



Proceedings of the Second Workshop on Cavitation and
Propeller Performance

The Fourth International Symposium on Marine Propulsors
smp'15

June 4 2015

Austin, Texas, USA

<http://www.marinepropulsors.com/index.php>

Edited by: S. Kinnas, M. Abdel-Maksoud,
U. Barkmann, L. Lübke, Y. Tian

Proceedings of



The Second Workshop on Cavitation and
Propeller Performance

The Fourth International Symposium on Marine Propulsors
smp'15

June 4 2015

Austin, Texas, USA

<http://www.marinepropulsors.com/>

Organized by:

Ocean Engineering Group, The University of Texas at Austin

SVA Potsdam GmbH

Sponsored by:

Marintek

www.marintek.com

Offshore Technology Research Center

<http://otrc.tamu.edu/>

Department of Department of Civil, Architectural and Environmental Engineering,
University of Texas at Austin

<http://www.caee.utexas.edu/>

©smp chair committee (Kourosch Koushan and Sverre Steen)

ISBN: 978-0-9964594-4-0

Layout: Kourosch Koushan and Sverre Steen

SMP'15 International Scientific Committee

Prof. Moustafa Abdel-Maksoud (Germany)

Prof. Jun Ando (Japan)

Prof. Mehmet Atlar (UK)

Prof. Rickard Bensow (Sweden)

Dr. Scott D. Black (USA)

Prof. Neil Bose (Australia)

Dr. Stefano Brizzolara (USA)

Prof. John Carlton (UK)

Prof. Pablo M. Carrica (USA)

Dr. Georges Chahine (USA)

Prof. Jose Falcao de Campos (Portugal)

Prof. Ching-Yeh Hsin (Taiwan)

Dr. Ki-Han Kim (USA)

Prof. Spyros A. Kinnas (USA)

Dr.-Ing. Kourosh Koushan (Norway)

Prof. Chang-Sup Lee (Korea)

Prof. Gerasimos Politis (Greece)

Prof. Shin Hyung Rhee (Korea)

Dr. Francesco Salvatore (Italy)

Dr. Antonio Sanchez Caja (Finland)

Prof. Sverre Steen (Norway)

Prof. Tom van Terwisga (The Netherlands)

Prof. Yin Lu Young (USA)

CHAIR COMMITTEE

Dr. –Ing. Kourosh Koushan (Norway)

Professor Sverre Steen (Norway)

LOCAL COMMITTEE

Prof. Spyros A. Kinnas, The University of Texas at Austin

Dr. Ye Tian, The University of Texas at Austin

Mr. Yiran Su, The University of Texas at Austin

Ms. Dori Eubank, The University of Texas at Austin

PREFACE

This draft contains the papers presented at the Second International Workshop on Cavitating Propeller Performance held at the Fourth International Symposium on Marine Propulsors – smp'15. The symposium was held at the University of Texas in Austin, from May 31 – June 3, 2015.

The first workshop on propeller performance was held in Hamburg, Germany 2011.

The editors would like to thank the authors and the presenters for their valuable contributions to the workshop. We would further like to thank the sponsors for their generosity.

The final workshop proceedings will be published shortly after the symposium.

Editors:

M. Abdel-Maksoud, U. Barkmann, S. Kinnas, L. Lübke, Y. Tian

Table of Contents

Table of Contents	i
1 Case 1	
Propeller Open Water Curves in Oblique Flow	1
1.1 Participants	2
1.2 Open water curves : ACCUSIM-CFX	3
1.3 Open water curves : ACCUSIM-OF	4
1.4 Open water curves : CNRS-ISIS	5
1.5 Open water curves : CRADLE-SCTetra steady	6
1.6 Open water curves : CRADLE-SCTetra unsteady	7
1.7 Open water curves : CSSRC-Fluent	8
1.8 Open water curves : MARIN-ReFresco	9
1.9 Open water curves : ROTAM-Fluent	10
1.10 Open water curves : TUHH-CFX	11
1.11 Open water curves : TUHH-OF	12
1.12 Open water curves : TUHH-panMARE	13
1.13 Open water curves : UDE-ISIS	14
1.14 Open water curves : UniGenoa-BEM	15
1.15 Open water curves : UniGenoa-StarCCM	16
1.16 Open water curves : UTAustin-PROPCAV	17
1.17 Open water curves : VTT-FinFlo	18
1.18 Comparison of open water characteristics, $J=0.6$	19
1.19 Comparison of open water characteristics, $J=0.8$	20
1.20 Comparison of open water characteristics, $J=1.0$	21
1.21 Comparison of open water characteristics, $J=1.2$	22
1.22 Comparison of open water characteristics, $J=1.4$	23
1.23 Absolute difference between measured and calculated values, $J=0.6$	24
1.24 Absolute difference between measured and calculated values, $J=0.8$	25
1.25 Absolute difference between measured and calculated values, $J=1.0$	26
1.26 Absolute difference between measured and calculated values, $J=1.2$	27
1.27 Absolute difference between measured and calculated values, $J=1.4$	28
1.28 Relative difference between measured and calculated values, $J=0.6$	29
1.29 Relative difference between measured and calculated values, $J=0.8$	30
1.30 Relative difference between measured and calculated values, $J=1.0$	31
1.31 Relative difference between measured and calculated values, $J=1.2$	32

1.32	Relative difference between measured and calculated values, $J=1.4$	33
2	Case 2	
	Cavitation Test in Oblique Flow	35
2.1	Participants	36
2.2	Case 2.1	37
	Case 2.1, ACCUSIM-CFX-FCM	37
	Case 2.1, ACCUSIM-CFX-Kunz	38
	Case 2.1, ACCUSIM-CFX-Zwart	39
	Case 2.1, CAT-OF	40
	Case 2.1, Chalmers-OF	41
	Case 2.1, CNRS-ISIS	42
	Case 2.1, CRADLE-SCTetra	43
	Case 2.1, CSSRC-Fluent	44
	Case 2.1, MARIN-ReFRESCO	45
	Case 2.1, ROTAM-Fluent	46
	Case 2.1, SSPA-Fluent-Sauer	47
	Case 2.1, SSPA-Fluent-Zwart1	48
	Case 2.1, SSPA-Fluent-Zwart2	49
	Case 2.1, TUHH-CFX	50
	Case 2.1, TUHH-panMARE	51
	Case 2.1, UniGenoa-BEM	52
	Case 2.1, UniGenoa-StarCCM+	53
	Case 2.1, UTAustin-PROPCAV	54
	Case 2.1, VTT-FinFlo	55
2.3	Case 2.2	56
	Case 2.2, ACCUSIM-CFX-FCM	56
	Case 2.2, ACCUSIM-CFX-Kunz	57
	Case 2.2, ACCUSIM-CFX-Zwart	58
	Case 2.2, CAT-OF	59
	Case 2.2, Chalmers-OF	60
	Case 2.2, CNRS-ISIS	61
	Case 2.2, CRADLE-SCTetra	62
	Case 2.2, CSSRC-Fluent	63
	Case 2.2, ROTAM-Fluent	64
	Case 2.2, SSPA-Fluent-Sauer	65
	Case 2.2, SSPA-Fluent-Zwart1	66
	Case 2.2, TUHH-CFX	67
	Case 2.2, TUHH-panMARE	68
	Case 2.2, UniGenoa-BEM	69
	Case 2.2, UniGenoa-StarCCM+	70
	Case 2.2, UTAustin-PROPCAV	71
	Case 2.2, VTT-FinFlo	72
2.4	Case 2.3	73
	Case 2.3, ACCUSIM-CFX-FCM	73
	Case 2.3, ACCUSIM-CFX-Kunz	74

Case 2.3, ACCUSIM-CFX-Zwart	75
Case 2.3, CAT-OF	76
Case 2.3, Chalmers-OF	77
Case 2.3, CNRS-ISIS	78
Case 2.3, CRADLE-SCTetra	79
Case 2.3, CSSRC-Fluent	80
Case 2.3, ROTAM-Fluent	81
Case 2.3, SSPA-Fluent-Sauer	82
Case 2.3, SSPA-Fluent-Zwart1	83
Case 2.3, TUHH-CFX	84
Case 2.3, TUHH-panMARE	85
Case 2.3, UniGenoa-BEM	86
Case 2.3, UniGenoa-StarCCM+	87
Case 2.3, VTT-FinFlo	88
2.5 Comparison	89
Thrust coefficient, non-cavitating	89
Difference in thrust coefficient, non cavitating	90
Thrust coefficient, cavitating	91
Difference in thrust coefficient, cavitating	92
Thrust breakdown, absolute difference	93
3 Case 3	
Propeller Pressure Pulses in Oblique Flow	95
3.1 Participants	96
3.2 Case 3.1: $J=1.019, \sigma_n=2.024$	98
Cradle-SCTetra, without Cavitation	98
Cradle-SCTetra, with Cavitation	99
MARIN-ReFresco, without Cavitation	100
MARIN-ReFresco, with Cavitation	101
ROTAM-ANSYS, without Cavitation	102
SSPA-FLUENT, without Cavitation	103
SSPA-FLUENT, with Cavitation	104
SSPA-FLUENT, with Cavitation, Sauer	105
TUHH-CFX, without Cavitation	106
TUHH-CFX, with Cavitation	107
TUHH-OpenFOAM, without Cavitation	108
TUHH-panMARE, without Cavitation	109
TUHH-panMARE, with Cavitation	110
UTAustin-PROPCAV, with Cavitation	111
UTAustin-PROPCAV, without Cavitation	112
VTT-FINFLO, without Cavitation	113
3.3 Case 3.2: $J=1.269, \sigma_n=1.424$	114
Cradle-SCTetra, without Cavitation	114
Cradle-SCTetra, with Cavitation	115
SSPA-FLUENT, without Cavitation	116
SSPA-FLUENT, with Cavitation	117

	SSPA-FLUENT, with Cavitation, Sauer	118
	TUHH-CFX, without Cavitation	119
	TUHH-CFX, with Cavitation	120
	TUHH-OpenFOAM, without Cavitation	121
	TUHH-panMARE, without Cavitation	122
	TUHH-panMARE, with Cavitation	123
	UTAustin-PROPCAV, without Cavitation	124
3.4	Case 3.3: $J=1.408$, $\sigma_n=2.000$	125
	Cradle-SCTetra, without Cavitation	125
	Cradle-SCTetra, with Cavitation	126
	SSPA-FLUENT, without Cavitation	127
	SSPA-FLUENT, with Cavitation	128
	SSPA-FLUENT, with Cavitation, Sauer	129
	TUHH-CFX, without Cavitation	130
	TUHH-CFX, with Cavitation	131
	TUHH-OpenFOAM, without Cavitation	132
	TUHH-panMARE, without Cavitation	133
	TUHH-panMARE, with Cavitation	134
	UTAustin-PROPCAV, without Cavitation	135
4	Papers by Participants	137
4.1	Numerical predictions of the PPTC model propeller in oblique flow (<i>Mitja Morgut, Enrico Nobile, Dragica Jošt, Aljaž Škerlavaj</i>)	138
4.2	Cavitation observation on the PPTC propeller in oblique flow (<i>Tobias Huuva, Simon Törnros</i>)	143
4.3	Computational Analysis of Cavitating Marine Propeller Performance using Open- FOAM (<i>Abolfazl Asnaghi, Andreas Feymark, Rickard E. Bensow</i>)	148
4.4	Numerical Simulations of the Cavitating and Non-Cavitating Flow around the Post- dam Propeller Test Case (<i>E. Guilmineau, G.B. Deng, A. Leroyer, P. Queutey, M. Visonneau, J. Wackers</i>)	156
4.5	Numerical Simulations of SMP'15 Marine Propeller with and without Cavitation (<i>Satoshi Nohara, Keita Fujiyama</i>)	166
4.6	The Numerical Predicted of VP1304 Propeller Cavitation Performance in Oblique Flow (<i>Dengcheng Liu, Min Gu</i>)	172
4.7	The Numerical Predicted of VP1304 Propeller Performance in Oblique Flow (<i>Dengcheng Liu</i>)	179
4.8	The Potsdam Propeller Test Case in oblique flow: prediction of propeller perfor- mance, cavitation patterns and pressure pulses (<i>Thomas Lloyd, Guilherme Vaz, Douwe Rijpkema, Bart Schuiling</i>)	182
4.9	Prediction of Performance of Test-Case Inclined Propeller SMP15 in Cavitating and Non Cavitating Conditions (<i>Emre Gungor</i>)	189

4.10 Prediction of pressure pulses and cavitation behavior of PPTC propeller in oblique flow with a 12 shaft inclination (<i>Da-Qing Li</i>)	198
4.11 A Comparative Study on Computational Methods with regard to Propeller Simulation in Oblique Inflow (<i>Martin Scharf, Keqi Wang, Sattar Al Jabair, Moustafa Abdel-Maksoud</i>)	205
4.12 Numerical Prediction of PPTC'2015 Propeller Performance in Oblique Flow (<i>Matthias Tenzer</i>)	212
4.13 PPTC 2015 Test Case: simulating non-cavitating and cavitating propeller performances in oblique flow (<i>Stefano Gaggero, Diego Villa and Michele Viviani</i>)	216
4.14 FINFLO two-phase URANS predictions of propeller performance in oblique flow (<i>V. Viitanen, J. Martio and T. Sipilä</i>)	225
4.15 Prediction of Performance of Cavitating Propeller in Oblique Inflow (<i>Ye Tian and Spyros Kinnas</i>)	232

Chapter 1

Case 1

Propeller Open Water Curves in Oblique Flow

1 Participants

The following institutes have participated:

Group	Solver	Acronym
ACCUSIM	ANSYS-CFX	ACCUSIM-CFX
	OpenFOAM	ACCUSIM-OF
CNRS-ECN	ISIS	CNRS-ISIS
CRADLE	SCTetra steady	CRADLE-SCTetra-st.
	SCTetra unsteady	CRADLE-SCTetra-unst.
CSSRC	ANSYS-Fluent	CSSRC-Fluent
ROTAM	ANSYS-Fluent	ROTAM-Fluent
MARIN	ReFresco	MARIN-ReFresco
TUHH	ANSYS-CFX	TUHH-CFX
	OpenFOAM	TUHH-OF
	panMARE	TUHH-panMARE
	ISIS	UDE-ISIS
UDE	ISIS	UDE-ISIS
University of Genoa	BEM	UniGenoa-BEM
	StarCCM+	UniGenoa-StarCCM
	PROPCAV	UTAustin-PROPCAV
UT Austin	PROPCAV	UTAustin-PROPCAV
VTT	FinFlo	VTT-FinFlo

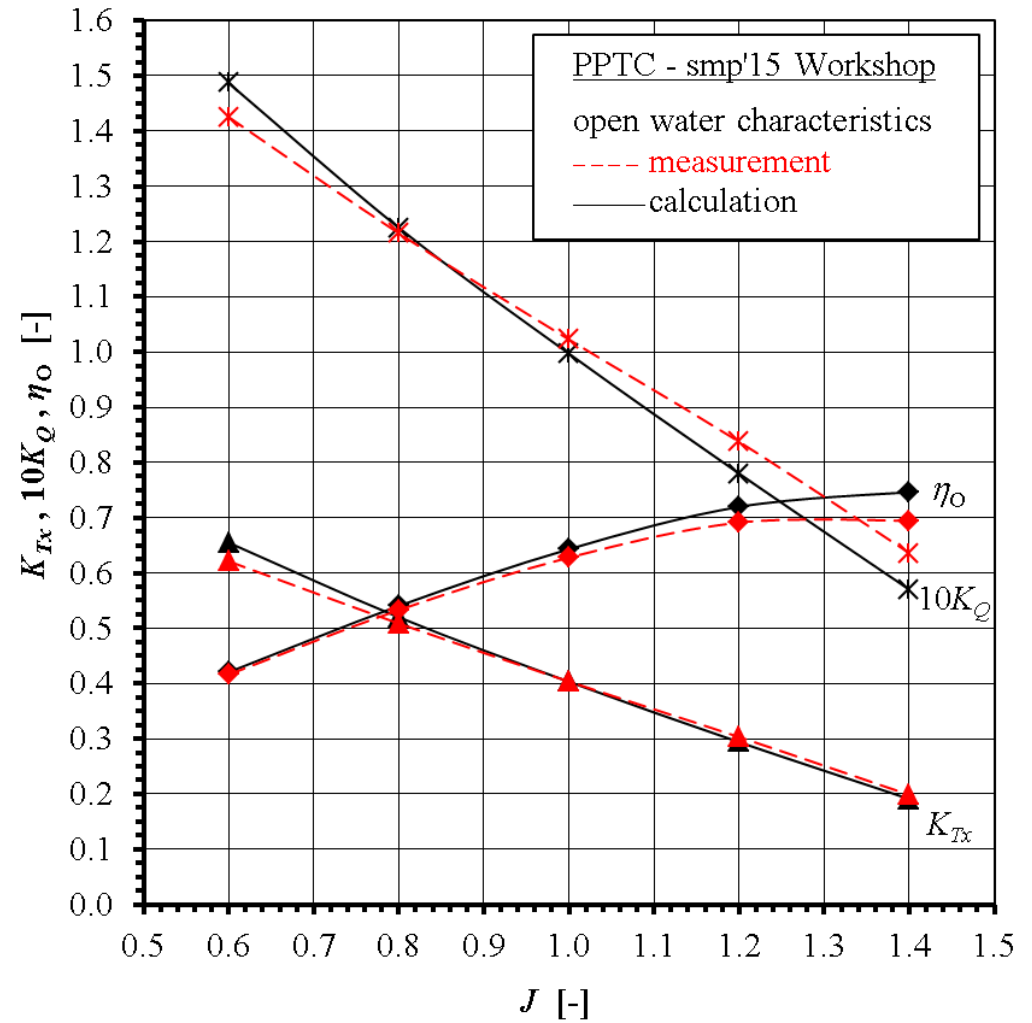
In the following the data is evaluated with respect to the thrust coefficient K_{Tx} (along the rotation axis, PCS coordinate system), the torque coefficient $10K_Q$ and the open water efficiency η_O (on basis of K_{Tx}), for an inclination angle between shaft and inflow direction of $\psi^{bP} = 12^\circ$. For each value an absolute (e.g. ΔK_{Tx}) and a relative comparison (e.g. ΔK_{Tx} [%]) to the measured value is made. The absolute difference is defined as the difference between the calculated to the measured value, while the relative difference is the same value expressed as percentage with respect to the measured value.

1.1 Open water curves for $\psi^{bP} = 12^\circ$: ACCUSIM-CFX

J	K_{Tx} EFD	K_{Tx} CFD	ΔK_{Tx}	ΔK_{Tx} [%]
0.60	0.621	0.655	0.034	5.4
0.80	0.509	0.520	0.011	2.2
1.00	0.404	0.403	-0.001	-0.1
1.20	0.303	0.294	-0.009	-3.0
1.40	0.198	0.191	-0.007	-3.7

J	$10K_Q$ EFD	$10K_Q$ CFD	$\Delta 10K_Q$	$\Delta 10K_Q$ [%]
0.60	1.425	1.487	0.062	4.3
0.80	1.215	1.225	0.010	0.8
1.00	1.023	0.997	-0.026	-2.5
1.20	0.838	0.780	-0.058	-6.9
1.40	0.636	0.570	-0.066	-10.4

J	η_o EFD	η_o CFD	$\Delta \eta_o$	$\Delta \eta_o$ [%]
0.60	0.416	0.421	0.004	1.0
0.80	0.533	0.540	0.007	1.4
1.00	0.628	0.643	0.015	2.4
1.20	0.691	0.720	0.029	4.1
1.40	0.695	0.747	0.052	7.5

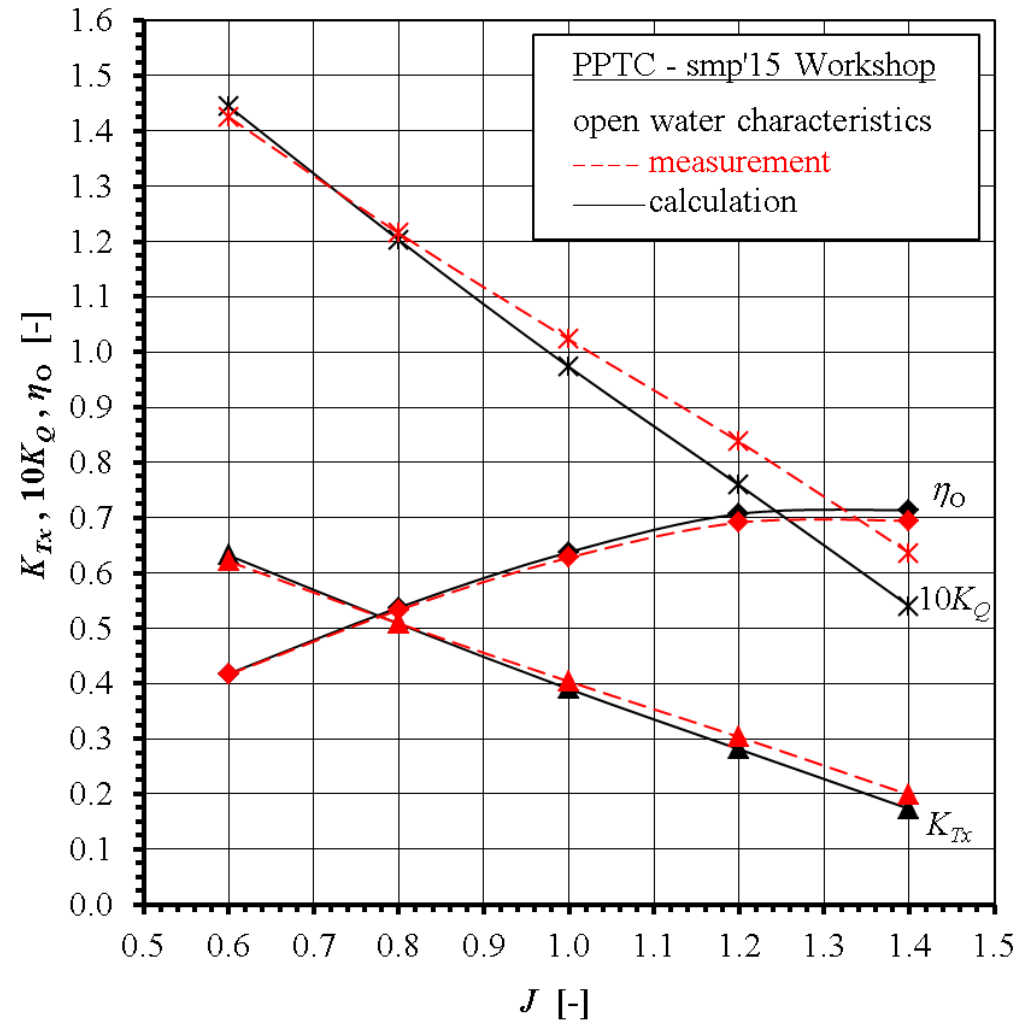


1.2 Open water curves for $\psi^{bP} = 12^\circ$: ACCUSIM-OF

J	K_{Tx} EFD	K_{Tx} CFD	ΔK_{Tx}	ΔK_{Tx} [%]
0.60	0.621	0.632	0.011	1.7
0.80	0.509	0.508	-0.001	-0.1
1.00	0.404	0.390	-0.014	-3.4
1.20	0.303	0.281	-0.022	-7.3
1.40	0.198	0.173	-0.025	-12.8

J	$10K_Q$ EFD	$10K_Q$ CFD	$\Delta 10K_Q$	$\Delta 10K_Q$ [%]
0.60	1.425	1.445	0.020	1.4
0.80	1.215	1.203	-0.012	-1.0
1.00	1.023	0.973	-0.050	-4.9
1.20	0.838	0.759	-0.079	-9.4
1.40	0.636	0.540	-0.096	-15.1

J	η_o EFD	η_o CFD	$\Delta \eta_o$	$\Delta \eta_o$ [%]
0.60	0.416	0.418	0.001	0.3
0.80	0.533	0.538	0.004	0.8
1.00	0.628	0.638	0.010	1.6
1.20	0.691	0.707	0.016	2.3
1.40	0.695	0.714	0.019	2.7

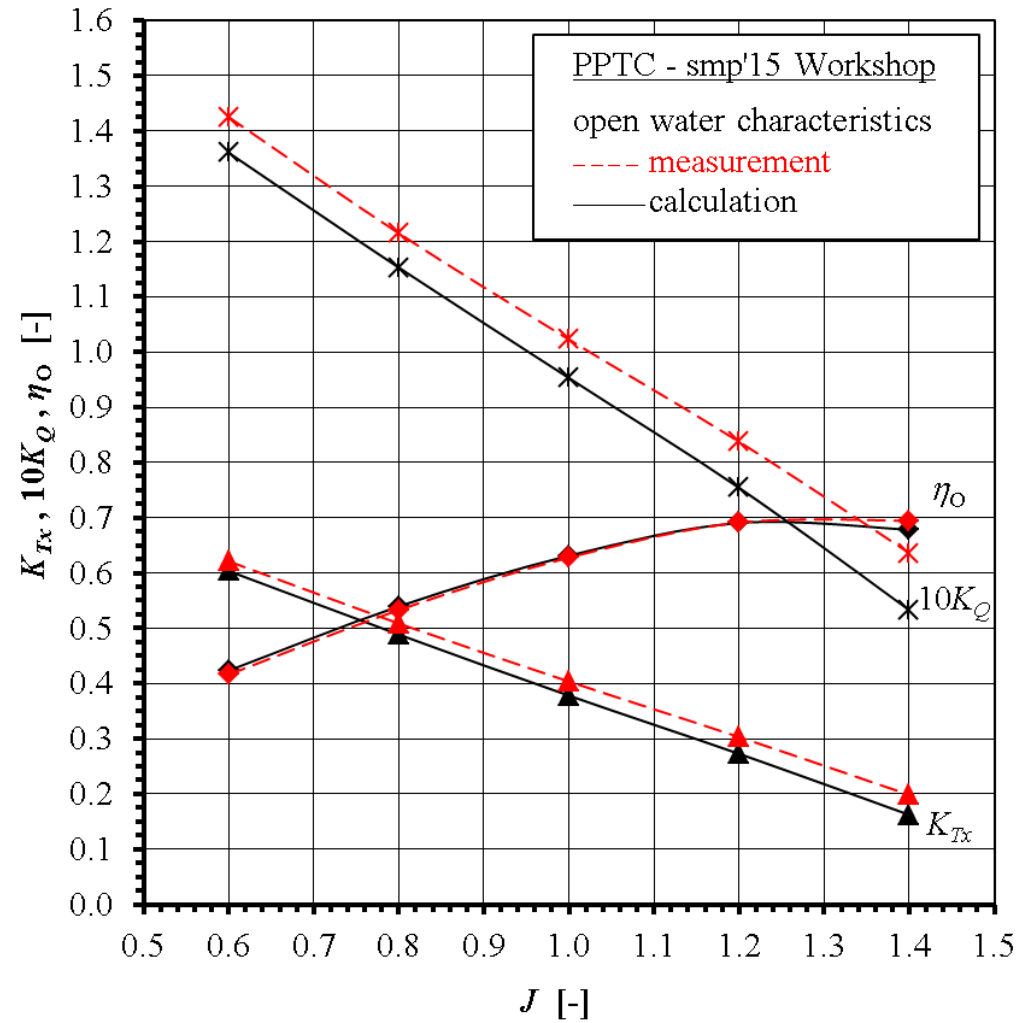


1.3 Open water curves for $\psi^{bP} = 12^\circ$: CNRS-ISIS

J	K_{Tx} EFD	K_{Tx} CFD	ΔK_{Tx}	ΔK_{Tx} [%]
0.60	0.621	0.604	-0.018	-2.9
0.80	0.509	0.489	-0.020	-3.9
1.00	0.404	0.378	-0.025	-6.3
1.20	0.303	0.273	-0.030	-10.0
1.40	0.198	0.162	-0.036	-18.2

J	$10K_Q$ EFD	$10K_Q$ CFD	$\Delta 10K_Q$	$\Delta 10K_Q$ [%]
0.60	1.425	1.361	-0.065	-4.5
0.80	1.215	1.153	-0.062	-5.1
1.00	1.023	0.953	-0.070	-6.8
1.20	0.838	0.754	-0.083	-10.0
1.40	0.636	0.533	-0.103	-16.2

J	η_o EFD	η_o CFD	$\Delta \eta_o$	$\Delta \eta_o$ [%]
0.60	0.416	0.424	0.007	1.7
0.80	0.533	0.540	0.007	1.2
1.00	0.628	0.632	0.003	0.5
1.20	0.691	0.691	-0.001	-0.1
1.40	0.695	0.679	-0.016	-2.3

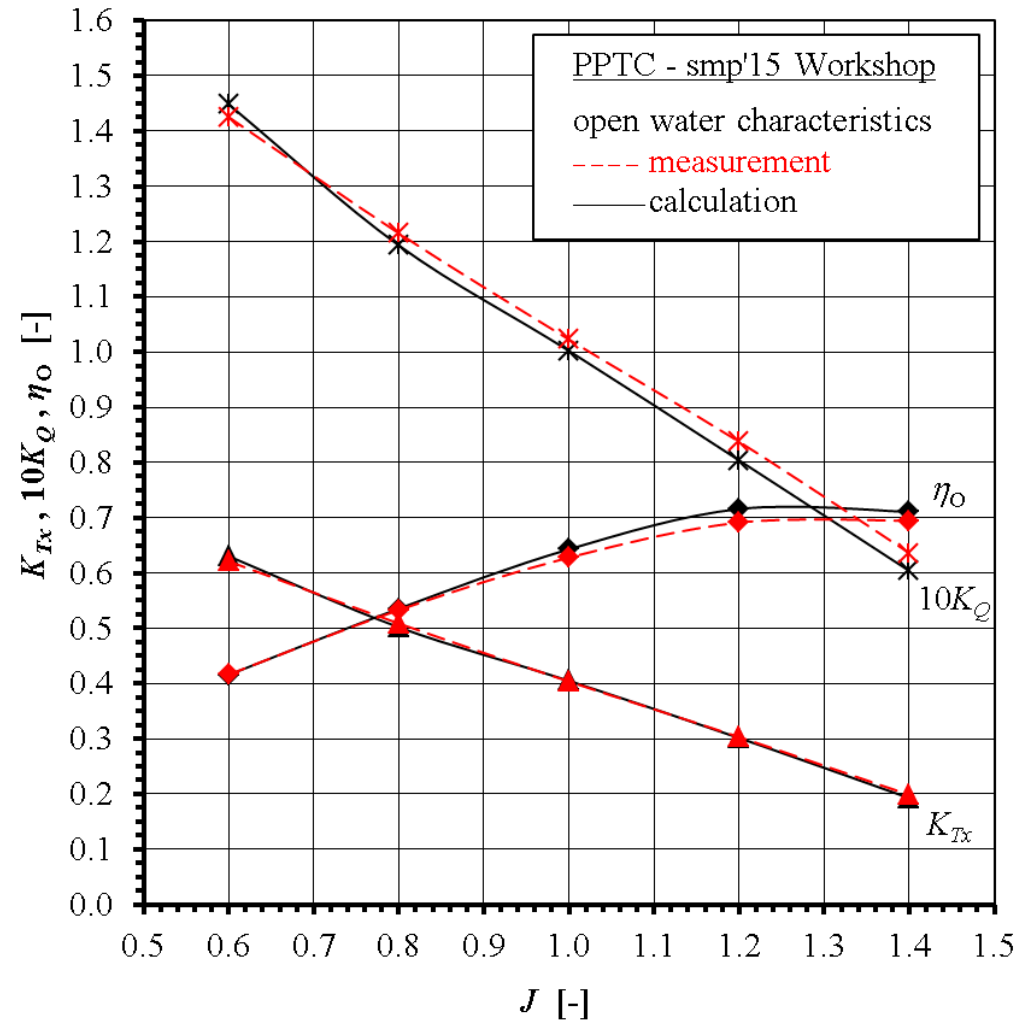


1.4 Open water curves for $\psi^{bP} = 12^\circ$: CRADLE-SCTetra steady

J	K_{Tx} EFD	K_{Tx} CFD	ΔK_{Tx}	ΔK_{Tx} [%]
0.60	0.621	0.631	0.009	1.5
0.80	0.509	0.502	-0.007	-1.3
1.00	0.404	0.405	0.001	0.4
1.20	0.303	0.301	-0.002	-0.6
1.40	0.198	0.193	-0.006	-2.9

J	$10K_Q$ EFD	$10K_Q$ CFD	$\Delta 10K_Q$	$\Delta 10K_Q$ [%]
0.60	1.425	1.449	0.023	1.6
0.80	1.215	1.193	-0.022	-1.8
1.00	1.023	1.002	-0.020	-2.0
1.20	0.838	0.804	-0.034	-4.0
1.40	0.636	0.604	-0.032	-5.1

J	η_o EFD	η_o CFD	$\Delta \eta_o$	$\Delta \eta_o$ [%]
0.60	0.416	0.416	-0.001	-0.1
0.80	0.533	0.536	0.003	0.5
1.00	0.628	0.643	0.015	2.4
1.20	0.691	0.716	0.025	3.6
1.40	0.695	0.711	0.016	2.3

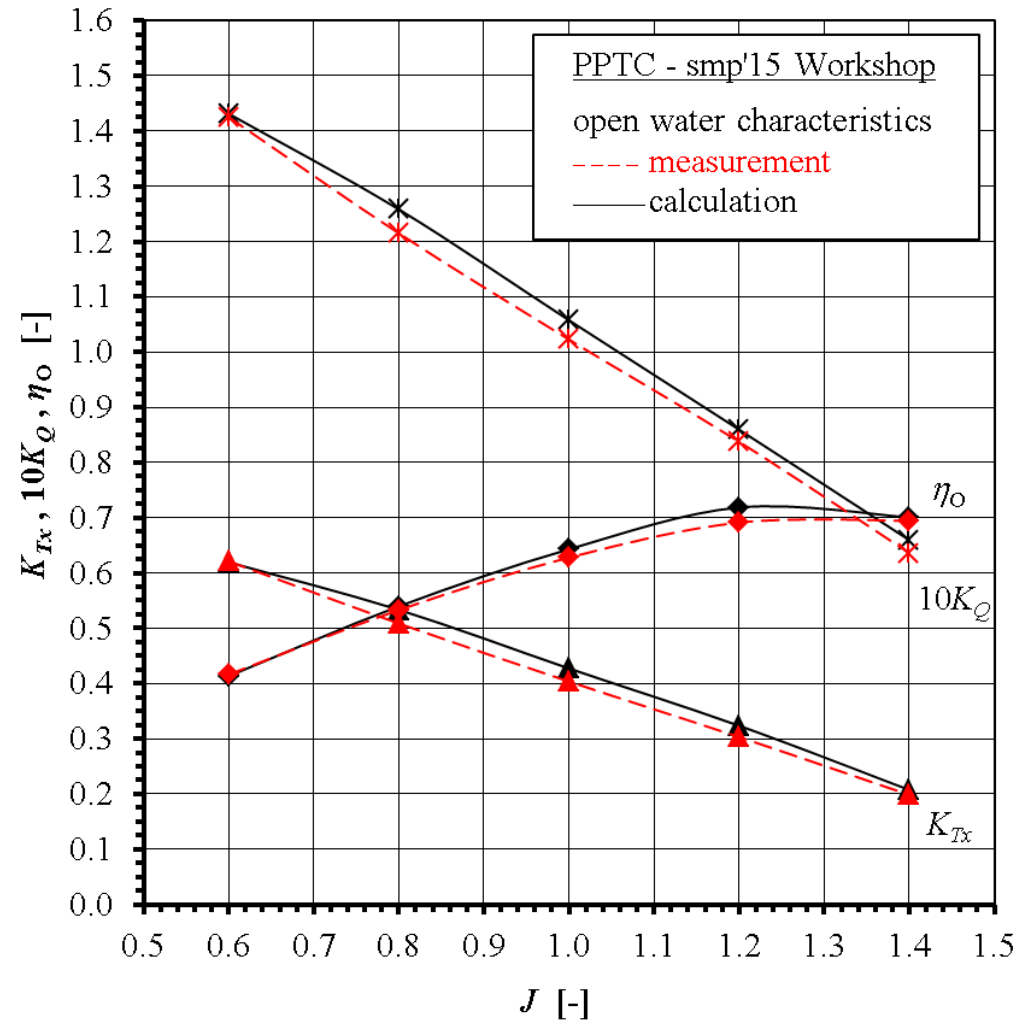


1.5 Open water curves for $\psi^{bP} = 12^\circ$: CRADLE-SCTetra unsteady

J	K_{Tx} EFD	K_{Tx} CFD	ΔK_{Tx}	ΔK_{Tx} [%]
0.60	0.621	0.620	-0.002	-0.3
0.80	0.509	0.533	0.025	4.9
1.00	0.404	0.427	0.024	5.9
1.20	0.303	0.324	0.020	6.7
1.40	0.198	0.207	0.009	4.6

J	$10K_Q$ EFD	$10K_Q$ CFD	$\Delta 10K_Q$	$\Delta 10K_Q$ [%]
0.60	1.425	1.431	0.006	0.4
0.80	1.215	1.258	0.043	3.6
1.00	1.023	1.058	0.035	3.4
1.20	0.838	0.860	0.022	2.6
1.40	0.636	0.660	0.023	3.7

J	η_o EFD	η_o CFD	$\Delta \eta_o$	$\Delta \eta_o$ [%]
0.60	0.416	0.413	-0.003	-0.7
0.80	0.533	0.540	0.007	1.2
1.00	0.628	0.643	0.015	2.4
1.20	0.691	0.719	0.027	4.0
1.40	0.695	0.701	0.006	0.9

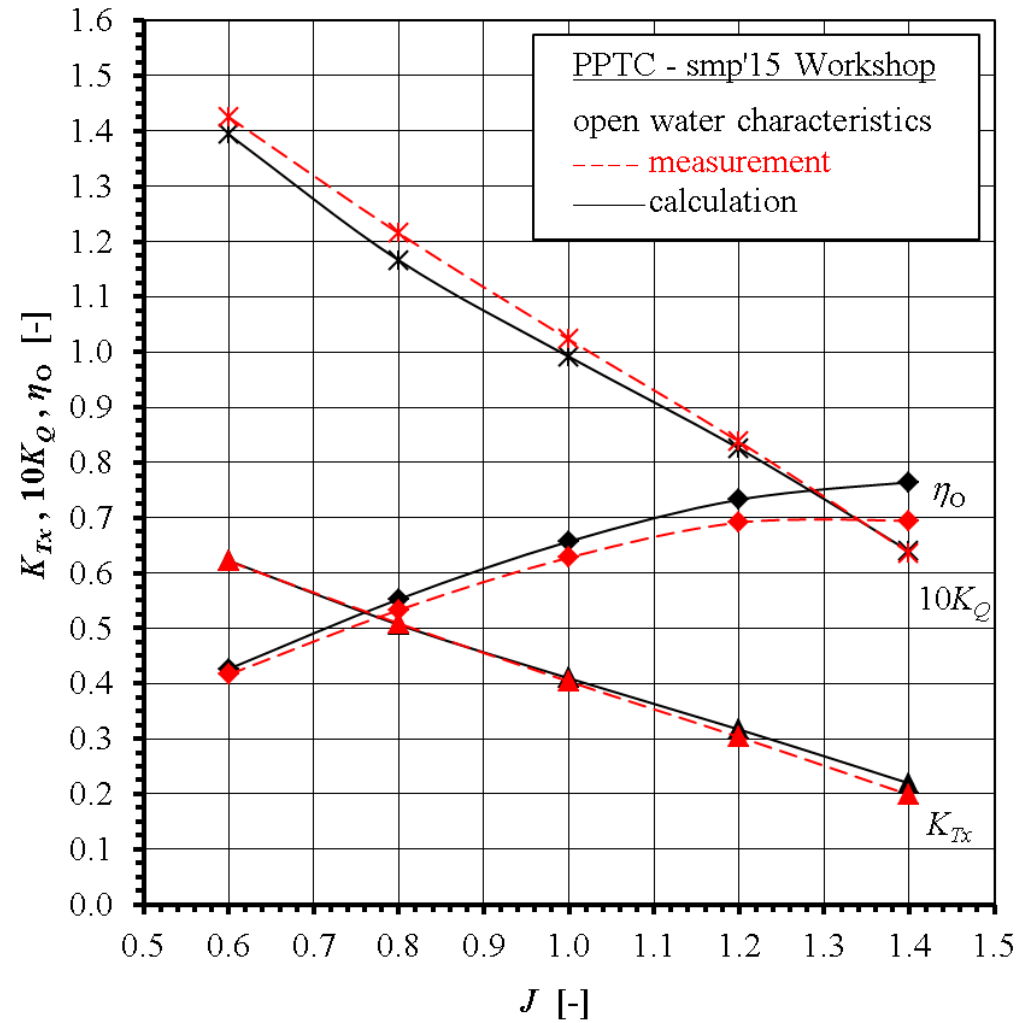


1.6 Open water curves for $\psi^{bP} = 12^\circ$: CSSRC-Fluent

J	K_{Tx} EFD	K_{Tx} CFD	ΔK_{Tx}	ΔK_{Tx} [%]
0.60	0.621	0.623	0.001	0.2
0.80	0.509	0.506	-0.003	-0.5
1.00	0.404	0.409	0.006	1.4
1.20	0.303	0.317	0.014	4.5
1.40	0.198	0.219	0.021	10.6

J	$10K_Q$ EFD	$10K_Q$ CFD	$\Delta 10K_Q$	$\Delta 10K_Q$ [%]
0.60	1.425	1.394	-0.031	-2.2
0.80	1.215	1.166	-0.049	-4.0
1.00	1.023	0.992	-0.031	-3.0
1.20	0.838	0.825	-0.012	-1.4
1.40	0.636	0.639	0.003	0.5

J	η_o EFD	η_o CFD	$\Delta \eta_o$	$\Delta \eta_o$ [%]
0.60	0.416	0.426	0.010	2.4
0.80	0.533	0.553	0.020	3.7
1.00	0.628	0.657	0.029	4.6
1.20	0.691	0.733	0.041	6.0
1.40	0.695	0.764	0.070	10.0

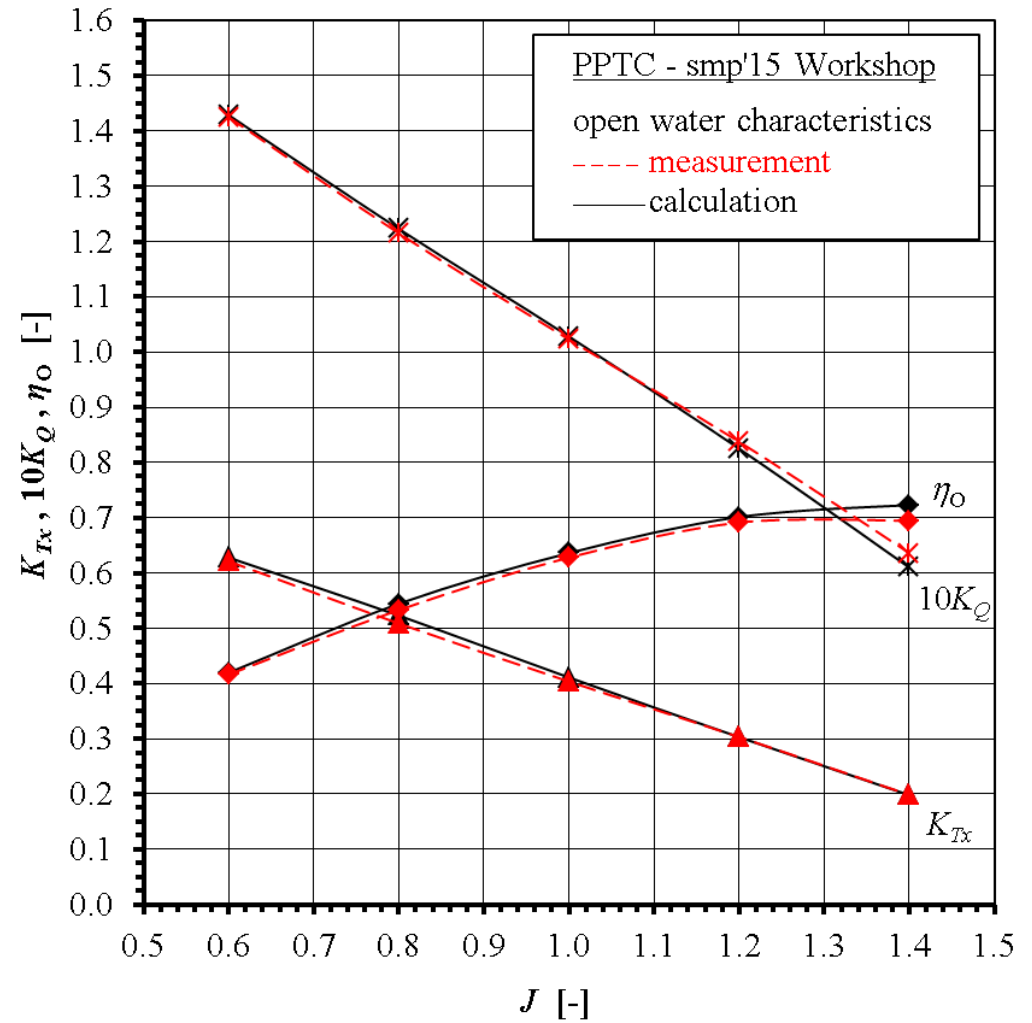


1.7 Open water curves for $\psi^{bP} = 12^\circ$: MARIN-ReFresco

J	K_{Tx} EFD	K_{Tx} CFD	ΔK_{Tx}	ΔK_{Tx} [%]
0.60	0.621	0.628	0.007	1.1
0.80	0.509	0.523	0.014	2.8
1.00	0.404	0.411	0.007	1.8
1.20	0.303	0.303	0.000	-0.1
1.40	0.198	0.198	0.000	-0.2

J	$10K_Q$ EFD	$10K_Q$ CFD	$\Delta 10K_Q$	$\Delta 10K_Q$ [%]
0.60	1.425	1.429	0.004	0.3
0.80	1.215	1.223	0.008	0.7
1.00	1.023	1.028	0.005	0.5
1.20	0.838	0.825	-0.013	-1.5
1.40	0.636	0.610	-0.026	-4.1

J	η_o EFD	η_o CFD	$\Delta \eta_o$	$\Delta \eta_o$ [%]
0.60	0.416	0.420	0.003	0.8
0.80	0.533	0.544	0.011	2.1
1.00	0.628	0.636	0.008	1.3
1.20	0.691	0.701	0.010	1.5
1.40	0.695	0.723	0.028	4.1

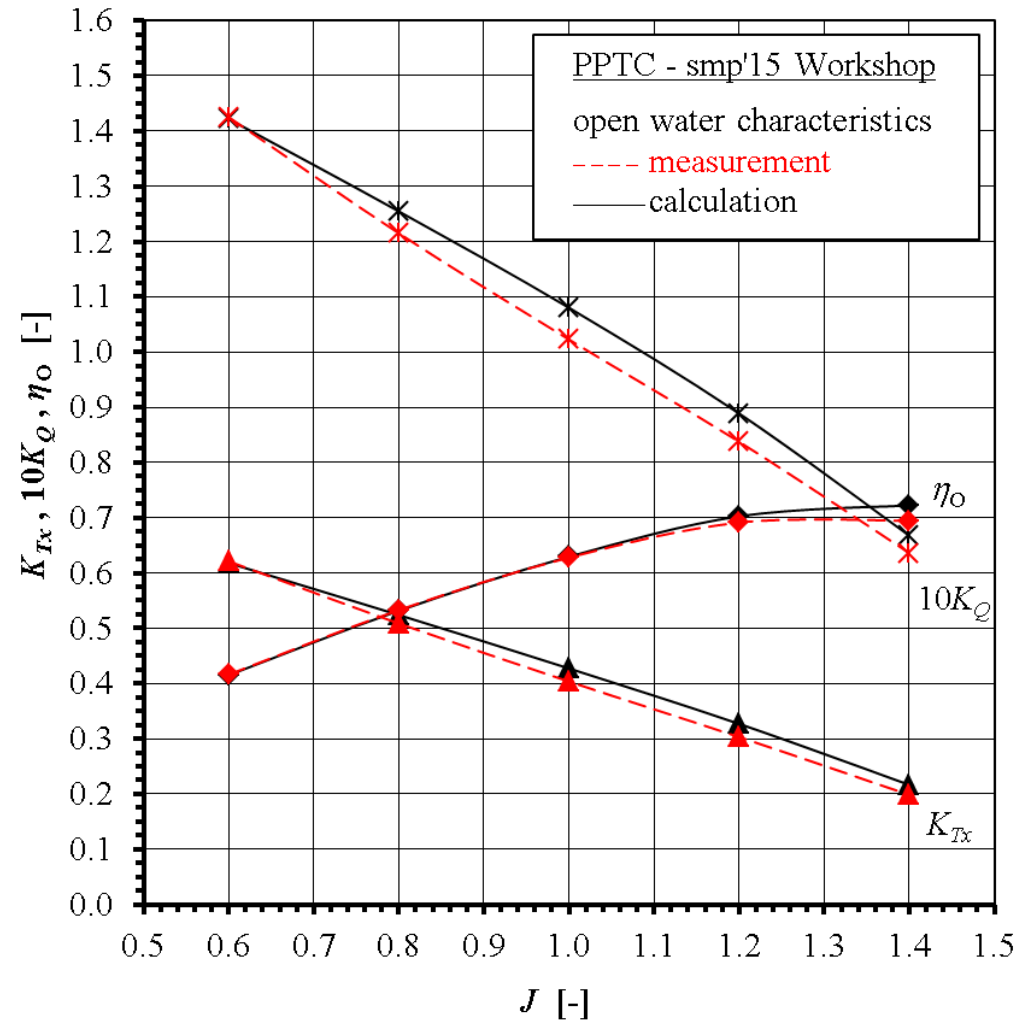


1.8 Open water curves for $\psi^{bP} = 12^\circ$: ROTAM-Fluent

J	K_{Tx} EFD	K_{Tx} CFD	ΔK_{Tx}	ΔK_{Tx} [%]
0.60	0.621	0.618	-0.003	-0.5
0.80	0.509	0.524	0.015	3.0
1.00	0.404	0.427	0.024	5.9
1.20	0.303	0.327	0.024	7.9
1.40	0.198	0.217	0.018	9.2

J	$10K_Q$ EFD	$10K_Q$ CFD	$\Delta 10K_Q$	$\Delta 10K_Q$ [%]
0.60	1.425	1.422	-0.003	-0.2
0.80	1.215	1.255	0.040	3.3
1.00	1.023	1.080	0.057	5.6
1.20	0.838	0.889	0.051	6.1
1.40	0.636	0.668	0.032	5.0

J	η_o EFD	η_o CFD	$\Delta \eta_o$	$\Delta \eta_o$ [%]
0.60	0.416	0.415	-0.001	-0.3
0.80	0.533	0.532	-0.001	-0.2
1.00	0.628	0.630	0.002	0.2
1.20	0.691	0.703	0.011	1.6
1.40	0.695	0.722	0.028	4.0

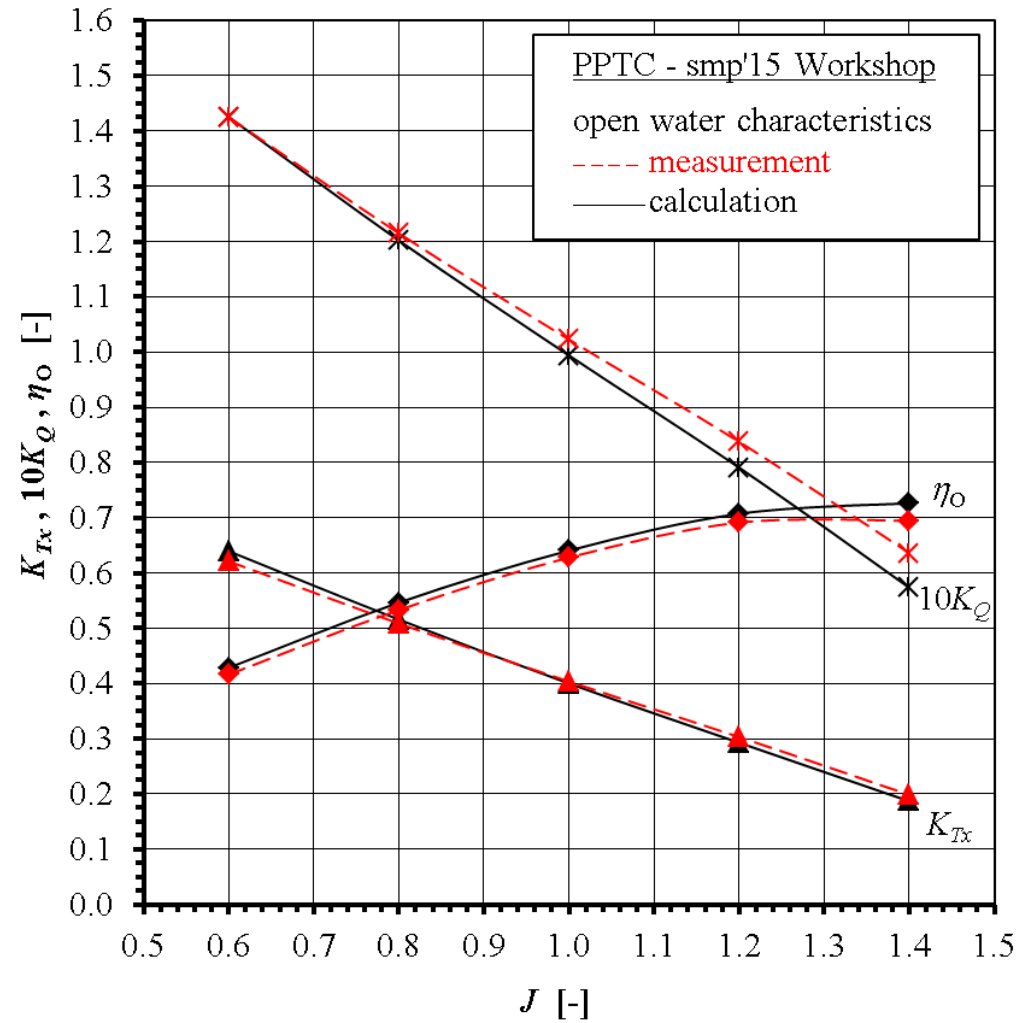


1.9 Open water curves for $\psi^{bP} = 12^\circ$: TUHH-CFX

J	K_{Tx} EFD	K_{Tx} CFD	ΔK_{Tx}	ΔK_{Tx} [%]
0.60	0.621	0.640	0.018	2.9
0.80	0.509	0.516	0.007	1.4
1.00	0.404	0.400	-0.003	-0.9
1.20	0.303	0.293	-0.010	-3.4
1.40	0.198	0.187	-0.011	-5.8

J	$10K_Q$ EFD	$10K_Q$ CFD	$\Delta 10K_Q$	$\Delta 10K_Q$ [%]
0.60	1.425	1.426	0.000	0.0
0.80	1.215	1.202	-0.013	-1.1
1.00	1.023	0.994	-0.029	-2.8
1.20	0.838	0.791	-0.047	-5.6
1.40	0.636	0.573	-0.063	-9.9

J	η_o EFD	η_o CFD	$\Delta \eta_o$	$\Delta \eta_o$ [%]
0.60	0.416	0.428	0.012	2.9
0.80	0.533	0.546	0.013	2.5
1.00	0.628	0.641	0.013	2.0
1.20	0.691	0.707	0.016	2.3
1.40	0.695	0.726	0.032	4.5

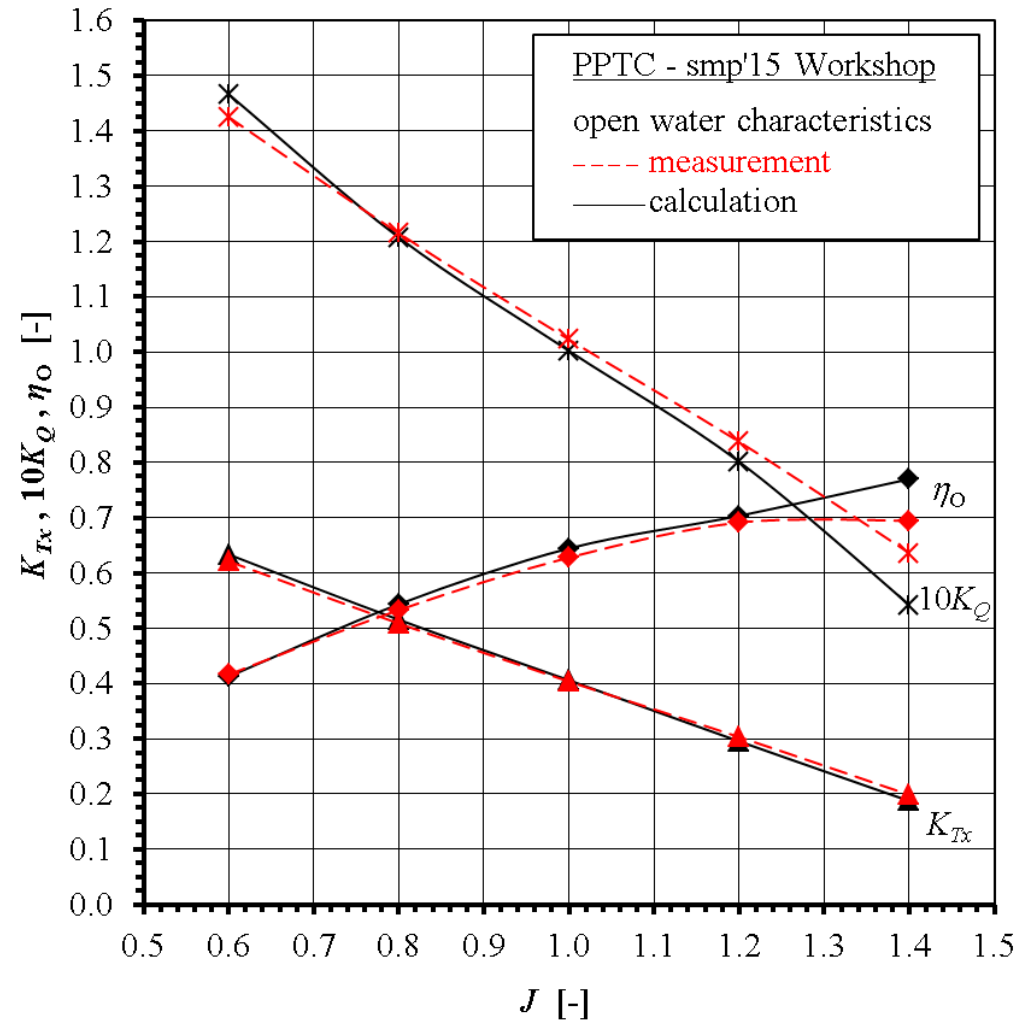


1.10 Open water curves for $\psi^{bP} = 12^\circ$: TUHH-OF

J	K_{Tx} EFD	K_{Tx} CFD	ΔK_{Tx}	ΔK_{Tx} [%]
0.60	0.621	0.634	0.012	2.0
0.80	0.509	0.516	0.007	1.3
1.00	0.404	0.406	0.002	0.6
1.20	0.303	0.295	-0.008	-2.6
1.40	0.198	0.187	-0.011	-5.5

J	$10K_Q$ EFD	$10K_Q$ CFD	$\Delta 10K_Q$	$\Delta 10K_Q$ [%]
0.60	1.425	1.467	0.041	2.9
0.80	1.215	1.207	-0.008	-0.6
1.00	1.023	1.002	-0.020	-2.0
1.20	0.838	0.801	-0.036	-4.3
1.40	0.636	0.542	-0.094	-14.8

J	η_o EFD	η_o CFD	$\Delta \eta_o$	$\Delta \eta_o$ [%]
0.60	0.416	0.413	-0.004	-0.9
0.80	0.533	0.544	0.010	2.0
1.00	0.628	0.645	0.017	2.6
1.20	0.691	0.704	0.012	1.8
1.40	0.695	0.770	0.075	10.8

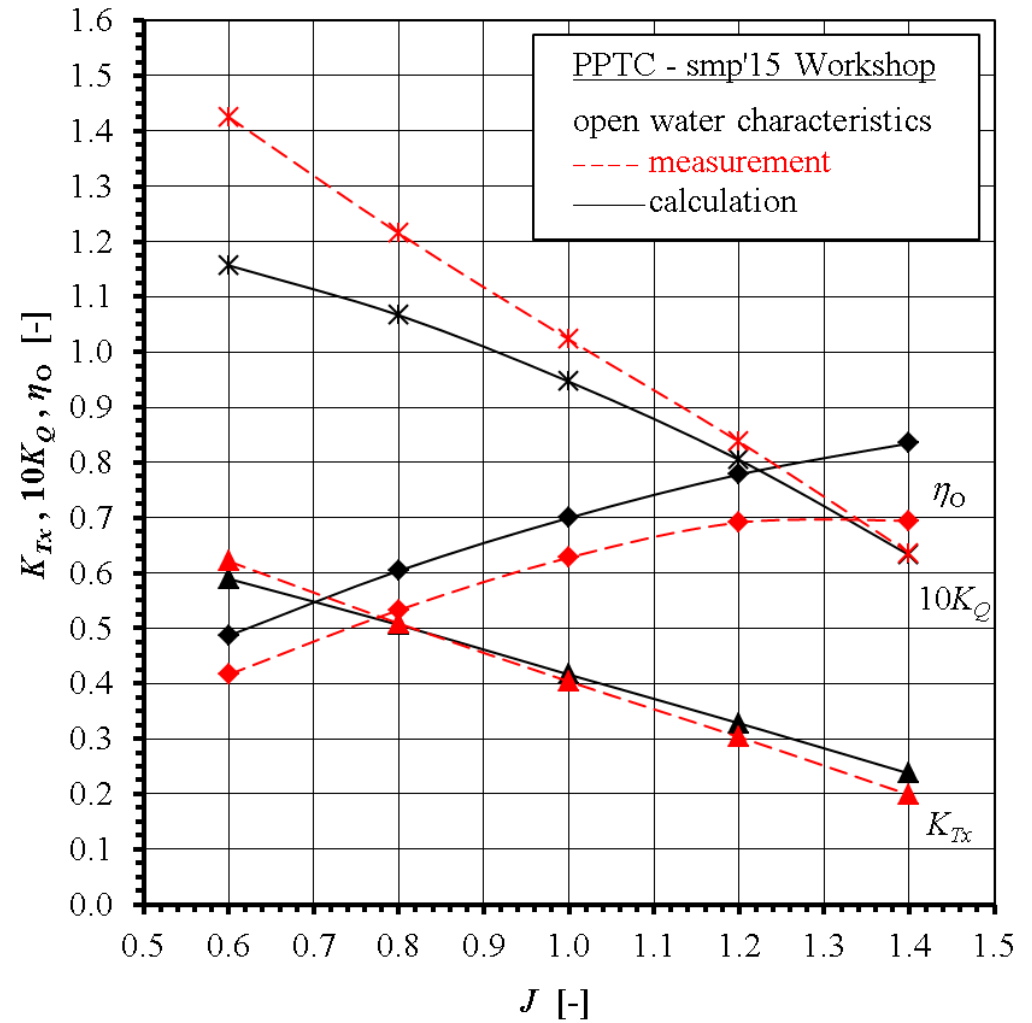


1.11 Open water curves for $\psi^{bP} = 12^\circ$: TUHH-panMARE

J	K_{Tx} EFD	K_{Tx} CFD	ΔK_{Tx}	ΔK_{Tx} [%]
0.60	0.621	0.590	-0.032	-5.1
0.80	0.509	0.506	-0.003	-0.5
1.00	0.404	0.416	0.013	3.1
1.20	0.303	0.328	0.025	8.2
1.40	0.198	0.237	0.039	19.5

J	$10K_Q$ EFD	$10K_Q$ CFD	$\Delta 10K_Q$	$\Delta 10K_Q$ [%]
0.60	1.425	1.157	-0.268	-18.8
0.80	1.215	1.067	-0.148	-12.2
1.00	1.023	0.946	-0.076	-7.5
1.20	0.838	0.805	-0.033	-3.9
1.40	0.636	0.633	-0.004	-0.6

J	η_o EFD	η_o CFD	$\Delta \eta_o$	$\Delta \eta_o$ [%]
0.60	0.416	0.487	0.070	16.9
0.80	0.533	0.604	0.071	13.3
1.00	0.628	0.700	0.072	11.4
1.20	0.691	0.778	0.087	12.6
1.40	0.695	0.835	0.140	20.2

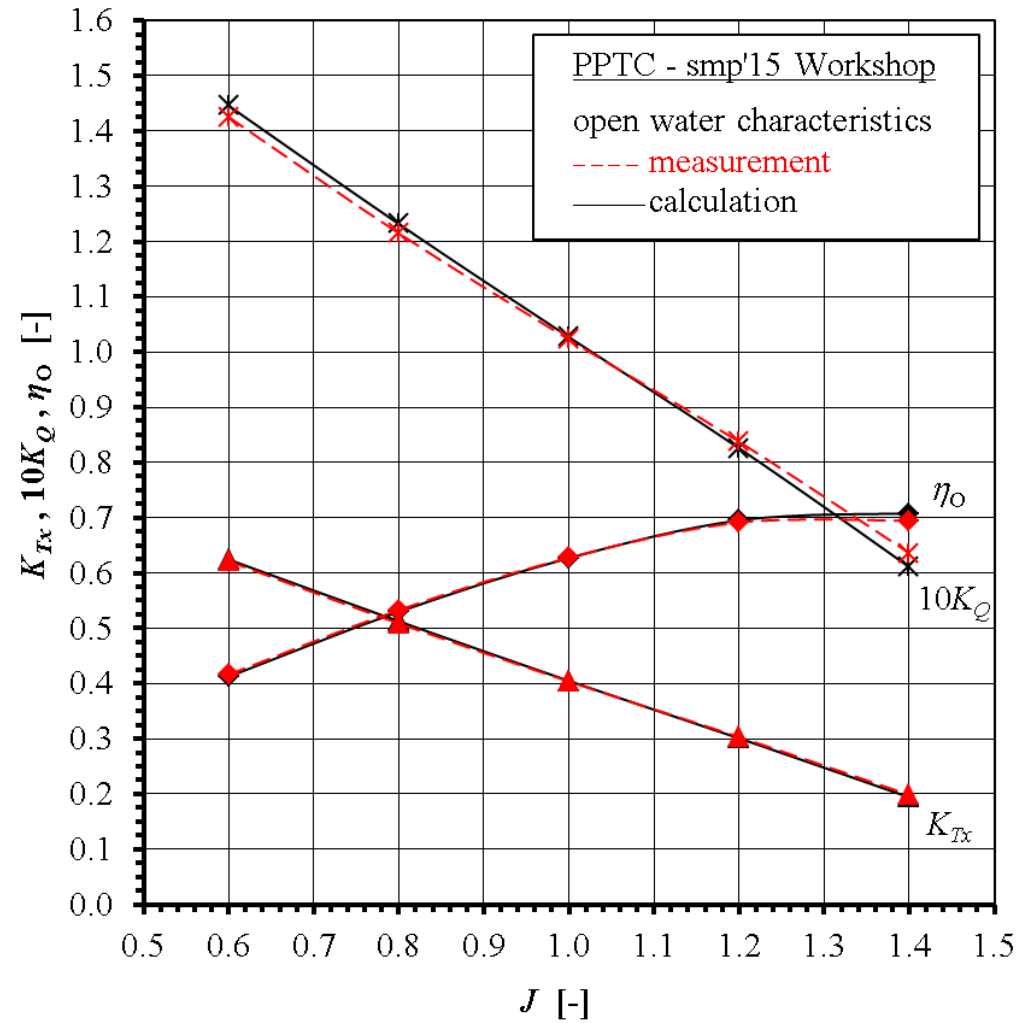


1.12 Open water curves for $\psi^{bP} = 12^\circ$: UDE-ISIS

J	K_{Tx} EFD	K_{Tx} CFD	ΔK_{Tx}	ΔK_{Tx} [%]
0.60	0.621	0.625	0.003	0.5
0.80	0.509	0.513	0.004	0.8
1.00	0.404	0.405	0.001	0.3
1.20	0.303	0.301	-0.002	-0.8
1.40	0.198	0.194	-0.004	-2.1

J	$10K_Q$ EFD	$10K_Q$ CFD	$\Delta 10K_Q$	$\Delta 10K_Q$ [%]
0.60	1.425	1.446	0.021	1.4
0.80	1.215	1.232	0.017	1.4
1.00	1.023	1.027	0.004	0.4
1.20	0.838	0.826	-0.012	-1.4
1.40	0.636	0.611	-0.025	-4.0

J	η_o EFD	η_o CFD	$\Delta \eta_o$	$\Delta \eta_o$ [%]
0.60	0.416	0.412	-0.004	-0.9
0.80	0.533	0.530	-0.003	-0.6
1.00	0.628	0.627	-0.001	-0.1
1.20	0.691	0.696	0.004	0.6
1.40	0.695	0.708	0.013	1.9

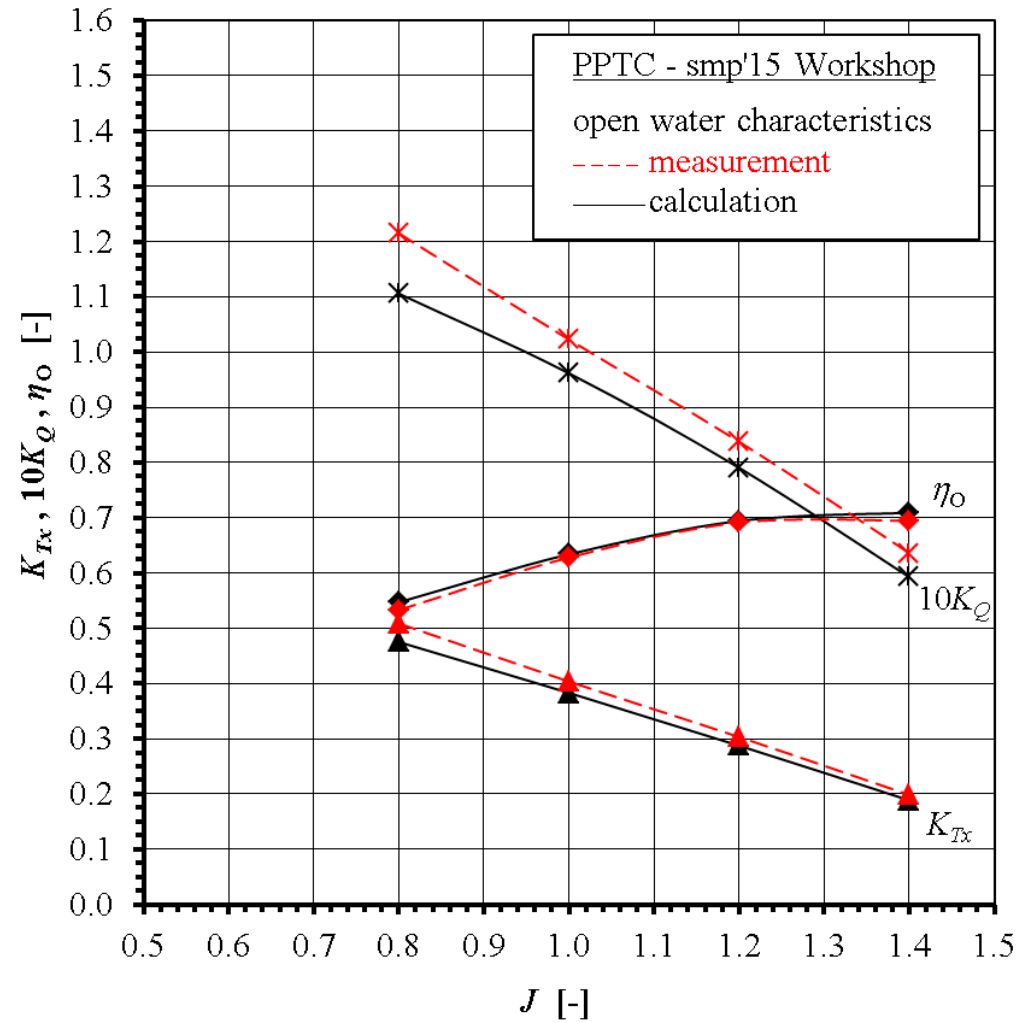


1.13 Open water curves for $\psi^{bP} = 12^\circ$: UniGenoa-BEM

J	K_{Tx} EFD	K_{Tx} CFD	ΔK_{Tx}	ΔK_{Tx} [%]
0.60				
0.80	0.509	0.475	-0.034	-6.6
1.00	0.404	0.383	-0.021	-5.1
1.20	0.303	0.287	-0.016	-5.2
1.40	0.198	0.189	-0.010	-4.9

J	$10K_Q$ EFD	$10K_Q$ CFD	$\Delta 10K_Q$	$\Delta 10K_Q$ [%]
0.60				
0.80	1.215	1.106	-0.109	-9.0
1.00	1.023	0.962	-0.061	-6.0
1.20	0.838	0.790	-0.047	-5.6
1.40	0.636	0.593	-0.044	-6.8

J	η_o EFD	η_o CFD	$\Delta \eta_o$	$\Delta \eta_o$ □[%]
0.60				
0.80	0.533	0.547	0.014	2.6
1.00	0.628	0.634	0.006	0.9
1.20	0.691	0.694	0.003	0.4
1.40	0.695	0.709	0.014	2.1

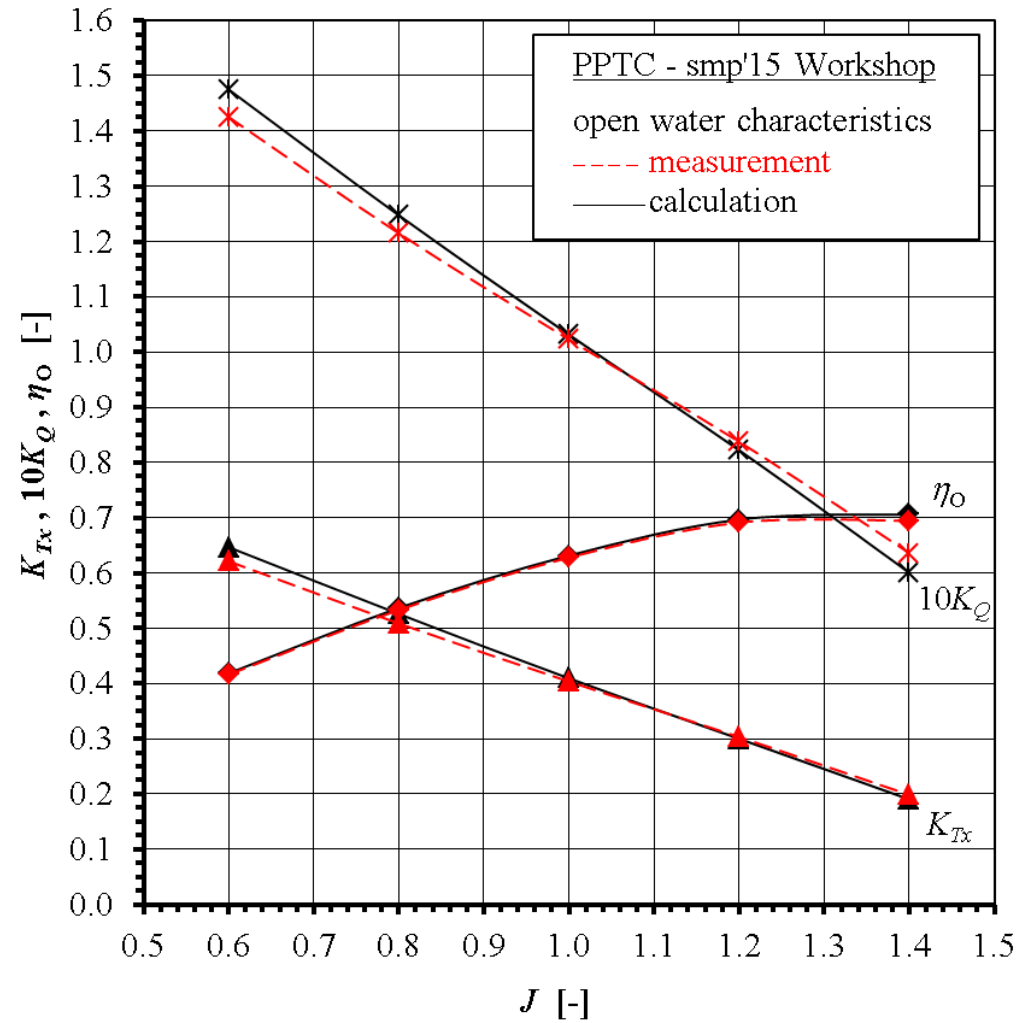


1.14 Open water curves for $\psi^{bP} = 12^\circ$: UniGenoa-StarCCM

J	K_{Tx} EFD	K_{Tx} CFD	ΔK_{Tx}	ΔK_{Tx} [%]
0.60	0.621	0.647	0.025	4.1
0.80	0.509	0.526	0.017	3.4
1.00	0.404	0.409	0.006	1.4
1.20	0.303	0.300	-0.003	-1.0
1.40	0.198	0.190	-0.008	-4.1

J	$10K_Q$ EFD	$10K_Q$ CFD	$\Delta 10K_Q$	$\Delta 10K_Q$ [%]
0.60	1.425	1.475	0.050	3.5
0.80	1.215	1.248	0.033	2.7
1.00	1.023	1.031	0.009	0.8
1.20	0.838	0.822	-0.015	-1.8
1.40	0.636	0.601	-0.036	-5.6

J	η_o EFD	η_o CFD	$\Delta \eta_o$	$\Delta \eta_o$ [%]
0.60	0.416	0.419	0.002	0.6
0.80	0.533	0.537	0.004	0.7
1.00	0.628	0.632	0.004	0.6
1.20	0.691	0.697	0.006	0.8
1.40	0.695	0.706	0.011	1.6

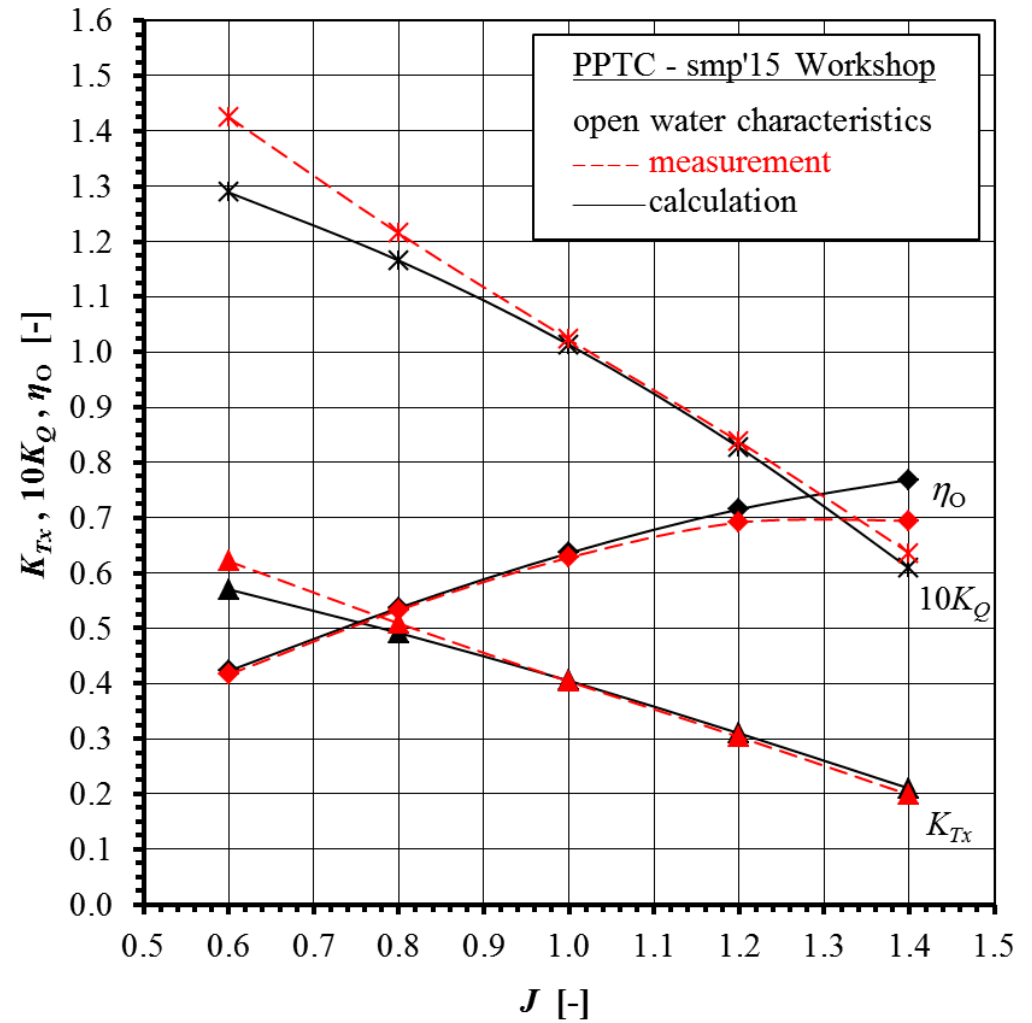


1.15 Open water curves for $\psi^{bP} = 12^\circ$: UTAustin-PROPCAV

J	K_{Tx} EFD	K_{Tx} CFD	ΔK_{Tx}	ΔK_{Tx} [%]
0.60	0.621	0.571	-0.051	-8.2
0.80	0.509	0.492	-0.017	-3.4
1.00	0.404	0.405	0.001	0.4
1.20	0.303	0.310	0.007	2.2
1.40	0.198	0.210	0.012	5.9

J	$10K_Q$ EFD	$10K_Q$ CFD	$\Delta 10K_Q$	$\Delta 10K_Q$ [%]
0.60	1.425	1.289	-0.136	-9.6
0.80	1.215	1.166	-0.049	-4.1
1.00	1.023	1.013	-0.009	-0.9
1.20	0.838	0.827	-0.010	-1.2
1.40	0.636	0.608	-0.028	-4.4

J	η_o EFD	η_o CFD	$\Delta \eta_o$	$\Delta \eta_o$ [%]
0.60	0.416	0.423	0.006	1.5
0.80	0.533	0.537	0.004	0.7
1.00	0.628	0.636	0.008	1.3
1.20	0.691	0.715	0.024	3.5
1.40	0.695	0.769	0.074	10.7

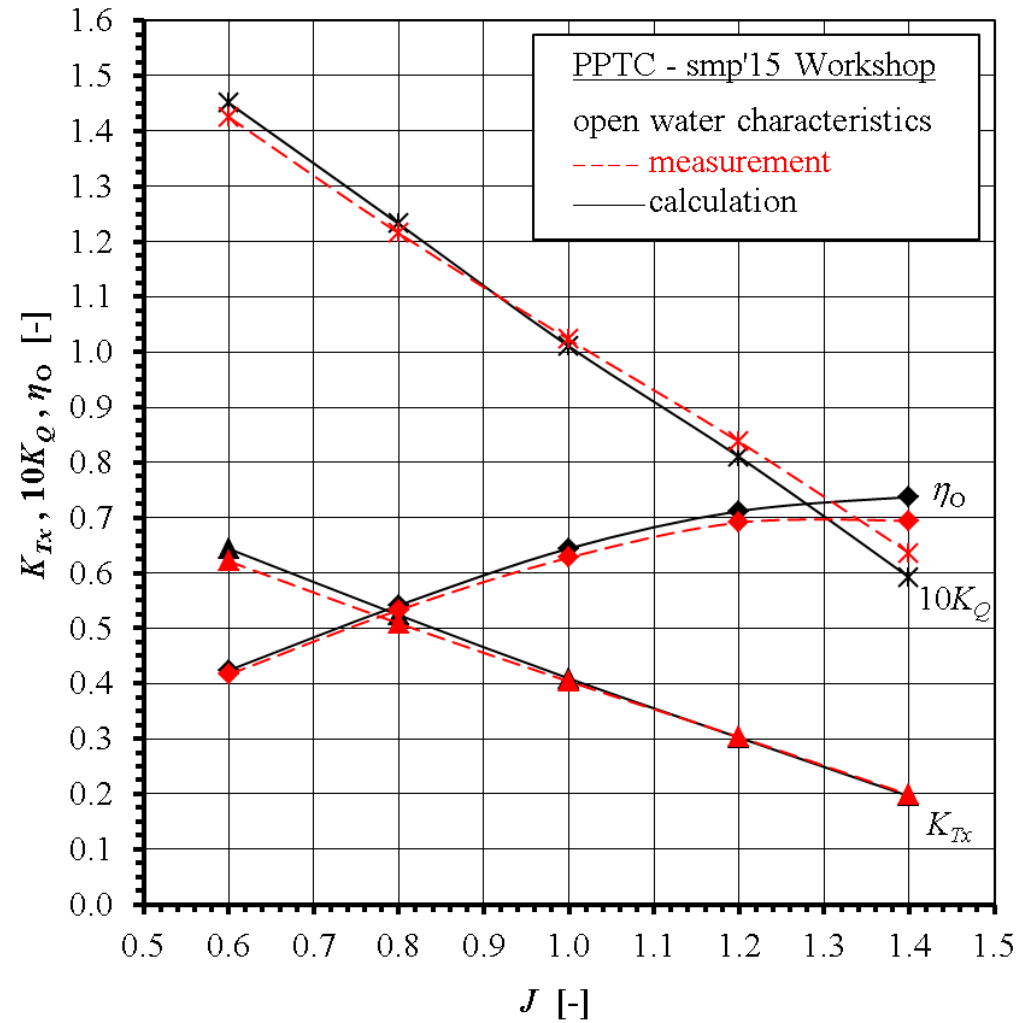


1.16 Open water curves for $\psi^{bP} = 12^\circ$: VTT-FinFlo

J	K_{Tx} EFD	K_{Tx} CFD	ΔK_{Tx}	ΔK_{Tx} [%]
0.60	0.621	0.644	0.023	3.6
0.80	0.509	0.524	0.015	3.0
1.00	0.404	0.409	0.005	1.3
1.20	0.303	0.302	-0.001	-0.4
1.40	0.198	0.196	-0.002	-1.2

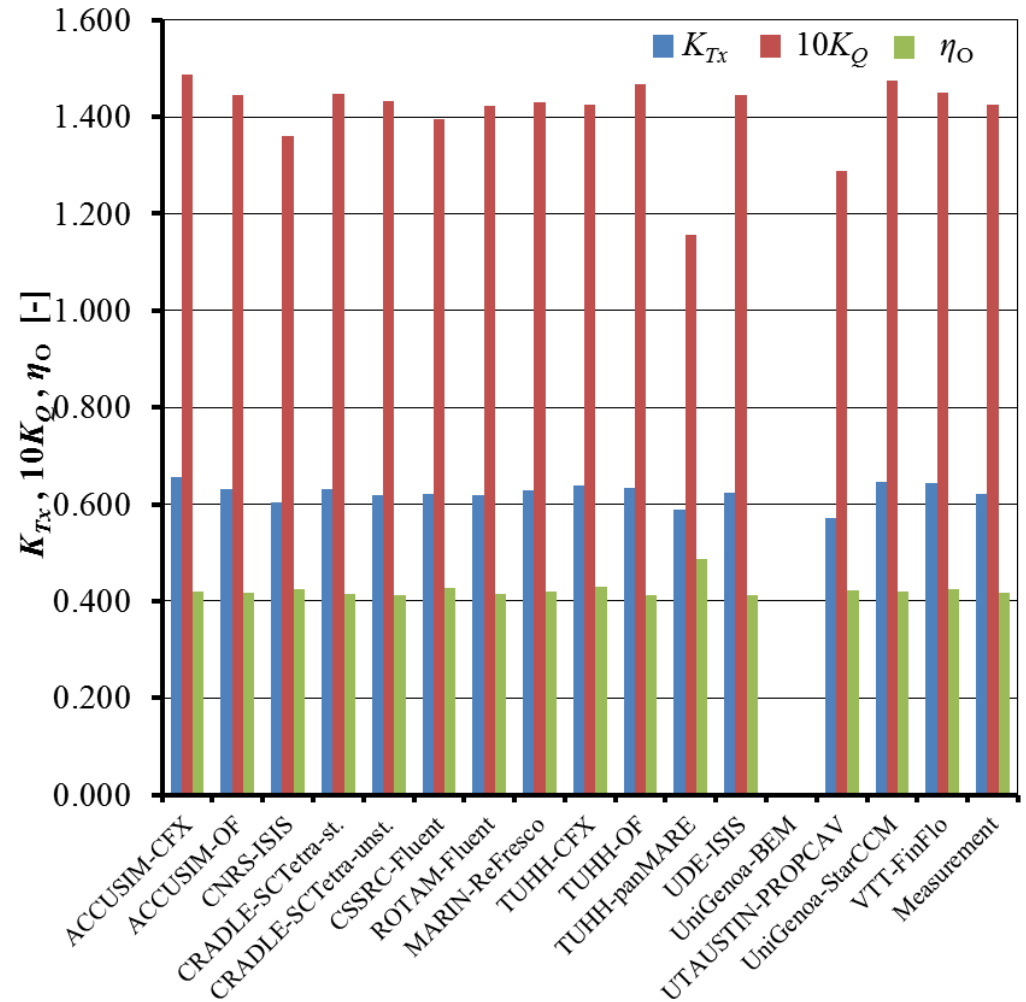
J	$10K_Q$ EFD	$10K_Q$ CFD	$\Delta 10K_Q$	$\Delta 10K_Q$ [%]
0.60	1.425	1.451	0.026	1.8
0.80	1.215	1.232	0.017	1.4
1.00	1.023	1.010	-0.013	-1.2
1.20	0.838	0.810	-0.028	-3.3
1.40	0.636	0.592	-0.044	-6.9

J	η_o EFD	η_o CFD	$\Delta \eta_o$	$\Delta \eta_o$ [%]
0.60	0.416	0.424	0.008	1.8
0.80	0.533	0.542	0.008	1.6
1.00	0.628	0.644	0.016	2.6
1.20	0.691	0.712	0.021	3.0
1.40	0.695	0.738	0.043	6.2



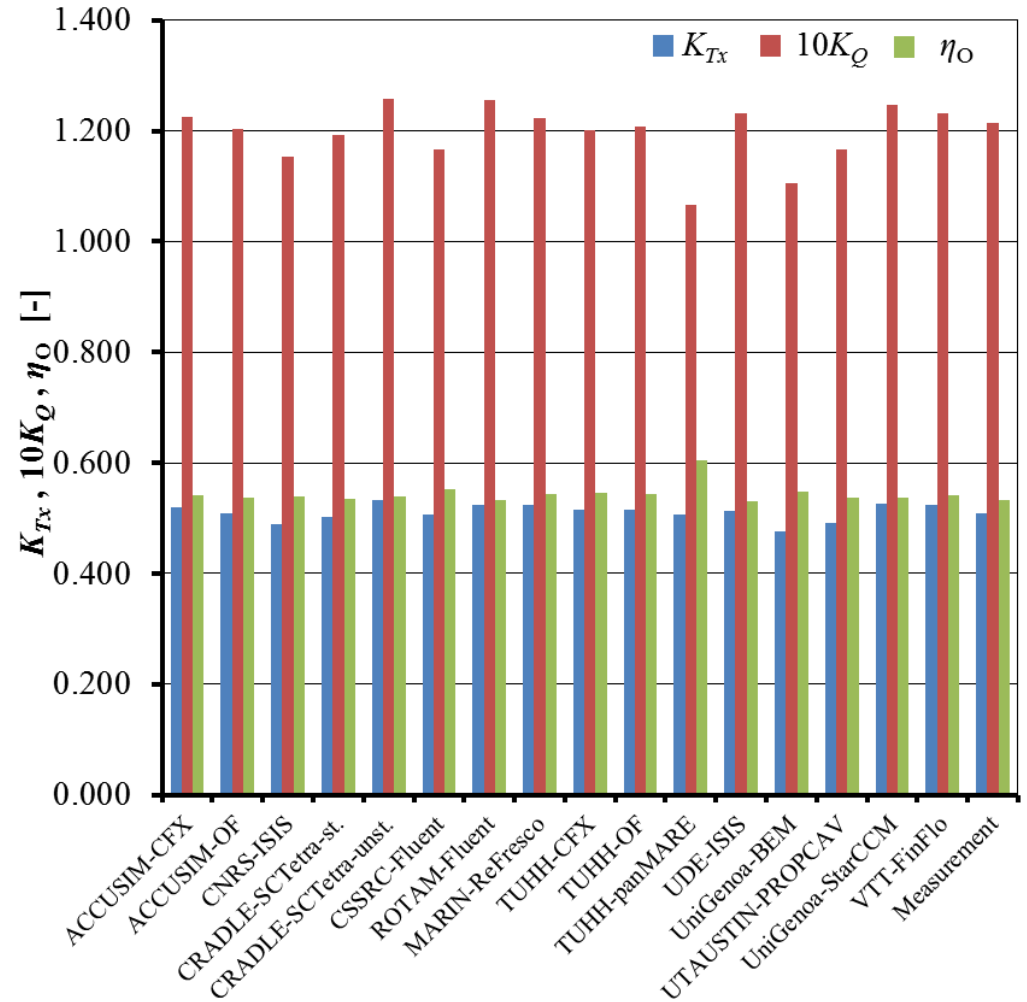
1.17 Comparison of open water characteristics, $\psi^{bP} = 12^\circ$, $J = 0.6$

	K_{Tx} [-]	$10K_Q$ [-]	η_o [-]
ACCUSIM-CFX	0.655	1.487	0.421
ACCUSIM-OF	0.632	1.445	0.418
CNRS-ISIS	0.604	1.361	0.424
CRADLE-SCTetra-st.	0.631	1.449	0.416
CRADLE-SCTetra-unst.	0.620	1.431	0.413
CSSRC-Fluent	0.623	1.394	0.426
ROTAM-Fluent	0.618	1.422	0.415
MARIN-ReFresco	0.628	1.429	0.420
TUHH-CFX	0.640	1.426	0.428
TUHH-OF	0.634	1.467	0.413
TUHH-panMARE	0.590	1.157	0.487
UDE-ISIS	0.625	1.446	0.412
UniGenoa-BEM			
UniGenoa-StarCCM	0.647	1.475	0.419
UTAustin-PROPCAV	0.571	1.289	0.423
VTT-FinFlo	0.644	1.451	0.424
Measurement	0.621	1.425	0.416



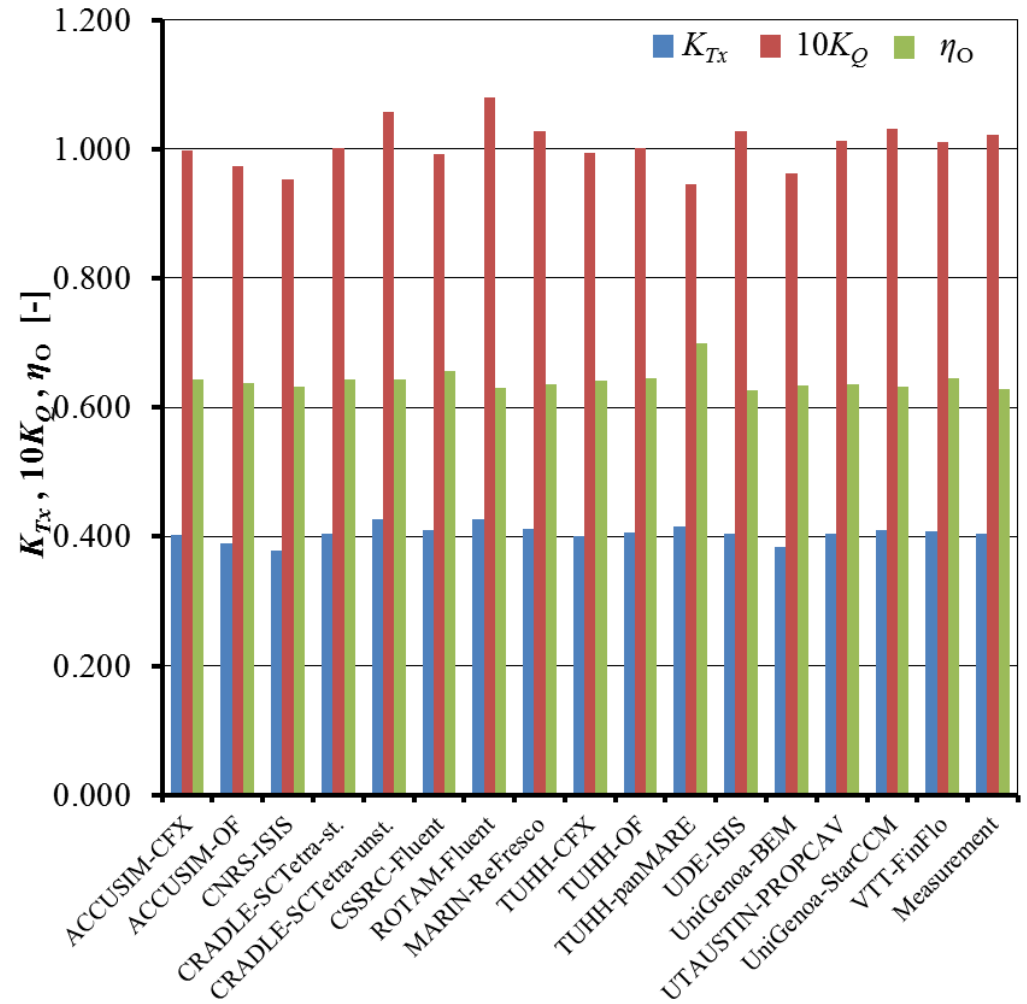
1.18 Comparison of open water characteristics, $\psi^{bP} = 12^\circ$, $J = 0.8$

	K_{Tx} [-]	$10K_Q$ [-]	η_o [-]
ACCUSIM-CFX	0.520	1.225	0.540
ACCUSIM-OF	0.508	1.203	0.538
CNRS-ISIS	0.489	1.153	0.540
CRADLE-SCTetra-st.	0.502	1.193	0.536
CRADLE-SCTetra-unst.	0.533	1.258	0.540
CSSRC-Fluent	0.506	1.166	0.553
ROTAM-Fluent	0.524	1.255	0.532
MARIN-ReFresco	0.523	1.223	0.544
TUHH-CFX	0.516	1.202	0.546
TUHH-OF	0.516	1.207	0.544
TUHH-panMARE	0.506	1.067	0.604
UDE-ISIS	0.513	1.232	0.530
UniGenoa-BEM	0.475	1.106	0.547
UniGenoa-StarCCM	0.526	1.248	0.537
UTAustin-PROPCAV	0.492	1.166	0.537
VTT-FinFlo	0.524	1.232	0.542
Measurement	0.509	1.215	0.533



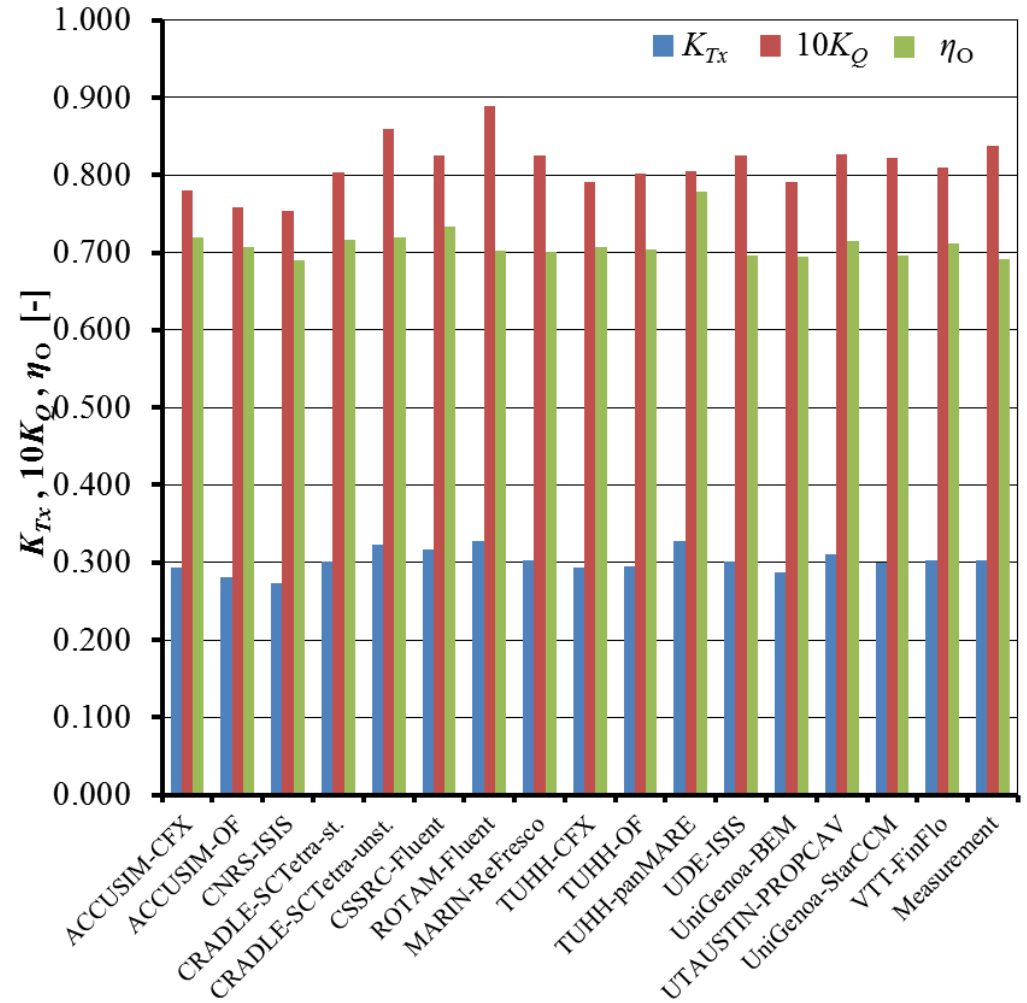
1.19 Comparison of open water characteristics, $\psi^{bP} = 12^\circ$, $J = 1.0$

	K_{Tx} [-]	$10K_Q$ [-]	η_o [-]
ACCUSIM-CFX	0.403	0.997	0.643
ACCUSIM-OF	0.390	0.973	0.638
CNRS-ISIS	0.378	0.953	0.632
CRADLE-SCTetra-st.	0.405	1.002	0.643
CRADLE-SCTetra-unst.	0.427	1.058	0.643
CSSRC-Fluent	0.409	0.992	0.657
ROTAM-Fluent	0.427	1.080	0.630
MARIN-ReFresco	0.411	1.028	0.636
TUHH-CFX	0.400	0.994	0.641
TUHH-OF	0.406	1.002	0.645
TUHH-panMARE	0.416	0.946	0.700
UDE-ISIS	0.405	1.027	0.627
UniGenoa-BEM	0.383	0.962	0.634
UniGenoa-StarCCM	0.409	1.031	0.632
UTAustin-PROPCAV	0.405	1.013	0.636
VTT-FinFlo	0.409	1.010	0.644
Measurement	0.404	1.023	0.628



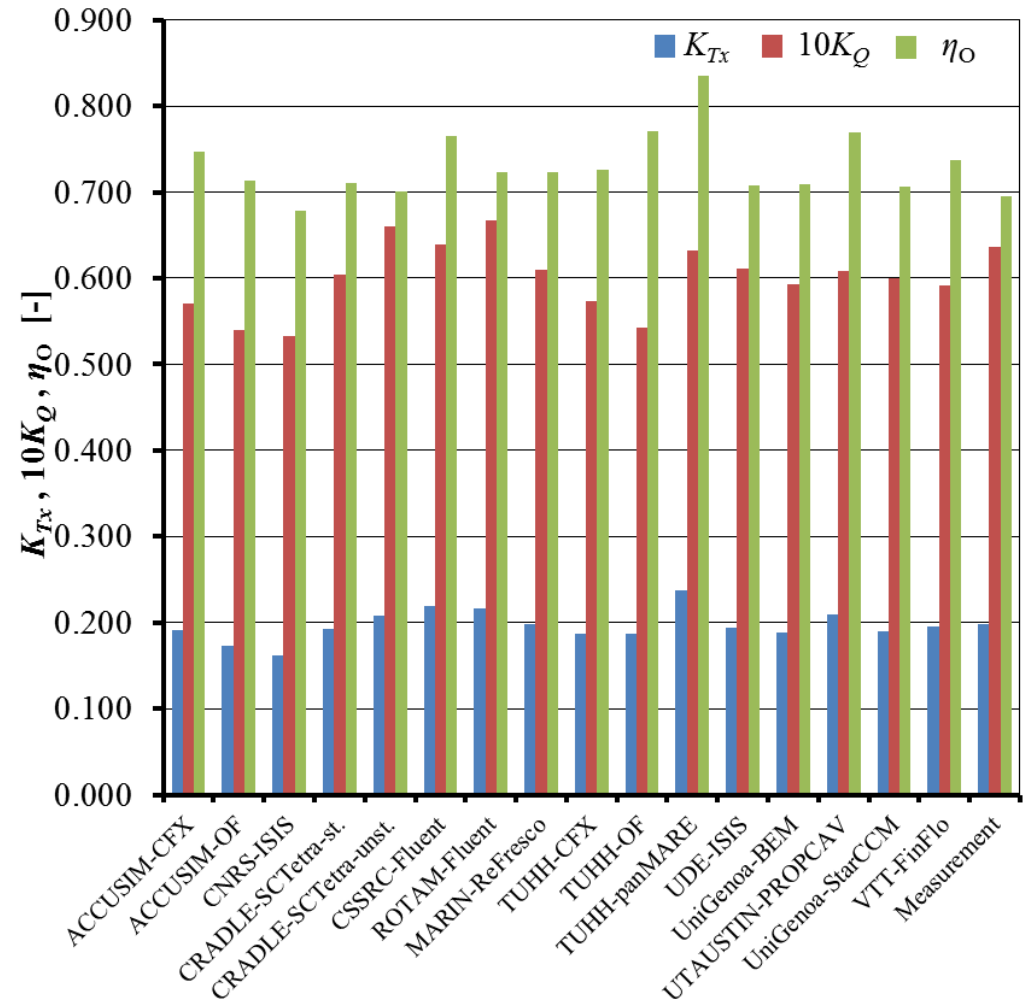
1.20 Comparison of open water characteristics, $\psi^{bP} = 12^\circ$, $J = 1.2$

	K_{Tx} [-]	$10K_Q$ [-]	η_o [-]
ACCUSIM-CFX	0.294	0.780	0.720
ACCUSIM-OF	0.281	0.759	0.707
CNRS-ISIS	0.273	0.754	0.691
CRADLE-SCTetra-st.	0.301	0.804	0.716
CRADLE-SCTetra-unst.	0.324	0.860	0.719
CSSRC-Fluent	0.317	0.825	0.733
ROTAM-Fluent	0.327	0.889	0.703
MARIN-ReFresco	0.303	0.825	0.701
TUHH-CFX	0.293	0.791	0.707
TUHH-OF	0.295	0.801	0.704
TUHH-panMARE	0.328	0.805	0.778
UDE-ISIS	0.301	0.826	0.696
UniGenoa-BEM	0.287	0.790	0.694
UniGenoa-StarCCM	0.300	0.822	0.697
UTAustin-PROPCAV	0.310	0.827	0.715
VTT-FinFlo	0.302	0.810	0.712
Measurement	0.303	0.838	0.691



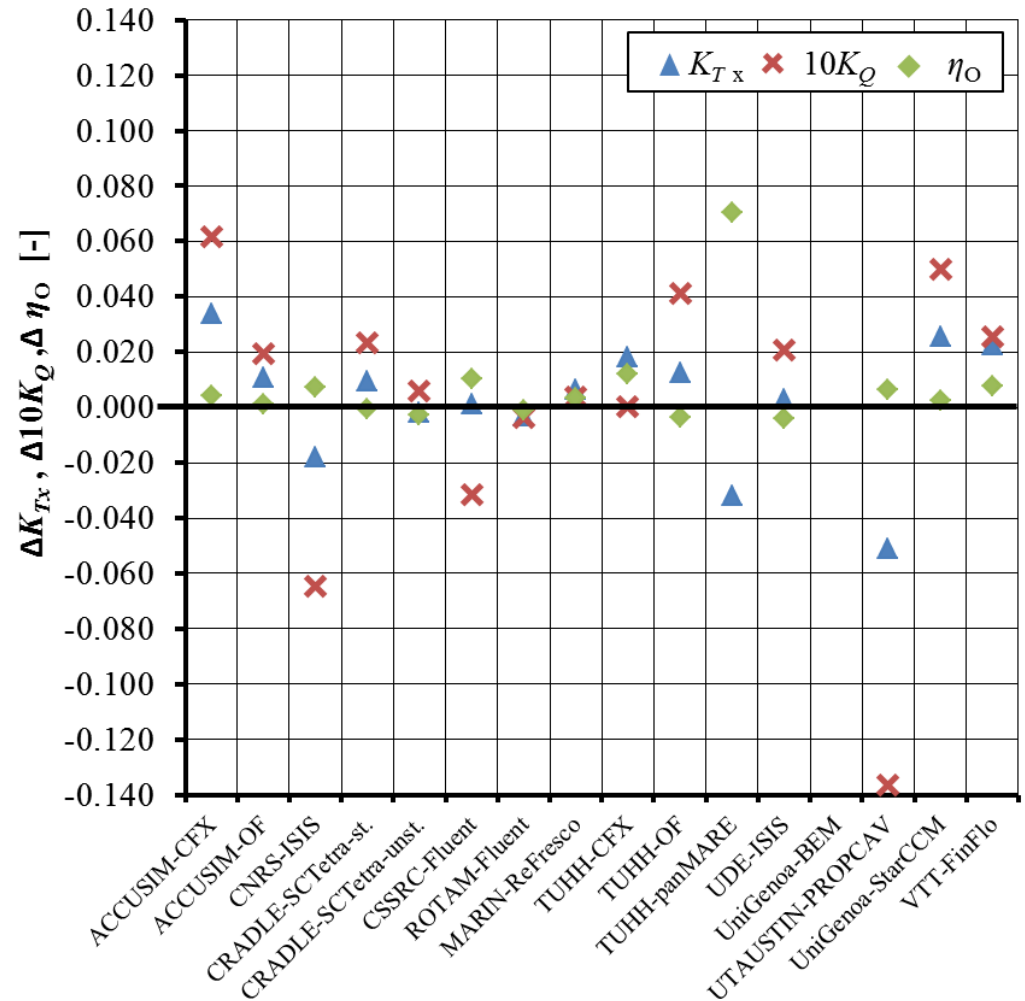
1.21 Comparison of open water characteristics, $\psi^{bP} = 12^\circ$, $J = 1.4$

	K_{Tx} [-]	$10K_Q$ [-]	η_o [-]
ACCUSIM-CFX	0.191	0.570	0.747
ACCUSIM-OF	0.173	0.540	0.714
CNRS-ISIS	0.162	0.533	0.679
CRADLE-SCTetra-st.	0.193	0.604	0.711
CRADLE-SCTetra-unst.	0.207	0.660	0.701
CSSRC-Fluent	0.219	0.639	0.764
ROTAM-Fluent	0.217	0.668	0.722
MARIN-ReFresco	0.198	0.610	0.723
TUHH-CFX	0.187	0.573	0.726
TUHH-OF	0.187	0.542	0.770
TUHH-panMARE	0.237	0.633	0.835
UDE-ISIS	0.194	0.611	0.708
UniGenoa-BEM	0.189	0.593	0.709
UniGenoa-StarCCM	0.190	0.601	0.706
UTAustin-PROPCAV	0.210	0.608	0.769
VTT-FinFlo	0.196	0.592	0.738
Measurement	0.198	0.636	0.695



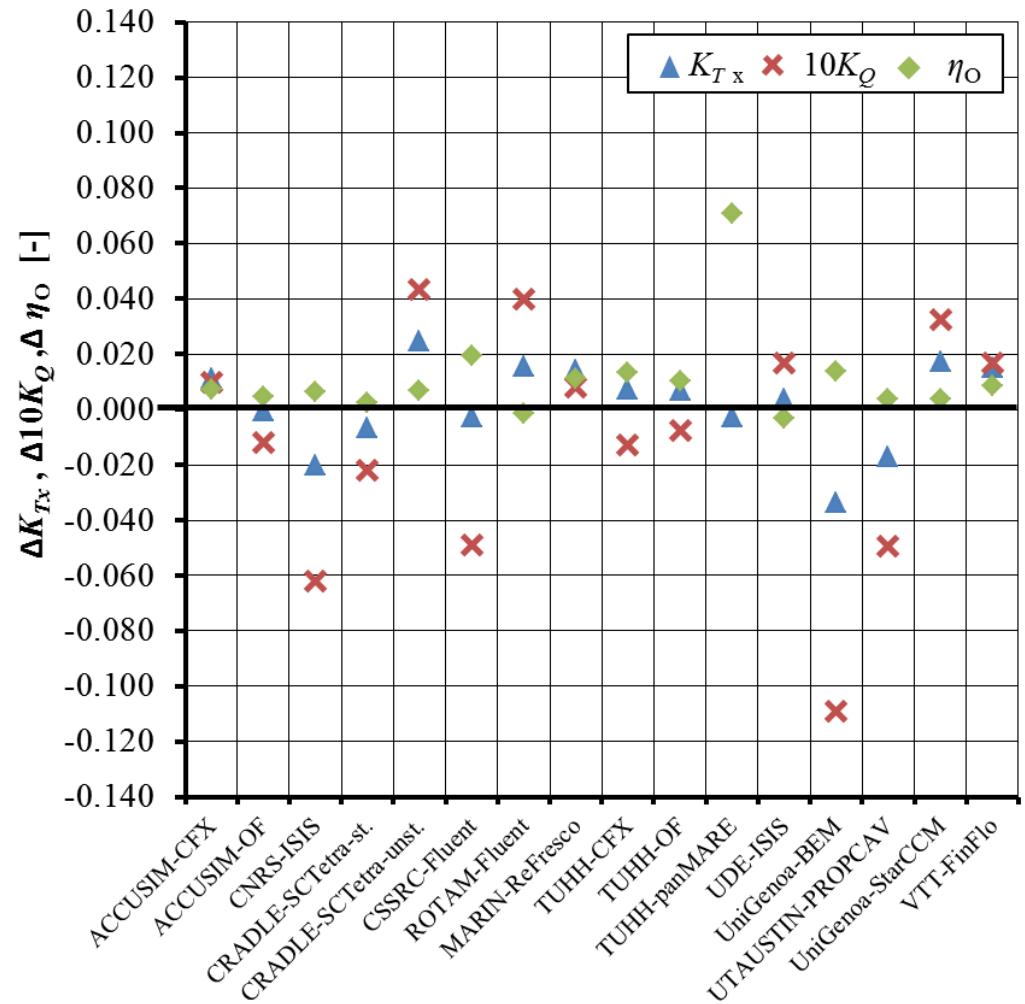
1.22 Absolute difference between measured and calculated values: $\psi^{bP} = 12^\circ, J = 0.6$

	ΔK_{Tx} [-]	$\Delta 10K_Q$ [-]	$\Delta \eta_O$ [-]
ACCUSIM-CFX	0.034	0.062	0.004
ACCUSIM-OF	0.011	0.020	0.001
CNRS-ISIS	-0.018	-0.065	0.007
CRADLE-SCTetra-st.	0.009	0.023	-0.001
CRADLE-SCTetra-unst.	-0.002	0.006	-0.003
CSSRC-Fluent	0.001	-0.031	0.010
ROTAM-Fluent	-0.003	-0.003	-0.001
MARIN-ReFresco	0.007	0.004	0.003
TUHH-CFX	0.018	0.000	0.012
TUHH-OF	0.012	0.041	-0.004
TUHH-panMARE	-0.032	-0.268	0.070
UDE-ISIS	0.003	0.021	-0.004
UniGenoa-BEM			
UniGenoa-StarCCM	0.025	0.050	0.002
UTAustin-PROPCAV	-0.051	-0.136	0.006
VTT-FinFlo	0.023	0.026	0.008



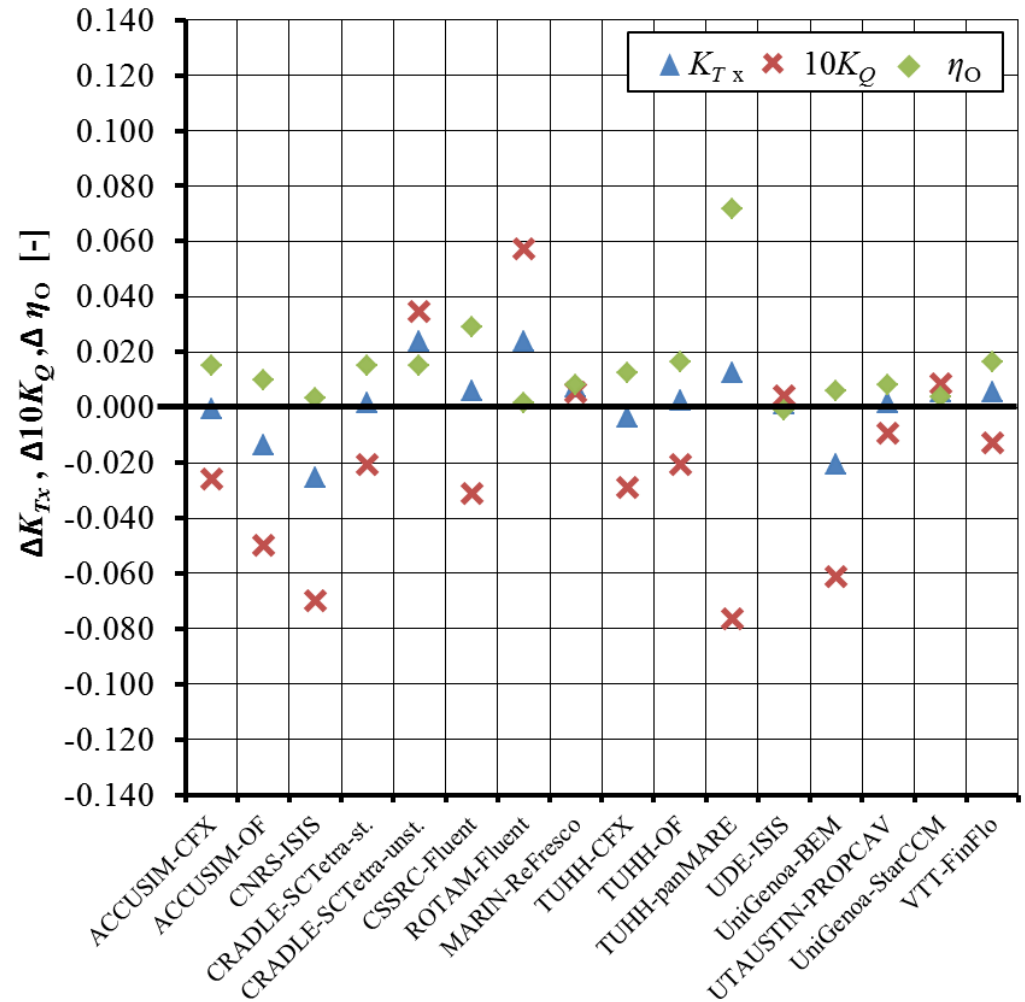
1.23 Absolute difference between measured and calculated values: $\psi^{pP} = 12^\circ, J = 0.8$

	ΔK_{Tx} [-]	$\Delta 10K_Q$ [-]	$\Delta \eta_O$ [-]
ACCUSIM-CFX	0.011	0.010	0.007
ACCUSIM-OF	-0.001	-0.012	0.004
CNRS-ISIS	-0.020	-0.062	0.007
CRADLE-SCTetra-st.	-0.007	-0.022	0.003
CRADLE-SCTetra-unst.	0.025	0.043	0.007
CSSRC-Fluent	-0.003	-0.049	0.020
ROTAM-Fluent	0.015	0.040	-0.001
MARIN-ReFresco	0.014	0.008	0.011
TUHH-CFX	0.007	-0.013	0.013
TUHH-OF	0.007	-0.008	0.010
TUHH-panMARE	-0.003	-0.148	0.071
UDE-ISIS	0.004	0.017	-0.003
UniGenoa-BEM	-0.034	-0.109	0.014
UniGenoa-StarCCM	0.017	0.033	0.004
UTAustin-PROPCAV	-0.017	-0.049	0.004
VTT-FinFlo	0.015	0.017	0.008



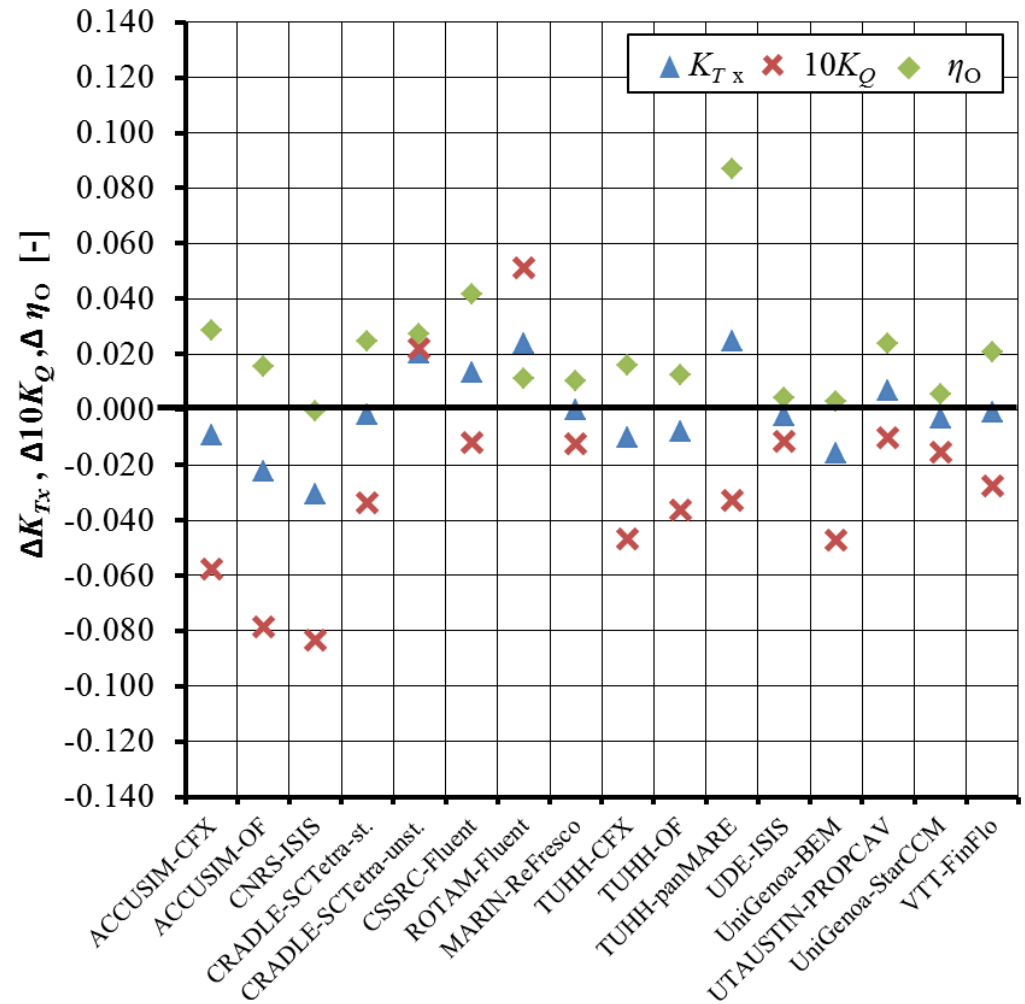
1.24 Absolute difference between measured and calculated values: $\psi^{pP} = 12^\circ, J = 1.0$

	ΔK_{Tx} [-]	$\Delta 10K_Q$ [-]	$\Delta \eta_O$ [-]
ACCUSIM-CFX	-0.001	-0.026	0.015
ACCUSIM-OF	-0.014	-0.050	0.010
CNRS-ISIS	-0.025	-0.070	0.003
CRADLE-SCTetra-st.	0.001	-0.020	0.015
CRADLE-SCTetra-unst.	0.024	0.035	0.015
CSSRC-Fluent	0.006	-0.031	0.029
ROTAM-Fluent	0.024	0.057	0.002
MARIN-ReFresco	0.007	0.005	0.008
TUHH-CFX	-0.003	-0.029	0.013
TUHH-OF	0.002	-0.020	0.017
TUHH-panMARE	0.013	-0.076	0.072
UDE-ISIS	0.001	0.004	-0.001
UniGenoa-BEM	-0.021	-0.061	0.006
UniGenoa-StarCCM	0.006	0.009	0.004
UTAustin-PROPCAV	0.001	-0.009	0.008
VTT-FinFlo	0.005	-0.013	0.016



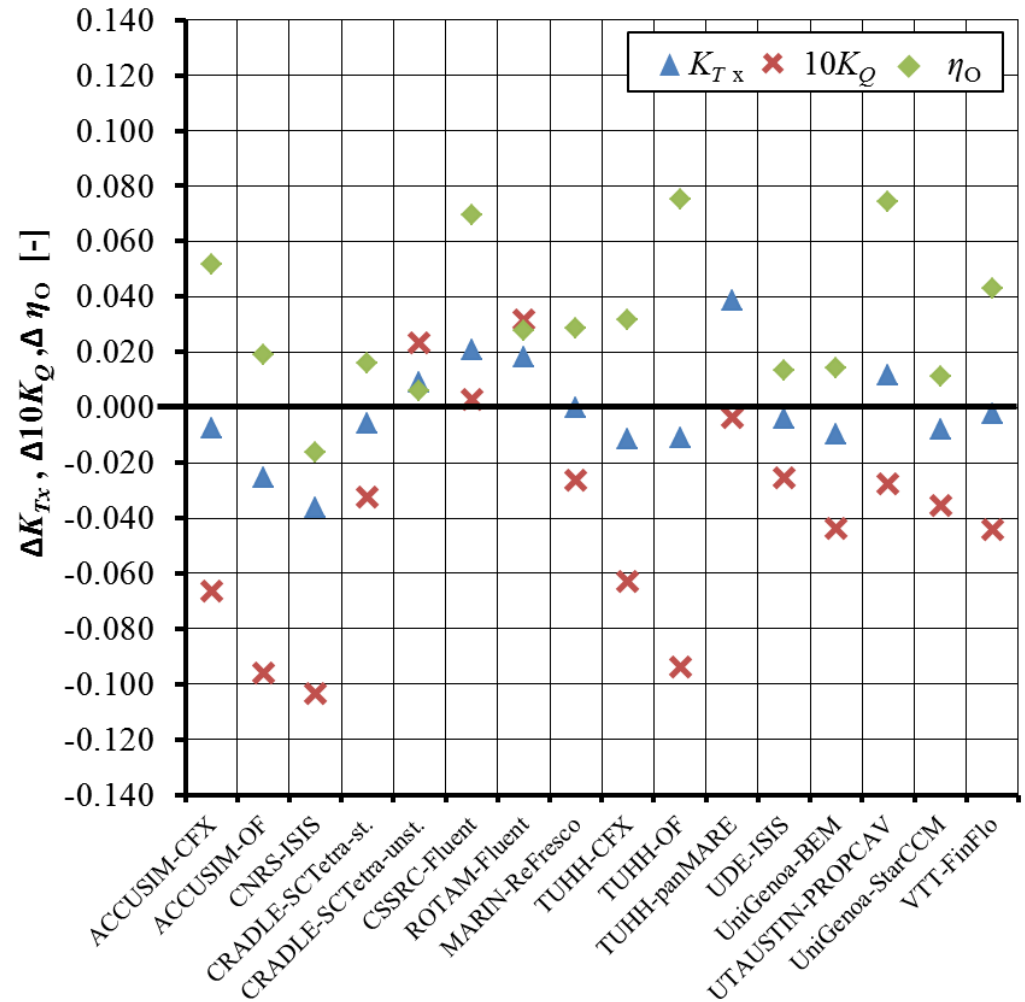
1.25 Absolute difference between measured and calculated values: $\psi^{pP} = 12^\circ, J = 1.2$

	ΔK_{Tx} [-]	$\Delta 10K_Q$ [-]	$\Delta \eta_o$ [-]
ACCUSIM-CFX	-0.009	-0.058	0.029
ACCUSIM-OF	-0.022	-0.079	0.016
CNRS-ISIS	-0.030	-0.083	-0.001
CRADLE-SCTetra-st.	-0.002	-0.034	0.025
CRADLE-SCTetra-unst.	0.020	0.022	0.027
CSSRC-Fluent	0.014	-0.012	0.041
ROTAM-Fluent	0.024	0.051	0.011
MARIN-ReFresco	0.000	-0.013	0.010
TUHH-CFX	-0.010	-0.047	0.016
TUHH-OF	-0.008	-0.036	0.012
TUHH-panMARE	0.025	-0.033	0.087
UDE-ISIS	-0.002	-0.012	0.004
UniGenoa-BEM	-0.016	-0.047	0.003
UniGenoa-StarCCM	-0.003	-0.015	0.006
UTAustin-PROPCAV	0.007	-0.010	0.024
VTT-FinFlo	-0.001	-0.028	0.021



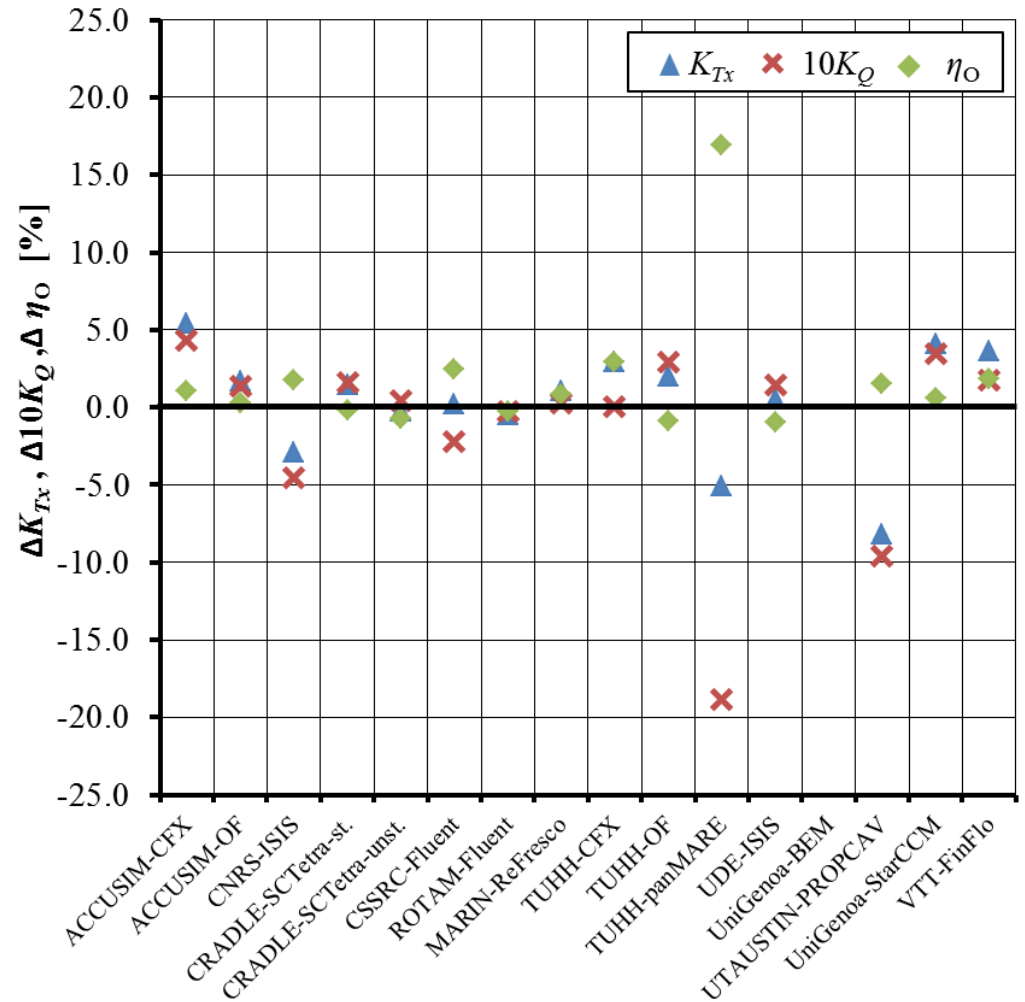
1.26 Absolute difference between measured and calculated values: $\psi^{pP} = 12^\circ, J = 1.4$

	ΔK_{Tx} [-]	$\Delta 10K_Q$ [-]	$\Delta \eta_o$ [-]
ACCUSIM-CFX	-0.007	-0.066	0.052
ACCUSIM-OF	-0.025	-0.096	0.019
CNRS-ISIS	-0.036	-0.103	-0.016
CRADLE-SCTetra-st.	-0.006	-0.032	0.016
CRADLE-SCTetra-unst.	0.009	0.023	0.006
CSSRC-Fluent	0.021	0.003	0.070
ROTAM-Fluent	0.018	0.032	0.028
MARIN-ReFresco	0.000	-0.026	0.028
TUHH-CFX	-0.011	-0.063	0.032
TUHH-OF	-0.011	-0.094	0.075
TUHH-panMARE	0.039	-0.004	0.140
UDE-ISIS	-0.004	-0.025	0.013
UniGenoa-BEM	-0.010	-0.044	0.014
UniGenoa-StarCCM	-0.008	-0.036	0.011
UTAustin-PROPCAV	0.012	-0.028	0.074
VTT-FinFlo	-0.002	-0.044	0.043



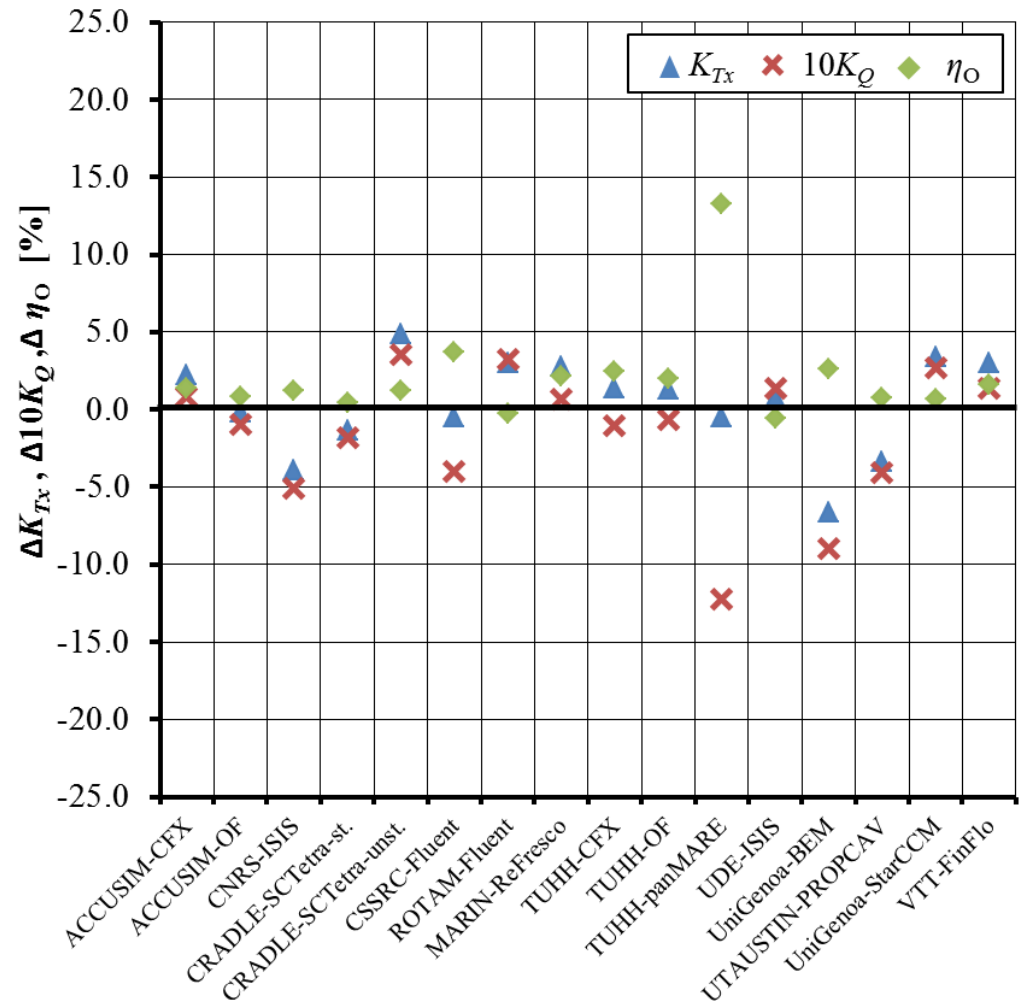
1.27 Relative difference between measured and calculated values: $\psi^{bP} = 12^\circ, J = 0.6$

	ΔK_{Tx} [%]	$\Delta 10K_Q$ [%]	$\Delta \eta_O$ [%]
ACCUSIM-CFX	5.4	4.3	1.0
ACCUSIM-OF	1.7	1.4	0.3
CNRS-ISIS	-2.9	-4.5	1.7
CRADLE-SCTetra-st.	1.5	1.6	-0.1
CRADLE-SCTetra-unst.	-0.3	0.4	-0.7
CSSRC-Fluent	0.2	-2.2	2.4
ROTAM-Fluent	-0.5	-0.2	-0.3
MARIN-ReFresco	1.1	0.3	0.8
TUHH-CFX	2.9	0.0	2.9
TUHH-OF	2.0	2.9	-0.9
TUHH-panMARE	-5.1	-18.8	16.9
UDE-ISIS	0.5	1.4	-0.9
UniGenoa-BEM			
UniGenoa-StarCCM	4.1	3.5	0.6
UTAustin-PROPCAV	-8.2	-9.6	1.5
VTT-FinFlo	3.6	1.8	1.8



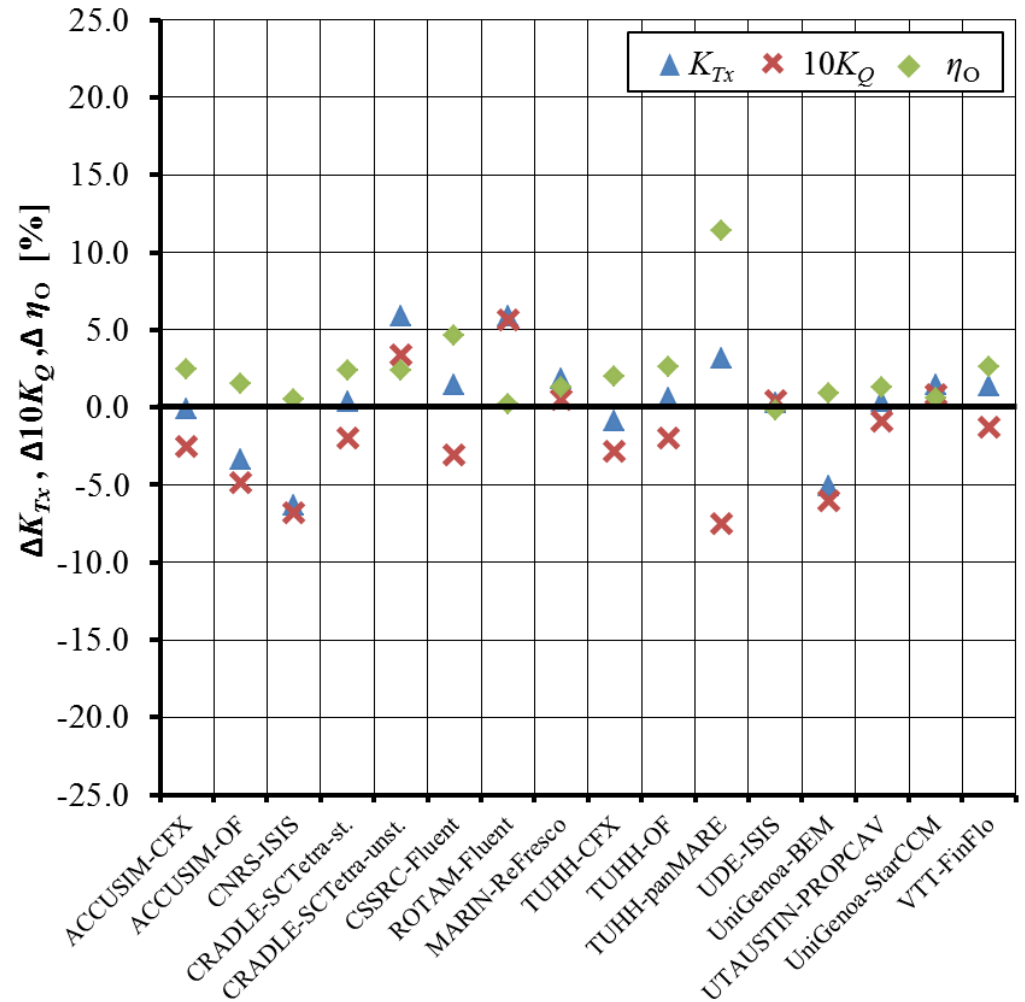
1.28 Relative difference between measured and calculated values: $\psi^{bP} = 12^\circ, J = 0.8$

	ΔK_{Tx} [%]	$\Delta 10K_Q$ [%]	$\Delta \eta_o$ [%]
ACCUSIM-CFX	2.2	0.8	1.4
ACCUSIM-OF	-0.1	-1.0	0.8
CNRS-ISIS	-3.9	-5.1	1.2
CRADLE-SCTetra-st.	-1.3	-1.8	0.5
CRADLE-SCTetra-unst.	4.9	3.6	1.2
CSSRC-Fluent	-0.5	-4.0	3.7
ROTAM-Fluent	3.0	3.3	-0.2
MARIN-ReFresco	2.8	0.7	2.1
TUHH-CFX	1.4	-1.1	2.5
TUHH-OF	1.3	-0.6	2.0
TUHH-panMARE	-0.5	-12.2	13.3
UDE-ISIS	0.8	1.4	-0.6
UniGenoa-BEM	-6.6	-9.0	2.6
UniGenoa-StarCCM	3.4	2.7	0.7
UTAustin-PROPCAV	-3.4	-4.1	0.7
VTT-FinFlo	3.0	1.4	1.6



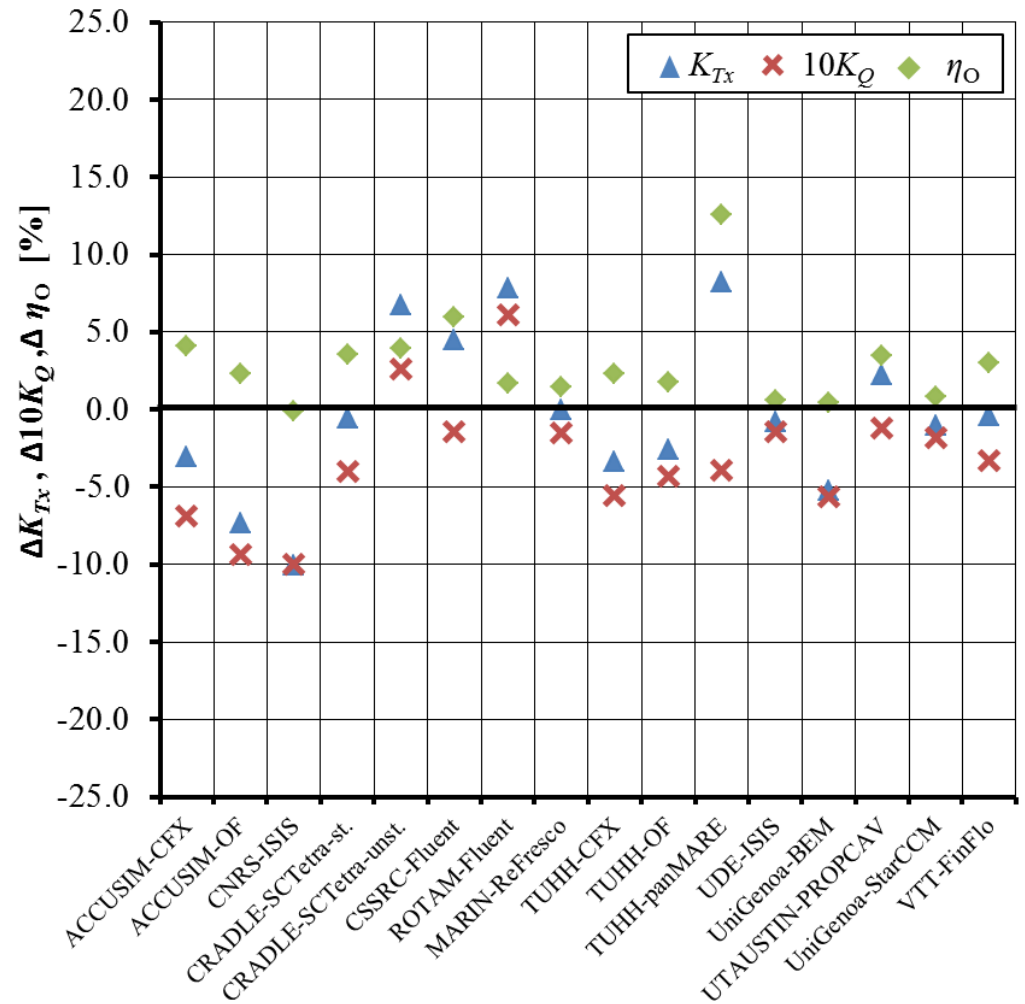
1.29 Relative difference between measured and calculated values: $\psi^{bP} = 12^\circ, J = 1.0$

	ΔK_{Tx} [%]	$\Delta 10K_Q$ [%]	$\Delta \eta_O$ [%]
ACCUSIM-CFX	-0.1	-2.5	2.4
ACCUSIM-OF	-3.4	-4.9	1.6
CNRS-ISIS	-6.3	-6.8	0.5
CRADLE-SCTetra-st.	0.4	-2.0	2.4
CRADLE-SCTetra-unst.	5.9	3.4	2.4
CSSRC-Fluent	1.4	-3.0	4.6
ROTAM-Fluent	5.9	5.6	0.2
MARIN-ReFresco	1.8	0.5	1.3
TUHH-CFX	-0.9	-2.8	2.0
TUHH-OF	0.6	-2.0	2.6
TUHH-panMARE	3.1	-7.5	11.4
UDE-ISIS	0.3	0.4	-0.1
UniGenoa-BEM	-5.1	-6.0	0.9
UniGenoa-StarCCM	1.4	0.8	0.6
UTAustin-PROPCAV	0.4	-0.9	1.3
VTT-FinFlo	1.3	-1.2	2.6



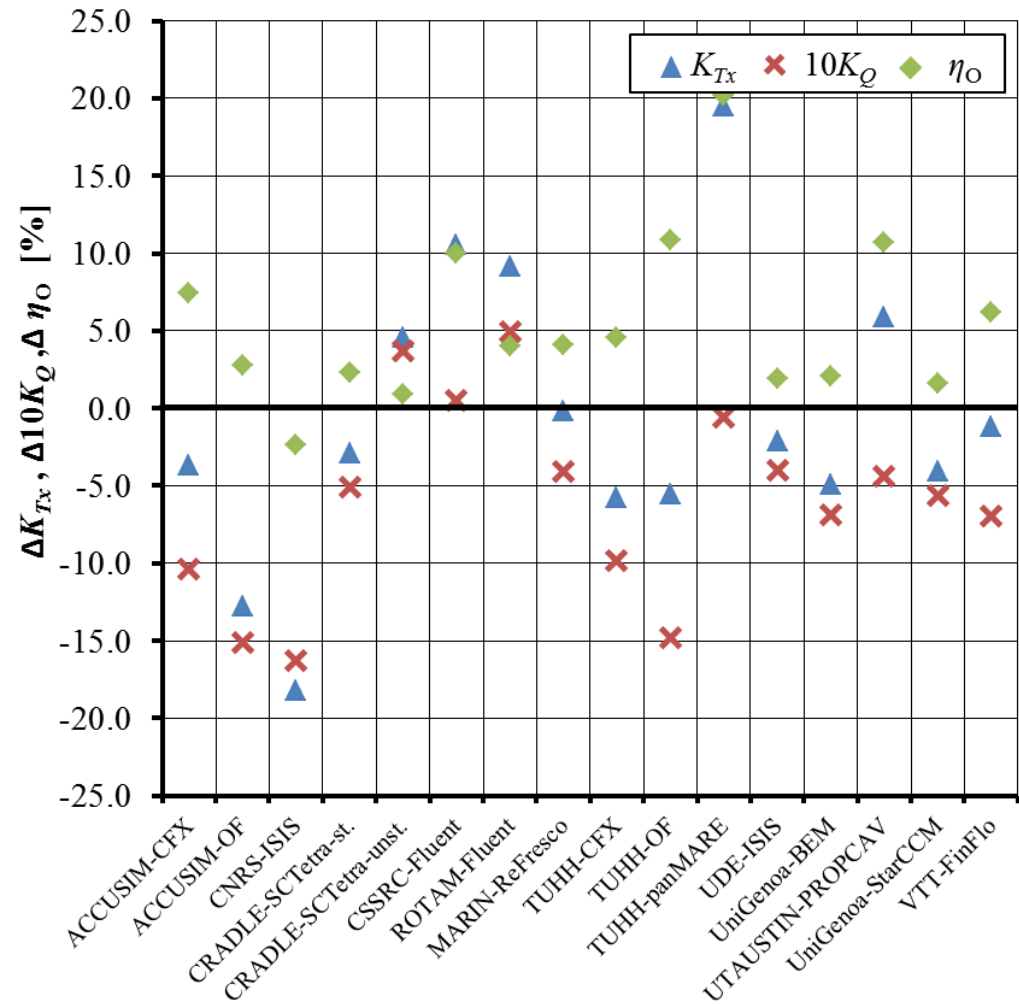
1.30 Relative difference between measured and calculated values: $\psi^{bP} = 12^\circ, J = 1.2$

	ΔK_{Tx} [%]	$\Delta 10K_Q$ [%]	$\Delta \eta_o$ [%]
ACCUSIM-CFX	-3.0	-6.9	4.1
ACCUSIM-OF	-7.3	-9.4	2.3
CNRS-ISIS	-10.0	-10.0	-0.1
CRADLE-SCTetra-st.	-0.6	-4.0	3.6
CRADLE-SCTetra-unst.	6.7	2.6	4.0
CSSRC-Fluent	4.5	-1.4	6.0
ROTAM-Fluent	7.9	6.1	1.6
MARIN-ReFresco	-0.1	-1.5	1.5
TUHH-CFX	-3.4	-5.6	2.3
TUHH-OF	-2.6	-4.3	1.8
TUHH-panMARE	8.2	-3.9	12.6
UDE-ISIS	-0.8	-1.4	0.6
UniGenoa-BEM	-5.2	-5.6	0.4
UniGenoa-StarCCM	-1.0	-1.8	0.8
UTAustin-PROPCAV	2.2	-1.2	3.5
VTT-FinFlo	-0.4	-3.3	3.0



1.31 Relative difference between measured and calculated values: $\psi^{bP} = 12^\circ, J = 1.4$

	ΔK_{Tx} [%]	$\Delta 10K_Q$ [%]	$\Delta \eta_o$ [%]
ACCUSIM-CFX	-3.7	-10.4	7.5
ACCUSIM-OF	-12.8	-15.1	2.7
CNRS-ISIS	-18.2	-16.2	-2.3
CRADLE-SCTetra-st.	-2.9	-5.1	2.3
CRADLE-SCTetra-unst.	4.6	3.7	0.9
CSSRC-Fluent	10.6	0.5	10.0
ROTAM-Fluent	9.2	5.0	4.0
MARIN-ReFresco	-0.2	-4.1	4.1
TUHH-CFX	-5.8	-9.9	4.5
TUHH-OF	-5.5	-14.8	10.8
TUHH-panMARE	19.5	-0.6	20.2
UDE-ISIS	-2.1	-4.0	1.9
UniGenoa-BEM	-4.9	-6.8	2.1
UniGenoa-StarCCM	-4.1	-5.6	1.6
UTAustin-PROPCAV	5.9	-4.4	10.7
VTT-FinFlo	-1.2	-6.9	6.2



Chapter 2

Case 2

Cavitation Test in Oblique Flow

1 Participants

The following institutes have participated:

Group	Solver	Acronym
ACCUSIM	ANSYS-CFX, FCM cav. model	ACCUSIM-CFX-FCM
	ANSYS-CFX, Kunz cav. model	ACCUSIM-CFX-Kunz
	ANSYS-CFX, Zwart cav. model	ACCUSIM-CFX-Zwart
CAT-Propulsion	OpenFOAM	CAT-OF
Chalmers	OpenFOAM	Chalmers-OF
CNRS-ECN	ISIS	CNRS-ISIS
CRADLE	SC-Tetra	CRADLE-SCTetra
CSSRC	ANSYS-Fluent	CSSRC-Fluent
MARIN	ReFRECSCO	MARIN-ReFRESCO
ROTAM	ANSYS-Fluent	ROTAM-Fluent
SSPA	ANSYS-Fluent	SSPA-Fluent-Sauer
	ANSYS-Fluent	SSPA-Fluent-Zwart1
	ANSYS-Fluent	SSPA-Fluent-Zwart2
TUHH	ANSYS-CFX	TUHH-CFX
	panMARE	TUHH-panMARE
University of Genoa	BEM	UniGenoa-BEM
	StarCCM+	UniGenoa-StarCCM+
UT Austin	PROPCAV	UTAustin-PROPCAV
VTT	FinFlo	VTT-FinFlo

At first the cavity surface for different vapour fractions are evaluated, followed by a summary of the computed thrust coefficient for the cavitating and non-cavitating propeller.

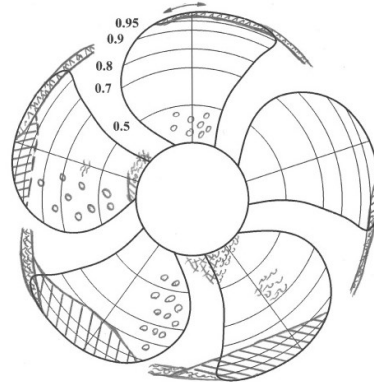
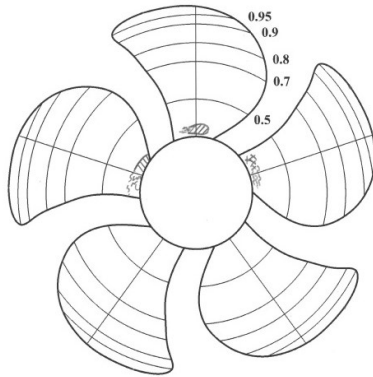
2 Case 2.1

2.1 Case 2.1, ACCUSIM-CFX-FCM

Pressure side

Suction side

Case 2.1
 $J = 1.019$
 $\sigma_n = 2.024$
 $\psi^{bP} = 12.0^\circ$

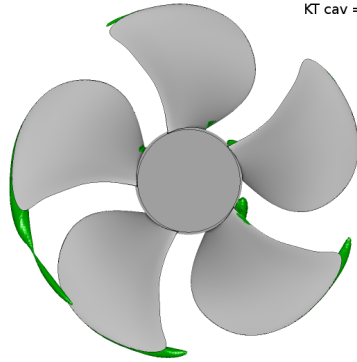


ACCUSIM-CFX-FCM

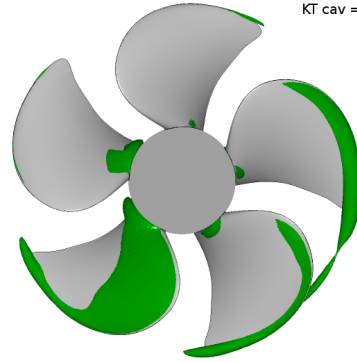
KT non-cav = 0.392
 KT cav = 0.365

ACCUSIM-CFX-FCM

KT non-cav = 0.392
 KT cav = 0.365



40 %
vapour
fraction

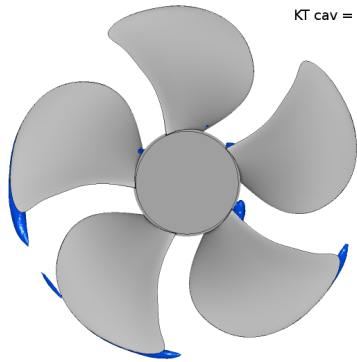


ACCUSIM-CFX-FCM

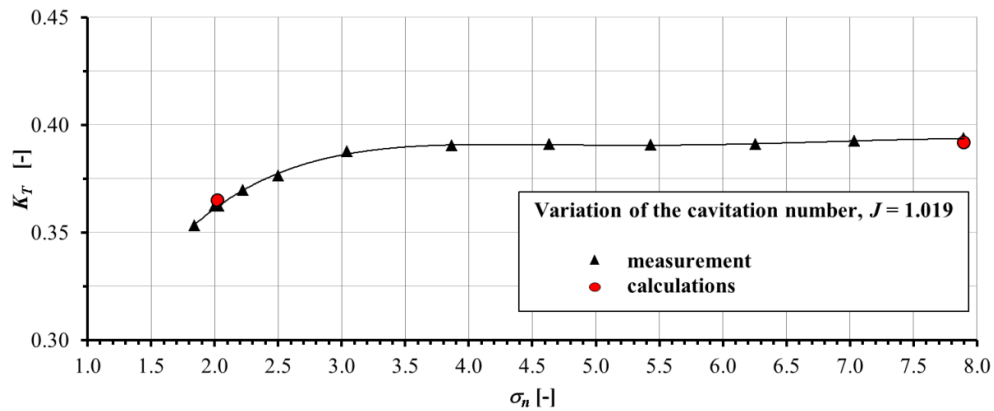
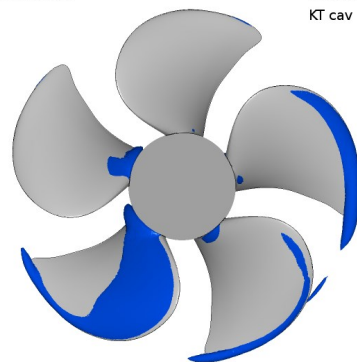
KT non-cav = 0.392
 KT cav = 0.365

ACCUSIM-CFX-FCM

KT non-cav = 0.392
 KT cav = 0.365



60 %
vapour
fraction

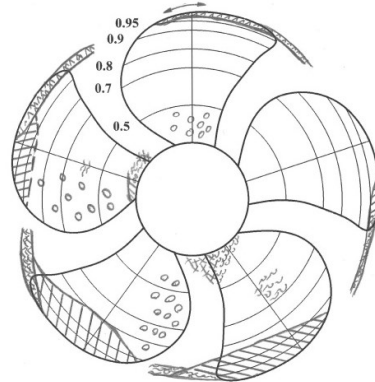
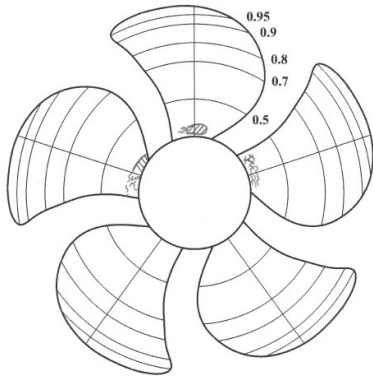


2.2 Case 2.1, ACCUSIM-CFX-Kunz

Pressure side

Suction side

Case 2.1
 $J = 1.019$
 $\sigma_n = 2.024$
 $\psi^{bP} = 12.0^\circ$

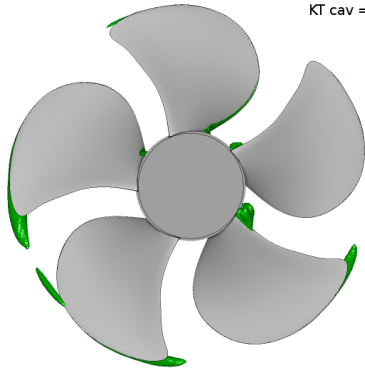


ACCUSIM-CFX-KUNZ

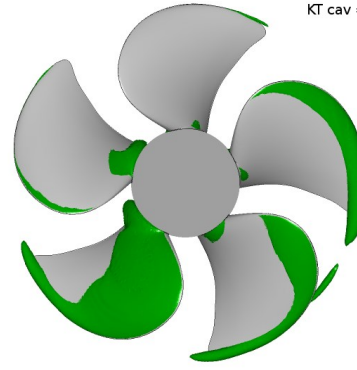
KT non-cav = 0.392
 KT cav = 0.368

ACCUSIM-CFX-KUNZ

KT non-cav = 0.392
 KT cav = 0.368



40 %
vapour
fraction

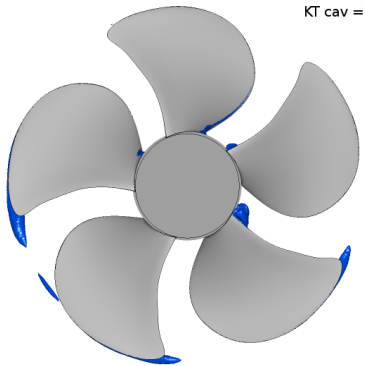


ACCUSIM-CFX-KUNZ

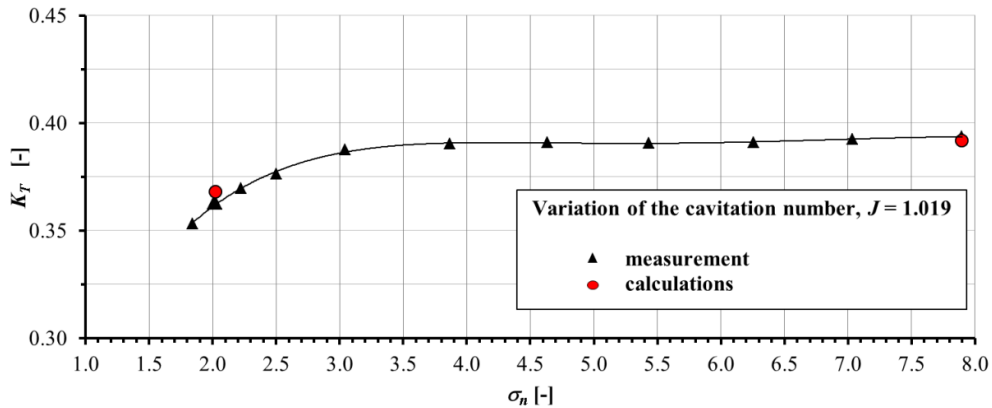
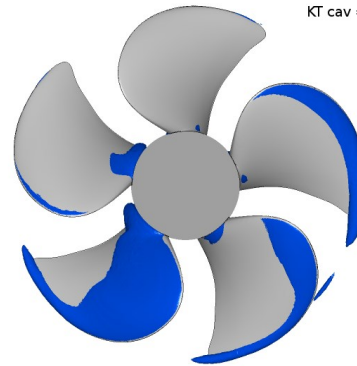
KT non-cav = 0.392
 KT cav = 0.368

ACCUSIM-CFX-KUNZ

KT non-cav = 0.392
 KT cav = 0.368



60 %
vapour
fraction

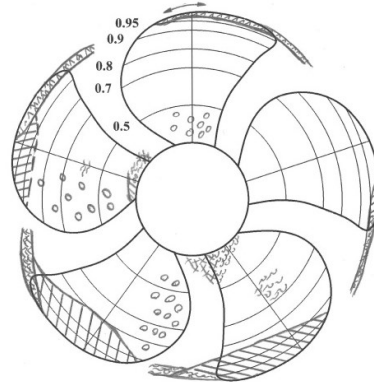
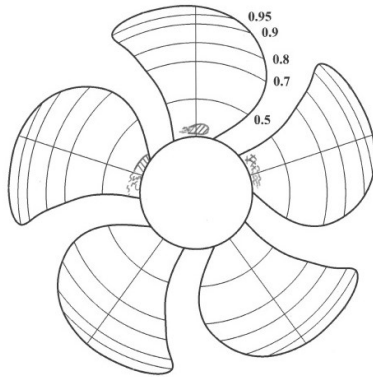


2.3 Case 2.1, ACCUSIM-CFX-Zwart

Pressure side

Suction side

Case 2.1
 $J = 1.019$
 $\sigma_n = 2.024$
 $\psi^{bP} = 12.0^\circ$

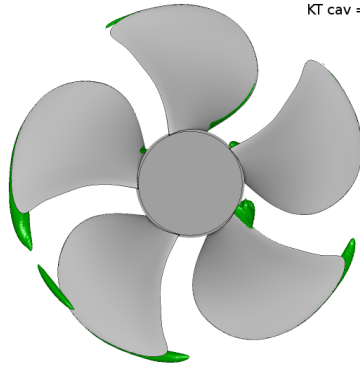


ACCUSIM-CFX-ZWART

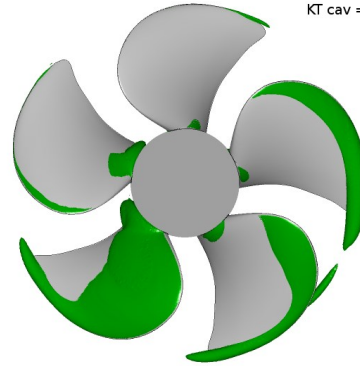
KT non-cav = 0.392
 KT cav = 0.365

ACCUSIM-CFX-ZWART

KT non-cav = 0.392
 KT cav = 0.365



40 %
vapour
fraction

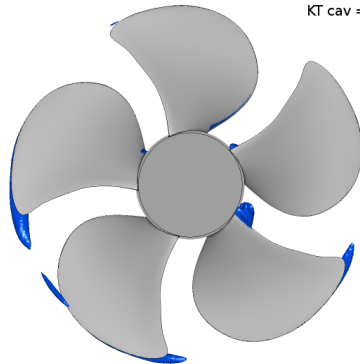


ACCUSIM-CFX-ZWART

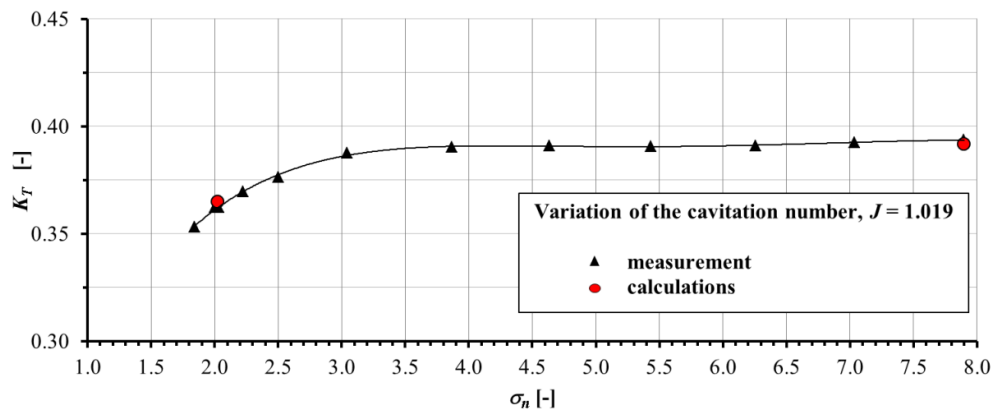
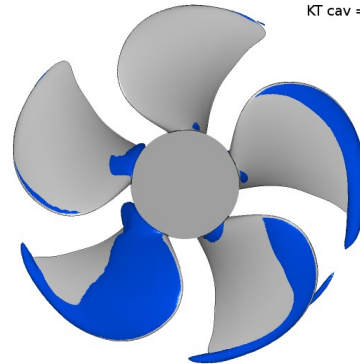
KT non-cav = 0.392
 KT cav = 0.365

ACCUSIM-CFX-ZWART

KT non-cav = 0.392
 KT cav = 0.365



60 %
vapour
fraction

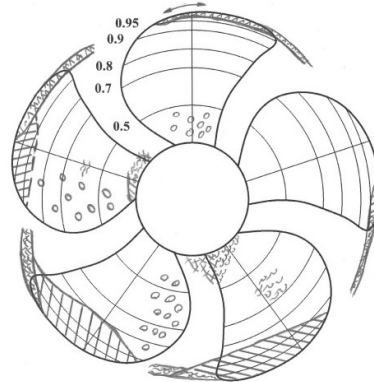
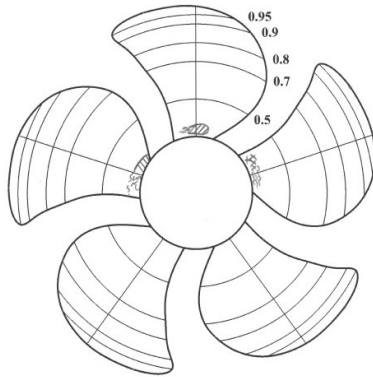


2.4 Case 2.1, CAT-OF

Pressure side

Suction side

Case 2.1
 $J = 1.019$
 $\sigma_n = 2.024$
 $\psi^{bP} = 12.0^\circ$

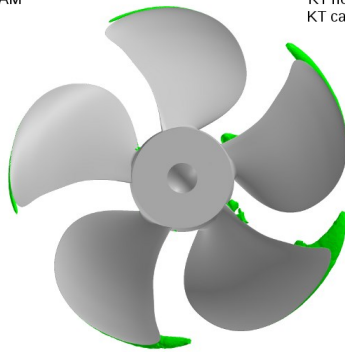


CAT-OpenFOAM

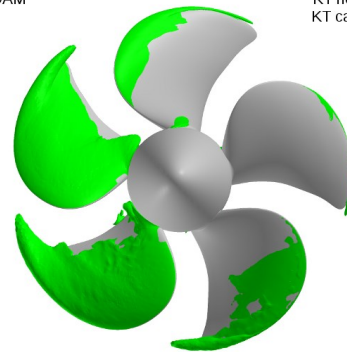
KT non-cav = 0.385
 KT cav = 0.349

CAT-OpenFOAM

KT non-cav = 0.385
 KT cav = 0.349



40 %
vapour
fraction

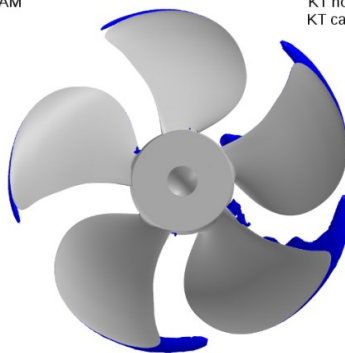


CAT-OpenFOAM

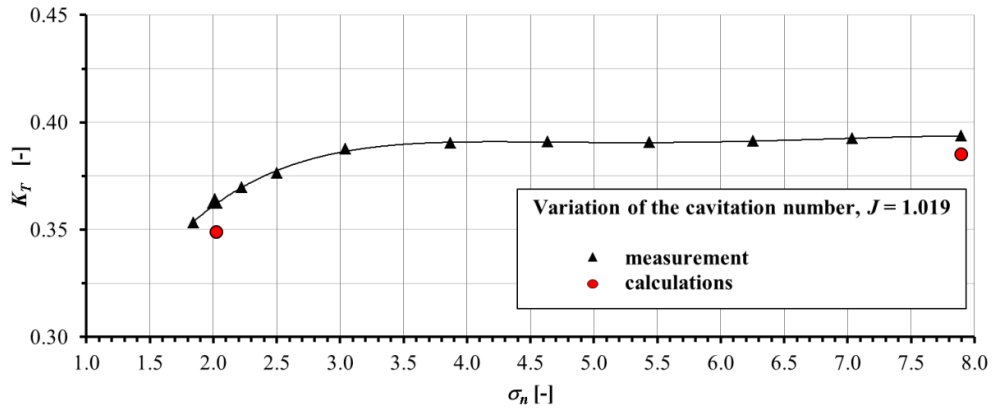
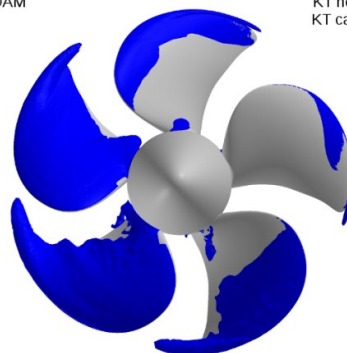
KT non-cav = 0.385
 KT cav = 0.349

CAT-OpenFOAM

KT non-cav = 0.385
 KT cav = 0.349



60 %
vapour
fraction

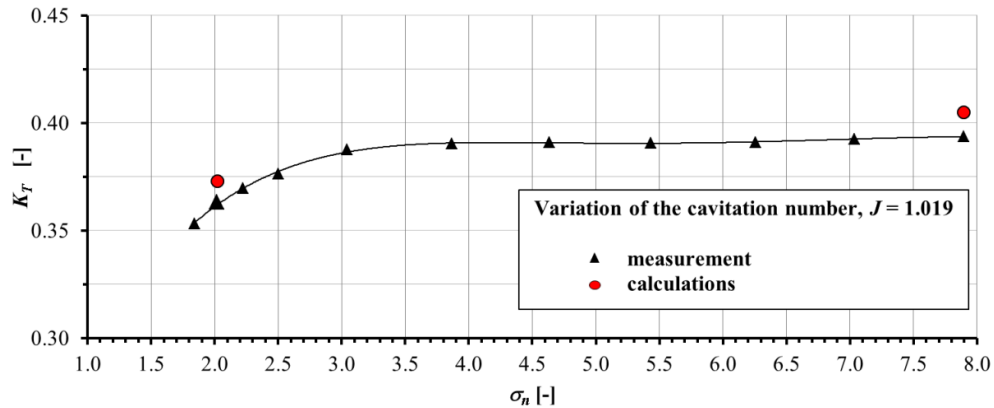
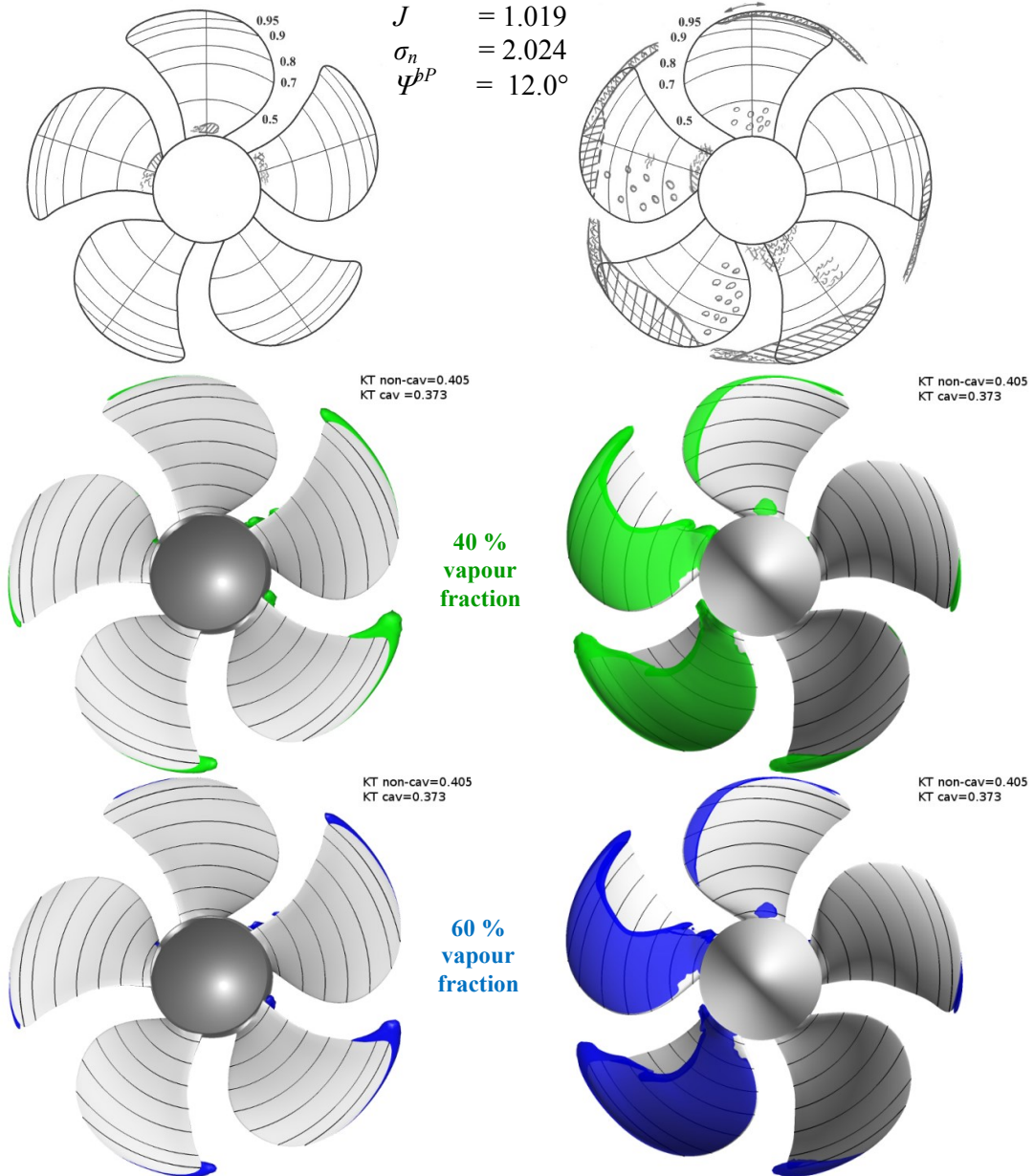


2.5 Case 2.1, Chalmers-OF

Pressure side

Suction side

Case 2.1
 $J = 1.019$
 $\sigma_n = 2.024$
 $\psi^{bP} = 12.0^\circ$



2.6 Case 2.1, CNRS-ISIS

Pressure side

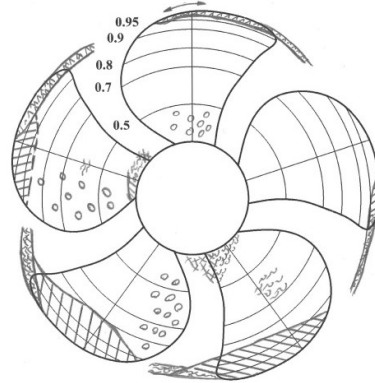
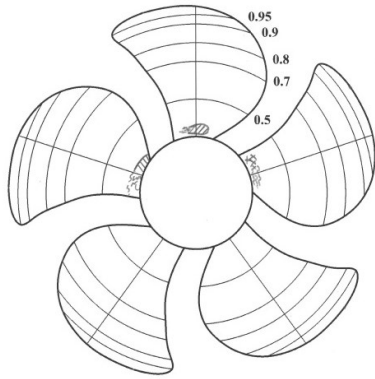
Suction side

Case 2.1

$$J = 1.019$$

$$\sigma_n = 2.024$$

$$\psi^{bP} = 12.0^\circ$$

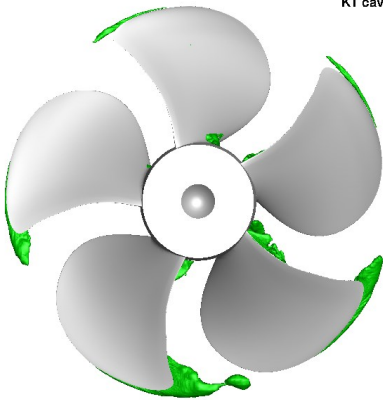


CNRS-ECN ISIS-CFD

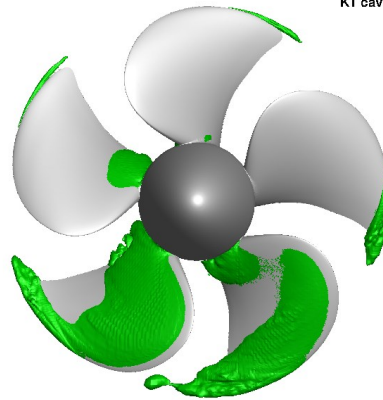
KT non-cav = 0.402
 KT cav = 0.353

CNRS-ECN ISIS-CFD

KT non-cav = 0.402
 KT cav = 0.353



40 %
 vapour
 fraction

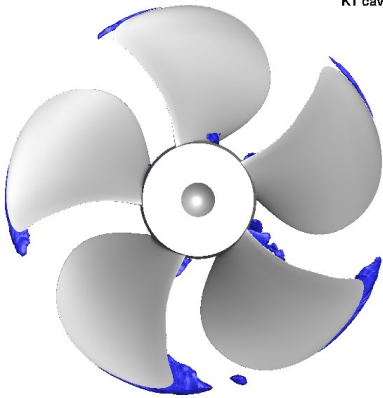


CNRS-ECN ISIS-CFD

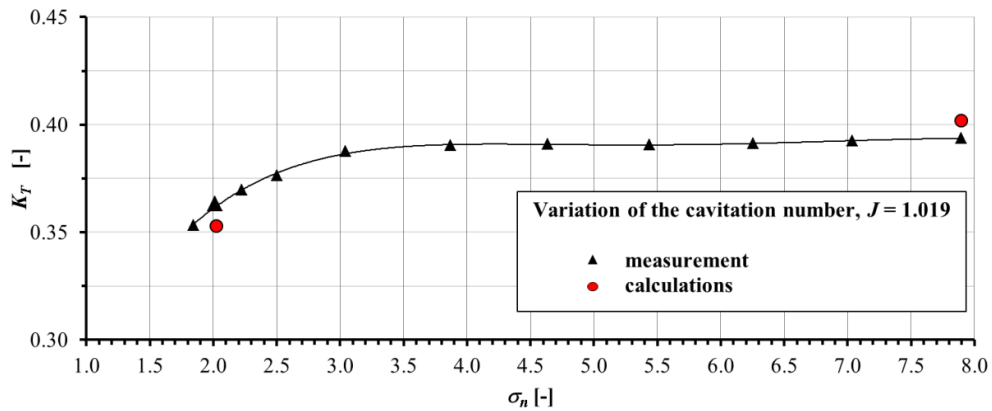
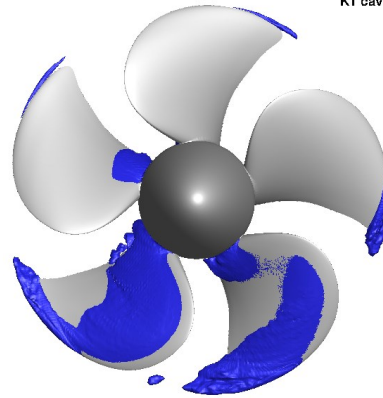
KT non-cav = 0.402
 KT cav = 0.353

CNRS-ECN ISIS-CFD

KT non-cav = 0.402
 KT cav = 0.353



60 %
 vapour
 fraction

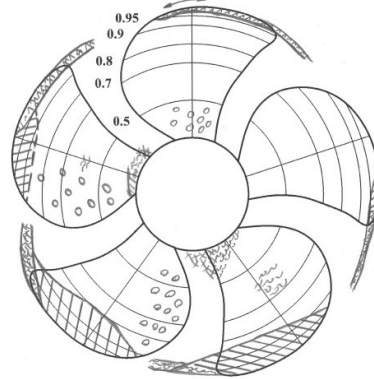
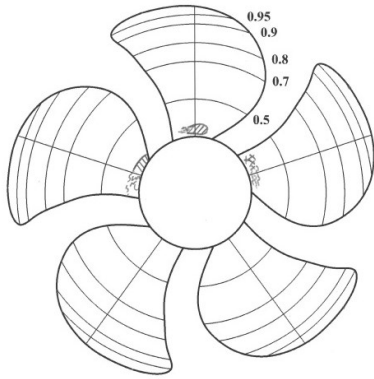


2.7 Case 2.1, CRADLE-SCTetra

Pressure side

Suction side

Case 2.1
 $J = 1.019$
 $\sigma_n = 2.024$
 $\psi^{bP} = 12.0^\circ$

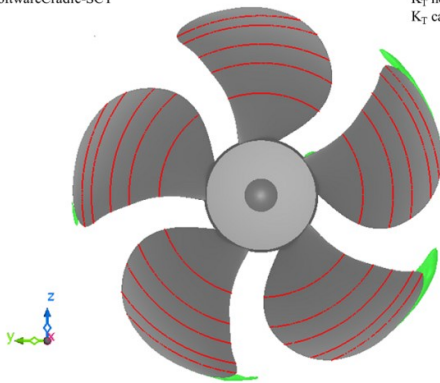


SoftwareCradle-SCT

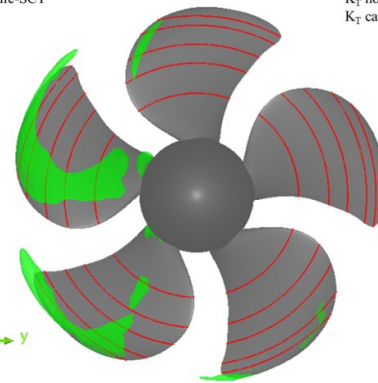
K_T non-cav = 0.417
 K_T cav = 0.372

SoftwareCradle-SCT

K_T non-cav = 0.417
 K_T cav = 0.372



40 %
vapour
fraction

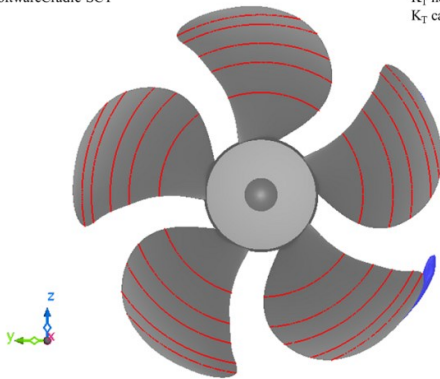


SoftwareCradle-SCT

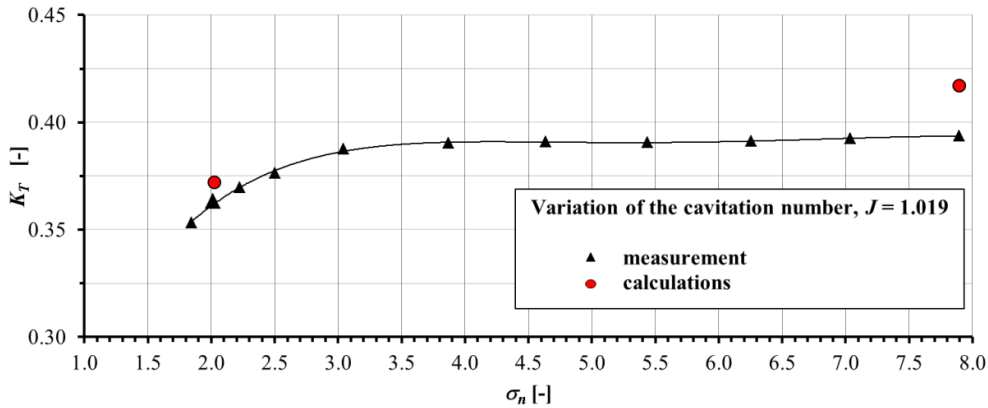
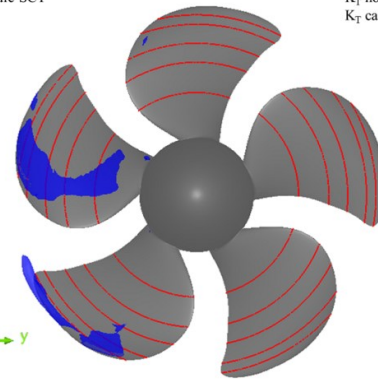
K_T non-cav = 0.417
 K_T cav = 0.372

SoftwareCradle-SCT

K_T non-cav = 0.417
 K_T cav = 0.372



60 %
vapour
fraction

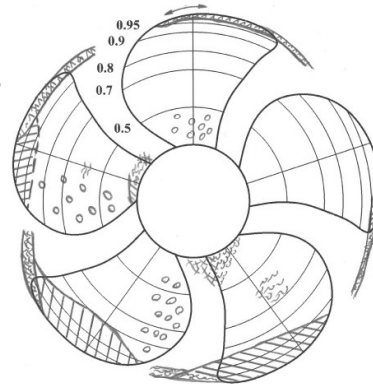
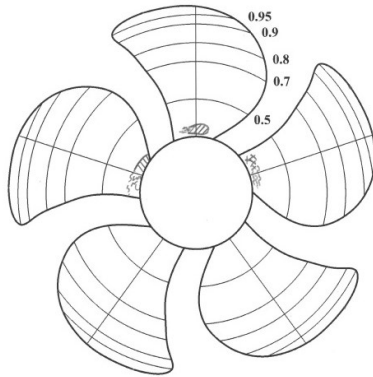


2.8 Case 2.1, CSSRC-Fluent

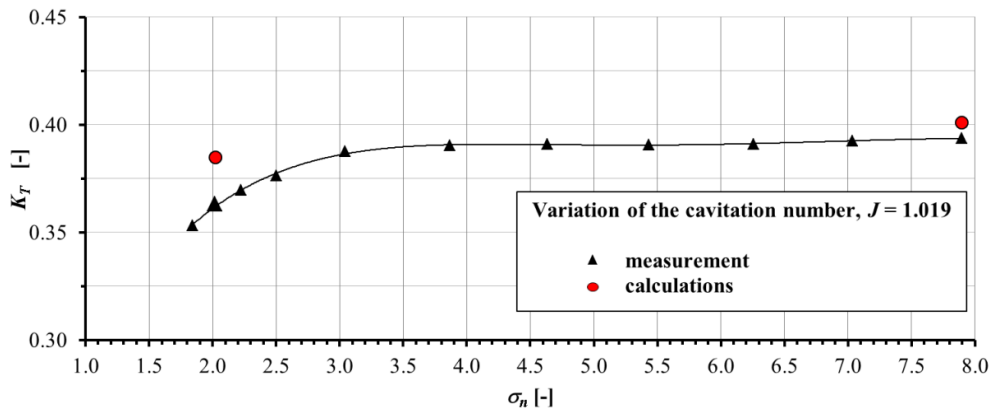
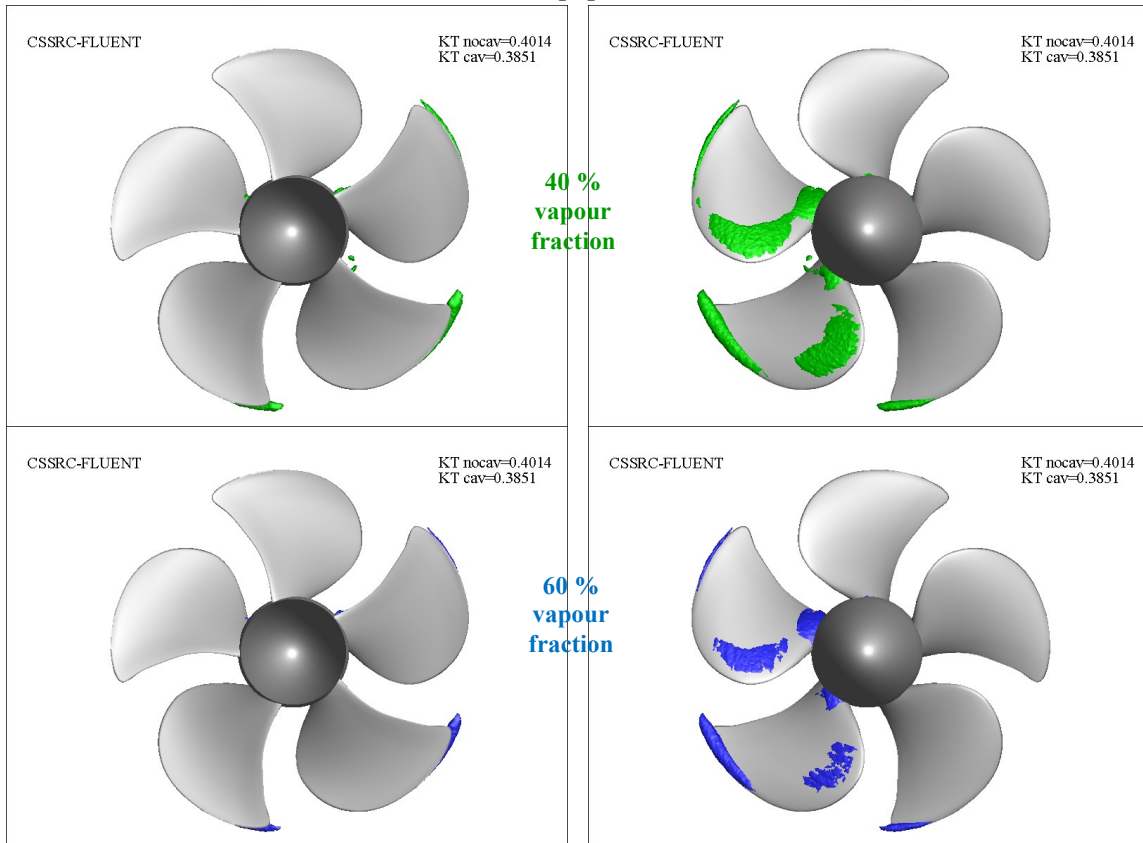
Pressure side

Suction side

Case 2.1
 $J = 1.019$
 $\sigma_n = 2.024$
 $\psi^{bP} = 12.0^\circ$



10% vapour fraction given in paper



2.9 Case 2.1, MARIN-ReFRESCO

Pressure side

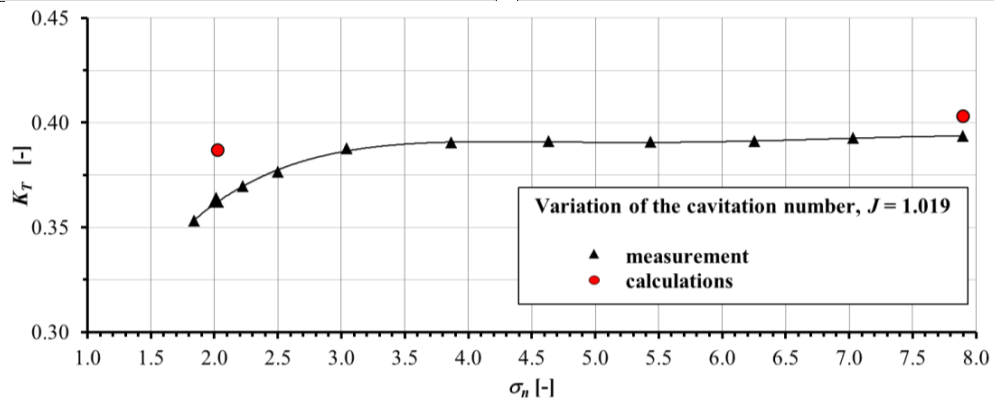
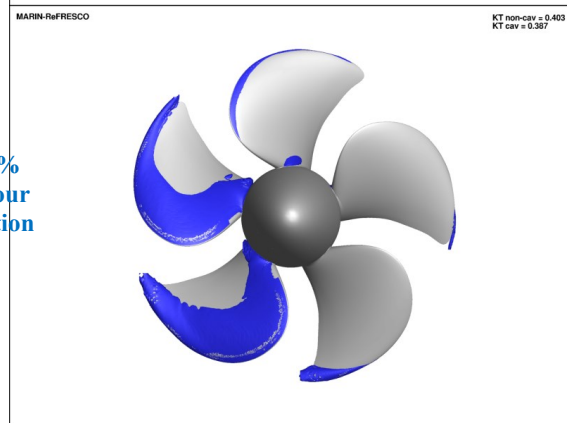
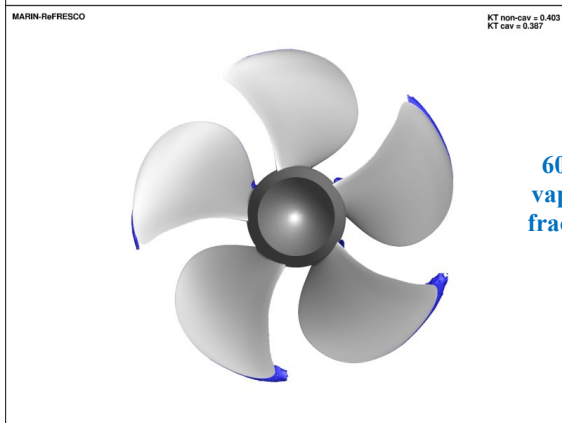
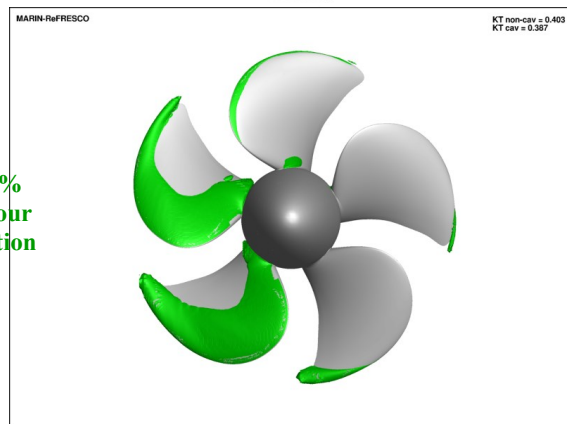
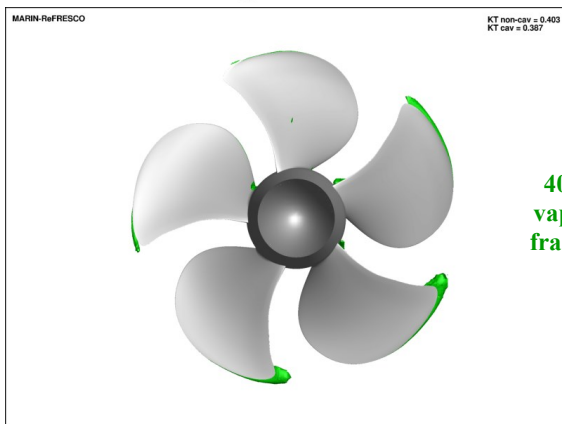
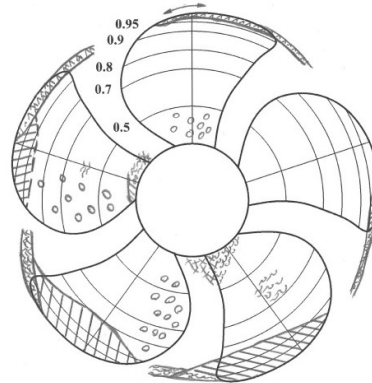
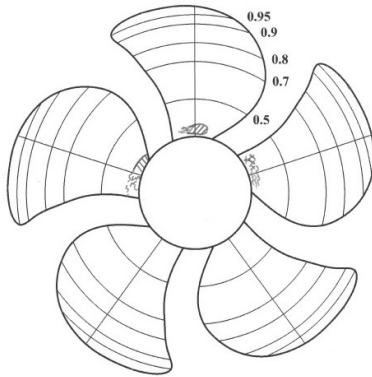
Suction side

Case 2.1

$$J = 1.019$$

$$\sigma_n = 2.024$$

$$\psi^{bP} = 12.0^\circ$$



2.10 Case 2.1, ROTAM-Fluent

Pressure side

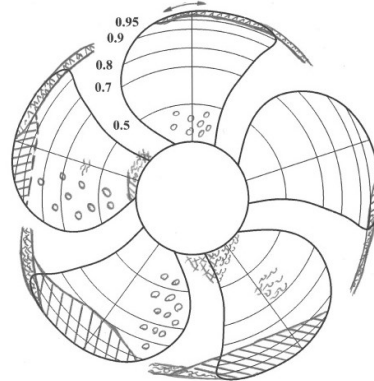
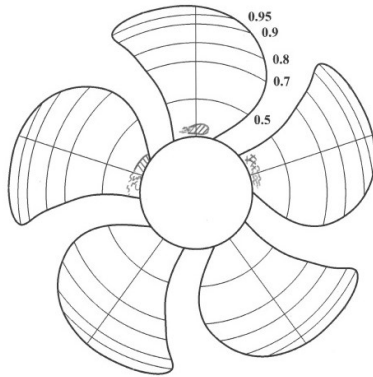
Suction side

Case 2.1

$$J = 1.019$$

$$\sigma_n = 2.024$$

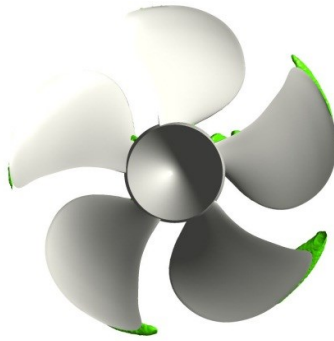
$$\psi^{bP} = 12.0^\circ$$



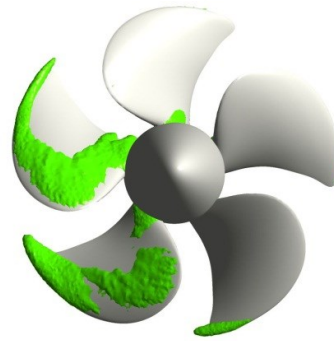
ROTAM-ANSYS

KT non-cav= 0.420
 KT cav= 0.385

KT non-cav= 0.420
 KT cav= 0.385



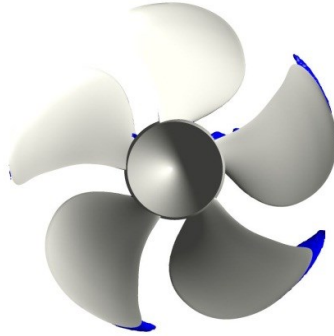
40 %
 vapour
 fraction



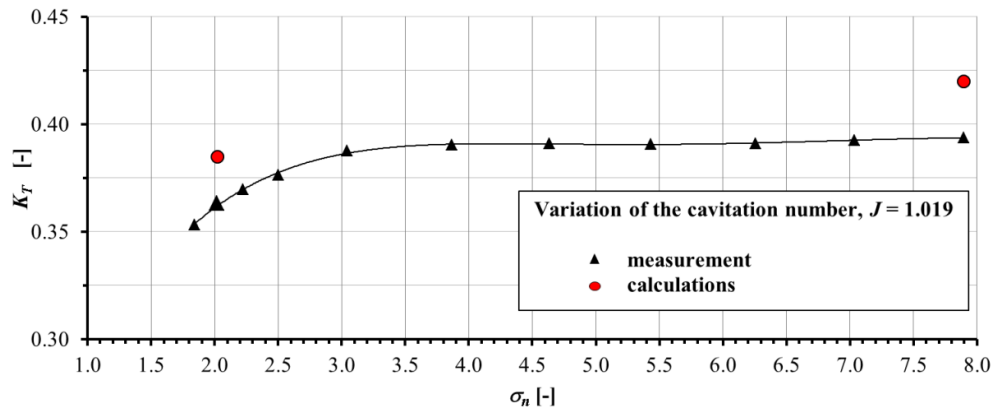
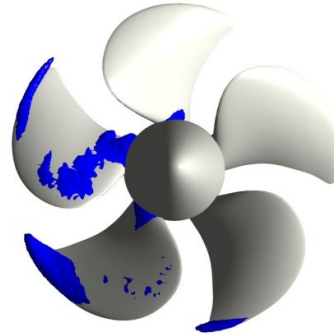
ROTAM-ANSYS

KT non-cav= 0.420
 KT cav= 0.385

KT non-cav= 0.420
 KT cav= 0.385



60 %
 vapour
 fraction

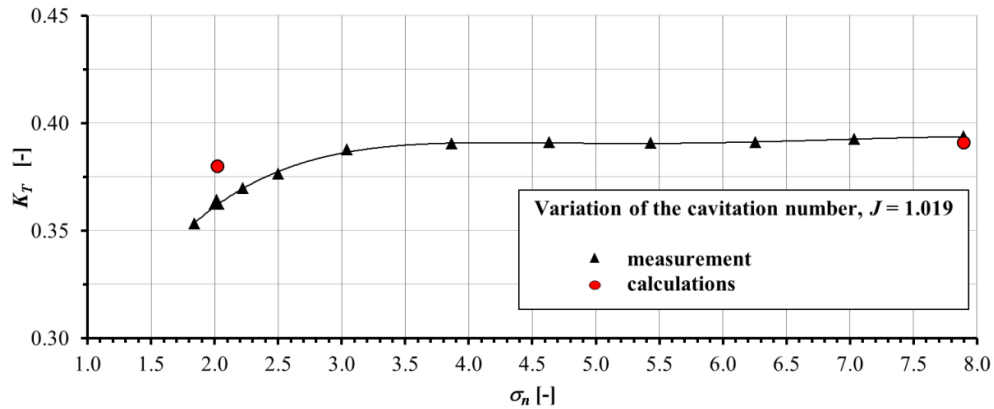
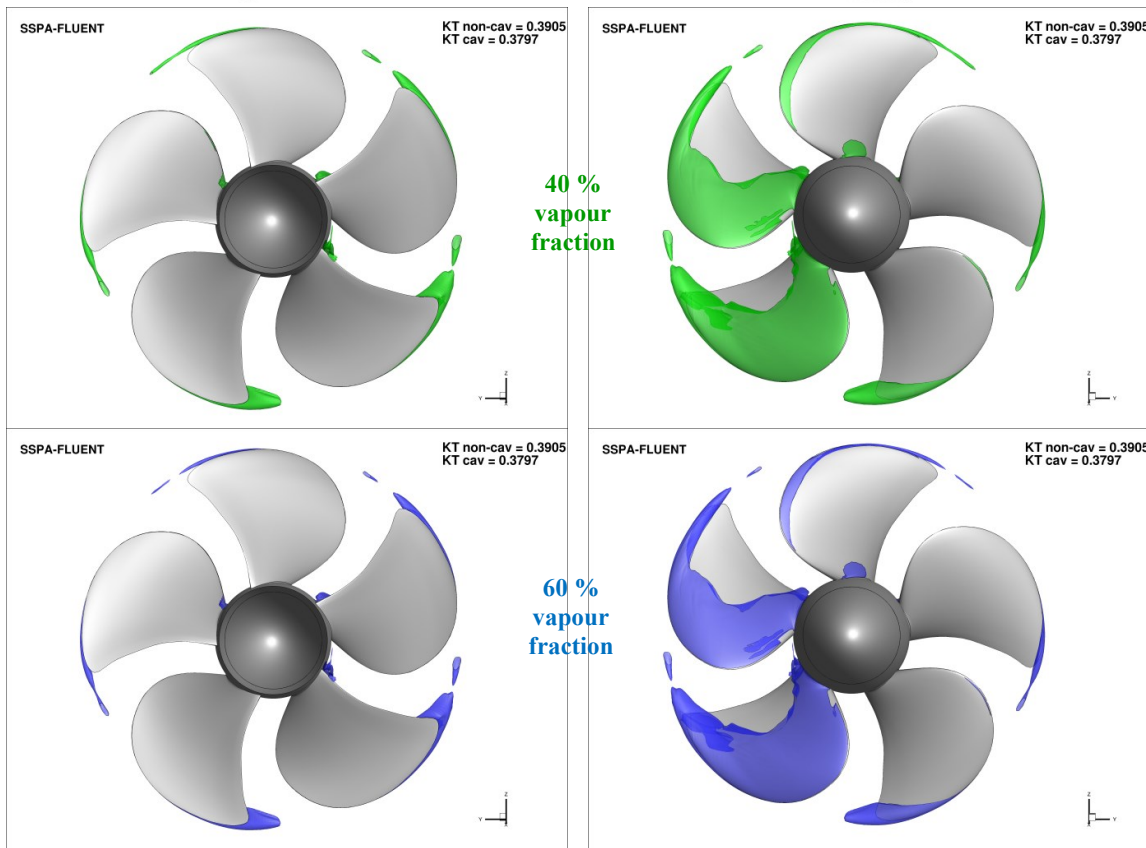
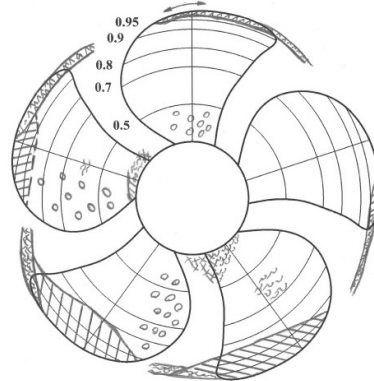
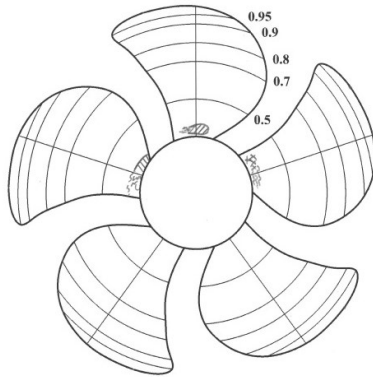


2.11 Case 2.1, SSPA-Fluent-Sauer

Pressure side

Suction side

Case 2.1
 $J = 1.019$
 $\sigma_n = 2.024$
 $\psi^{bP} = 12.0^\circ$



2.12 Case 2.1, SSPA-Fluent-Zwart1

Pressure side

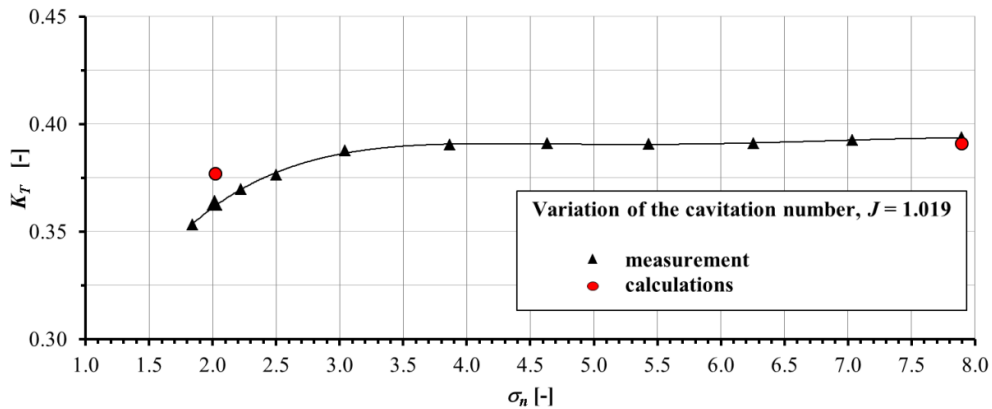
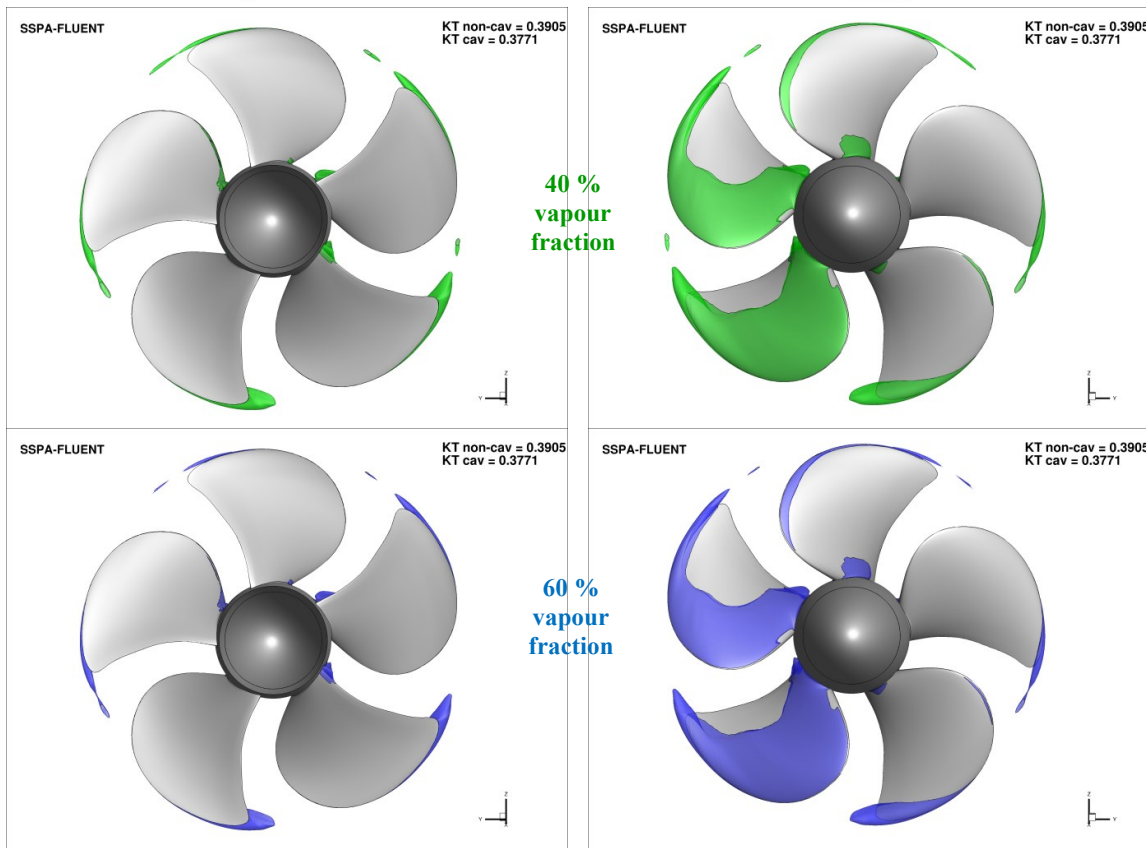
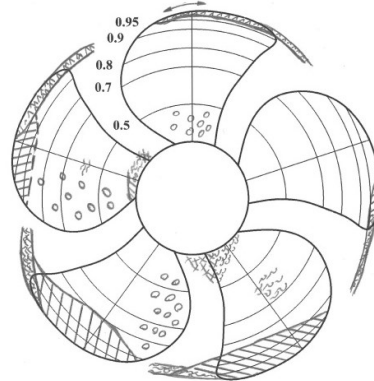
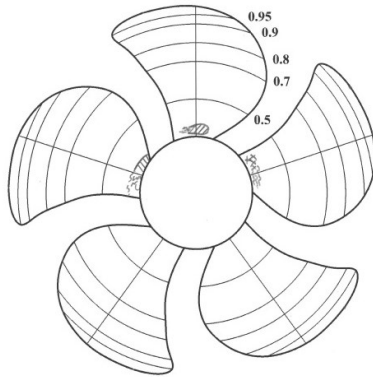
Suction side

Case 2.1

$$J = 1.019$$

$$\sigma_n = 2.024$$

$$\psi^{bP} = 12.0^\circ$$



2.13 Case 2.1, SSPA-Fluent-Zwart2

Pressure side

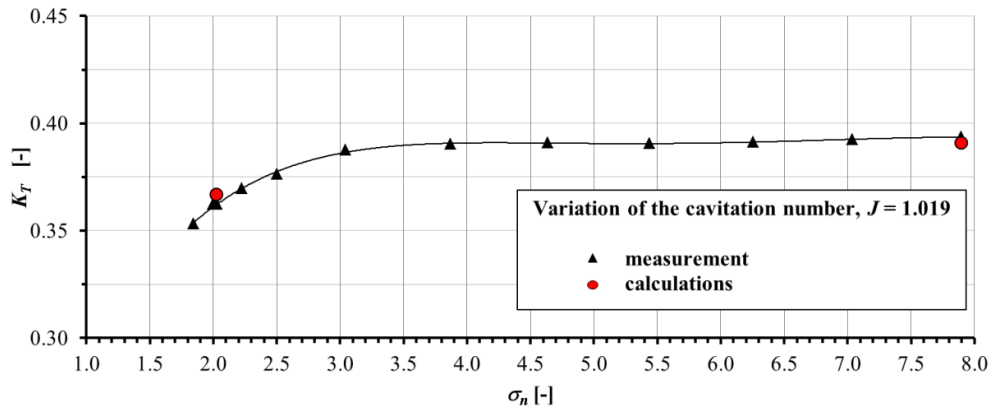
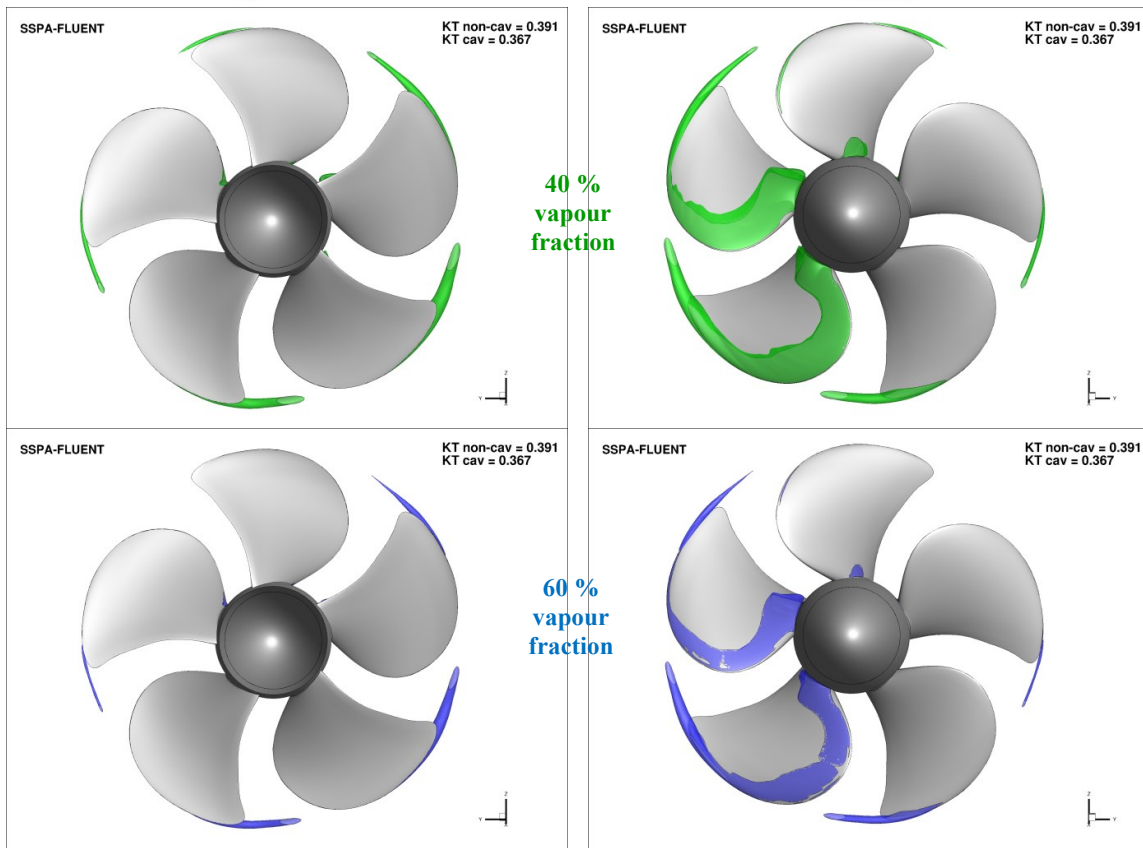
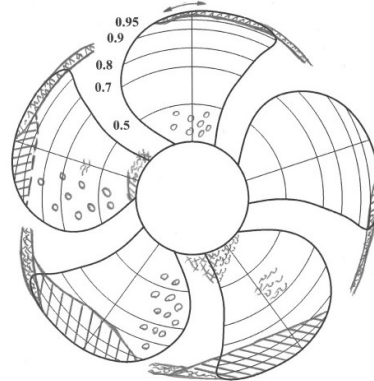
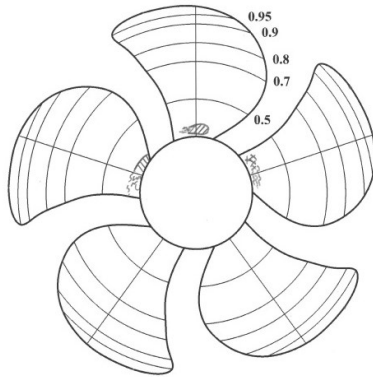
Suction side

Case 2.1

$$J = 1.019$$

$$\sigma_n = 2.024$$

$$\psi^{bP} = 12.0^\circ$$



2.14 Case 2.1, TUHH-CFX

Pressure side

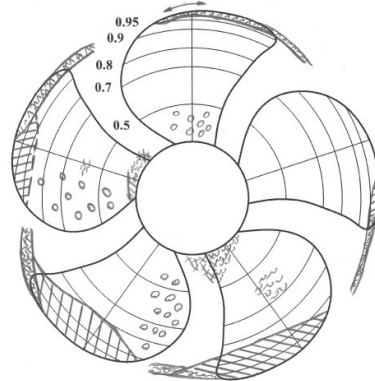
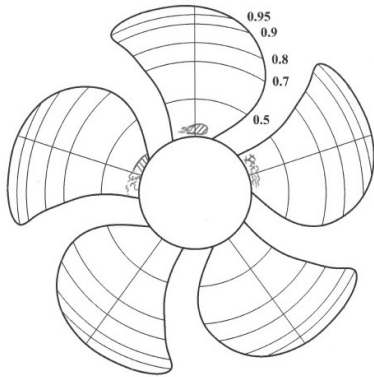
Suction side

Case 2.1

$$J = 1.019$$

$$\sigma_n = 2.024$$

$$\psi^{bP} = 12.0^\circ$$

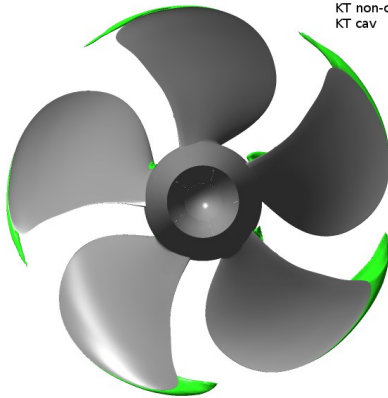


TUHH-CFX

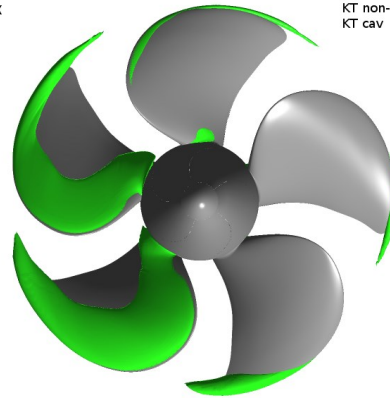
KT non-cav = 0.3946
 KT cav = 0.3862

TUHH-CFX

KT non-cav = 0.3946
 KT cav = 0.3862



40 %
 vapour
 fraction

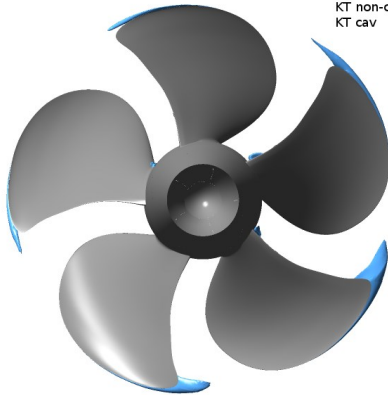


TUHH-CFX

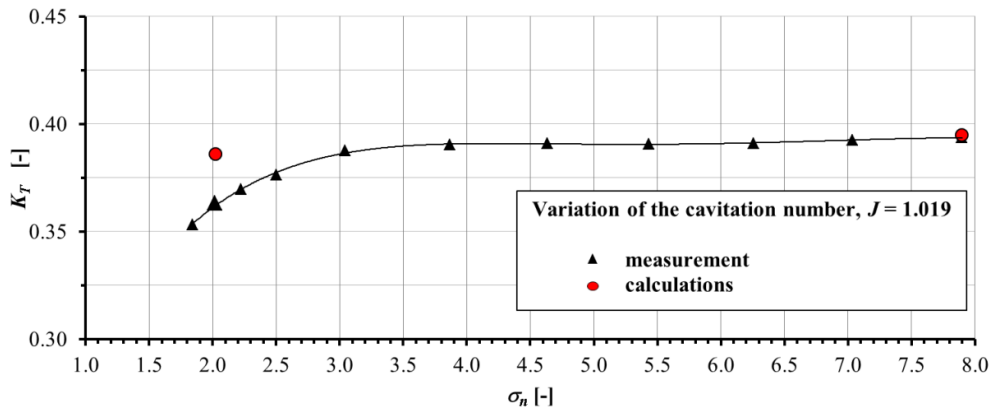
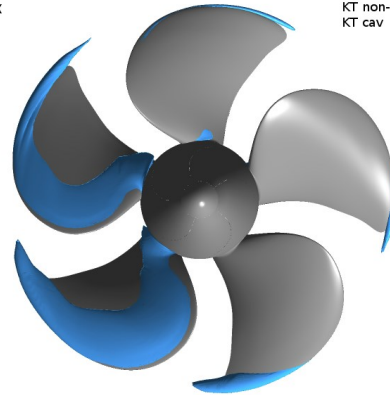
KT non-cav = 0.3946
 KT cav = 0.3862

TUHH-CFX

KT non-cav = 0.3946
 KT cav = 0.3862



60 %
 vapour
 fraction



2.15 Case 2.1, TUHH-panMARE

Pressure side

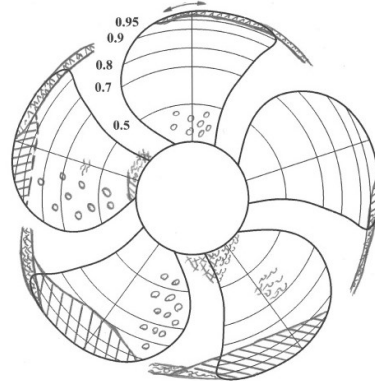
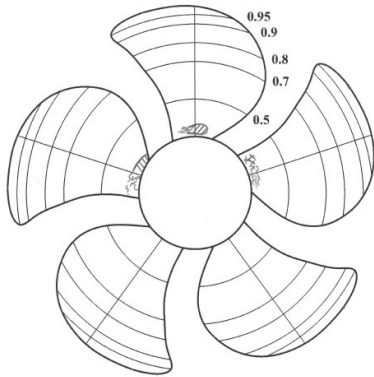
Suction side

Case 2.1

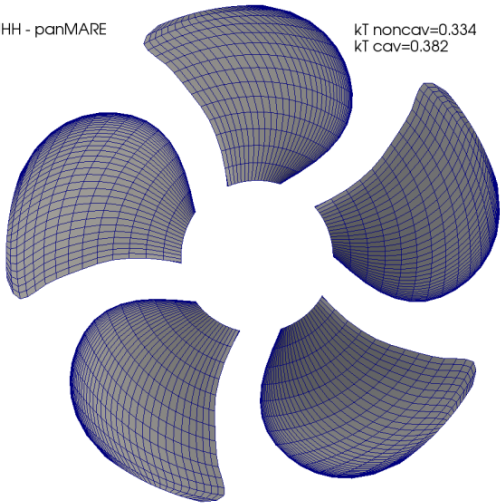
$$J = 1.019$$

$$\sigma_n = 2.024$$

$$\psi^{bP} = 12.0^\circ$$

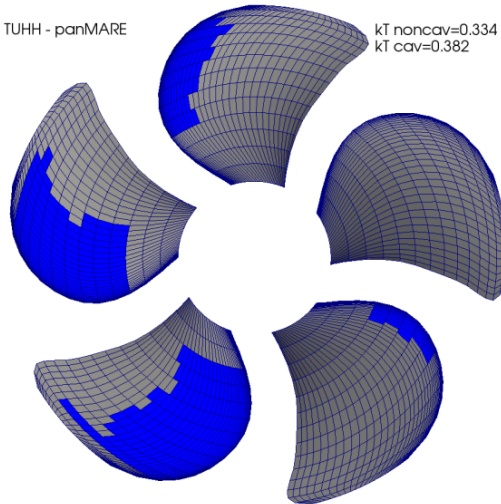


TUHH - panMARE

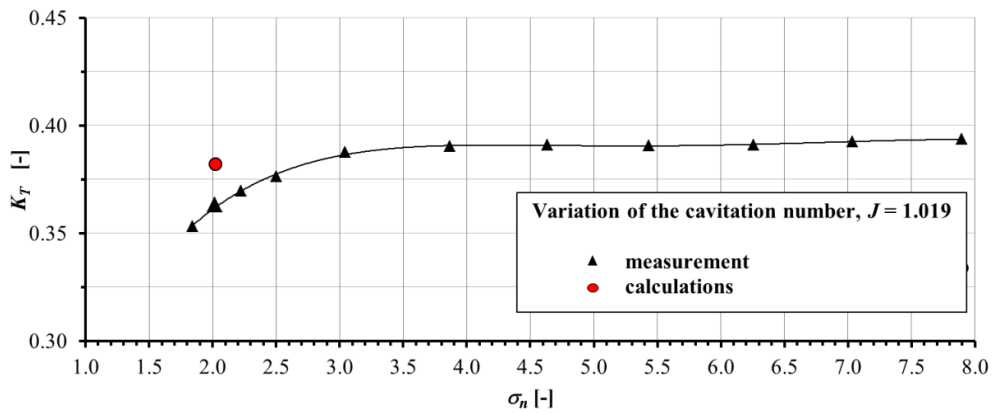


kT noncav=0.334
kT cav=0.382

TUHH - panMARE



kT noncav=0.334
kT cav=0.382



2.16 Case 2.1, UniGenoa-BEM

Pressure side

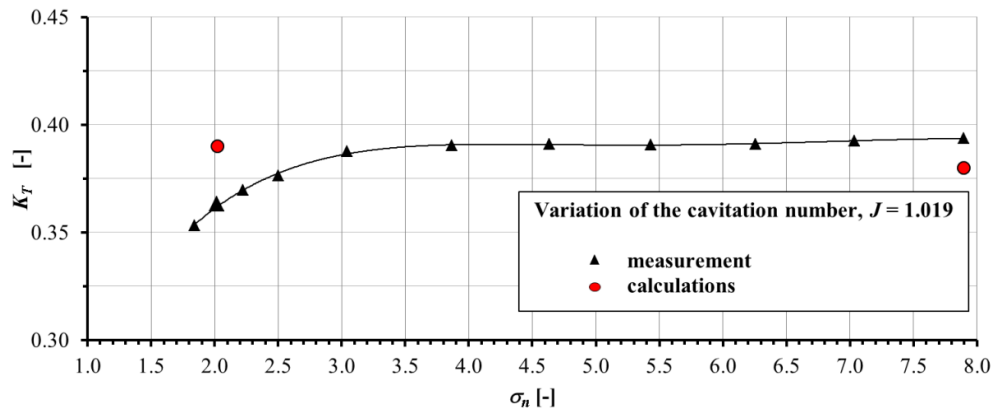
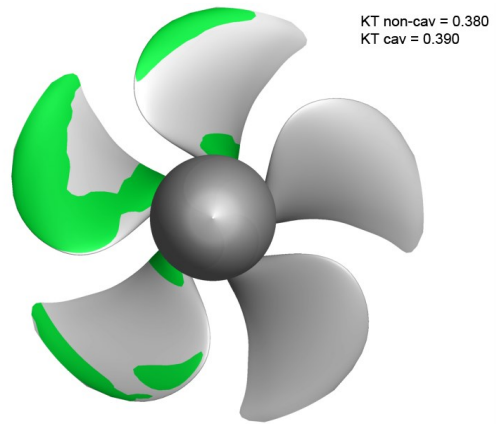
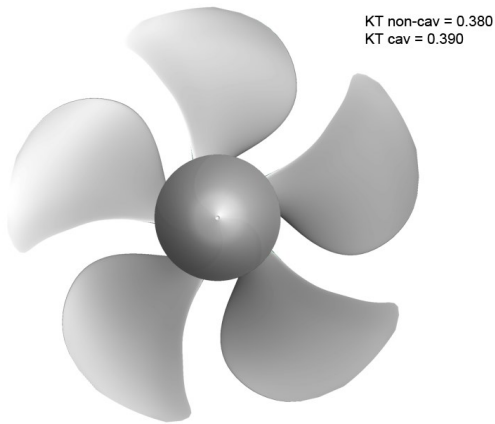
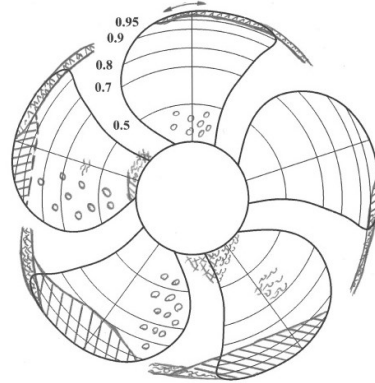
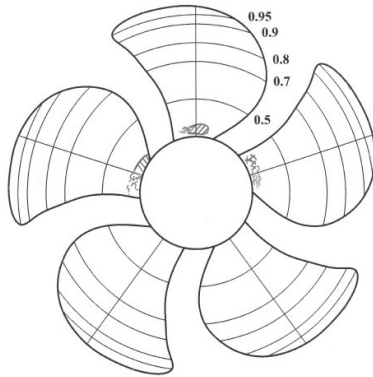
Case 2.1

Suction side

$$J = 1.019$$

$$\sigma_n = 2.024$$

$$\psi^{bP} = 12.0^\circ$$



2.17 Case 2.1, UniGenoa-StarCCM+

Pressure side

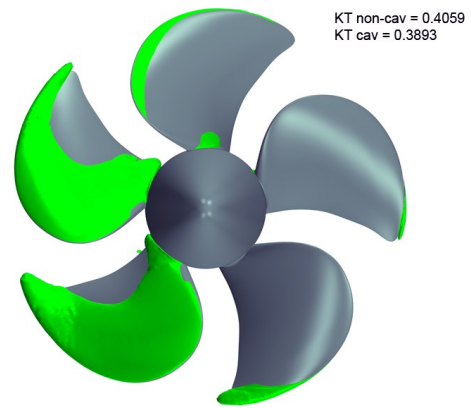
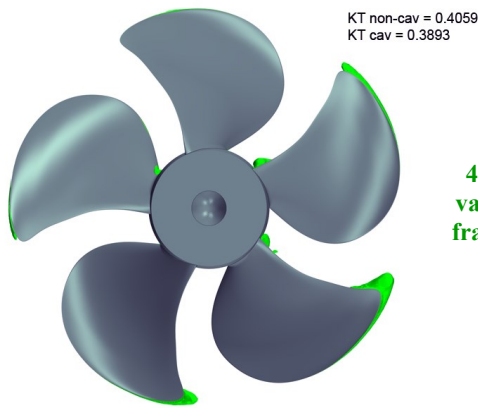
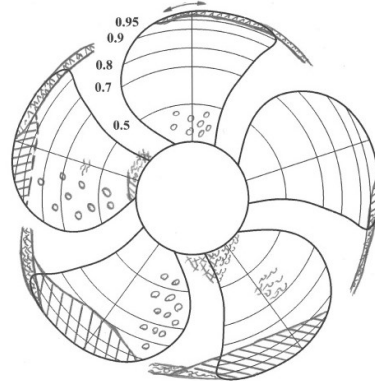
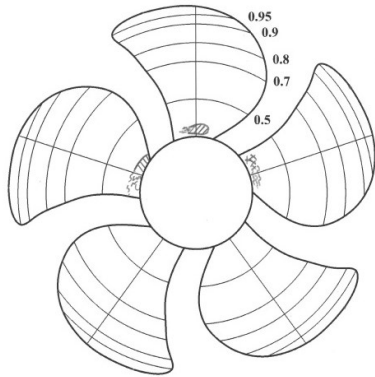
Suction side

Case 2.1

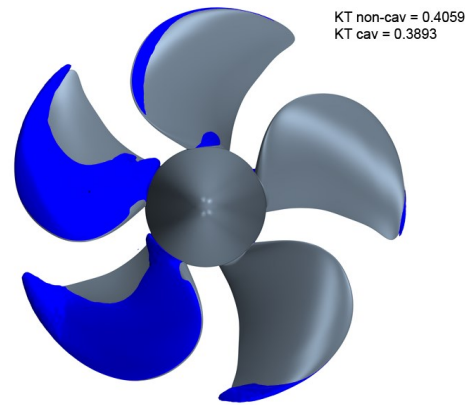
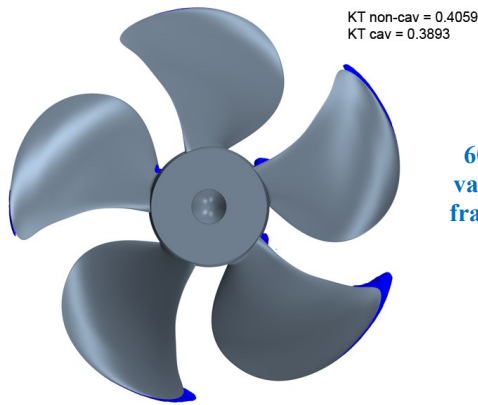
$$J = 1.019$$

$$\sigma_n = 2.024$$

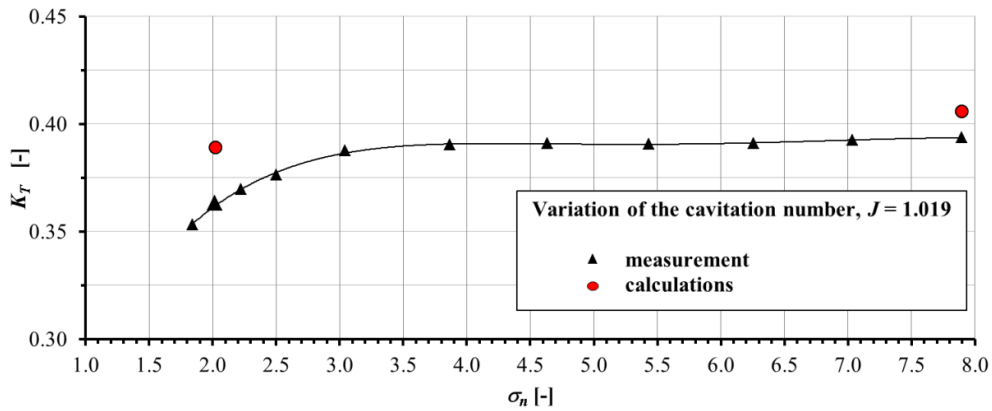
$$\psi^{bP} = 12.0^\circ$$



40 %
vapour
fraction



60 %
vapour
fraction



2.18 Case 2.1, UTAustin-PROPCAV

Pressure side

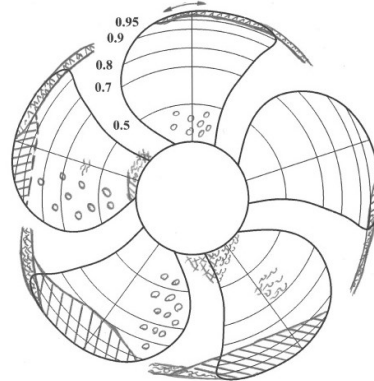
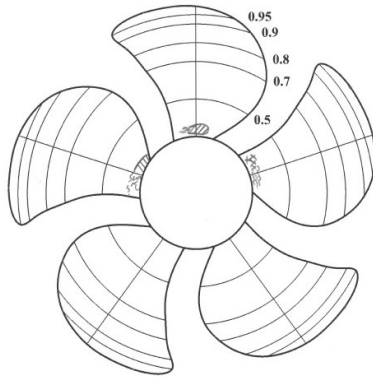
Suction side

Case 2.1

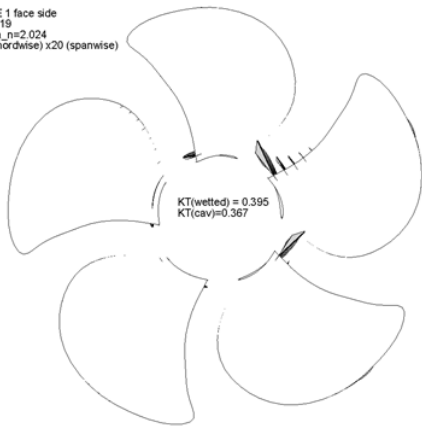
$$J = 1.019$$

$$\sigma_n = 2.024$$

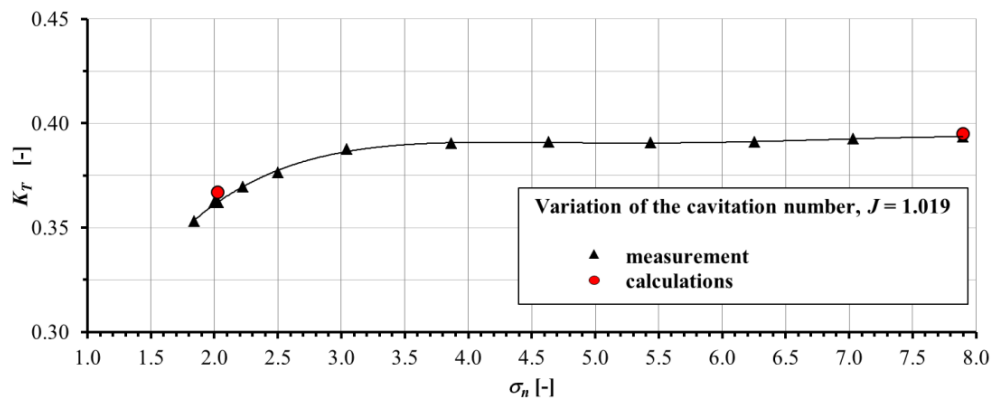
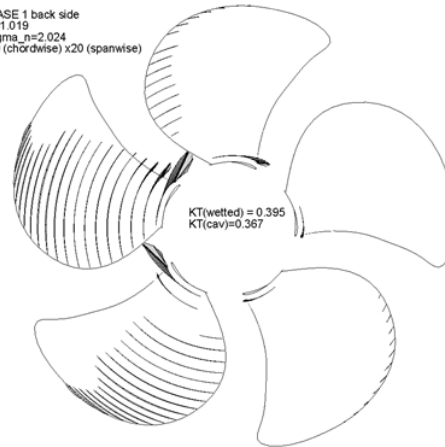
$$\psi^{bP} = 12.0^\circ$$



CASE 1 face side
 J=1.019
 sigma_n=2.024
 60 (chordwise) x20 (spanwise)



CASE 1 back side
 J=1.019
 sigma_n=2.024
 60 (chordwise) x20 (spanwise)

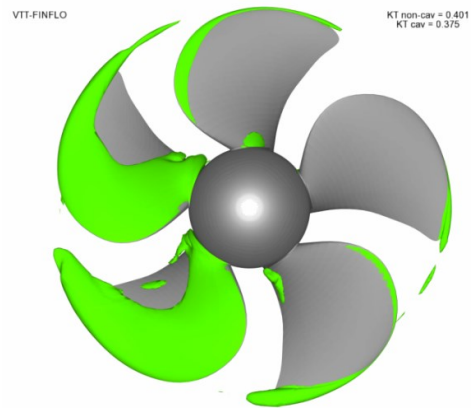
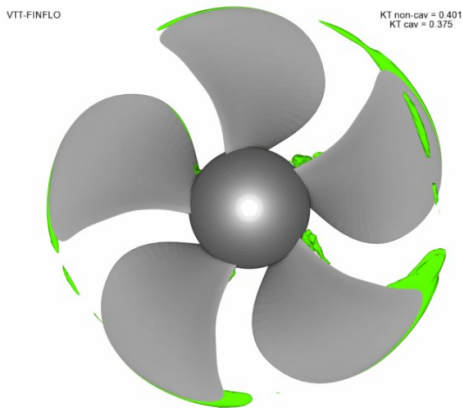
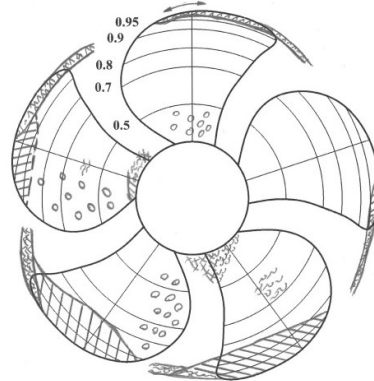
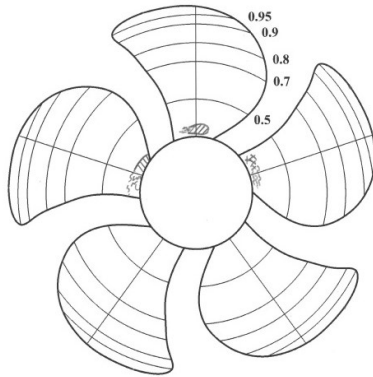


2.19 Case 2.1, VTT-FinFlo

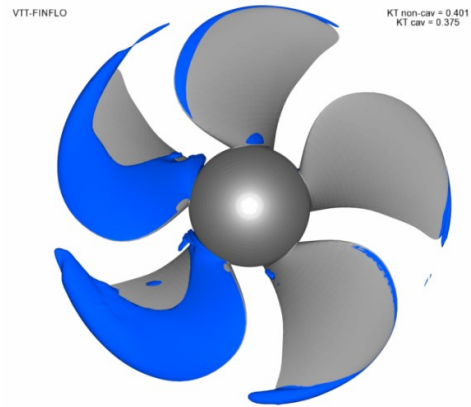
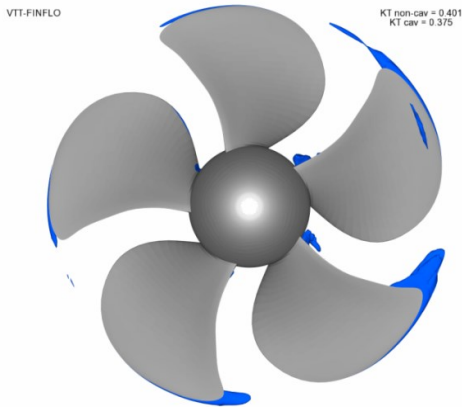
Pressure side

Suction side

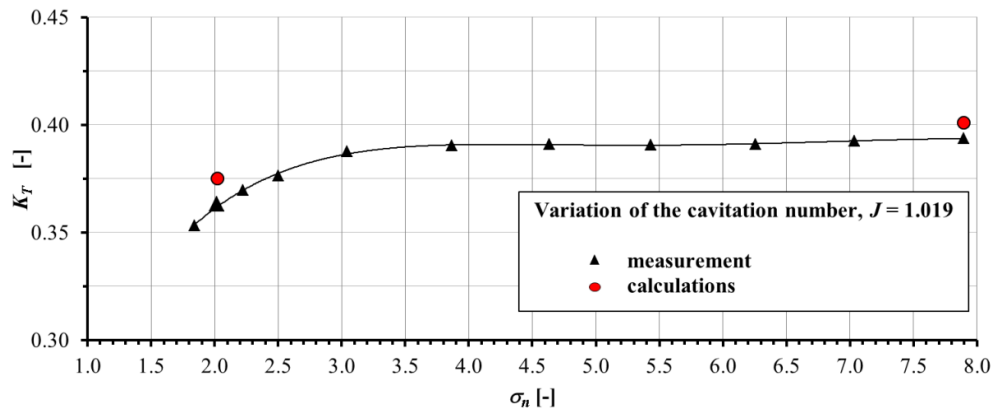
Case 2.1
 $J = 1.019$
 $\sigma_n = 2.024$
 $\psi^{bP} = 12.0^\circ$



40 %
vapour
fraction



60 %
vapour
fraction



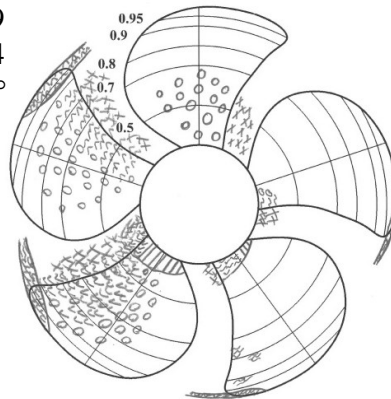
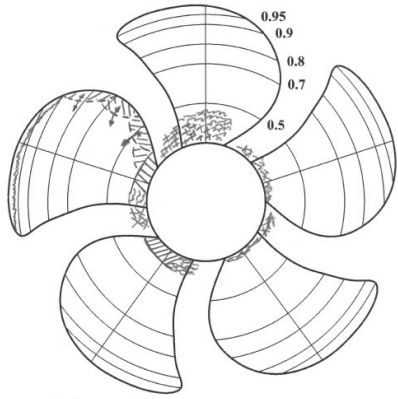
3 Case 2.2

3.1 Case 2.2, ACCUSIM-CFX-FCM

Pressure side

Suction side

Case 2.2
 $J = 1.269$
 $\sigma_n = 1.424$
 $\psi^{bP} = 12.0^\circ$

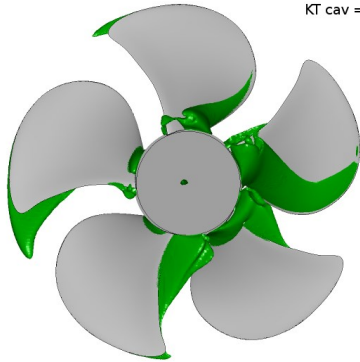


ACCUSIM-CFX-FCM

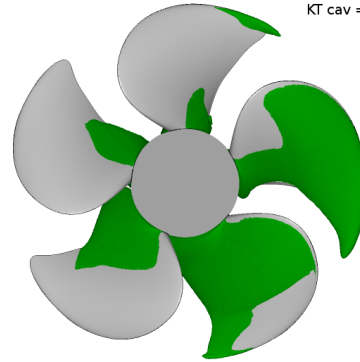
KT non-cav = 0.255
 KT cav = 0.173

ACCUSIM-CFX-FCM

KT non-cav = 0.255
 KT cav = 0.173



40 %
vapour
fraction

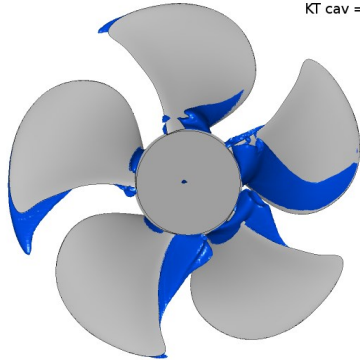


ACCUSIM-CFX-FCM

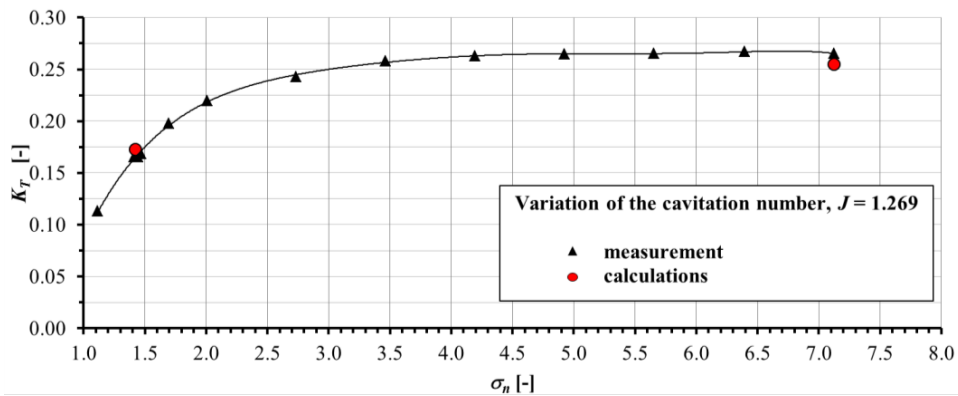
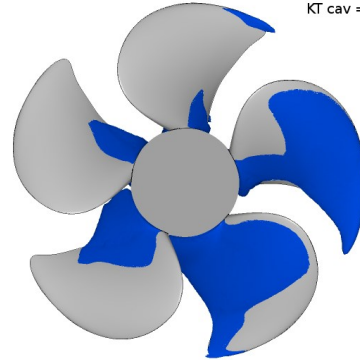
KT non-cav = 0.255
 KT cav = 0.173

ACCUSIM-CFX-FCM

KT non-cav = 0.255
 KT cav = 0.173



60 %
vapour
fraction

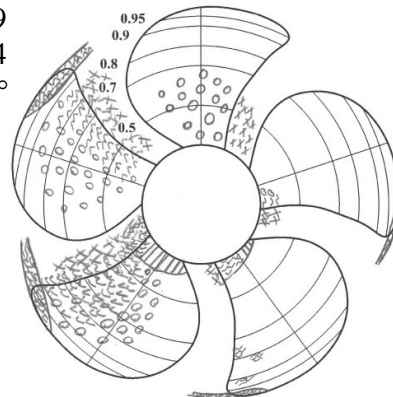
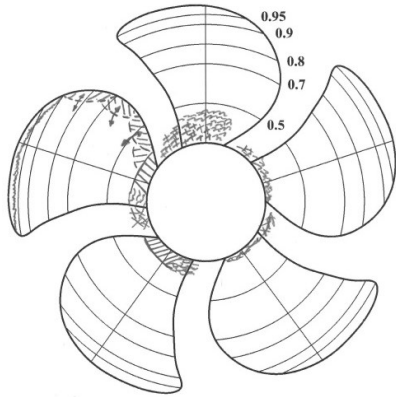


3.2 Case 2.2, ACCUSIM-CFX-Kunz

Pressure side

Suction side

Case 2.2
 $J = 1.269$
 $\sigma_n = 1.424$
 $\psi^{bP} = 12.0^\circ$

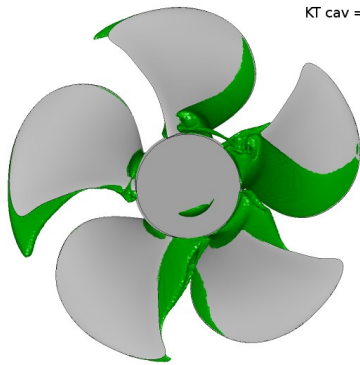


ACCUSIM-CFX-KUNZ

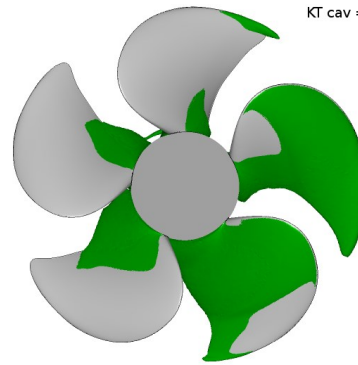
KT non-cav = 0.255
 KT cav = 0.166

ACCUSIM-CFX-KUNZ

KT non-cav = 0.255
 KT cav = 0.166



40 %
vapour
fraction

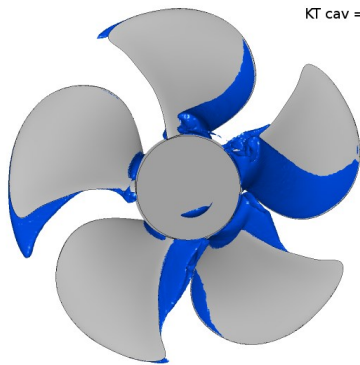


ACCUSIM-CFX-KUNZ

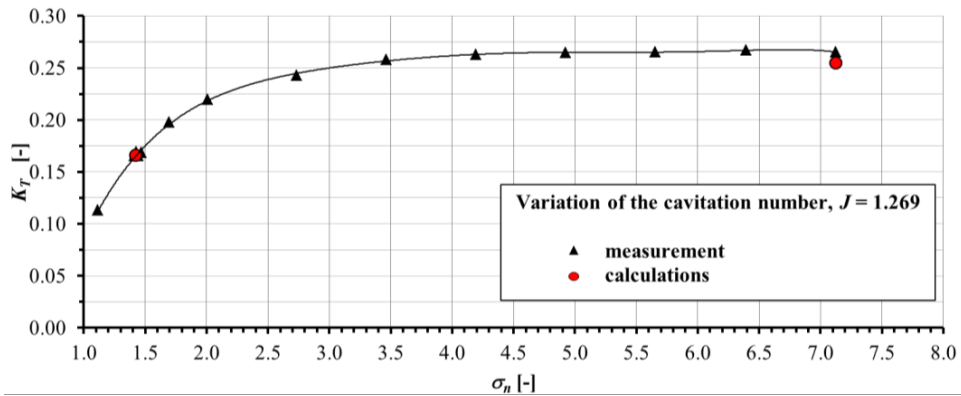
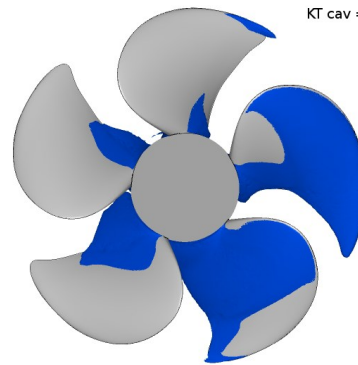
KT non-cav = 0.255
 KT cav = 0.166

ACCUSIM-CFX-KUNZ

KT non-cav = 0.255
 KT cav = 0.166



60 %
vapour
fraction

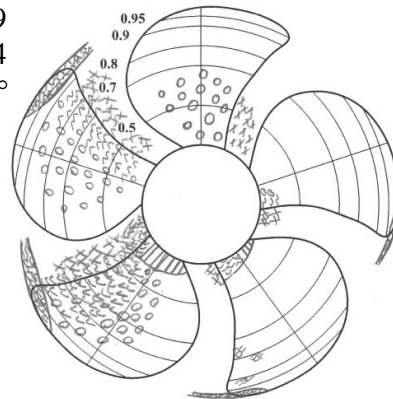
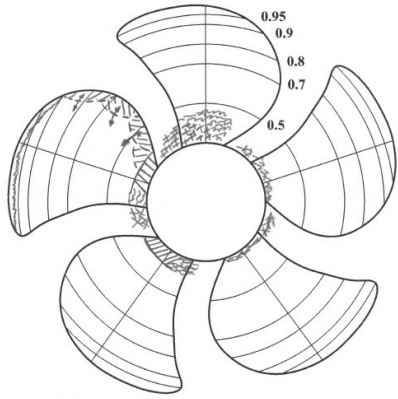


3.3 Case 2.2, ACCUSIM-CFX-Zwart

Pressure side

Suction side

Case 2.2
 $J = 1.269$
 $\sigma_n = 1.424$
 $\psi^{bP} = 12.0^\circ$

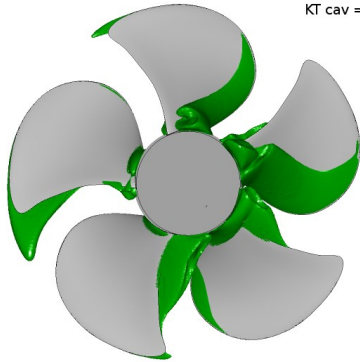


ACCUSIM-CFX-ZWART

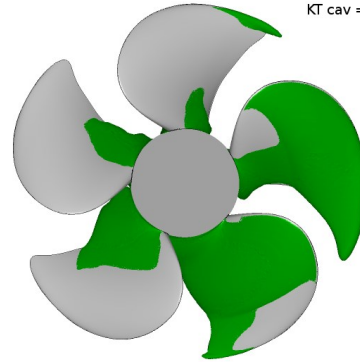
KT non-cav = 0.255
 KT cav = 0.166

ACCUSIM-CFX-ZWART

KT non-cav = 0.255
 KT cav = 0.166



40 %
vapour
fraction

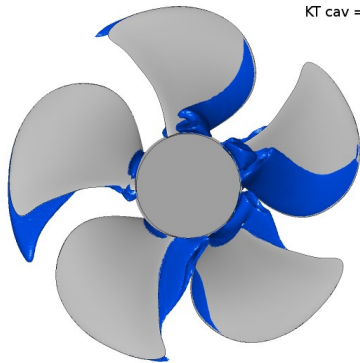


ACCUSIM-CFX-ZWART

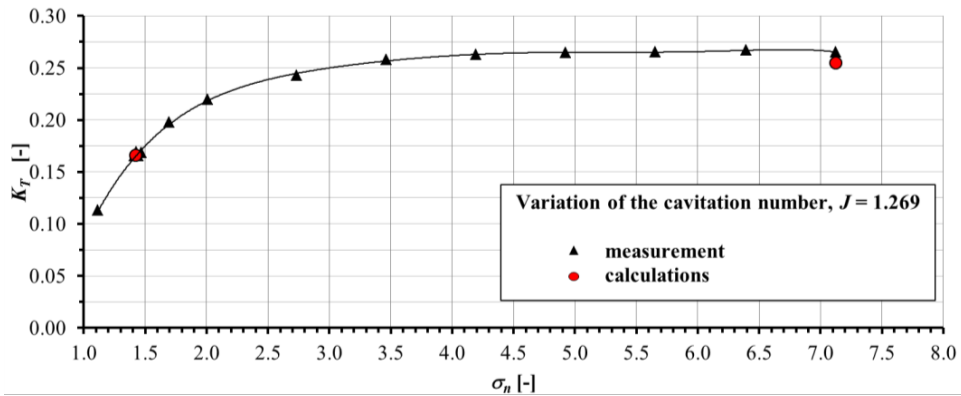
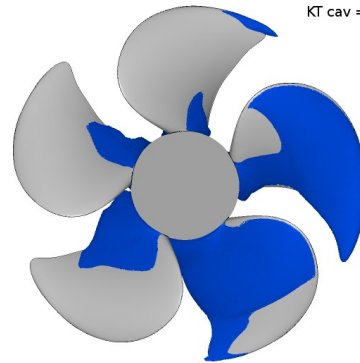
KT non-cav = 0.255
 KT cav = 0.166

ACCUSIM-CFX-ZWART

KT non-cav = 0.255
 KT cav = 0.166



60 %
vapour
fraction

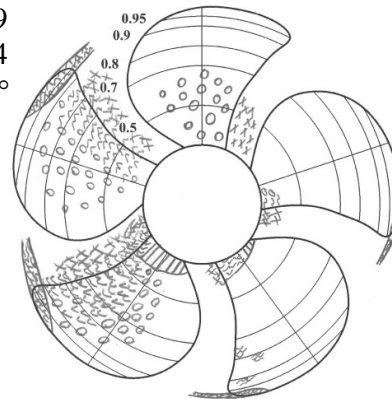
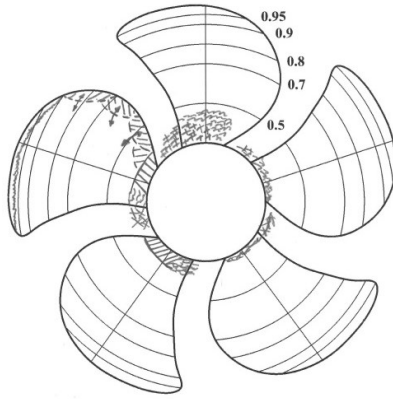


3.4 Case 2.2, CAT-OF

Pressure side

Suction side

Case 2.2
 $J = 1.269$
 $\sigma_n = 1.424$
 $\psi^{bP} = 12.0^\circ$

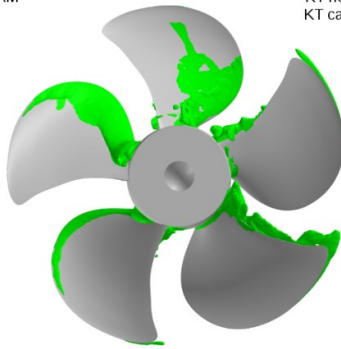


CAT-OpenFOAM

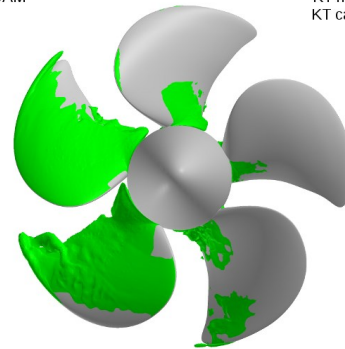
KT non-cav = 0.287
 KT cav = 0.157

CAT-OpenFOAM

KT non-cav = 0.287
 KT cav = 0.157



40 %
vapour
fraction

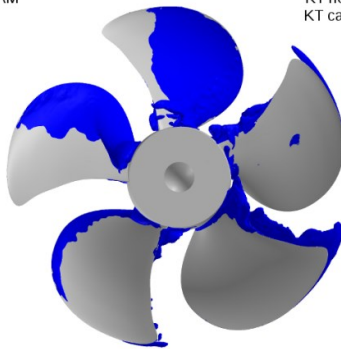


CAT-OpenFOAM

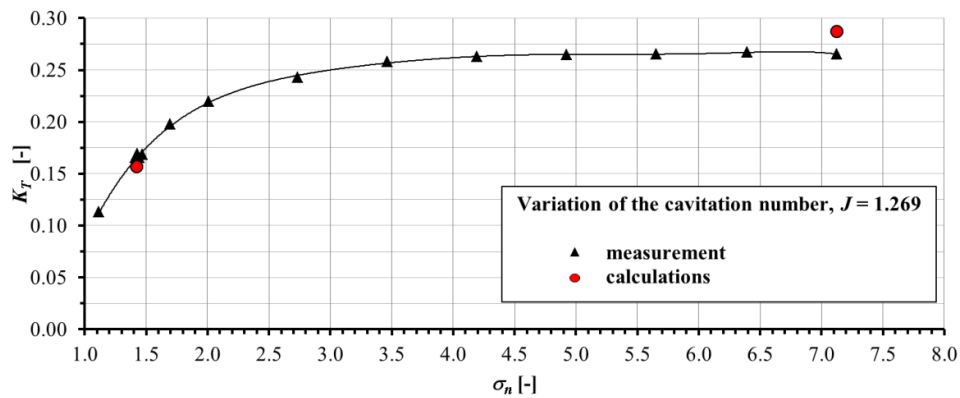
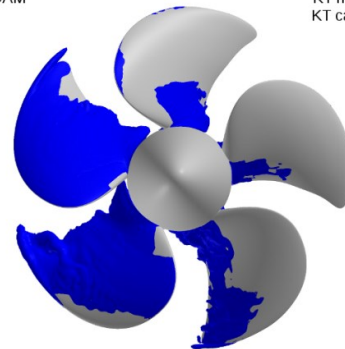
KT non-cav = 0.287
 KT cav = 0.157

CAT-OpenFOAM

KT non-cav = 0.287
 KT cav = 0.157



60 %
vapour
fraction

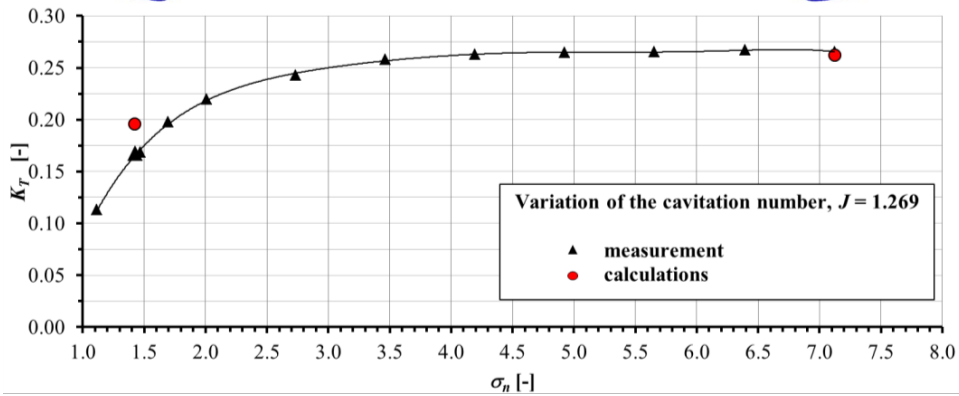
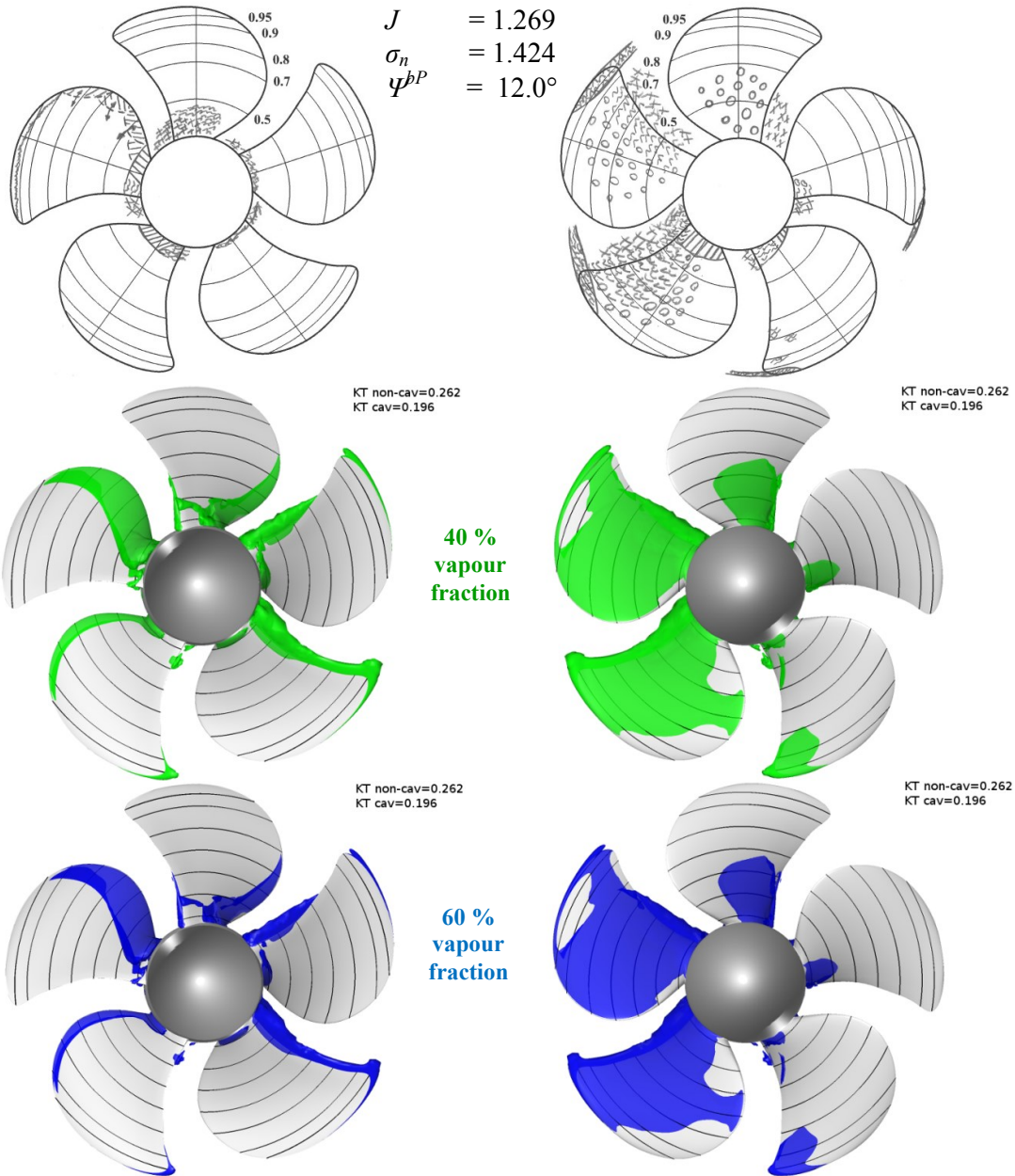


3.5 Case 2.2, Chalmers-OF

Pressure side

Suction side

Case 2.2
 $J = 1.269$
 $\sigma_n = 1.424$
 $\psi^{bP} = 12.0^\circ$

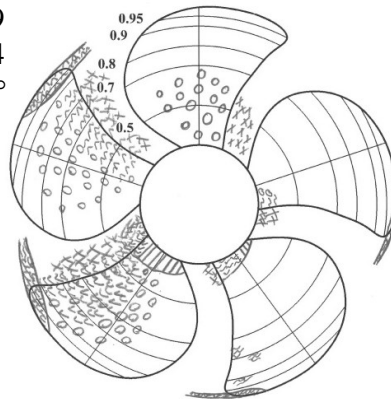
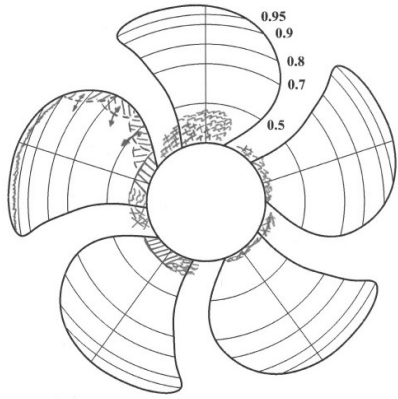


3.6 Case 2.2, CNRS-ISIS

Pressure side

Suction side

Case 2.2
 $J = 1.269$
 $\sigma_n = 1.424$
 $\psi^{bP} = 12.0^\circ$

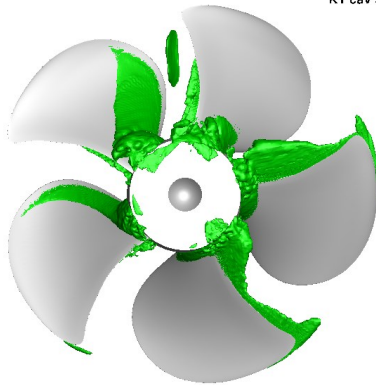


CNRS-ECN ISIS-CFD

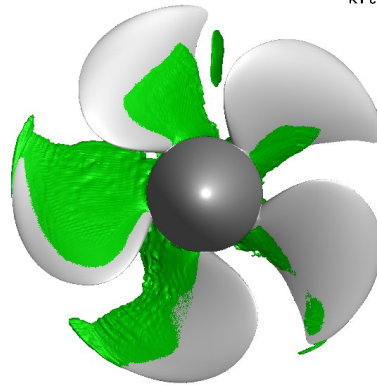
KT non-cav = 0.266
 KT cav = 0.122

CNRS-ECN ISIS-CFD

KT non-cav = 0.266
 KT cav = 0.122



40 %
vapour
fraction

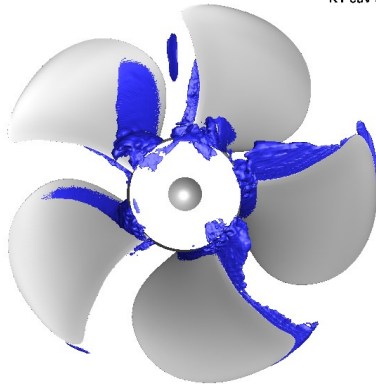


CNRS-ECN ISIS-CFD

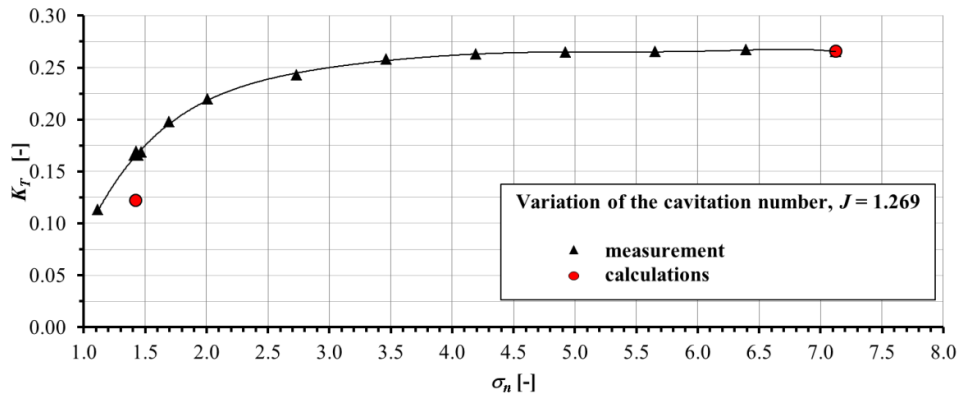
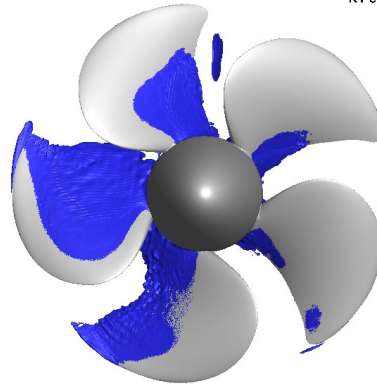
KT non-cav = 0.266
 KT cav = 0.122

CNRS-ECN ISIS-CFD

KT non-cav = 0.266
 KT cav = 0.122



60 %
vapour
fraction

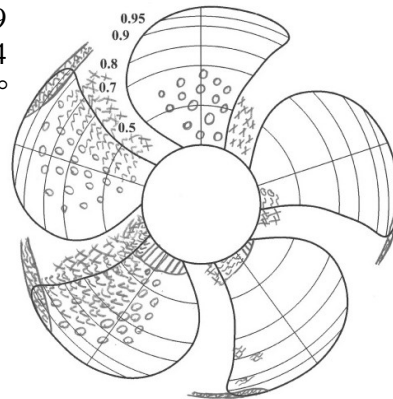
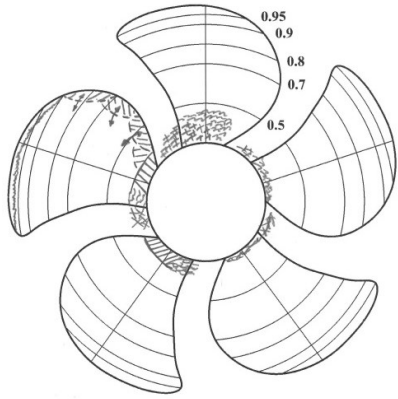


3.7 Case 2.2, CRADLE-SCTetra

Pressure side

Suction side

Case 2.2
 $J = 1.269$
 $\sigma_n = 1.424$
 $\psi^{bP} = 12.0^\circ$

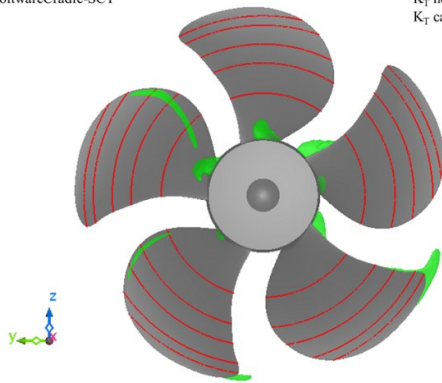


SoftwareCradle-SCT

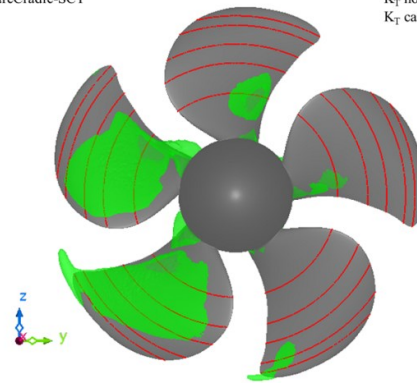
K_T non-cav = 0.279
 K_T cav = 0.212

SoftwareCradle-SCT

K_T non-cav = 0.279
 K_T cav = 0.212



40 %
vapour
fraction

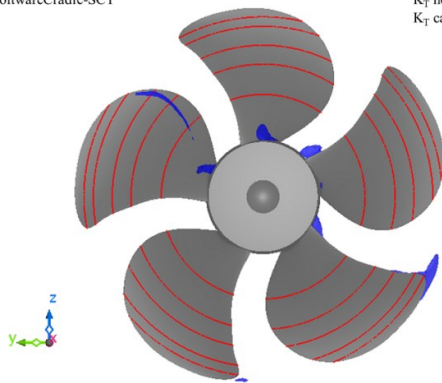


SoftwareCradle-SCT

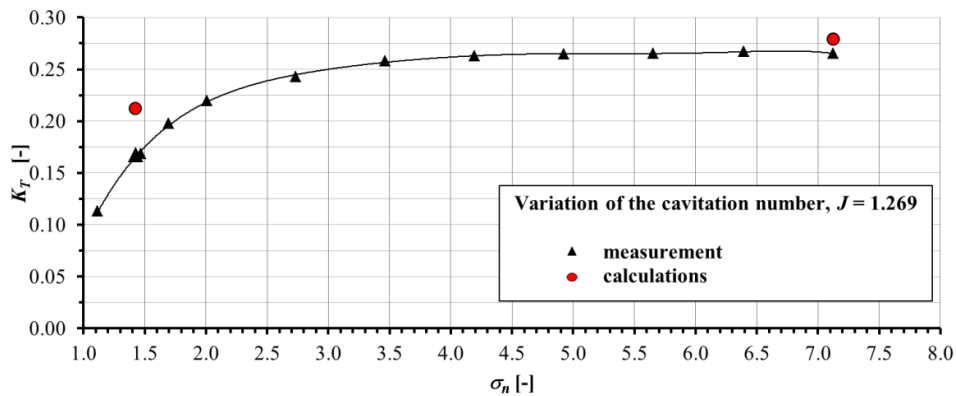
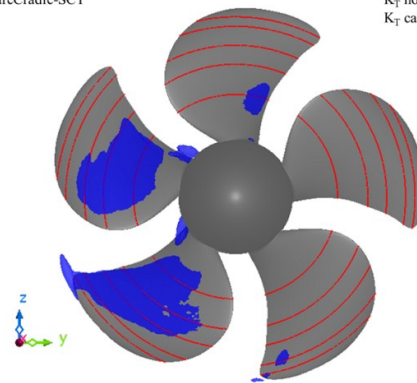
K_T non-cav = 0.279
 K_T cav = 0.212

SoftwareCradle-SCT

K_T non-cav = 0.279
 K_T cav = 0.212



60 %
vapour
fraction



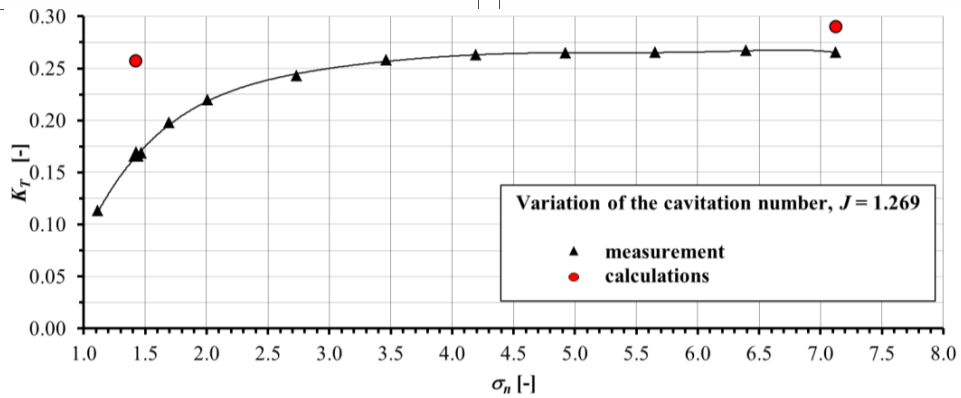
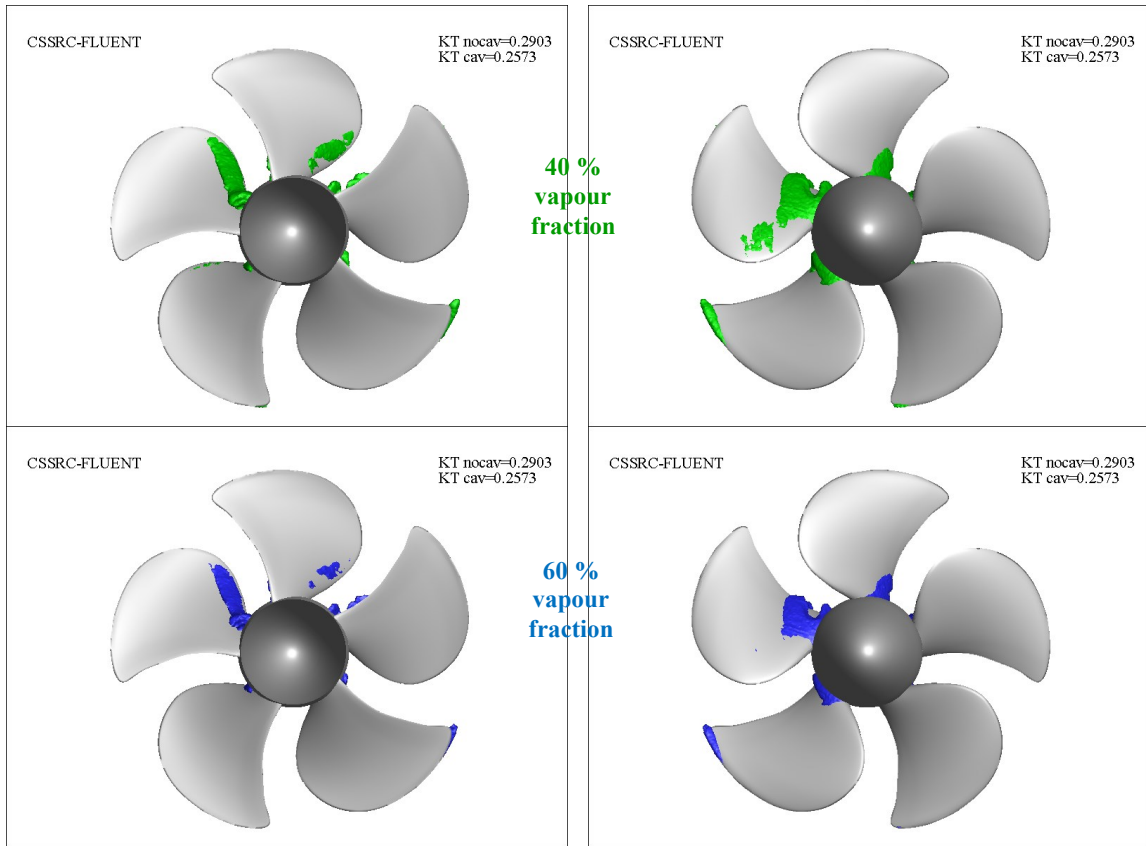
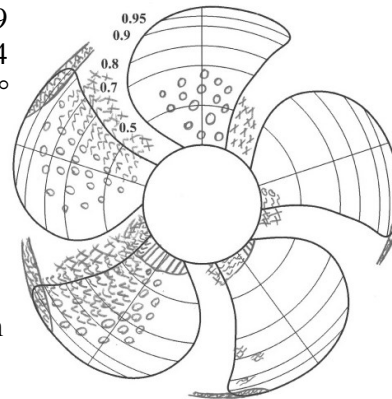
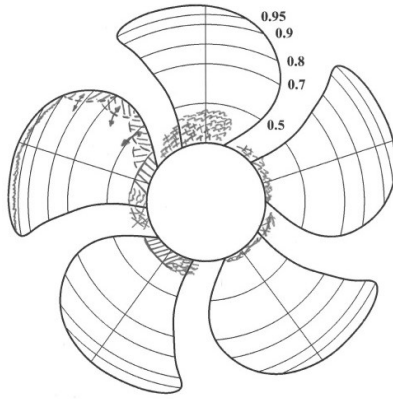
3.8 Case 2.2, CSSRC-Fluent

Pressure side

Suction side

Case 2.2
 $J = 1.269$
 $\sigma_n = 1.424$
 $\psi^{bP} = 12.0^\circ$

10% vapour fraction given in paper

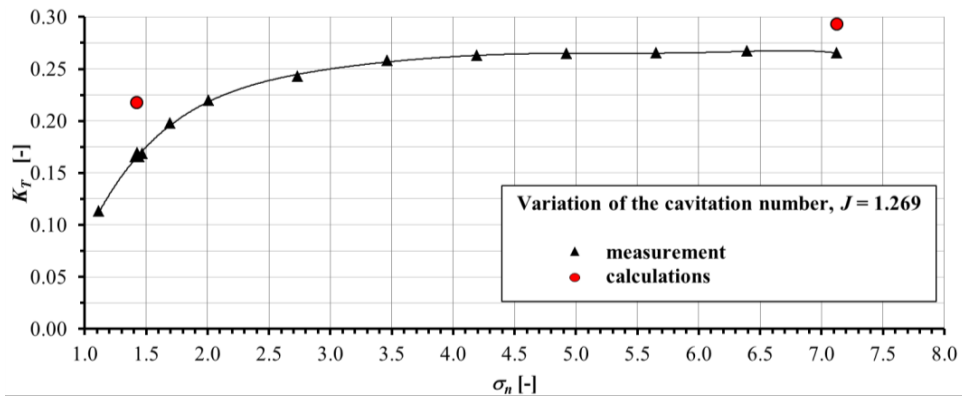
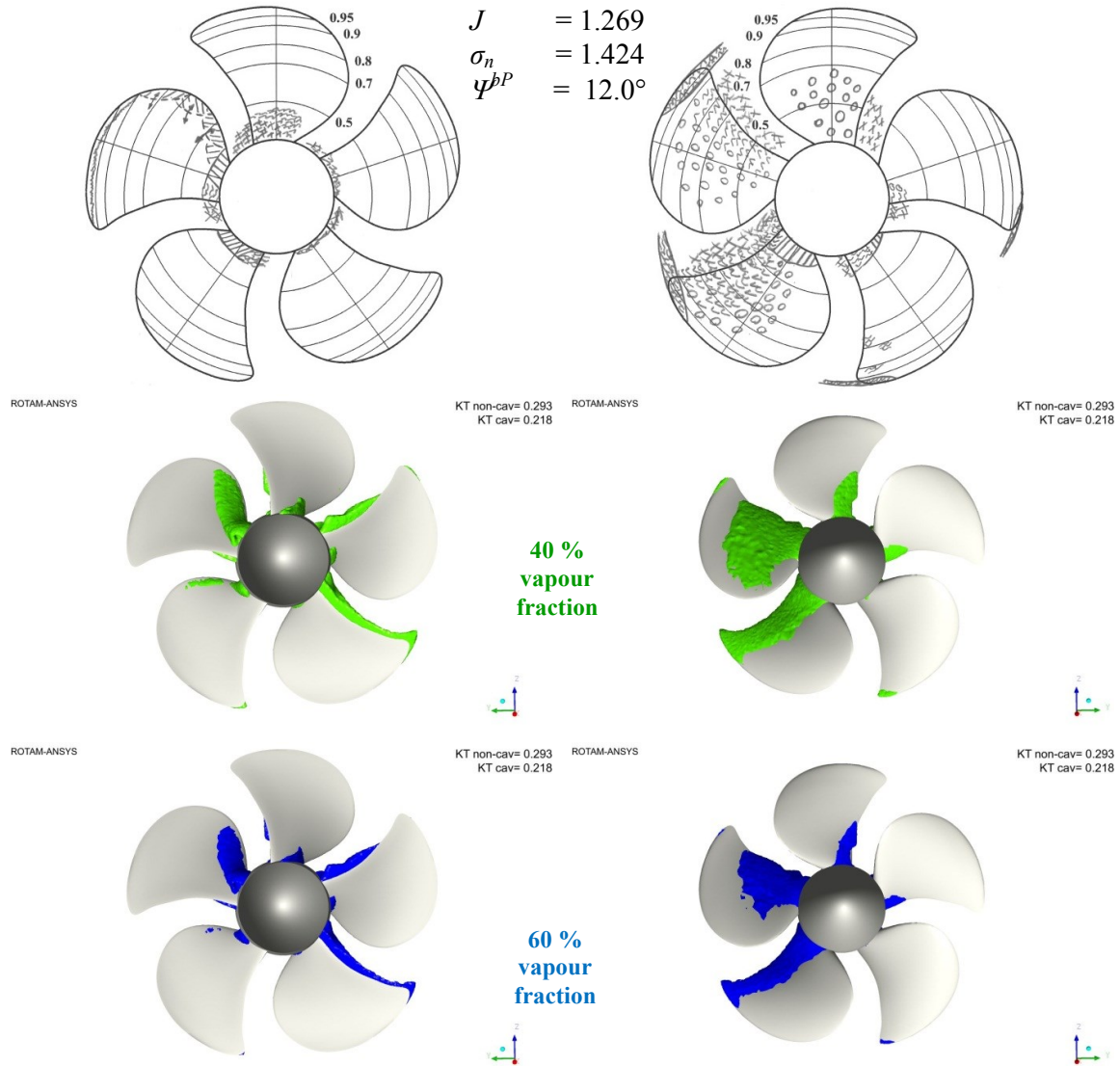


3.9 Case 2.2, ROTAM-Fluent

Pressure side

Suction side

Case 2.2
 $J = 1.269$
 $\sigma_n = 1.424$
 $\psi^{bP} = 12.0^\circ$

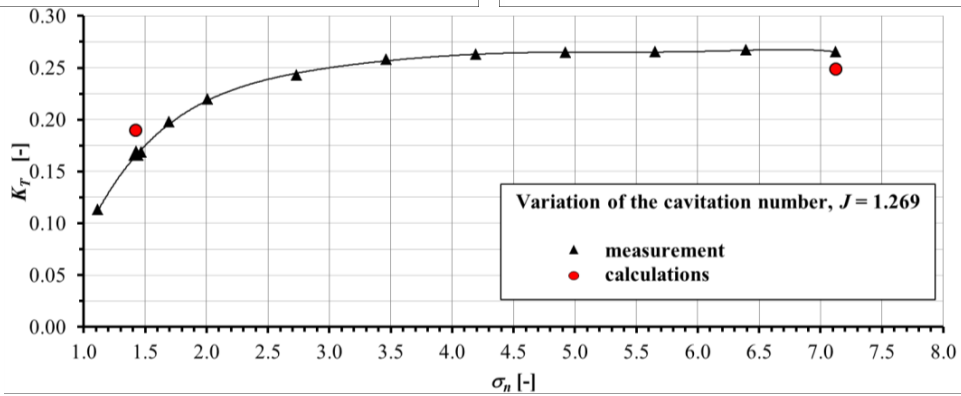
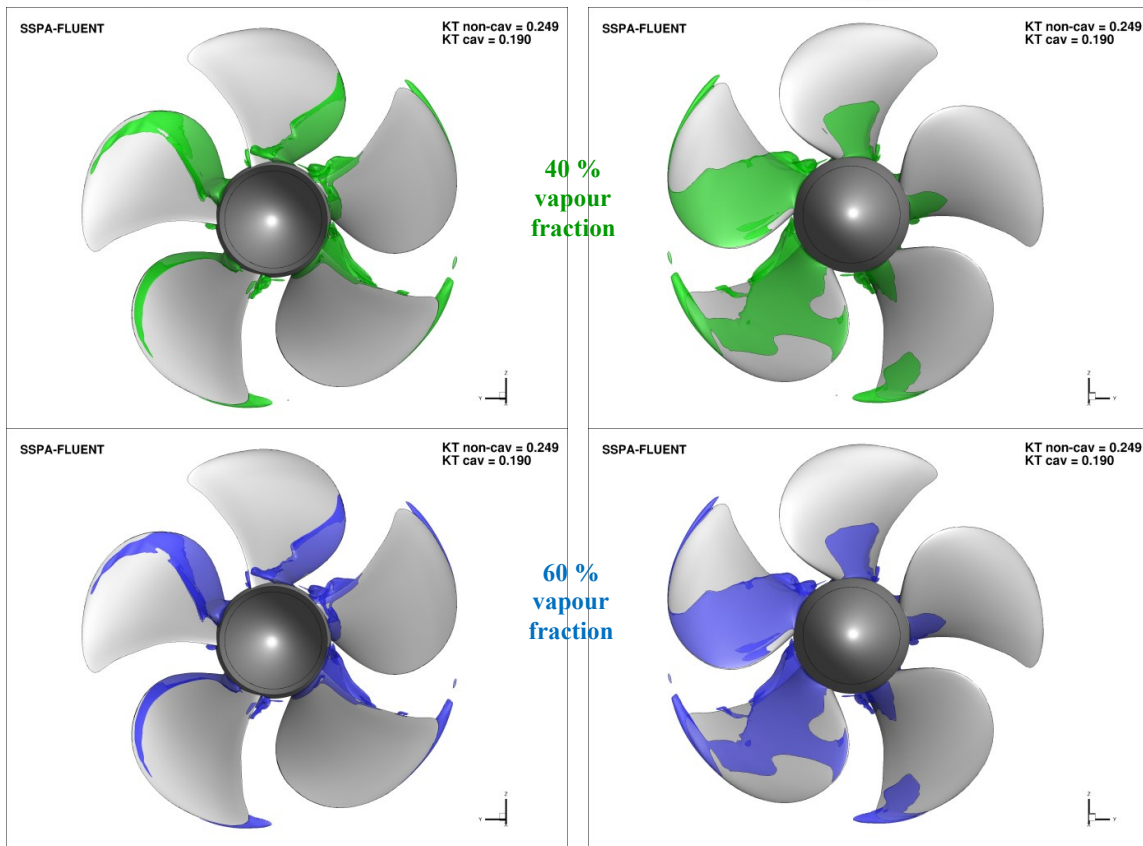
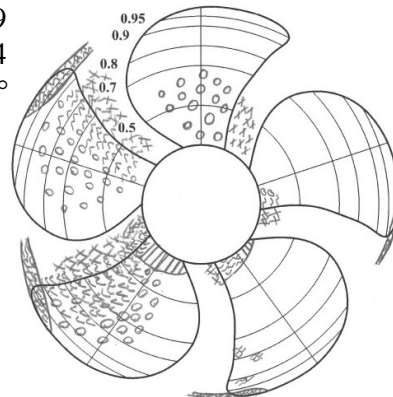
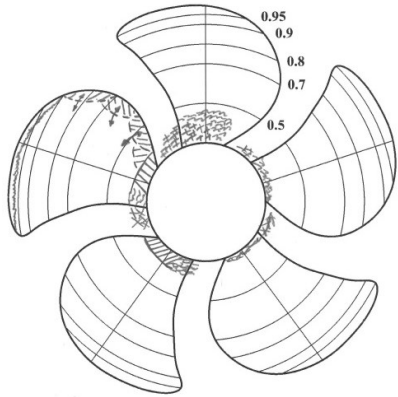


3.10 Case 2.2, SSPA-Fluent-Sauer

Pressure side

Suction side

Case 2.2
 $J = 1.269$
 $\sigma_n = 1.424$
 $\psi^{bP} = 12.0^\circ$

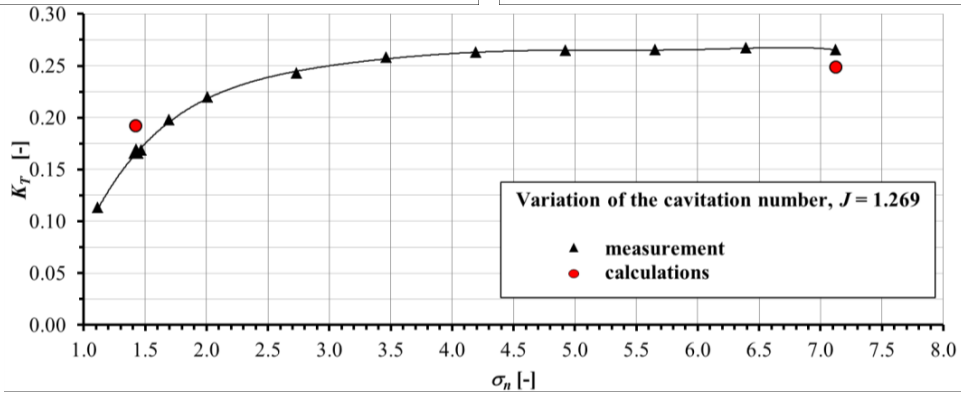
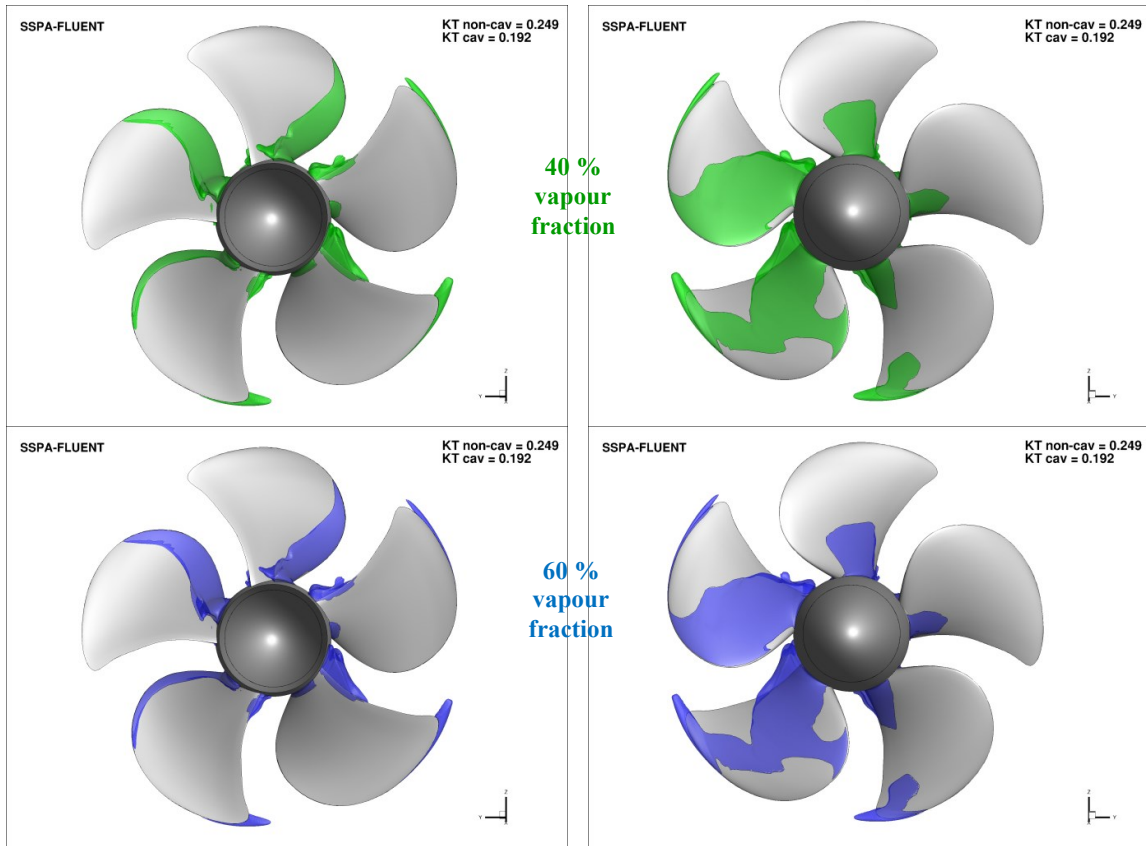
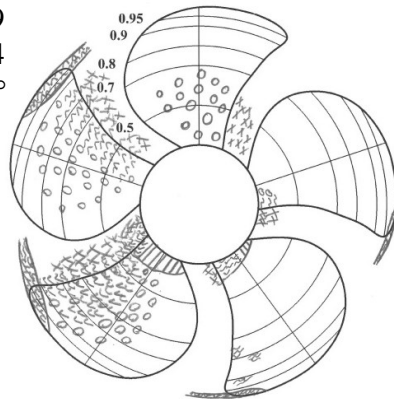
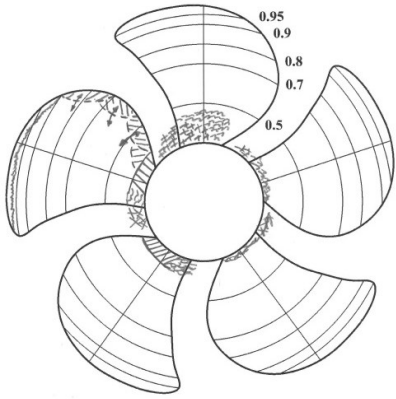


3.11 Case 2.2, SSPA-Fluent-Zwart1

Pressure side

Suction side

Case 2.2
 $J = 1.269$
 $\sigma_n = 1.424$
 $\psi^{bP} = 12.0^\circ$



3.12 Case 2.2, TUHH-CFX

Pressure side

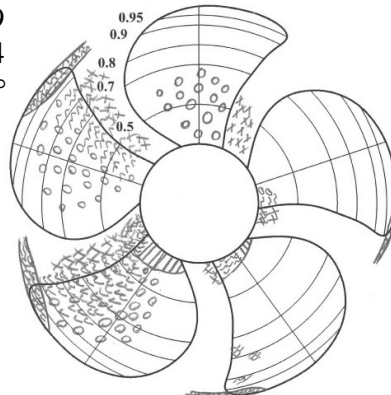
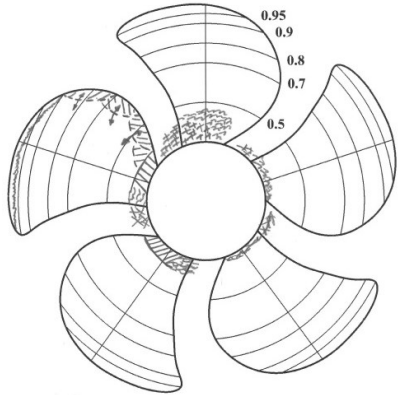
Suction side

Case 2.2

$$J = 1.269$$

$$\sigma_n = 1.424$$

$$\psi^{bP} = 12.0^\circ$$

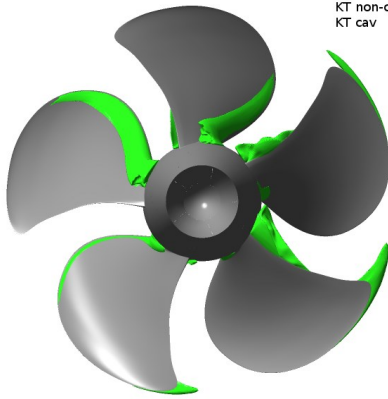


TUHH-CFX

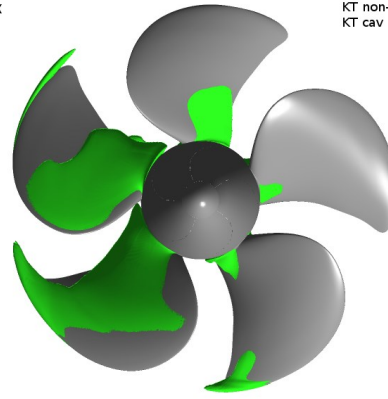
KT non-cav = 0.2584
 KT cav = 0.2045

TUHH-CFX

KT non-cav = 0.2584
 KT cav = 0.2045



40 %
vapour
fraction

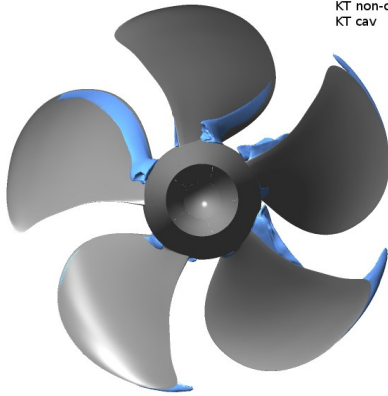


TUHH-CFX

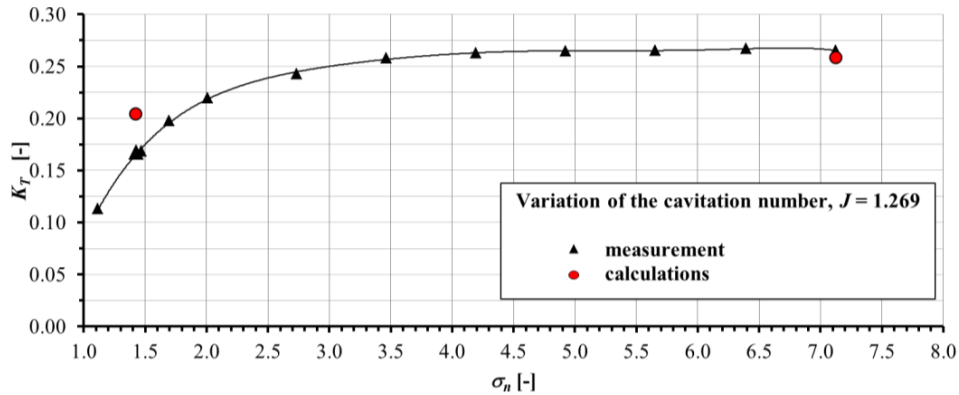
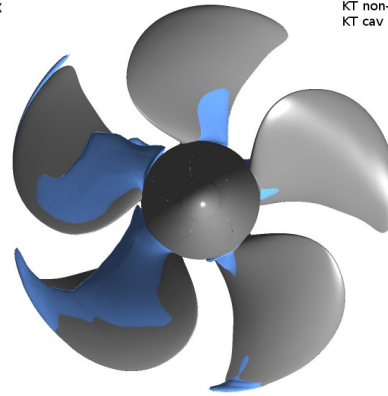
KT non-cav = 0.2584
 KT cav = 0.2045

TUHH-CFX

KT non-cav = 0.2584
 KT cav = 0.2045



60 %
vapour
fraction



3.13 Case 2.2, TUHH-panMARE

Pressure side

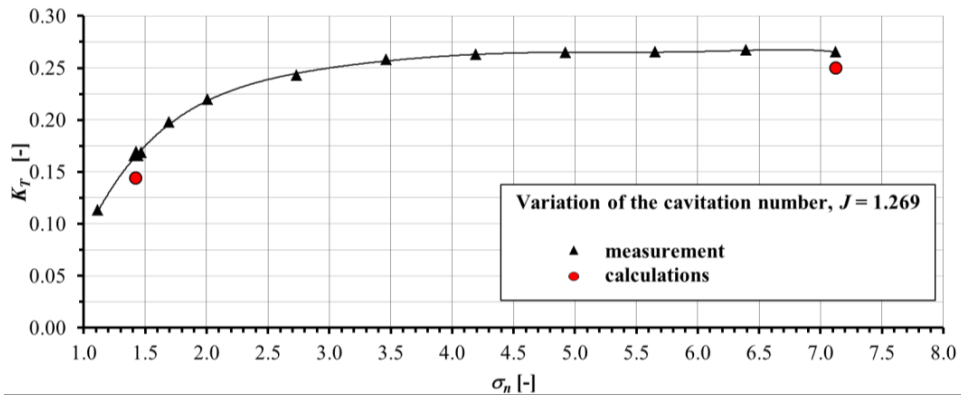
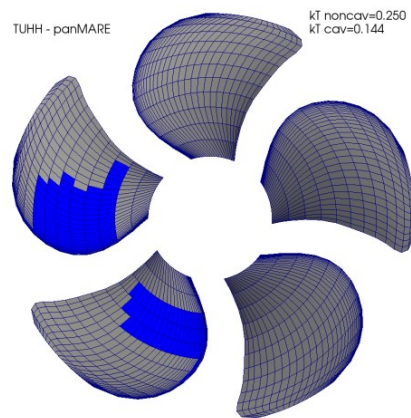
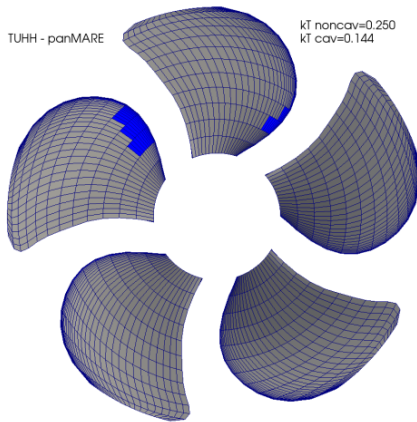
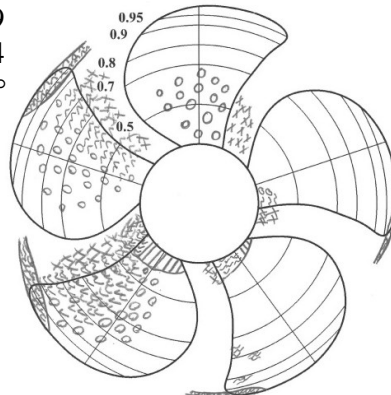
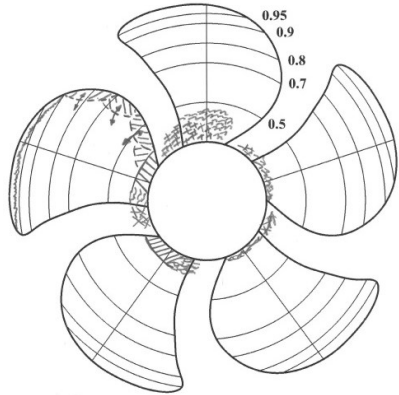
Suction side

Case 2.2

$$J = 1.269$$

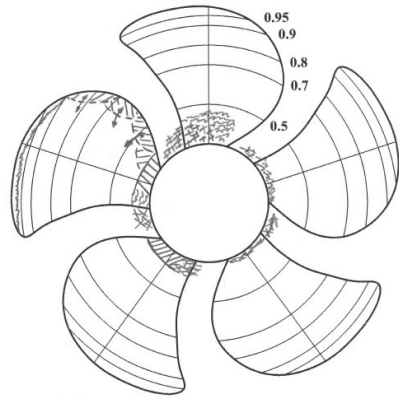
$$\sigma_n = 1.424$$

$$\psi^{bP} = 12.0^\circ$$



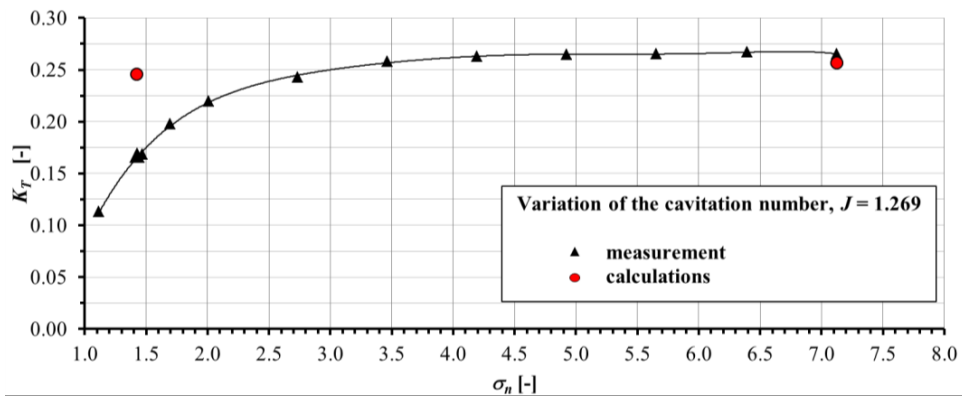
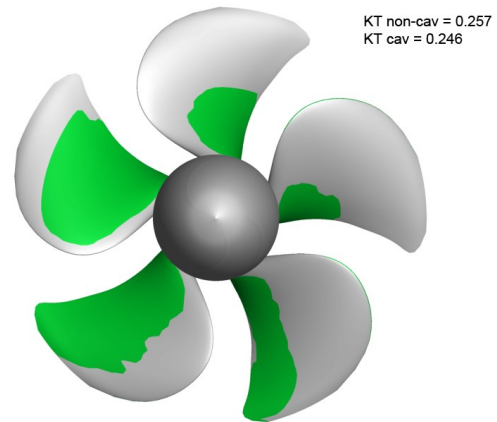
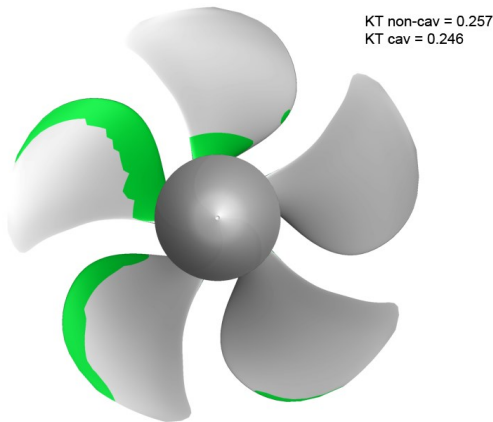
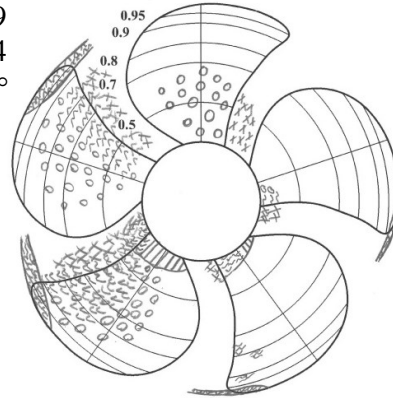
3.14 Case 2.2, UniGenoa-BEM

Pressure side



Case 2.2
 $J = 1.269$
 $\sigma_n = 1.424$
 $\psi^{BP} = 12.0^\circ$

Suction side



3.15 Case 2.2, UniGenoa-StarCCM+

Pressure side

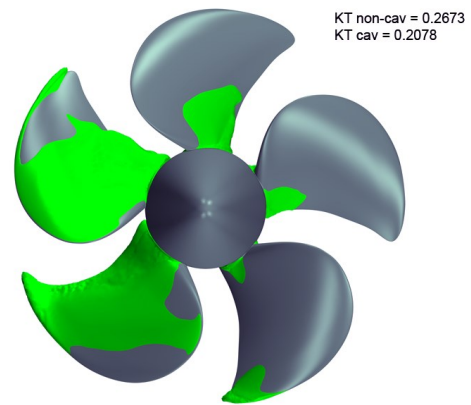
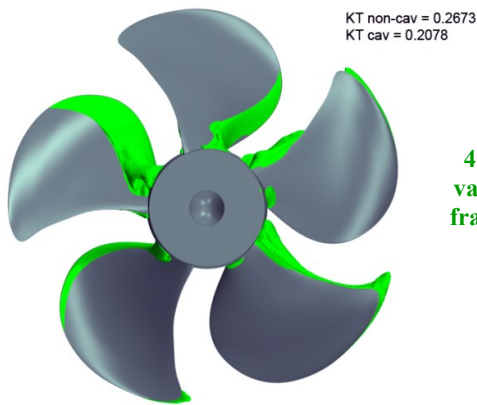
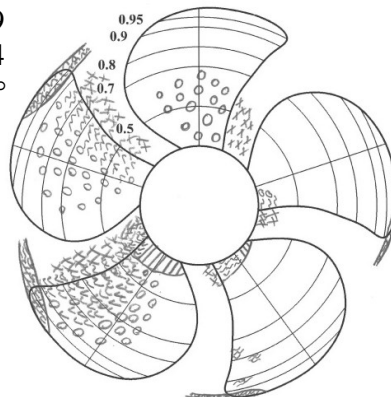
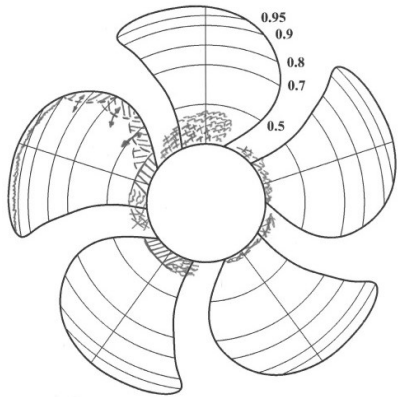
Suction side

Case 2.2

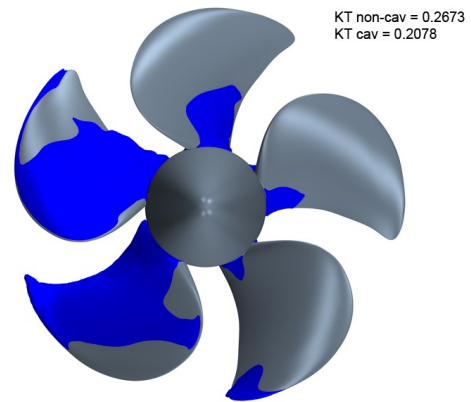
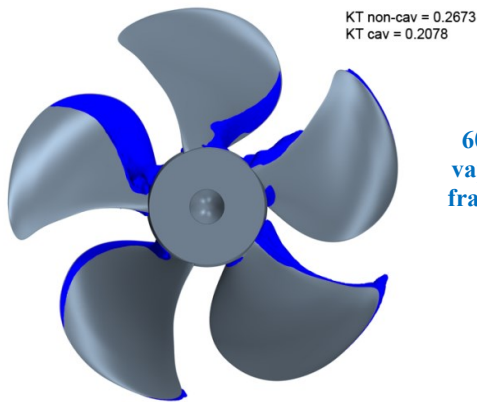
$$J = 1.269$$

$$\sigma_n = 1.424$$

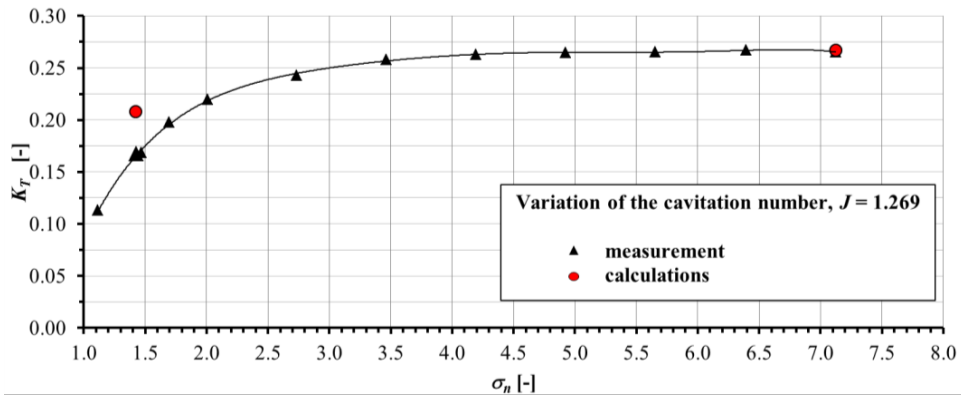
$$\psi^{bP} = 12.0^\circ$$



40 %
vapour
fraction



60 %
vapour
fraction



3.16 Case 2.2, UTAustin-PROPCAV

Pressure side

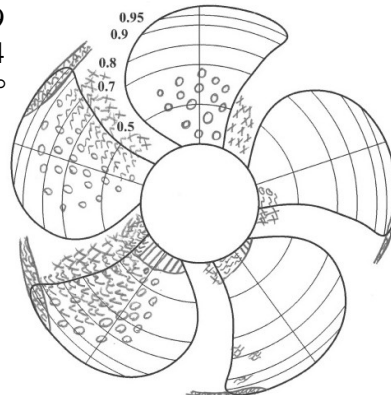
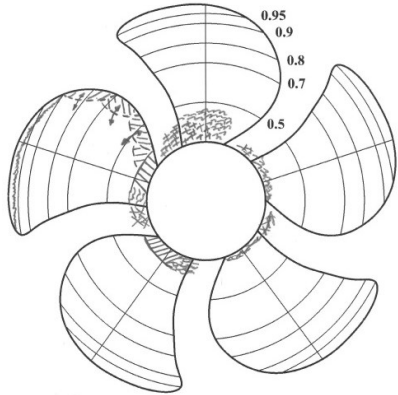
Suction side

Case 2.2

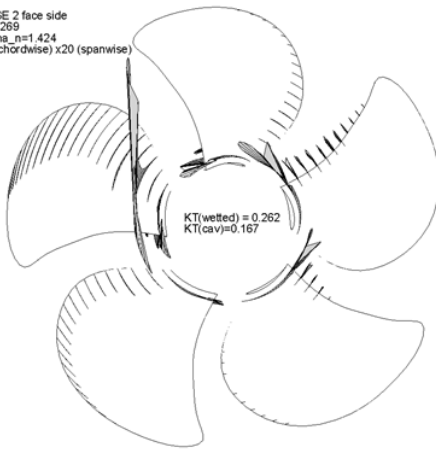
$$J = 1.269$$

$$\sigma_n = 1.424$$

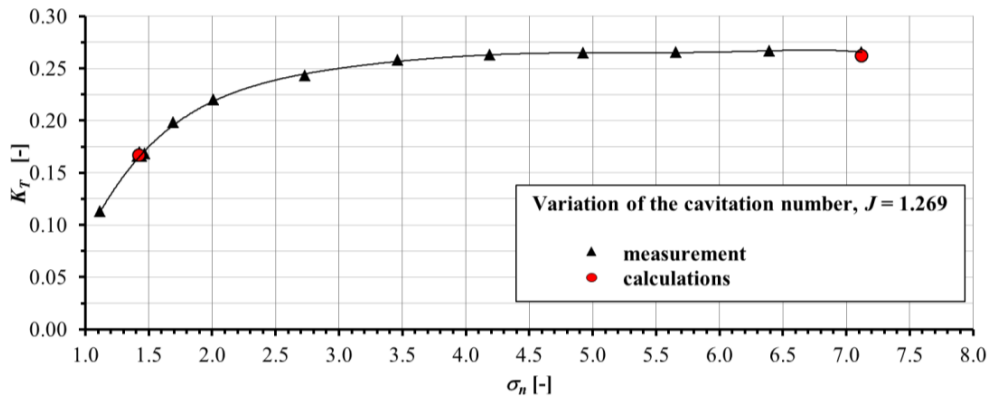
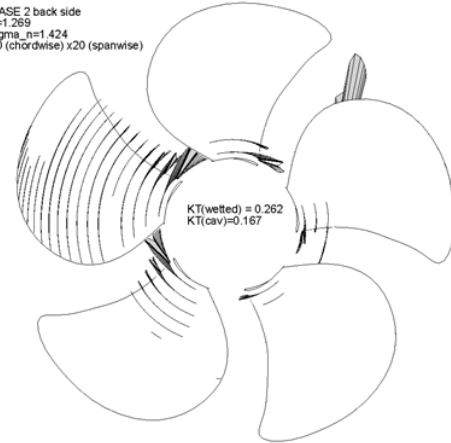
$$\psi^{BP} = 12.0^\circ$$



CASE 2 face side
 J=1.269
 sigma_n=1.424
 60 (chordwise) x20 (spanwise)



CASE 2 back side
 J=1.269
 sigma_n=1.424
 60 (chordwise) x20 (spanwise)



3.17 Case 2.2, VTT-FinFlo

Pressure side

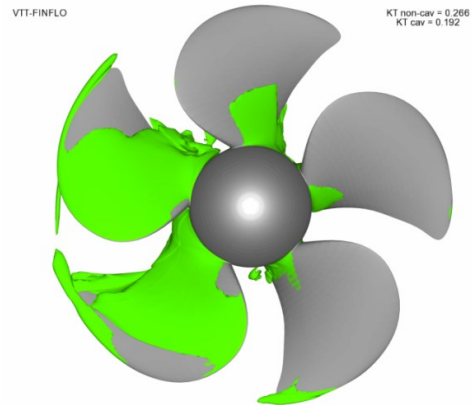
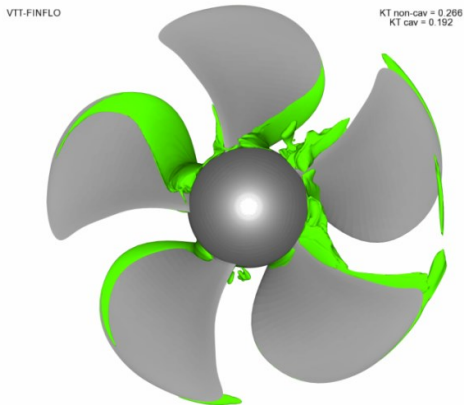
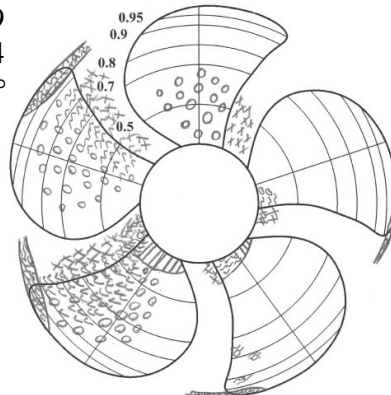
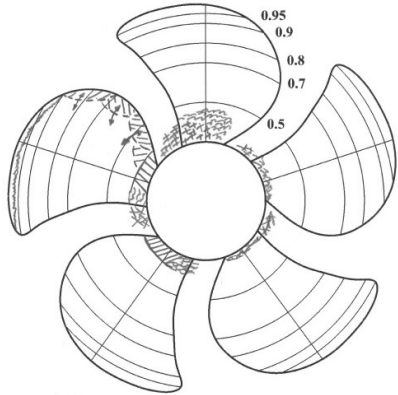
Suction side

Case 2.2

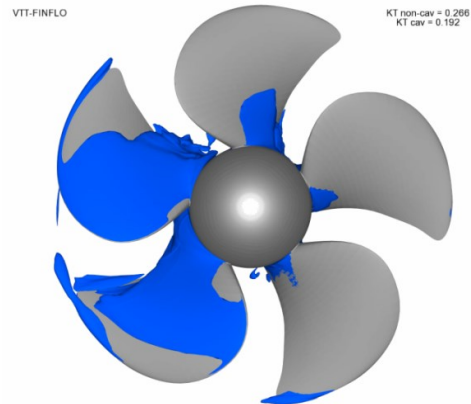
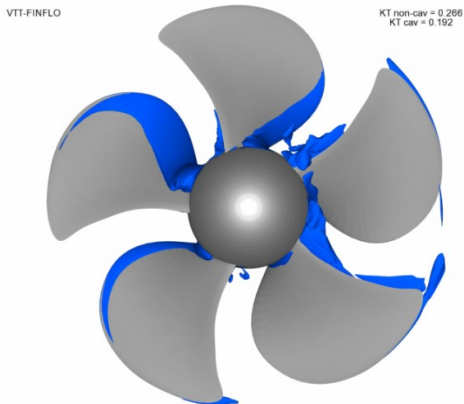
$$J = 1.269$$

$$\sigma_n = 1.424$$

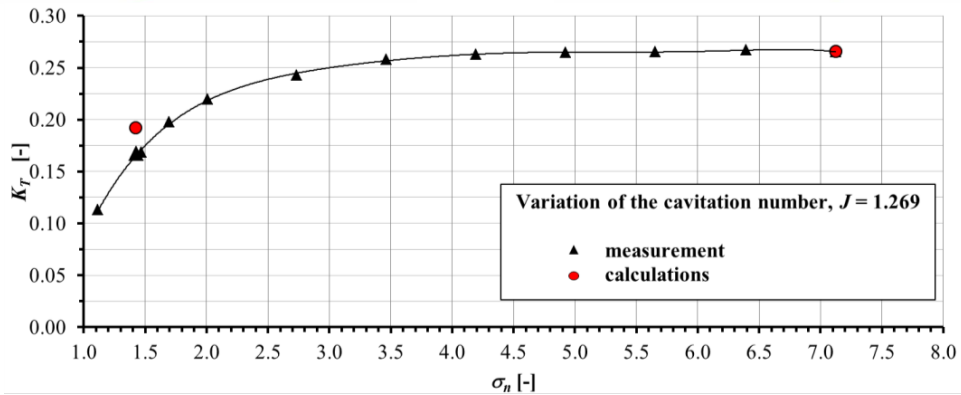
$$\psi^{bP} = 12.0^\circ$$



40 %
vapour
fraction



60 %
vapour
fraction



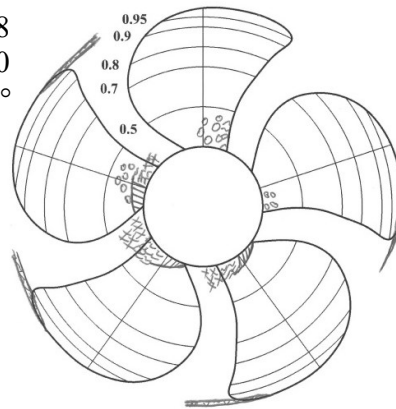
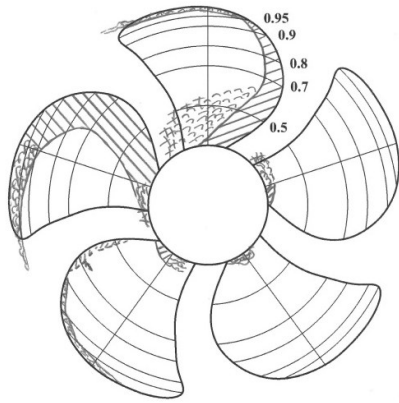
4 Case 2.3

4.1 Case 2.3, ACCUSIM-CFX-FCM

Pressure side

Suction side

Case 2.3
 $J = 1.408$
 $\sigma_n = 2.000$
 $\psi^{bP} = 12.0^\circ$

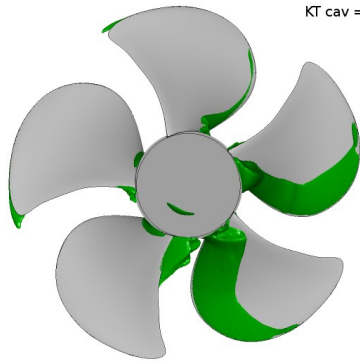


ACCUSIM-CFX-FCM

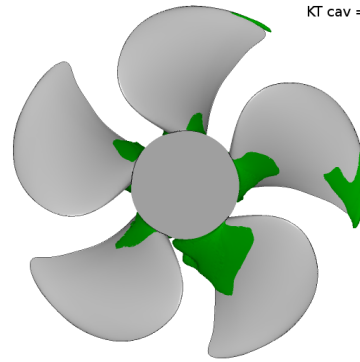
KT non-cav = 0.181
 KT cav = 0.131

ACCUSIM-CFX-FCM

KT non-cav = 0.181
 KT cav = 0.131



40 %
vapour
fraction

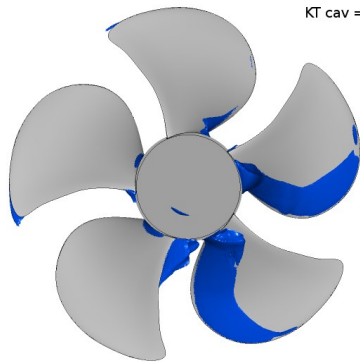


ACCUSIM-CFX-FCM

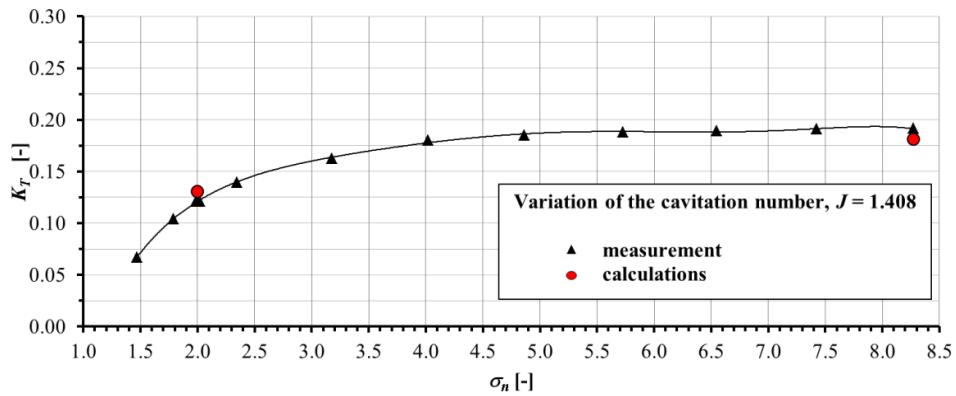
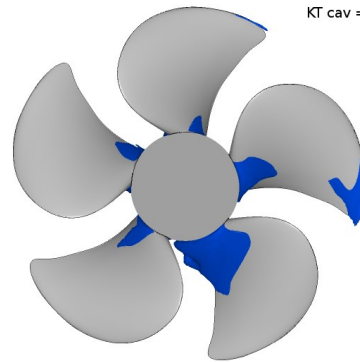
KT non-cav = 0.181
 KT cav = 0.131

ACCUSIM-CFX-FCM

KT non-cav = 0.181
 KT cav = 0.131



60 %
vapour
fraction

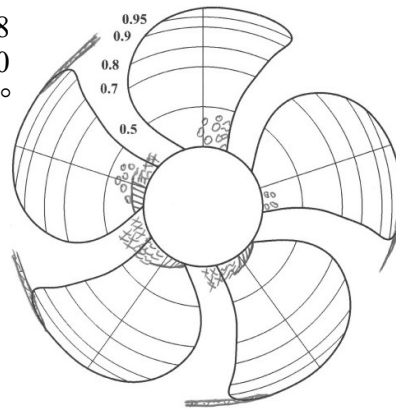
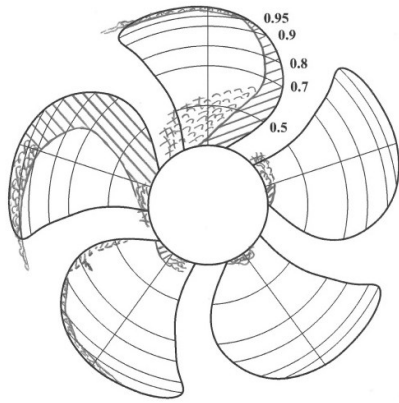


4.2 Case 2.3, ACCUSIM-CFX-Kunz

Pressure side

Suction side

Case 2.3
 $J = 1.408$
 $\sigma_n = 2.000$
 $\psi^{bP} = 12.0^\circ$

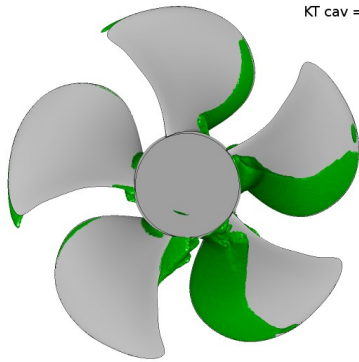


ACCUSIM-CFX-KUNZ

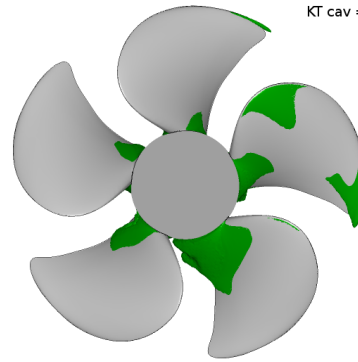
KT non-cav = 0.181
 KT cav = 0.128

ACCUSIM-CFX-KUNZ

KT non-cav = 0.181
 KT cav = 0.128



40 %
vapour
fraction

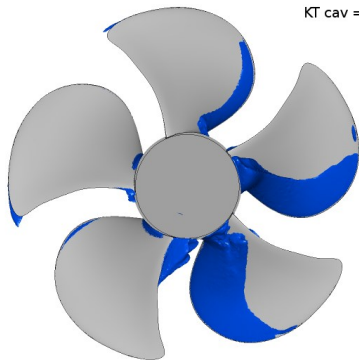


ACCUSIM-CFX-KUNZ

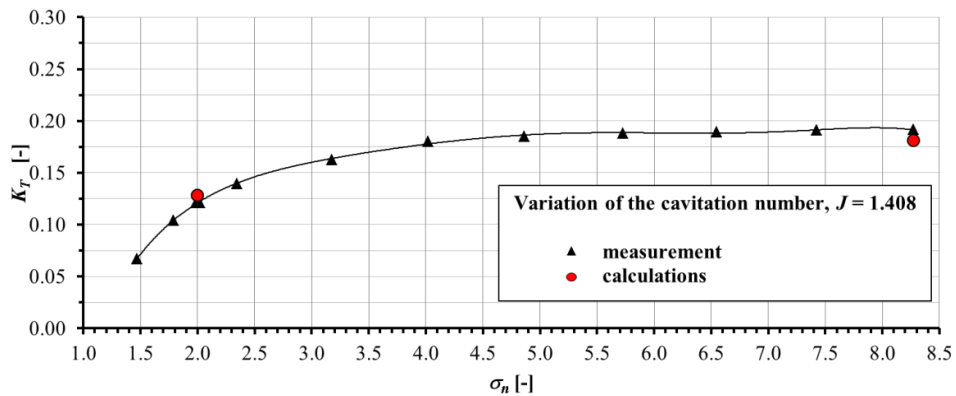
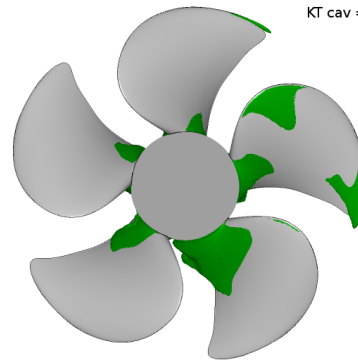
KT non-cav = 0.181
 KT cav = 0.128

ACCUSIM-CFX-KUNZ

KT non-cav = 0.181
 KT cav = 0.128



60 %
vapour
fraction

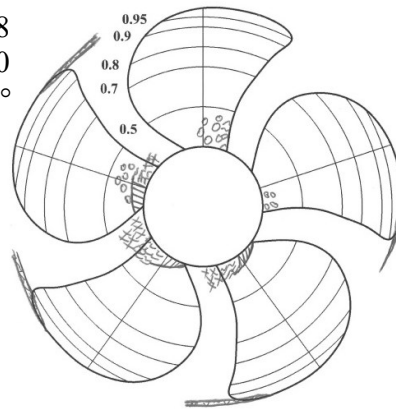
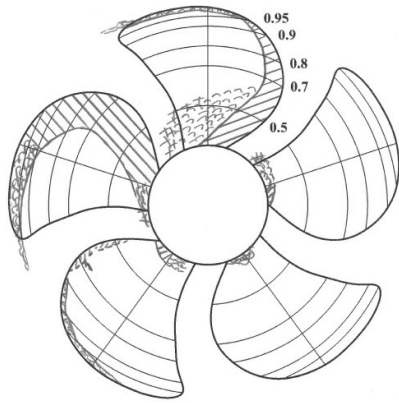


4.3 Case 2.3, ACCUSIM-CFX-Zwart

Pressure side

Suction side

Case 2.3
 $J = 1.408$
 $\sigma_n = 2.000$
 $\psi^{bP} = 12.0^\circ$

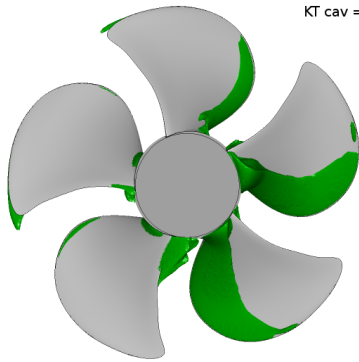


ACCUSIM-CFX-ZWART

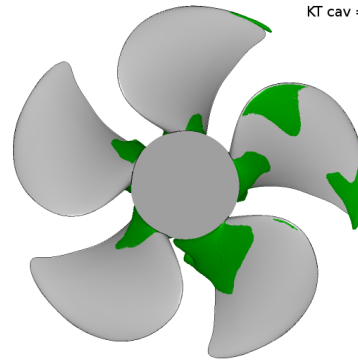
KT non-cav = 0.181
 KT cav = 0.130

ACCUSIM-CFX-ZWART

KT non-cav = 0.181
 KT cav = 0.130



40 %
vapour
fraction

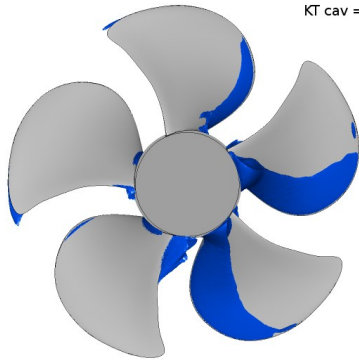


ACCUSIM-CFX-ZWART

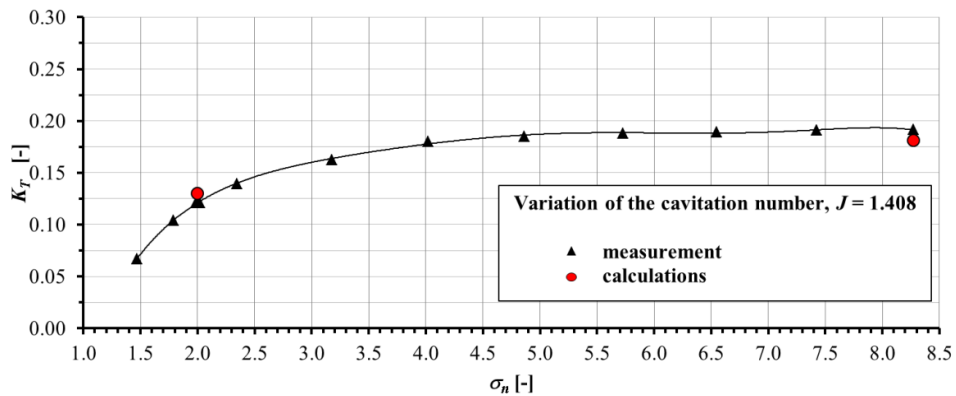
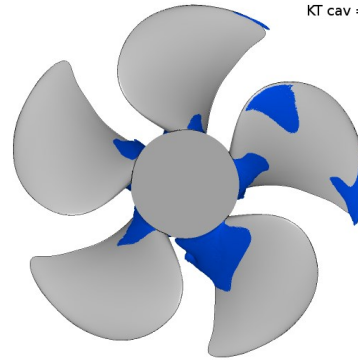
KT non-cav = 0.181
 KT cav = 0.130

ACCUSIM-CFX-ZWART

KT non-cav = 0.181
 KT cav = 0.130



60 %
vapour
fraction

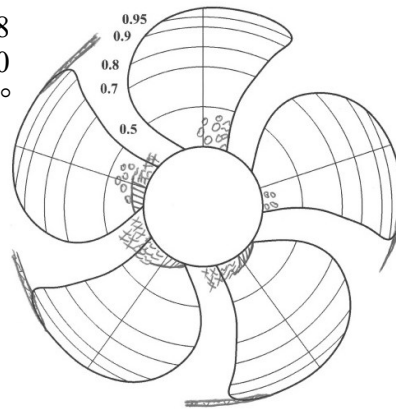
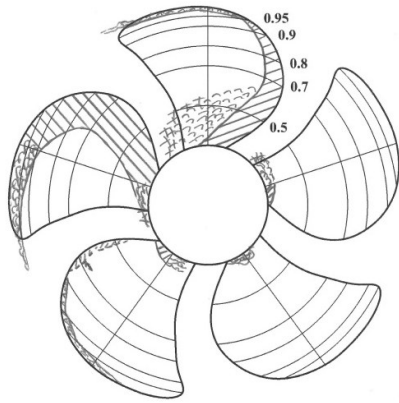


4.4 Case 2.3, CAT-OF

Pressure side

Suction side

Case 2.3
 $J = 1.408$
 $\sigma_n = 2.000$
 $\psi^{bP} = 12.0^\circ$

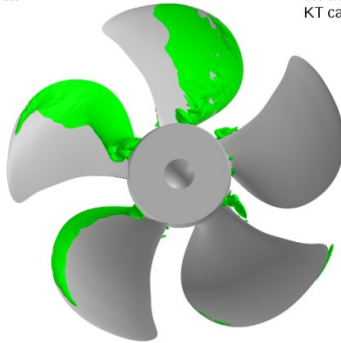


CAT-OpenFOAM

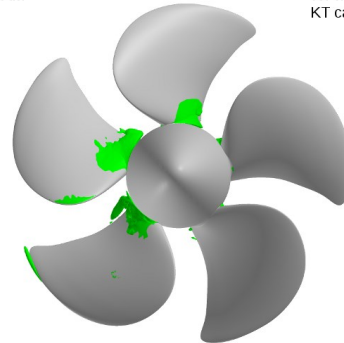
KT non-cav = 0.208
 KT cav = 0.084

CAT-OpenFOAM

KT non-cav = 0.208
 KT cav = 0.084



40 %
vapour
fraction

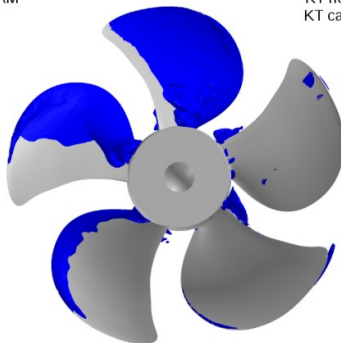


CAT-OpenFOAM

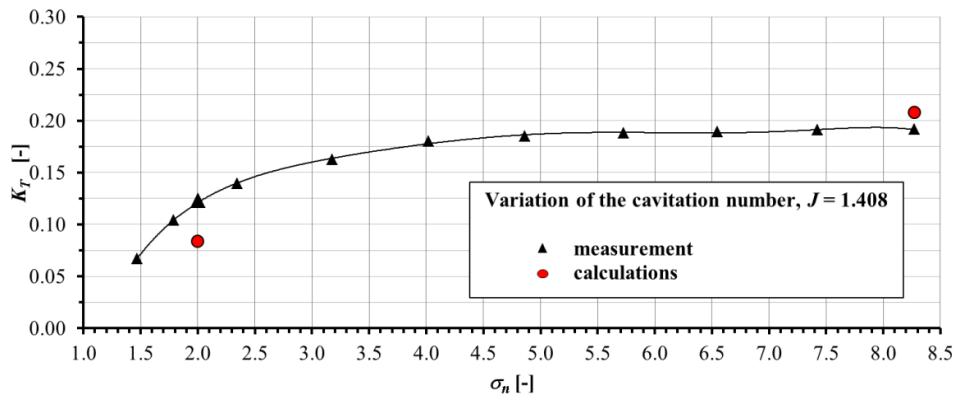
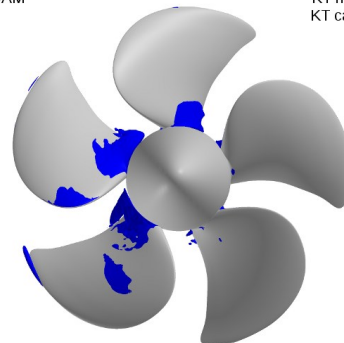
KT non-cav = 0.208
 KT cav = 0.084

CAT-OpenFOAM

KT non-cav = 0.208
 KT cav = 0.084



60 %
vapour
fraction

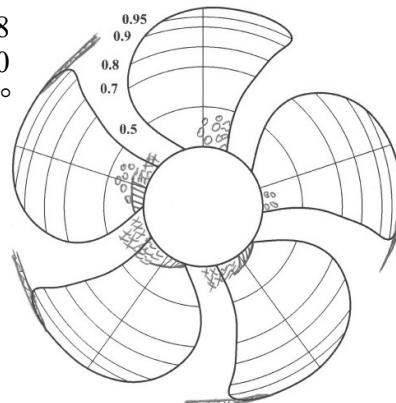
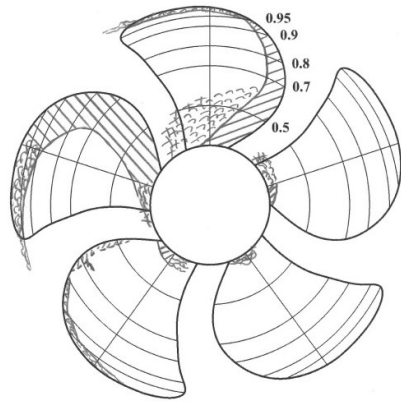


4.5 Case 2.3, Chalmers-OF

Pressure side

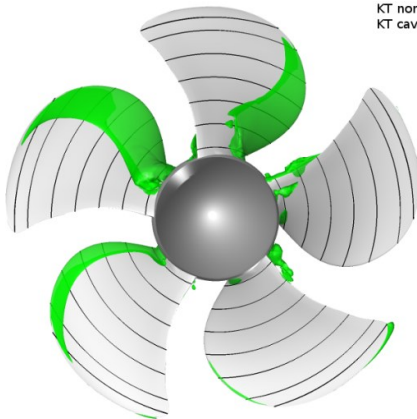
Suction side

Case 2.3
 $J = 1.408$
 $\sigma_n = 2.000$
 $\psi^{bP} = 12.0^\circ$

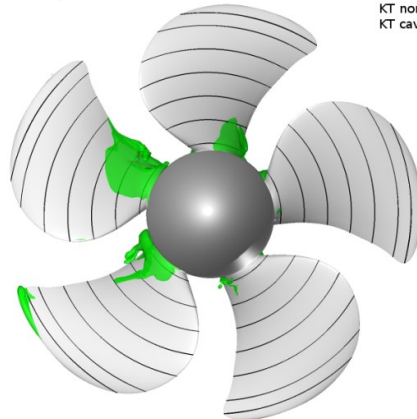


KT non-cav=0.181
 KT cav=0.157

KT non-cav=0.181
 KT cav=0.157

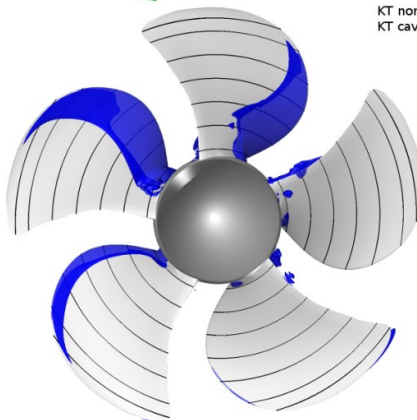


40 %
 vapour
 fraction

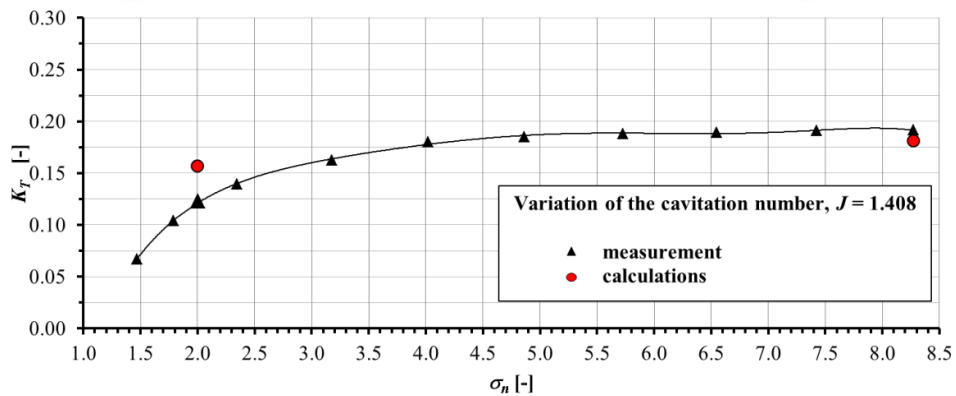
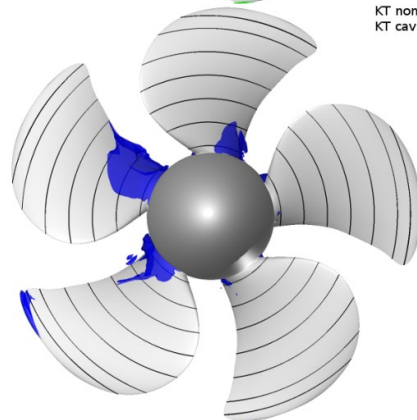


KT non-cav=0.181
 KT cav=0.157

KT non-cav=0.181
 KT cav=0.157



60 %
 vapour
 fraction



4.6 Case 2.3, CNRS-ISIS

Pressure side

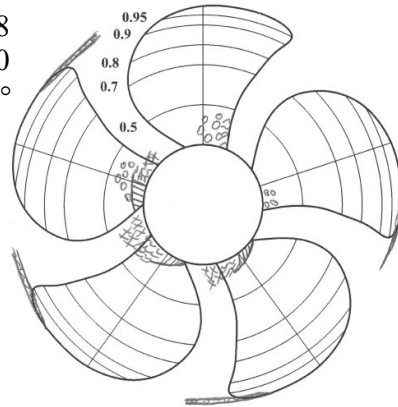
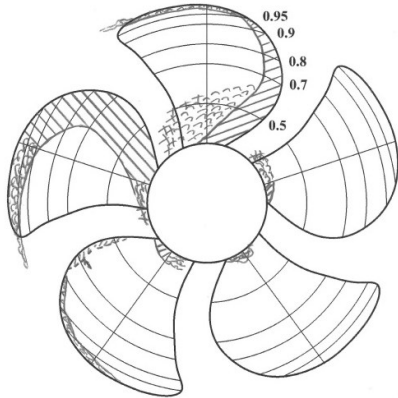
Suction side

Case 2.3

$$J = 1.408$$

$$\sigma_n = 2.000$$

$$\psi^{bP} = 12.0^\circ$$

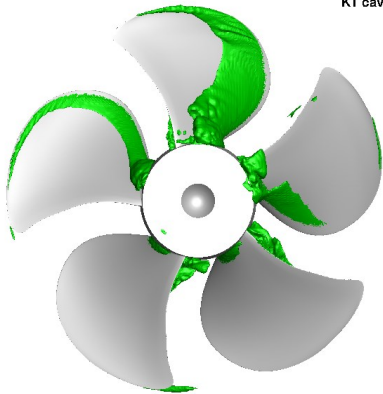


CNRS-ECN ISIS-CFD

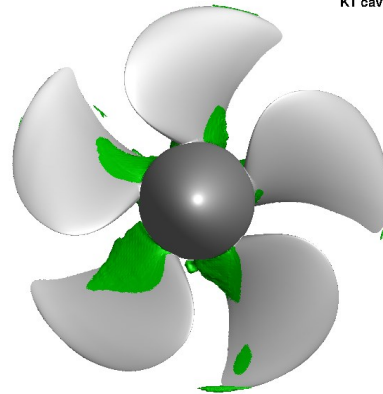
KT non-cav = 0.182
 KT cav = 0.084

CNRS-ECN ISIS-CFD

KT non-cav = 0.182
 KT cav = 0.084



40 %
 vapour
 fraction

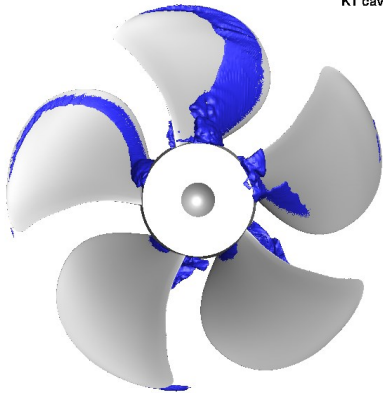


CNRS-ECN ISIS-CFD

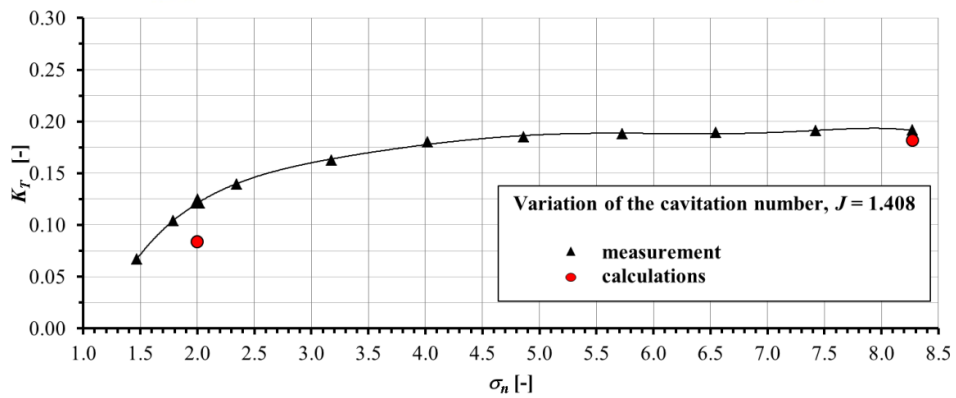
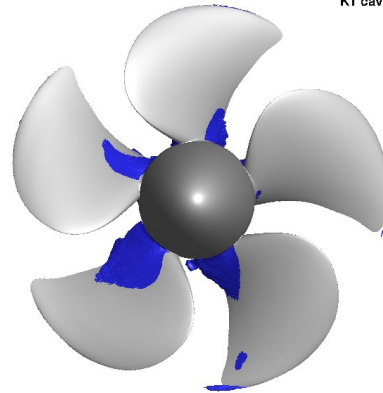
KT non-cav = 0.182
 KT cav = 0.084

CNRS-ECN ISIS-CFD

KT non-cav = 0.182
 KT cav = 0.084



60 %
 vapour
 fraction



4.7 Case 2.3, CRADLE-SCTetra

Pressure side

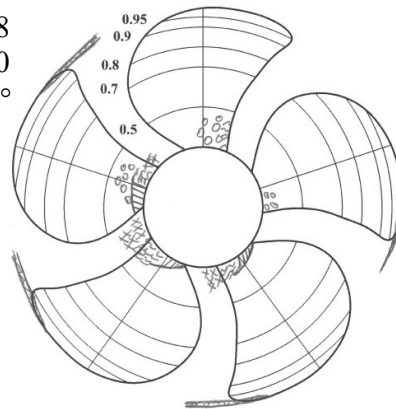
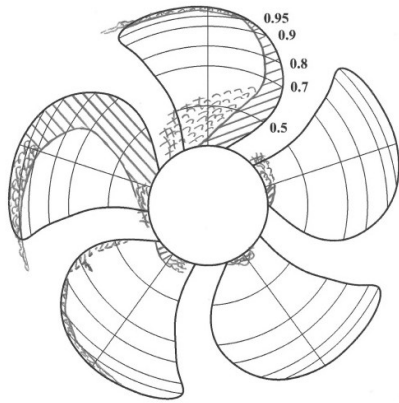
Suction side

Case 2.3

$$J = 1.408$$

$$\sigma_n = 2.000$$

$$\psi^{bP} = 12.0^\circ$$

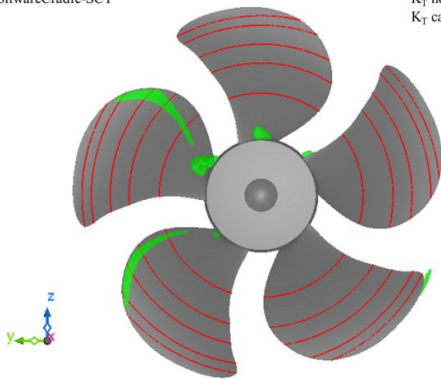


SoftwareCradle-SCT

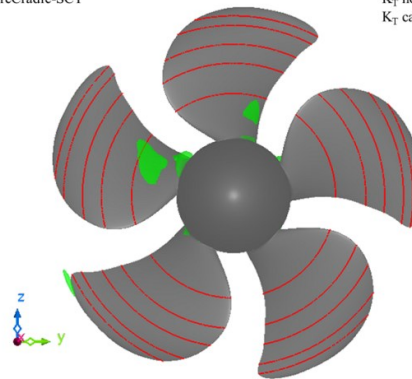
K_T non-cav = 0.200
 K_T cav = 0.146

SoftwareCradle-SCT

K_T non-cav = 0.200
 K_T cav = 0.146



40 %
vapour
fraction

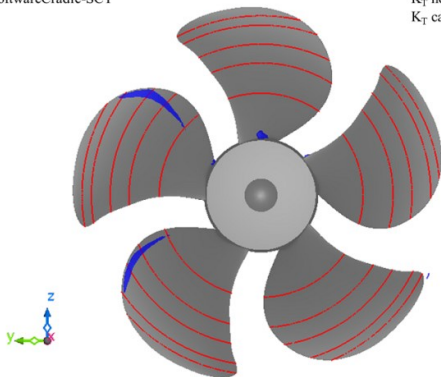


SoftwareCradle-SCT

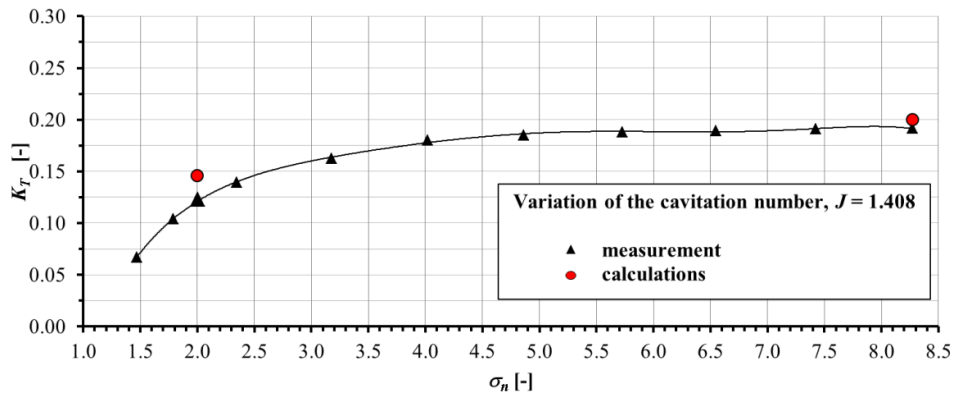
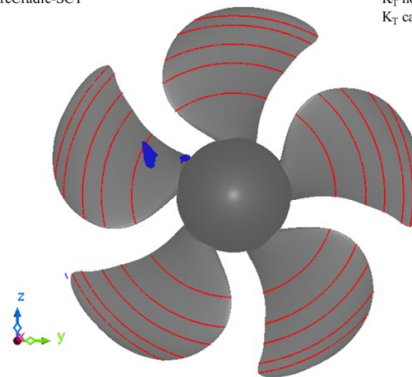
K_T non-cav = 0.200
 K_T cav = 0.146

SoftwareCradle-SCT

K_T non-cav = 0.200
 K_T cav = 0.146



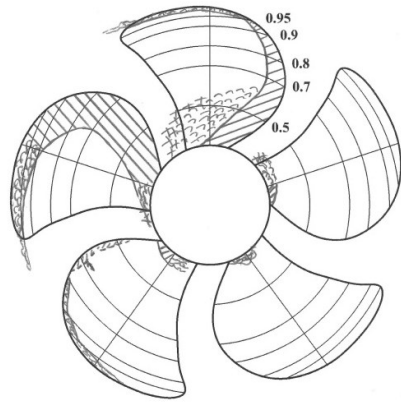
60 %
vapour
fraction



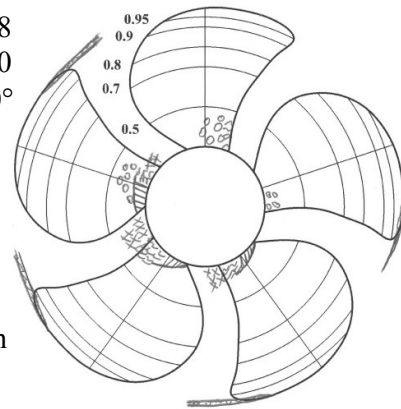
4.8 Case 2.3, CSSRC-Fluent

Pressure side

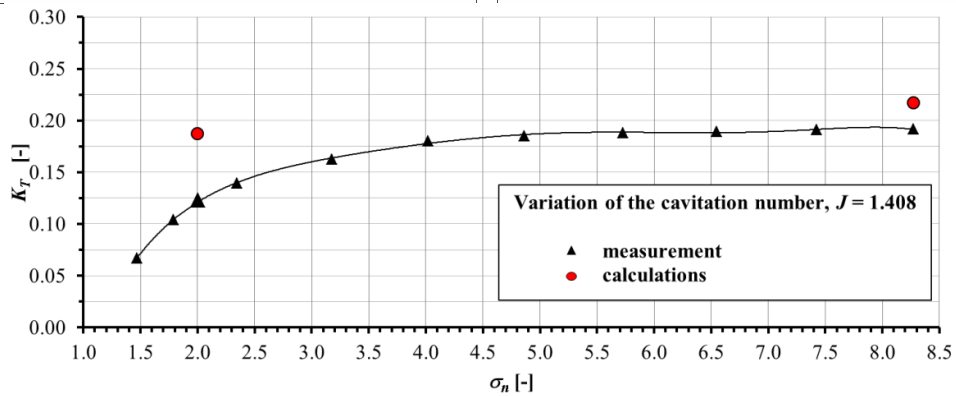
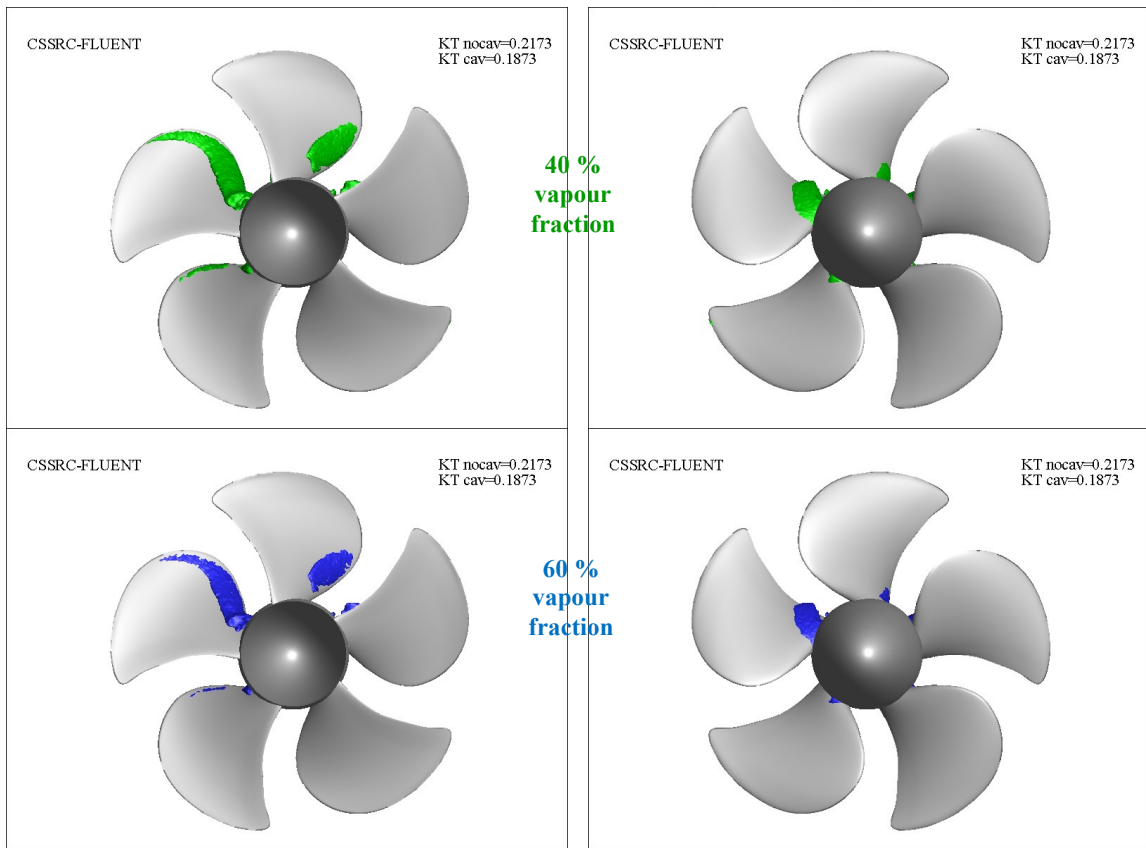
Suction side



Case 2.3
 $J = 1.408$
 $\sigma_n = 2.000$
 $\psi^{bP} = 12.0^\circ$



10% vapour fraction given in paper

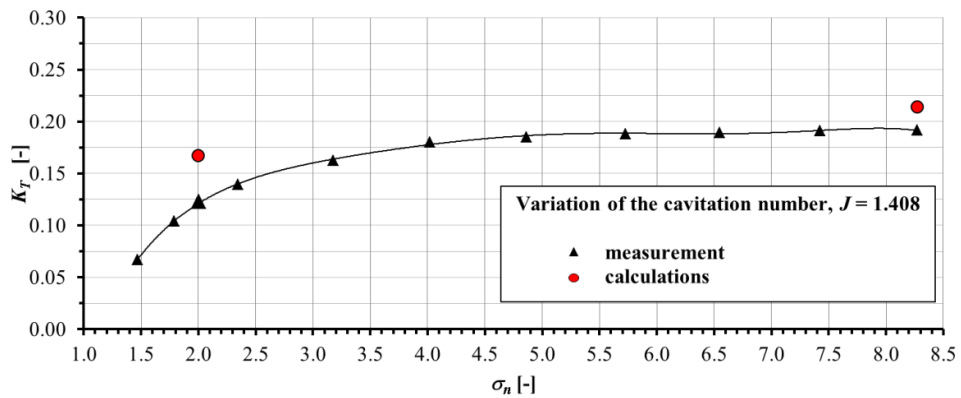
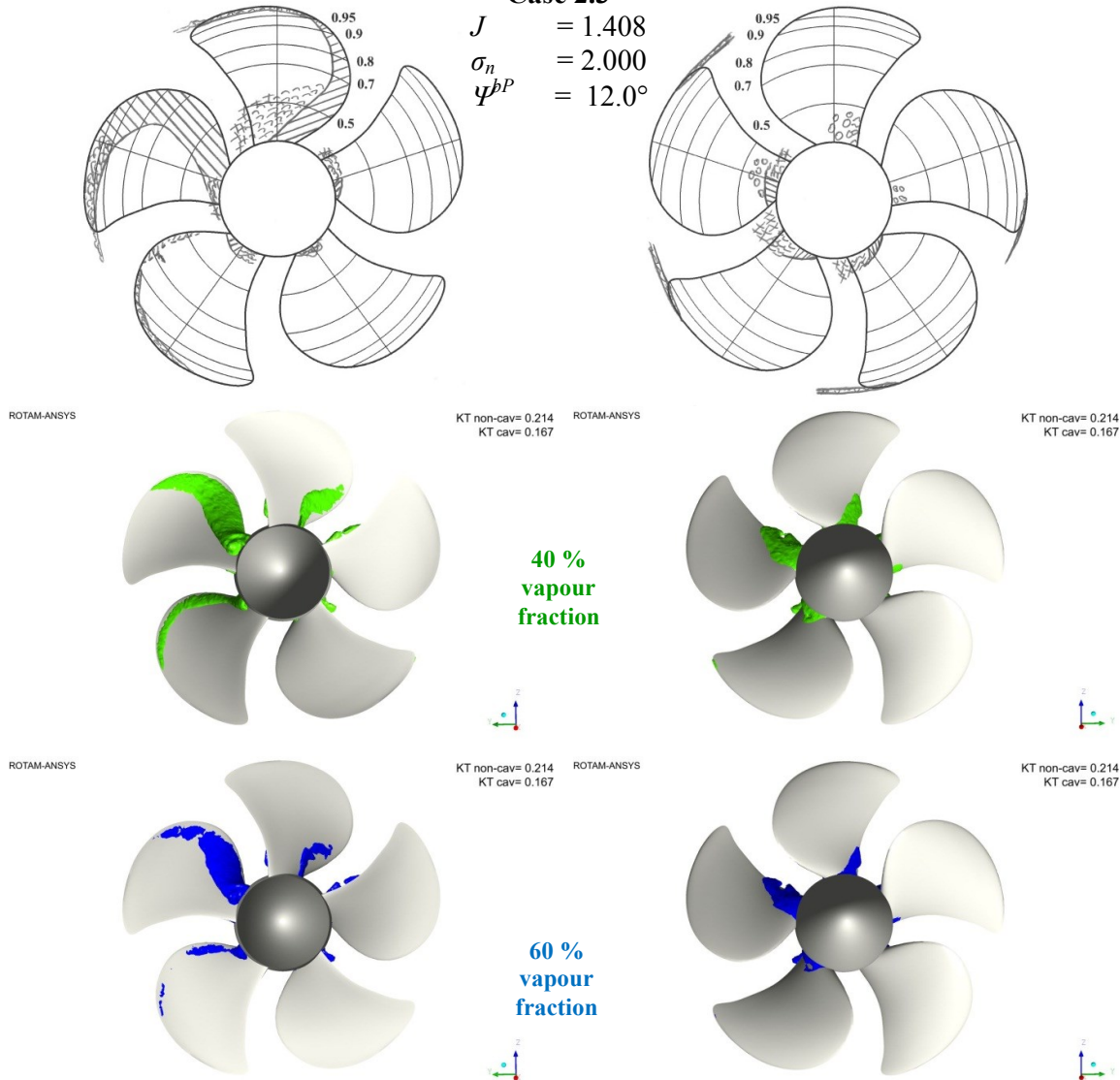


4.9 Case 2.3, ROTAM-Fluent

Pressure side

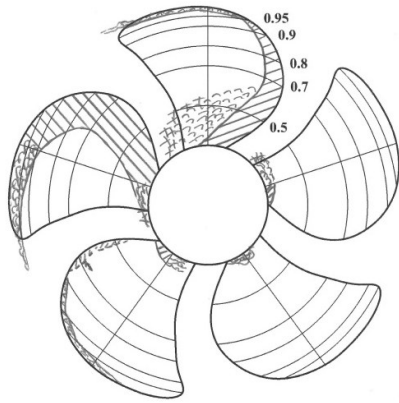
Suction side

Case 2.3
 $J = 1.408$
 $\sigma_n = 2.000$
 $\psi^{bP} = 12.0^\circ$



4.10 Case 2.3, SSPA-Fluent-Sauer

Pressure side



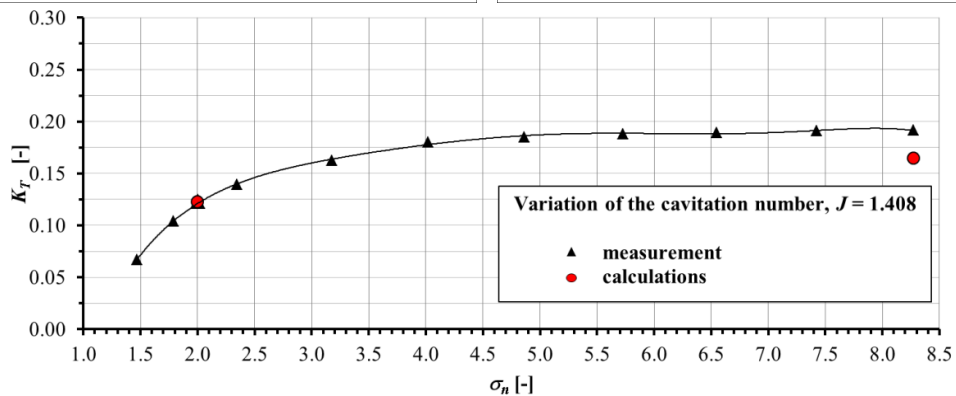
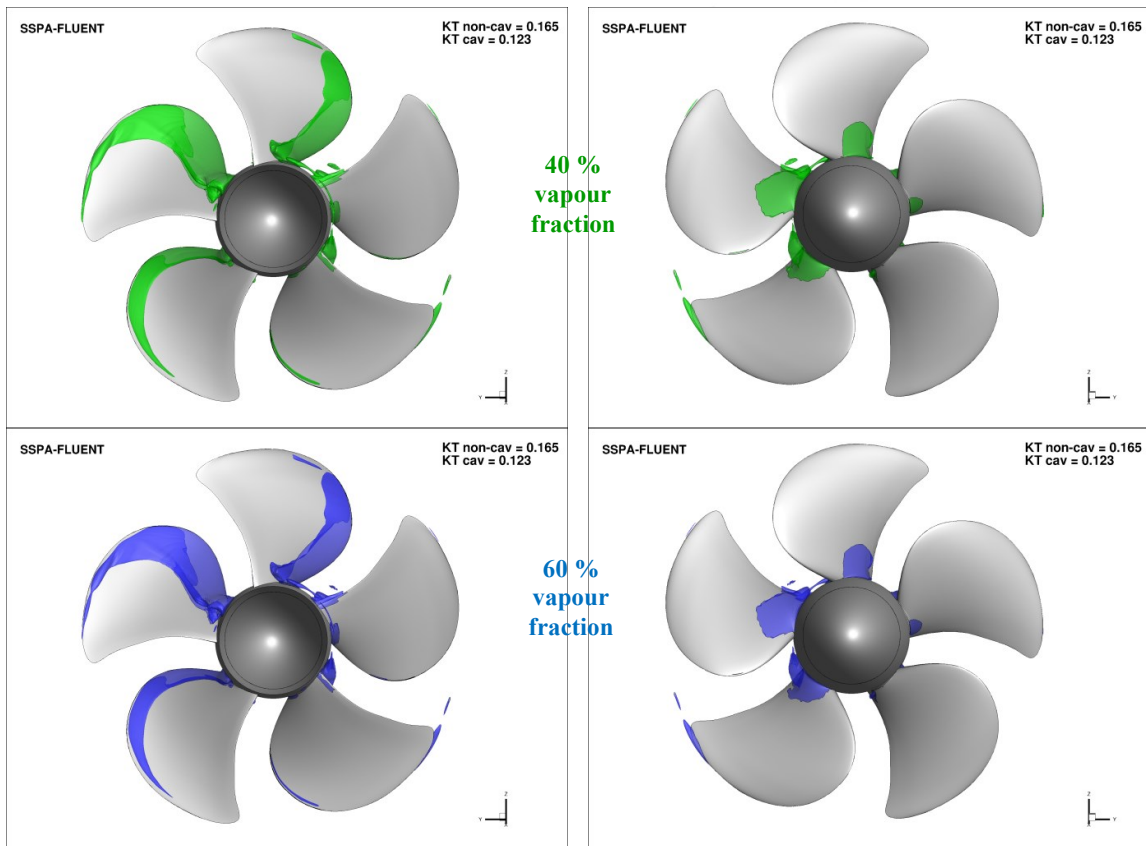
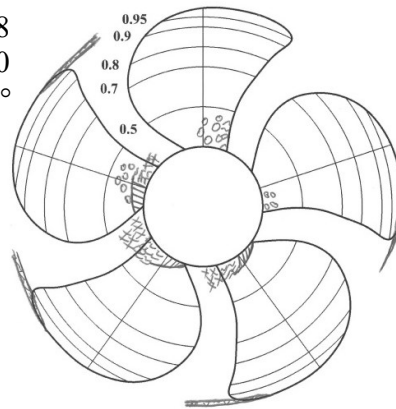
Case 2.3

$$J = 1.408$$

$$\sigma_n = 2.000$$

$$\psi^{bP} = 12.0^\circ$$

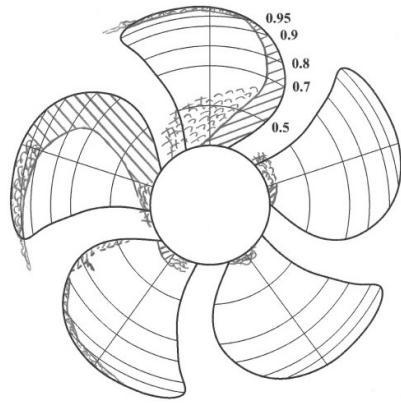
Suction side



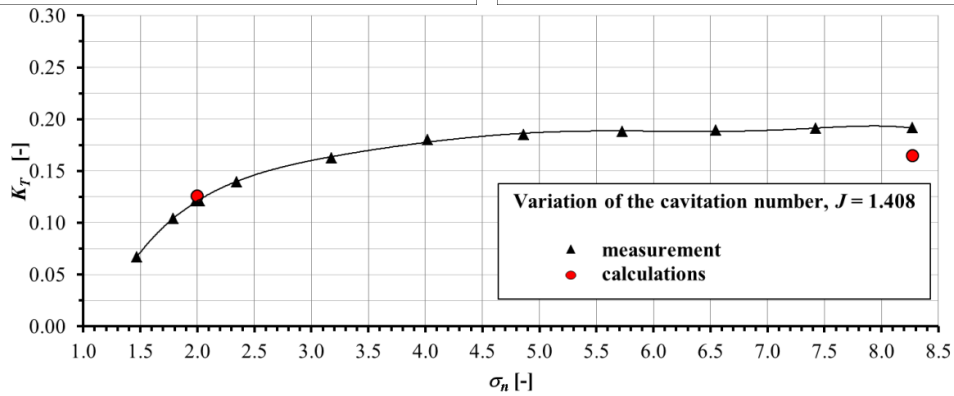
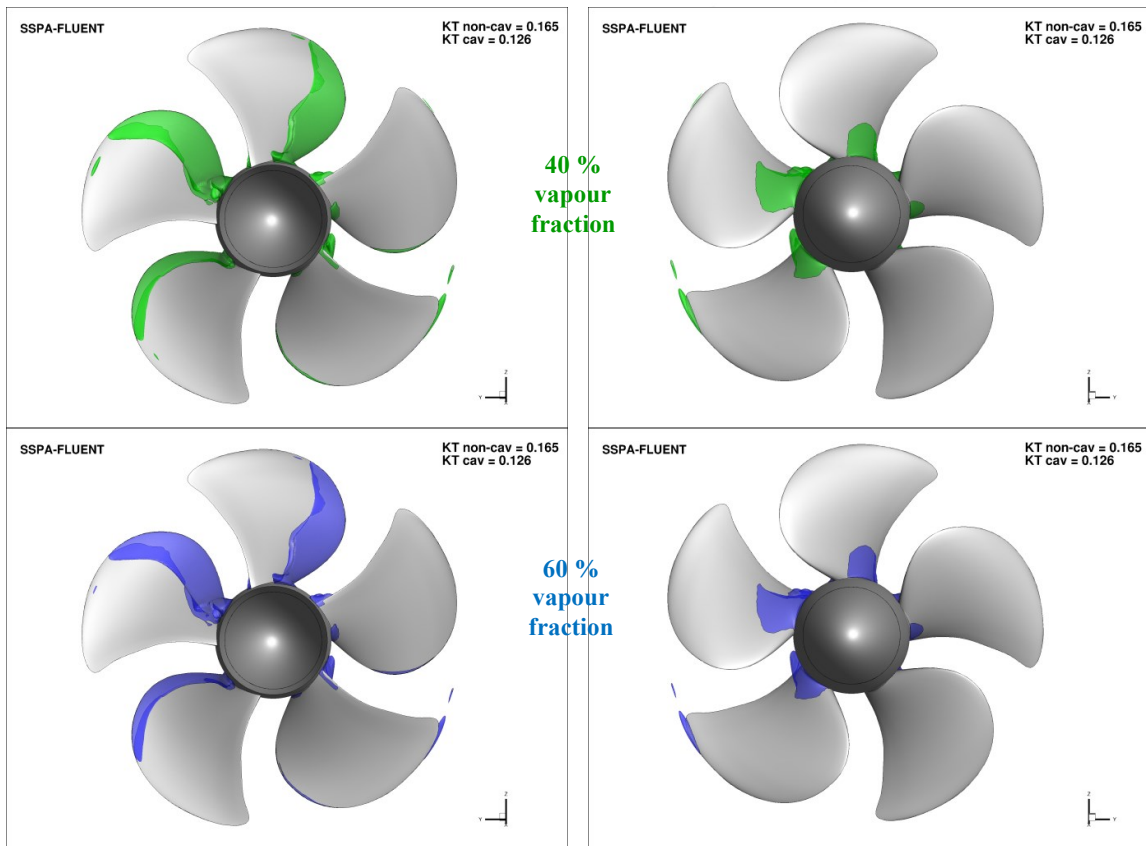
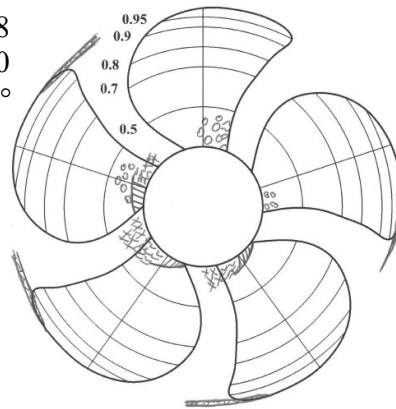
4.11 Case 2.3, SSPA-Fluent-Zwart1

Pressure side

Suction side



Case 2.3
 $J = 1.408$
 $\sigma_n = 2.000$
 $\psi^{bP} = 12.0^\circ$

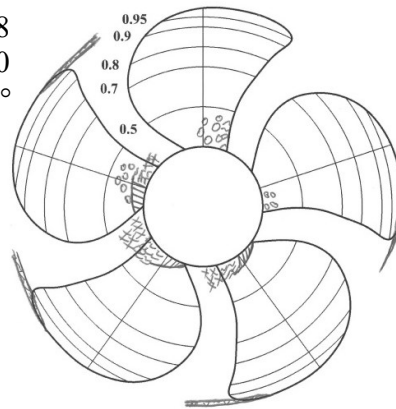
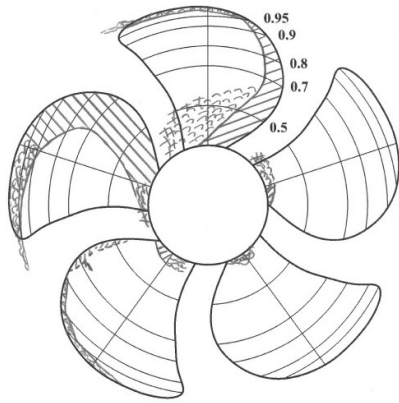


4.12 Case 2.3, TUHH-CFX

Pressure side

Suction side

Case 2.3
 $J = 1.408$
 $\sigma_n = 2.000$
 $\psi^{bP} = 12.0^\circ$

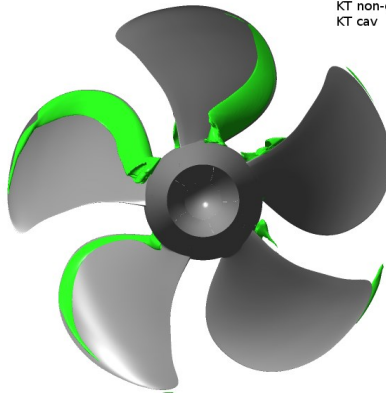


TUHH-CFX

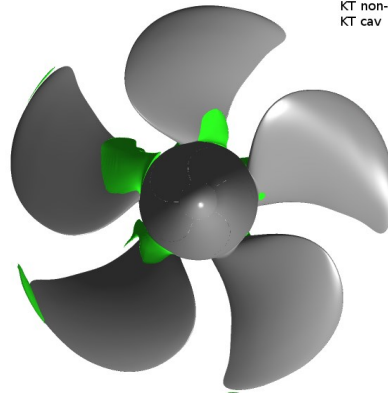
KT non-cav = 0.1847
 KT cav = 0.1470

TUHH-CFX

KT non-cav = 0.1847
 KT cav = 0.1470



40 %
vapour
fraction

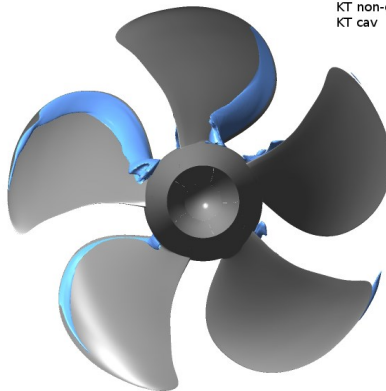


TUHH-CFX

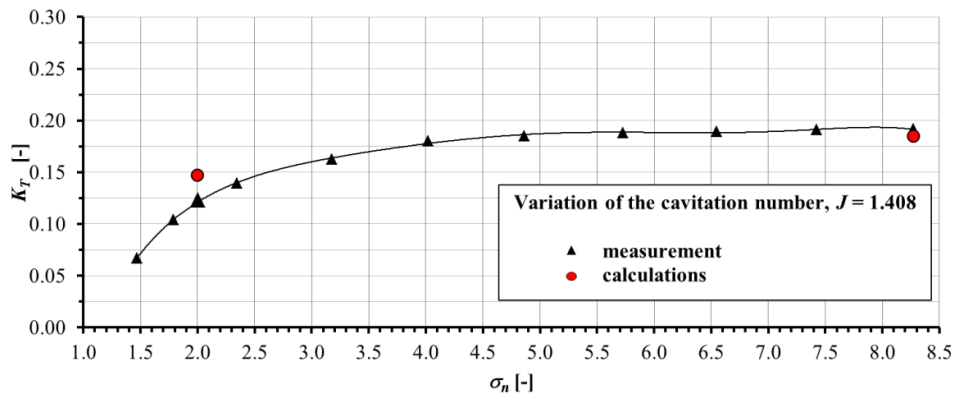
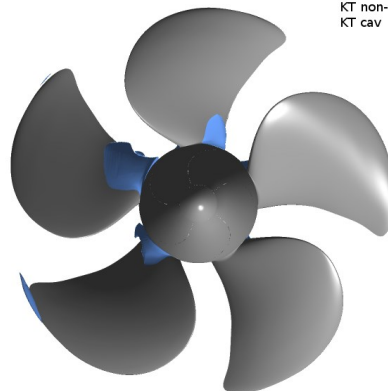
KT non-cav = 0.1847
 KT cav = 0.1470

TUHH-CFX

KT non-cav = 0.1847
 KT cav = 0.1470

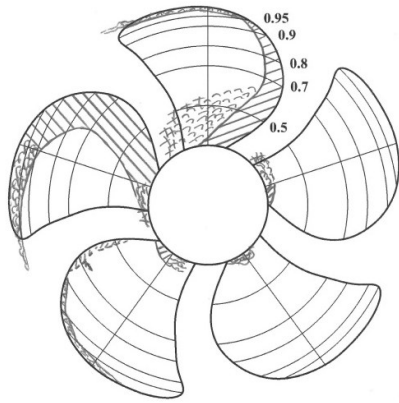


60 %
vapour
fraction



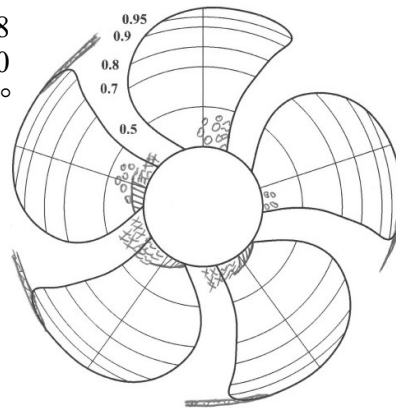
4.13 Case 2.3, TUHH-panMARE

Pressure side



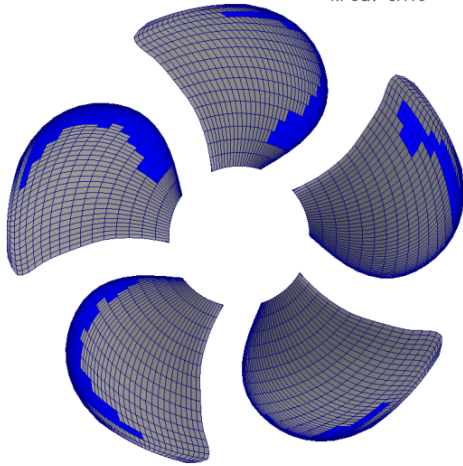
Case 2.3
 $J = 1.408$
 $\sigma_n = 2.000$
 $\psi^{bP} = 12.0^\circ$

Suction side



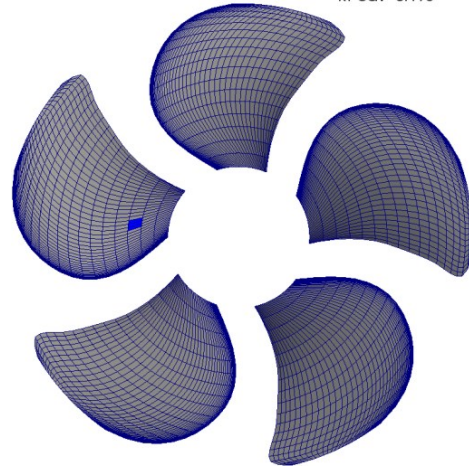
TUHH - panMARE

kT noncav=0.194
 kT cav=0.193

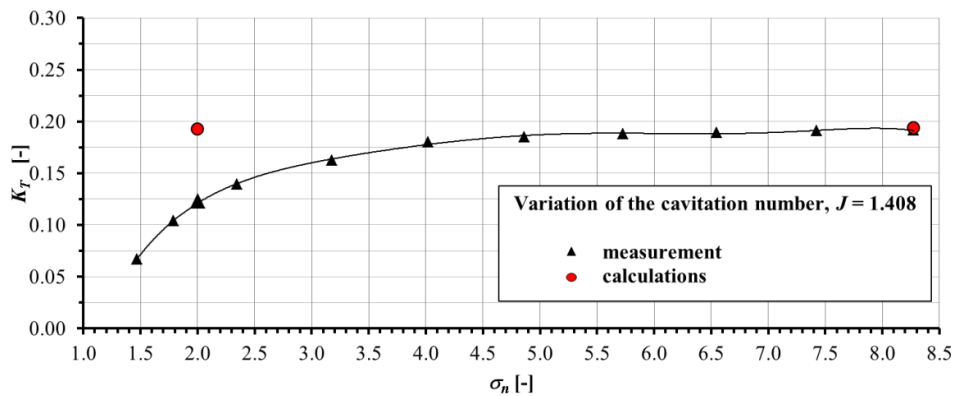


TUHH - panMARE

kT noncav=0.194
 kT cav=0.193

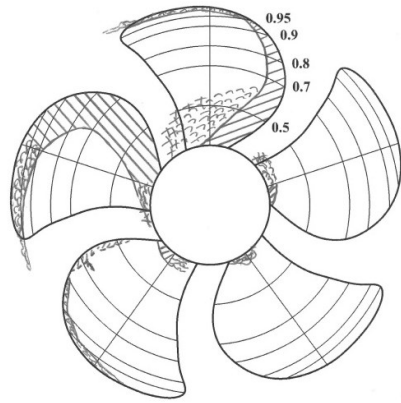


60 %
 vapour
 fraction



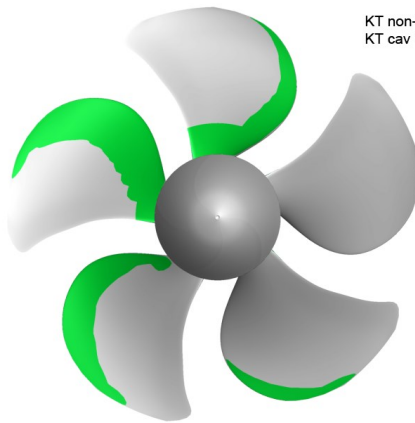
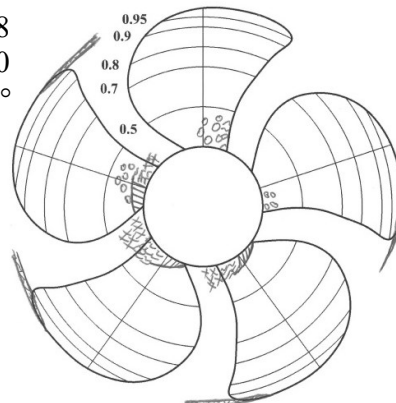
4.14 Case 2.3, UniGenoa-BEM

Pressure side



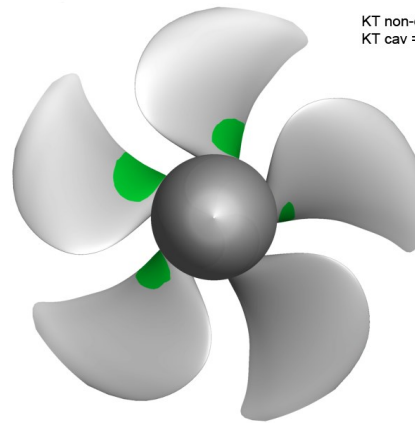
Case 2.3
 $J = 1.408$
 $\sigma_n = 2.000$
 $\psi^{bP} = 12.0^\circ$

Suction side

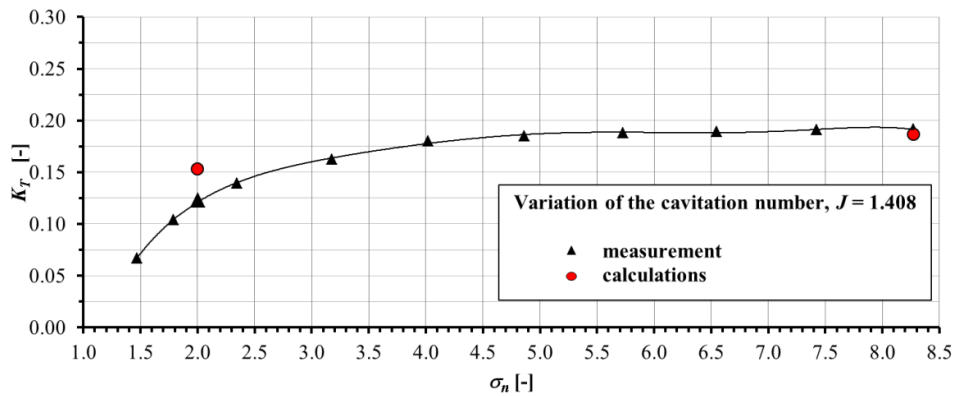


KT non-cav = 0.187
 KT cav = 0.153

40 %
 vapour
 fraction



KT non-cav = 0.187
 KT cav = 0.153



4.15 Case 2.3, UniGenoa-StarCCM+

Pressure side

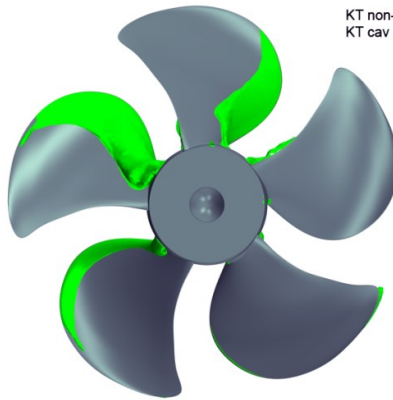
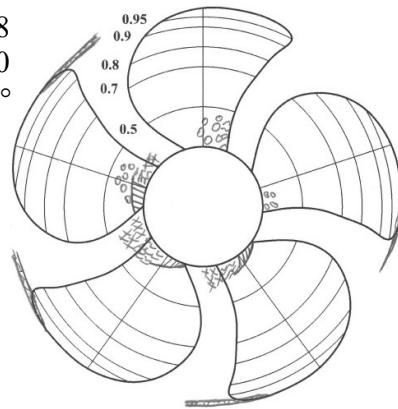
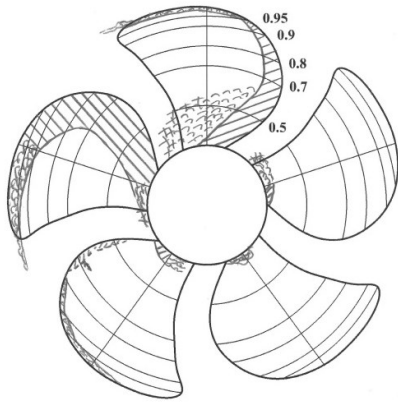
Suction side

Case 2.3

$$J = 1.408$$

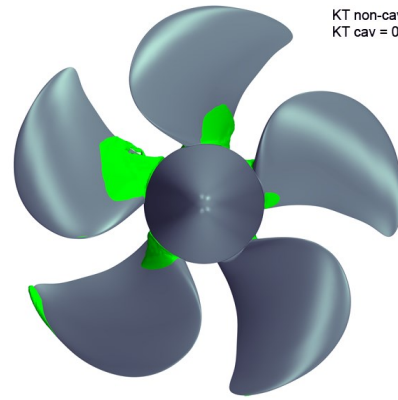
$$\sigma_n = 2.000$$

$$\psi^{bP} = 12.0^\circ$$

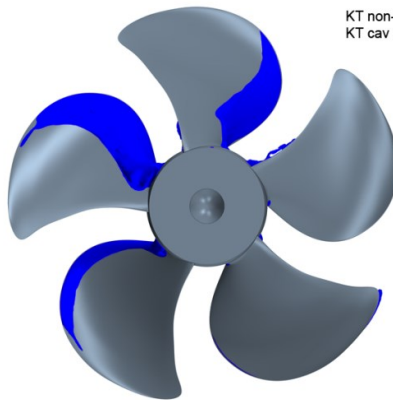


KT non-cav = 0.1890
 KT cav = 0.1452

40 %
 vapour
 fraction

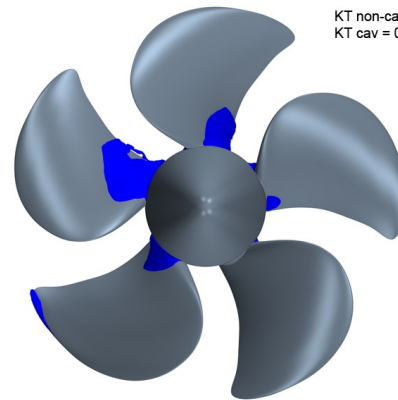


KT non-cav = 0.1890
 KT cav = 0.1452

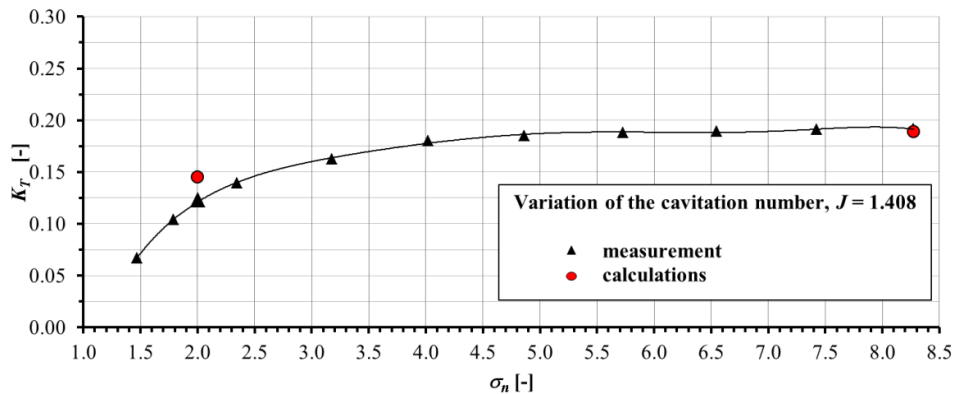


KT non-cav = 0.1890
 KT cav = 0.1452

60 %
 vapour
 fraction



KT non-cav = 0.1890
 KT cav = 0.1452

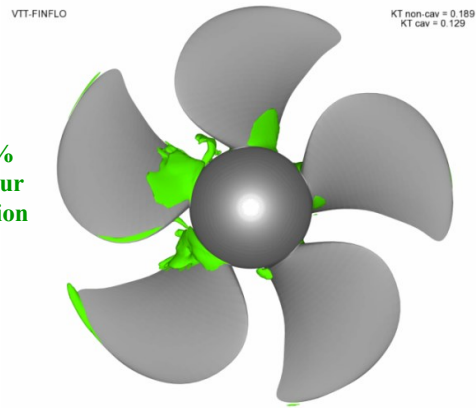
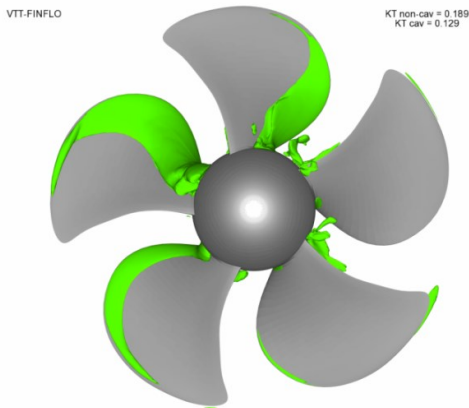
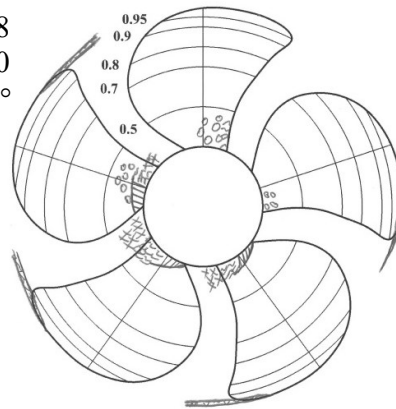
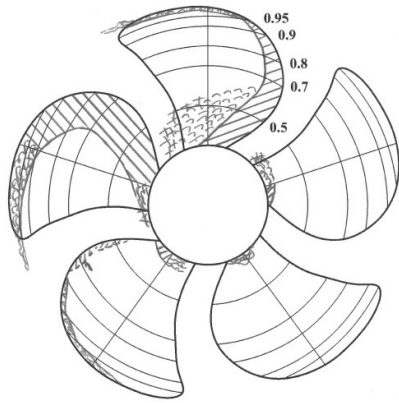


4.16 Case 2.3, VTT-FinFlo

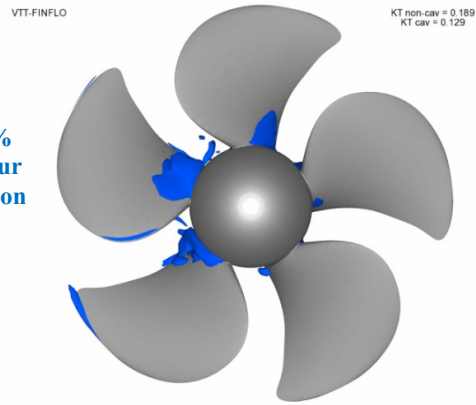
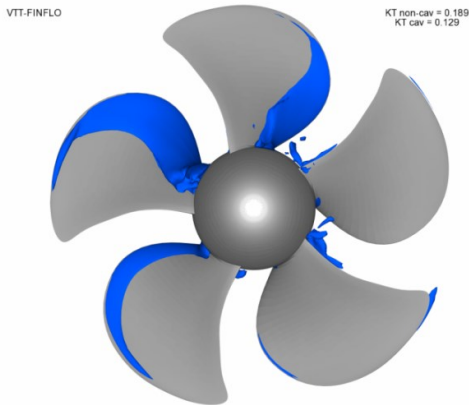
Pressure side

Suction side

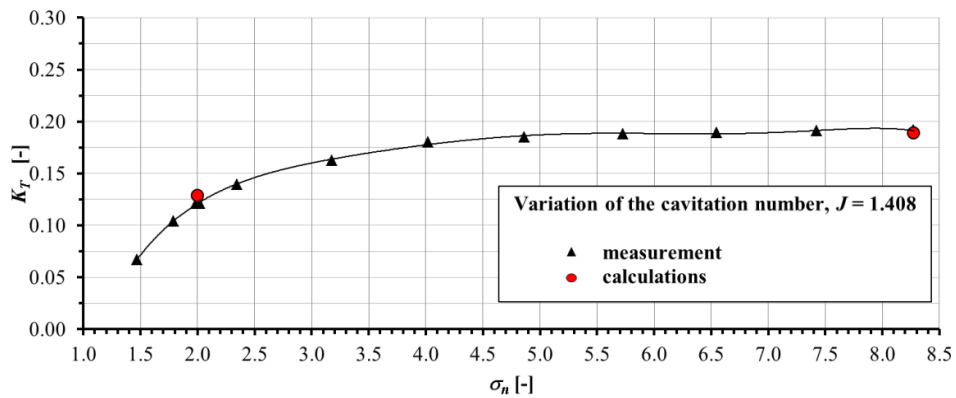
Case 2.3
 $J = 1.408$
 $\sigma_n = 2.000$
 $\psi^{bP} = 12.0^\circ$



40 %
 vapour
 fraction



60 %
 vapour
 fraction



5 Comparison

5.1 Thrust coefficient, non-cavitating

	case 2.1	case 2.2	case 2.3
	K_T [-]	K_T [-]	K_T [-]
Exp. (non-cavitating)	0.392	0.265	0.189
ACCUSIM-CFX-FCM	0.392	0.255	0.181
ACCUSIM-CFX-Kunz	0.392	0.255	0.181
ACCUSIM-CFX-Zwart	0.392	0.255	0.181
CAT-OF	0.385	0.287	0.208
Chalmers-OF	0.405	0.262	0.181
CNRS-ISIS	0.402	0.266	0.182
CRADLE-SCTetra	0.417	0.279	0.200
CSSRC-Fluent	0.401	0.290	0.217
MARIN-ReFresco	0.403		
ROTAM-Fluent	0.420	0.293	0.214
SSPA-Fluent-Sauer	0.391	0.249	0.165
SSPA-Fluent-Zwart1	0.391	0.249	0.165
SSPA-Fluent-Zwart2	0.391		
TUHH-CFX	0.395	0.258	0.185
TUHH-panMARE	0.334	0.250	0.194
UniGenoa-BEM	0.380	0.257	0.187
UniGenoa-StarCCM+	0.406	0.267	0.189
UTAustin-PROPCAV	0.395	0.262	
VTT-FinFlo	0.401	0.266	0.189

5.2 Difference in thrust coefficient, non cavitating

	case 2.1	case 2.2	case 2.3
	ΔK_T [%]	ΔK_T [%]	ΔK_T [%]
ACCUSIM-CFX-FCM	0.00	-3.77	-4.23
ACCUSIM-CFX-Kunz	0.00	-3.77	-4.23
ACCUSIM-CFX-Zwart	0.00	-3.77	-4.23
CAT-OF	-1.79	8.30	10.05
Chalmers-OF	3.32	-1.13	-4.23
CNRS-ISIS	2.55	0.38	-3.70
CRADLE-SCTetra	6.38	5.28	5.82
CSSRC-Fluent	2.30	9.55	14.97
MARIN-ReFresco	2.81		
ROTAM-Fluent	7.14	10.57	13.23
SSPA-Fluent-Sauer	-0.26	-6.04	-12.70
SSPA-Fluent-Zwart1	-0.26	-6.04	-12.70
SSPA-Fluent-Zwart2	-0.26		
TUHH-CFX	0.77	-2.49	-2.28
TUHH-panMARE	-14.80	-5.66	2.65
UniGenoa-BEM	-3.06	-3.02	-1.06
UniGenoa-StarCCM+	3.57	0.87	0.00
UTAustin-PROPCAV	0.77	-1.13	
VTT-FinFlo	2.30	0.38	0.00

5.3 Thrust coefficient, cavitating

	case 2.1	case 2.2	case 2.3
	K_T [-]	K_T [-]	K_T [-]
Exp. (cavitating)	0.363	0.167	0.123
ACCUSIM-CFX-FCM	0.365	0.173	0.131
ACCUSIM-CFX-Kunz	0.368	0.166	0.128
ACCUSIM-CFX-Zwart	0.365	0.166	0.130
CAT-OF	0.349	0.157	0.084
Chalmers-OF	0.373	0.196	0.157
CNRS-ISIS	0.353	0.122	0.084
CRADLE-SCTetra	0.372	0.212	0.146
CSSRC-Fluent	0.385	0.257	0.187
MARIN-ReFresco	0.387		
ROTAM-Fluent	0.385	0.218	0.167
SSPA-Fluent-Sauer	0.380	0.190	0.123
SSPA-Fluent-Zwart1	0.377	0.192	0.126
SSPA-Fluent-Zwart2	0.367		
TUHH-CFX	0.386	0.205	0.147
TUHH-panMARE	0.382	0.144	0.193
UniGenoa-BEM	0.390	0.246	0.153
UniGenoa-StarCCM+	0.389	0.208	0.145
UTAustin-PROPCAV	0.367	0.167	
VTT-FinFlo	0.375	0.192	0.129

5.4 Difference in thrust coefficient, cavitating

	case 2.1	case 2.2	case 2.3
	ΔK_T [%]	ΔK_T [%]	ΔK_T [%]
ACCUSIM-CFX-FCM	0.55	3.59	6.50
ACCUSIM-CFX-Kunz	1.38	-0.60	4.07
ACCUSIM-CFX-Zwart	0.55	-0.60	5.69
CAT-OF	-3.86	-5.99	-31.71
Chalmers-OF	2.75	17.37	27.64
CNRS-ISIS	-2.75	-26.95	-31.71
CRADLE-SCTetra	2.48	26.95	18.70
CSSRC-Fluent	6.06	54.07	52.28
MARIN-ReFresco	6.61		
ROTAM-Fluent	6.06	30.54	35.77
SSPA-Fluent-Sauer	4.68	13.77	0.00
SSPA-Fluent-Zwart1	3.86	14.97	2.44
SSPA-Fluent-Zwart2	1.10		
TUHH-CFX	6.34	22.46	19.51
TUHH-panMARE	5.23	-13.77	56.91
UniGenoa-BEM	7.44	47.31	24.39
UniGenoa-StarCCM+	7.16	24.43	18.05
UTAustin-PROPCAV	1.10	0.00	
VTT-FinFlo	3.31	14.97	4.88

5.5 Thrust breakdown, absolute difference

	case 2.1	case 2.2	case 2.3
	ΔK_T [-]	ΔK_T [-]	ΔK_T [-]
Experiment	0.029	0.098	0.066
ACCUSIM-CFX-FCM	0.027	0.082	0.050
ACCUSIM-CFX-Kunz	0.024	0.089	0.053
ACCUSIM-CFX-Zwart	0.027	0.089	0.051
CAT-OF	0.036	0.130	0.124
Chalmers-OF	0.032	0.066	0.024
CRADLE-SCTetra	0.049	0.144	0.098
CNRS-ISIS	0.045	0.067	0.054
CSSRC-Fluent	0.016	0.033	0.030
MARIN-ReFresco	0.016		
ROTAM-Fluent	0.035	0.075	0.047
SSPA-Fluent-Sauer	0.011	0.059	0.042
SSPA-Fluent-Zwart	0.014	0.057	0.039
TUHH-CFX	0.024		
TUHH-panMARE	0.009	0.054	0.038
UniGenoa-BEM	-0.048	0.106	0.001
UniGenoa-StarCCM+	-0.010	0.011	0.034
UTAustin-PROPCAV	0.028	0.095	
VTT-FinFlo	0.017	0.060	0.044

Chapter 3

Case 3

Propeller Pressure Pulses in Oblique Flow

3 Participants

The following institutes have participated:

Case 3.1

Group	Solver	Acronym	Cavitation	N / turn
Cradle	SCTetra	Cradle-SCTetra	without	512
Cradle	SCTetra	Cradle-SCTetra	with	1024
MARIN	ReFresco	MARIN-ReFresco	without	128
MARIN	ReFresco	MARIN-ReFresco	with	256
ROTAM	ANSYS	ROTAM-ANSYS	without	256
SSPA	FLUENT	SSPA-FLUENT	without	256
SSPA	FLUENT	SSPA-FLUENT	with	256
SSPA	FLUENT	SSPA-FLUENT	with	256
TUHH	CFX	TUHH-CFX	without	256
TUHH	CFX	TUHH-CFX	with	256
TUHH	OpenFOAM	TUHH-OpenFOAM	without	256
TUHH	panMARE	TUHH-panMARE	without	64
TUHH	panMARE	TUHH-panMARE	with	32
UTAustin	PROPCAV	UTAustin-PROPCAV	without	60
UTAustin	PROPCAV	UTAustin-PROPCAV	with	60
VTT	FINFLO	VTT-FINFLO	without	256

Case 3.2

Group	Solver	Acronym	Cavitation	N / turn
Cradle	SCTetra	Cradle-SCTetra	without	512
Cradle	SCTetra	Cradle-SCTetra	with	1024
MARIN	ReFresco	MARIN-ReFresco	without	128
MARIN	ReFresco	MARIN-ReFresco	with	256
ROTAM	ANSYS	ROTAM-ANSYS	without	256
SSPA	FLUENT	SSPA-FLUENT	without	256
SSPA	FLUENT	SSPA-FLUENT	with	256
SSPA	FLUENT	SSPA-FLUENT	with	256
TUHH	CFX	TUHH-CFX	without	256
TUHH	CFX	TUHH-CFX	with	256
TUHH	OpenFOAM	TUHH-OpenFOAM	without	256
TUHH	panMARE	TUHH-panMARE	without	64
TUHH	panMARE	TUHH-panMARE	with	16
UTAustin	PROPCAV	UTAustin-PROPCAV	without	60

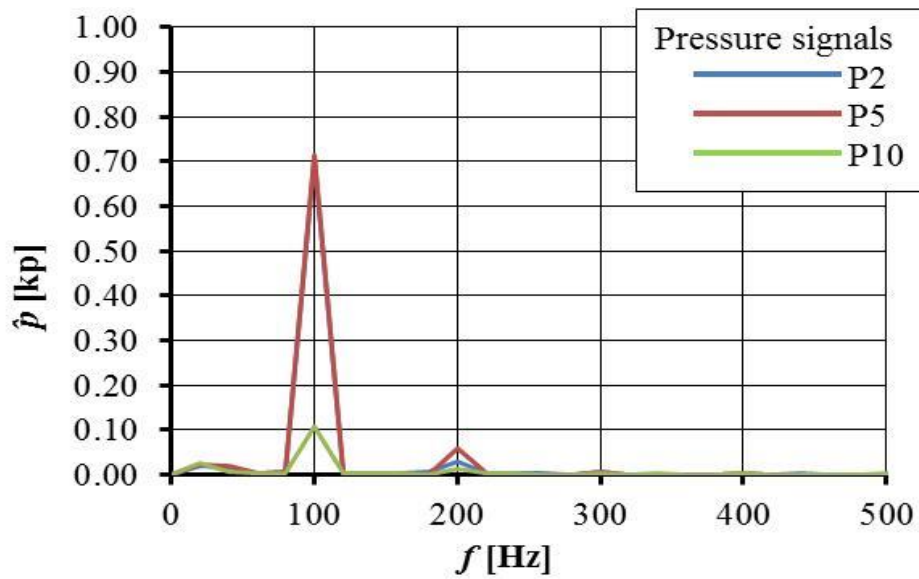
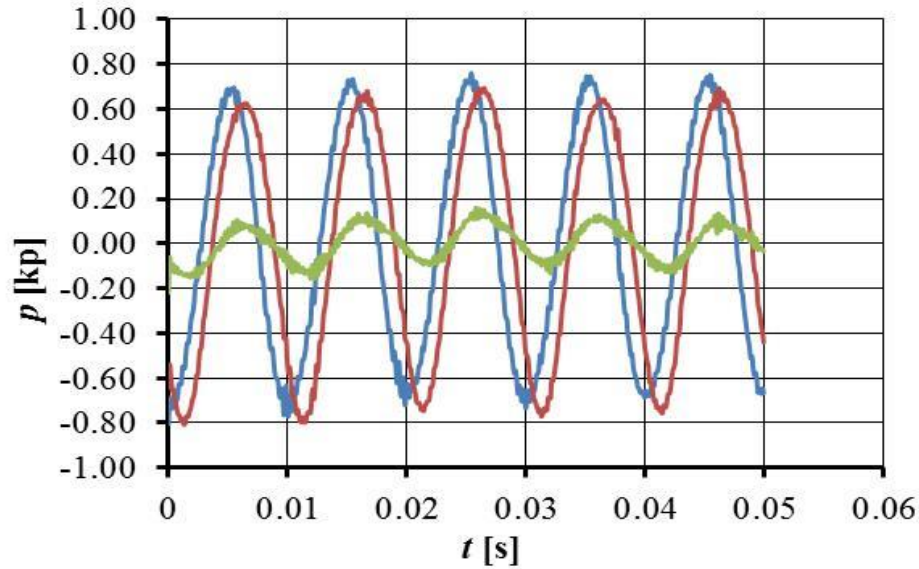
3 Participants

The following institutes have participated:

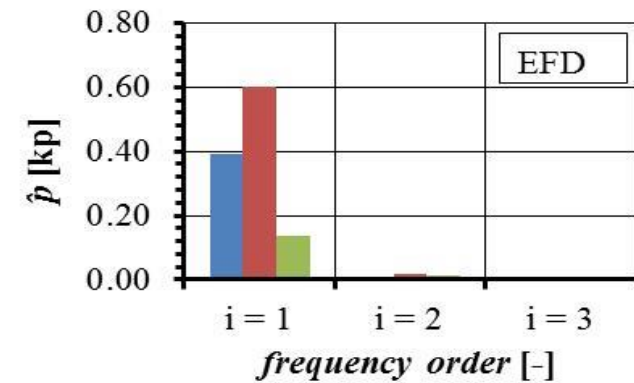
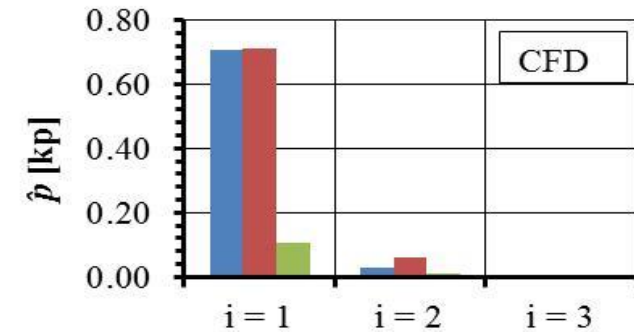
Case 3.3

Group	Solver	Acronym	Cavitation	N / turn
Cradle	SCTetra	Cradle-SCTetra	without	512
Cradle	SCTetra	Cradle-SCTetra	with	1024
MARIN	ReFresco	MARIN-ReFresco	without	128
MARIN	ReFresco	MARIN-ReFresco	with	256
ROTAM	ANSYS	ROTAM-ANSYS	without	256
SSPA	FLUENT	SSPA-FLUENT	without	256
SSPA	FLUENT	SSPA-FLUENT	with	256
SSPA	FLUENT	SSPA-FLUENT	with	256
TUHH	CFX	TUHH-CFX	without	256
TUHH	CFX	TUHH-CFX	with	256
TUHH	OpenFOAM	TUHH-OpenFOAM	without	256
TUHH	panMARE	TUHH-panMARE	without	64
TUHH	panMARE	TUHH-panMARE	with	32
UTAustin	PROPCAV	UTAustin-PROPCAV	without	60

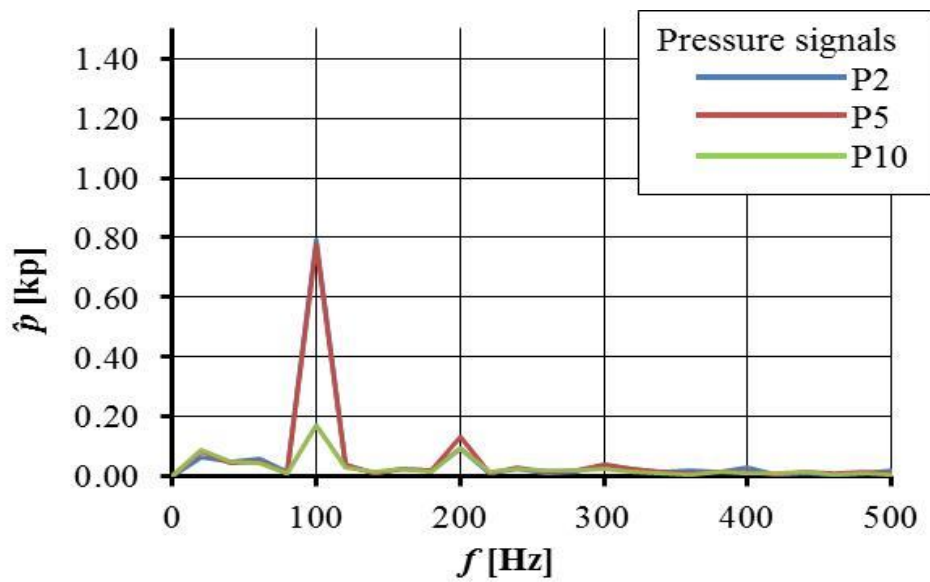
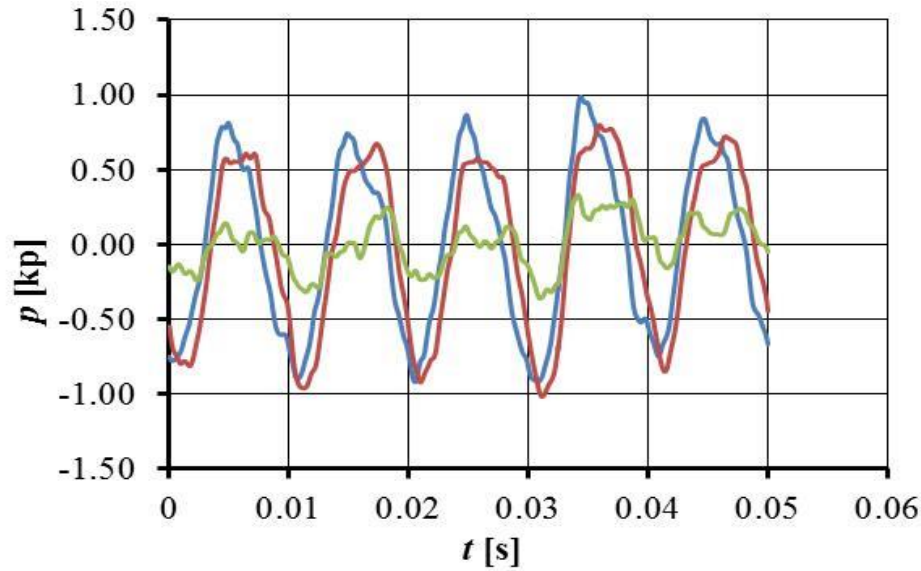
3.1.1 Pressure pulses for $\Psi^{bP} = 12^\circ$: Cradle-SCTetra, without Cavitation



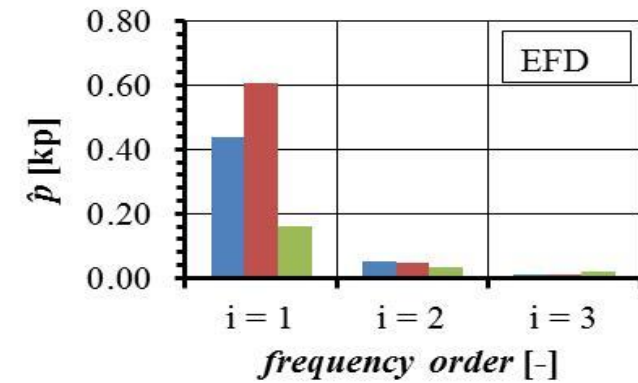
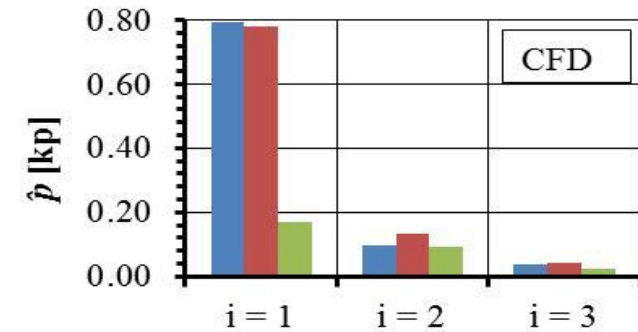
Sensor		$i = 1$	$i = 2$	$i = 3$
p2	(CFD)	0.7085	0.0294	0.0051
p5	(CFD)	0.7129	0.0582	0.0059
P10	(CFD)	0.1074	0.0116	0.0038
p2	(EFD)	0.3899	0.0107	0.0047
p5	(EFD)	0.6017	0.0159	0.0081
P10	(EFD)	0.1373	0.0113	0.0076



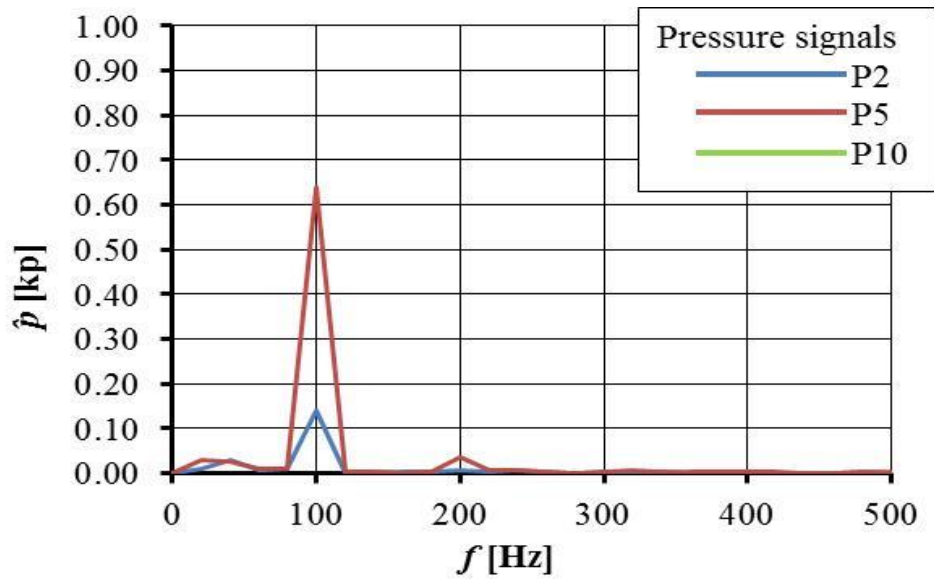
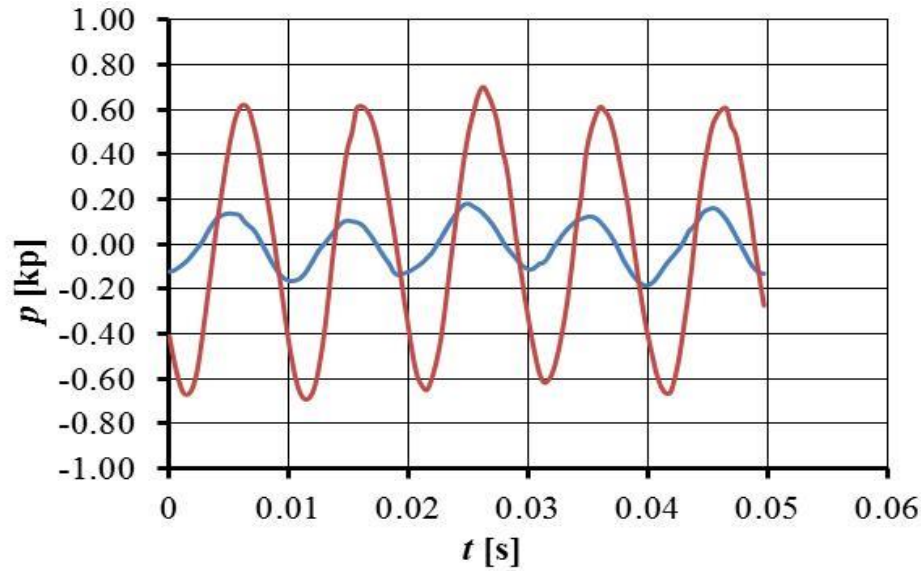
3.1.2 Pressure pulses for $\Psi^{bP} = 12^\circ$: Cradle-SCTetra, with Cavitation



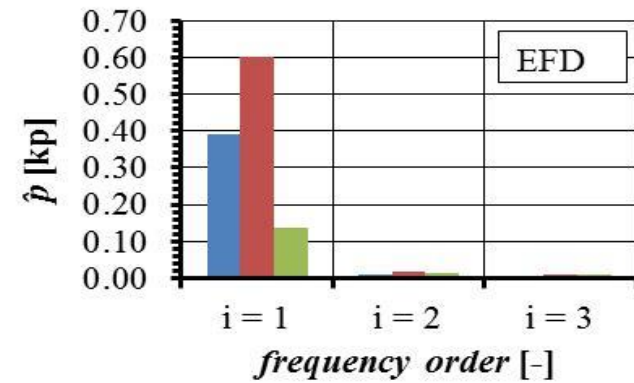
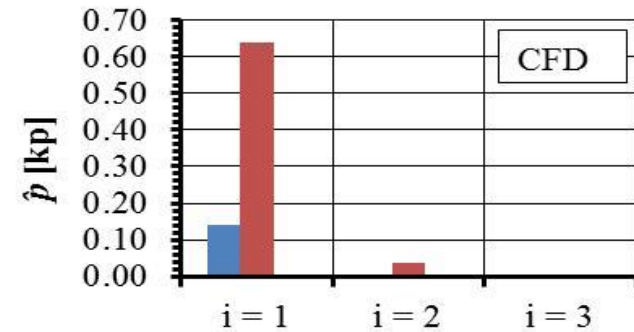
Sensor		$i = 1$	$i = 2$	$i = 3$
p2	(CFD)	0.7933	0.0948	0.0385
p5	(CFD)	0.7784	0.1337	0.0397
P10	(CFD)	0.1696	0.0941	0.0244
p2	(EFD)	0.4372	0.0525	0.0079
p5	(EFD)	0.6053	0.0484	0.0087
P10	(EFD)	0.1611	0.0318	0.0178



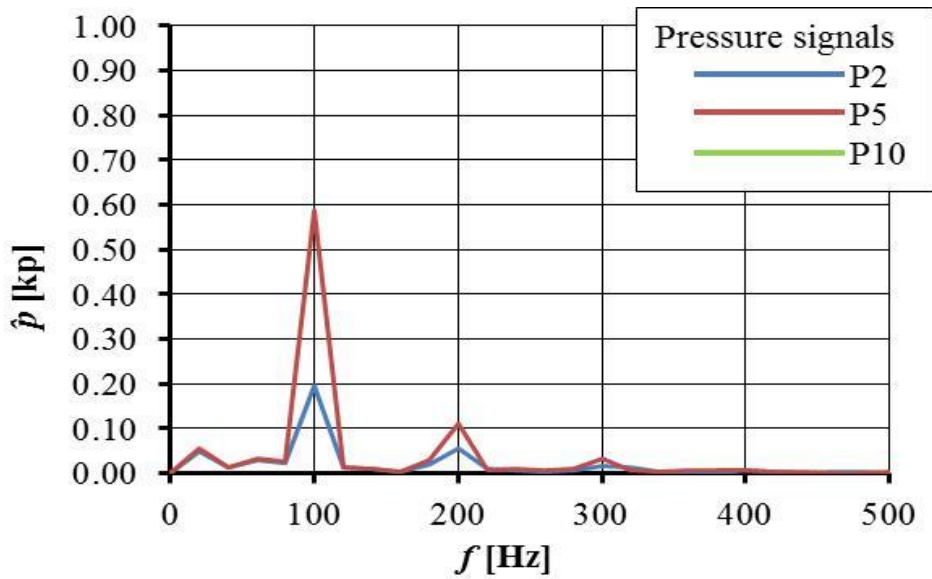
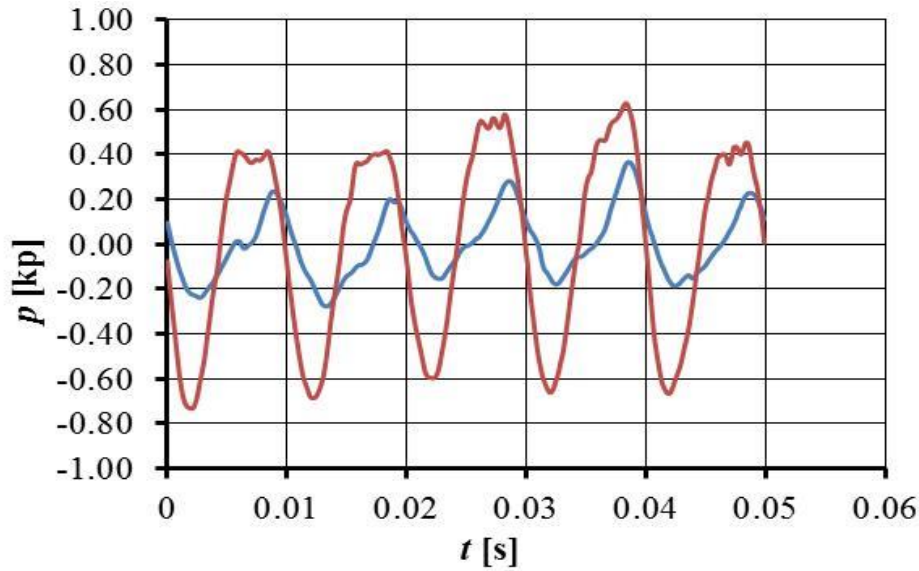
3.1.3 Pressure pulses for $\Psi^{bP} = 12^\circ$: MARIN-ReFresco, without Cavitation



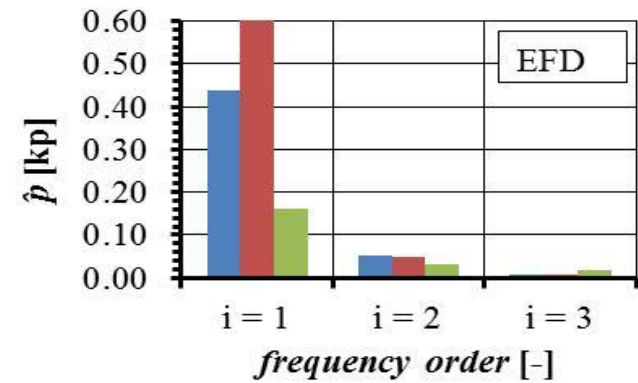
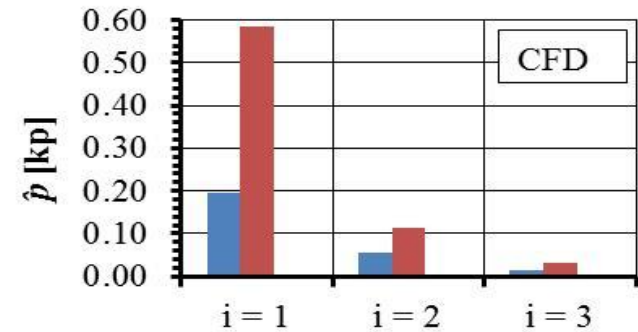
Sensor		$i = 1$	$i = 2$	$i = 3$
p2	(CFD)	0.1404	0.0057	0.0024
p5	(CFD)	0.6399	0.0354	0.0017
p2	(EFD)	0.3899	0.0107	0.0047
p5	(EFD)	0.6017	0.0159	0.0081
P10	(EFD)	0.1373	0.0113	0.0076



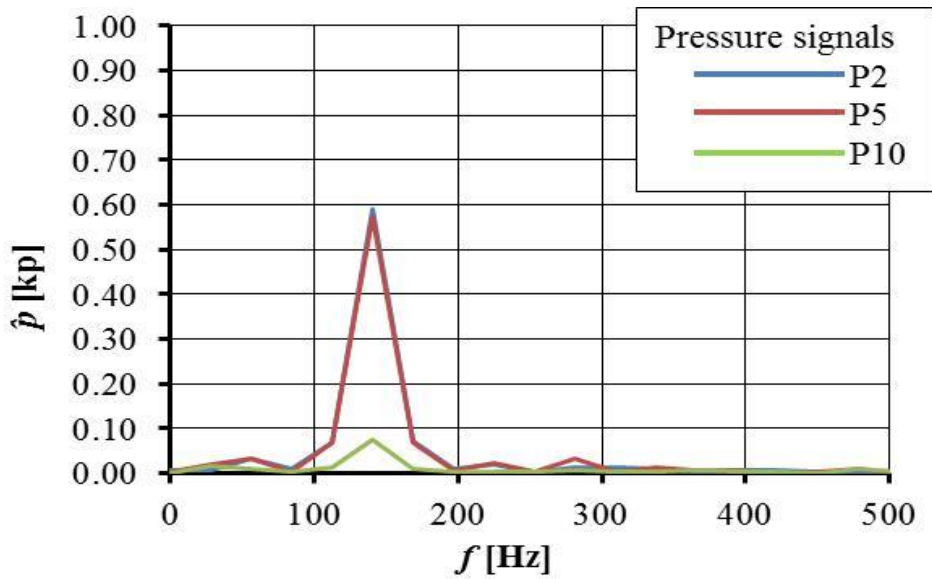
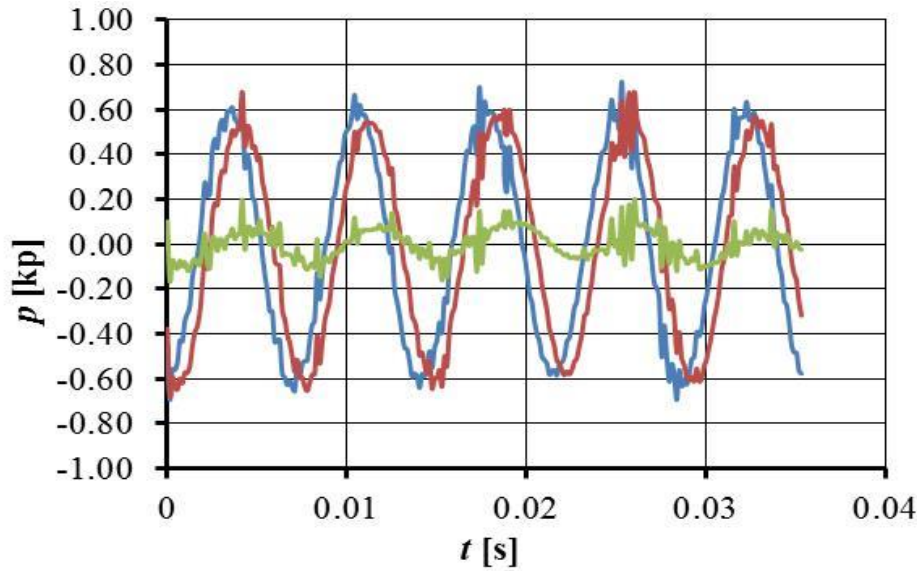
3.1.4 Pressure pulses for $\Psi^{bP} = 12^\circ$: MARIN-ReFresco, with Cavitation



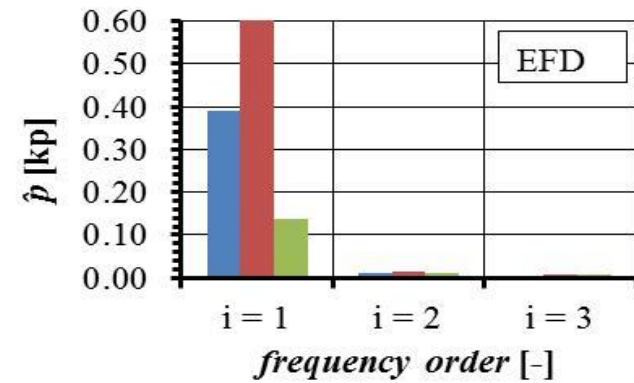
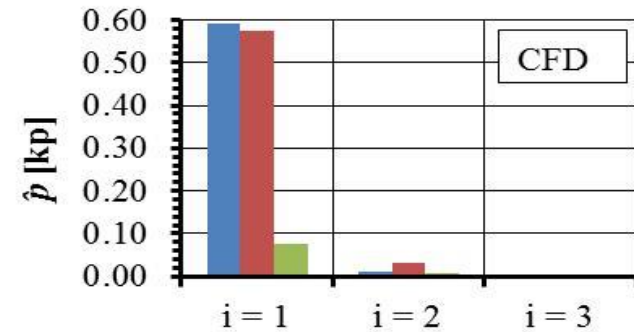
Sensor		$i = 1$	$i = 2$	$i = 3$
p2	(CFD)	0.1950	0.0546	0.0158
p5	(CFD)	0.5855	0.1118	0.0319
p2	(EFD)	0.4372	0.0525	0.0079
p5	(EFD)	0.6053	0.0484	0.0087
P10	(EFD)	0.1611	0.0318	0.0178



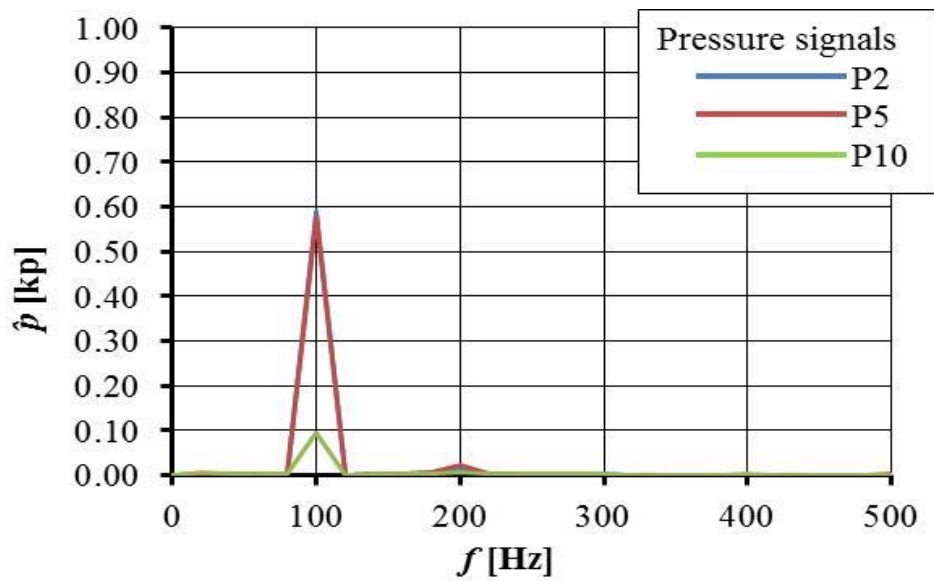
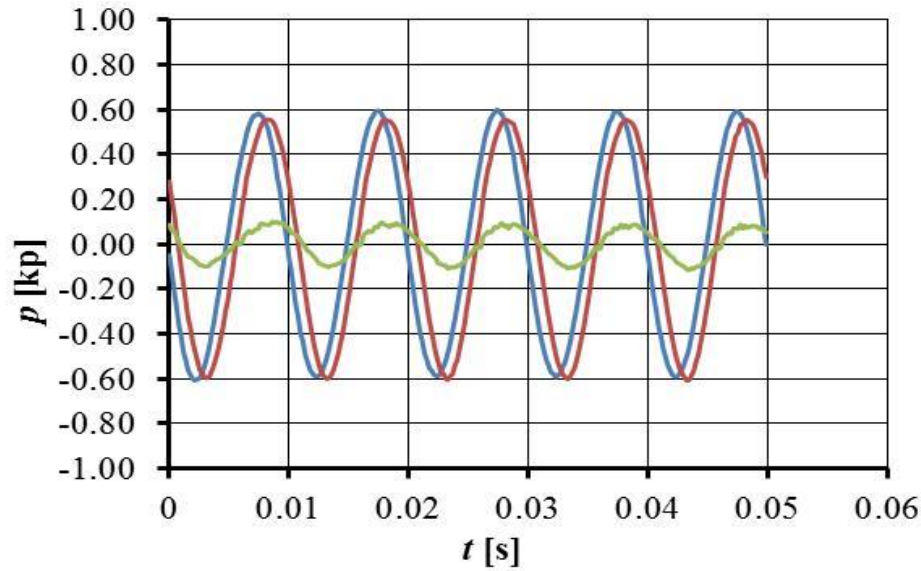
3.1.5 Pressure pulses for $\Psi^{bP} = 12^\circ$: ROTAM-ANSYS, without Cavitation



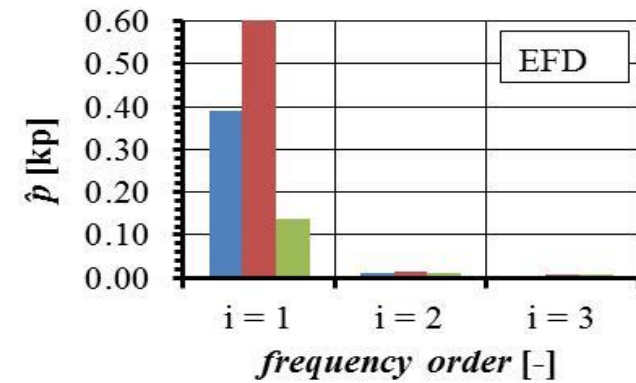
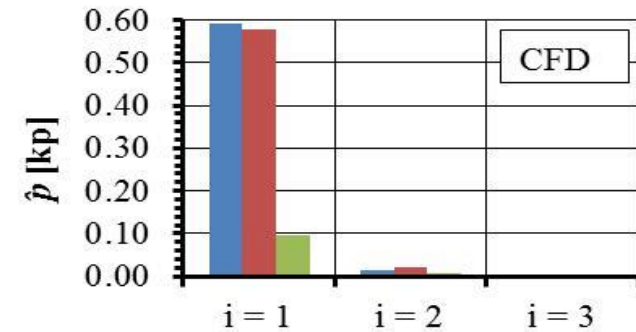
Sensor		$i = 1$	$i = 2$	$i = 3$
p2	(CFD)	0.5896	0.0125	0.0059
p5	(CFD)	0.5734	0.0314	0.0004
P10	(CFD)	0.0761	0.0061	0.0027
p2	(EFD)	0.3899	0.0107	0.0047
p5	(EFD)	0.6017	0.0159	0.0081
P10	(EFD)	0.1373	0.0113	0.0076



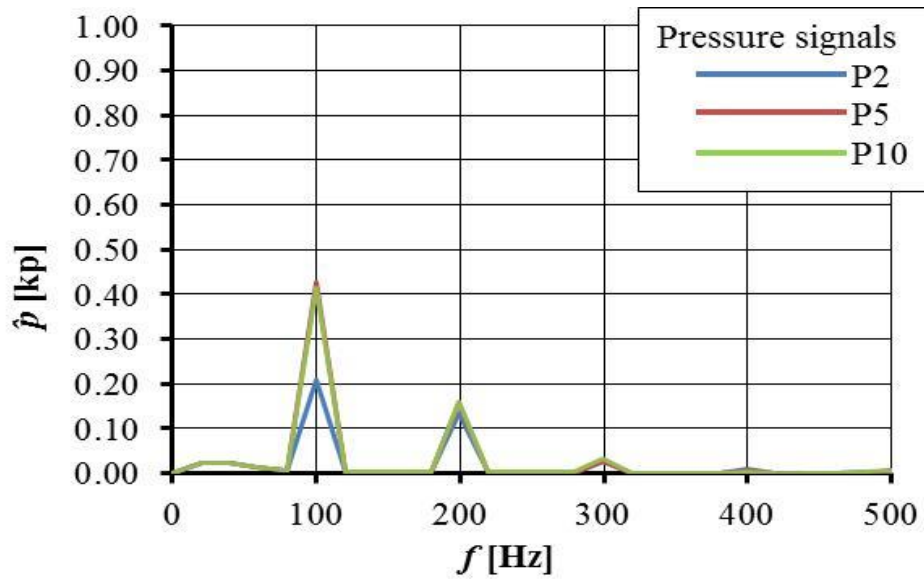
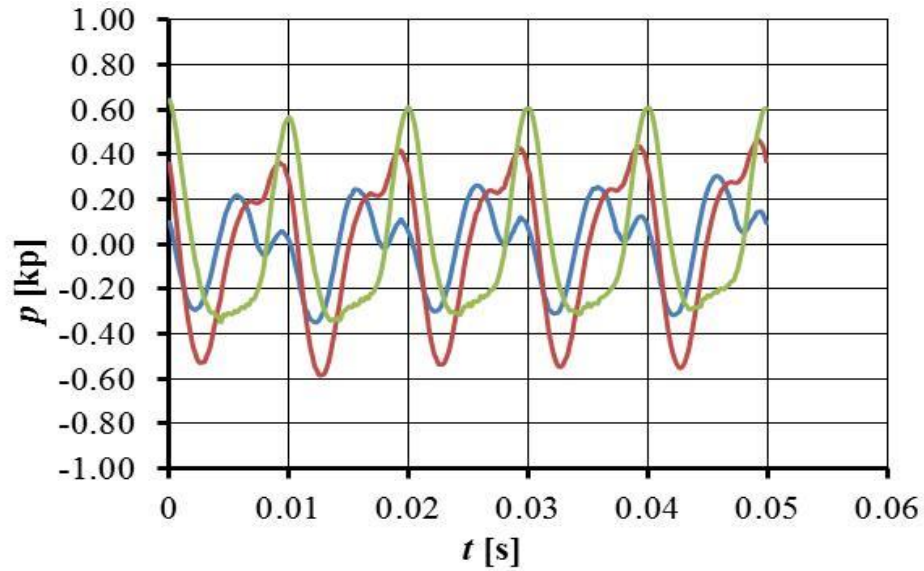
3.1.6 Pressure pulses for $\Psi^{bP} = 12^\circ$: SSPA-FLUENT, without Cavitation



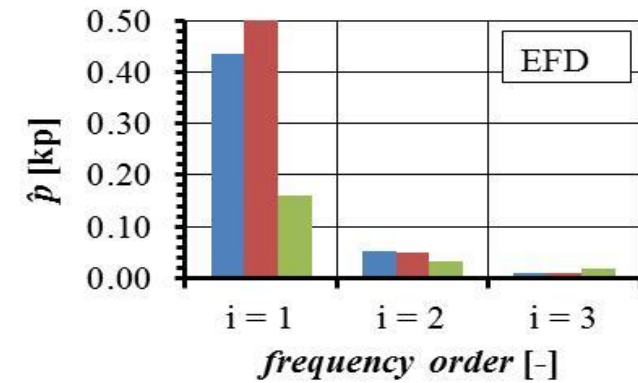
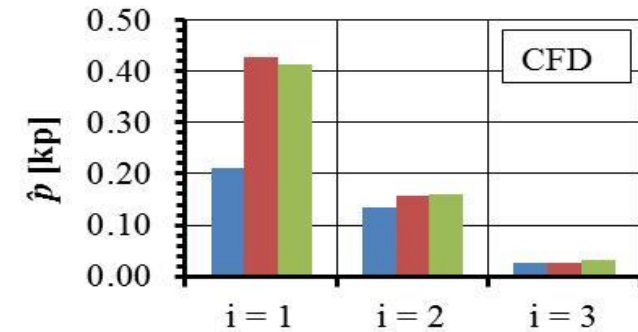
Sensor		$i = 1$	$i = 2$	$i = 3$
p2	(CFD)	0.5907	0.0132	0.0017
p5	(CFD)	0.5778	0.0212	0.0011
P10	(CFD)	0.0955	0.0069	0.0018
p2	(EFD)	0.3899	0.0107	0.0047
p5	(EFD)	0.6017	0.0159	0.0081
P10	(EFD)	0.1373	0.0113	0.0076



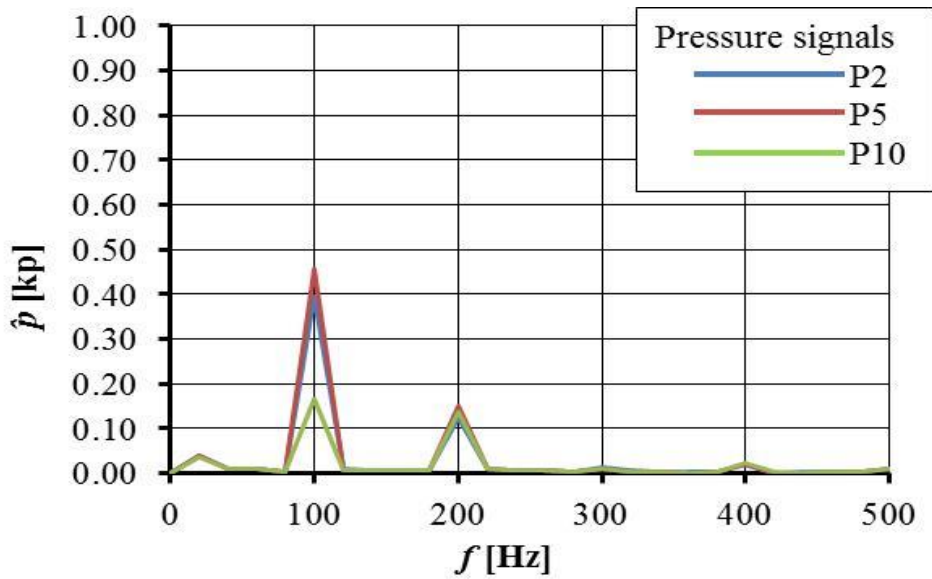
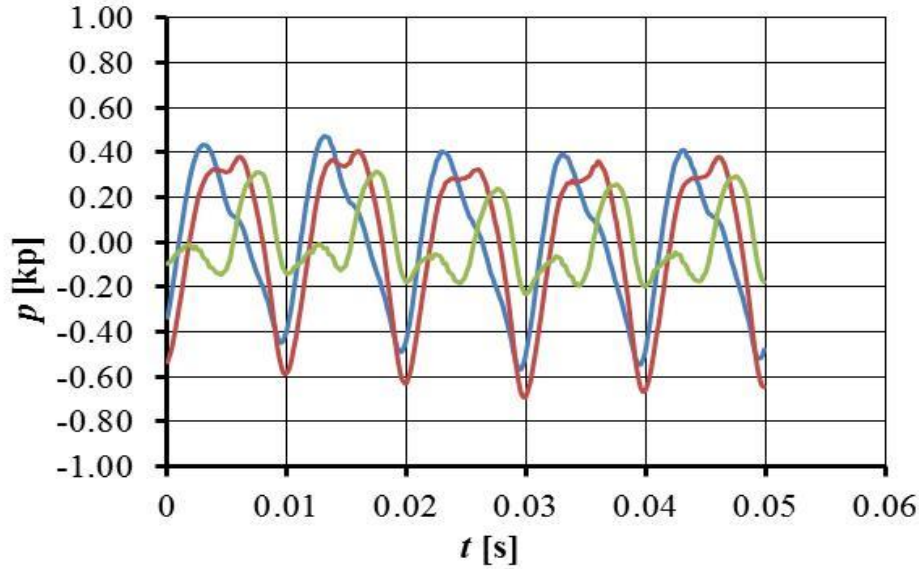
3.1.7 Pressure pulses for $\Psi^{bP} = 12^\circ$: SSPA-FLUENT, with Cavitation



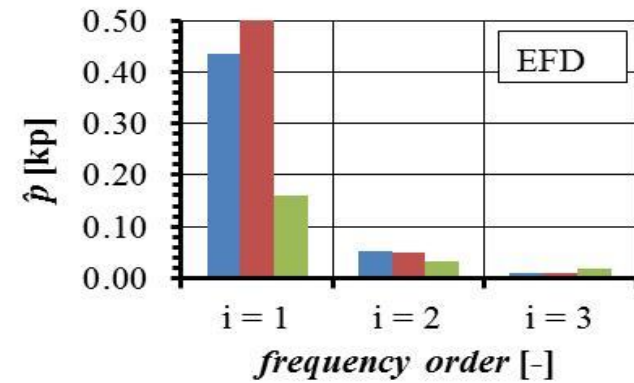
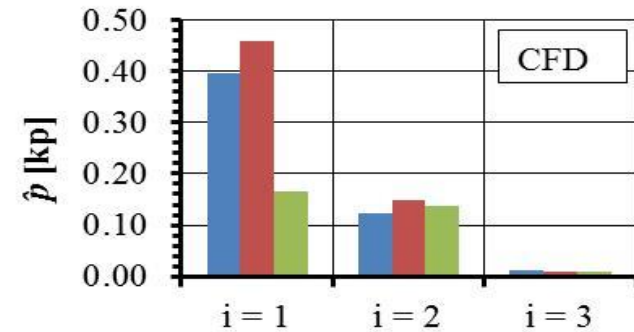
Sensor		$i = 1$	$i = 2$	$i = 3$
p2	(CFD)	0.2100	0.1348	0.0265
p5	(CFD)	0.4285	0.1578	0.0257
P10	(CFD)	0.4144	0.1610	0.0313
p2	(EFD)	0.4372	0.0525	0.0079
p5	(EFD)	0.6053	0.0484	0.0087
P10	(EFD)	0.1611	0.0318	0.0178



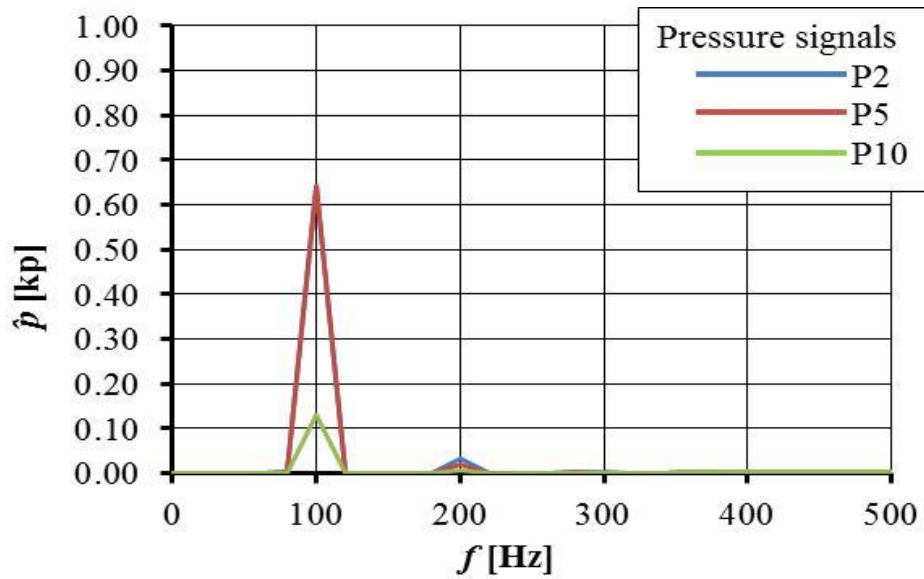
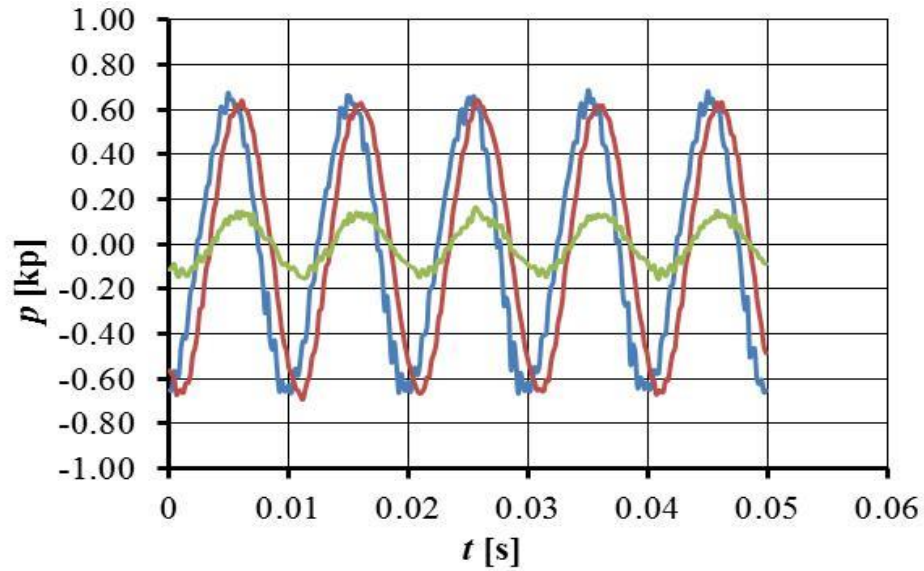
3.1.8 Pressure pulses for $\Psi^{bP} = 12^\circ$: SSPA-FLUENT, with Cavitation, Sauer



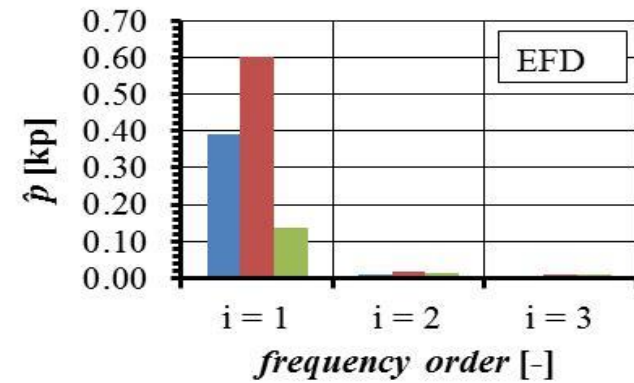
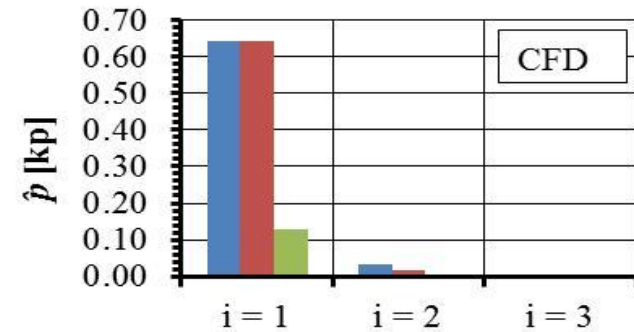
Sensor		$i = 1$	$i = 2$	$i = 3$
p2	(CFD)	0.3961	0.1238	0.0113
p5	(CFD)	0.4574	0.1483	0.0104
P10	(CFD)	0.1668	0.1360	0.0101
p2	(EFD)	0.4372	0.0525	0.0079
p5	(EFD)	0.6053	0.0484	0.0087
P10	(EFD)	0.1611	0.0318	0.0178



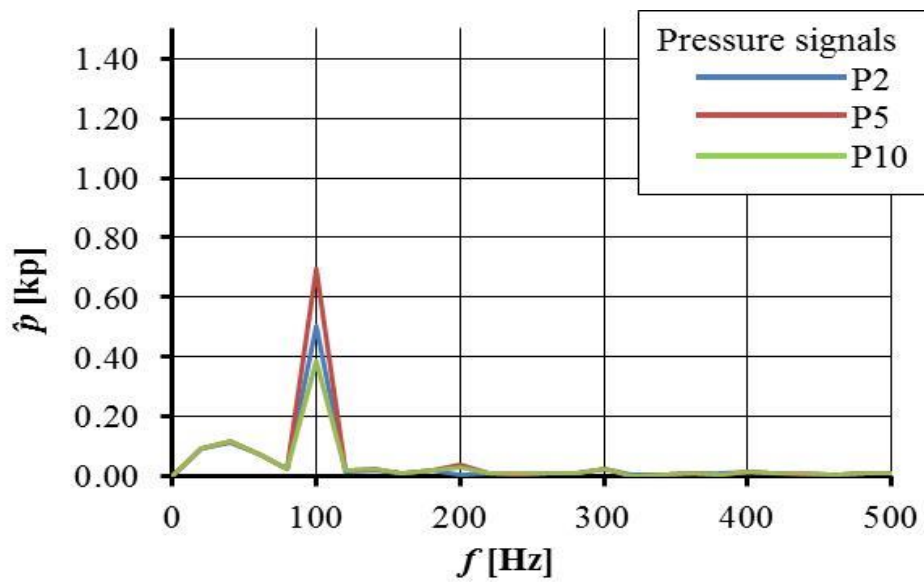
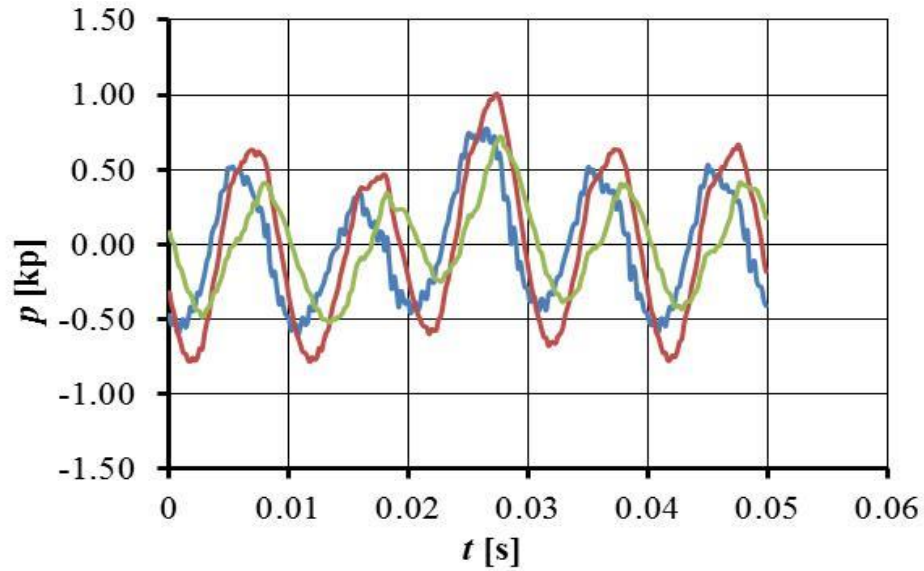
3.1.9 Pressure pulses for $\Psi^{bP} = 12^\circ$: TUHH-CFX, without Cavitation



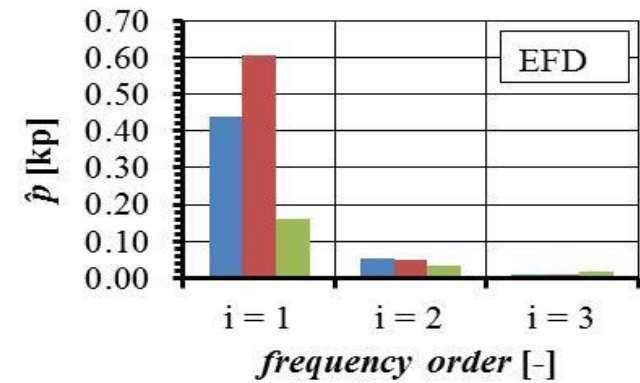
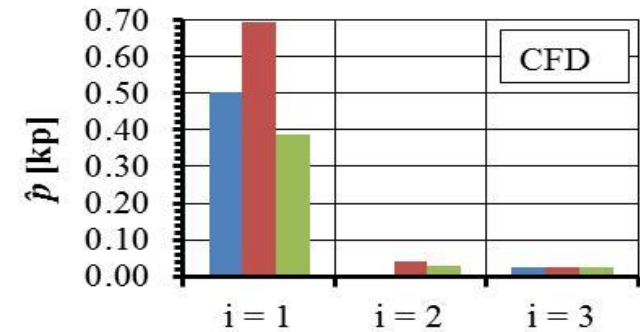
Sensor		$i = 1$	$i = 2$	$i = 3$
p2	(CFD)	0.6435	0.0308	0.0034
p5	(CFD)	0.6413	0.0178	0.0004
P10	(CFD)	0.1297	0.0047	0.0007
p2	(EFD)	0.3899	0.0107	0.0047
p5	(EFD)	0.6017	0.0159	0.0081
P10	(EFD)	0.1373	0.0113	0.0076



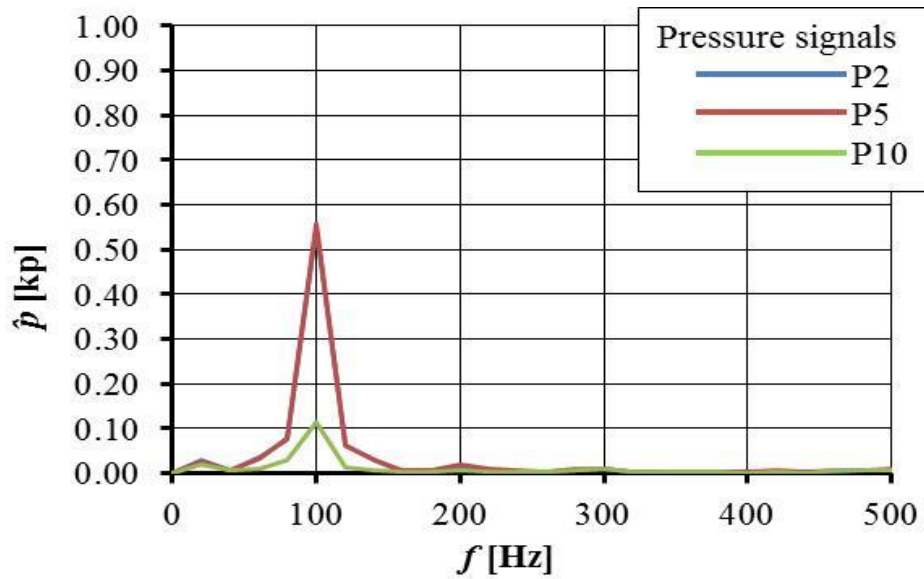
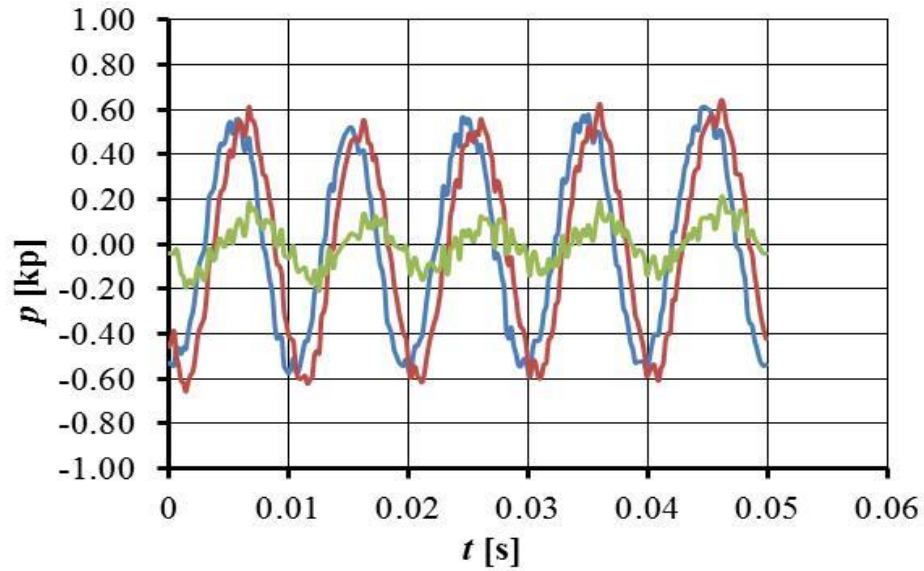
3.1.10 Pressure pulses for $\Psi^{bP} = 12^\circ$: TUHH-CFX, with Cavitation



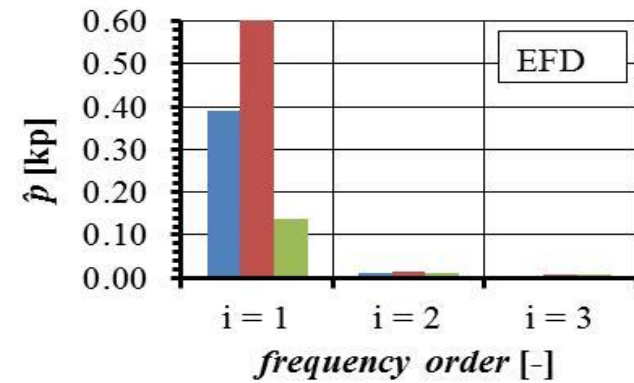
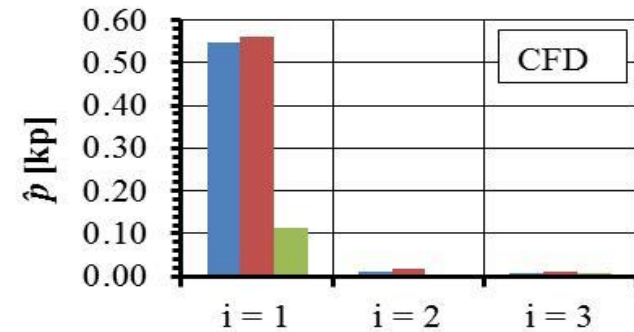
Sensor		$i = 1$	$i = 2$	$i = 3$
p2	(CFD)	0.5020	0.0023	0.0229
p5	(CFD)	0.6949	0.0406	0.0254
P10	(CFD)	0.3874	0.0283	0.0259
p2	(EFD)	0.4372	0.0525	0.0079
p5	(EFD)	0.6053	0.0484	0.0087
P10	(EFD)	0.1611	0.0318	0.0178



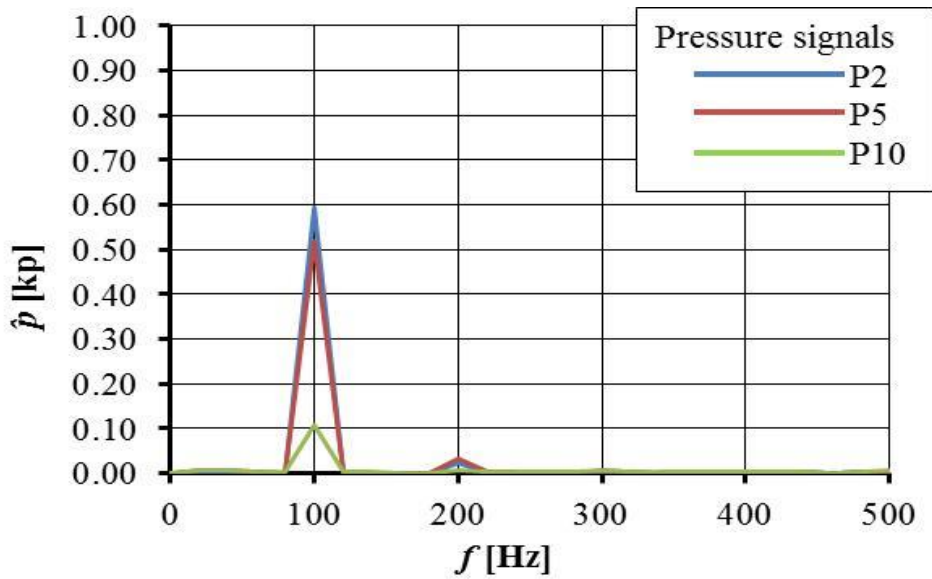
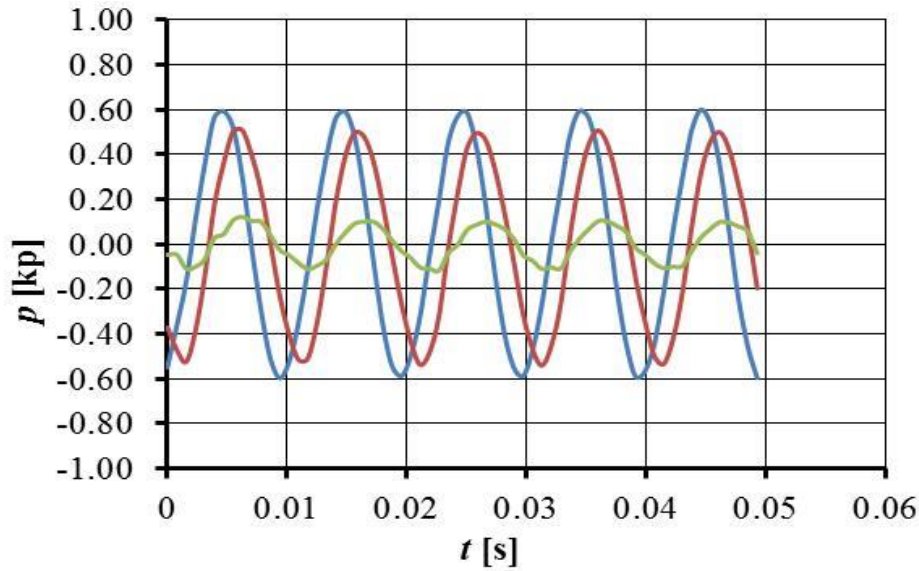
3.1.11 Pressure pulses for $\Psi^{bP} = 12^\circ$: TUHH-OpenFOAM, without Cavitation



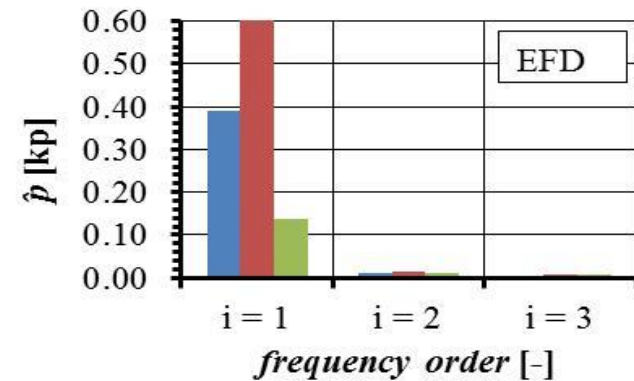
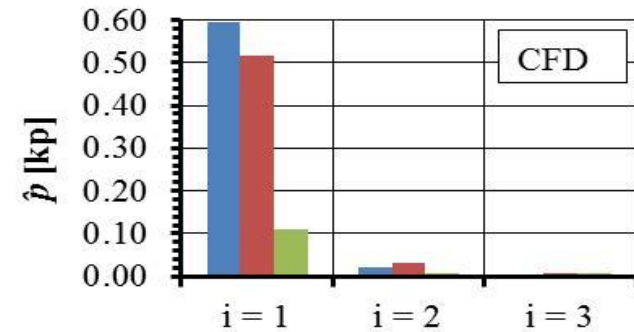
Sensor		$i = 1$	$i = 2$	$i = 3$
p2	(CFD)	0.5471	0.0126	0.0081
p5	(CFD)	0.5591	0.0193	0.0106
P10	(CFD)	0.1134	0.0047	0.0085
p2	(EFD)	0.3899	0.0107	0.0047
p5	(EFD)	0.6017	0.0159	0.0081
P10	(EFD)	0.1373	0.0113	0.0076



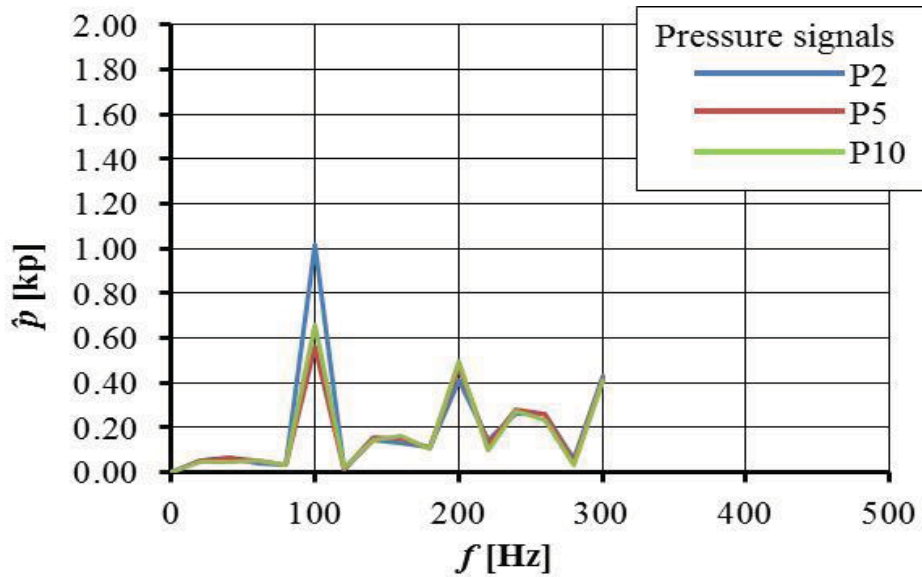
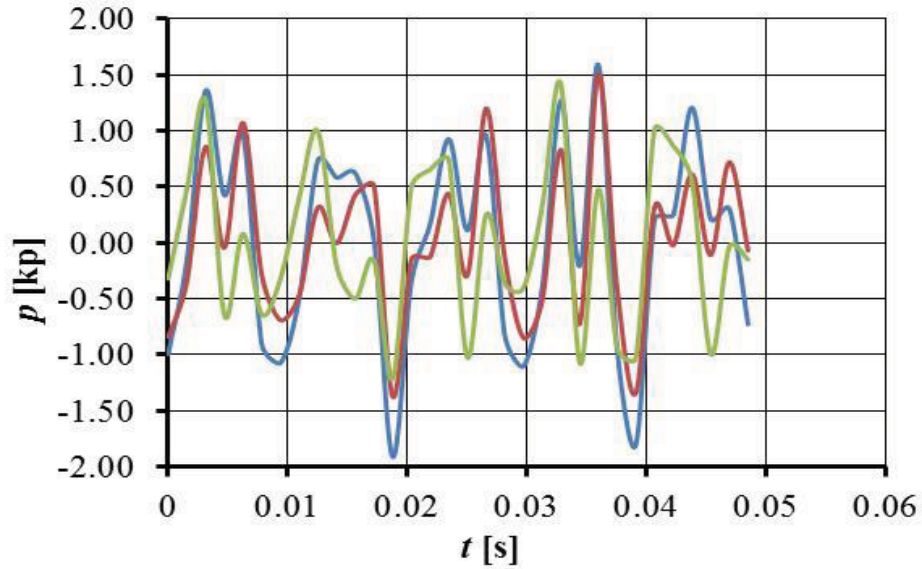
3.1.12 Pressure pulses for $\Psi^{bP} = 12^\circ$: TUHH-panMARE, without Cavitation



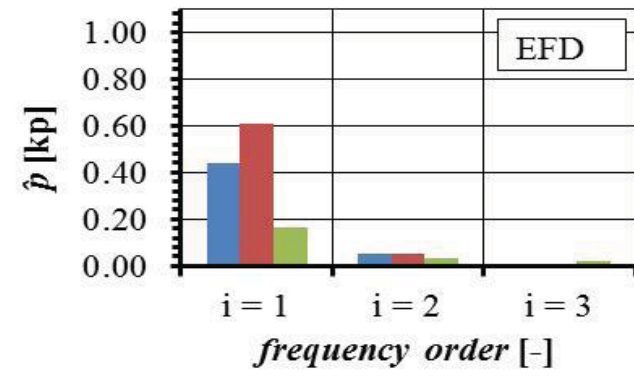
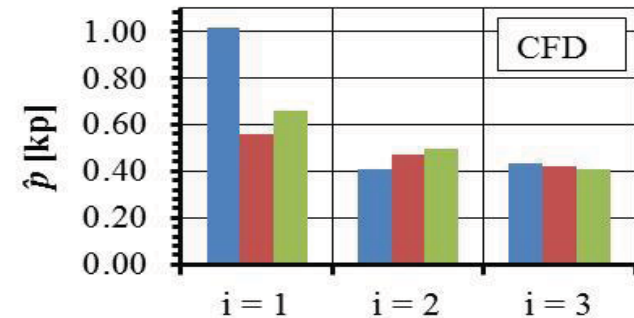
Sensor		$i = 1$	$i = 2$	$i = 3$
p2	(CFD)	0.5941	0.0222	0.0020
p5	(CFD)	0.5170	0.0310	0.0066
P10	(CFD)	0.1085	0.0065	0.0075
p2	(EFD)	0.3899	0.0107	0.0047
p5	(EFD)	0.6017	0.0159	0.0081
P10	(EFD)	0.1373	0.0113	0.0076



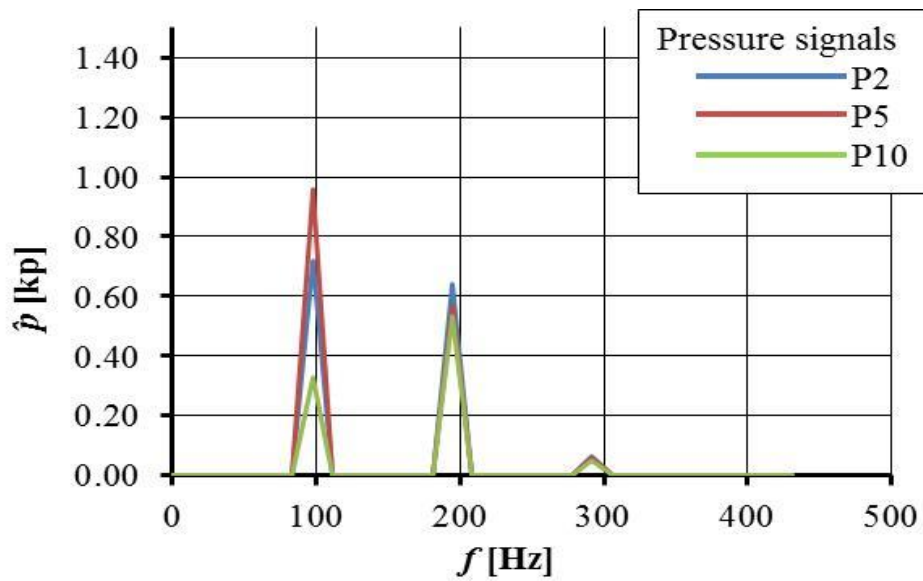
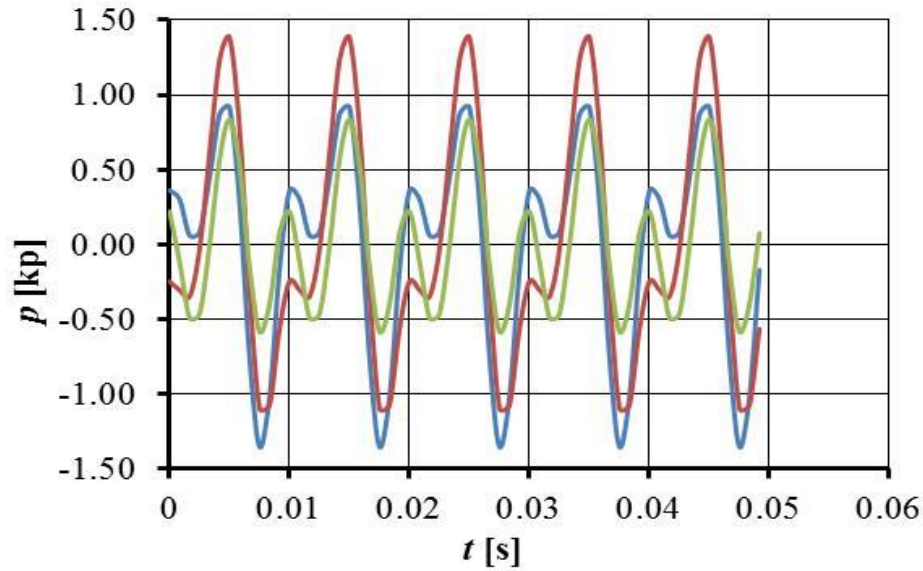
3.1.13 Pressure pulses for $\Psi^{bP} = 12^\circ$: TUHH-panMARE, with Cavitation



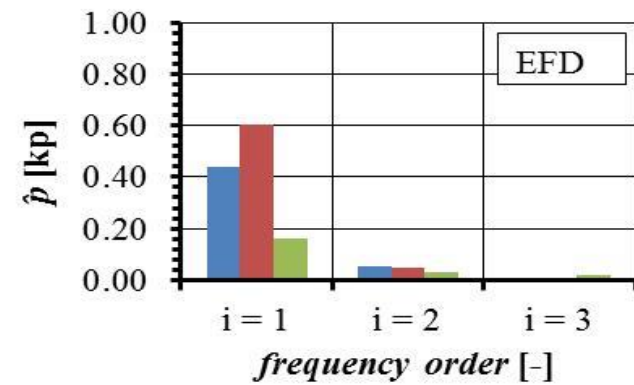
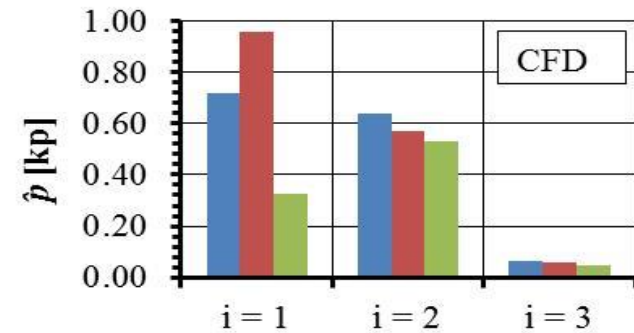
Sensor		$i = 1$	$i = 2$	$i = 3$
p2	(CFD)	1.0153	0.4112	0.4322
p5	(CFD)	0.5582	0.4725	0.4190
P10	(CFD)	0.6599	0.4959	0.4102
p2	(EFD)	0.4372	0.0525	0.0079
p5	(EFD)	0.6053	0.0484	0.0087
P10	(EFD)	0.1611	0.0318	0.0178



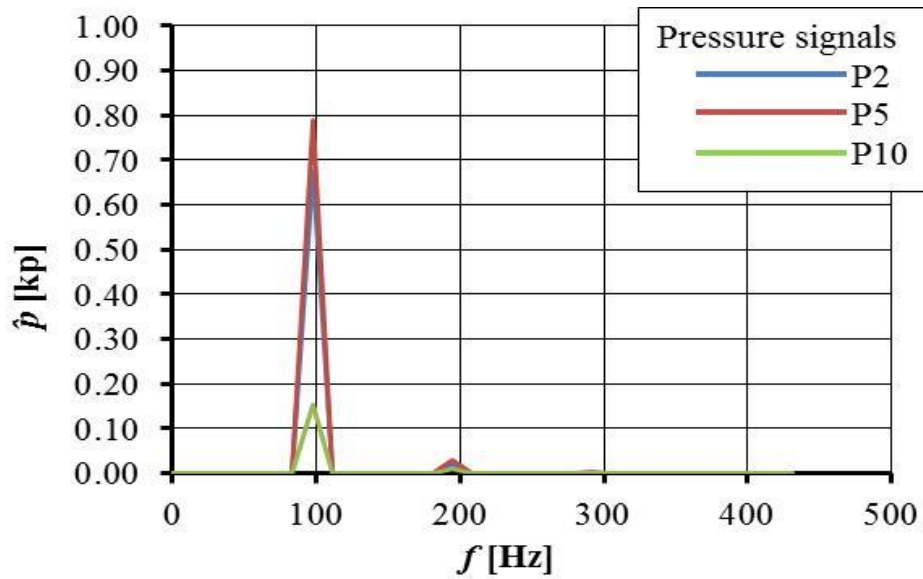
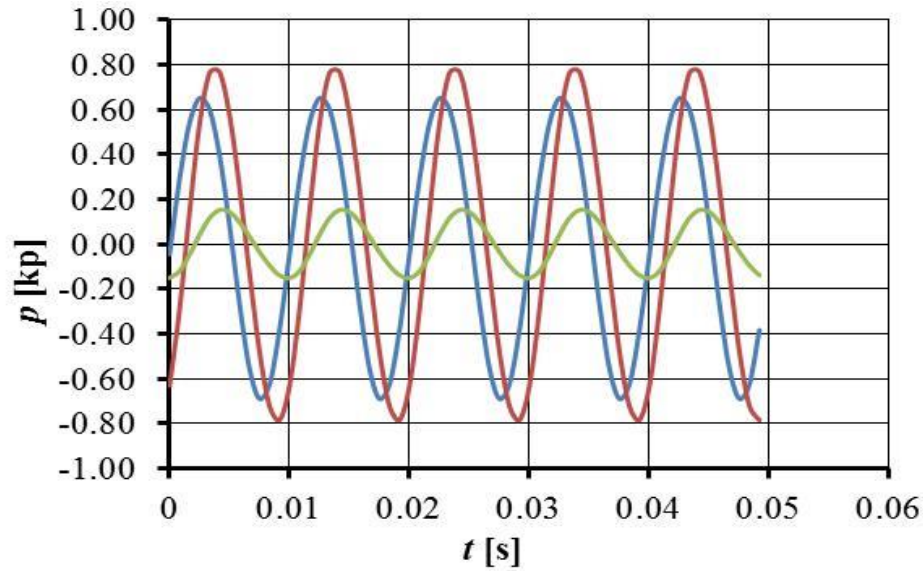
3.1.13 Pressure pulses for $\psi^{bP} = 12^\circ$: UTAustin-PROPCAV, with Cavitation



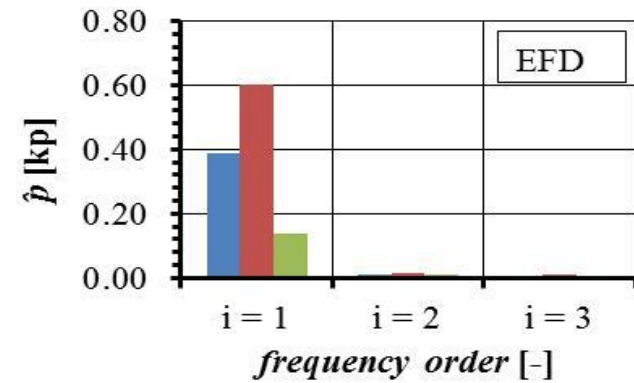
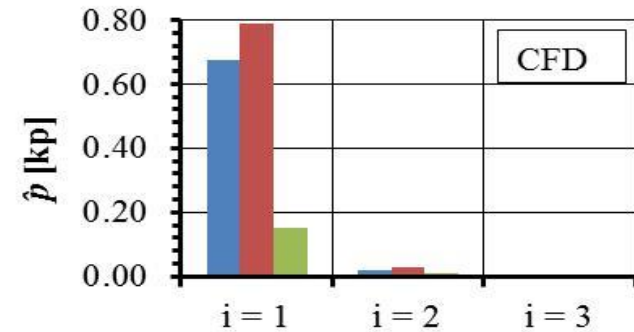
Sensor	$i = 1$	$i = 2$	$i = 3$
p2 (CFD)	0.7195	0.6388	0.0641
p5 (CFD)	0.9578	0.5697	0.0606
P10 (CFD)	0.3280	0.5310	0.0495
p2 (EFD)	0.4372	0.0525	0.0079
p5 (EFD)	0.6053	0.0484	0.0087
P10 (EFD)	0.1611	0.0318	0.0178



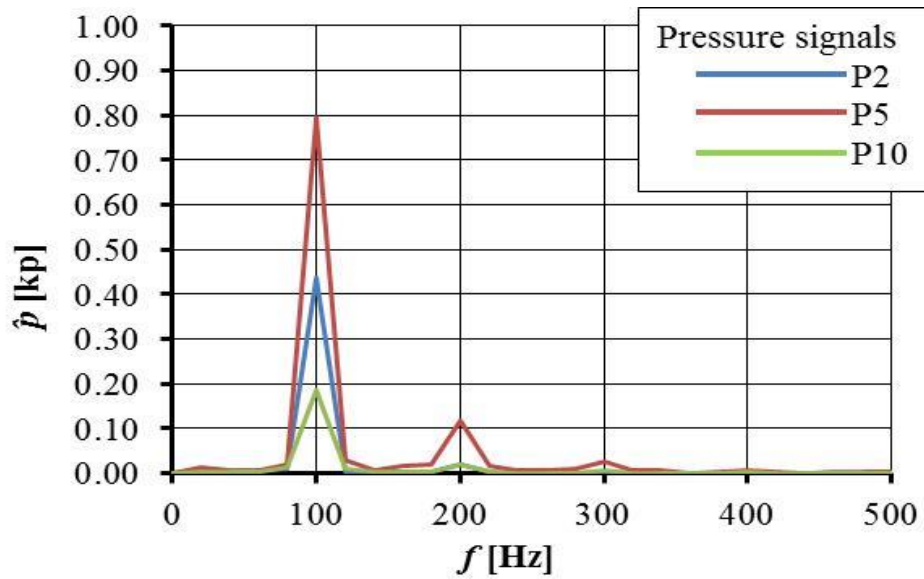
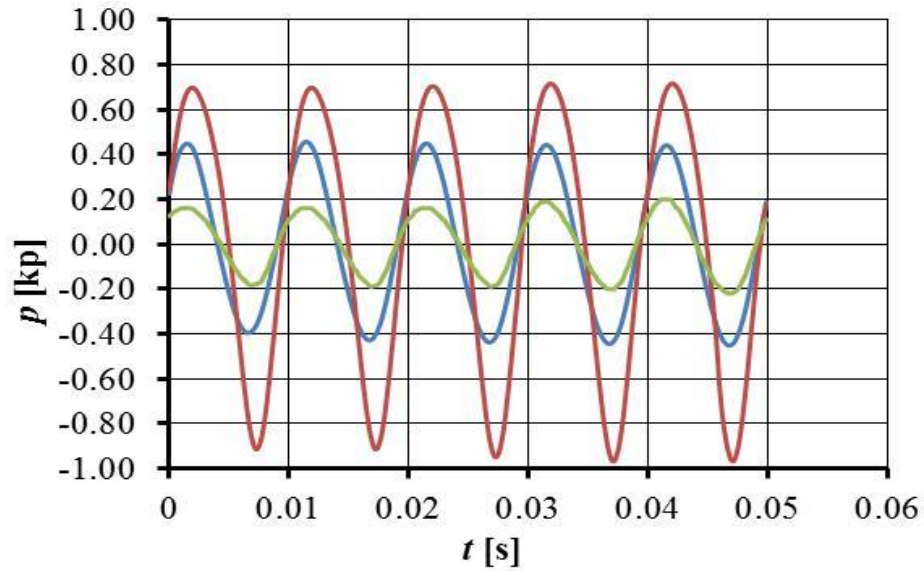
3.1.14 Pressure pulses for $\Psi^{bP} = 12^\circ$: UTAustin-PROPCAV, without Cavitation



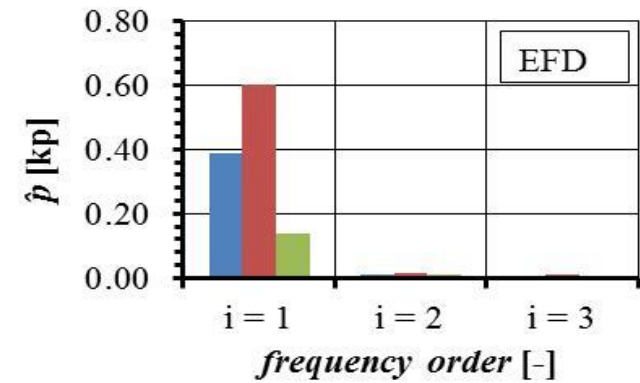
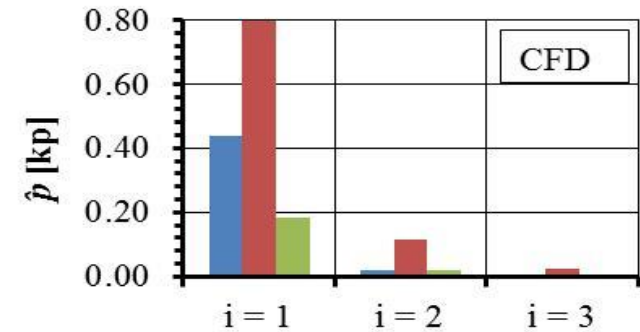
Sensor		$i = 1$	$i = 2$	$i = 3$
p2	(CFD)	0.6737	0.0193	0.0010
p5	(CFD)	0.7901	0.0293	0.0018
P10	(CFD)	0.1519	0.0108	0.0008
p2	(EFD)	0.3899	0.0107	0.0047
p5	(EFD)	0.6017	0.0159	0.0081
P10	(EFD)	0.1373	0.0113	0.0076



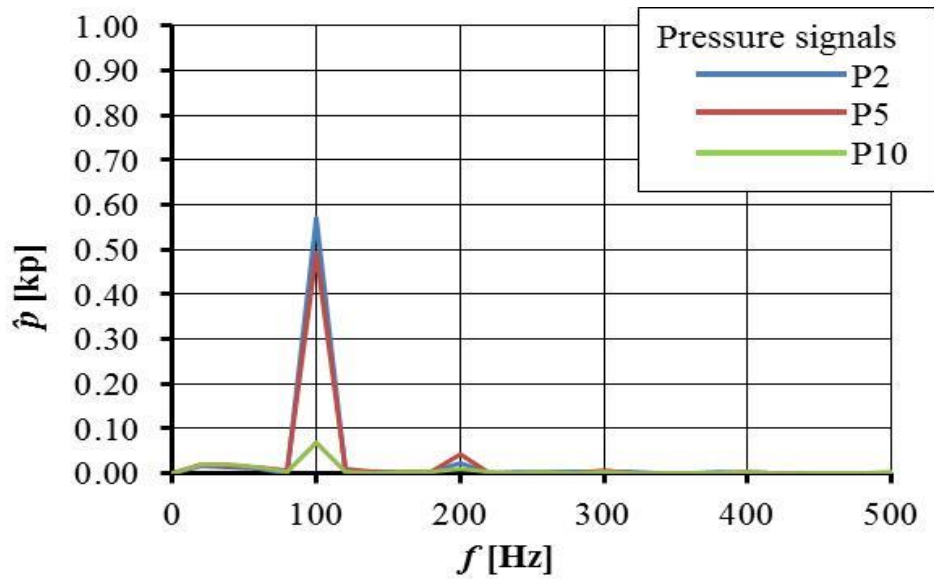
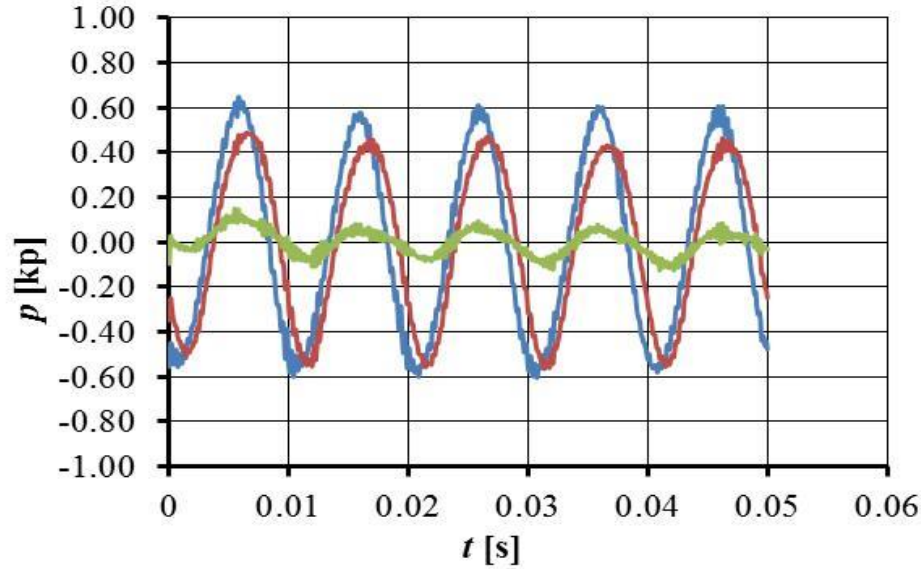
3.1.15 Pressure pulses for $\Psi^{bP} = 12^\circ$: VTT-FINFLO, without Cavitation



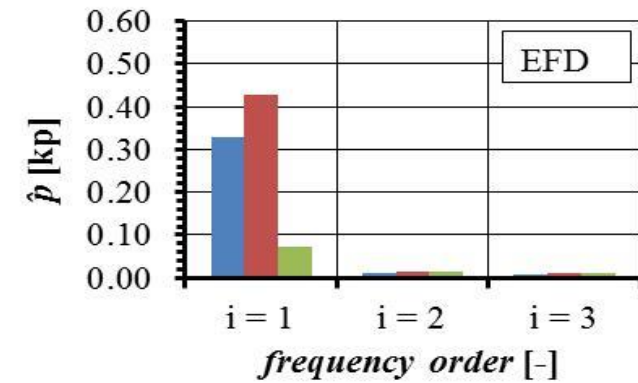
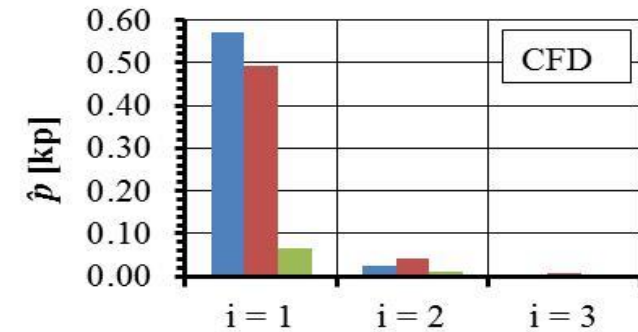
Sensor		$i = 1$	$i = 2$	$i = 3$
p2	(CFD)	0.4367	0.0180	0.0030
p5	(CFD)	0.7963	0.1161	0.0255
P10	(CFD)	0.1842	0.0182	0.0050
p2	(EFD)	0.3899	0.0107	0.0047
p5	(EFD)	0.6017	0.0159	0.0081
P10	(EFD)	0.1373	0.0113	0.0076



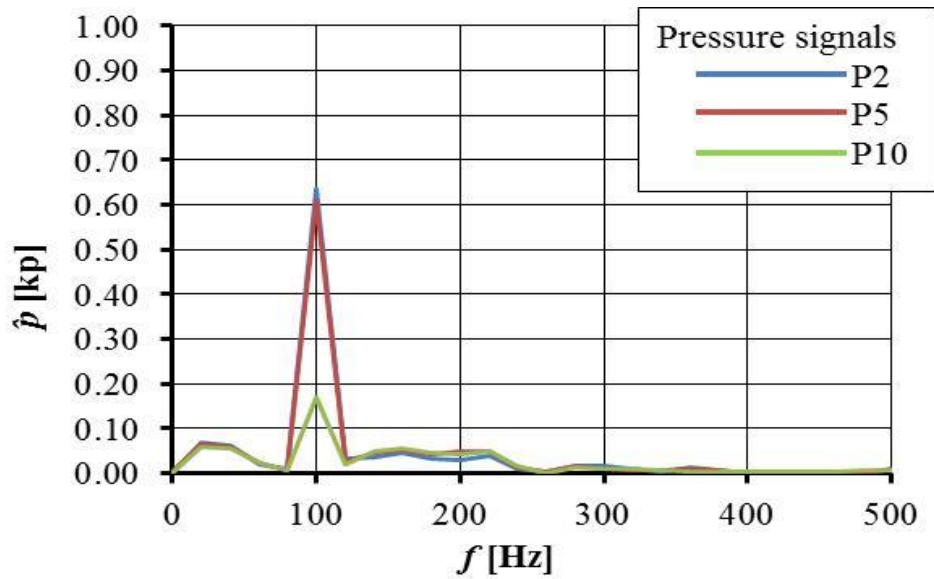
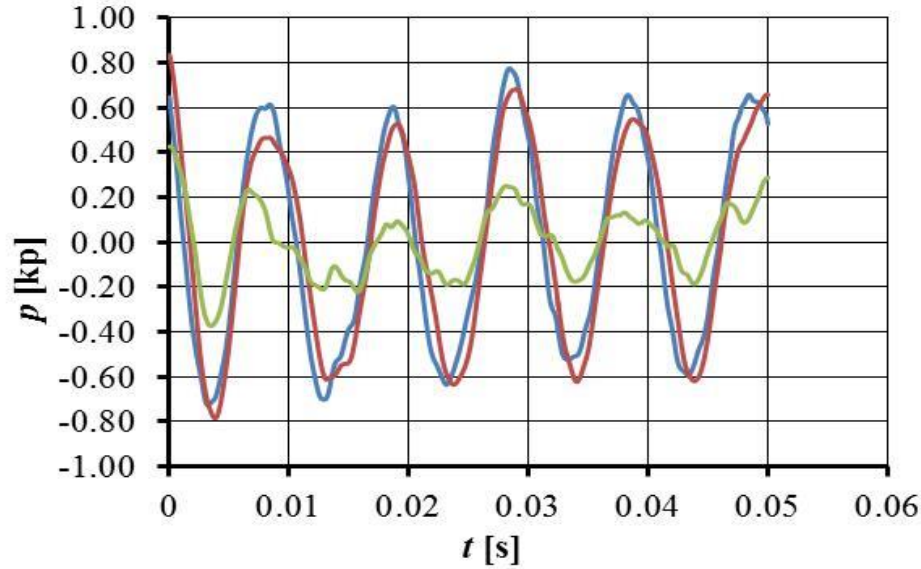
3.2.1 Pressure pulses for $\Psi^{bP} = 12^\circ$: Cradle-SCTetra, without Cavitation



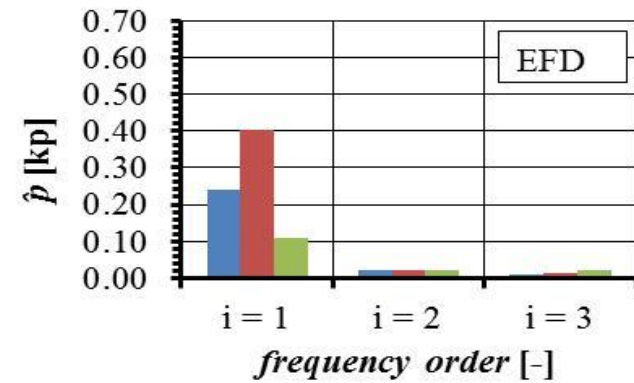
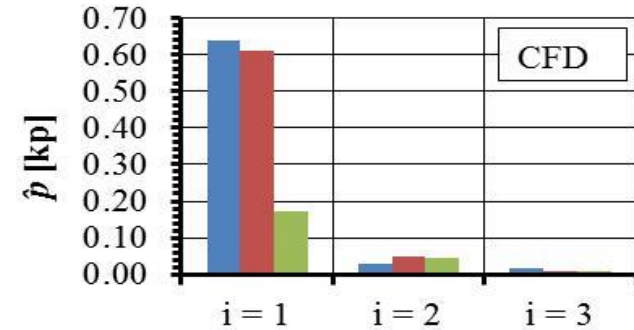
Sensor		$i = 1$	$i = 2$	$i = 3$
p2	(CFD)	0.5701	0.0236	0.0031
p5	(CFD)	0.4918	0.0432	0.0062
P10	(CFD)	0.0672	0.0105	0.0017
p2	(EFD)	0.3277	0.0103	0.0080
p5	(EFD)	0.4266	0.0152	0.0108
P10	(EFD)	0.0711	0.0142	0.0104



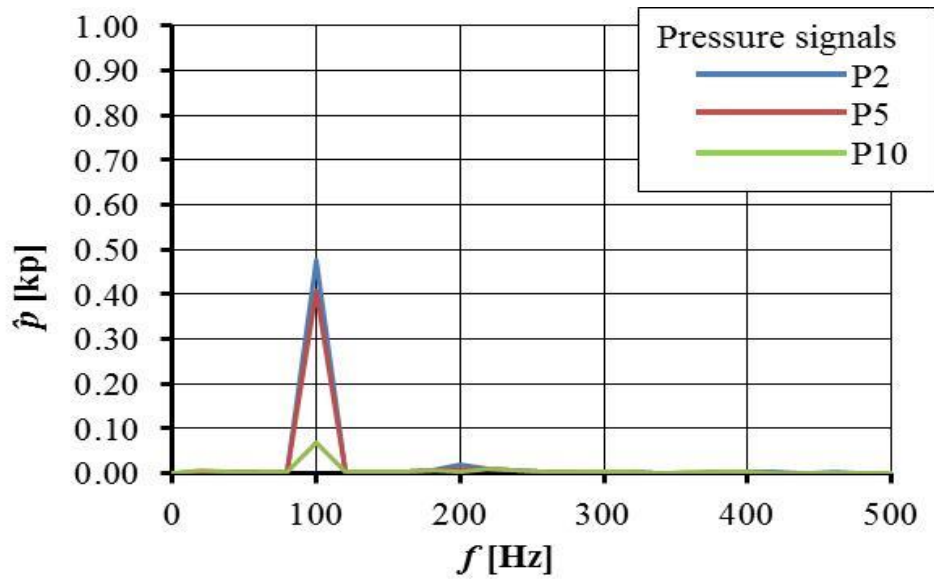
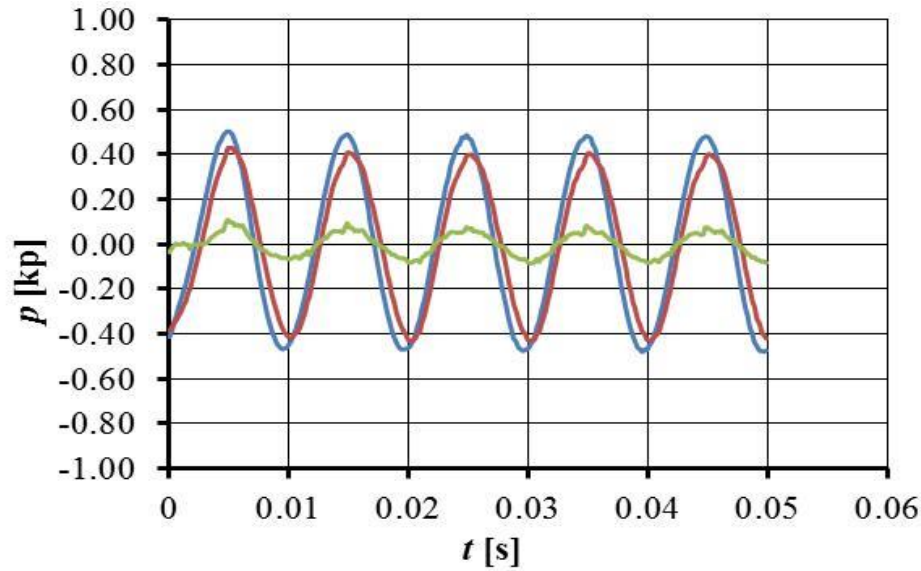
3.2.2 Pressure pulses for $\Psi^{bP} = 12^\circ$: Cradle-SCTetra, with Cavitation



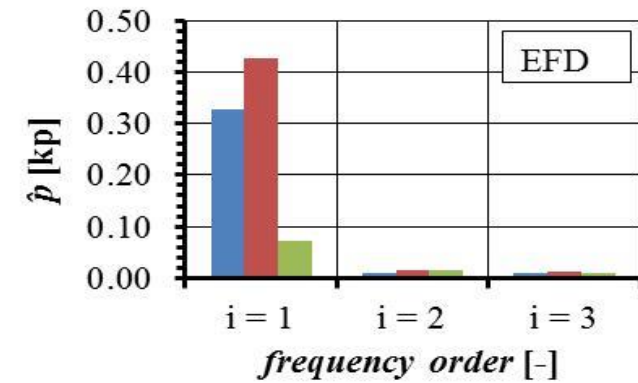
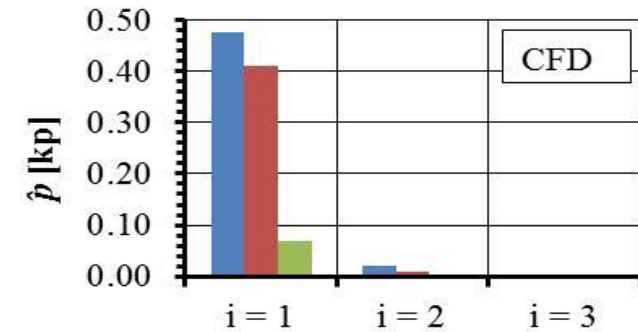
Sensor		$i = 1$	$i = 2$	$i = 3$
p2	(CFD)	0.6369	0.0280	0.0153
p5	(CFD)	0.6105	0.0499	0.0107
P10	(CFD)	0.1707	0.0435	0.0098
p2	(EFD)	0.2387	0.0206	0.0091
p5	(EFD)	0.4017	0.0196	0.0130
P10	(EFD)	0.1096	0.0227	0.0207



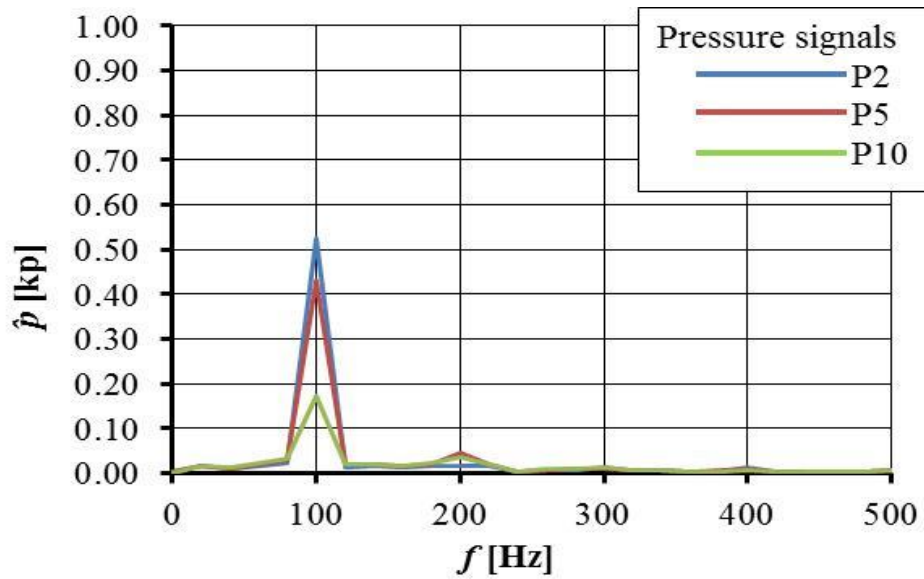
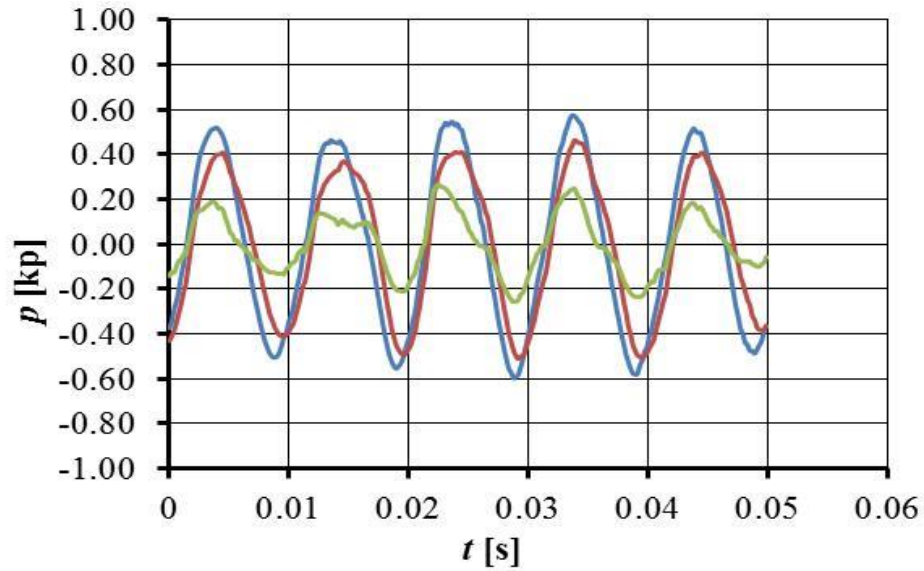
3.2.3 Pressure pulses for $\Psi^{bP} = 12^\circ$: SSPA-FLUENT, without Cavitation



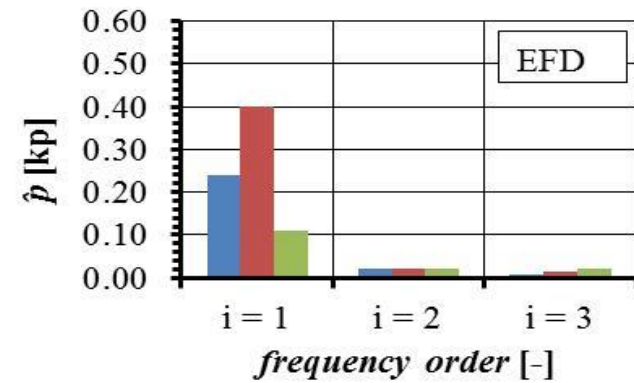
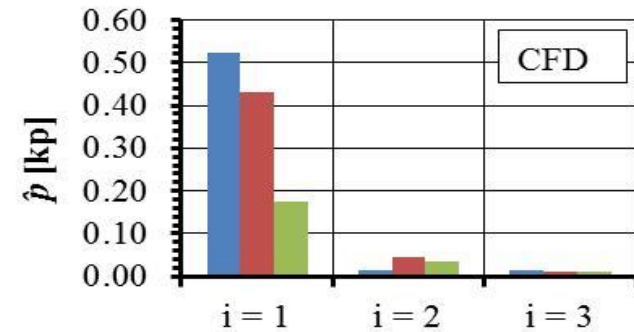
Sensor		$i = 1$	$i = 2$	$i = 3$
p2	(CFD)	0.4770	0.0205	0.0015
p5	(CFD)	0.4090	0.0097	0.0013
P10	(CFD)	0.0691	0.0031	0.0015
p2	(EFD)	0.3277	0.0103	0.0080
p5	(EFD)	0.4266	0.0152	0.0108
P10	(EFD)	0.0711	0.0142	0.0104



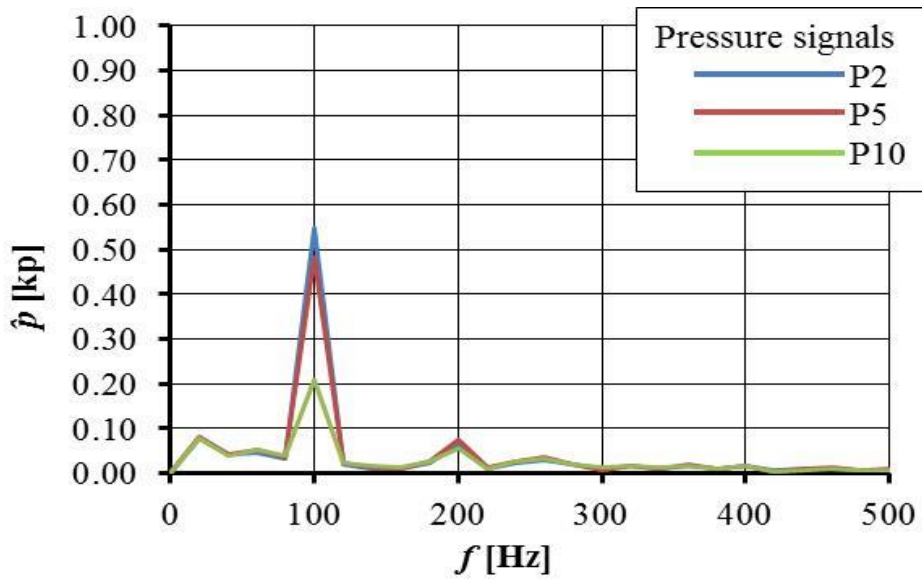
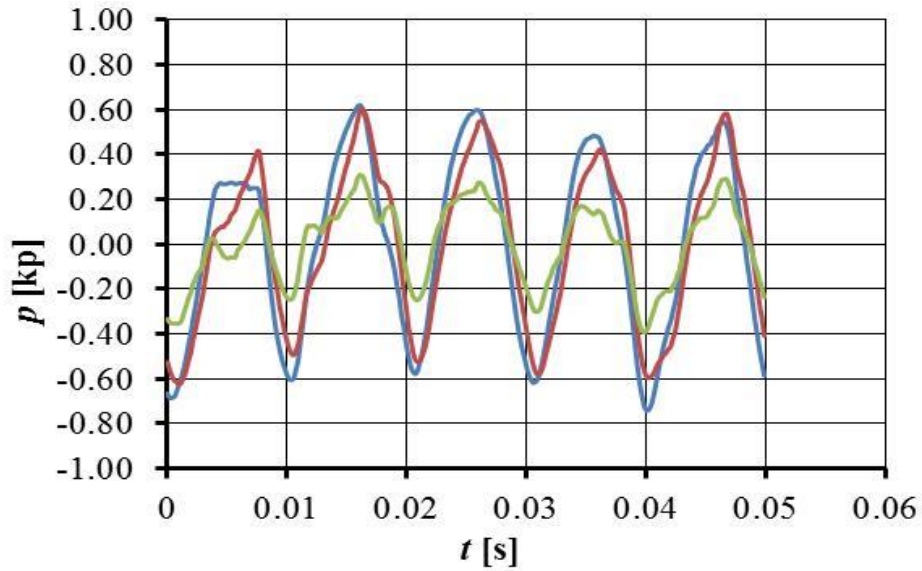
3.2.4 Pressure pulses for $\Psi^{bP} = 12^\circ$: SSPA-FLUENT, with Cavitation



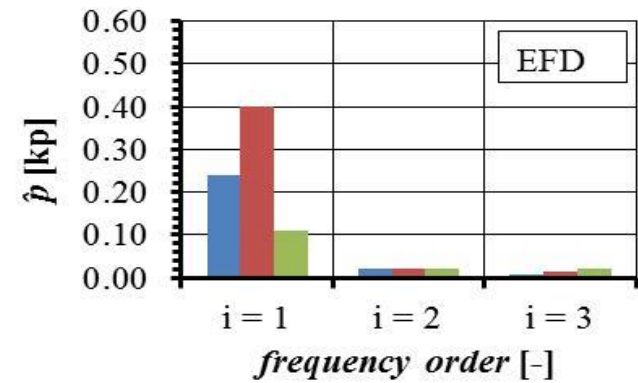
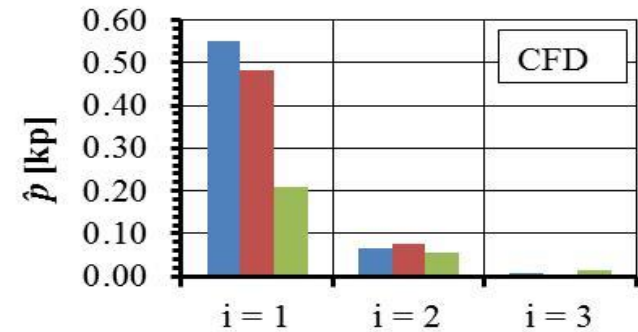
Sensor		$i = 1$	$i = 2$	$i = 3$
p2	(CFD)	0.5237	0.0155	0.0138
p5	(CFD)	0.4315	0.0468	0.0100
P10	(CFD)	0.1732	0.0343	0.0124
p2	(EFD)	0.2387	0.0206	0.0091
p5	(EFD)	0.4017	0.0196	0.0130
P10	(EFD)	0.1096	0.0227	0.0207



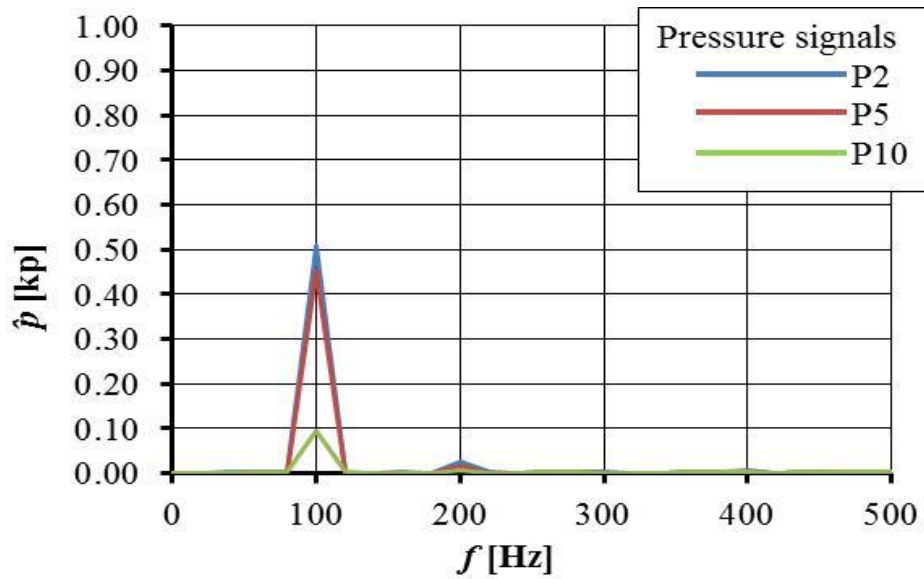
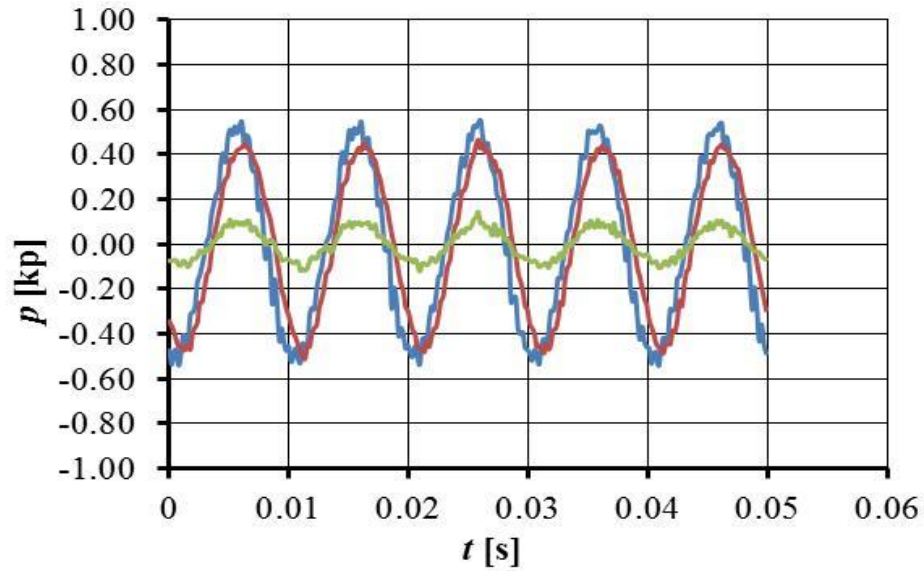
3.2.5 Pressure pulses for $\Psi^{bP} = 12^\circ$: SSPA-FLUENT, with Cavitation, Sauer



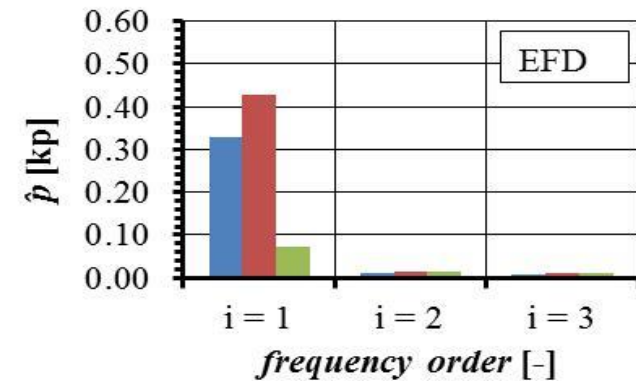
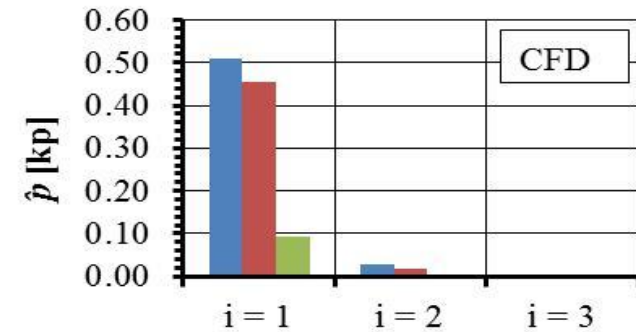
Sensor		$i = 1$	$i = 2$	$i = 3$
p2	(CFD)	0.5488	0.0651	0.0092
p5	(CFD)	0.4814	0.0750	0.0050
P10	(CFD)	0.2079	0.0566	0.0132
p2	(EFD)	0.2387	0.0206	0.0091
p5	(EFD)	0.4017	0.0196	0.0130
P10	(EFD)	0.1096	0.0227	0.0207



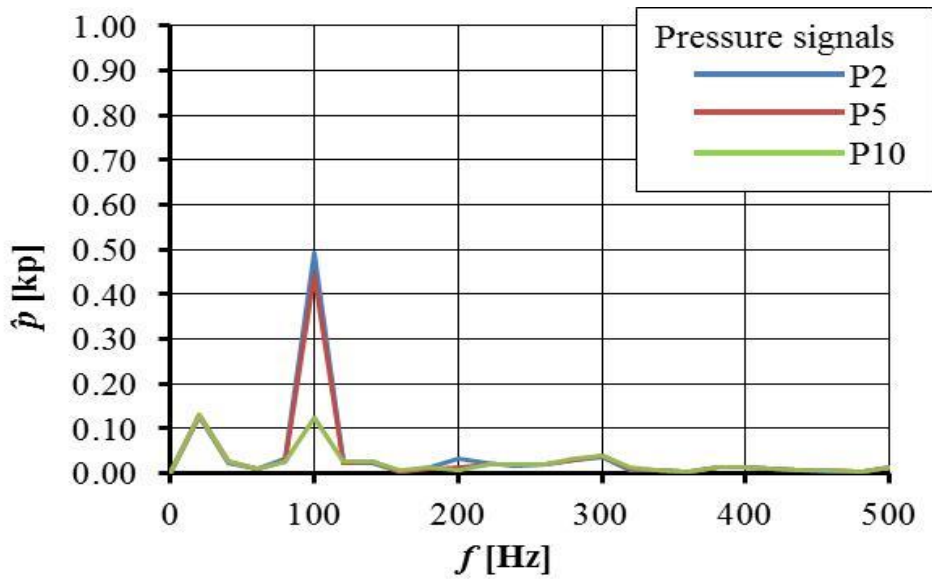
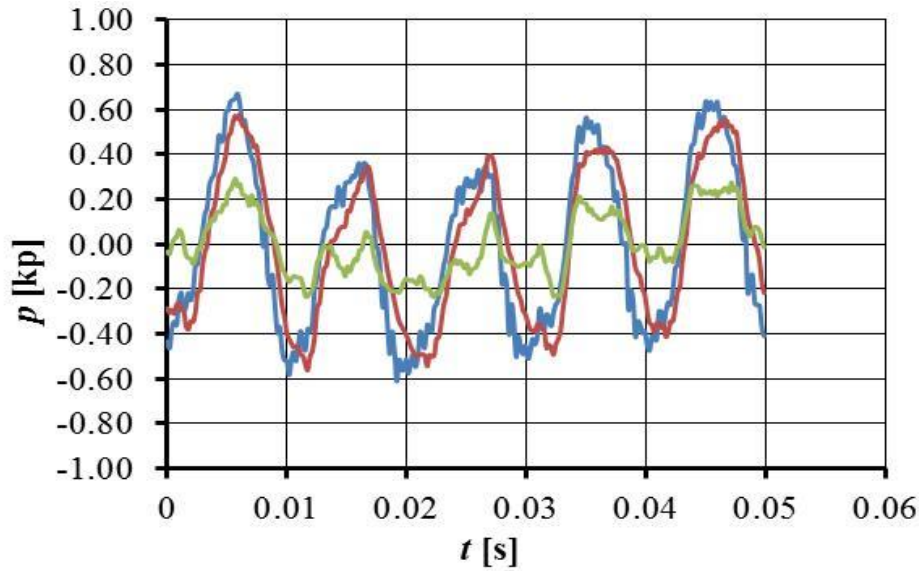
3.2.6 Pressure pulses for $\Psi^{bP} = 12^\circ$: TUHH-CFX, without Cavitation



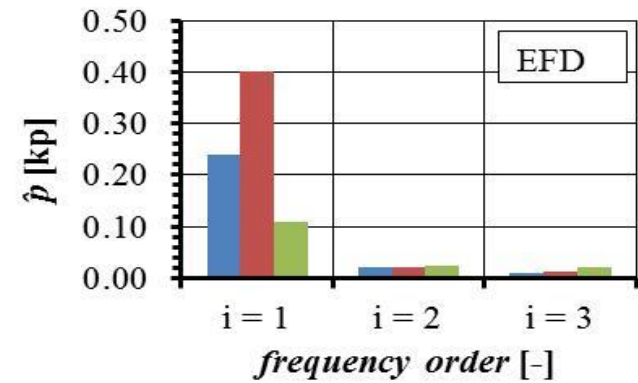
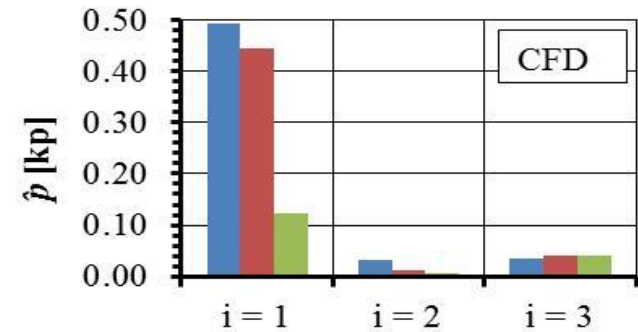
Sensor		$i = 1$	$i = 2$	$i = 3$
p2	(CFD)	0.5086	0.0266	0.0036
p5	(CFD)	0.4535	0.0167	0.0005
P10	(CFD)	0.0928	0.0048	0.0006
p2	(EFD)	0.3277	0.0103	0.0080
p5	(EFD)	0.4266	0.0152	0.0108
P10	(EFD)	0.0711	0.0142	0.0104



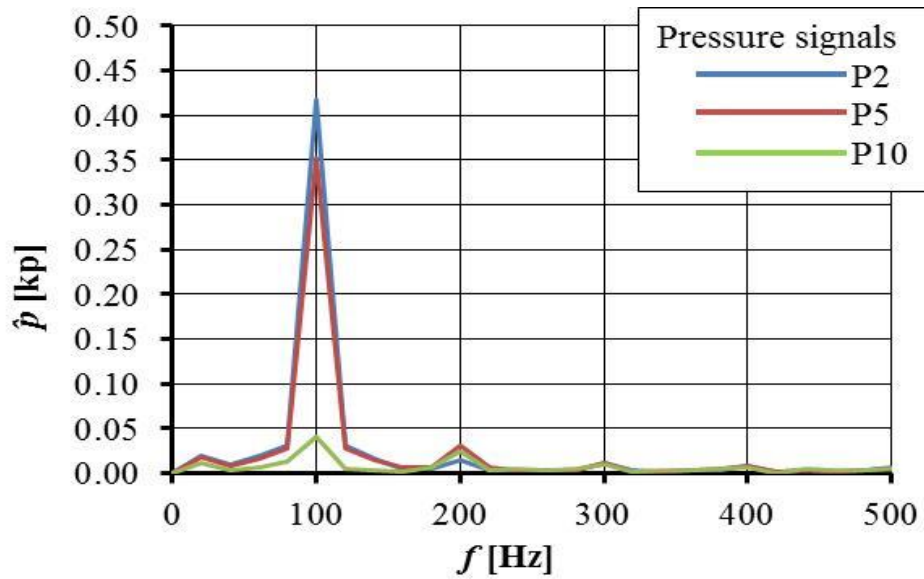
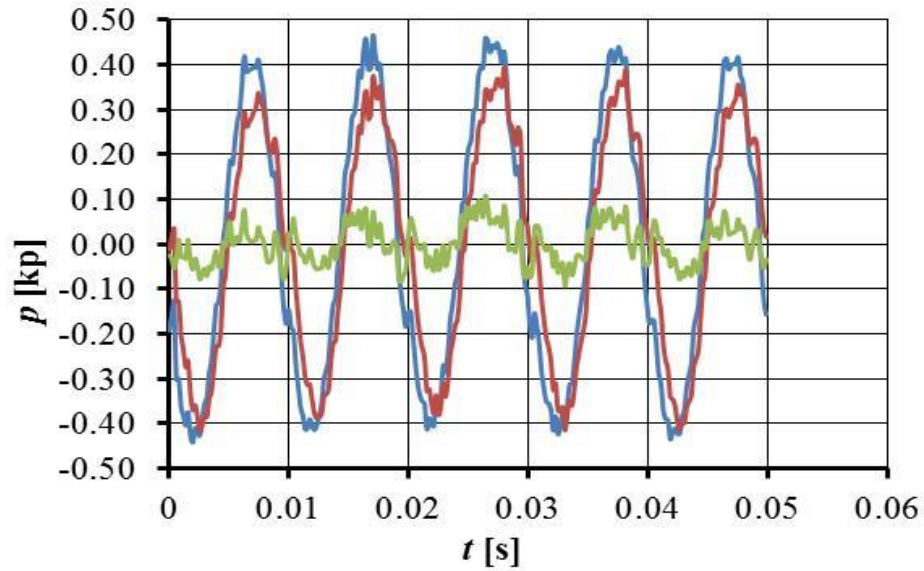
3.2.7 Pressure pulses for $\Psi^{bP} = 12^\circ$: TUHH-CFX, with Cavitation



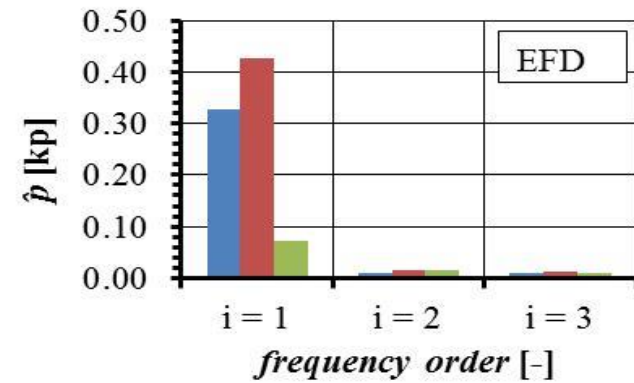
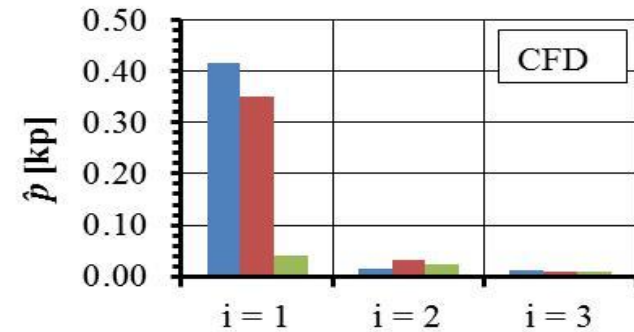
Sensor		$i = 1$	$i = 2$	$i = 3$
p2	(CFD)	0.4925	0.0309	0.0361
p5	(CFD)	0.4445	0.0119	0.0403
P10	(CFD)	0.1229	0.0074	0.0399
p2	(EFD)	0.2387	0.0206	0.0091
p5	(EFD)	0.4017	0.0196	0.0130
P10	(EFD)	0.1096	0.0227	0.0207



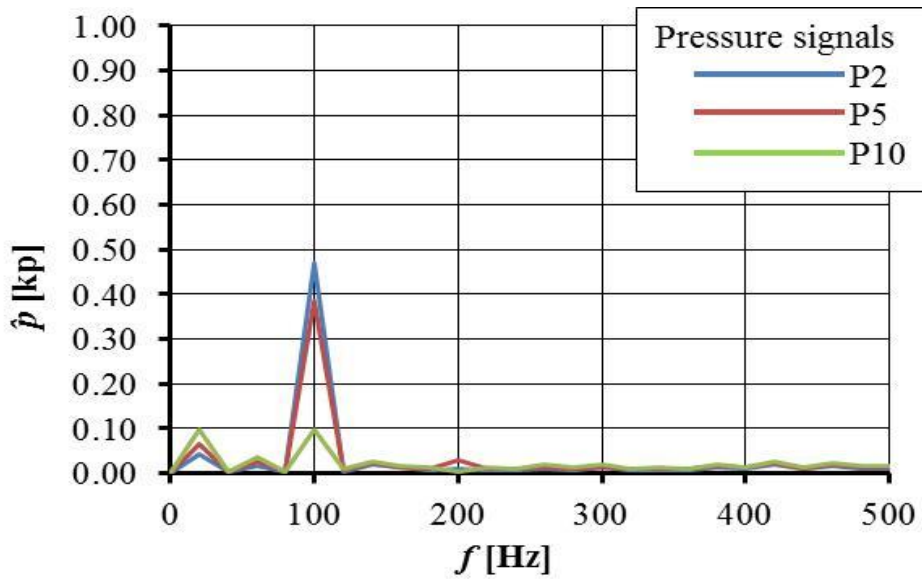
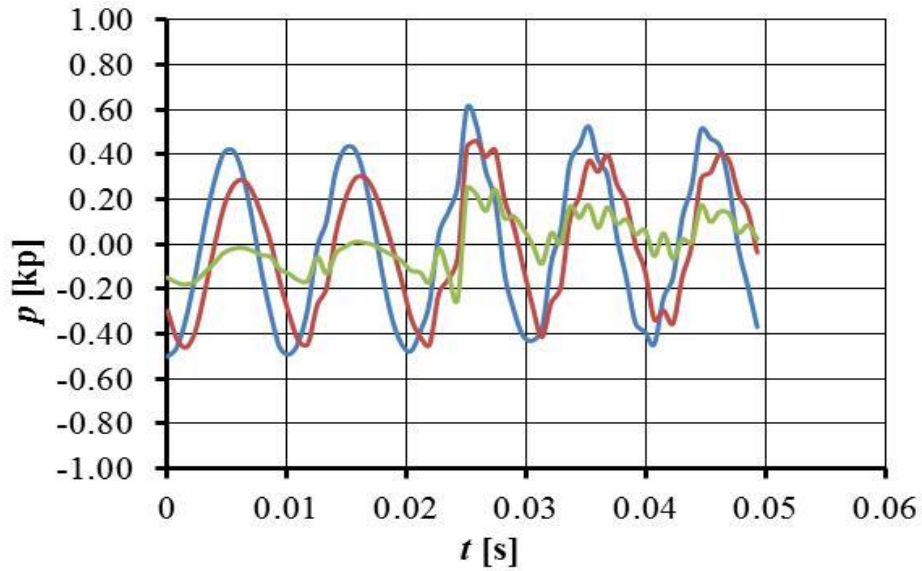
3.2.8 Pressure pulses for $\Psi^{bP} = 12^\circ$: TUHH-OpenFOAM, without Cavitation



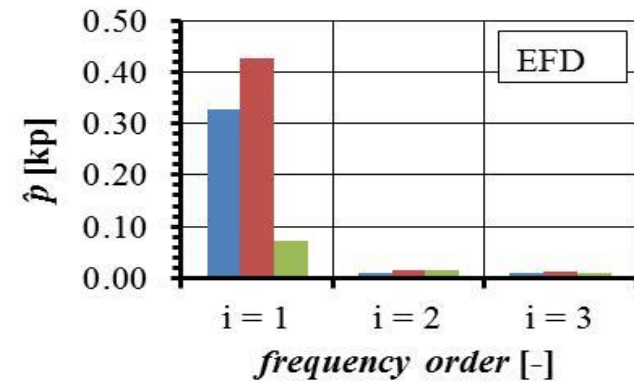
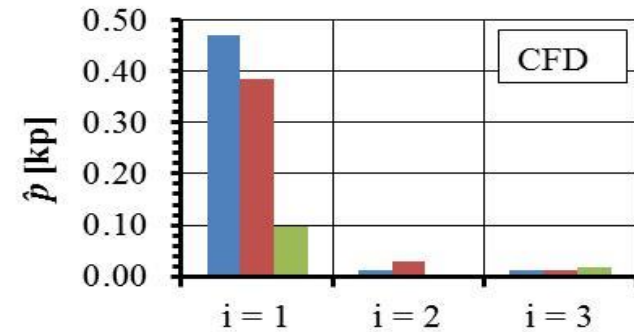
Sensor		$i = 1$	$i = 2$	$i = 3$
p2	(CFD)	0.4168	0.0152	0.0118
p5	(CFD)	0.3517	0.0315	0.0105
P10	(CFD)	0.0408	0.0239	0.0098
p2	(EFD)	0.3277	0.0103	0.0080
p5	(EFD)	0.4266	0.0152	0.0108
P10	(EFD)	0.0711	0.0142	0.0104



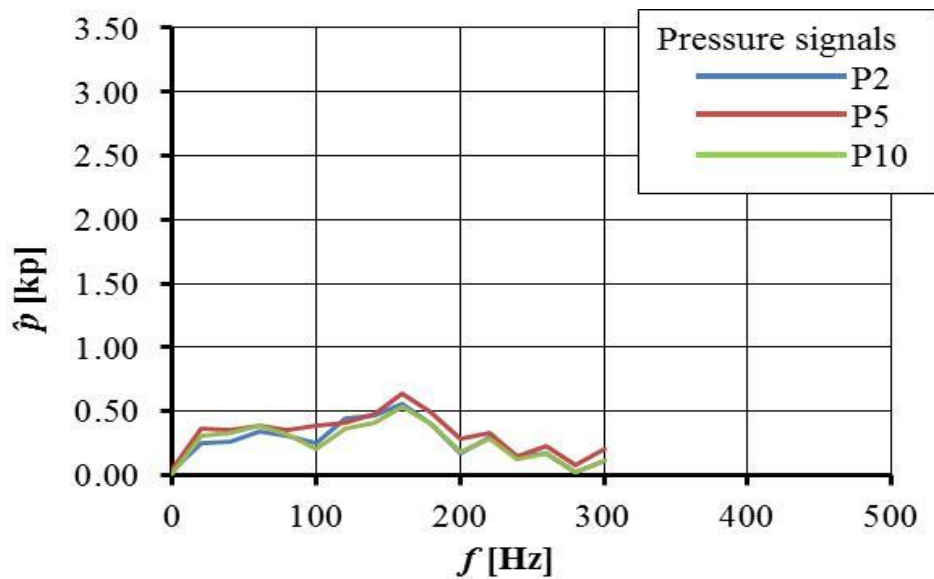
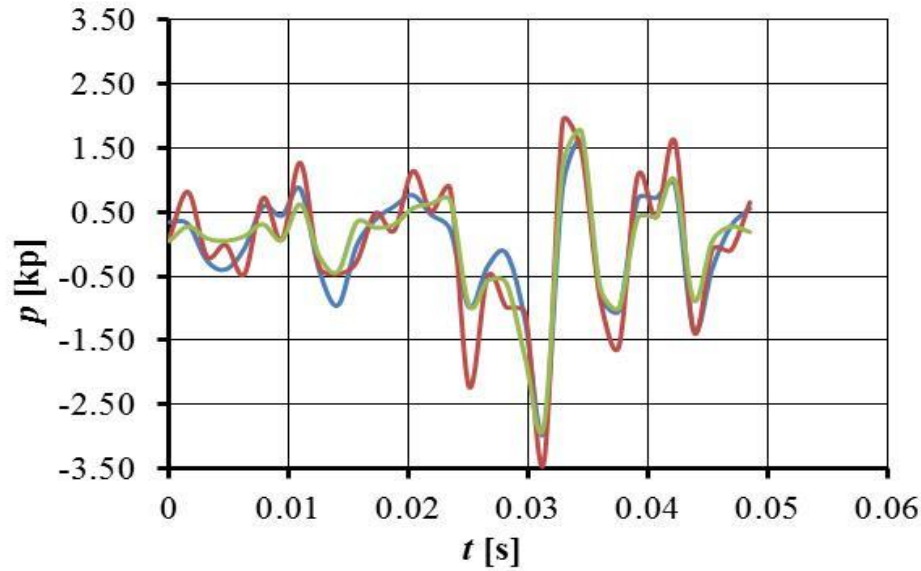
3.2.9 Pressure pulses for $\Psi^{bP} = 12^\circ$: TUHH-panMARE, without Cavitation



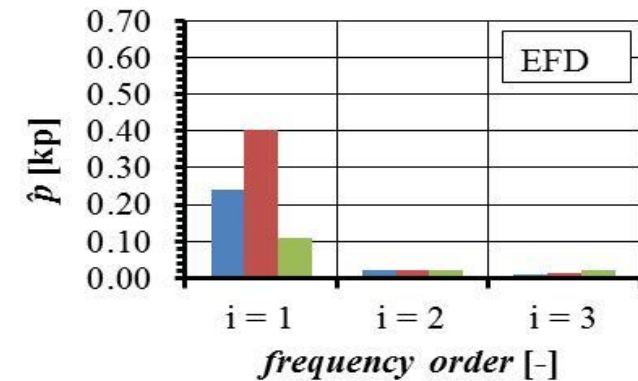
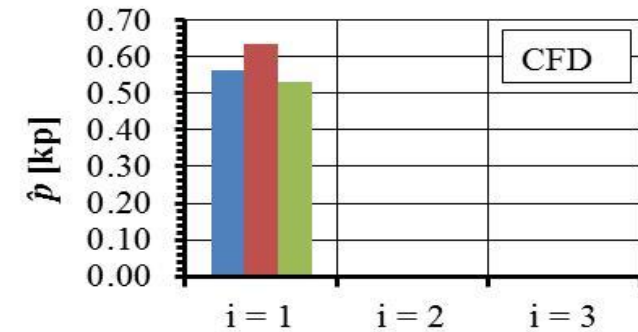
Sensor		$i = 1$	$i = 2$	$i = 3$
p2	(CFD)	0.4699	0.0109	0.0120
p5	(CFD)	0.3841	0.0285	0.0121
P10	(CFD)	0.0985	0.0044	0.0183
p2	(EFD)	0.3277	0.0103	0.0080
p5	(EFD)	0.4266	0.0152	0.0108
P10	(EFD)	0.0711	0.0142	0.0104



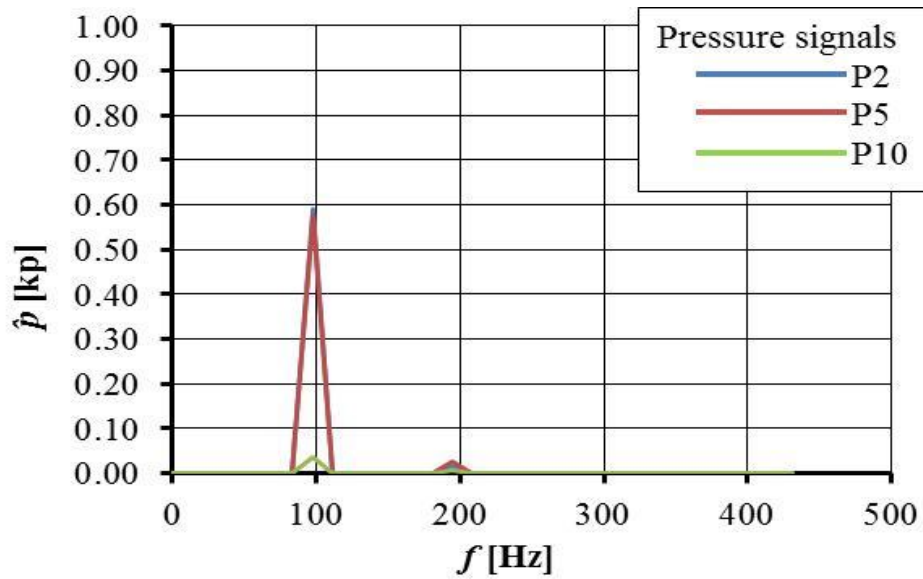
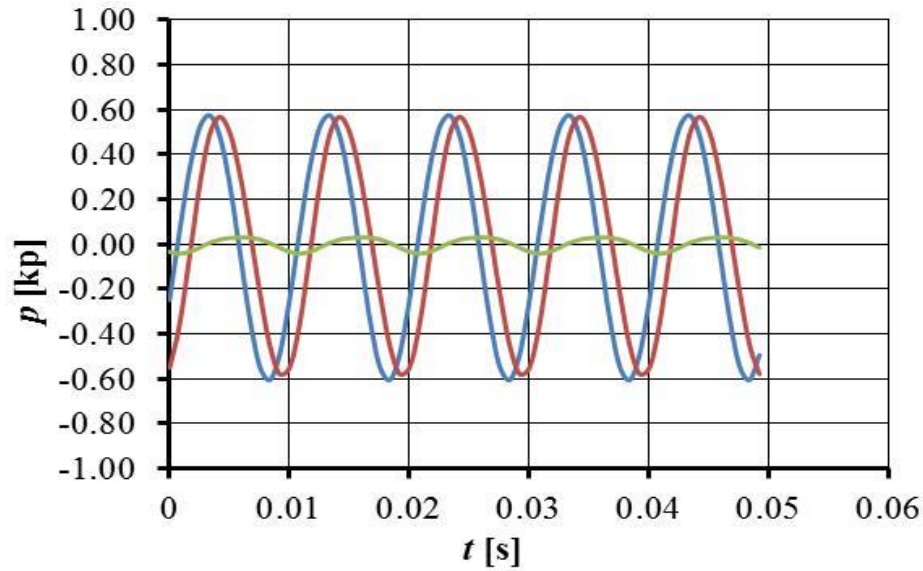
3.2.10 Pressure pulses for $\Psi^{bP} = 12^\circ$: TUHH-panMARE, with Cavitation



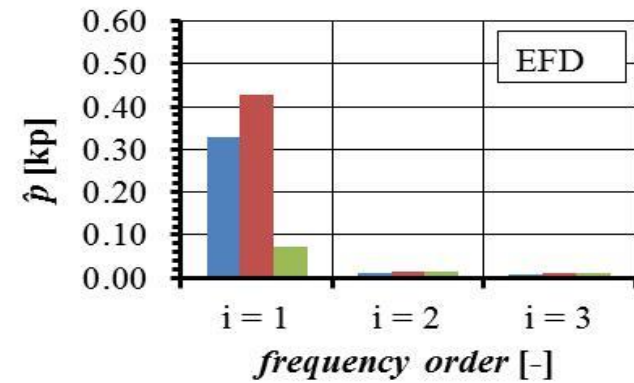
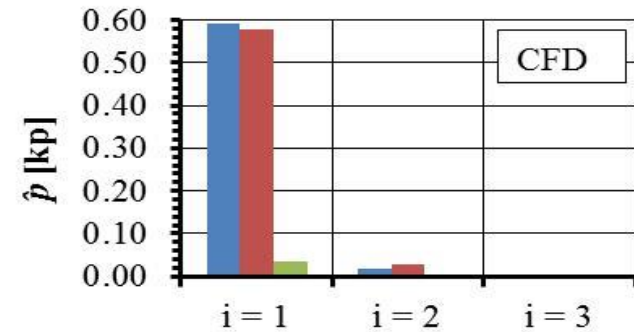
Sensor		$i = 1$	$i = 2$	$i = 3$
p2	(CFD)	0.5619	0.0000	0.0000
p5	(CFD)	0.6338	0.0000	0.0000
P10	(CFD)	0.5303	0.0000	0.0000
p2	(EFD)	0.2387	0.0206	0.0091
p5	(EFD)	0.4017	0.0196	0.0130
P10	(EFD)	0.1096	0.0227	0.0207



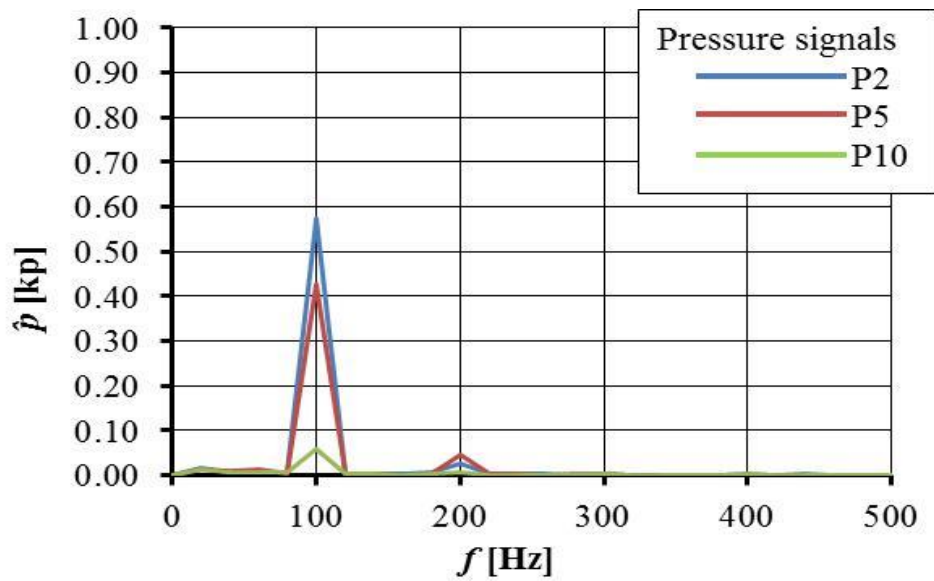
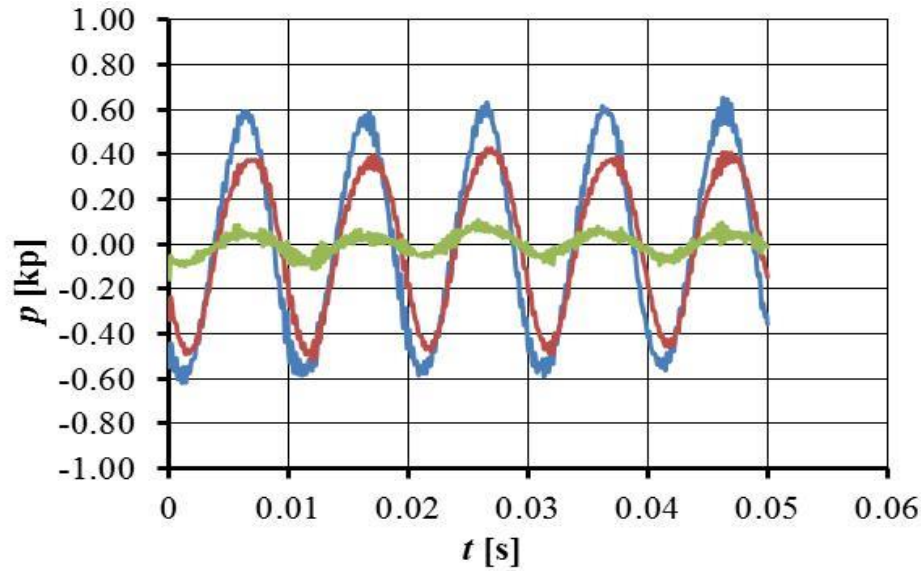
3.2.11 Pressure pulses for $\psi^{bP} = 12^\circ$: UTAustin-PROPCAV, without Cavitation



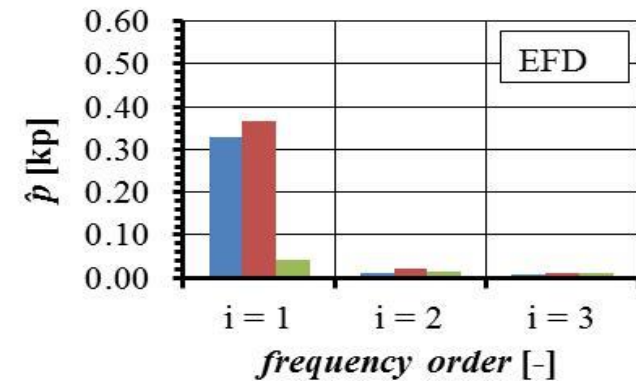
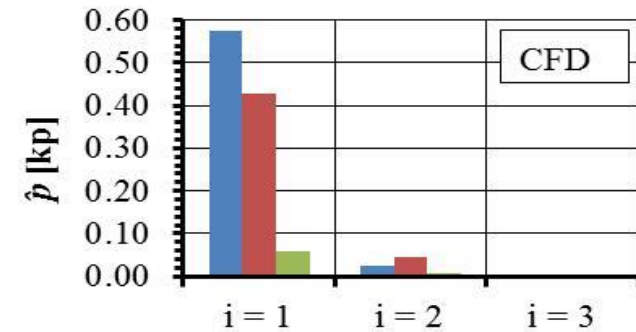
Sensor		$i = 1$	$i = 2$	$i = 3$
p2	(CFD)	0.5919	0.0162	0.0009
p5	(CFD)	0.5770	0.0266	0.0012
P10	(CFD)	0.0362	0.0058	0.0006
p2	(EFD)	0.3277	0.0103	0.0080
p5	(EFD)	0.4266	0.0152	0.0108
P10	(EFD)	0.0711	0.0142	0.0104



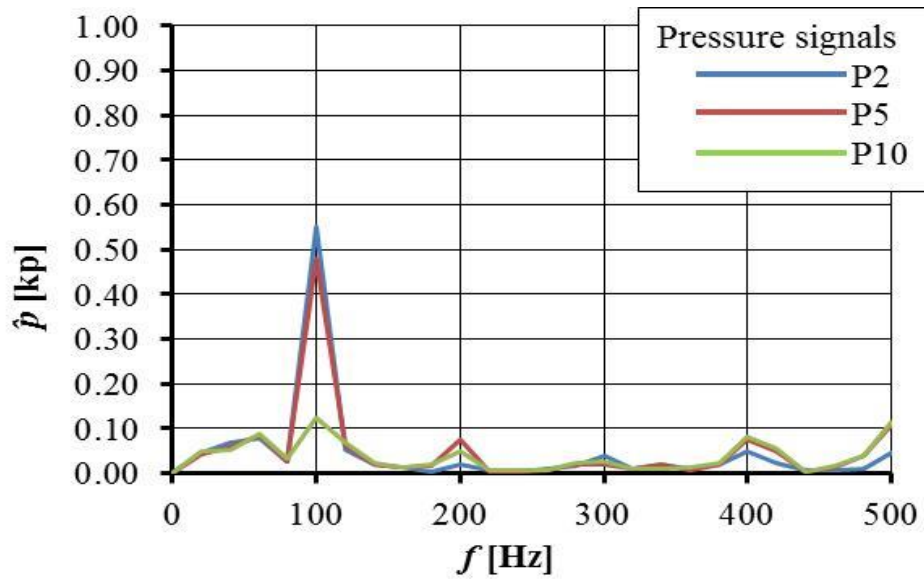
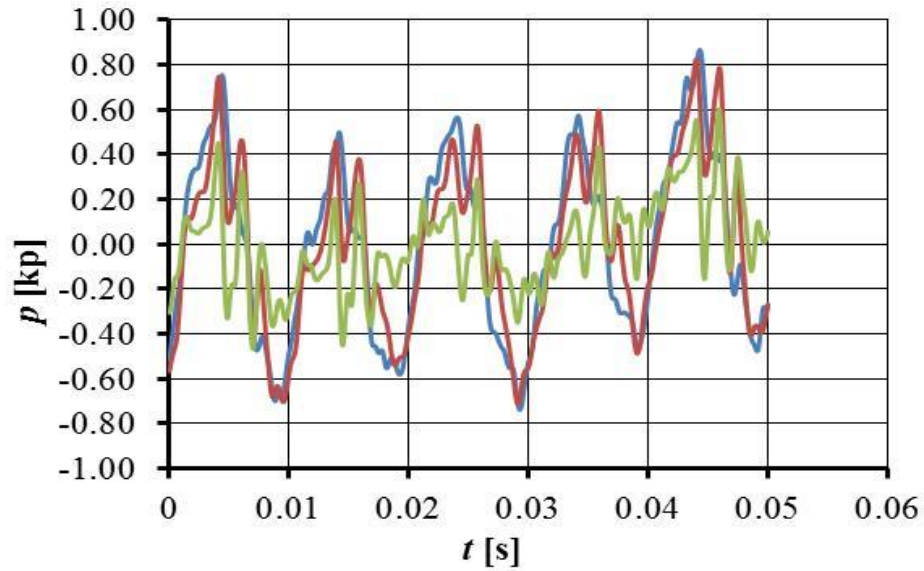
3.3.1 Pressure pulses for $\Psi^{bP} = 12^\circ$: Cradle-SCTetra, without Cavitation



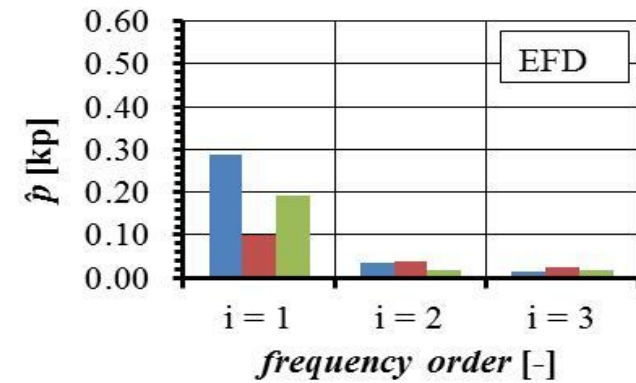
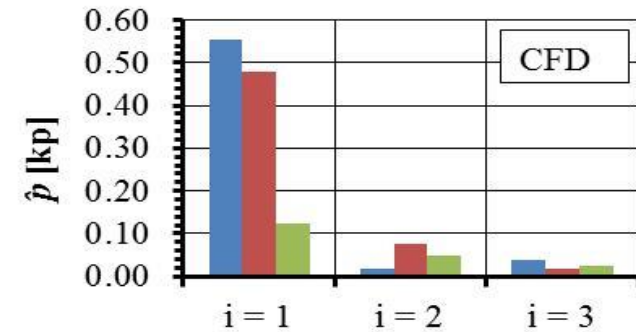
Sensor		$i = 1$	$i = 2$	$i = 3$
p2	(CFD)	0.5727	0.0256	0.0024
p5	(CFD)	0.4275	0.0457	0.0042
P10	(CFD)	0.0580	0.0078	0.0040
p2	(EFD)	0.3289	0.0122	0.0077
p5	(EFD)	0.3671	0.0204	0.0125
P10	(EFD)	0.0404	0.0141	0.0093



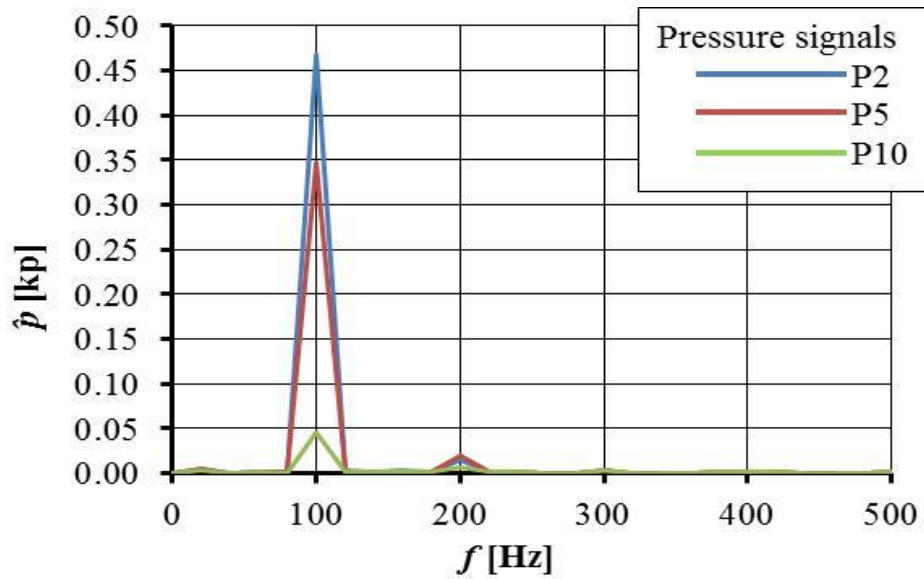
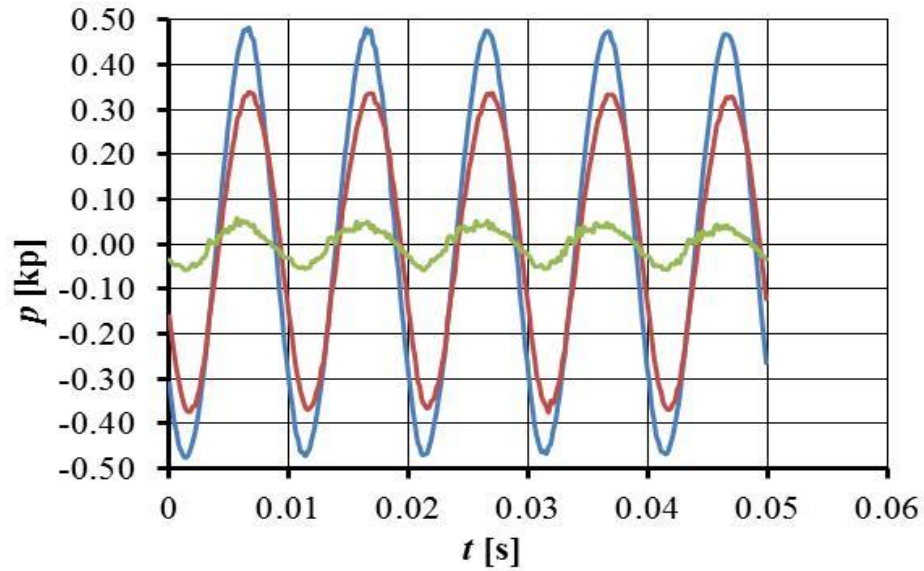
3.3.2 Pressure pulses for $\Psi^{bP} = 12^\circ$: Cradle-SCTetra, with Cavitation



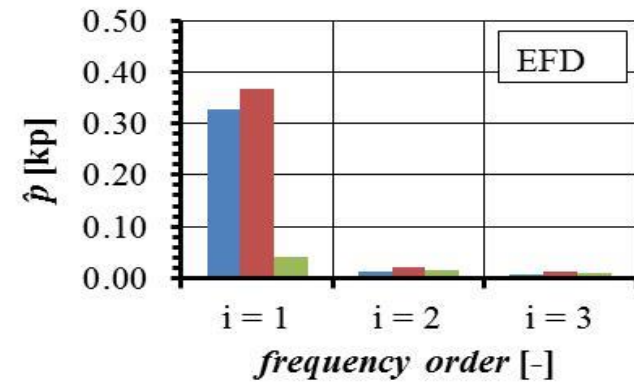
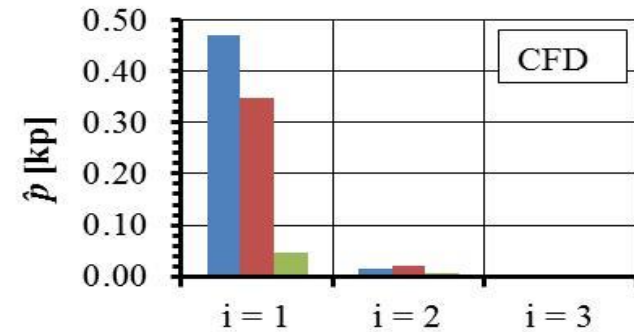
Sensor		$i = 1$	$i = 2$	$i = 3$
p2	(CFD)	0.5527	0.0194	0.0380
p5	(CFD)	0.4779	0.0758	0.0194
P10	(CFD)	0.1222	0.0497	0.0258
p2	(EFD)	0.2872	0.0355	0.0128
p5	(EFD)	0.1014	0.0395	0.0238
P10	(EFD)	0.1904	0.0183	0.0162



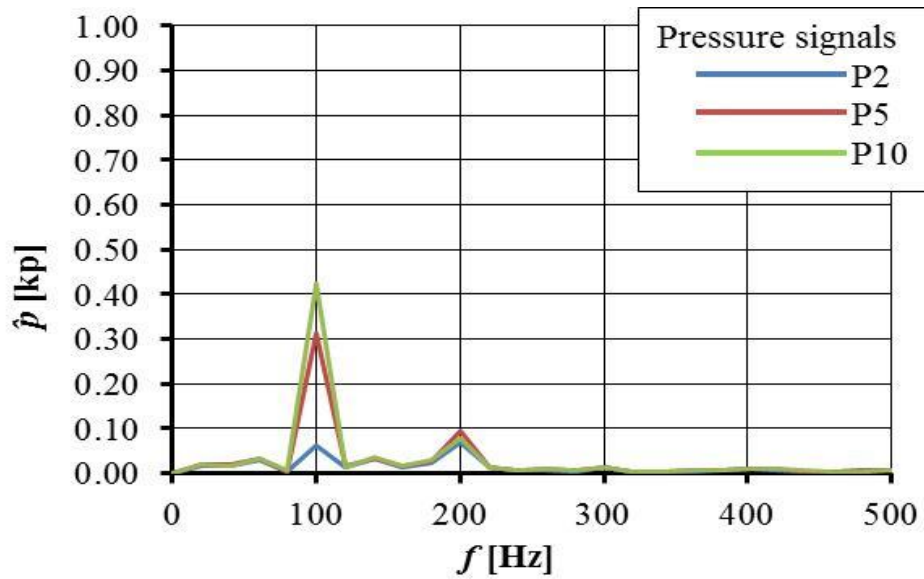
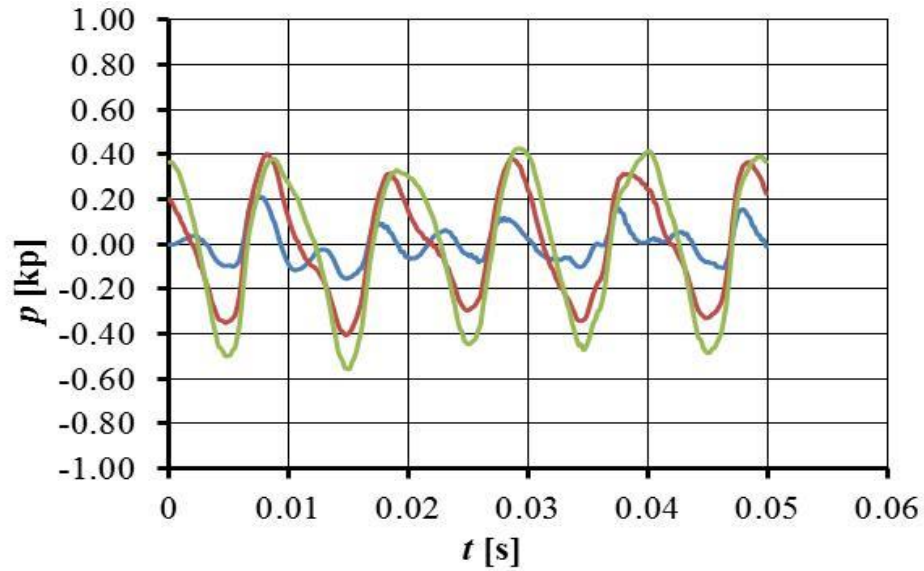
3.3.3 Pressure pulses for $\Psi^{bP} = 12^\circ$: SSPA-FLUENT, without Cavitation



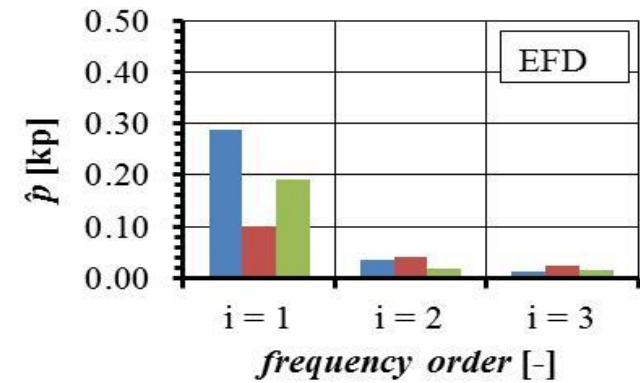
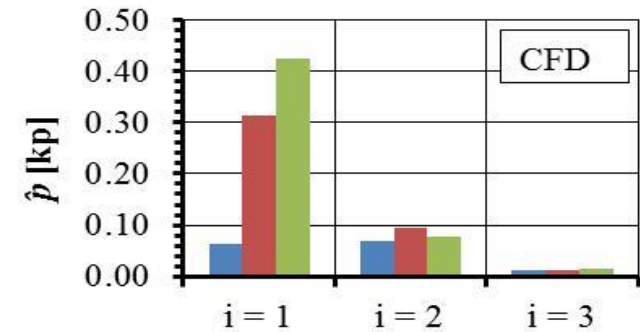
Sensor		$i = 1$	$i = 2$	$i = 3$
p2	(CFD)	0.4686	0.0142	0.0032
p5	(CFD)	0.3478	0.0197	0.0037
P10	(CFD)	0.0463	0.0058	0.0026
p2	(EFD)	0.3289	0.0122	0.0077
p5	(EFD)	0.3671	0.0204	0.0125
P10	(EFD)	0.0404	0.0141	0.0093



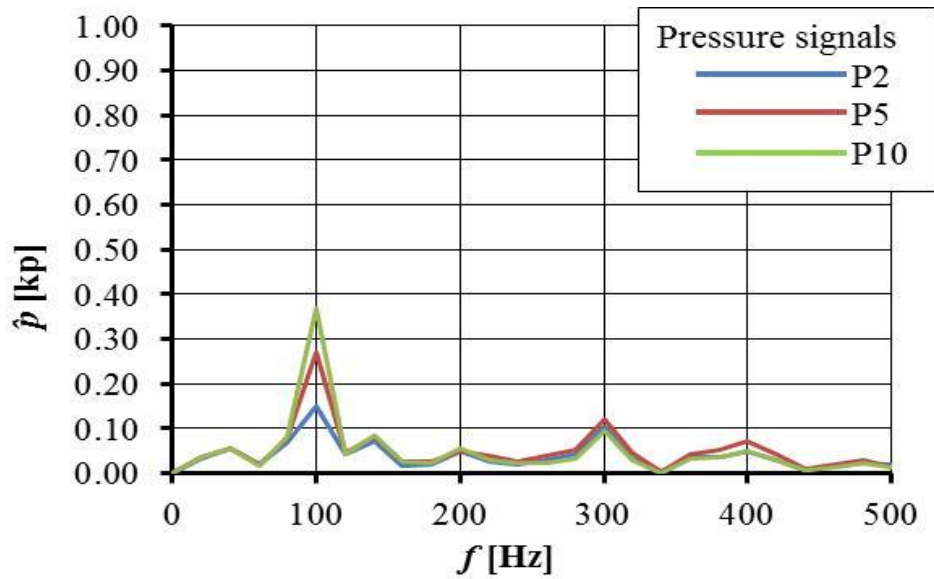
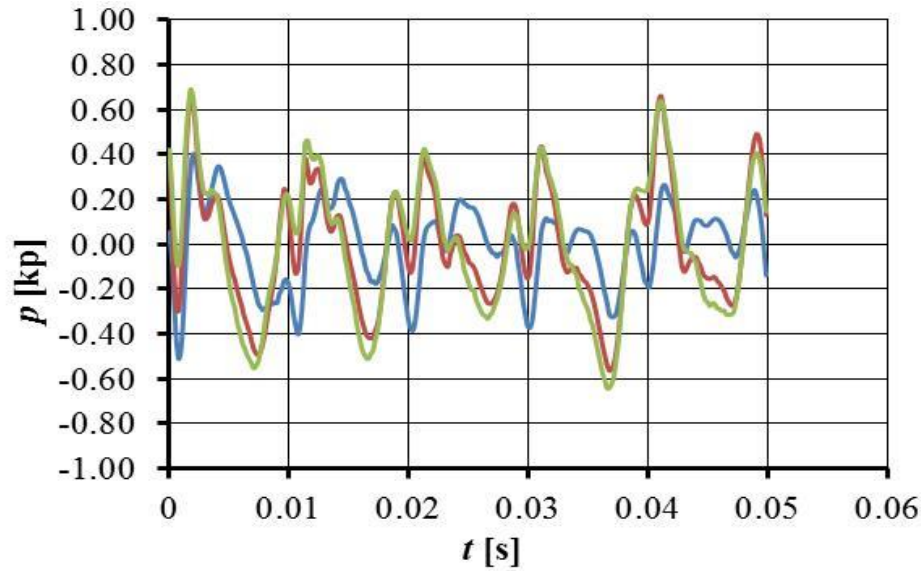
3.3.4 Pressure pulses for $\Psi^{bP} = 12^\circ$: SSPA-FLUENT, with Cavitation



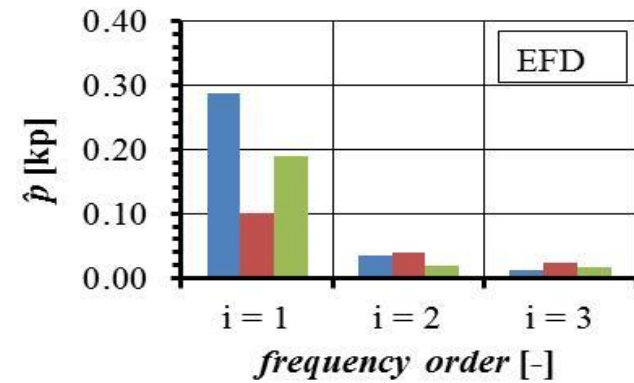
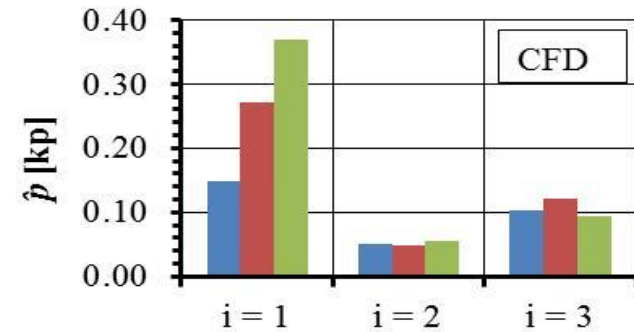
Sensor		$i = 1$	$i = 2$	$i = 3$
p2	(CFD)	0.0620	0.0689	0.0122
p5	(CFD)	0.3128	0.0937	0.0120
P10	(CFD)	0.4232	0.0765	0.0141
p2	(EFD)	0.2872	0.0355	0.0128
p5	(EFD)	0.1014	0.0395	0.0238
P10	(EFD)	0.1904	0.0183	0.0162



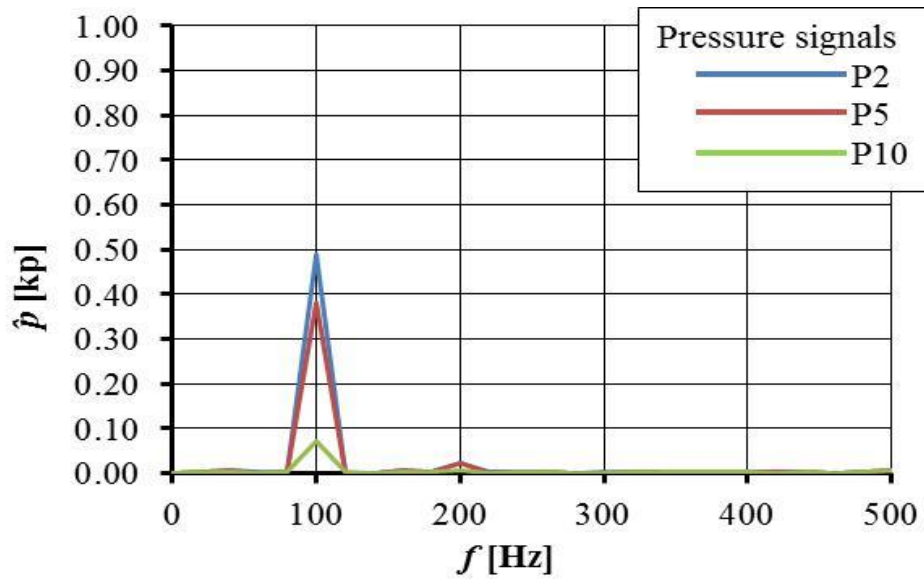
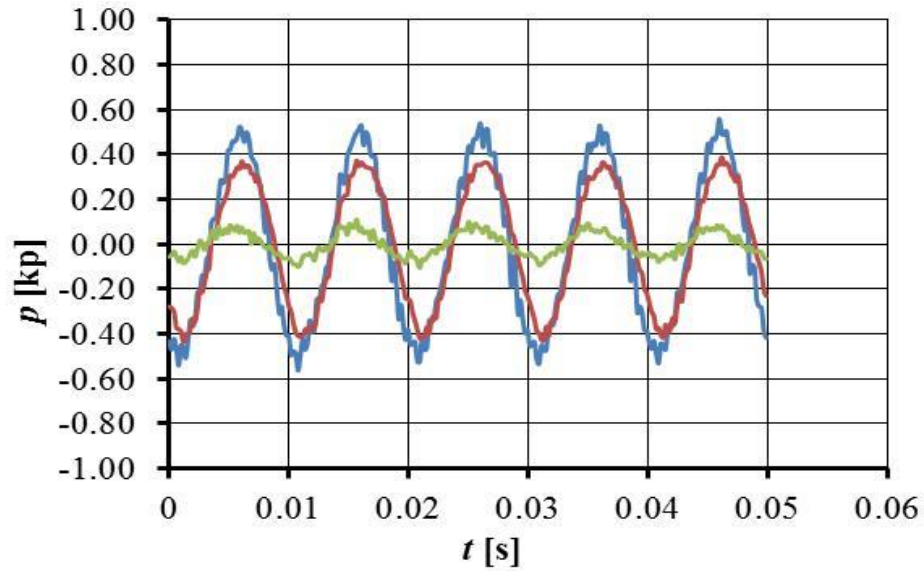
3.3.5 Pressure pulses for $\Psi^{bP} = 12^\circ$: SSPA-FLUENT, with Cavitation, Sauer



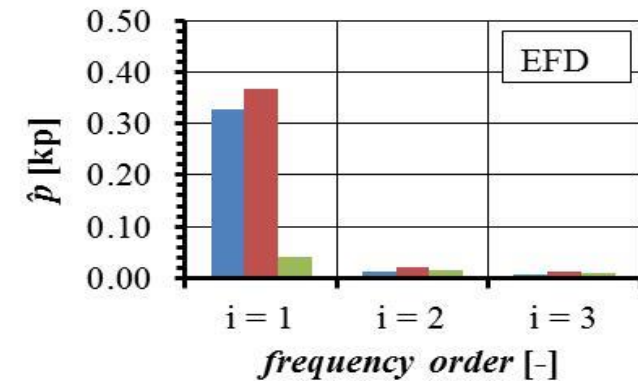
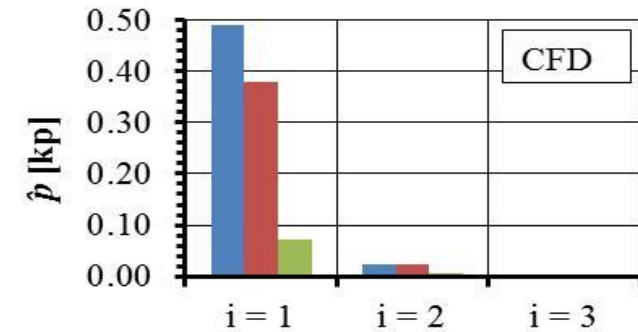
Sensor		$i = 1$	$i = 2$	$i = 3$
p2	(CFD)	0.1492	0.0500	0.1031
p5	(CFD)	0.2719	0.0488	0.1213
P10	(CFD)	0.3690	0.0541	0.0941
p2	(EFD)	0.2872	0.0355	0.0128
p5	(EFD)	0.1014	0.0395	0.0238
P10	(EFD)	0.1904	0.0183	0.0162



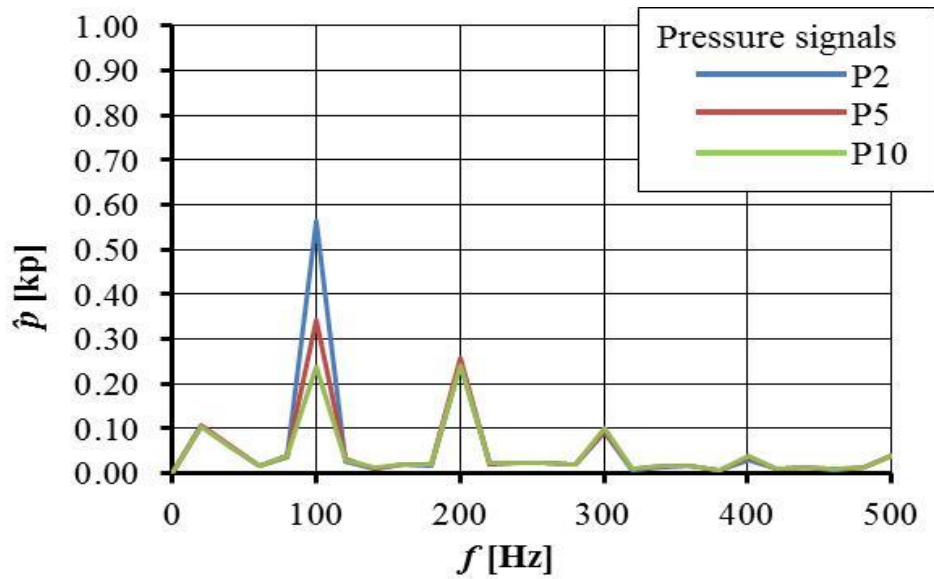
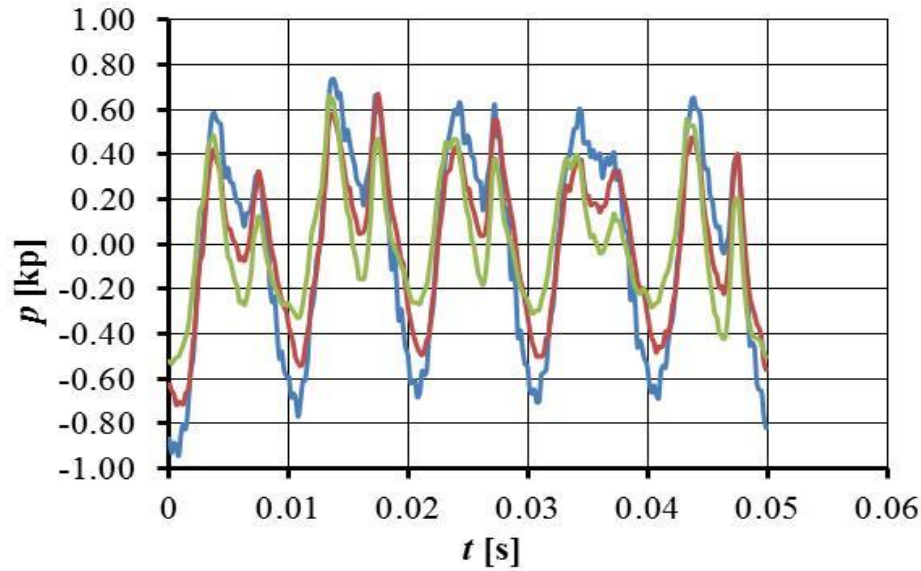
3.3.6 Pressure pulses for $\Psi^{bP} = 12^\circ$: TUHH-CFX, without Cavitation



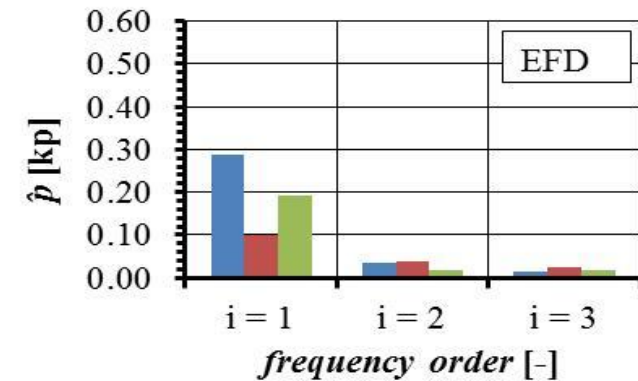
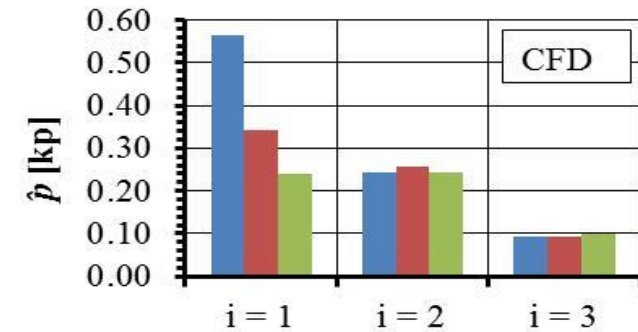
Sensor		$i = 1$	$i = 2$	$i = 3$
p2	(CFD)	0.4894	0.0230	0.0035
p5	(CFD)	0.3802	0.0227	0.0006
P10	(CFD)	0.0705	0.0065	0.0003
p2	(EFD)	0.3289	0.0122	0.0077
p5	(EFD)	0.3671	0.0204	0.0125
P10	(EFD)	0.0404	0.0141	0.0093



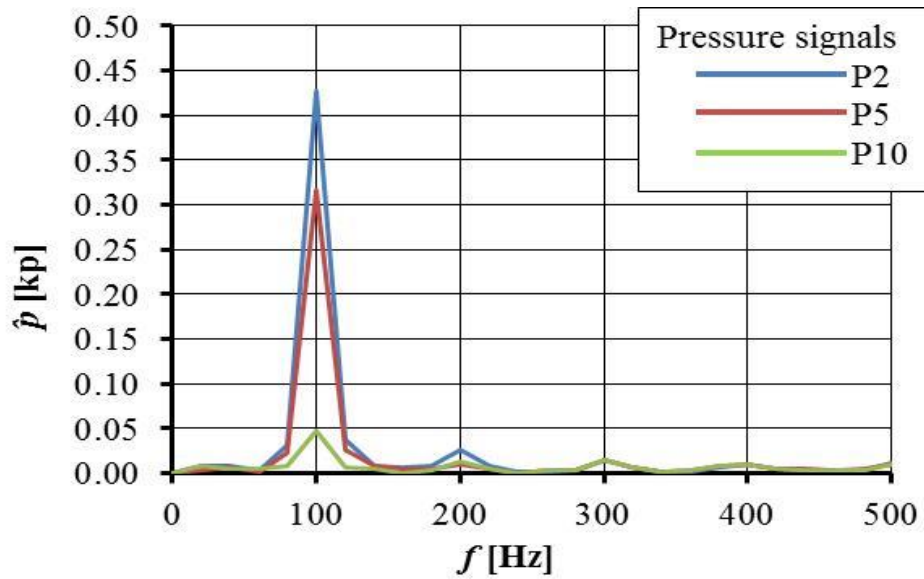
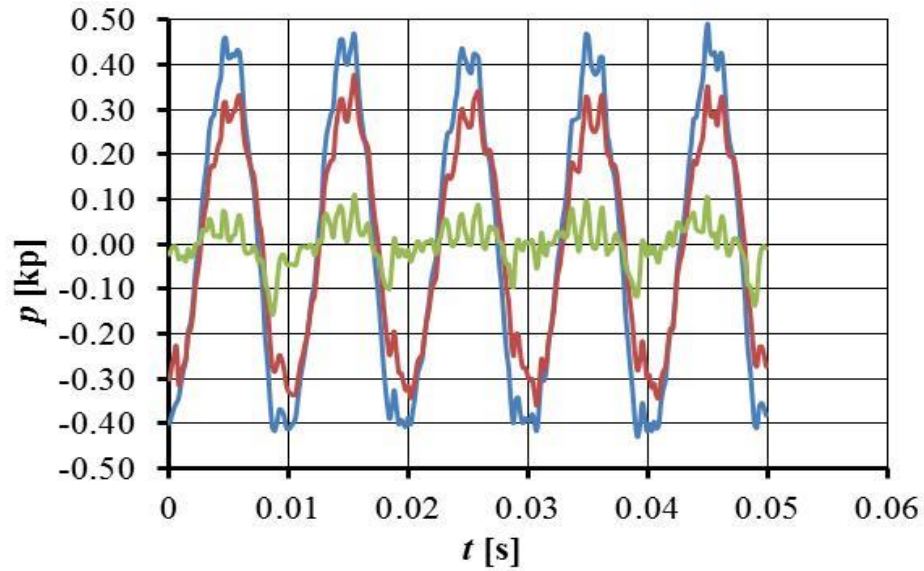
3.3.7 Pressure pulses for $\Psi^{bP} = 12^\circ$: TUHH-CFX, with Cavitation



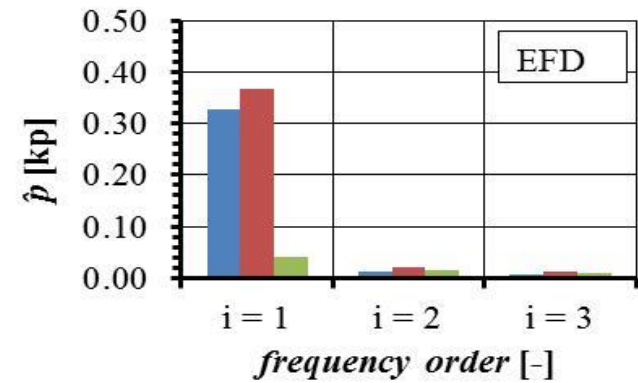
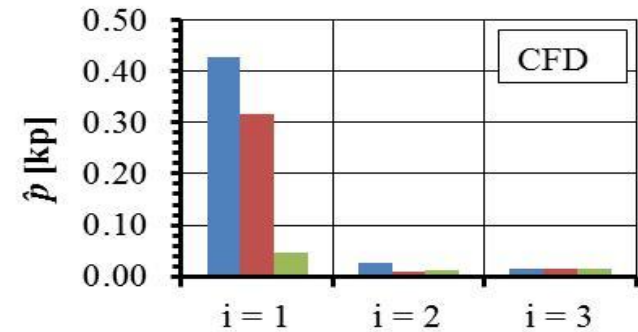
Sensor		$i = 1$	$i = 2$	$i = 3$
p2	(CFD)	0.5653	0.2435	0.0914
p5	(CFD)	0.3419	0.2576	0.0939
P10	(CFD)	0.2392	0.2422	0.1004
p2	(EFD)	0.2872	0.0355	0.0128
p5	(EFD)	0.1014	0.0395	0.0238
P10	(EFD)	0.1904	0.0183	0.0162



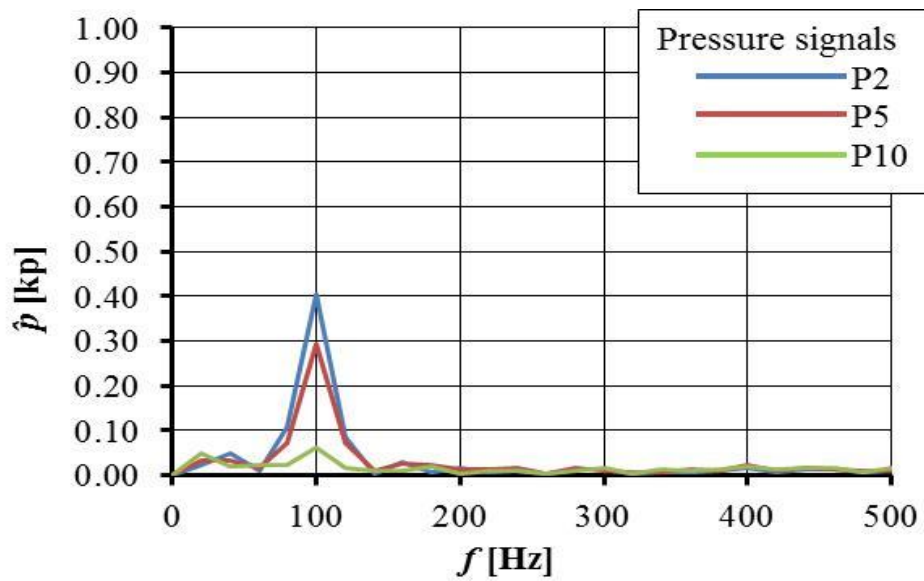
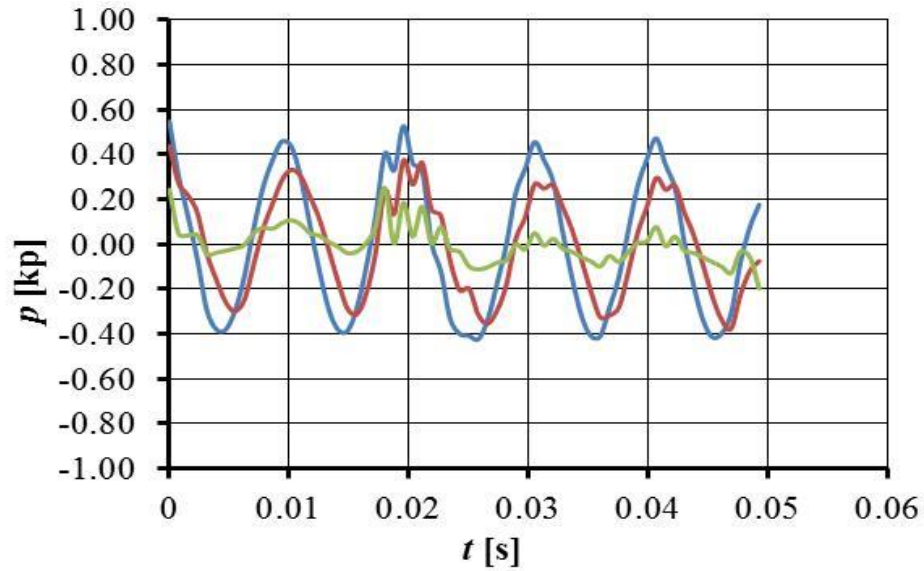
3.3.8 Pressure pulses for $\Psi^{bP} = 12^\circ$: TUHH-OpenFOAM, without Cavitation



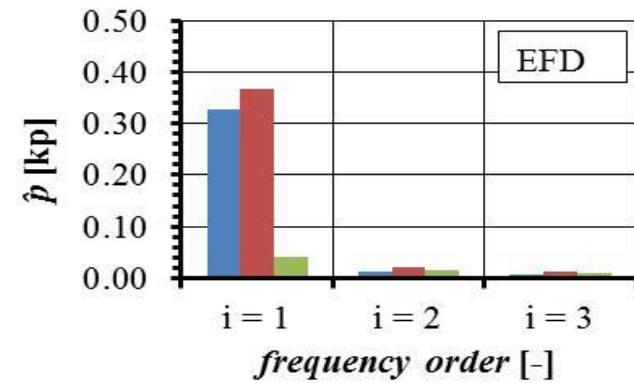
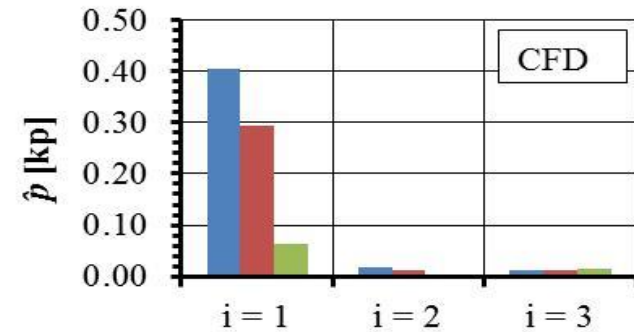
Sensor		$i = 1$	$i = 2$	$i = 3$
p2	(CFD)	0.4281	0.0267	0.0141
p5	(CFD)	0.3169	0.0101	0.0144
P10	(CFD)	0.0470	0.0125	0.0139
p2	(EFD)	0.3289	0.0122	0.0077
p5	(EFD)	0.3671	0.0204	0.0125
P10	(EFD)	0.0404	0.0141	0.0093



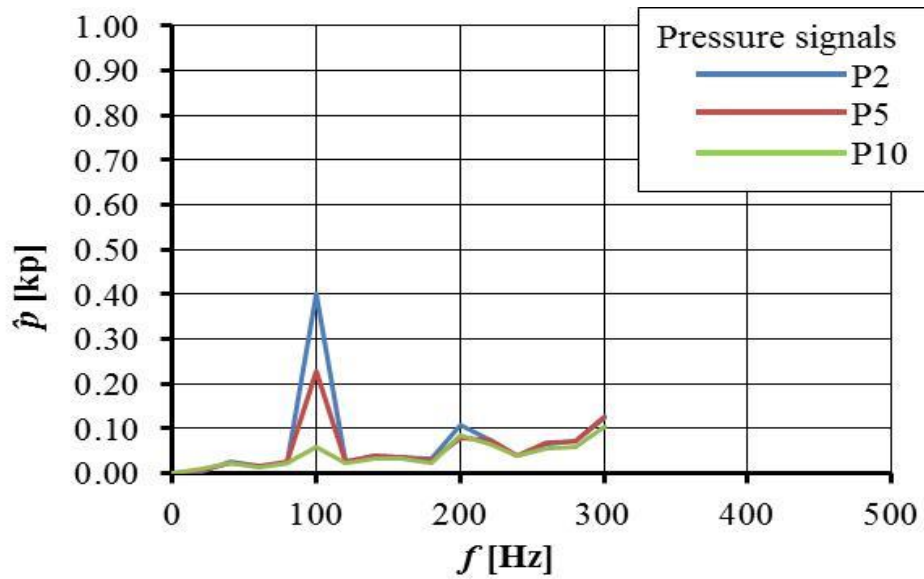
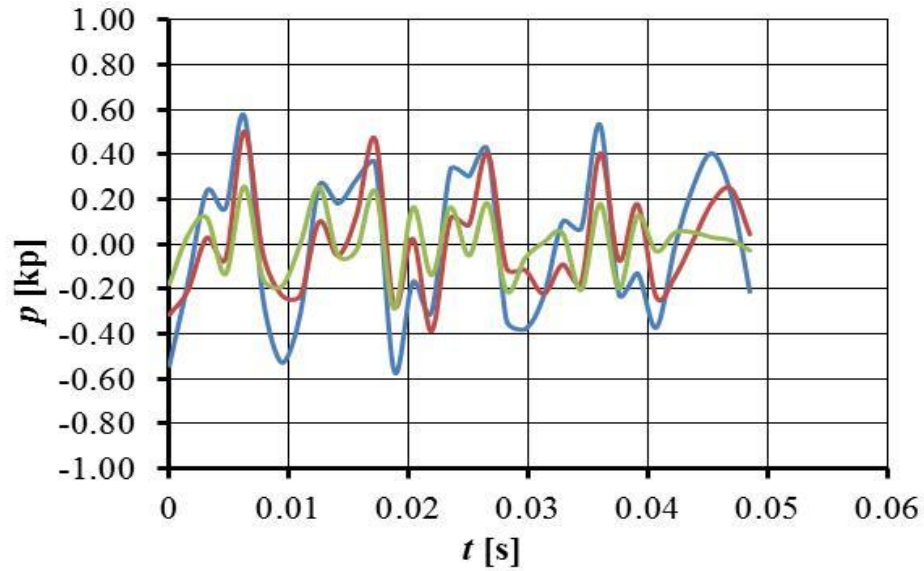
3.3.9 Pressure pulses for $\Psi^{bP} = 12^\circ$: TUHH-panMARE, without Cavitation



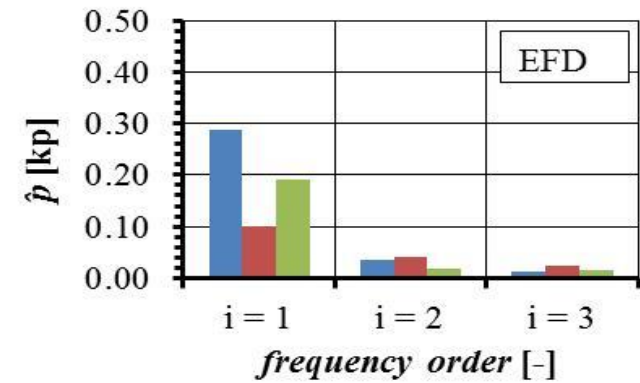
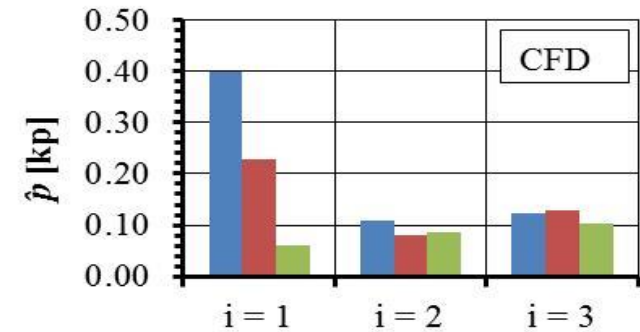
Sensor		$i = 1$	$i = 2$	$i = 3$
p2	(CFD)	0.4050	0.0177	0.0118
p5	(CFD)	0.2946	0.0122	0.0109
P10	(CFD)	0.0630	0.0046	0.0155
p2	(EFD)	0.3289	0.0122	0.0077
p5	(EFD)	0.3671	0.0204	0.0125
P10	(EFD)	0.0404	0.0141	0.0093



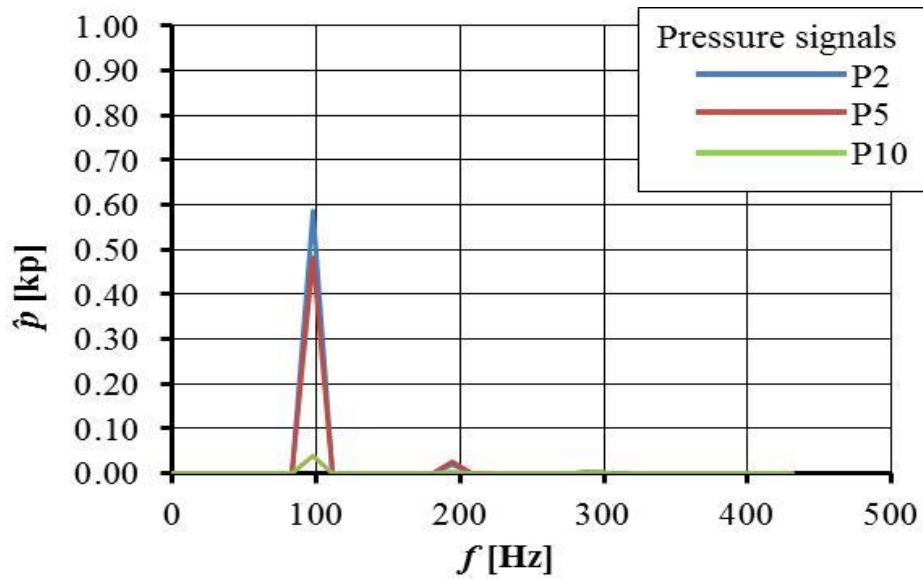
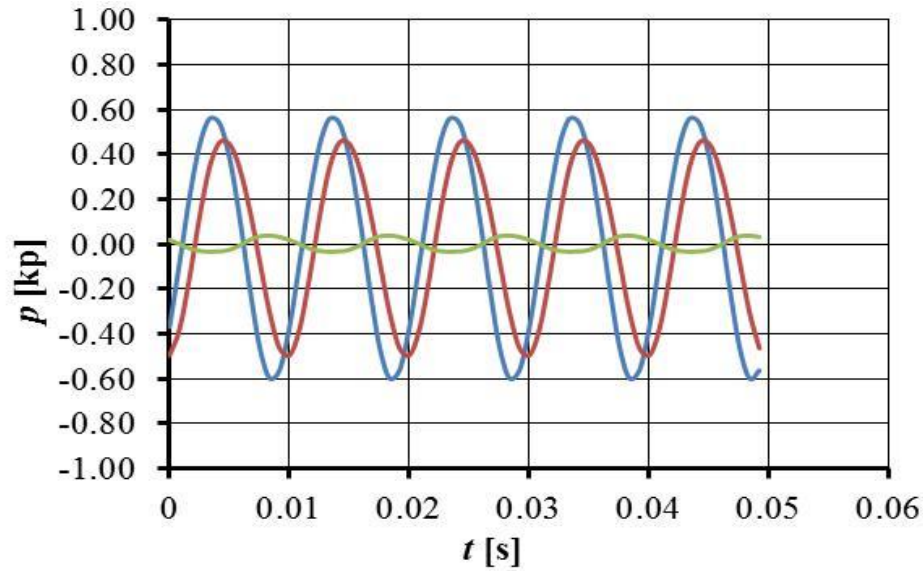
3.3.10 Pressure pulses for $\Psi^{bP} = 12^\circ$: TUHH-panMARE, with Cavitation



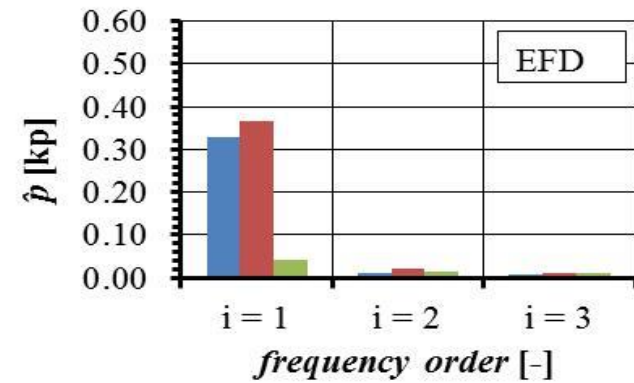
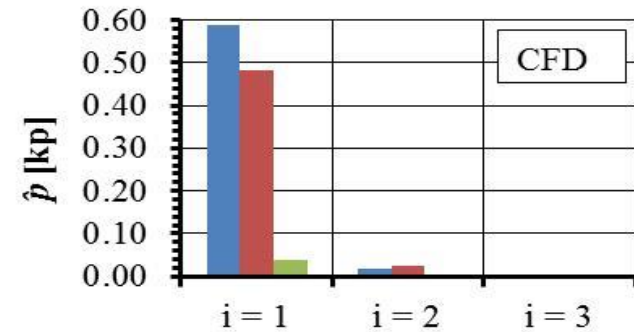
Sensor		$i = 1$	$i = 2$	$i = 3$
p2	(CFD)	0.4002	0.1084	0.1224
p5	(CFD)	0.2290	0.0792	0.1273
P10	(CFD)	0.0596	0.0856	0.1033
p2	(EFD)	0.2872	0.0355	0.0128
p5	(EFD)	0.1014	0.0395	0.0238
P10	(EFD)	0.1904	0.0183	0.0162



3.3. Pressure pulses for $\psi^{bP} = 12^\circ$: UTAustin-PROPCAV, without Cavitation



Sensor		$i = 1$	$i = 2$	$i = 3$
p2	(CFD)	0.5873	0.0192	0.0014
p5	(CFD)	0.4831	0.0257	0.0018
P10	(CFD)	0.0377	0.0031	0.0019
p2	(EFD)	0.3289	0.0122	0.0077
p5	(EFD)	0.3671	0.0204	0.0125
P10	(EFD)	0.0404	0.0141	0.0093



Chapter 4

Papers by Participants

Numerical predictions of the PPTC model propeller in oblique flow

Mitja Morgut¹, Enrico Nobile², Dragica Jošt³, Aljaž Škerlavaj⁴

¹Turboinštitut d.d., Rovšnikova 7, 1210 Ljubljana (SLOVENIA)

² Dipartimento di Ingegneria e Architettura, Università degli Studi di Trieste, via A. Valerio 10, 34127 Trieste (ITALY)

^{3,4} Turboinštitut d.d., Rovšnikova 7, 1210 Ljubljana (SLOVENIA), presently at Dipartimento di Ingegneria e Architettura, Università degli Studi di Trieste, via A. Valerio 10, 34127 Trieste (ITALY)

ABSTRACT

The numerical predictions of the non-cavitating and cavitating flow around the PPTC model scale propeller, working in oblique flow, are presented. The simulations are performed using both commercial and open source CFD codes. The homogeneous multiphase model is used and three widespread mass transfer models, previously calibrated, are employed. The turbulence is modelled using the RANS (Reynolds Averaged Navier Stokes) approach with a two-equation turbulence model.

Keywords

RANS, cavitation, PPTC propeller, oblique flow.

1 INTRODUCTION

In this work the numerical predictions of the non-cavitating and cavitating flow are presented for the PPTC propeller in oblique flow. The simulations are carried out following the experimental setups, kindly provided by the workshop organizers, for the Case 1: *Propeller open water curves in oblique flow* and Case 2: *Cavitation observations in oblique flow* (see www.sva-potsdam.de/pptc_data_15.html). For Case 1 the numerical predictions are carried out using ANSYS-CFX 15, a commercial CFD solver (for brevity CFX), and OpenFOAM, an OpenSource CFD toolbox (for brevity OF). As far as the Case 2 is concerned, it is important to point out that all the simulations are performed using CFX in combination with three different calibrated mass transfer models following the approach used during the former smp'11 workshop (Morgut and Nobile, 2011).

In the following the propeller model and the coordinate system conventions used in this work are first presented. Then, the descriptions of the Case 1 and Case 2 are given. Eventually some brief conclusions are given.

2 PROPELLER MODEL AND CONVENTIONS

In this study the PPTC model propeller was consider. It is a five bladed controllable pitch propeller with a diameter

$D = 250 \text{ mm}$. In Fig. 1 it is visible the propeller CAD model used in all the simulations.

The propeller had an incidence inclination of 12 degrees towards the inflow direction. Thus the propeller performances were evaluated in the PCS (Propeller Coordinate System) depicted in Fig. 1.

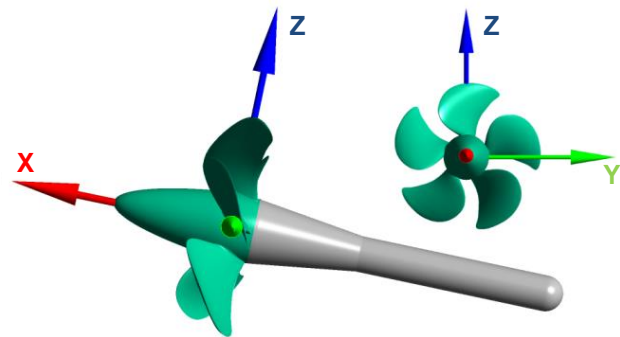


Fig.1: Propeller model and Propeller Coordinate System

In the following the survey of the formulae used to evaluate the required quantities is given for the sake of clarity.

$$K_{T_i} = \frac{T_i}{\rho_l n^2 D^4} \quad K_Q = \frac{Q}{\rho_l n^2 D^5}$$

$$J = \frac{V}{nD} \quad \sigma_n = \frac{P_{ref} - P_v}{0.5 \rho_l (nD)^2}$$

It is important to note that the forces were integrated on the blade surfaces and the portion of the hub depicted with green colour in Fig. 1 following the organizers' suggestion. In the above equations T_i stays for the force component projected along x-direction, y-direction and z-direction. Q is the propeller torque, ρ_l is the water density, n is the propeller rotation speed and V is the free-stream (inlet) flow velocity.

3 CASE 1

3.1 Numerical Strategy

The numerical simulations were carried out following the experimental/numerical setup provided by the workshop organizers. In current simulations the computational domain roughly sketched in Fig. 2 was used.

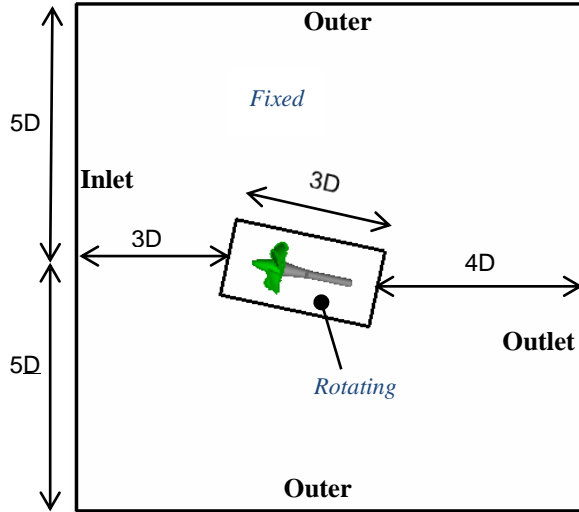


Fig 2: Computational domain for PPTC propeller. View looking through Y- direction. The *Rotating* region is a cylinder having diameter equal to $1.52D$.

The following boundary conditions were set. On the solid surfaces the no slip wall boundary condition was set, except for the Outer (radial) domain surface where the free-slip condition was imposed. On the Outlet boundary a fixed value of static pressure was set and on the Inlet boundary the inlet flow conditions were defined according to the considered operational point. Even though the considered problem has an unsteady character, the simulations were performed, for the sake of computational costs, using an approximated steady state approach. In particular the steady state MRF (Multiple Reference Frame) approach was used with both CFX and OF solvers. In Fig. 2 the *Rotating* and *Fixed* regions are shown. In all the simulations the propeller rotation was $n = 15 \text{ rps}$. Since the numerical investigations were carried out solving the RANS equations the workhorse SST (Shear Stress Transport) model was selected for the turbulence closure. The high resolution and the second order linear upwind schemes were used in CFX and OF, respectively, for the discretization of the convective terms.

3.2 Meshing

All the meshes were generated using ANSYS - ICEM CFD 15, a commercial meshing tool. The two different domain regions, i.e. *Rotating* and *Fixed*, were discretized using the hybrid approach (tetrahedra + pyramids + prisms). A higher

resolution was enforced close to the shaft and propeller surfaces.

The mesh independence study was first carried out in CFX considering three progressively refined grids. The study was performed for $J = 0.8$. In Table 1 the details of the mesh resolutions (number of nodes) are collected. Fig. 3 shows a snapshot of the mesh CFX-OW-2.

Table 1: Number of nodes for the meshes used in CFX

Solver-Mesh Id	Rotating	Fixed
CFX-OW-1	1,739,688	212,641
CFX-OW-2	6,558,812	212,641
CFX-OW-3	10,586,761	212,641

Table 2: Number of elements for the mesh used in OF

Solver-Mesh Id	Rotating	Fixed
OF-OW-2	4,512,194	208,231

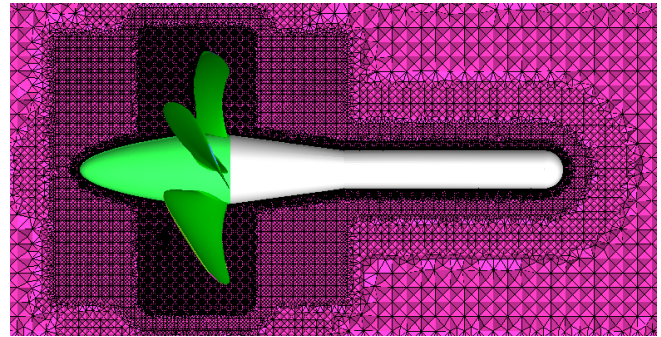


Fig. 3: Mesh CFX-OW-2 close to the propeller

In the case of OF, by taking advantage of the former mesh independence study, only one mesh was generated. In particular in order to maintain as much as possible the mesh congruency (with CFX case) an additional mesh with approximately the same number of cells, as the number of elements of the mesh CFX-OW-2, was generated. We remind that while OF is based on a cell centered FV method, ANSYS-CFX rely on a node centered CVFEM (Control Volume Finite Element Method) approach. As a matter of fact while in OF the number of solved variables is proportional to the number of cells, in CFX it is proportional to the number of nodes. It is important to add that both CFX and OF meshes had a similar averaged value of y^+ on blade surfaces. (approximately 40 for $J = 0.8$).

3.3 Results

In Table 3 the results of the mesh independence study carried out with CFX, considering the operating point $J = 0.8$, are reported. Moreover in the same table the values predicted with OF are given.

Table 3: Results of the mesh independence study carried out with CFX for $J=0.8$, and values predicted with OF.

Solver-Mesh Id	K_{Tx}	$10 K_Q$
CFX-OW-1	0.532	1.255
CFX-OW-2	0.520	1.225
CFX-OW-3	0.522	1.227
OF-OW-2	0.508	1.203

Fig. 4 highlights that the performances predicted with the two different solvers were similar to each other.

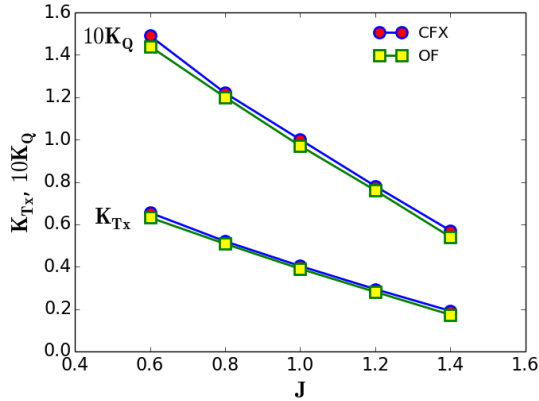


Fig. 4: Performances predicted with CFX and OF

It is important to point out that in both cases (CFX and OF) the convergence of the solver variables (U_x , U_y , U_z , p) was poor as expected due to the approximated method (steady state MRF) adopted to carry out the simulations. For this reason in all the cases the simulations were stopped when the *steady* trend of the forces was achieved.

4 CASE 2

4.1 Numerical Strategy

In these simulations the propeller was placed in the cavitation tunnel domain provided by the workshop organizers.

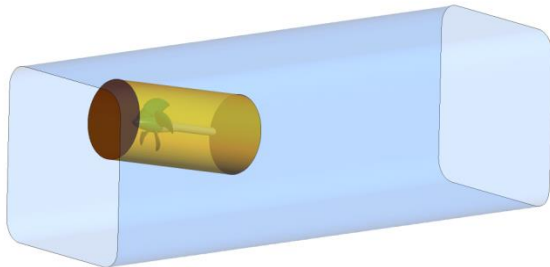


Fig. 5: Computational domain for Case 2

Fig. 5: shows the computational domain where the yellow cylinder represents the *Rotating* domain region. As a matter of fact this region had exactly the same dimensions of the former *Rotating* region used for Case 1.

The simulations were performed using the following boundary conditions. On the solid boundaries the no-slip wall condition was imposed. On the Inlet boundary the inflow velocity was set according to the prescribed operating point. On the Outlet boundary a fixed static pressure was set. The propeller rotation was simulated using the steady state MRF approach where the rotation velocity was always equal to $n = 20$ rps. In this case the turbulent cavitating flow was simulated using the homogeneous model in combination with three different calibrated mass transfer models (Morgut and Nobile 2011, 2012). Here we remind, for the sake of clarity, that were calibrated the following models: the Kunz et al. (2000) model (for brevity Kunz), the Singhal et al. (2002) model (known as the *Full Cavitation Model*, thus FCM hereafter), the Zwart et al. model (2004), (for brevity Zwart). As far as the turbulent treatment is concerned, also in this case the RANS approach was selected, and following the former study the SST model was used for turbulence closure. The simulations were carried out using CFX where for the discretization of the convective terms the high resolution method was used.

4.2 Meshing

Only one mesh was generated for the cavitation tunnel tests. Since we focused exclusively on the predictions of the mean global problem values, thrust and torque, we assumed that the considered mesh, based on the grid-independence study carried out for Case 1, could ensure sufficient accuracy to evaluate the behavior of the considered operating points.

Also in this case the mesh was well refined close to the propeller blade surfaces and shaft.

In Table 4 the main mesh characteristics are summarized, while in Fig. 6 a snapshot of the propeller surface mesh is shown.

Table 4: Number of nodes of the computational mesh

Solver-Mesh Id	Rotating	Fixed
CFX-CT	4,312,560	260,450

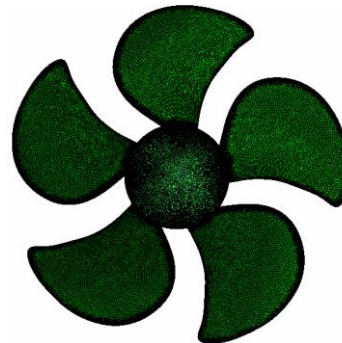


Fig. 6 : Propeller surface mesh. View looking suction side.

4.3 Results

The simulations were performed for three different values of the advance coefficient, J , considering fully wetted flow

as well as cavitating flow conditions. In the case of cavitation the following operational points were considered: ($J = 1.019, \sigma_n = 2.024$), ($J = 1.269, \sigma_n = 1.424$), ($J = 1.408, \sigma_n = 2.000$). Analogously to Case 1 the simulations were stopped when the forces were almost steady.

In Fig. 7 the numerical predictions for the fully wetted flow conditions and cavitating flow conditions are plotted.

Fig. 8 shows for the simulations performed at point ($J = 1.019, \sigma_n = 2.014$) with the cavitation model deactivated the regions on the blades surfaces where the pressure was lower than the vapour saturation pressure.

Finally, in Fig. 9 the sketches of the cavitation patters predicted with the three different calibrated mass transfer models are compared.

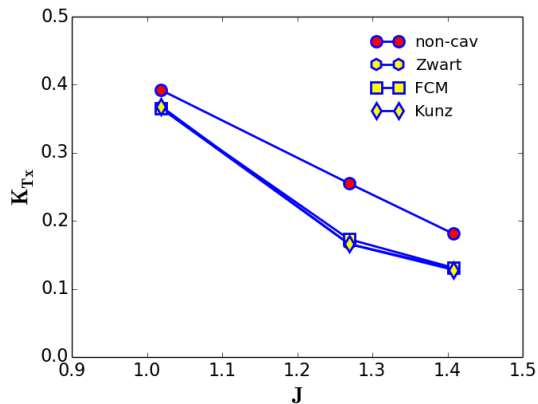


Fig. 7: Performances predicted using CFX in combination with three different mass transfer models.

5 CONCLUSIONS

In this report the numerical predictions of the PPTC model propeller in oblique flow were presented. In particular the results obtained for the case 1: *Propeller open water curves in oblique flow* and case 2: *Cavitation observations in oblique flow*, were presented.

All the simulations were carried out using the steady state MRF approach. For turbulence modelling the RANS approach was used and following former studies the SST turbulence model was employed. As far as the cavitating flow predictions are concerned, three different calibrated mass transfer models were alternatively used.

ANSYS-CFX 14, a commercial CFD solver as well as OpenFOAM-2.3.x, an open source CFD toolbox, were used for the Case 1. The numerical results obtained with the two different solvers were similar.

The predictions corresponding to the Case 2 were performed using exclusively ANSYS-CFX 14 because the major interest was focused on the evaluation of the behavior of the three different calibrated mass transfer models. As a matter of fact, despite the currently unknown accuracy of the obtained results, it is interesting to point out that similarly to the former experience of the smp'11 workshop

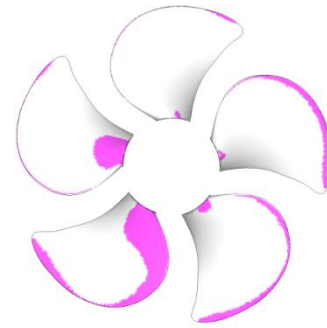


Fig. 8: Operating point: $J = 1.019, \sigma_n = 2.024$, cavitation model deactivated. In cyan are shown the regions on the blade surfaces where pressure was dropped below the vapour pressure P_v . View looking propeller suction side.

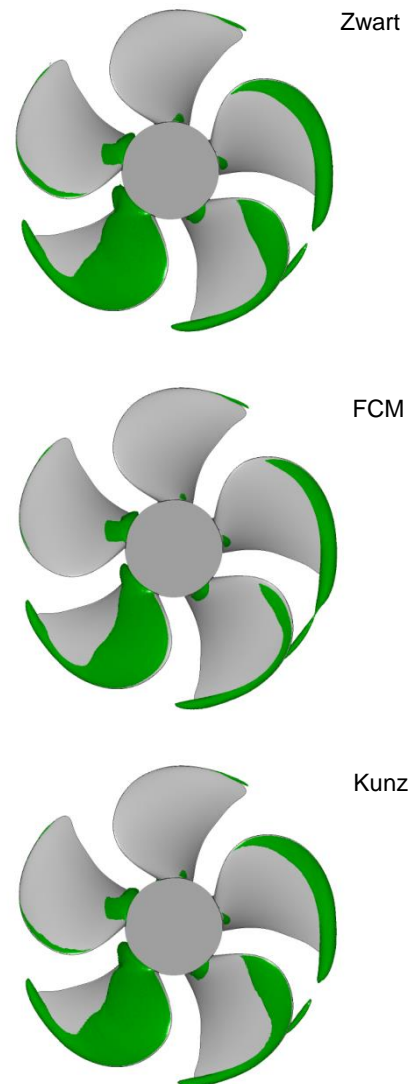


Fig. 9: Operating point: $J = 1.019, \sigma_n = 2.024$. Cavitation patterns predicted using different mass transfer models. Cavitation patterns depicted as isosurfaces of vapour volume fraction equal to 0.4. View looking propeller suction side.

also in this case the numerical results obtained with the different calibrated mass transfer models were very close to each other.

Finally, it is important to note that this study aimed to evaluate the effective application of the steady state MRF approach to the predictions of the performances of the marine propellers in oblique flow leaving the more detailed local flow analysis to the *higher fidelity models* based on more expensive, from the computational point of view, time dependent approaches.

6 ACKNOWLEDGEMENTS

The research leading to these results has received funding from the People Programme (Marie Curie Actions) of the European Union's Seventh Framework Programme FP7/2007-2013/ under REA grant agreement n°612279.

7 REFERENCES

- Kunz, R. F. , Boger, D. A., Stinebring, D. R., Chyczewski, T. S., Lindau, J. W., Gibeling, H. J., Venkateswaran, S., and Govindan, T. R. (2000), "A preconditioned Navier-Stokes method for two-phase flows with application to cavitation prediction". Computers and Fluids 29(8), 849-875.
- Morgut, M., and Nobile, E. (2011) "Numerical Predictions of the Cavitating and Non-Cavitating Flow Around the Model Scale Propeller PPTC", Proc. of the Workshop on Cavitation and Propeller Performance, the 2nd International Symposium on Marine Propulsors, Hamburg, Germany.
- Morgut, M. and Nobile, E. (2012), "Numerical Predictions of Cavitating Flow around Model Scale Propellers by CFD and Advanced Model Calibration", International Journal of Rotating Machinery, special issue: Marine Propulsors and Current Turbines: State of the Art and Current Challenges.
- Singhal, A. K., Athavale, M. M., Li, H. and Jiang, Y. (2002), "Mathematical Basis and Validation of the Full Cavitation Model". Journal of Fluids Engineering 124, 617-624.
- Zwart, P., Gerber, A. G. and Belamri, T. (2004). "A Two-Phase Model for Predicting Cavitation Dynamics", ICMF 2004 International Conference on Multiphase Flow, Yokohama, Japan

Cavitation observation on the PPTC propeller in oblique flow

Tobias Huuva¹, Simon Törnros¹

¹ Caterpillar Propulsion Production AB
Andvägen 26, SE-475 40 Hönö, Sweden

1 INTRODUCTION

The Second International Workshop on Cavitating Propeller Performance is to be held at the Fourth International Symposium on Marine Propulsors (SMP'15). The first workshop was held at the Second International Symposium on Marine Propulsors (SMP'11) and focused on open water performance, cavitation observation and tip vortex flow of the PPTC propeller in homogenous inflow. The second workshop focuses on open water performance and cavitation observation in oblique flow using the same propeller. The test is setup as a blind test but it is stated that the inclination has a decisive impact on the propeller performance.

Three cases constitutes the second workshop

- Case 1: Propeller open water curves in oblique flow
- Case 2: Cavitation observation in oblique flow
- Case 3: Propeller induced pressure pulses

Caterpillar Propulsion has chosen to participate in the study of only one of these cases. Case number 2 is chosen as it is found to be the most interesting for the validation of the numerical methodology of Caterpillar Propulsion.

2 TEST CASE

The test consists of the PPTC propeller in pulling configuration with an inclination of 12°. The model test was made in the cavitation tunnel K 15 A (Kempf & Remmers) of SVA Potsdam, Figure 1.

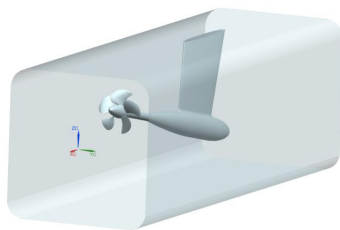


Figure 1 Test setup

The PPTC propeller is a controllable pitch propeller designed to generate a stable tip vortex for academic purposes. The propeller can be seen in Figure 2. The propeller performance is evaluated as the forces on the green parts, Figure 2 (left), scalar projected on the unit vector of rotation.

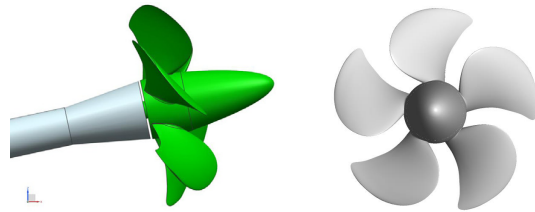


Figure 2 Potsdam Propeller Test Case (PPTC)

Important propeller design parameters are shown in Table 1.

Table 1 Propeller properties

Propeller diameter	D_p	[mm]	250
Pitch ratio	$P_{0.7}/D$	[-]	1.635
Chord ratio	$C_{0.7}/D$	[-]	0.416668
Area ratio	A_e/A_o	[-]	0.779
Skew	Θ_{eff}	[°]	18.8
Hub diameter ratio	D_h/D_p	[-]	0.15
Number of blades	z	[-]	5
Direction of rotation			Right-handed

Three operating conditions referred to as 2-1, 2-2 and 2-3 constitutes case 2. Case 2-2 is the design point while 2.1 is operating at a lower advance ratio and 2-3 at a higher advance ratio. Details of the three operation points can be seen in Table 2.

Table 2 Case properties

Case			2.1	2.2	2.3
Advance coefficient	J	[-]	1.019	1.269	1.408
Cavitation number	σ_n	[-]	2.024	1.424	2.000
Rotational speed	n	[s ⁻¹]	20	20	20

Water density	ρ	[kgm ⁻³]	997.78	997.8	997.41
Water Kinematic viscosity	ν	[m ² s ⁻¹]	9.567·10 ⁻⁷	9.591·10 ⁻⁷	9.229·10 ⁻⁷
Vapour pressure	p_v	[Pa]	2643	2626	2904
Water temperature	T	[°]	22.0	21.9	23.2

The following vaporous water properties are used, see Table 3. Note that surface tension as well as gravity is ignored.

Table 3 Vapor properties

Water vapour density	ρ	[kgm ⁻³]	0.023
Water vapour kinematic viscosity	ν	[m ² s ⁻¹]	6·10 ⁻⁴

The cavitation number is set by a Dirichlet boundary condition for the pressure field on the outlet.

3 NUMERICAL SETUP

The two phases are considered using the Volume Of Fluid (VOF) method by an in-house modified solver originating from the C++ finite volume library OpenFOAM 2.3. Turbulence is modelled using Unsteady Reynolds Averaged Navier Stokes (URANS). Large Eddy Simulation (LES) has shown ability of resolving more details than URANS for cavitating flows, however URANS requires a significantly lower computational effort which makes URANS a suitable approach for industrial CFD for cavitating flows. Cavitation is taken into account by using the mass transfer model by Kunz et al. (1999).

3.1 Solver

The in-house modified solver is based on the C++ finite volume library OpenFOAM 2.3. The modifications constitutes of a damping function of the turbulent viscosity and a ramp function for the cavitation constants. The solver is a multiphase solver, taking two fluids into account using the Volume Of Fluid (VOF) approach. The solver utilizes the semi-implicit Multidimensional Universal Limited with Explicit Solution (MULES) to allow for higher courant numbers and still maintain boundedness.

3.2 Turbulence modelling

The turbulent viscosity μ_t needs to be modelled using a turbulence model. A modified version of the RANS turbulence model RNG (Renormalization Group Theorem) k- ϵ was used together with wall functions. The modification (Reboud, Coutier-Delgosha, & Fortes-Patella, 2002) aims to deal with an over prediction of turbulent viscosity in the mixture region. This over prediction is commonly experienced when using RANS and dampens unsteadiness. The modification is applied by exchanging the density in the

expression for turbulent viscosity with a damping function $f(\rho)$.

$$\mu_t = f(\rho) C_\mu \frac{k^2}{\epsilon}$$

$$f(\rho) = \rho_v + \frac{(\rho_m - \rho_v)^{10}}{(\rho_l - \rho_v)^9}$$

This modification dampens the turbulent viscosity in the mixture region but returns the physical density value for pure liquid and vapor, see Figure 3.

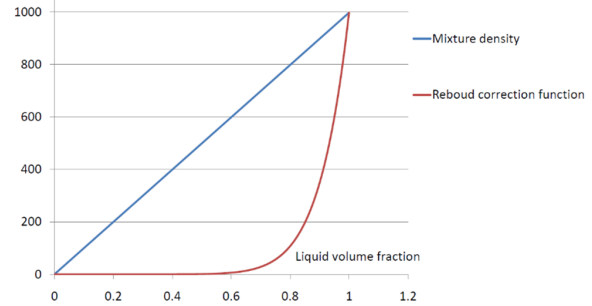


Figure 3 Employed damping function

Wall functions are employed for all stationary patches while the rotating patches are wall resolved. The dimensionless wall normal distance Y^+ to the first cell on the blades is 1.1 on average.

3.3 Cavitation model

The mass transfer term \dot{m} appearing in the source term in the continuity equation and in the transport equation for the liquid volume fraction needs to be modelled by a cavitation model.

The pressure driven model developed by Kunz is used due to prior experience and successful simulations of cavitating propeller flows as shown by Huuva (2008) and Törnros (2013). In this model the vaporization and condensation are treated separately.

$$\dot{m} = \dot{m}^+ + \dot{m}^-$$

The vaporization term \dot{m}^+ is active when the pressure is lower than the vaporization pressure and depends on the liquid volume fraction to avoid negative volume fraction values.

$$\dot{m}^+ = \left(\frac{C_{prod}}{U_{\infty}^2 t_{\infty}} \right) \frac{\rho_v}{\rho_l} \alpha_l \min[0, p - p_v]$$

The condensation term \dot{m}^- on the other hand is always present where there is mixture, independently of the pressure. The condensation term has its maximum where the liquid volume fraction is 2/3.

$$\dot{m}^- = \left(\frac{C_{dest}}{t_{\infty}} \right) \rho_v \alpha_l^2 [1 - \alpha_l]$$

The model constants for the Kunz cavitation model can be seen in Table 4.

Table 4 Kunz cavitation model constants

$\frac{C_{prod}}{U_{\infty}^2 t_{\infty}}$	12500
$\frac{C_{dest}}{t_{\infty}}$	320

The cavitating flow simulation is started by employing a linear increase of the cavitation constants from zero to their maximum values over the simulated time corresponding to 18° rotation.

3.4 Rotor modelling

The mesh is a composition of two meshes, one stator and one rotor. The rotor contains all rotating geometries. The rotation of the rotor is achieved using moving mesh with sliding interfaces. The interfaces between the rotor and the stator mesh volumes uses Arbitrary Mesh Interface (AMI) which allows simulation across unmatched and unconnected patches.

3.5 Discretization

The domain is discretized into 9.6 million polyhedrals using ANSA by BETA CAE. Polyhedrals are used due to the many faces which are beneficial for rotating flows as it is difficult to align the mesh with the flow. The mesh is visualized by a Y-normal plane through the center of the domain in Figure 4. Note that the contour of the AMI boundaries are shown in red and rotating geometries in green.

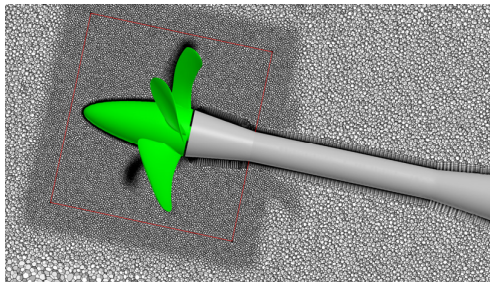


Figure 4 Cut through the domain visualizing the mesh

Second order schemes are used for the convection terms, except for the turbulent quantities which together with the time discretization utilizes first order schemes.

4 RESULTS AND DISCUSSION

The transient wetted flow simulations are initialized from steady state simulations using the frozen rotor technique. A very short time step of 0.1° in wetted condition and 0.025° in cavitating condition was used due to numerical instability of unknown origin.

4.1 Wetted flow

The history of thrust and torque coefficient is shown in Figure 5. The propeller performance is converged after about 2 revolutions and onwards.

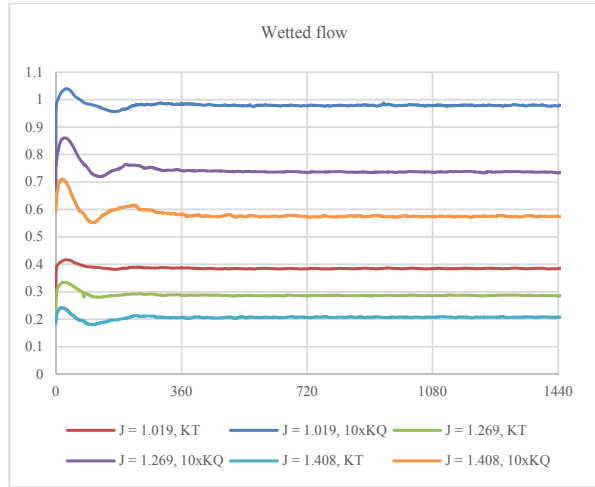


Figure 5 Wetted flow performance history

The average performance during one revolution, 1080° to 1440°, is shown in Table 5.

Table 5 Wetted flow average performance

J [-]	Average K_T [-]	Average $10xK_Q$ [-]
1.019	0.385	0.979
1.269	0.287	0.737
1.408	0.208	0.575

4.2 Cavitating flow

The cavitating flow performance history can be seen in Figure 6. Case 2-1 is not fully converged due to time constraints.

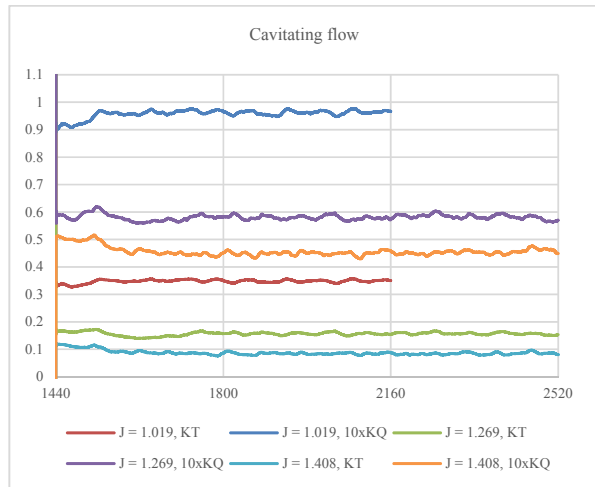


Figure 6 Cavitating flow performance history

The average performance of the last 360° can be seen in Table 6. The load on the propeller is decreased in cavitating condition for all three cases.

Table 6 Cavitating flow average performance

J [-]	Average K_T [-]	Average $10 \times K_Q$ [-]
1.019	0.349	0.962
1.269	0.157	0.583
1.408	0.084	0.454

Previous experience has shown best correspondence to experimental observation when visualizing sheet cavitation using a low isosurface value for the liquid volume fraction. A higher isovalue should be used for the often underpredicted tip vortex cavitation. The RANS turbulence model assumes turbulent flow, while the experiment may suffer from laminar flow especially on lower radii. This is expected to overestimate the cavitation at lower radii. Isosurfaces are shown for 10, 40, 60 and 90 % liquid volume fraction.

Case 2-1 is visualized in Figure 7. All isosurfaces shows leading edge cavitation on blades at 0°, 72° and 144°. Tip vortex cavitation is always present at 72° and 144°. For higher liquid volume fractions tip vortex cavitation is present on all blades. Root cavitation is present for all volume fractions on the three blades at 0°, 72° and 144°. For higher volume fractions the root cavitation is also present on the blade at 216°.

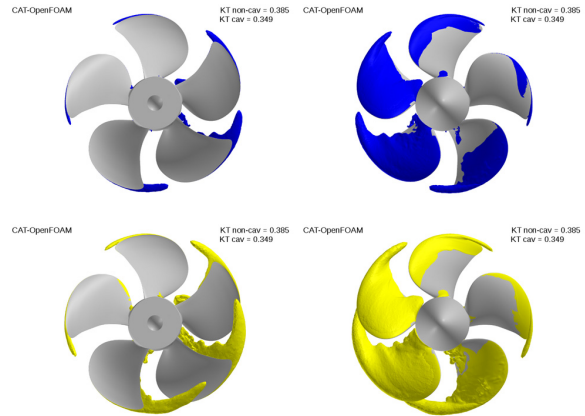
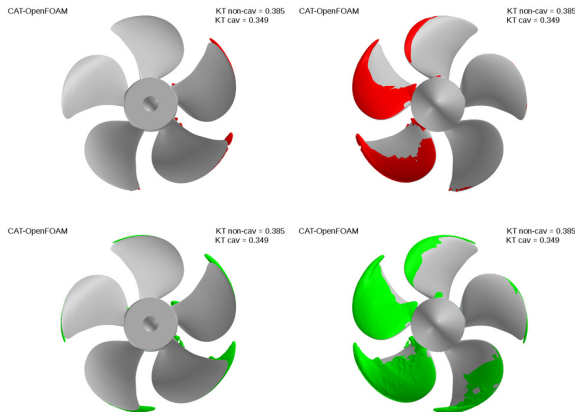
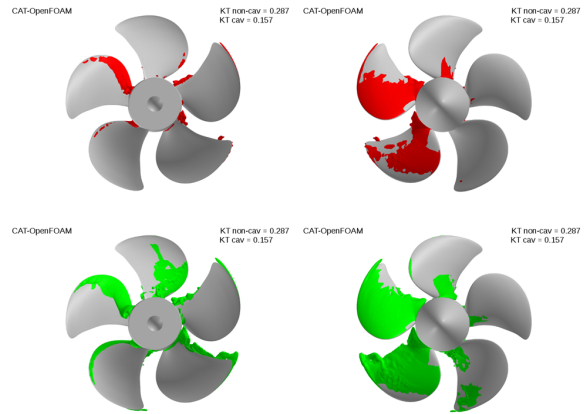


Figure 7 Case 2.1: Pressure side (left), suction side (right). Liquid volume fraction of 10% (red), 40% (green), 60% (blue) and 90% (yellow)

Case 2-2, Figure 8, shows sheet cavitation and tip vortex cavitation on the suction side of the 72° blade for all isovalues. Root cavitation is present for all isovalues on blades at 0°, 72° and 144°. For higher isovalues the root cavitation is present on all blades. Pressure side cavitation is present near the leading edge on the 288° blade for all isovalues. For higher isovalues pressure side cavitation is present on all blades.



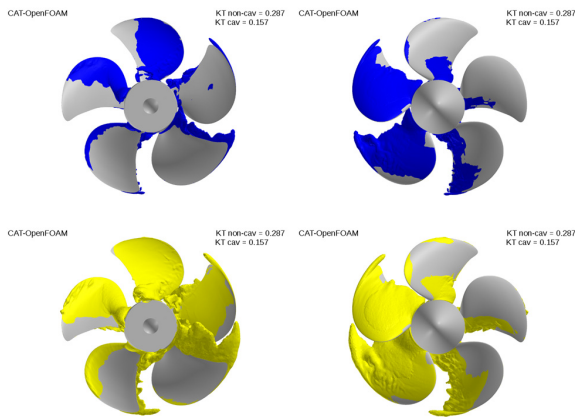


Figure 8 Case 2.2: Pressure side (left), suction side (right). Liquid volume fraction of 10% (red), 40% (green), 60% (blue) and 90% (yellow)

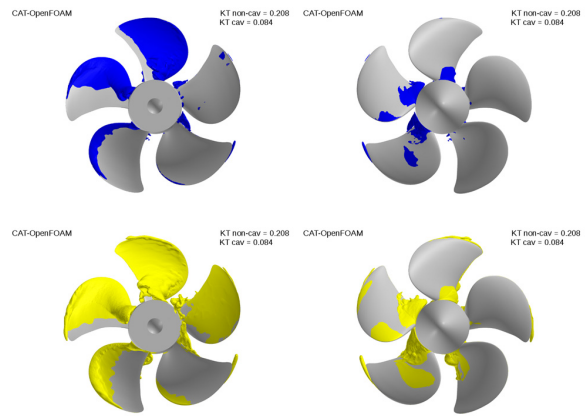
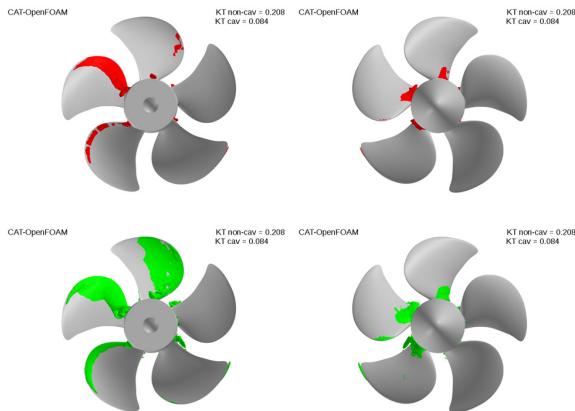


Figure 9 Case 2.3: Pressure side (left), suction side (right). Liquid volume fraction of 10% (red), 40% (green), 60% (blue) and 90% (yellow)

Case 2-3, Figure 9, shows root cavitation on blades at 0° , 72° and 144° . For higher isovalues a tendency to sheet cavitation can be seen on the blade at 72° . Small amount of tip vortex cavitation is present on all blades except 216° for the highest isovalue. On the pressure side a significant amount on cavitation is present. Sheet cavitation and root cavitation is largest at the blade at 288° . Cavitation is present on the pressure side near the leading edge for all blades for the highest isosurface of 90%.



REFERENCES

- Huuva, T. (2008), "Large eddy simulation of cavitating and non-cavitating flows", PhD thesis, Chalmers University of Technology, Gothenburg, Sweden.
- Kunz, R. F., Boger, D. A., Chyczewski, T. S., Stinebring, D. R., Gibeling, H.J., Venkateswaran, S., and Govindan, T. R. (1999), "A Preconditioned Navier Stokes Method for Two-Phase Flows with Application to Cavitation Problems". Proceedings of 14th AIAA CFD Conference, 849-875). Norfolk
- Törnros, S. (2013), "Propeller Cavitation Simulation using RANS and OpenFOAM", MSc thesis. Chalmers University of Technology, Gothenburg

Computational Analysis of Cavitating Marine Propeller Performance using OpenFOAM

Abolfazl Asnaghi, Andreas Feymark, Rickard E. Bensow

Department of Shipping and Marine Technology,
Chalmers University of Technology, Gothenburg, Sweden

ABSTRACT

In this paper, numerical results, based on implicit LES and transport equation mass transfer modelling approach, submitted to the Second International Workshop on Cavitating Propeller Performance at the Fourth International Symposium on Marine Propulsors (SMP'15) are presented. The numerical simulations are performed using OpenFOAM. The present work is focused on the second task of the workshop, *Propeller in oblique flow inside tunnel in wetted and cavitating conditions*. We summarise results from the three different operating conditions given in the task, where the experimental data of one condition is revealed, and the two other conditions are put forward as blind tests to workshop participants. For the condition where experimental data is known, we see good agreement for the forces in wetted conditions that slightly deteriorate in cavitating conditions. Cavitation extent is over predicted, where mid-span bubbly cavitation in the experiments is predicted as a sheet cavity; cavitation in the tip region does however seem reasonable. This is also likely the reason for the larger error in force prediction. A limited mesh resolution study has been performed.

Keywords

Cavitation, Numerical Simulation, OpenFOAM.

1 INTRODUCTION

A controllable pitch propeller with extensive experimental data is provided by SVA Potsdam to be considered for SMP'15 Workshop on Cavitation and Propeller Performance. The current work covers the performance prediction of the propeller in the cavitating conditions (Case 2) in three different operating conditions. The workshop is organized in a 'blind test' format where none of the participants knows the experiment results prior to the workshop.

The current numerical simulations have been conducted using a modified interPhaseChangeDyMFOam solver of OpenFOAM (OpenFOAM foundation). Implicit LES

approach is adopted to account for turbulence (Bensow and Bark, 2010). The Schnerr-Sauer mass transfer model is employed to mimic the phase change between vapour and liquid (Schnerr and Sauer, 2001).

The presented results consist of simulations of three different operating conditions for wetted and cavitating flows, denoted as Case2.1, 2.2, and 2.3, see Table 1. For each of the operating conditions, the thrust and torque coefficients are presented. The effects of the mesh resolution, the inlet location and also the time discretization scheme on the numerical simulation are also investigated in this work and reported for Case2.1. The cavitation pattern at different blade positions for suction side and pressure side are presented. For Case2.1 that the experimental data are available the numerical results are analysed and compared with experiment.

2 Governing Equations

In the current study, the effective flow and each phase have been considered incompressible and isothermal which is a common engineering approach for cavitating flows. A mixture assumption is adopted using Transport Equation Modelling of volume fraction (TEM) for the phase distribution.

2.1 Mass and momentum equations

The conservation equations of mass and momentum for the effective fluid can be written as follow,

$$\frac{\partial \rho_m}{\partial t} + \frac{\partial (\rho_m u_i)}{\partial x_i} = 0 \quad (1)$$

$$\frac{\partial (\rho_m u_i)}{\partial t} + \frac{\partial (\rho_m u_i u_j)}{\partial x_j} = \tau_{ij} + \rho_m g_i \quad (2)$$

The stress tensor in Newtonian fluids is conventionally written in the form of summation of pressure stress and shear stresses as follow.

$$\tau_{ij} = -p \delta_{ij} + S_{ij} - \frac{2}{3} \mu \frac{\partial u_m}{\partial x_m} \delta_{ij} \quad (3)$$

$$S_{ij} = 2\mu D_{ij} \quad (4)$$

In these equations, p is the static pressure, μ is the effective viscosity and S is the viscous stress tensor and D is the deformation rate tensor (symmetric part of the velocity strain), defined as $D_{ij} = (\partial u_i / \partial x_j + \partial u_j / \partial x_i) / 2$.

2.2 Turbulence modelling

For turbulence modelling, implicit Large Eddy Simulation approach, ILES, is used. This turbulence model has been used and proved effective previously by the authors for simulation of the cavitating flows (Bensow and Bark, 2010), as well as for wetted flows.

Using the low pass filtering approach, the momentum equation in LES model can be written as Eq. (5).

$$\frac{\partial(\rho_m \bar{u}_i)}{\partial t} + \frac{\partial(\rho_m \bar{u}_i \bar{u}_j)}{\partial x_j} = -\frac{\bar{p}}{\partial x_i} + \frac{\partial}{\partial x_j} (\bar{S}_{ij} - B_{ij}) + \rho_m g_i \quad (5)$$

The over bar denotes the low pass filtering quantities. In this equation, the subgrid stress tensor is $B_{ij} = \rho(u_i u_j - \bar{u}_i \bar{u}_j)$.

In ILES approach no explicit model is applied for B , instead the numerical dissipation is considered enough to mimic the action of B (Bensow and Bark, 2010). Therefore, for momentum convection term, a relatively dissipative scheme should be used to provide appropriate numerical diffusion in the solution procedure.

2.3 Multiphase modelling

TEM, Transport Equation Model, is used in this study to model the transport of phases. In the TEM approach the spatial distribution of each phase is specified using a volume fraction function. Using the volume fraction, it is possible to calculate the mixture density and mixture viscosity based on the homogenous flow assumption.

$$\rho_m = \alpha_l \rho_l + (1 - \alpha_l) \rho_v, \quad \mu_m = \alpha_l \mu_l + (1 - \alpha_l) \mu_v \quad (6)$$

$$\frac{\partial \alpha_l}{\partial t} + \frac{\partial(\alpha_l u_i)}{\partial x_i} = \dot{m} \quad (7)$$

In Eq. (7), which represents the transport equation of liquid volume fraction, the source term is the rate of phase change between vapour and liquid phases.

Based on the fluid properties and also the local flow properties, different models have been proposed to predict the cavitation phase change rate, \dot{m} in the Eq. (7). In the current study, the mass transfer model proposed by Schnerr and Sauer is employed, Eq. (8), where average nucleus per liquid volume is considered constant and in this study equal to $n_0 = 10^8$, and the initial nuclei radius is $d_{Nuc} = 10^{-4}$ m.

$$\dot{m} = \text{sign}(P_{sat} - P) \frac{n_0}{1 + n_0 \frac{4}{3} \pi R^3} 4\pi R^2 \sqrt{\frac{2|P_{sat} - P|}{3\rho_l}} \quad (8)$$

Using the saturation pressure as the pressure threshold for phase change in the cavitating flows is based upon the liquid rupturing at the static or quasi-static conditions. In these conditions, the static pressure in the major part of the liquid is much larger than the viscous shear stresses. Although this estimation, using the saturation pressure as the pressure threshold, has been used widely in numerical simulation of cavitation, it does not take into account the effects of the shear stresses in the liquid rupturing and initiating phase change. In order to consider the viscous stresses, the eigenvalue of the stress tensor should be considered as the criteria on whether the fluid withstands rupturing or phase change. Here the modification proposed in Asnaghi et al. (2014) has been employed.

$$P_{threshold} = \mu \dot{\gamma} + P_{saturation} \quad (9)$$

$$\dot{\gamma} = \sqrt{2D_{ij}D_{ij}} \quad (10)$$

The added term is important if either shear strain rate or effective viscosity is large enough, and comparable with the static pressure value. For the flow around the foils, this is the case near the leading edge or during the collapse when the velocity variation is very high, and for the flow around the propellers this is the case both at the tip and leading edge regions.

2.4 Non-dimensional parameters

The definition of advance coefficient (J), cavitation number (σ_n), thrust coefficient (K_T) and torque coefficient (K_Q) are as follow,

$$J = V_A / (n \cdot D_p) \quad (11)$$

$$\sigma_n = (p - p_{sat}) / (0.5 \cdot \rho \cdot n^2 \cdot D_p^2) \quad (12)$$

$$K_{Tx} = T_x / (\rho \cdot n^2 \cdot D_p^4) \quad (13)$$

$$K_Q = Q / (\rho \cdot n^2 \cdot D_p^5) \quad (14)$$

where in these equations, V_A is the advance velocity (i.e. in this case the inlet velocity), n is the rotational speed of the propeller, p is the tunnel outlet pressure, T is the propeller thrust, and Q is the propeller torque.

3 Solution Procedure and Discretization

In order to solve the governing equations, OpenFOAM-2.3.x which is an open source CFD software package developed by OpenCFD Ltd at ESI Group and distributed by the OpenFOAM Foundation is used. In this software, the spatial discretization is performed using a cell centered co-located finite volume (FV) method for unstructured meshes with arbitrary cell-shapes, and a multi-step scheme is used for the time derivatives. The interPhaseChangeDyMFOam solver is employed to simulate the cavitation. The implicit LES model is implemented into the original code and in order to reduce the mesh resolution requirement for LES simulations near the walls, the Spalding wall model is employed to correct the turbulent viscosity at the first cell.

The PIMPLE algorithm is used to solve the coupling between the velocity and pressure. The residual of solving pressure and velocity in each iteration is set equal to $1e-6$ for wetted flow and $1e-12$ for cavitation simulation. A second order implicit time scheme (backward scheme) is used for time discretization. For one condition, the effects of using first order Euler scheme, often suggested sufficient when using small time steps, is also investigated and discussed.

A blending scheme of first order upwind and second order central difference schemes is used for the convective term. The constant of this blending is set equal to 0.2. All of the gradients have been corrected to consider non-orthogonality effects of neighbouring cells. For the volume fraction transport equation, first order upwind scheme is utilized.

In order to handle the rotation of the propeller, the computational domain is decomposed in two regions, the rotating region close to the propeller and the outer region, coupled via the standard sliding mesh implementation in OpenFOAM. The data across the regions are interpolated through the AMI boundaries in OpenFOAM.

4 Test Conditions

The propeller geometry and three different operating conditions are provided by SMP'15 workshop organisers. The propeller is a model scale, five bladed propeller with a diameter equal to 250 mm, Fig. 1.

The cavitation tests were conducted in the cavitation tunnel K 15 A of the SVA Potsdam. During testing the propeller was positioned according to the Fig. 2 with a 12° inclination of the propeller towards the inflow direction. In Table 1, the operating conditions are briefly presented.

Table 1: Operating conditions

Case	J	σ_n	V_{inlet} (m/s)	n (rev/sec)
2.1	1.019	2.024	5.095	20
2.2	1.269	1.424	6.345	20
2.3	1.408	2.0	7.04	20

5 RESULTS AND DISCUSSION

The numerical results consist of propeller performance (i.e. thrust and torque coefficients) predictions in the wetted and cavitating flows for three different operating conditions, described in Table 1. For the cavitating flows, the cavitation pattern at different blade positions are also plotted and investigated. The angular positions of the blades are described according to the right-handed rotation of the propeller with zero degree being equivalent to the 12 o'clock position.

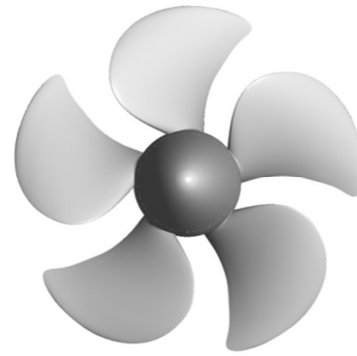


Figure 1: Propeller geometry

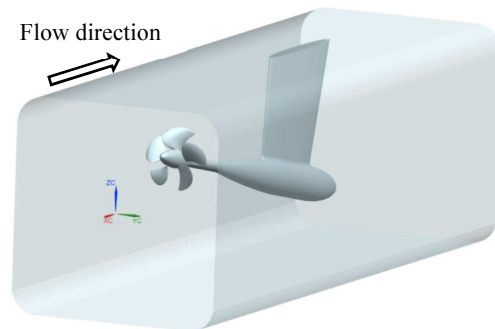


Figure 2: Test section

Since the experimental data are provided just for Case2.1, the numerical results are compared with the experimental data just for this case.

In order to elaborate the study, for the operating condition Case2.1, effects of using first order Euler time scheme, distance of the inlet boundary location relative to the propeller, and also mesh resolution are investigated and results are presented and compared with experimental data.

5.1 Boundary conditions

A summary of the numerical boundary setup is presented in Table 2. In order to reduce the requirement of mesh resolution near the tunnel wall, slip boundary condition is applied for the tunnel wall. The uniform inlet velocity and uniform outlet pressure are adopted to adjust the flow advance ratio and cavitation number.

5.2 Mesh specifications

The blades surface mesh consists of quad surfaces, which then have been extruded in the wall normal direction ($y^+=10$) to create prism cells (hexahedrals) in order to better capture the boundary layer over the blades. The rest of the domain is filled with unstructured tetrahedral cells. Since the flow has higher gradients near the leading and trailing edges and also near the tip region of the blades, the mesh has finer resolution at these areas. In order to limit the mesh size in a reasonable range, the mesh gets coarser by increasing distance from the blades.

Table 2: Numerical boundary setup

Boundary	Velocity	Pressure	ν_{sgs}	Vapour (α)
Inlet	Fixed	Zero gradient	Zero gradient	Fixed
Outlet	Zero gradient	Fixed	Zero gradient	Zero gradient
Propeller surfaces	No-slip	Zero gradient	Wall model	Zero gradient
Tunnel wall	Slip	Zero gradient	Zero gradient	Zero gradient

In order to handle the rotation of the propeller, the computational domain is decomposed in two regions, the rotating region close to the propeller, and the stationary region where the total size of the mesh is around 4.7 M cells, called MeshI in this paper. For this mesh, the domain size has been kept the same as the geometry provided by the workshop committee.

In the provided geometry of the tunnel, the inlet is located almost in 2D upstream of the propeller. Since the inlet is relatively close to the propeller, it is possible that using uniform inflow as inlet velocity boundary condition affects the flow around the propeller (e.g. pressure distribution and cavitation pattern). Therefore, another mesh is also created where the inlet is moved 4D further upstream, MeshII in Fig. 3.

In order to investigate the effects of the mesh resolution on the results, MeshIII is created from MeshII where the prism cells around one blade are refined using refineMesh command in OpenFOAM. This command splits a hex cell into 2 cells in each direction. Therefore, the final cells are 8 times smaller than the original one. The final total cell size for this mesh is around 8.5 M cells. The blades surface mesh is presented in Fig. 4.

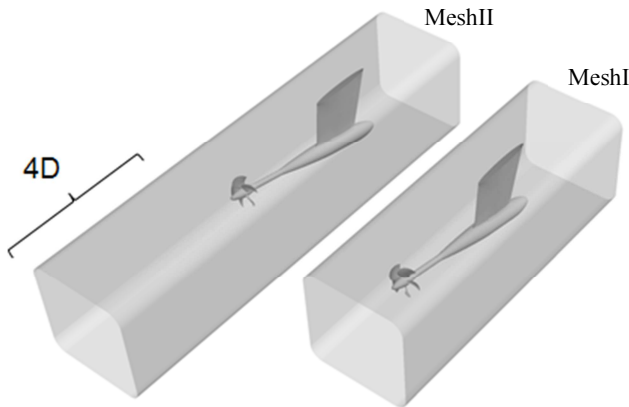


Figure 3: The inlet locations for MeshI and MeshII

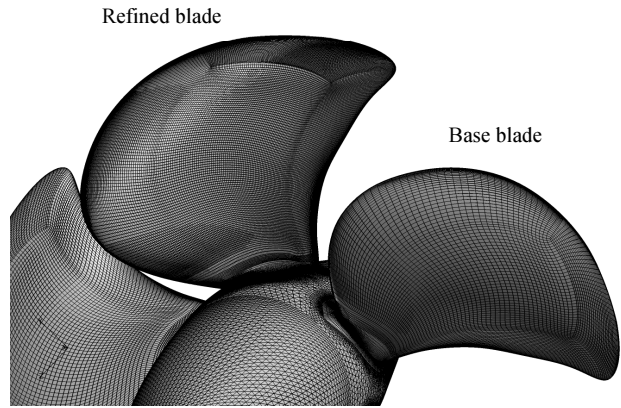


Figure 4: The blade surface mesh for MeshIII

5.3 Wetted flow results

In Table 3, the thrust and torque coefficients for the three different operating conditions are presented. Comparison between the experimental data and numerical results for Case2.1 shows that the obtained results have a good agreement with the experiment.

Table 3: Thrust and torque coefficients for wetted flow simulations

Operating conditions	Mesh	Time scheme	Method	K_{Tx}	$10K_Q$
Case2.1	-----		Exp	0.397	1.02
	MeshI	backward	ILES	0.405	1.01
	MeshI	Euler	ILES	0.408	1.01
	MeshII	backward	ILES	0.404	1.00
	MeshIII	backward	ILES	0.406	1.01
Case2.2	MeshI	backward	ILES	0.262	0.72
Case2.3	MeshI	backward	ILES	0.181	0.55

5.4 Cavitating flow results

In Table 4, the thrust and torque coefficients for the three different operating conditions of cavitating flow are presented. For Case2.1, where the experimental data are available, comparison between numerical results and experimental data reveals that the comparison error is around 8% for K_Q and 4% for K_{Tx} prediction using backward scheme. However, the results related to Euler scheme show a severe over prediction of K_Q by 35%.

5.4.1 Case2.1

In Fig. 5, cavitation pattern for two iso-surfaces of alpha (40% and 60%) are presented for suction and pressure sides of the propeller. These results are related to the MeshI with backward time scheme. Note that we do not see any pressure side cavitation, but the image only reveals the extended sheet of the suction side.

Table 4: Thrust and torque coefficients for cavitating flow simulations

Operating conditions	Mesh	Time scheme	Method	K_{Tx}	$10K_Q$
Case2.1			Exp	0.36	0.94
	MeshI	backward	ILES	0.373	1.07
	MeshI	Euler	ILES	0.351	1.34
	MeshII	backward	ILES	0.374	1.05
	MeshIII	backward	ILES	0.375	1.04
Case2.2	MeshI	backward	ILES	0.196	0.73
Case2.3	MeshI	backward	ILES	0.157	0.53

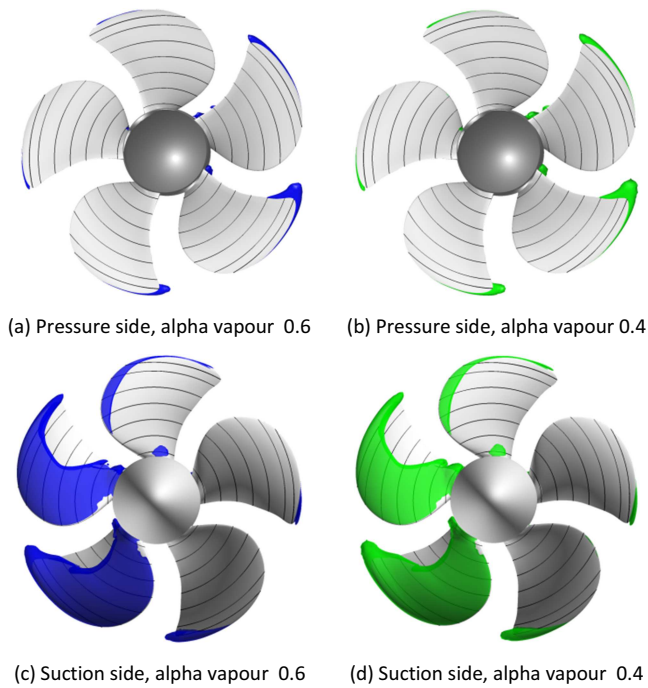


Figure 5: Case2.1, view along x-axis

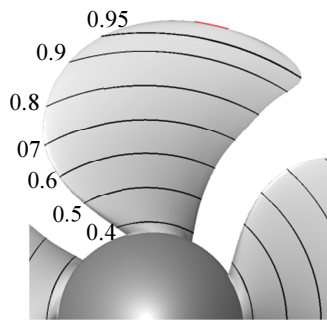


Figure 6: Description of radius ratio over the blade surface, view along x-axis

The lines on the surface of the blade represent the radius ratio, r/R , where R is the propeller radius and r is the distance from the centre of the propeller in the cylindrical coordinate system aligned with the propeller shaft, Fig. 6.

In Fig.7, the cavitation prediction for different settings and mesh resolutions are presented for Case2.1 where the vapour iso-surface is 60%.

For MeshIII, the picture is modified in a way that each blade position is replaced with the corresponding results of the blade having the refined mesh. Therefore, the picture somehow represents the results for an imaginary fully refined propeller.

Comparison between results of Fig. 7-c and Fig. 7-d will reveal the effects of mesh resolution on the cavitation prediction. From the results it can be deduced that the finer mesh is more capable of capturing and preserving the vortex rolled up into the blade tip region; note that the only the region around the blade is refined and not when the vortex has left the blade. From blade positions zero degree, it can be seen that finer mesh resolution was able to preserve the tip vortex cavitation longer, till the end of blade tip while in the coarser mesh cavitation is ended before reaching the blade tip. From the blade position 72 degree, it can be seen that in the finer mesh the vortex is rolled up earlier into blade tip region, and also from the blade position 216 degree, it can be seen that the preserved cavity is bigger than in the coarser mesh. These three main effects are highlighted by yellow ovals in the figures. We remark that the mesh refinement does not affect the over predicted mid radii sheet.

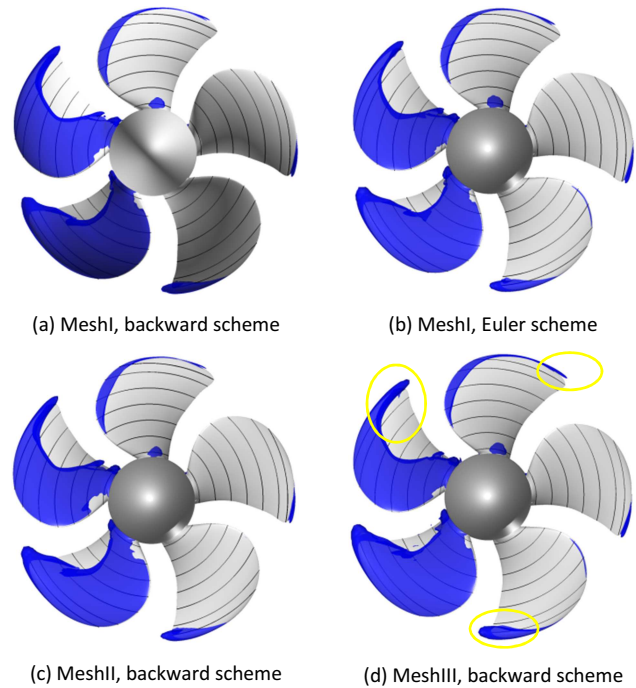


Figure 7: Case2.1, view along x-axis, Suction side, vapour iso-surface 0.6

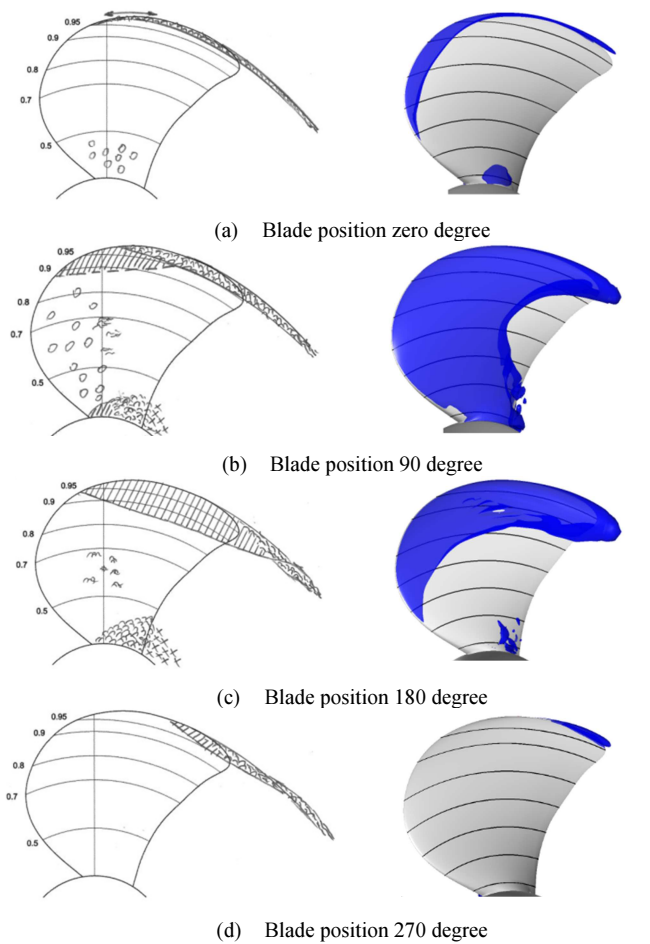


Figure 8: Comparison between numerical results and experimental sketches for cavitation in Case2.1, view along x-axis, suction side, numerical results: MeshIII, vapour iso-surface: 0.6

In Figs. 8 and 9, the cavitation predictions are compared with the experimental sketches for Case2.1 for the suction side and pressure side at different blade positions. As it is shown in Fig. 8, the general trend of the cavitation has been predicted reasonably well. The main difference between numerical results and the experimental data is related to the region with the bubbly cavitation pattern. In Fig.8-a, the bubbly root cavitation is predicted as sheet cavity, and in Fig.8-b the bubbly cavitation near the leading edge is predicted with the sheet leading edge cavitation. This sheet cavity then is attached to the near tip sheet cavity (radius 0.9) and covers almost all of the suction side of the blade. The type of bubble cavitation in the experiments indicates a blade pressure close to, or even below, vapour pressure. The modelling used here can not accommodate the growth of individual nuclei to this type of bubble cavitation, instead leading to this formation of a sheet over the leading half of the blade. The pressure side of the blade experiences root cavitation at blade positions of zero and 270 degrees during the experiment. The numerical simulation under predicts root cavitation at zero degree position, and 270 degree blade position.

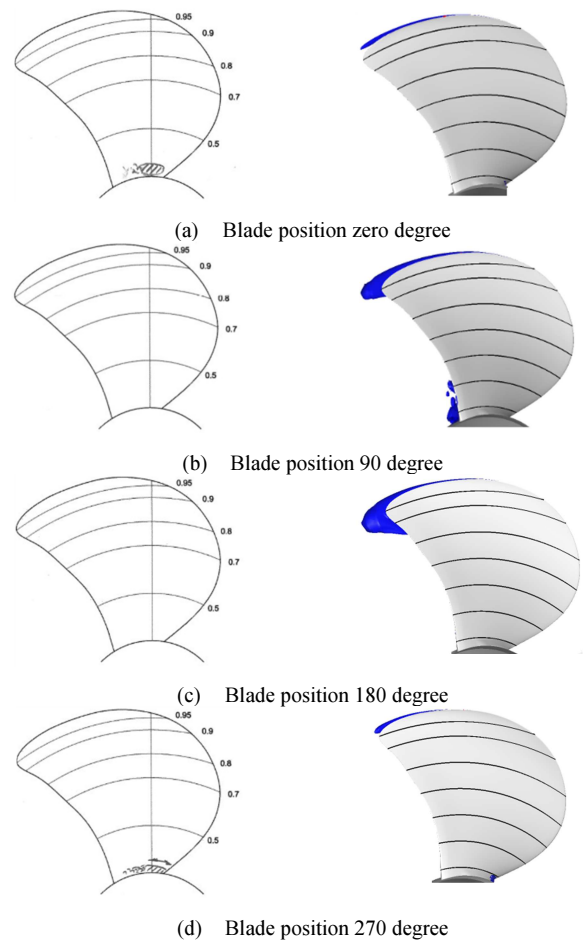


Figure 9: Comparison between numerical results and experimental sketches for cavitation in Case2.1, view along x-axis, pressure side, numerical results: MeshIII, Vapour Iso-surface: 0.6

In Fig. 10, the pressure coefficient of the wetted flow and also the vapour iso-surface 60% are presented for Case2.1. The pressure coefficient values, Fig. 10-a, are adjusted to show the values below $C_p = -2$, which represent regions with pressure lower than the saturation pressure.

As it is discussed before, the main discrepancy between numerical prediction of cavitation extent and the experimental observations is related to the prediction of leading edge sheet cavitation, e.g. at the blade positions 72 and 144 degrees in Fig. 10.

In the leading edge regions where the numerical prediction show pressure lower than the saturation pressure, the computational model will start to produce vapour. In the experiments, the formation of a sheet cavity depends as well on the nuclei content and nuclei residence time in the low pressure region. This is a modelling discrepancy between the numerical and experimental procedures.

Bubble cavitation is observed in the experiment to incept from the leading edge at these positions which suggests a blade pressure close to, or possibly even below, vapour pressure while the numerically predicted pressure at the leading edge is far lower than the saturation pressure in a considerable region. Without further experimental data,

clarifying the actual blade pressure, it's difficult to assess whether the difference in prediction is related to an error in the flow modelling, or if there are, e.g., geometrical differences between the tested and modelled propeller causing this deviation. However, it is also known that a laminar boundary layer can suppress the cavitation inception even though pressure is far below the saturation pressure.

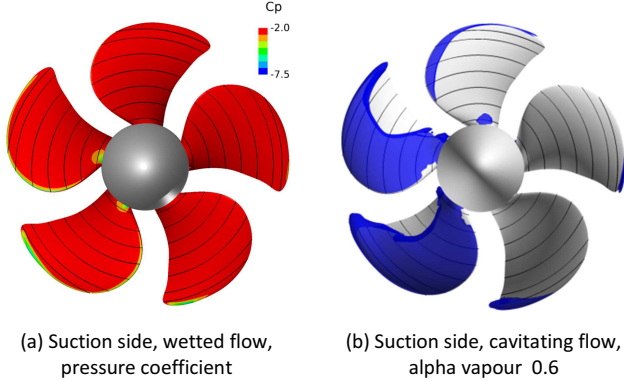


Figure 10: Case2.1, MeshI, backward scheme, view along x-axis

5.4.2 Case2.2

Cavitation prediction of Case2.2, presented in Fig. 11, shows cavitation appearances in both pressure side and suction side of the blade. It should be noted that the mesh is constructed in a way that has finer resolution in the suction side of the blades. As a result the cavitation is less resolved on the leading edge of the pressure side comparing to the suction side. The most pronounced feature is the leading edge cavitation which seems to start from the mid-chord of the blade on the suction side and then cavity extends till the trailing edge.

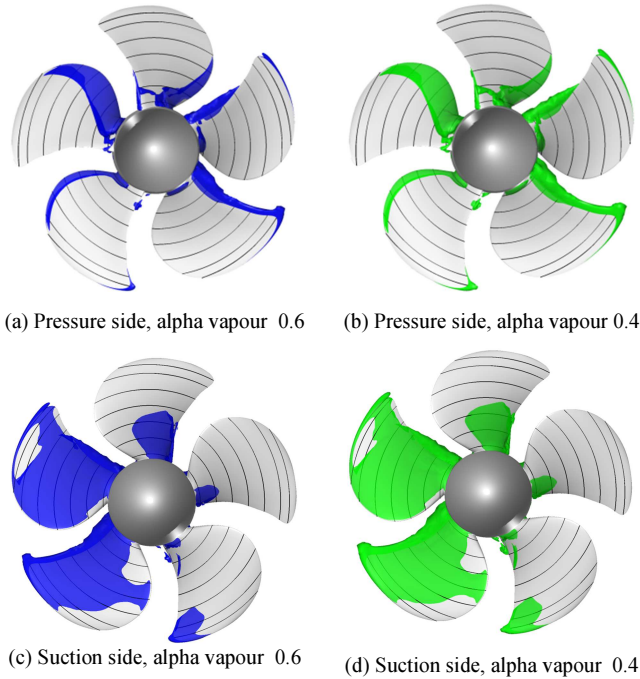


Figure 11: Case2.2, view along x-axis

5.4.3 Case2.3

In Fig. 12, cavitation prediction of Case2.3 is presented. The root cavitation is predicted for both suction and pressure sides of the blade at different positions. The leading edge cavitation is predicted for just the pressure side of the blade. At position 135 degree, tip cavitation is predicted for both sides of the blade.

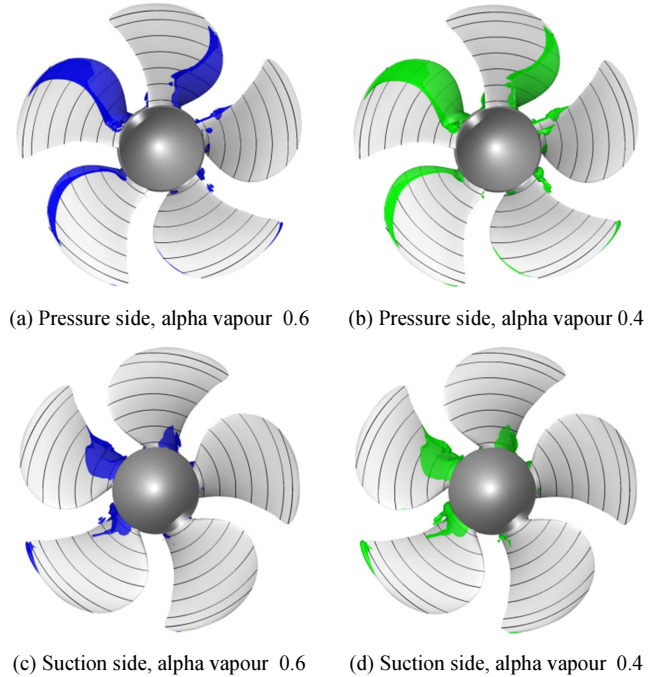


Figure 12: Case2.3, view along x-axis

6 CONCLUSION

Numerical simulations of cavitation of the Potsdam propeller test case (Case2) at three operating conditions are presented in this paper. For Case2.1 that the experimental data are available, results indicate that the employed numerical tool can predict the thrust and torque coefficients in the wetted and cavitating flows reasonably well. The cavitation simulation shows over prediction of the cavity size especially at the region that the bubbly cavitation is observed during the experiment.

ACKNOWLEDGMENTS

Financial support of this work has been provided by Rolls-Royce Marine through the University Technology Centre in Computational Hydrodynamics hosted at the Department of Shipping and Marine Technology, Chalmers. Computational resources have been provided by Chalmers Centre for Computational Science and Engineering, C3SE.

REFERENCES

- Asnaghi, A., Feymark, A., and Bensow, R.E., (2014), “Shear Stress Effects in Cavitating Flows”, 17th Numerical Towing Tank Symposium, 28-30 Sep., 2014, Marstrand, Sweden
- Bensow, R.E. and Bark, G. (2010). “Implicit LES Predictions of The Cavitating Flow on a Propeller”. J. Fluids Engineering 132.
- Fourth International Symposium on Marine Propulsors & Second International Workshop on Cavitating Propeller Performance, May 31- June 4, 2015, Austin, Texas, USA, <http://www.cae.utexas.edu/smp15/>
- OpenFOAM foundation, <http://www.openfoam.com/>, 28 April 2015
- Propeller workshop smp'15, http://www.sva-potsdam.de/pptc_data_15.html, 28 April 2015
- Schnerr, G. H. and Sauer J., (2001), “Physical and Numerical Modeling of Unsteady Cavitation Dynamics”, In Fourth International Conference on Multiphase Flow, New Orleans, USA

Numerical Simulations of the Cavitating and Non-Cavitating Flow around the Postdam Propeller Test Case

E. Guilmineau, G.B. Deng, A. Leroyer, P. Queutey, M. Visonneau, J. Wackers

LHEEA CNRS UMR 6598, Ecole Centrale de Nantes
BP 92101, 44321 Nantes Cedex, France

ABSTRACT

In this paper, the cavitating performance and open water performance of the SMP'15 propeller are numerically simulated using the flow solver ISIS-CFD. A cavitation model based on a transport equation and the $k-\omega$ SST turbulence model are coupled in the flow solver. The thrust and torque coefficients are presented for the open water case. The pressure distribution on the propeller blades is also presented. For the cavitating case, the cavity surface is presented as well as the thrust and torque coefficients.

Keywords

Propeller, Open water, Cavitation, Numerical simulation, ISIS-CFD, Oblique flow.

1 INTRODUCTION

Numerous studies based on experiments or computations have been carried out to investigate propeller open water characteristics. Most studies only consider the case of a propeller in straight ahead flow. However, under real conditions, a working propeller operates behind a ship usually in a complex wake, so that the propeller shows quite different hydrodynamic performance. Moreover the consequence of the disturbance of the ship is that the angle of attack is different from blade to blade and the loads acting on the blades in axial direction is not symmetric.

Few authors have reported on hydrodynamic characteristics of a marine propeller in oblique flow. El Moctar and Bertram used a Reynolds-averaged Navier-Stokes (RANS) solver to investigate the flow around a four-bladed modern propeller at oblique angles up to 12° . They found that the forces oscillate and the frequency of the oscillations increases with the angle of attack. Krasilnikov et al. (2009) used an unsteady RANS method to investigate the blade forces acting on a podded propeller operating in oblique flow conditions. They found that blades of pulling propeller experience comparable amplitudes and load levels at positive and negative heading angles, being mainly affected by the crossflow. The amplitudes and load levels on the blades of a pushing propeller are different at positive and

negative headings due to the interaction of the propeller with the separated strut wake. Shamsi and Ghassemi (2013) evaluated the performance of a podded propulsor in straight and azimuthing condition by using a RANS approach with Moving Reference Frame. They found that the propeller thrust coefficient and the torque coefficient increase with increasing yaw angles. Their results also indicate that side force coefficients increase with increasing yaw angle and velocity advance ratio. Dubbioso et al. (2013, 2014) analyzed the performance of the CNR-INSEAN E779A propeller model in oblique flow by unsteady RANS and dynamically overlapping grid approach. Their main focus is on hydrodynamic loads that act on a single blade. They also discuss the flow features around the propeller. Unfortunately, due to the lack of experiments in oblique flow conditions, they did not perform a validation of the numerical computations. Yao (2015) investigated the hydrodynamic performance of a 6-bladed propeller in oblique flow. The hydrodynamic forces and moment showed a good agreement with experimental data under no cavitation condition or under weak cavitation condition.

A propeller data in oblique flow was provided by SVA Postdam with well-defined cases and conditions for the SMP'15 Workshop on Cavitating Propeller Performance. The experiments datasets cover the open water characteristics and cavitation tests. The workshop for this propeller is organized in a "blind test" format that none of the participants knows the experiment results prior to the workshop. The numerical simulation will be performed with the ISIS-CFD flow solver and only the propeller in oblique flow in open water case and the cavitation observation in oblique flow will be investigated.

2 NUMERICAL METHOD

The solver ISIS-CFD, available as a part of FINETM/Marine computing suite, is an incompressible unsteady Reynolds-averaged Navier-Stokes method mainly devoted to marine applications. The method features several sophisticated turbulence models: apart from the classical two-equation $k-$

ϵ and $k-\omega$ models, the anisotropic two-equation Explicit Algebraic Reynolds Stress Model (EARSM), as well as Reynolds Stress Transport Model (RSTM), are available, see Deng & Visonneau (1999) and Duvigneau et al. (2003). All models are available with wall-function or low-Reynolds near wall formulation. Hybrid LES (Large Eddy Simulation) turbulence models based on Detached Eddy Simulation (DES) are also implemented and have been validated on automotive flows characterized by large separations, see Guilmineau et al. (2011). Additionally, several cavitation models, such as the Merkle model, Sauer model or Kuntz mode, are available in the solver.

The solver is based on the finite volume method to build the spatial discretization of the transport equations. The unstructured discretization is faced-based. While all unknown variables are cell-centered, the system of equations used in the implicit time stepping procedure are constructed face by face and the contribution of each face is then added to the two cells next to the face. This technique poses no specific requirements on the topology of the cells. Therefore, the grid can be completely unstructured: cells with an arbitrary number of arbitrarily-shaped faces are accepted. Pressure-velocity coupling is enforced through a Rhie & Chow SIMPLE like method: at each time step, the velocity updates come from the momentum equation and the pressure is given by the mass conservation law. In the case of turbulent flows, transport equations for the variables in the turbulence model are added to the discretization.

Free-surface flow is simulated with multi-phase flow approach: the water surface is captured with a conservation equation for the volume fraction of water, discretized with a specific compressive scheme, see Queutey & Visonneau (2007). The technique included for the 6 degrees of freedom simulation is combined with analytical weighted analogy grid deformation to adapt the fluid mesh to the moving ship, see Leroyer & Visonneau (2005). To enable relative motions of appendages, propellers or bodies without having recourse to overlapping grids, a sliding grid approach has been implemented. Propellers can be modeled by actuator disc theory, by coupling with boundary element codes (RANS-BEM coupling), see Deng et al. (2013) or with direct discretization through e.g. the rotating frame method or sliding interface approaches.

Finally, an automatic grid refinement procedure has been developed which is controlled by various flow related criteria, see Wackers et al. (2014). Parallelization is based on domain decomposition. The grid is divided into different partitions, which contain the cells. The interface faces on the boundaries between the partitions are shared between the partitions: information on these faces is exchanged with MPI (Message Passing Interface) protocol. The method works with the sliding grid approach and the different sub-domains can be distributed arbitrarily over the processors

without loss of generality. Moreover, the automatic grid refinement procedure is fully parallelized with a dynamic load balancing working transparently with or without sliding grids.

3 COMPUTATIONAL CONDITIONS

3.1 Geometry model and test cases

In this paper, the model case is a five bladed Postdam Propeller Test Case (PPTC). It is a controllable pitch propeller with diameter $D = 0.250$ m, hub ratio of 0.3 and, pitch-to-diameter ratio of 1.635 at 0.7 radial section, skewed angle of 19.12° . The propeller is operating in a pull configuration with the hub cap pointing upstream. The propeller axis is inclined by 12° . Table 1 gives the case of open water simulation and Table 2 the case of cavitation simulation. n is the number of revolution per second, $J = U_\infty / (nD)$ is the advance coefficient obtained by changing the inflow velocity U_∞ , and σ_n the cavitation number, with respect to n . For case 1, J varies between 0.6 and 1.4. The Reynolds number, Re is based on the radius of the propeller ($L_{ref} = D/2 = 0.125$ m) and the velocity of the tips of the blades ($U_{ref} = \pi nD$). For the case 1, the Reynolds number is $Re = 1.39 \cdot 10^6$ while, for the case 2, $Re = 2.05 \cdot 10^6$.

Table 1: Case 1 - Conditions for the open water simulation.

Water density	ρ [kg/m ³]	998.62
Kinematic viscosity of water	ν [m ² /s]	1.057E-06
Number of revolution	n [1/s]	15

Table 2: Case 2 - Conditions for the cavitation simulation.

Case	2.1	2.2	2.3
Advance coefficient J	1.019	1.269	1.408
Cavitation number σ_n	2.024	1.424	2.000
Number of revolution n [1/s]	20	20	20
Water density ρ [kg/m ³]	997.78	997.80	997.41
Kinematic viscosity of water ν [m ² /s]	9.567E-07	9.591E-07	9.229E-07

3.1 Computational meshes and conditions

For both cases, the computational mesh is created with HEXPRESSTM, an automatic unstructured mesh generator. This software generates meshes containing only hexahedrons.

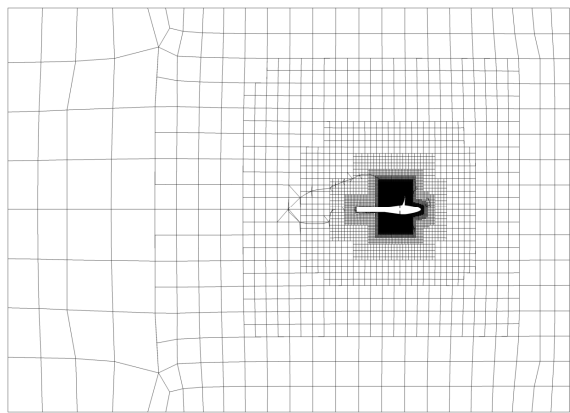
For the case 1, the computational domain consists of a cylinder domain whose the diameter is 10 times the propeller diameter, and the length is 17.04 times the propeller diameter. It starts 5.04D before the propeller plane and it extends until 12D after the propeller plane. At the inlet boundary and at the external boundary, the velocity components of the given inflow speeds calculated by the advance coefficient are imposed taking into account the incidence (12°) of the propeller. At the outlet boundary, the pressure is imposed. On the blades and the hub of the

propeller, no-slip conditions are imposed while for the shaft, a wall-function is used. On the blades and on the hub, the average y^+ value is below 0.6 and on the shaft, the average y^+ value is below 28.

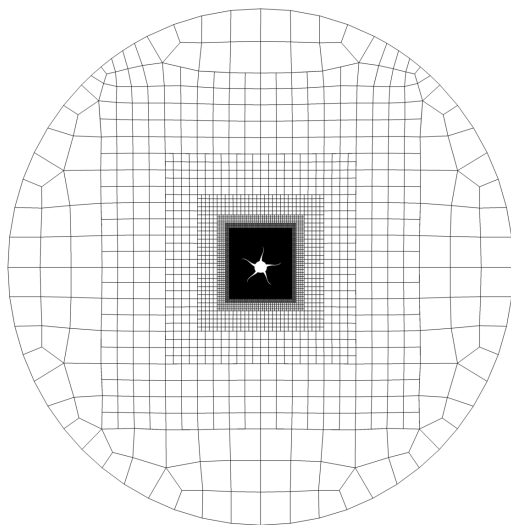
In order to establish a grid-independent solution for the case 1, computations have been performed for three meshes with approximately $11.9 \cdot 10^6$ cells, $30.0 \cdot 10^6$ cells, and $51.1 \cdot 10^6$ cells. The characteristics of these meshes are detailed in Table 3. Figure 1 shows the medium mesh and the size of the computational domain while Figure 2 presents grid details in the plane $Y = 0$, see Figure 2(a), and the propeller plane, see Figure 2(b). Around the propeller, a refinement box with cells of 1.5 mm size is adding.

Table 3: Case 1 - Characteristics of the three meshes.

	Coarse	Medium	Fine
Nb of cells	11,921,137	29,970,465	51,140,754
Nb of nodes	12,848,819	31,482,232	53,343,827
Nb of faces on the propeller	442,244	749,105	1,120,046
Nb of faces on one blade	77,796	131,369	195,932

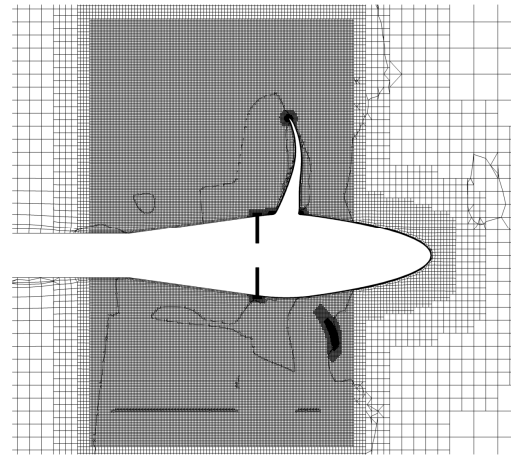


(a) Mesh in the plane $Y = 0$

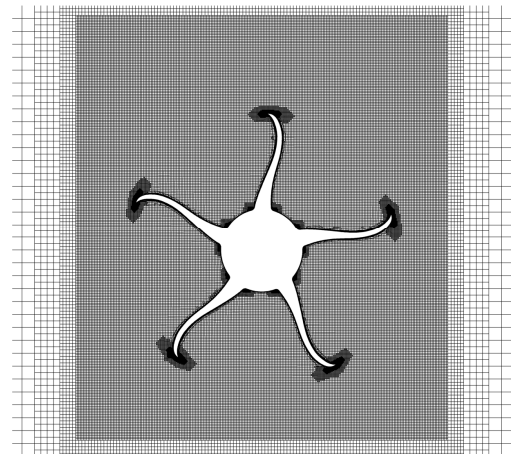


(b) Mesh in the lane $X = 0$

Figure 1: Case 1 - View of the mesh and the computational domain.



(a) Mesh in the plane $Y = 0$



(b) Mesh in the plane $X = 0$

Figure 2: Case 1 - Details of the mesh.

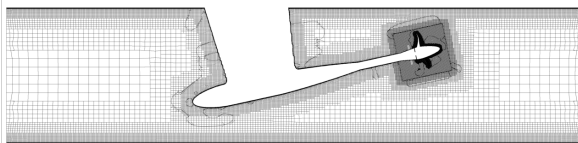
For the case 2, the cavitation tunnel and the mounting bracket of propeller are taken into account. In this case, the propeller is in incidence contrary to the previous case. The inlet of the cavitation tunnel is located at $4.15D$ of the propeller plane while the outlet is located at $10.6D$ of the

propeller plane. The cross-section of the cavitation tunnel is $0.850 \times 0.850 \text{ m}^2$. At the inlet boundary, the velocity components of the given inflow speeds are calculated by the advance coefficient. At the outlet boundary, the pressure is imposed. On the blades and on the hub of the propeller, a no-slip condition is imposed while for the shaft and the cavitation tunnel, a wall-function is used. Two sub-domains are used: the first one attached to the cavitation tunnel including the mounted bracket of the propeller and a second one attached to the rotating propeller. The communication between the two domains is performed across a cylindrical boundary with the sliding grid communication strategy.

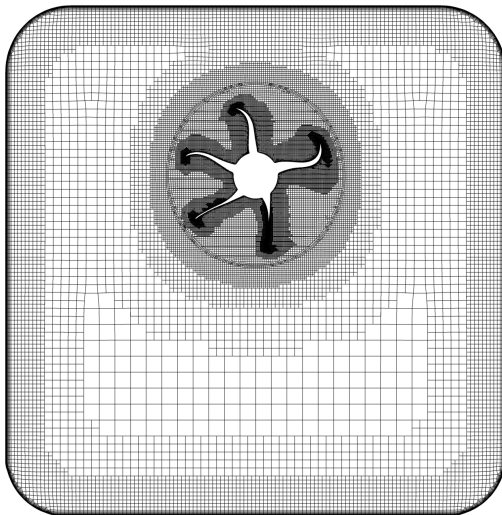
Table 5 gives the characteristics of the mesh used for the case 2. Figure 3 shows the mesh and the size of the computational domain for the case 2. Figure 4 presents details of the mesh in the plane $Y = 0$ and in the propeller plane.

Table 5: Case 2 - Characteristics of the mesh

Nb of cells	Nb of nodes	Nb of faces on the propeller	Nb of faces on one blade
25,772,598	27,304,872	562,487	100,603

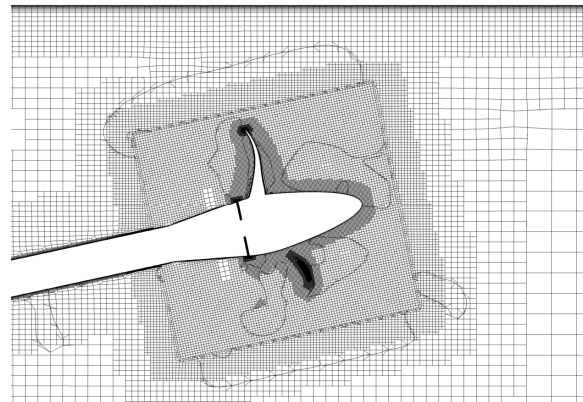


(a) Mesh in the plane $Y = 0$

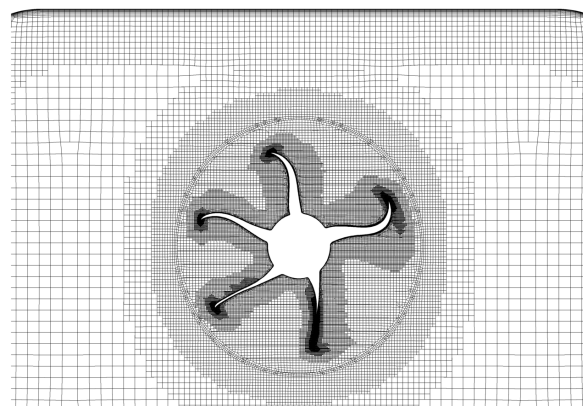


(b) Mesh in the vertical plane through the propeller centre

Figure 3: Case 2 - View of the mesh and the computational domain.



(a) Mesh in the plane $Y = 0$



(b) Mesh in the vertical plane through the propeller centre

Figure 4: Case 2 - Details of the mesh.

4 RESULTS

4.1 Case 1: Open water test case

In order to establish a grid-independent solution for the case 1, computations have been performed for three meshes. Table 4 presents the propeller loads for $J = 1.0$. The results are obtained with the $k-\omega$ SST turbulence model. For the KT_y thrust coefficient, the maximum difference between the three simulations is 1.5%, for the KQ_z torque coefficient, the maximum is 1.4% while for the other coefficients the difference is below 1%. Then, the medium mesh is used for all further numerical simulations for the case 1.

For the advance coefficient $J = 1.0$, a study of the turbulence modelization is performed. The first model used is the $k-\omega$ SST and the second is the EARSM model. Table 6 presents the propeller loads obtained with these turbulence models. The results are quite similar. Thus, in the remainder of the paper, only the $k-\omega$ SST turbulence model is used

Table 4: Case 1 - $J = 1.0$ - Influence of the mesh for the propeller loads.

	Coarse mesh	Medium mesh	Fine mesh
KT_x	0.3791	0.3781	0.3784
KT_y	-0.0281	-0.0286	-0.0282
KT_z	0.0743	0.0731	0.0737
KT	0.3873	0.3862	0.3866
KQ_x	0.0960	0.0953	0.0956
KQ_y	0.0212	0.0212	0.0213
KQ_z	-0.0264	-0.0262	-0.02655
KQ	0.1018	0.1011	0.1014

Table 6: Case 1 - $J = 1.0$ - Influence of the turbulence models for the propeller loads.

	KT_x	KT_y	KT_z	KQ_x
k- ω SST	0.3786	-0.0286	0.0731	0.0953
EARSM	0.3790	-0.0280	0.0743	0.0959

Figure 5 presents the open water characteristics curve in the propeller coordinate system (PCS). As a direct consequence of the non-uniform inflow, the loads generated by the blades are not constant during the revolution. This behavior can be seen in Figures 6, 7 and 8, that represent the blade forces and moments in the PCS for $J = 0.6$, $J = 1.0$ and $J = 1.4$. The forces and moments decrease as the advance coefficient increase, and for $J = 1.4$, KT_x and KT_z are of the same order of magnitude.

Figure 9 presents a non-dimensional iso-surface of the second invariant of the velocity gradient. As the advance coefficient increases, the size of the vortices decreases and

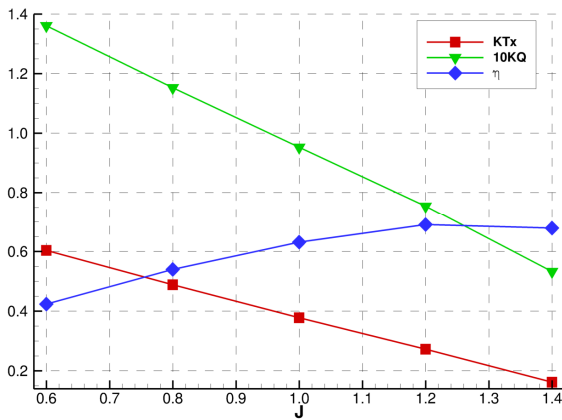
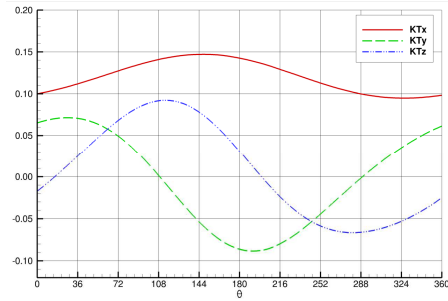
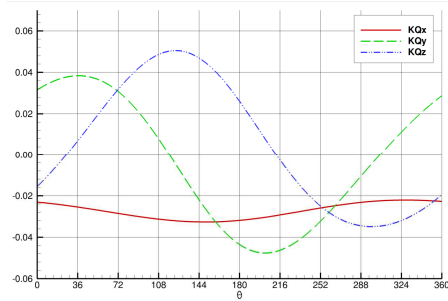


Figure 5: Case 1 - Computed open water characteristics.

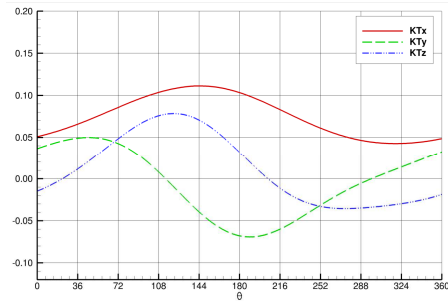


(a) Forces

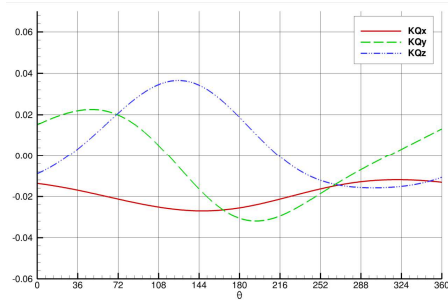


(b) Moments

Figure 6: Case 1 - $J = 0.6$ - Forces and moments developed by one blade, in PCS.



(a) Forces



(b) Moments

Figure 7: Case 1 - $J = 1.0$ - Forces and moments developed by one blade, in PCS.

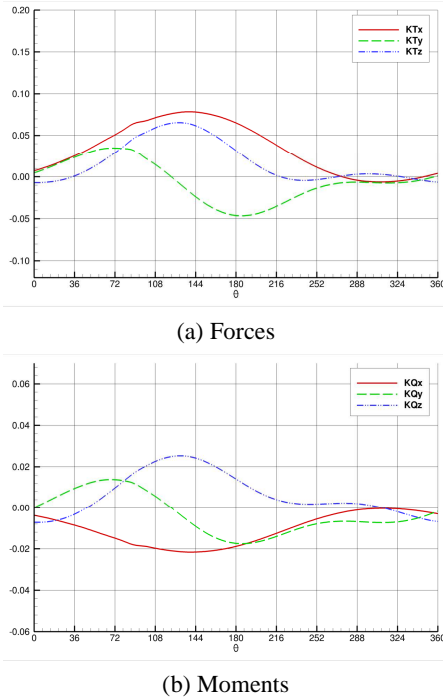


Figure 8: Case 1 - $J = 1.4$ - Forces and moments developed by one blade, in PCS.

the wake is more and more aligned with the incoming flow. The deviation of the wake is also visible in Figure 10 which presents the pressure coefficient $C_p = P/(0.5\rho U_{ref}^2)$ where P is the pressure. With the same pressure levels, the deflection of the vortex structures is clearly observed as the advance coefficient increases. It is also observed that the pressure intensity in the core of the vortex decreases at high J . The tip vortex suddenly vanishes as the vortex enters the region where the grid is coarser.

In Figures 11, 12 and 13 the pressure generated on the propeller blades and the hub cap is visualized for three advance coefficients. For all figures, the blades are in the same position with the blade 1 at 0° , equivalent to the 12 O'clock position. Due to the incidence of the propeller, the pressure is not the same on each blade when the advance coefficient increases. On the suction side, the pressure on the blade 1 increases while on the pressure side, the pressure decreases. We observe a reversal in the pressure at the leading edge of the blade 1 when the advance coefficient increases. For the small J , the pressure is negative on the section side while at the high J , the pressure is positive.

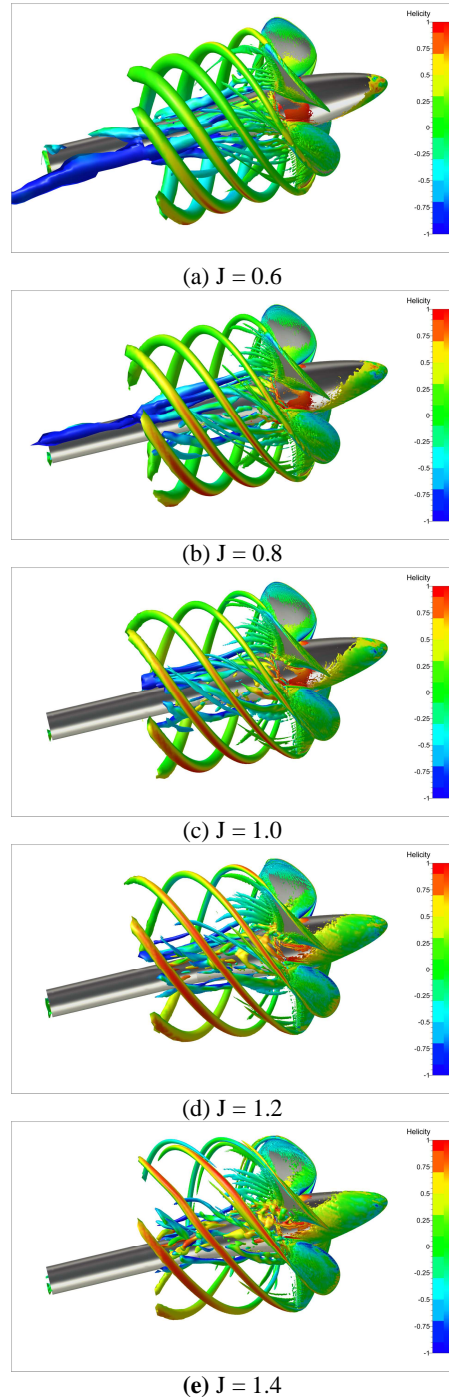
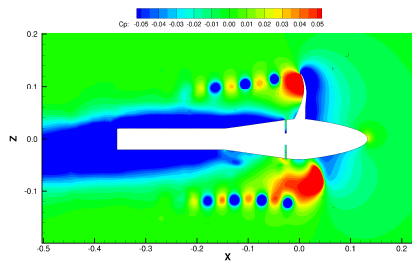
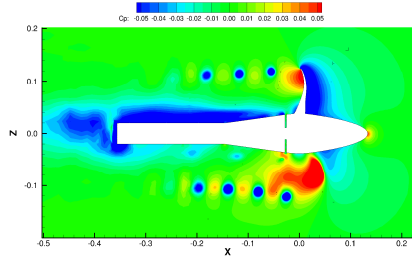


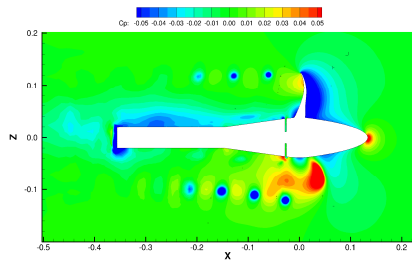
Figure 9: Case 1 - Visualizations of vortical structures ($Q^* = 1$)



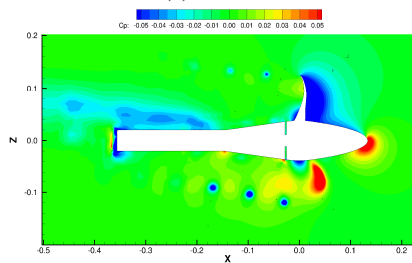
(a) $J = 0.6$



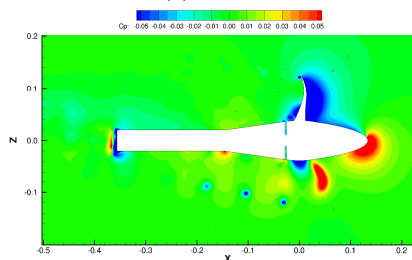
(b) $J = 0.8$



(c) $J = 1.0$

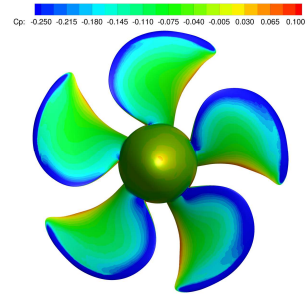


(d) $J = 1.2$

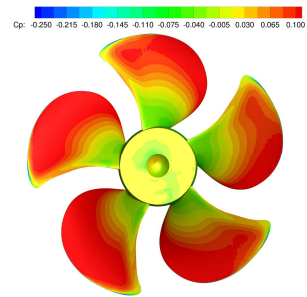


(e) $J = 1.4$

Figure 10: Case 1 - Pressure in the plane $Y = 0$.

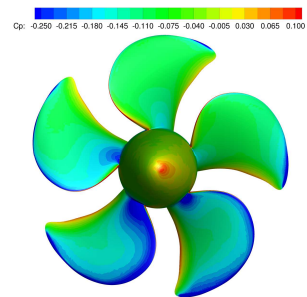


(a) Suction side

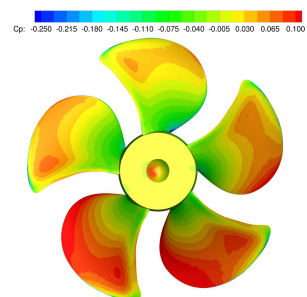


(b) Pressure side

Figure 11: Case 1 - $J = 0.6$ - Pressure fields on propeller blades.



(a) Suction side



(b) Pressure side

Figure 12: Case 1 - $J = 1.0$ - Pressure fields on propeller blades.

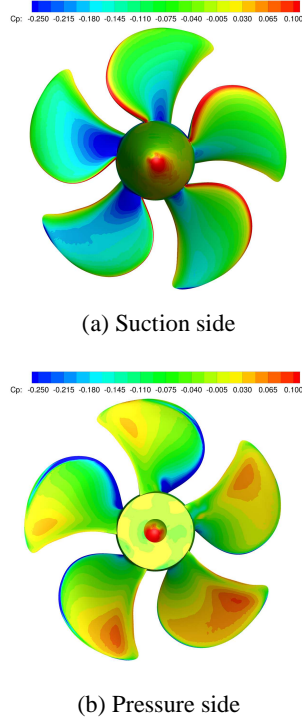


Figure 13: Case 1 - $J = 1.4$ - Pressure fields on propeller blades.

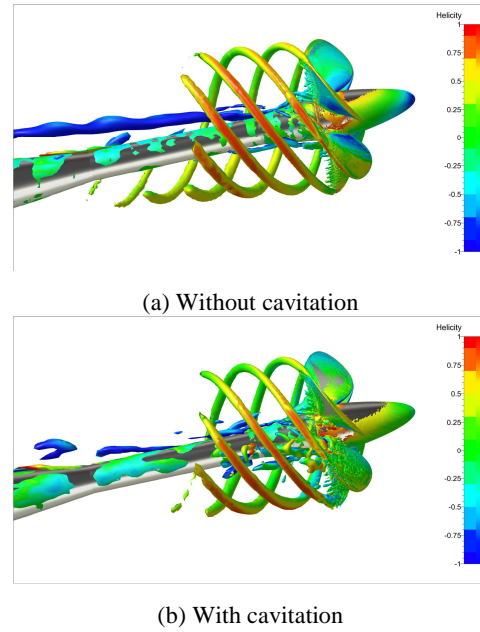


Figure 14: Case 2-1 - Visualizations of vortical structures ($Q=1$)

4.2 Case 2: Cavitation test case

For all the simulations, the Sauer model is used to predict the cavitation.

In order to evaluate the influence of the cavitating behavior on the propeller performance, we compare the results of the non-cavitating and cavitating flow at three advance coefficients. In Table 7, the predicted values of the thrust and torque coefficients, for the non-cavitating and cavitating flow regimes, are collected. For all the operational conditions, cavitation affects the propeller thrust negatively.

Table 7: Case 2 - Thrust and torque coefficients in PCS.

Forces & Torque	$J = 1.019$		$J = 1.269$		$J = 1.408$	
	No cav	$\sigma = 2.024$	No cav	$\sigma = 1.424$	No cav	$\sigma = 2.000$
KT_x	0.4021	0.3527	0.2663	0.1220	0.1825	0.0838
KT_y	-0.044	-0.026	-0.058	-0.032	-0.066	-0.037
KT_z	0.0835	0.0786	0.1158	0.0590	0.1393	0.0995
KQ	0.1005	0.0903	0.0487	0.0484	0.0581	0.0443

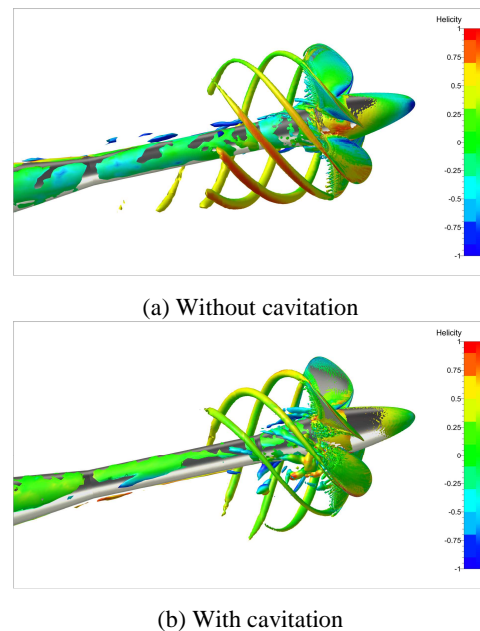
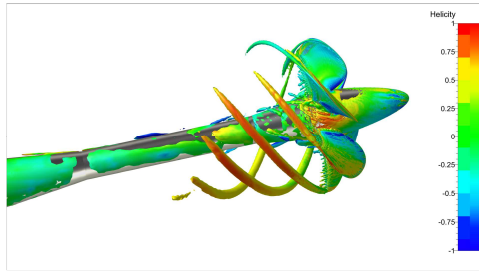
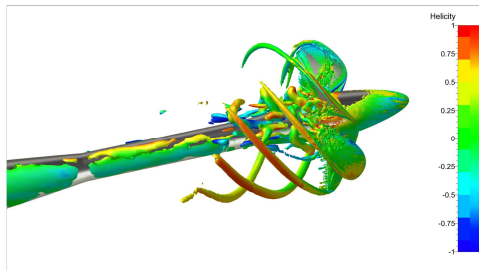


Figure 15: Case 2-2 - Visualizations of vortical structures ($Q=1$)



(a) Without cavitation



(b) With cavitation

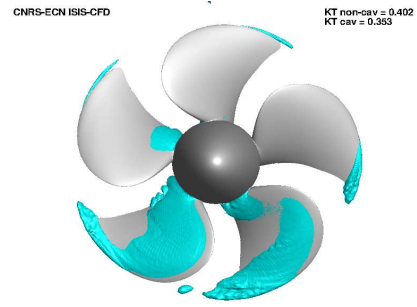
Figure 16: Case 2-3 - Visualizations of vortical structures ($Q^* = 1$)

Figures 14, 15 and 16 show the vortical structures for the three advance coefficients with and without cavitation. For all cases, we observe the vortex generated by the tip vortices. As for the case of open water, these vortices disappear when the mesh is not fine enough.

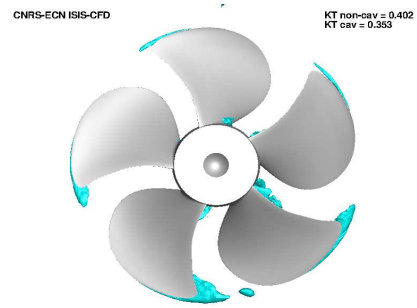
Figures 17, 18 and 19 show cavity patterns on the blades for each test case. With these figures, we observe that the cavity patterns are only located on the blades while with the previous figures, we note that the vortices going to the wake of the propeller have not vapor fraction inside. Then it is not clear to conclude that this damping of the vapor fraction is due to the turbulence modeling and/or the cavitation model itself.

5 CONCLUSIONS AND FUTURE WORK

In this paper, the cavitating performance and open water performance of the PPTC model at an incidence was numerically simulated using the ISIS-CFD flow solver. The turbulence is modeled with the $k-\omega$ SST model and the cavitation with the Sauer model. Simulations were carried out following the recommendations of the SMP'15 Workshop. The requested thrust and torque coefficient are presented for open water case. The cavity surface on the propeller is presented for the cavitating cases.

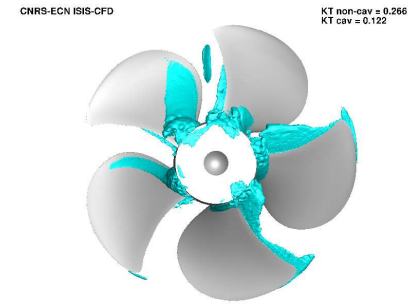


(a) Suction side

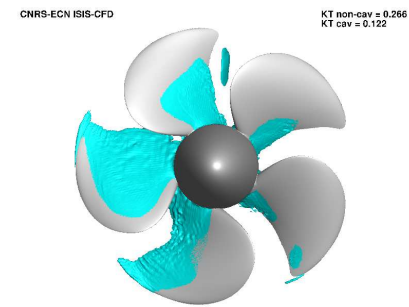


(b) Pressure side

Figure 17: Case 2-1 - Cavitation patterns.



(a) Suction side



(b) Pressure side

Figure 18: Case 2-2 - Cavitation patterns.

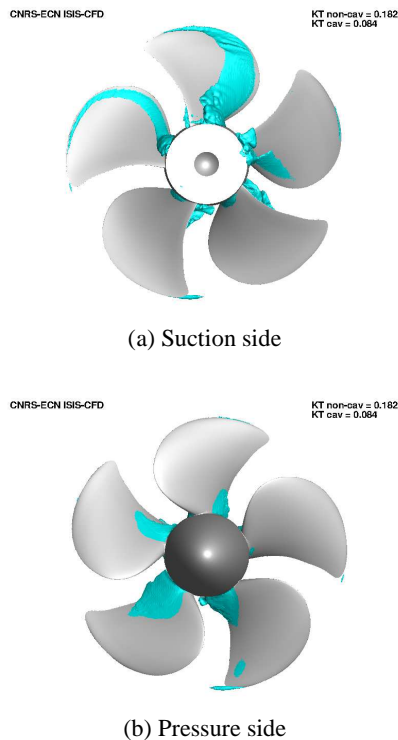


Figure 19: Case 2-3 - Cavitation patterns.

ACKNOWLEDGMENTS

This work was granted access to the HPC resources of CINES/IDRIS under the allocation 2015-2a0129 made by GENCI.

REFERENCES

- Deng, G.B., Queutey, P., Visonneau, M., and Salvatore, F. (2013), "Ship Propulsion Prediction with a Coupled RANS-BEM Approach," Proc. of V. International Conference on Computational Methods in Marine Engineering, MARINE 2013, Hamburg, Germany.
- Deng, G.B., and Visonneau, M. (1999), "Comparison of Explicit Algebraic Stress Models and Second-Order Turbulence Closures for Steady Flow around Ships," Proc. of 7th Symposium on Numerical Ship Hydrodynamics, Nantes, France, 4.4-1-4.4-15.

Dubbioso, G., Muscari, R., and Di Mascio, A. (2013), "Analysis of the Performance of a Marine Propeller Operating in Oblique Flow," Computers & Fluids, 75, 86-102.

Dubbioso, G., Muscari, R., and Di Mascio, A. (2014), "Analysis of the Performance of a Marine Propeller Operating in Oblique Flow. Part 2: Very High Incidence Angles," Computers & Fluids, 92, 56-81.

Duvigneau, R., Deng, G.B. and Visonneau, M. (2003), "On the Role Played by Turbulence Closures in Hull Ship Optimization at model and Full Scale," J. Mar. Sci. Technol., 8, 11-25.

El Moctar, O., and Bertram, V. (2000), "RANS Simulation of Propeller in Oblique Flow," Proc. of 3rd Numerical Towing Tank Symposium, Tjärnö, Sweden, 46-48.

Guilmineau, E., Deng, G.B., and Wackers, J. (2011), "Numerical Simulation with DES Approach for Automotive Flows," Journal of Fluids & Structures, 27, 807-8016.

Krasilnikov, V., Zhang, Z.R., and Hong, F.W. (2009), "Analysis of Unsteady Propeller Blade Forces by RANS," Proc. of the First International Symposium on Marine Propulsors, SMP'09, Trondheim, Norway.

Leroyer, A., and Visonneau, M. (2005), "Numerical Methods for RANSE Simulations of Self-Propelled Fish-like Body," Journal of Fluids & Structures, 20, 975-991.

Queutey, P., and Visonneau, M. (2007), "An Interface Capturing Method for Free-Surface Hydrodynamic Flows," Computers & Fluids, 36, 1481-1510.

Shamsi, R., and Ghassemi, H. (2013), "Numerical Investigation of Yaw Angle Effects on Propulsive Characteristics of Podded Propulsors," Int. J. Nav. Archit. Ocean Eng., 5, 287-301.

Wackers, J., Deng, G.B., Guilmineau, E., Leroyer, A., Queutey, P., and Visonneau, M. (2014), "Combined Refinement Criteria for Anisotropic Grid Refinement in Free-Surface Flow Simulations," Computers & Fluids, 92, 209-222.

Yao, J. (2015), "Investigation on Hydrodynamic Performance of a Marine Propeller in Oblique Flow by RANS Computations," Int. J. Nav. Archit. Ocean Eng., 7, 56-69.

Numerical Simulations of SMP'15 Marine Propeller with and without Cavitation

Satoshi Nohara¹, Keita Fujiyama¹

¹Software Cradle Co., Ltd., Osaka, JAPAN

▪ ABSTRACT

SC/Tetra is general-purpose computational fluid dynamics (CFD) software using unstructured mesh finite volume method. SC/Tetra implements both RANS-based turbulence models for transitional flows and models for cavitating flows. This paper shows the calculation results of the problems provided by SMP'15 workshop, and evaluation of the accuracy and reliability of SC/Tetra obtained from the analyses of the flows on marine propellers.

In Case1, numerical simulations of a non-cavitating flow, i.e., open water tests, are performed by using the LKE $k-k_L-\omega$ model and the transitional flow behaviors on a propeller surface are analyzed. This paper shows the thrust and torque obtained from the simulations of the propeller.

In Case2 and Case3, numerical simulations of cavitating flow are performed by using the full-cavitation model (Singhal's model) and SST-SAS turbulence model derived from SST $k-\omega$ model. This paper shows the comparison of cavitation patterns obtained from the simulations, particularly such as tip vortices, the thrust of the propeller, and pressure pulses in the cavitation tunnel.

▪ Keywords

Numerical Simulation, Cavitation, Pressure Fraction, Tip Vortex

▪ 1 INTRODUCTION

SC/Tetra, developed by Software Cradle Co., Ltd. in Japan from 2001, is general purpose CFD software using unstructured mesh finite volume method. SC/Tetra has been developed as a design tool for mechanical engineers and designers, and is widely used mainly the automotive, electrical appliance, and turbo-machinery fields.

In the marine engineering field, CFD is used for large-scale simulations such as cavitation analyses. SC/Tetra implements some advanced turbulence models, some cavitation models, and various functions, effective for the field.

This paper presents the calculations of marine propellers and cavitating flows performed by SC/Tetra version 11, and the evaluation of the accuracy and the performance of SC/Tetra.

▪ 2 NUMERICAL MODEL

All simulations presented in this paper are performed with SC/Tetra version 11 which is the finite volume solver for general purpose. SC/Tetra implements low-Raynolds-number turbulence model, cavitation models, and various physical models.

In this paper, we used the LKE $k-k_L-\omega$ model for the open water tests (Case1) and SST-SAS model for cavitating flows (Case2, Case3). In addition, Cavitating flows are calculated by the full-cavitation model.

▪ 2.1 LKE $k-k_L-\omega$ Turbulence Model

It is important to predict the location of transition in a simulation of a flow around a body. Laminar Kinetic Energy (LKE) model proposed by Walters and Lylek is one of RANS based approaches to predict the transitional flow.

In the LKE model, the energy of the disturbances in the pre-transitional region of a boundary layer is expressed as "Laminar Kinetic Energy (k_L)" while the turbulence energy is as k , and the transport equation of k_L is solved with two equations of fully turbulent model. SC/Tetra introduces the following $k-k_L-\omega$ model which was developed based on the $k-\omega$ model:

$$\frac{\partial \rho k}{\partial t} + \frac{\partial u_i \rho k}{\partial x_i} = \rho(P_k + R_{BP} + R_{NAT} - \omega k - D_T) + \frac{\partial}{\partial x_i} \left[\left(\mu + \frac{\rho \alpha_T}{\sigma_k} \right) \frac{\partial k}{\partial x_i} \right] \quad (1)$$

$$\frac{\partial \rho k_L}{\partial t} + \frac{\partial u_i \rho k_L}{\partial x_i} = \rho(P_{k_L} + R_{BP} + R_{NAT} - D_L) + \frac{\partial}{\partial x_i} \left[\mu \frac{\partial k_L}{\partial x_i} \right] \quad (2)$$

$$\frac{\partial \rho \omega}{\partial t} + \frac{\partial u_i \rho \omega}{\partial x_i} = \rho \left[C_{\omega 1} \frac{\omega}{k} P_k + \left(\frac{C_{\omega R}}{f_W} - 1 \right) \frac{\omega}{k} (R_{BP} + R_{NAT}) - C_{\omega 2} f_W^{\frac{4}{3}} \omega^2 + C_{\omega 3} f_W \alpha_T f_W^2 \frac{\sqrt{k}}{d^3} \right] + \frac{\partial}{\partial x_i} \left[\left(\mu + \frac{\rho \alpha_T}{\sigma_\omega} \right) \frac{\partial \omega}{\partial x_i} \right] \quad (3)$$

P_k and P_{k_L} are respectively production terms of k and k_L :

$$P_k = \nu_{T,S} S^2 \quad (4)$$

$$P_{kL} = \nu_{T,l} S^2 \quad (5)$$

$\nu_{T,s}$ and $\nu_{T,l}$ are respectively the eddy viscosities of small scale and large scale. The sum of these values ($\nu_t = \nu_{T,s} + \nu_{T,l}$) is used for the eddy viscosity of the momentum equation. R_{BP} and R_{NAT} are the contributions of the bypass transition and the natural transition, respectively. The contribution of the bypass transition increases as the turbulent intensity in the external flow increases.

For the definitions of other variables and constants, please refer the references [1] [2].

2.2 SST-SAS Turbulence Model

The SST (Shear-Stress Transport) model developed by Menter solves the two equations for k and ω with a zonal treatment: the conventional k - ω equations developed by Wilcox are solved in near-wall regions, and they are shifted toward outer regions to be equivalent to the k - ε model, which promises an accurate and robust computation. Also, the concept of Shear-Stress Transport avoids the over-estimate of eddy viscosity under adverse pressure-gradients, and properly reproduces complicated separation phenomena that the conventional eddy viscosity models may fail to capture.

In the k - ω model, the eddy viscosity is expressed as follows:

$$\mu_t|_{k-\omega} = \rho \frac{k}{\omega} \quad (7)$$

The k transport equation has the same form as that solved in other low-Rayolds-number k - ε models, except the different energy-dissipation expression $\varepsilon = C_\mu k \omega$. The ω transport equation is written as follows:

$$\frac{\partial \rho \omega}{\partial t} + \frac{\partial u_j \rho \omega}{\partial x_j} = \frac{\partial}{\partial x_j} \left[\left(\mu + \frac{\mu_t}{\sigma_\omega} \right) \frac{\partial \omega}{\partial x_j} \right] + \frac{\gamma \rho}{\mu_t} G_s - \beta \rho \omega^2 \quad (8)$$

By adding the following cross-diffusion term to RHS of the above ω equation, the k - ω equations become analytically equivalent to the k - ε model:

$$CD_{k\omega} = 2 \frac{\rho}{\sigma_\omega \omega} \frac{\partial k}{\partial x_j} \frac{\partial \omega}{\partial x_j} \quad (9)$$

In the SST model, the smooth zonal shift from the k - ω model to k - ε is achieved by introducing a blending function, which has wall distance and turbulence quantities as its argument, multiplied by the above cross diffusion term.

Furthermore, the Shear-Stress Transport is represented by the following eddy viscosity expression:

$$\mu_t|_{SST} = \rho \frac{a_1 k}{\Omega} \quad (10)$$

Here, Ω is magnitude of mean vorticity.

The SST model is suitable for the analysis of flow with separation phenomena. However, as a general feature of RANS models, to reproduce unsteady flow in the separation zone is difficult. SST-SAS (Scale-Adaptive Simulation) model is which is derived

from the SST model is proposed to solve the problem. Specifically, the following additional source term Q_{SAS} is added in the transport equation of ω to control the production of the turbulence energy:

$$Q_{SAS} = \max \left[\rho \zeta_2 \kappa S^2 \left(\frac{L}{L_{VK}} \right)^2 - C \frac{2\rho k}{\sigma_\phi} \max \left(\frac{|\nabla \omega|^2}{\omega^2}, \frac{|\nabla k|^2}{k^2} \right), 0 \right] \quad (11)$$

The value L in the above equation is the modeled length scale on the assumption of homogeneous turbulent flow, and the L_{VK} (von Karman length scale) is the length scale which is derived from the velocity gradients to indicate inhomogeneous nature of the turbulent flow. Those are defined as follows:

$$L = \frac{\sqrt{k}}{C_\mu^{\frac{1}{4}} \cdot \omega} \quad (12)$$

$$L_{VK} = \max \left(\frac{\kappa S}{|\nabla^2 U|}, C_s \sqrt{\frac{\kappa \zeta_2}{\beta}} \frac{\Delta}{C_\mu - \alpha} \right), \quad \Delta = \Omega^{-\frac{1}{3}} \quad (13)$$

For the definitions of other variables and constants, please refer the references [3][4].

2.3 Cavitation Model

To simulate a two-phase cavitating flow, the single fluid approach is used. In addition, the mixture density is given by barotropic relation. Evaporation and condensation are modeled using a full cavitation model [5].

A non-condensable gas is taken into account in the full cavitation model as well.

$$\rho = \frac{P(P + P_c) \rho_g}{K(1 - Y - Y_g)P(T + T_0) \rho_g + RY(P + P_c)T \rho_g + Y_g P(P + P_c)} \quad (14)$$

where ρ stands for density of homogenous media, P pressure, T absolute temperature and Y mass fraction of the vapor. The lower suffix g stands for the non-condensable gas. The following equation of the mass fraction including sink (condensation) term as well as source (evaporation) term is solved in the full cavitation model.

$$\frac{\partial \rho Y}{\partial t} + \frac{\partial \rho u_j Y}{\partial x_j} = R_e - R_c \quad (15)$$

The evaporation and the condensation terms are as follows:

$$R_e = C_e \frac{\sqrt{k}}{\sigma_s} \rho_l \rho_v \sqrt{\frac{2P_v - P}{3} \frac{1}{\rho_l}} (1 - Y - Y_g) \quad \text{if } P < P_v \quad (16)$$

$$R_c = C_c \frac{\sqrt{k}}{\sigma_s} \rho_l \rho_l \sqrt{\frac{2P - P_v}{3} \frac{1}{\rho_l}} Y \quad \text{if } P > P_v \quad (17)$$

where $C_e = 0.02$, $C_c = 0.01$ are model constants and k turbulent kinetic energy. The lower suffix 1 stands for the liquid, σ_s surface tension of the liquid. In the full cavitation model, the effect of turbulence to the vapor pressure is taken into account as follows.

$$P_V = P_s + \frac{0.39\rho k}{2} \quad (18)$$

P_s is the saturated vapor pressure.

3 RESULTS

The test conditions and the propeller model geometry are given by SMP'15 workshop. Table 1 and Figure 1 show the propeller geometry data, and inclination angle of the propeller is 12[deg].

The numerical mesh generated by SC/Tetra is unstructured mesh which consists of tetrahedral, prism, and pyramid elements. Prism layers are inserted to resolve boundary layers around surfaces. To use a low-Raynolds-number turbulence model, the first layers around surfaces are generated under the condition that $y^+ < 1$ is satisfied in all the cases.

Table 1: Propeller Geometry Data

Number of Blades	5
Propeller Diameter [mm]	250.0000
Pitch Ratio r/R=0.7	1.6350
Skew [deg]	18.8000

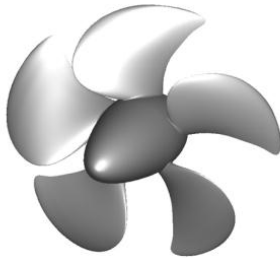


Figure 1: Propeller

3.1 Open Water Test (Case 1)

Table 2 shows conditions for the open water tests. Figure 2 shows the computational domain and Figure 3 shows the mesh on the propeller surface. The mesh data is listed in Table 3.

The simulations are performed as steady-state and transient analyses using the advance coefficient J of 0.6, 0.8, 1.0, 1.2, and 1.4. In the steady-state analyses, the mesh around the propeller does not move. However, the rotational force is added in order to satisfy what flow is steady state in rotational frame.

To simulate a transitional flow, LKE $k-k_L-\omega$ turbulence model is used. For coupling between momentum and mass conservation, SIMPLEC method is used. The convective term is discretized by using the second order scheme.

Figure 4 shows curves of the thrust coefficients K_T , the torque

coefficients K_Q , and the efficiency η with the advance coefficients J in the steady-state and the transient analysis. Figure 5 shows limiting streamlines at the propeller surface and the transition caused by the effect of the turbulence model can be checked.

Table 2: Condition of Case 1

Water density ρ [Kg/m ³]	998.62
Kinematic viscosity ν [m ² /s]	$1.057 \cdot 10^{-7}$
Number of revolutions n [1/s]	15

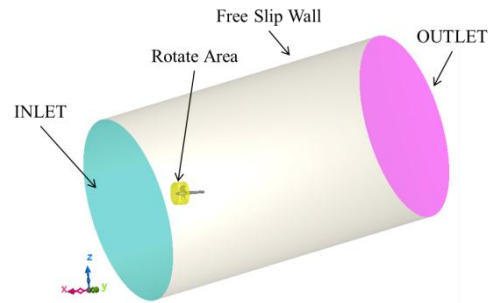


Figure 2: Computational Region (Case 1)



Figure 3: Propeller Surface Mesh (Case 1)

Table 3: Condition of Mesh (Case 1)

Total node number	3,700,000
Total element number	9,800,000
y^+	< 1
Prism layers	20

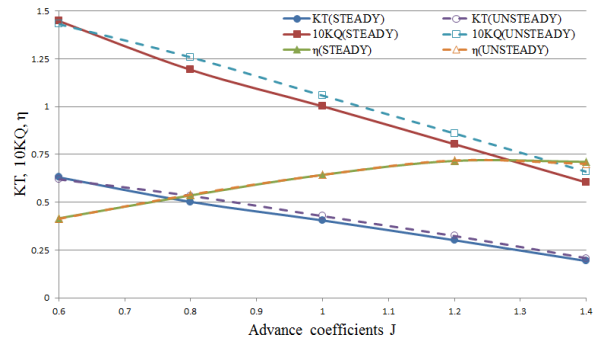


Figure 4: K_T , K_Q and η Curves (Case 1)

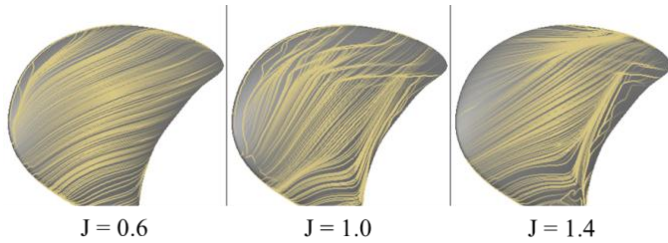


Figure 5: Limiting Streamlines of Propeller Surface (Case 1)

3.2 Analysis of Cavitating flows (Case 2)

Table 4 shows the conditions of Case 2, including cavitation. Figure 6 shows the computational domain and Figure 7 shows the mesh on the propeller surface and fine mesh area (purple). The mesh data is listed in Table 5.

In this analysis, SST-SAS turbulence model and SIMPLEC method are used. In addition, full-cavitation model is used for cavitating flows. For generating finer mesh at tip vortex regions, the mesh adaptation technique is used.

Figure 8 shows the cavity surfaces where the volume fraction of vapor is 10% and 40% at a blade position of 0 [deg]. Figure 9 shows the comparison of the cavitation patterns between the simulation with $J = 1.019$ and the open data. The tip vortices are also well simulated in comparison with the open data.

Table 4: Condition of Case 2

	Case2.1	Case2.2	Case2.3
Advanced coefficient J	1.019	1.269	1.408
Cavitation number σ_n	2.024	1.424	2.000
Number of revolutions n [1/s]	20		
Water density ρ [Kg/m ³]	997.780	997.900	997.410
Kinematic viscosity ν [m ² /s]	$9.567 \cdot 10^{-7}$	$9.591 \cdot 10^{-7}$	$9.229 \cdot 10^{-7}$
Vapor pressure P_V [Pa]	2643	2626	2904

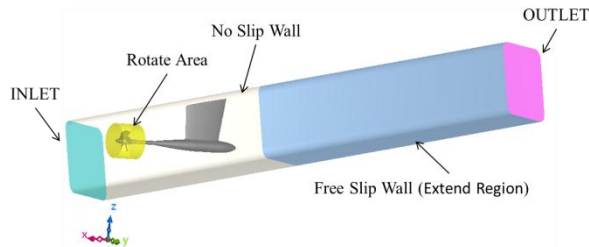


Figure 6: Computational Region (Case 2)

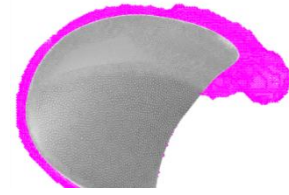


Figure 7: Propeller Surface Mesh and Fine Mesh Area (Case 2)

Table 5: Condition of Mesh (Case 2)

Total node number	7,000,000
Total element number	30,000,000
y^+	< 1
Prism layers	20

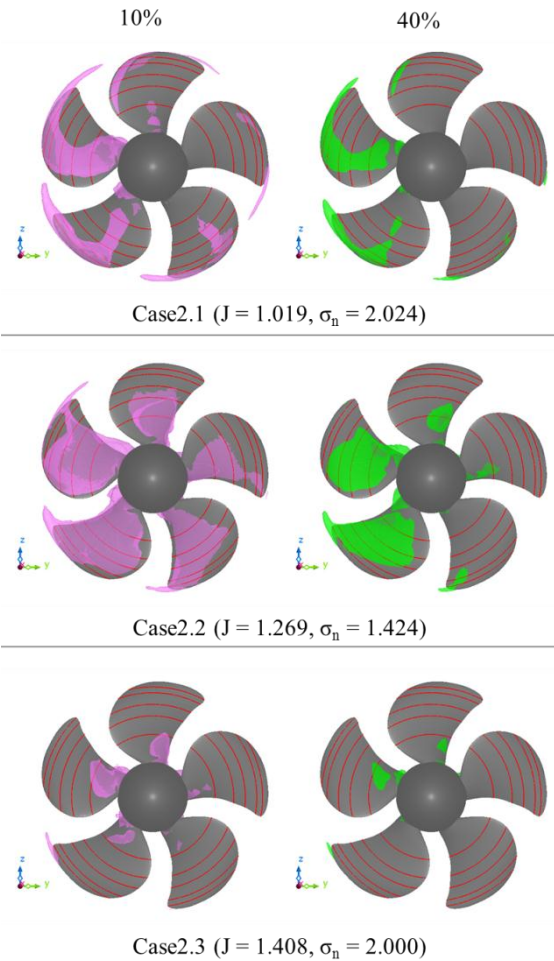


Figure 8: Cavity surfaces where The Volume Fractions of Vapor is 10% and 40% (Case 2)

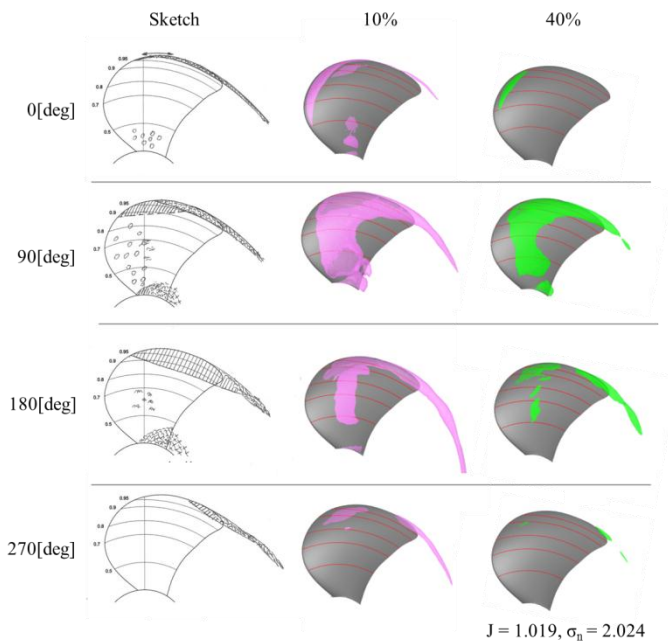


Figure 9: Comparison of Cavitation Patterns (Case 2.1)

3.2 Analysis of Pressure Pulse (Case 3)

Table 6 shows the conditions of Case 3. Figure 10 shows the computational domain and Figure 11 shows measuring points (p2, p5 and p10) of pressure pulse viewed from above. The points are positioned 50 [mm] above the propeller tip at intervals of 50 [mm]. The mesh data is listed in Table 7.

In this analysis, SST-SAS turbulence model and SIMPLEC method is used. In addition, full-cavitation model is used for cavitating flows. The mesh is also generated by the mesh adaptation technique in the same manner for the mesh of Case2.

Figure 12 shows the pressure pulses with cavitation of 8 revolutions at three measuring points (p2, p5 and p10). The data of the graph is created by editing pressure pulse of 4 - 5 revolutions. Periodic pressure pulses at three measuring points are obtained in each condition.

Table 6: Condition of Case 3

	Case3.1	Case3.2	Case3.3
Advanced coefficient J	1.019	1.269	1.408
Cavitation number σ_n	2.024	1.424	2.000
Number of revolutions n [1/s]	20		
Water density ρ [Kg/m ³]	997.380		
Kinematic viscosity ν [m ² /s]	$9.199 \cdot 10^{-7}$		
Vapor pressure P_V [Pa]	2929		

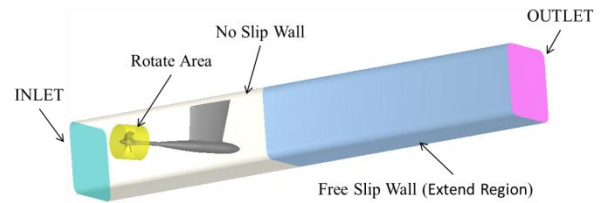


Figure 10: Computational Region (Case 3)

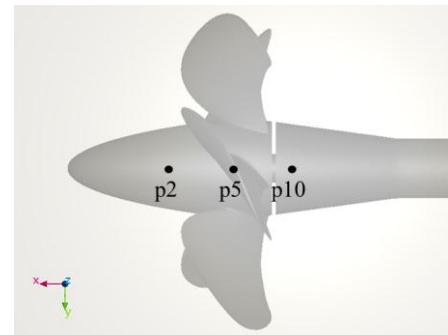


Figure 11: Measuring Points of Pressure Pulse (Case 3)

Table 7: Condition of Mesh (Case 3)

Total node number	6,800,000
Total element number	29,000,000
y^+	< 1
Prism layers	20

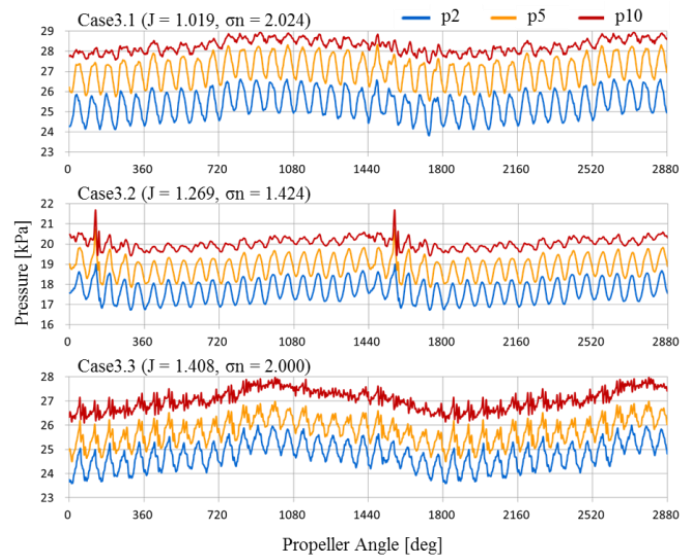


Figure 12: Pressure Pulses (Case 3)

▪4 CONCLUSIONS

In this paper, the marine propeller and cavitating flows has been analyzed by using SC/Tetra based on RANS solver. SC/Tetra implements effective RANS turbulence models and a full cavitation model. LKE $k-k_L-\omega$ turbulence model is effective for the transitional flows of a marine propeller and the cavitating flows around the marine propeller have been obtained by using RANS model and full cavitation model. In addition, generating fine mesh around the tip of blade by using the mesh adaptation technique is effective to simulate tip vortices.

▪FORMULA

Advance coefficient J :

$$J = \frac{V_A}{n \cdot D_p}$$

Thrust coefficient K_{Tx} :

$$K_{Tx} = \frac{T_x}{\rho \cdot n^2 \cdot D_p^4}$$

Torque coefficient K_Q :

$$K_Q = \frac{Q}{\rho \cdot n^2 \cdot D_p^5}$$

Cavitation number σ_n with respect to n :

$$\sigma_n = \frac{(p - p_v)}{0.5 \cdot \rho \cdot (n \cdot D_p)^2}$$

With D_p being the propeller diameter, T_x the propeller thrust along the shaft axis (PCS), Q the propeller torque, p the tunnel pressure and p_v the vapor pressure.

▪Propeller Coordinate System (PCS)

An orthogonal coordinate system is used for the propeller, with the x-axis pointing upstream against the flow direction and the z-axis upwards. Figure 13 shows PCS. PCS is used all calculations in this paper.

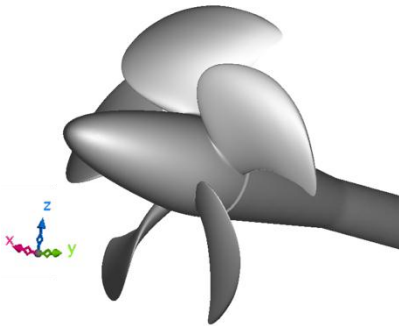


Figure 13: Propeller Coordinate System

▪REFERENCES

- [1] Walters, D.K. and Leylek, J.H. (2004)
"A New Model for Boundary Layer Transition Using a Single-Point RANS Approach," ASME Journal of Turbomachinery, 126, pp.193-202.
- [2] Walters, D.K. and Cokljat, D. (2008)
"A Three-Equation Eddy-Viscosity Model for Reynolds-Averaged Navier-Stokes Simulations of Transitional Flow," ASME J. of Fluids Eng., 130, 121401.
- [3] Menter, F., Zonal. (1993)
"Two Equation $k-\omega$ Turbulence Models for Aerodynamic Flows", AIAA 93-2906.
- [4] Egorov, Y., Menter, F. (2008)
"Development and Application of SST-SAS Turbulence Model in the DESIDER Project", Hybrid RANS-LES Modelling, p.261-270.
- [5] Singhal, A.K. et al., (2002)
"Mathematical basis and validation of the full cavitation model", J. Fluid Eng., Vol.124.
- [6] Fujiyama, K., Kim, C., Hitomi, D. (2011)
"Performance and Cavitation Evaluation of Marine Propeller using Numerical Simulations", smp'11 - Workshop on Cavitation and Propeller Performance, p 50 - 56

The Numerical Predicted of VP1304 Propeller Cavitation Performance in Oblique Flow

Dengcheng Liu, Min Gu

China Ship Scientific Research Center (CSSRC), Wuxi, China

ABSTRACT

Second international workshop on cavitating propeller performance will hold in Austin, USA, at the end of smp'15. The workshop emphasis will be on prediction of propeller hydrodynamic performance and propeller cavitation performance in oblique flow, and the blind test will be performed at Potsdam Model Basin. In this paper, the cavitating performance of VP1304 propeller in oblique flow was numerically simulated using a hybrid mesh based on unsteady RANS solver. A full cavitation model based on transport equation and SST $\kappa-\omega$ turbulence model were coupled in the RANS solver. The appointed cavity surfaces for different volume fraction were present for the cavitation cases. The thrust and torque coefficient and open water efficiency were present with and without cavitation. In addition, the cavity surfaces with added volume fraction were given for analyzing propeller cavitating shape.

Keywords

PPTC, Cavitation, Oblique, Numerical simulation.

1 INTRODUCTION

Cavitating flows are highly complicated because it is a rapid phase change phenomenon, which often occurs in the high-speed or rotating fluid machineries. It is well known that the cavitating flow raise up the vibration, the noise and the erosion. Therefore, the research on the cavitating flow is of great interest.

Numerical method is highly important approach for studying the cavitating flow. Computational methods for cavitation have been studied since over two decades ago. In general, the methods can be largely categorized into two groups: single-phase modeling with cavitation interface tracking and multi-phase modeling with cavitation interface capturing.

The first workshop on cavitation and propeller performance held in Hamburg, Germany, at the end of smp'11. the workshop emphasis will be on prediction of propeller VP1304 hydrodynamic performance and propeller cavitation performance in uniform flow, the test were blind test at Potsdam Model Basin. A large number

of different research groups participated, and the workshop become a success.

Now the second international workshop on cavitating propeller performance will hold in Austin, USA, at the end of smp'15. The workshop emphasis will be on prediction of propeller hydrodynamic performance and propeller cavitation performance in oblique flow, and the blind test will also be performed at Potsdam Model Basin.

In this paper, the cavitation performance of VP1304 propeller in oblique flow was numerically simulated. The requested data of SMP15 workshop were given.

2 Numerical Method

We used a commercial CFD code FLUENT14.0 which employs a cell-centered finite volume method based on unstructured mesh. The cavitation performance of VP1304 propeller in oblique flow was numerically simulated using a hybrid mesh based on unsteady RANS solver. The SST $\kappa-\omega$ turbulence model was chosen. Convection terms are discretized using a second order accurate upwind scheme, while diffusion terms are discretized using a second order accurate central differencing scheme. A segregated solver with SIMPLE as the velocity-pressure coupling algorithm was selected. The discrete equations are solved using pointwise Gauss-Seidel iterations, and algebraic multi-grid method accelerates the solution convergence.

2.1 Governing Equations

The governing equations are written for the mass and momentum conservation of mixture fluid as follows:

$$\frac{\partial(\rho_m)}{\partial t} + \frac{\partial(\rho_m u_i)}{\partial x_i} = 0 \quad (1)$$

$$\frac{\partial(\rho_m u_i)}{\partial t} + \frac{\partial(\rho_m u_i u_j)}{\partial x_j} = -\frac{\partial p}{\partial x_i} + \frac{\partial}{\partial x_j} \left[(\mu + \mu_t) \left(\frac{\partial u_i}{\partial x_j} + \frac{\partial u_j}{\partial x_i} \right) \right] \quad (2)$$

Where μ is the mixed viscosity, μ_t is the mixed eddy viscosity.

2.2 Full Cavitation Model

The mixed density is controlled by vapor volume fraction f :

$$\frac{1}{\rho_m} = \frac{f}{\rho_v} + \frac{f_g}{\rho_g} + \frac{1-f-f_g}{\rho_l} \quad (1)$$

The vapor transport equation is written as:

$$\frac{\partial(\rho_m f)}{\partial t} + \nabla \cdot (\rho_m \mathbf{u} f) = R_g - R_c \quad (4)$$

Where ρ_v , ρ_g and ρ_l are the density of vapor, non-condensable gas and liquid, respectively. R_g and R_c are the rates of vapor generation and condensation, respectively. To solve the Equation, R_g and R_c need to be given. Singhal et al (2002) derived the expressions.

$$R_g = -C_g \frac{\sqrt{k}}{S} \rho_l \rho_v \left(\frac{2(p - p_v)}{3\rho_l} \right)^{1/2} (1 - f_v - f_g) \quad \text{if } p < p_v \quad (5)$$

$$R_c = C_c \frac{\sqrt{k}}{S} \rho_l \rho_l \left(\frac{2(p - p_v)}{3\rho_l} \right)^{1/2} f_v \quad \text{if } p > p_v \quad (6)$$

Where p_v is saturated vapor pressure. C_g and C_c are two empirical constants and k is the local turbulent kinetic energy. Singhal et al. (2002) used 0.02 and 0.01 for C_g and C_c , respectively, after careful study of numerical stability and physical behavior of the solution. Their values are adopted in the present study. S is surface tension. f_g is non-condensable gas mass fraction.

3 Computational Condition

3.4 Geometry model and the cases

In this paper, the research object is a five bladed propeller. It is a controllable pitch propeller with diameter $D=0.250\text{m}$, hub diameter ratio of 0.3, pitch-to-diameter ratio of 1.635 at 0.7 radial section, skewed angle of 19.12° and area ratio of 0.78. Table 1~Table3 are the cases of cavitation computational. J is advance ratio. N is rotational speed of propeller. The expression of advance ratio, cavitation number, thrust and torque coefficient is written as follow:

$$J = \frac{V}{ND}, \quad Kt = \frac{T}{\rho N^2 D^4} \quad (7)$$

$$Kq = \frac{T}{\rho N^2 D^5}, \quad \sigma_n = \frac{p - p_v}{0.5 \rho (ND)^2}$$

Table.1 the case2-1 of cavitation computational

Advanced coefficient	1.019
Cavitation number	2.024
Water density(kg/m ³)	997.78
Kinematic viscosity of water(m ² /s)	9.567e-7
Rate of revolutions(1/s)	20
Inclination angle(°)	12

Table.2 the case2-2 of cavitation computational

Advanced coefficient	1.269
Cavitation number	1.424
Water density(kg/m ³)	997.8
Kinematic viscosity of water(m ² /s)	9.591e-7
Rate of revolutions(1/s)	20
Inclination angle(°)	12

Table.3 the case2-3 of cavitation computational

Advanced coefficient	1.408
Cavitation number	2.000
Water density(kg/m ³)	997.41
Kinematic viscosity of water(m ² /s)	9.229e-7
Rate of revolutions(1/s)	20
Inclination angle(°)	12

3.5 Computational mesh and conditions

For oblique flow simulation, the computational domain was created as cylinder surrounding propeller. A hybrid mesh was generated using GAMBIT. The blade and hub surface was meshed with triangles which the size is 4% propeller diameter. The volume cells are grew form the wall surface with the 1.1 ratio, and the limited size is 12% propeller diameter. The number of tetrahedral cells was about 6.8 million. The remaining region in the domain was filled with hexahedral cells, and the number of hexahedral cells was about 2.8 million. Figure 1 presents the propeller surface mesh.

Boundary conditions were set to simulate the flow around a rotating propeller: on the inlet boundary and the outer boundary, x-velocity components and z-velocity components of uniform stream with the given inflow speeds were imposed which is calculated by advance coefficient and oblique angle; on the blade and hub surface, the no slip condition was imposed; on the exit boundary, the static pressure was set to a constant value.

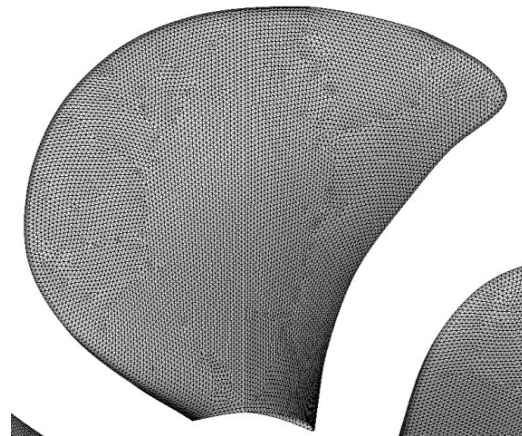


Figure.1 the propeller surface mesh

4 Results

4.1 Open water performance w/o cavitation

Figure 2 presents the coordinate system. Table 4 and table 5 presents the predicted thrust and torque coefficient with and without cavitation respectively. Table 6 present the thrust breakdown because of cavitation.

Table.4 predicted open water performance

J	Ktx	10Kq	ETA0
1.019	0.4014	0.9869	0.6596
1.269	0.2903	0.7684	0.7630
1.408	0.2173	0.6336	0.7685

Table.5 predicted open water performance with cavitation

J	Ktx	10Kq	ETA0
1.019	0.3851	0.9616	0.6495
1.269	0.2573	0.7367	0.7344
1.408	0.1873	0.6061	0.7105

Table.6 thrust breakdown with cavitation

case	J	Kt(no cav)	Kt(cav)	Error(%)
2-3-1	1.019	0.4014	0.3851	-4.06%
2-3-2	1.269	0.2903	0.2573	-11.37%
2-3-3	1.408	0.2173	0.1873	-13.81%

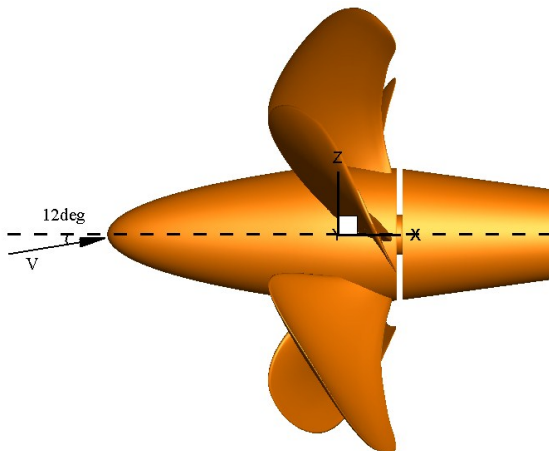


Figure.2 the coordinate coordinate

4.2 Cavitation surface

We simulated propeller cavitation performance in oblique flow at three different advance ratios, and we can gain the propeller cavitation surface.

According to my experience, the cavity shape defined by iso-surface of vapor volume fraction of 0.1 will agree well with experiment. So the appointed cavity surface (iso-surface of vapor volume fraction of 0.4, 0.6) and cavity surface defined by iso-surface of vapor volume fraction of 0.1 are also given.

Figure 3~Figure 5 presents the computed cavity shapes of different cases respectively. From Figure 3 we clearly see that cavitation is to occur in the tip, root and leading edge of middle radial section of suction side of propeller at case2-1, the cavitation is not occur on the pressure side of propeller, the cavitation area is periodic change with the propeller angle. From Figure 4 we clearly see that there are face cavitation or back cavitation when propeller locate different site. From Figure 5 we clearly see that there are serious face cavitations at leading edge of most radial section, and there is no face cavitation except at root region.

4 Conclusions

In this paper, the cavitation performance of VP1304 propeller in oblique flow was numerically simulated using a hybrid mesh based on unsteady RANS solver. SST $\kappa\omega$ turbulence model were coupled in the RANS solver. The appointed cavity surfaces for different volume fraction were present for the cavitation cases. The thrust and torque coefficient and open water efficiency were present with and without cavitation. In addition, the cavity surfaces with added volume fraction were given for analyzing propeller cavitating shape.

REFERENCES

- Coutier-Delgosha, O., Reboud, J.L., and Fortes-Patella, R., Evaluation of the Turbulence Model Influence on the Numerical Simulations of Unsteady Cavitation [J], Journal of Fluids Engineering, Vol. 125, Issue 1, pp. 38-45, 2003.
- Dengcheng Liu. (2008). The CFD analysis of propeller sheet cavitation. Proceedings of the 8th International Conference on Hydrodynamics. Nantes France. 2008
- Dengcheng Liu. (2010). The Numerical Research on Unsteady Cloud Cavitating Flow of 3D Twisted Hydrofoil and Compared with Experiment. [J]. Chinese Journal of Hydrodynamics, Vol.25 No.6. 721-726.
- Dengcheng Liu, Fangwen Hong. (2010). The Numerical and Experimental Research on Unsteady Cloud Cavitating Flow of 3D Elliptical Hydrofoil. Proceedings of the 9th International Conference on Hydrodynamics. Shanghai China. 2010
- D.Q.Li, Grekula, Prediction of dynamic shedding of cloud cavitation on a 3D twisted foil and comparison with experiments [C], 27th Symposium on Naval Hydrodynamics (Cav2003), Seoul, Korea, Oct. 5-10, 2008
- Francisco Pereira et al. 2002. Experimental and Numerical Investigation of the Cavitation Pattern on a Marine Propeller.[C]. 24th Symposium on Naval Hydrodynamics. Fukuoka, Japan, 8-13 July.
- Francesco Salvatore et al. 2003. A Viscous/Inviscous Coupled Formulation for Unsteady Sheet Cavitation

- Modelling of Marine Propellers. [C]. Fifth International Symposium on Cavitation (cav2003) Osaka, Japan, November 1-4.
- Inanc Senocak, Wei Shyy. 2002. A Pressure-Based Method for Turbulent Cavitating Flow Computation. [J].Journal of Computational Physics. 176,363-383.
- Kubota, A., Kato, H., and Yamaguchi, H., 1992. A New Modeling of Cavitating Flows: A Numerical Study of Unsteady Cavitation on A Hydrofoil Section. [J]. J. of Fluid Mechanics, Vol.240, 1992, pp.59-96.
- Kunz, R.F., Boger, D.A., Stinebring, D.R., Chyczewski, T.S., Lindau, J.W., Gibeling, H.J., Venkateswaran, S., and Govindan, T.R., 1996. A preconditioned Navier-Stokes method for two-phase flows with application to cavitation prediction,[J]. Computers and Fluids, Vol.29, 2000, pp.849-875.
- Merkle. C. L, Feng. J, Buelow. P. E. O. 1998. Computational Modeling of the Dynamics of Sheet Cavitation. [C].Proceedings of 3rd International Symposium on Cavitation, Grenoble, France.
- Niklas, Christer Fureby. 2003. LES of the Flow past Simplified Submarine Hulls. [C]. The 8th International Conference on Numerical Ship Hydrodynamics. Busan. Korea. September 22-25.
- Singhal.A.K, Athavale. M.M.. 2002. Mathematical Basis and Validation of the Full Cavitation Model. [J].Journal of Fluids Engineering.Vol.124.617-624.
- Shin Hyung Rhee, Takarumi Kawamura. 2003. A Study of Propeller Cavitation Using A RANS CFD Method. [C]. The 8th International Conference on Numerical Ship Hydrodynamics. Busan. Korea. September 22-25.

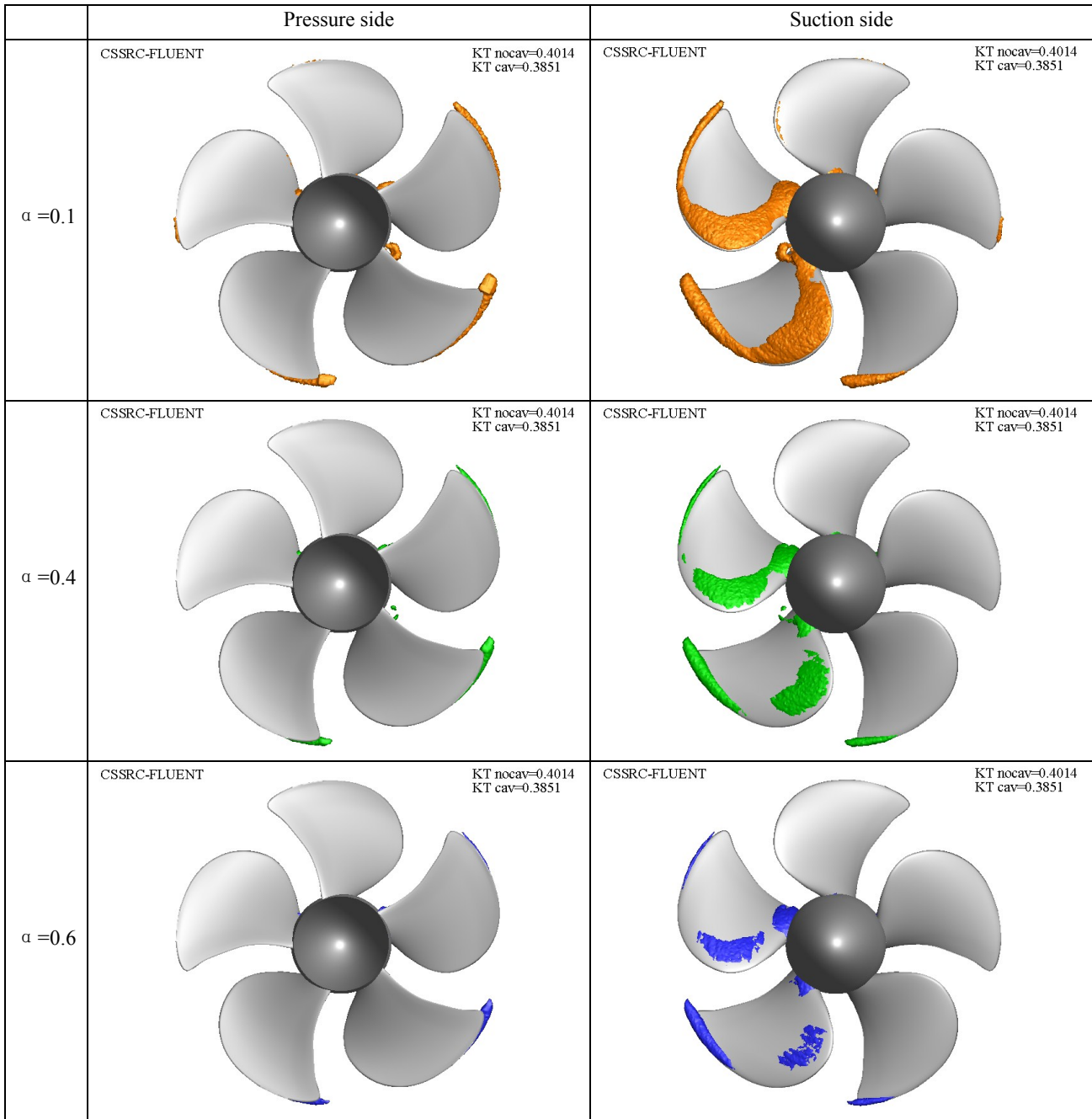


Figure.3 computed cavity shapes of case2-1(J=1.019)

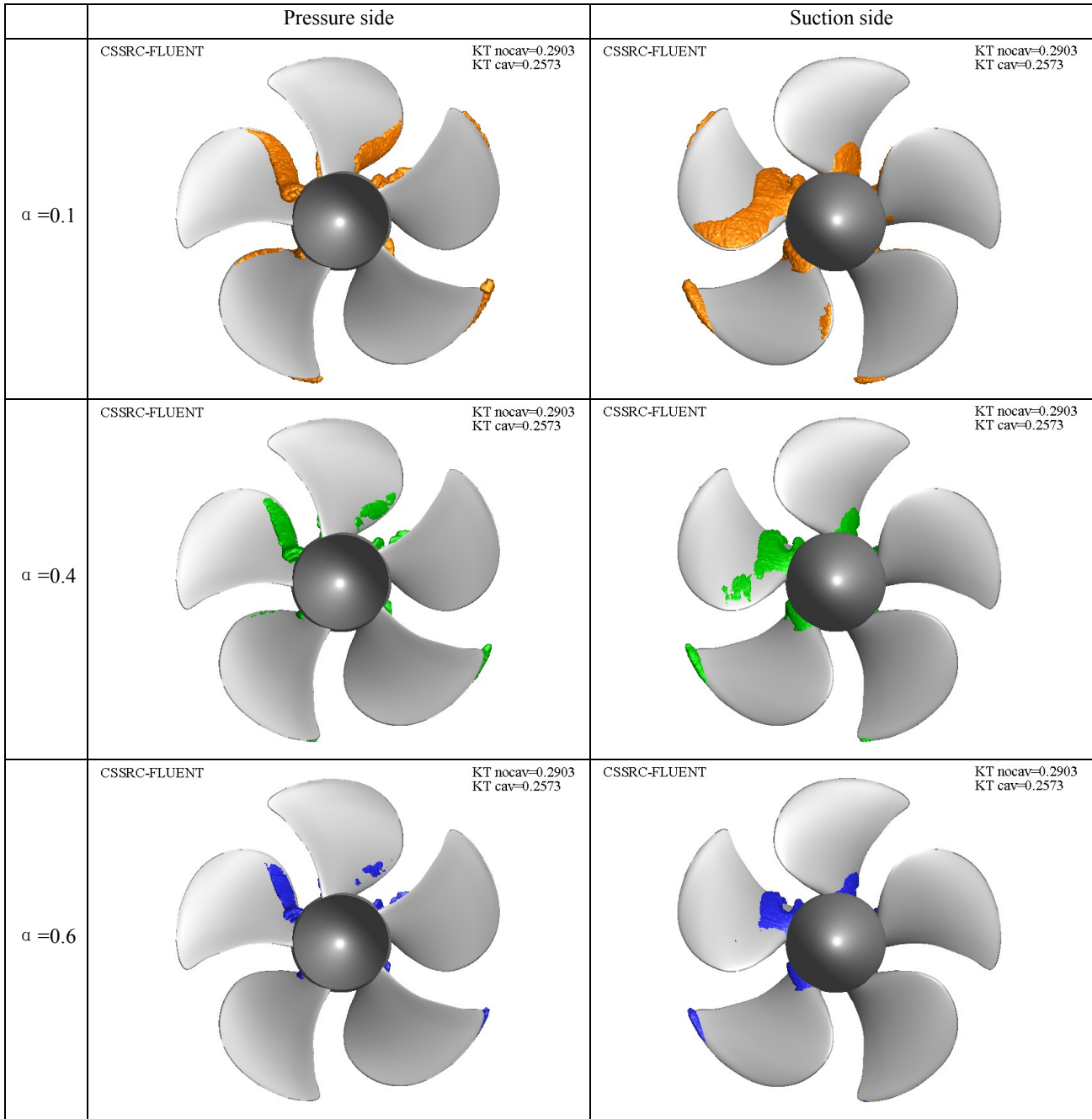


Figure.4 computed cavity shapes of case2-2($J=1.269$)

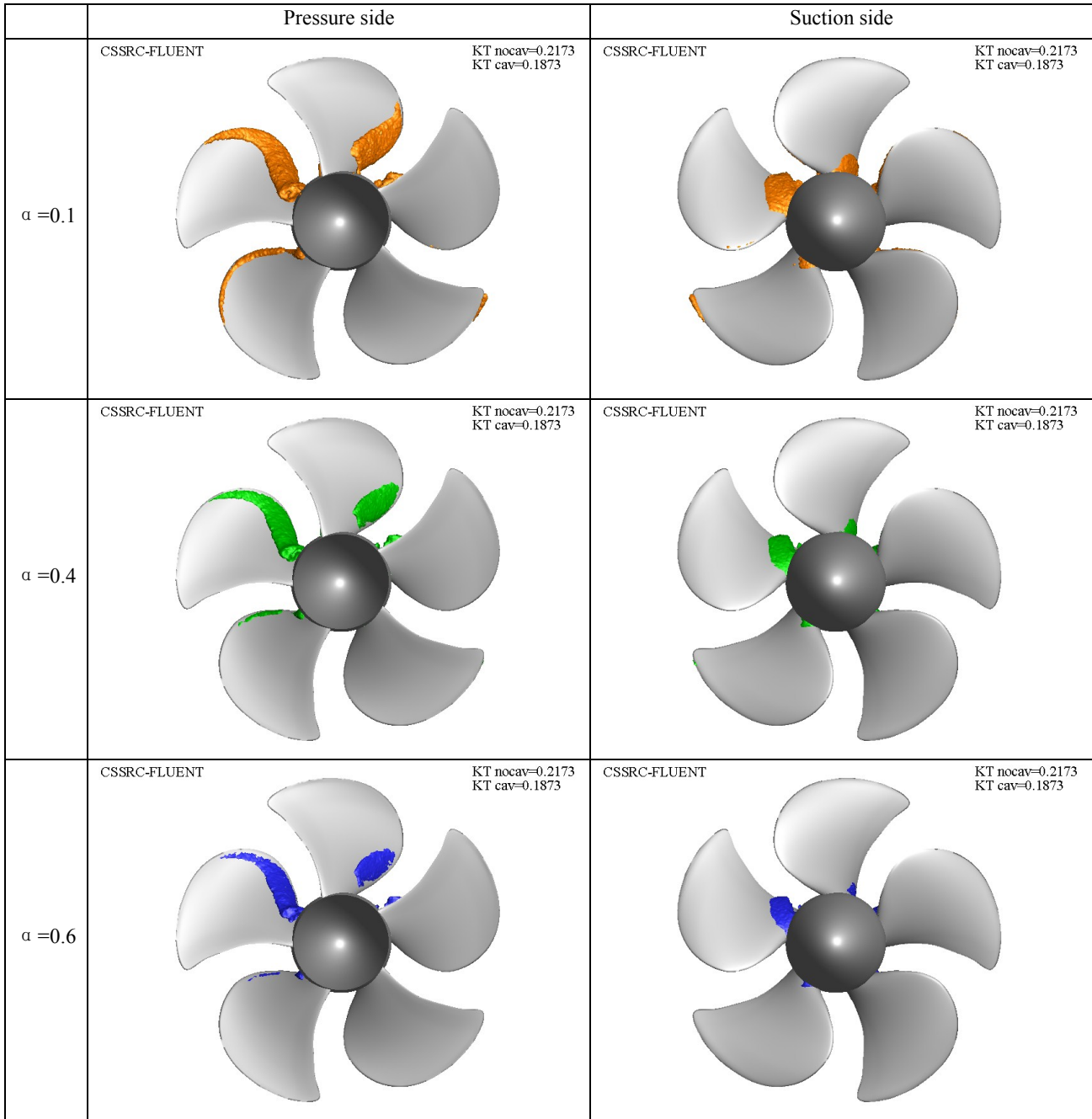


Figure.5 computed cavity shapes of case2-3($J=1.408$)

The Numerical Predicted of VP1304 Propeller Performance in Oblique Flow

Dengcheng Liu

China Ship Scientific Research Center (CSSRC), Wuxi, China

ABSTRACT

Second international workshop on cavitating propeller performance will hold in Austin, USA, at the end of smp'15. The workshop emphasis will be on prediction of propeller hydrodynamic performance and propeller cavitation performance in oblique flow, and the blind test will be performed at Potsdam Model Basin. In this paper, the open water performance of VP1304 propeller in oblique flow was numerically simulated using a hybrid mesh based on steady RANS solver. RSM turbulence model were coupled in the RANS solver. The requested force and torque coefficient were present for appointed case. In addition, the added results of pressure contour were given for analyzing propeller performance.

Keywords

PPTC, Oblique, Numerical simulation.

1 INTRODUCTION

The propeller hydrodynamic performance in oblique were investigated more than 10 years, the famous test cases are the D4679 propeller in 7.5 degree oblique flow and HSP propeller in 10 degree oblique flow. Recently some researchers from Canada and Norway have published some experimental data on pod propulsors at static azimuthing angles. These test data are used to develop and validate the CFD method.

The first workshop on cavitation and propeller performance held in Hamburg, Germany, at the end of smp'11. the workshop emphasis will be on prediction of propeller VP1304 hydrodynamic performance and propeller cavitation performance in uniform flow, the test were blind test at Potsdam Model Basin. A large number of different research groups participated, and the workshop become a success.

Now the second international workshop on cavitating propeller performance will hold in Austin, USA, at the end of smp'15. The workshop emphasis will be on prediction of propeller hydrodynamic performance and propeller cavitation performance in oblique flow, and the blind test will also be performed at Potsdam Model Basin.

In this paper, the open water performance of VP1304 propeller in oblique flow was numerically simulated. The requested data of SMP11 workshop were given.

2 Numerical Method

We used a commercial CFD code FLUENT14.0 which employs a cell-centered finite volume method based on unstructured mesh. The open water performance of VP1304 propeller in oblique flow was numerically simulated using a hybrid mesh based on steady RANS solver. The RSM turbulence model was chosen. Convection terms are discretized using a second order accurate upwind scheme, while diffusion terms are discretized using a second order accurate central differencing scheme. A segregated solver with SIMPLE as the velocity-pressure coupling algorithm was selected. The discrete equations are solved using pointwise Gauss-Seidel iterations, and algebraic multi-grid method accelerates the solution convergence.

The governing equations are written for the mass and momentum conservation of mixture fluid as follows:

$$\frac{\partial (\rho u_i)}{\partial x_i} = 0 \quad (1)$$

$$\frac{\partial (\rho u_i u_j)}{\partial x_j} = -\frac{\partial p}{\partial x_i} + \frac{\partial}{\partial x_j} \left[(\mu + \mu_t) \left(\frac{\partial u_i}{\partial x_j} + \frac{\partial u_j}{\partial x_i} \right) \right] \quad (2)$$

Where μ is the mixed viscosity, μ_t is the mixed eddy viscosity.

3 Computational Condition

3.4 Geometry model and the cases

In this paper, the research object is a five bladed propeller. It is a controllable pitch propeller with diameter $D=0.250\text{m}$, hub diameter ratio of 0.3, pitch-to-diameter ratio of 1.635 at 0.7 radial section, skewed angle of 19.12° and area ratio of 0.78. Table 1 is the cases of open water computational. J is advance ratio. N is rotational

speed of propeller. The expression of advance ratio, thrust and torque coefficient is written as follow:

$$J = \frac{V}{ND}, \quad K_t = \frac{T}{\rho N^2 D^4}, \quad K_q = \frac{T}{\rho N^2 D^5} \quad (3)$$

Table.1 the cases of open water computational

Water density(kg/m ³)	998.62
Kinematic viscosity of water(m ² /s)	1.057e-6
Rate of revolutions(1/s)	15
Inclination angle(°)	12

3.5 Computational mesh and conditions

For steady oblique flow simulation, the computational domain was created as cylinder surrounding propeller. A hybrid mesh was generated using GAMBIT. The blade and hub surface was meshed with triangles which the size is 4% propeller diameter. The volume cells are grew from the wall surface with the 1.1 ratio, and the limited size is 12% propeller diameter. The number of tetrahedral cells was about 6.8 million. The remaining region in the domain was filled with hexahedral cells, and the number of hexahedral cells was about 2.8 million. Figure 1 presents the propeller surface mesh.

Boundary conditions were set to simulate the flow around a rotating propeller: on the inlet boundary and the outer boundary, x-velocity components and z-velocity components of uniform stream with the given inflow speeds were imposed which is calculated by advance coefficient and oblique angle; on the blade and hub surface, the no slip condition was imposed; on the exit boundary, the static pressure was set to a constant value.

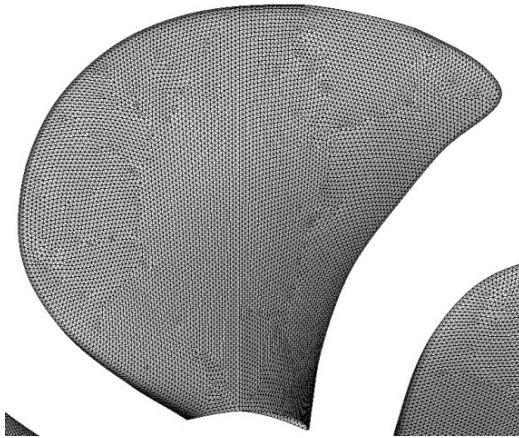


Figure.1 the propeller surface mesh

4 Results

4.1 Open water performance

Figure 2 presents the coordinate system. Table 2 presents the predicted thrust and torque coefficient. Especially the propeller force in z-direction becomes bigger when the advance ratio increases.

Table.2 predicted open water performance

J	Ktx	Kty	Ktz	10Kq
0.6	0.6225	0.0241	0.0384	1.3940
0.8	0.5062	0.0201	0.0601	1.1660
1.0	0.4094	0.0141	0.0863	0.9915
1.2	0.3167	0.0073	0.1150	0.8254
1.4	0.2193	0.0024	0.1419	0.6392

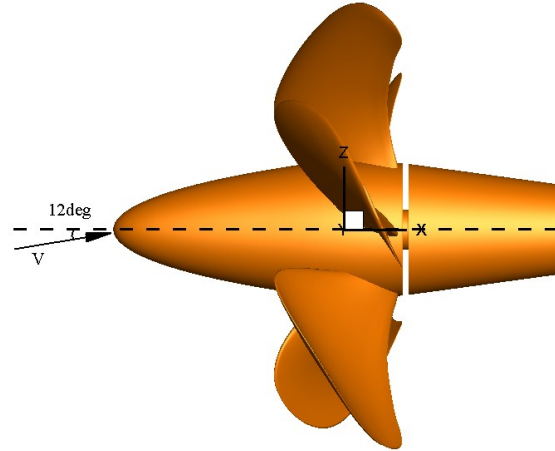


Figure.2 the coordinate coordinate

4.2 Pressure distribution

We simulated propeller open water performance in oblique flow at five different advance ratios, and we can gain the pressure coefficient distribution of propeller surface. Figure 3 ~ figure 7 present the pressure coefficient distribution at different cases. The expression of pressure coefficient is written as follow:

$$C_p = \frac{P - P_0}{\frac{1}{2} \rho V^2} \quad (4)$$

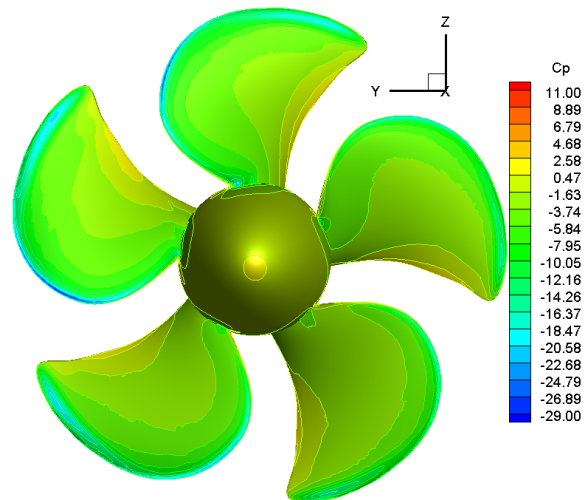


Figure.3 the pressure coefficient distribution (J=0.6)

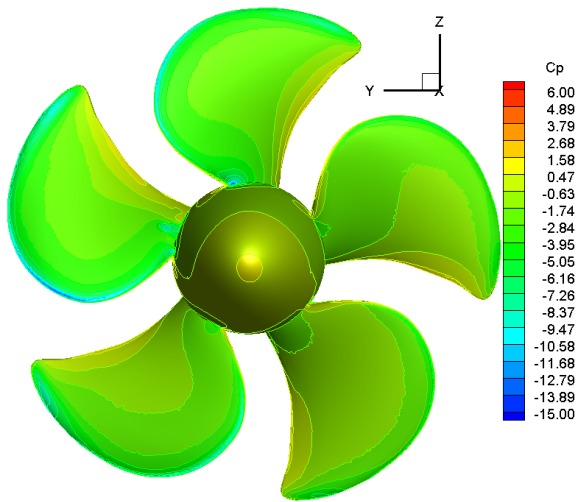


Figure.4 the pressure coefficient distribution ($J=0.8$)

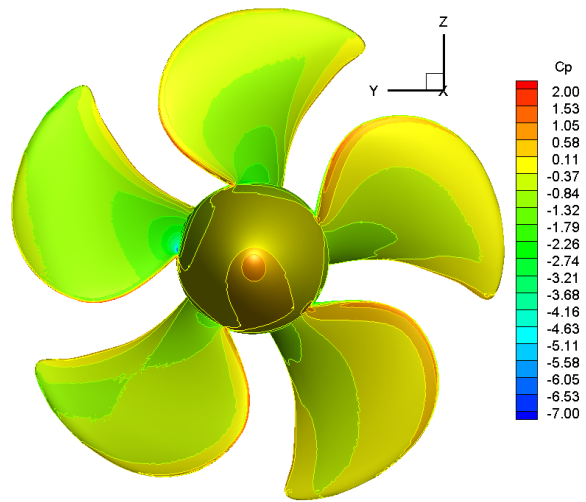


Figure.7 the pressure coefficient distribution ($J=1.4$)

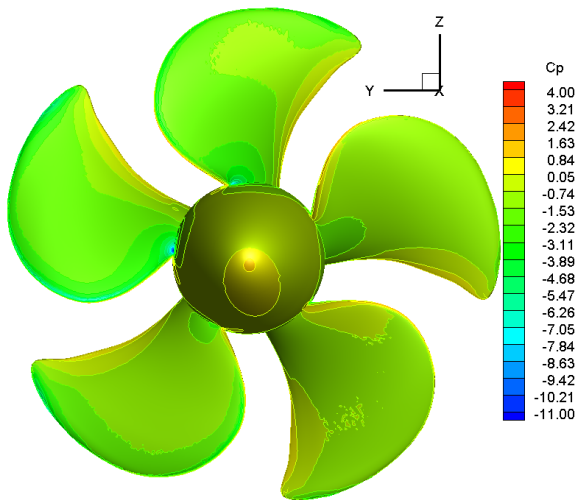


Figure.5 the pressure coefficient distribution ($J=1.0$)

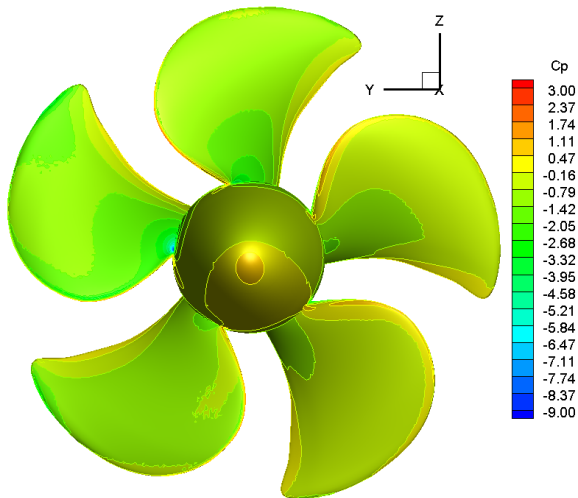


Figure.6 the pressure coefficient distribution ($J=1.2$)

4 Conclusions

In this paper, the open water performance of VP1304 propeller in oblique flow was numerically simulated using a hybrid mesh based on steady RANS solver. RSM turbulence model were coupled in the RANS solver. The requested force and torque coefficient were present for appointed case. In addition, the added results of pressure contour were given for analyzing propeller performance.

REFERENCES

- The propulsion committee, Final report and recommendations to the 22nd IITC. 1998.
- Islam, Mohammed F et al, Performance characteristics of static and dynamic azimuthing podded propulsor. Proceedings of the First international symposium on marine propulsors, smp'09, pp.482-492, 2009-01-01.
- SVA PPTC team. Case1: Propeller forces in oblique flow of 12°. Second international workshop on cavitating propeller performance, May 31- June 4, 2015..

The Potsdam Propeller Test Case in oblique flow: prediction of propeller performance, cavitation patterns and pressure pulses

Thomas Lloyd¹, Guilherme Vaz², Douwe Rijpkema², Bart Schuiling²

{t.lloyd; g.vaz; d.r.rijpkema; b.schuiling}@marin.nl

¹ MARIN Academy, Wageningen, The Netherlands; ² MARIN, Wageningen, The Netherlands

ABSTRACT

We report computations performed as part of the Second International Workshop on Cavitating Propeller Performance, using the Potsdam Propeller Test Case. The requested computations differ from the previous workshop in that the propeller was tested with a shaft inclination of 12 degrees. Hence all computations were performed unsteady. Results are reported for both open-water (non-cavitating) and cavitating conditions, including prediction of pressure pulses inside the cavitation tunnel, using the computational fluid dynamics code *ReFresco*.

Three unstructured grids were generated: one designed for use with wall functions (Coarse); and two with a wall resolved grid (Medium and Fine). The Fine grid also had increased refinement in the region of the sliding interface. Small differences in the prediction of the propeller performance coefficients were found between the three grid types (less than one percent).

The grids were seen to resolve the wake flow well, including transport of the tip vortex and capture of the shaft vortex which impinges onto the strut. Due to the shaft inclination, a strong circumferentially varying propeller loading distribution and cavity pattern was seen. Differences in the predicted cavity patterns were small between the Coarse and Medium grids. The reduction in thrust and torque due to cavitation was underpredicted compared to the experimental observations. Propeller thrust increases slightly for the pressure pulses case, due to the reduced distance between the blade tip and the tunnel ceiling. The pressure pulse amplitudes are seen to increase due to cavitation, including additional higher frequency content.

1 INTRODUCTION

Benchmarking of numerical tools is important as part of code development. Hence validation cases are a valuable means to analyse code performance. In this paper we report our contribution to the Potsdam Propeller Test Case (PPTC) workshop 2015, wherein comparisons will be made to experimental observations as well as other codes. The test case aims at providing a dataset for examining the performance of computational tools for predicting both non-cavitating and cavitating propeller flows, in both open-

water and cavitation tunnel setups. The first workshop (SMP11, 2011) considered the more common straight-ahead condition, while in the present workshop computations were performed for the same propeller with a shaft inclination of 12 degrees.

In §2, key details of the numerical approach are given. Next, the test case is summarised in §3. §4 outlines the simulation setup and data processing. The results are divided into three main sections, namely open water simulations in §5.1, cavitation observation in §5.2 and pressure pulses in §5.3. Finally, a summary is given in §6.

2 NUMERICAL APPROACH

We solved the governing flow equations using the computational fluid dynamics (CFD) code *ReFresco* (www.refresco.org), developed by MARIN in collaboration with various universities worldwide. The code has previously been used for verification and validation studies of propulsors (Rijpkema and Vaz, 2011). The code adopts a finite volume face-based approach, permitting the use of grid cells with an arbitrary number of faces, which eases the gridding of complex engineering geometries. Flow variables are colocated at cell centres, and the equations coupled using a segregated SIMPLE-type solution algorithm. Parallelisation is achieved using Message Passing Interface and domain decomposition.

Numerous turbulence modelling approaches, cavitation models and numerical schemes are available; here we focus on details relevant to the present work. We performed Reynolds-averaged Navier-Stokes computations, using the $k - \omega$ SST 2003 model for turbulence. Using this approach, all the turbulence is modelled. For cavitation we used a modified version of the Sauer model (Sauer and Schnerr, 2001), which we prefer based on previous experience (Hoekstra and Vaz, 2009; Vaz *et al.*, 2015). All flow variables were discretised in space using second-order schemes, except for the convective flux of the turbulence quantities which was treated using a first-order upwind scheme. Time stepping was achieved using an implicit three time level (second-order) scheme for wetted flow computations, with an Euler (first-order) scheme used for cavitation simulations.

3 TEST CASE DESCRIPTION

3.1 Case overview

A brief overview is provided here; full details of the test case are provided by SMP15 (2015) and SVA (2015). The current workshop considers similar cases to those previously reported, but with a shaft inclination angle of 12 degrees (see Figure 1). This setup causes the propeller to experience an inhomogeneous inflow velocity, leading to circumferentially varying loading and cavitation. Therefore all simulations were performed in unsteady mode.

The propeller itself is five-bladed, has a diameter (D_P) of 0.25 m, and rotates in a clockwise (right-handed) direction relative to the x -axis ($+ve$ upstream; see Figure 1). The advance ratio is defined as

$$J = \frac{U_0}{nD_P} = \frac{U_0}{U_{ref}}, \quad (1)$$

where U_0 is the inflow speed and n is the rotation rate.

We present results from each of the three requested cases: Cases 1 (open-water), 2 (cavitation observation) and 3 (pressure pulses). Information specific to each will be presented in the relevant results section.

3.2 Domain design

Figure 1 provides an overview of the domain used, including the distances to the boundaries and the boundary conditions. The upstream and downstream length was used for both open-water and cavitation tunnel computations. This meant the tunnel geometry provided was extended. The domain size was based on our previous studies (Lloyd *et al.*, 2015), although a downstream length of $10D_P$ was used due to the strong wake expected from the strut. Boundary conditions are shown briefly in Figure 1 and are the same as those used in Lloyd *et al.* (2015), who provide mathematical details.

3.3 Grid generation

Unstructured grids were generated using *Hexpress*[®]. Views of the grid are provided in Figure 2. Figure 2a shows the refinement used on the sliding interface, and in the propeller wake. Due to the complex propeller geometry, a large number of cells were required at the blade edges (as seen in Figure 2b). Three grids were designed:

- “Coarse”: the wall-normal grid resolution is suitable for using wall functions to model the inner part of the boundary layer on all walls; total of $\sim 7M$ cells.
- “Medium”: the wall-normal resolution on the propeller blades was increased so that wall functions were not necessary; $\sim 14M$ cells.
- “Fine”: the sliding interface was refined by a factor of two relative to the “Medium” grid; $\sim 16M$ cells.

Thus the effects of near-wall viscous flow modelling and near-wake resolution could be studied.

4 SETUP AND DATA PROCESSING

A summary of the timesteps and number of computed revolutions for each case is given in Table 1. The timestep used for cavitating flow simulations is much lower than for wetted flow in order to improve time accuracy and maintain stability of the cavitation model. Within each timestep, a total of 100 loops were used to couple the governing equations. Since the propeller forces were seen to still be converging during the first revolution, a minimum of two revolutions were used for all cases. Initialisation of the flow field was achieved using a steady *frozen rotor* solution, computed using the *absolute formulation* of the governing equations (see Rijpkema and Vaz, 2011).

Table 1: Summary of time steps and total simulation time for computed cases: $\Delta\theta$ - timestep in degrees; N_{rev} - total number of computed revolutions.

Case	wetted		cavitating	
	$\Delta\theta/^\circ$	N_{rev}	$\Delta\theta/^\circ$	N_{rev}
1.x	3.0	6	-	-
2.1	3.0	2	1.0	2
3.1	2.8	6	1.4	4

Transformation of the forces from the grid Cartesian coordinate system to the propeller coordinate system (PCS) were made using

$$F_X = F_x \cos \Psi + F_z \sin \Psi, \quad (2a)$$

$$F_Y = F_y \quad (2b)$$

and

$$F_Z = F_x \sin \Psi + F_z \cos \Psi, \quad (2c)$$

where lower case subscripts refer to the grid coordinate system, and upper case to the PCS. The angle Ψ is the shaft inclination, defined as an anticlockwise (left-handed) rotation about the y -axis. The mean force and moment coefficients in the PCS are defined as

$$\bar{K}_{Ti} = \frac{\bar{T}_i}{\rho_0 U_{ref}^2 D_P^2} \quad (3a)$$

and

$$\bar{K}_{Qi} = \frac{\bar{Q}_i}{\rho_0 U_{ref}^2 D_P^3}, \quad (3b)$$

where i denotes a force or moment component, T is thrust, and Q is torque. In all cases, the predicted performance coefficients were computed using an ensemble average over the last complete propeller revolution.

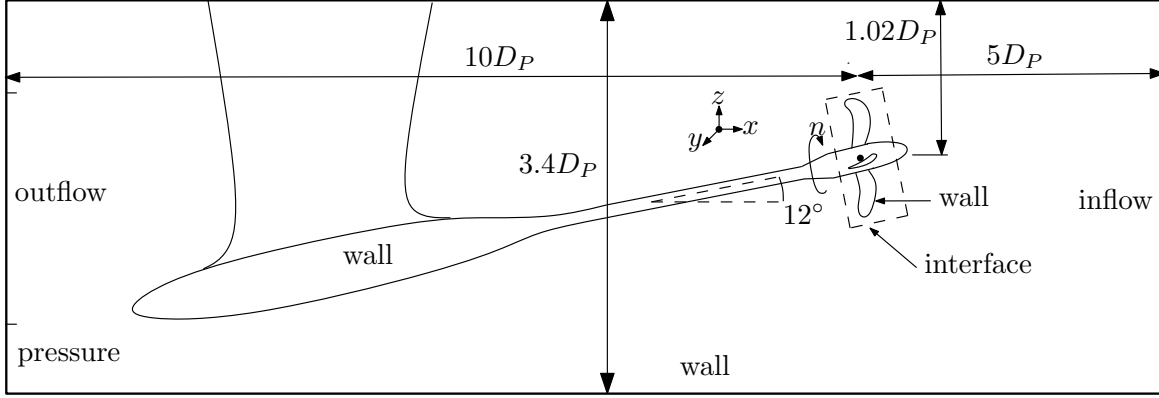


Figure 1: Schematic of domain layout for Case 2. Global origin situated at the centre of the propeller plane. Tunnel geometry extended in axial direction to dimensions shown. For Case 1, domain extends $5D_P$ in the radial direction. Position of the propeller shifted closer to the tunnel ceiling for Case 3. The radial boundary condition for Case 1 is set to a zero pressure condition, while for Cases 2 and 3, this condition is prescribed on the outer part of the outlet boundary. The inner part of the outlet boundary uses an outflow condition to reduce reflections of the propeller and strut wakes.

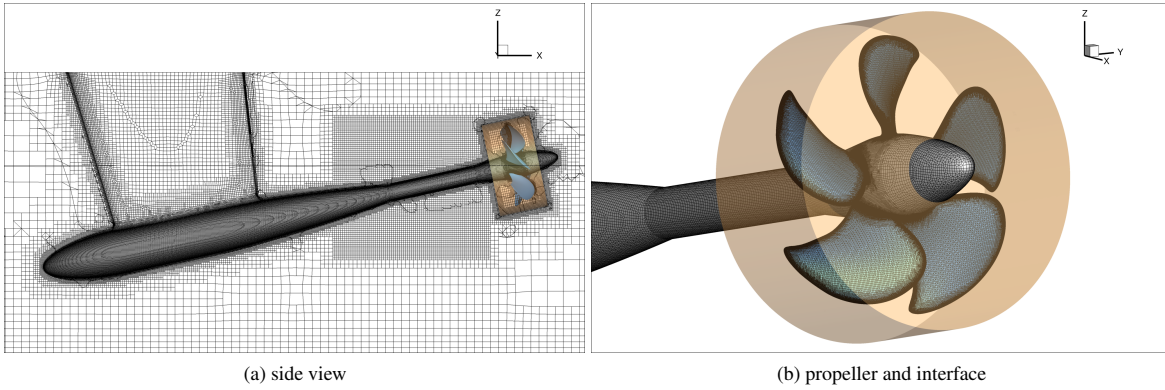


Figure 2: Views of grid (Coarse grid shown)

5 RESULTS

5.1 Case 1: Open-water

In total, five advance ratios were computed for Case 1. Table 2 summarises the propeller performance coefficients in the PCS. The variation in thrust and torque for $J = 0.6$ between the Coarse and Fine grids was found to be less than 1%. In order to reduce computational expense, all further advance ratios were computed using the Coarse grid. The shaft inclination results in large force components in the Y - and Z - directions. A strong reduction in the ratio between K_{TX} and K_{TZ} is also seen as J increases.

Based on the results in Table 2, it was assumed that the Coarse grid, was sufficient to predict the open-water (wetted flow) performance of the PPTC. It was still important however to examine the effect of the near-wall grid resolution on cavitation prediction. Due to limited time, only the Coarse and Medium grids were used for cavitation prediction. A single advance ratio was computed (Case 2.1), although this represented the highest loading condition, and

therefore potentially the most challenging simulation.

5.2 Case 2: Cavitation observation

In this section, we compare results from wetted and cavitating flow computations for Case 2.1. Case 2.1 was chosen since some experimental data were already available. The advance ratio is $J = 1.019$, with a rotation rate of $n = 20$ Hz. The cavitation number, defined as

$$\sigma_n = \frac{2(p_0 - p_v)}{\rho_w U_{ref}^2}, \quad (4)$$

where p_0 is the reference pressure, p_v the vapour pressure and ρ_w the water density, is equal to 2.024.

Visualisation of the flow field is provided in terms of the “Q-criterion” in Figure 3a and normalised axial vorticity $\omega_x^* = \omega_x/n$ in Figure 3b. Figure 3 reveals a number of flow features, including:

- the propeller tip vortex, which is well resolved through the sliding interface and inside the wake refinement region;

Table 2: Summary of performance coefficients for all open-water cases (K_Q values multiplied by 10).

Case	J	Grid	K_{TX}	K_{TY}	K_{TZ}	K_{QX}	K_{QY}	K_{QZ}
1.1	0.6	C	0.628	-0.016	0.286	1.429	-0.150	0.374
		M	0.630	-0.015	0.286	1.421	-0.148	0.372
		F	0.628	-0.015	0.285	1.418	-0.148	0.370
1.2	0.8	C	0.523	-0.019	0.267	1.223	-0.195	0.263
1.3	1.0	C	0.411	-0.025	0.238	1.028	-0.217	0.163
1.4	1.2	C	0.303	-0.030	0.213	0.825	-0.236	0.069
1.5	1.4	C	0.198	-0.038	0.195	0.610	-0.256	-0.032

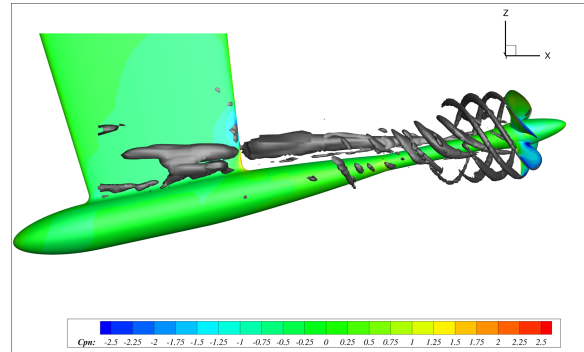
Table 3: Summary of performance coefficients for all cavitation tunnel cases (K_Q values multiplied by 10). Experimental values from SVA (2015) denoted as 'exp'.

Case	J	Flow	Grid	K_{TX}	K_{TY}	K_{TZ}	K_{QX}	K_{QY}	K_{QZ}
2.1	1.019	wetted	C	0.400	-0.022	0.238	1.004	-0.221	0.142
			M	0.403	-0.026	0.237	0.999	-0.224	0.144
			exp	0.397	-	-	1.020	-	-
		cavitating	C	0.386	-0.019	0.238	0.983	-0.195	0.142
			M	0.387	-0.019	0.236	0.979	-0.195	0.147
			exp	0.360	-	-	0.960	-	-
3.1	1.019	wetted	C	0.408	-0.027	0.244	1.000	-0.237	0.130
		cavitating	C	0.389	-0.019	0.237	0.977	-0.199	0.143

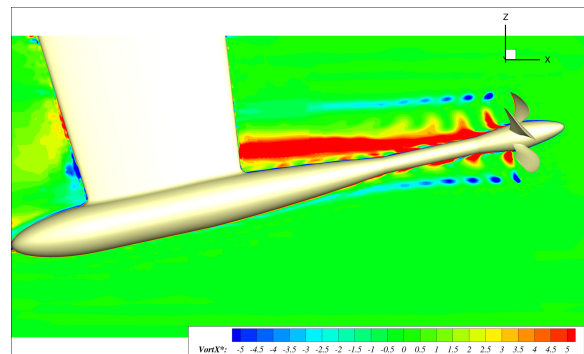
- counter-rotating hub vortices which wrap around the inclined shaft;
- flow separation on the shaft, which propagates to the strut before splitting.

Differences in the propeller forces (K_{TX}) between wetted and cavitating flow solutions are shown in Figure 4. The wetted flow force is not periodic, which may be due to differences in the grid on each blade surface when using Hexpress. The variation in K_{TX} for wetted flow is small however ($< 1\%$), with a larger fluctuation seen for the cavitating flow due to the cavity dynamics ($\sim 4\%$). The cavitating solution shows periodicity in the total propeller force, as well as a lower mean value. This is expected due to the thrust reduction caused by the cavitation, which is seen in the experimental values in Table 3. Figure 4a also shows some higher frequency content due to the cavity dynamics; the blade forces for wetted flow are more sinusoidal. As for Case 1, the differences in the predicted performance coefficients between Coarse and Medium grids is small. The reduction in thrust and torque due to the presence of cavitation is however seen to be much smaller than in the experiment (K_{TX} reduces by $\sim 4\%$ compared to $\sim 9\%$ in the experiment).

Figure 5a shows the blade surface pressure and limiting streamlines. This highlights the strong circumferential variation in the propeller loading due to the shaft inclination. For this loading condition ($J = 1.019$) we also see some flow separation on the downgoing blade, close to the



(a) $Q = 1 \text{ s}^{-1}$



(b) normalised vorticity on a slice at $y = 0$

Figure 3: Visualisation of flow field for Case 2.1 (wetted flow) using Medium grid.

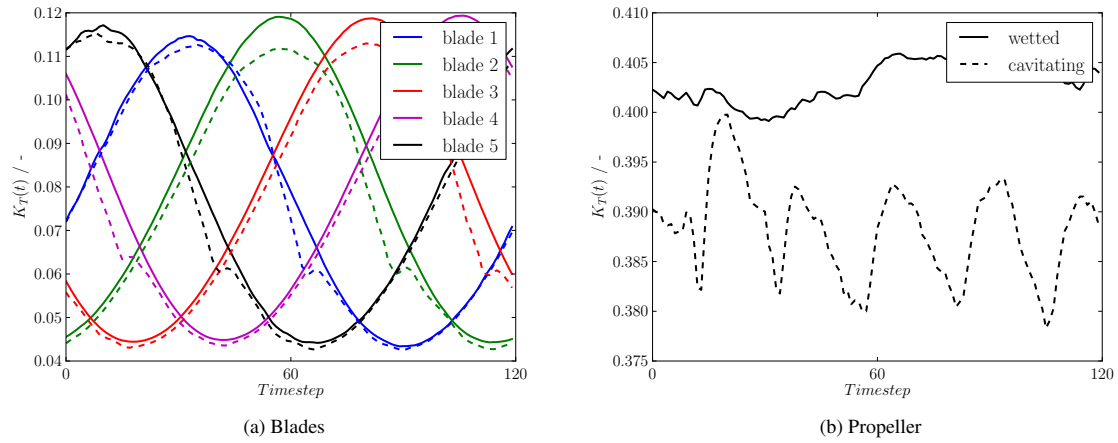


Figure 4: Time traces of forces for wetted and cavitating flow (Case 2.1) using Medium grid.

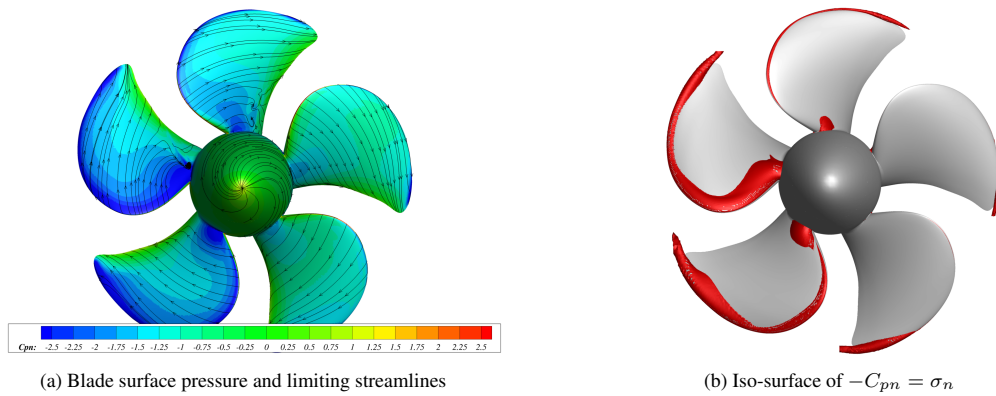


Figure 5: Blade surface pressure for Case 2.1 using Medium grid.



Figure 6: Iso-surfaces of vapour volume fraction $\alpha_v = 0.4$ on suction side for Case 2.1. Chosen value of α_v corresponds to that requested as part of workshop; we see little sensitivity in the cavity extent to the choice of α_v .

blade root. In Figure 5b, an iso-surface of $-C_{pn} = \sigma_n$ reveals where cavitation inception would take place. We predict continuous cavitation in the tip region, while the downgoing blade experiences cavitation along the entire leading edge.

Next we compare cavitation pattern prediction for both Coarse and Medium grids. Figure 6 reveals that the prediction of the vapour extent is remarkably similar between the two grids; the cavitation pattern has not been significantly affected by the use of wall functions. A small difference is seen on the downgoing blade, where the Coarse grid gives a larger cavity extent. At the top dead centre (TDC) position however, the predictions are very similar. Figure 7 compares the predicted cavity extent in the TDC position to the experimental sketch. Clearly the tip vortex cavity is under-predicted, which is a common issue for RANS computations. We do predict however a leading edge cavity along a large part of the blade span, which leads to questions concerning the nucleation process used in the experiments. In addition, the bubble cavitation seen in the experiment at the lower radii manifests as a small sheet in the computations close to the root.

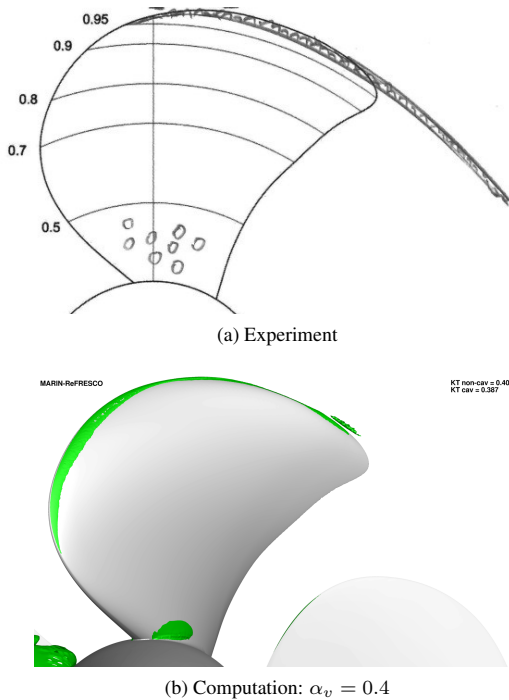


Figure 7: Comparison of cavity extent at blade top dead centre position for Case 2.1.

Finally in this section, we show the development of the total vapour volume for Case 2.1 (Figure 8). After initialisation of the cavitation model, the volume is seen to overshoot before reducing to a lower mean level. The total vapour volume predicted by the Medium grid is smaller than that for the Coarse grid. The fluctuation in total vol-

ume is seen to be relatively small, primarily due to the high blade number (blade area ratio of 0.779).

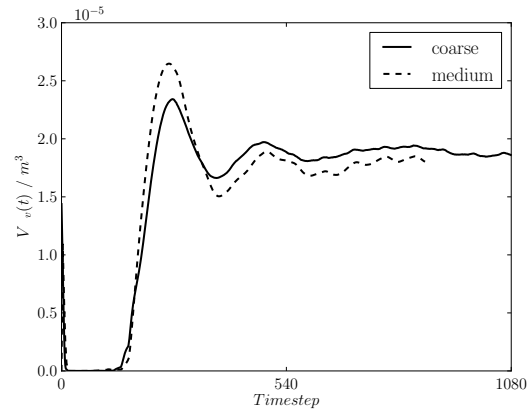


Figure 8: Total vapour volume for Case 2.1.

5.3 Case 3: Pressure pulses

Based on the similarity between the Coarse and Medium grid results for Case 2.1, it was decided to only compute the pressure pulses using the Coarse grid.

Table 3 also shows the performance coefficients predicted for Case 3.1. Small increases in thrust coefficient (K_{TX}) are seen for Case 3.1 compared to Case 2.1; approximately 2% and 1% respectively, for wetted and cavitating flow. The torque coefficient is seen to reduce in both cases, by less than 1%. These differences are likely due to the increased local blockage in the tip region at the blade top dead centre position. Further analysis in this region may reveal local differences in the flow field, but is outside the scope of this paper.

Finally, in Figure 9, we present pressure pulse predictions for wetted and cavitating flow at the three probe positions specified. For Probes 2 and 10, the amplitude of the signals clearly increases when cavitation is present. For Probe 5, the first harmonic does not increase. This makes sense however, since Probe 5 is closest to the propeller, and thus experiences a stronger near-field pressure loading than the other probes. The wetted and cavitating signals also exhibit a noticeable phase difference compared to Probes 2 and 10. All signals contain more higher frequency components for the cavitating compared to the wetted flow, particularly Probes 2 and 10.

6 SUMMARY

The main outcomes of this work are summarised as:

- Refinement in the near-wall and sliding interface regions of the grid led to only small differences in the predicted performance coefficients (Case 1).
- Shaft inclination causes strong spatial variation of the propeller loading distribution and therefore cavity pattern (Case 2.1).

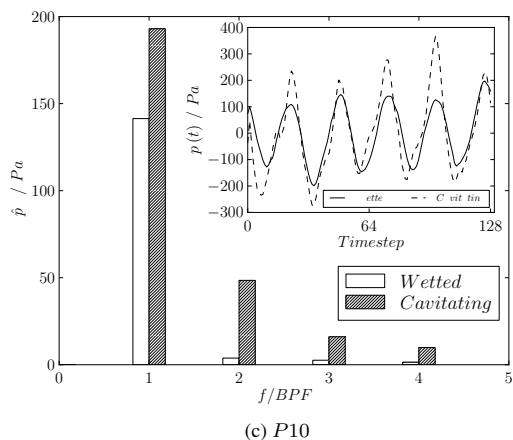
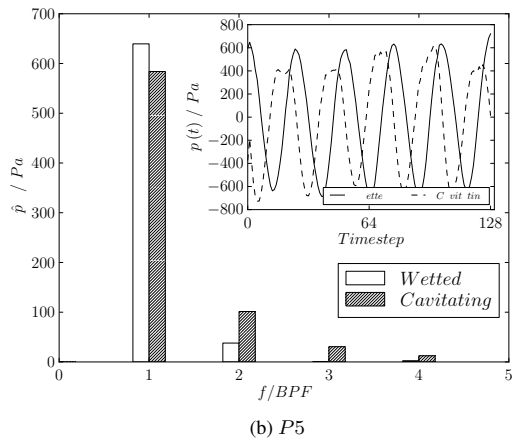
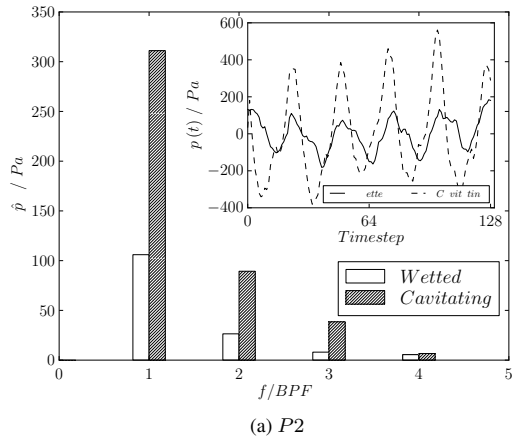


Figure 9: Harmonic amplitudes and time traces for pressure pulses over one propeller revolution for Case 3.1. Probe locations in metres: P2 - (-0.081, 0.0, 0.173); P5 - (-0.031, 0.0, 0.173); P10 - (0.019, 0.0, 0.173). Frequency f normalised by blade passing frequency (BPF).

- The predicted cavity pattern is very similar for both Coarse and Medium grids. Therefore the influence of the wall function approach for near-wall modelling has not had a significantly negative effect on cavitation prediction (Case 2.1).
- The presence of unsteady cavitation increases the amplitude of pressure pulses, especially for probes not directly above the propeller, as well as adding more higher frequency content to the signals (Case 3.1).

Due to limited time available, not all of the advance ratios requested have been completed. As part of future work it would be interesting to examine the behaviour of the PPTC for different advance ratios and cavitation numbers.

REFERENCES

- Hoekstra, M. and Vaz, G. (2009), The partial cavity on a 2D foil revisited. In: *Proceedings of CAV2009*, 17th-22nd August, Michigan.
- Lloyd, T.P., Rijpkema, D. and van Wijngaarden, E. (2015), Propeller acoustic modelling: comparing CFD results with an acoustic analogy approach. In: *Proceedings of the 4th Symposium on Marine Propulsors*, 31 May-4 June, Austin.
- Rijpkema, D. and Vaz, G. (2011), Viscous flow computations on propulsors: verification, validation and scale effects. In: *Proceedings of Marine CFD*, London.
- Sauer, J. and Schnerr, G.H. (2001), Development of a new cavitation model based on bubble dynamics. *ZAMM - Journal of Applied Mathematics and Mechanics / Zeitschrift für Angewandte Mathematik und Mechanik*, **81**(S3): pp. 561–562, doi:10.1002/zamm.20010811559.
- SMP11 (2011), Workshop on cavitation and propeller performance. URL http://www.marinepropulsors.com/smp/files/downloads/smp11_workshop/smp11_workshop/.
- SMP15 (2015), 2nd International Workshop on Cavitating Propeller Performance. URL http://www.cae.utexas.edu/smp15/smp_workshop_2015.html.
- SVA (2015), Propeller workshop SMP'15. URL http://www.sva-potsdam.de/pptc_data_15.html.
- Vaz, G., Hally, D., Huuva, T., Bulten, N., Muller, P., Becchi, P., Herrero, J.L.R., Whitworth, S., Macé, R. and Korsström, A. (2015), Cavitating flow calculations for the E779A propeller in open water and behind conditions : code comparison and solution validation. In: *Proceedings of the 4th Symposium on Marine Propulsors*, 31 May-4 June, Austin.

Prediction of Performance of Test-Case Inclined Propeller SMP15 in Cavitating and Non Cavitating Conditions

Emre Gungor^{1,2}

¹ School of Mechanical Engineering, Istanbul Technical University, Gumussuyu, 34437, Istanbul, Turkey

² Roketsan Technology and Research Center (ROTAM), Roketsan Missiles Inc., Istanbul, Turkey

ABSTRACT

In this paper, performance of inclined Propeller in cavitating and non cavitating conditions which is handled in test-case program in SMP15 Workshop was investigated using finite volume based solvers. Experiments were performed at Potsdam Model Basin (Germany) by Schiffbau-Versuchsanstalt Potsdam Team (SVA-PPTC). The three cases for numerical simulations consist of propeller open water test in oblique flow, cavitation observations in oblique flow and calculation of propeller induced pressure pulses. Propeller is operating in inhomogeneous inflow, therefore the characteristics are deeply influenced by inclination angle. Design and off-design conditions were investigated through simulations in pull configuration and cavitating propeller. Performances of those points were all evaluated with CFD analysis to realize the effects of mesh generation, discretization method and turbulence model in numerical process. In order to visualize cavitation behavior, cavitation models are studied in respect of convergence criteria and reasonable output values. Steady and transient mode is so different that pressure fluctuations can be attained accurately using unsteady revolutions. Additionally, pressure pulses for each time step was obtained in three point located in different place of cavitation tunnel.

Keywords

Cavitation, Computational fluid dynamics, Finite volume-based solver, Test-case propeller, validation.

1 INTRODUCTION

Propellers are special propulsion systems which are utilized to propel marine systems as well as underwater vehicles. Propeller design should have high efficiency so as to reduce fuel costs and have high performance in order to attain robust control of vehicles. Reference [1] gives useful information about preliminary stage of propeller design by implementing lifting line theory to foil elements. Combining Reynolds averaged Navier Stokes (RANS) solver with vortex lattice method improves the development of ducted propellers [2]. Boswell [3] obtained main characteristics of propeller series 4382-82-83 and 84 in

cavitation tunnel and represented dimensionless parameters for thrust and torque of them. The experimental results of Boswell's study were used to investigate differences of RANS and panel method in [4]. Liu and Hong [5] dealt with computational fluid dynamics (CFD) problems on a propeller for which experimental results were done in University of Potsdam. As [6] flow simulations of operational conditions for submarine and its propeller can be investigated in finite-volume solvers. Large eddy simulations (LES) are required to establish a proper model for unsteady cases such as ducted propeller in which fixed blades are positioned in front of rotating ones [7]. In comparison to the studies that neglect cavitation effect, Xia et al. [8] handled cavitation occurring on blade surfaces. Cavitation is a deep scope relating to two phase flow which is taken into account in this paper.

The performance characteristics of propeller such as horsepower, thrust, torque and flow behavior can be determined in exclusive test facilities, however they are not cheap enough to execute and need remarkable work, resulting in slower progress. Numerical calculations of computational fluid dynamics take over the studies due to the cost, reliability and time considerations of test facilities. Although experimental tests are trustworthy for many cases, they also consist of uncertainty and errors in a margin so thus special care should be given in applications. Boswell [3] and Denny [9] give the experimental results in graphs for various design points of 4382 and 4119 propellers. In validation part, those test results had been used before to show nice compatibility between test and numerical calculations. Gungor and Ozdemir (2014) showed the whole validation procedure and illustrated the steps to determine the most proper and efficient way of numerical calculation methods [13].

The numerical analyses were done on finite volume method which utilizes the integral formulation of Navier Stokes equations [10]. Second order discretization scheme was chosen for the convective and viscous terms of each governing equation. Turbulence model is so important that suitable model depends on the present case. Mesh

generation should be enough fine and appropriate to get successful result. Therefore physical domain was subdivided into a number of grids in which tetrahedral forms are preferred. The validated steps as in [14] are followed to achieve similar nice results with experiments.

2 NUMERICAL METHOD FOR CFD

2.1 Governing Equations and Turbulence Models

The conservation of mass, momentum and energy are main laws in fluid dynamics and the dynamical behavior of fluid is determined by these laws. The amount of quantity crossing boundary is determined by convective transport and molecular motion. The flow properties around propeller are mainly viscous, incompressible, constant density and viscosity. Equations relating to energy conservation can be neglected. Mass and momentum conservation can be stated as,

$$\nabla \cdot V_i = 0 \quad (1)$$

$$\rho \frac{DV}{Dt} = \rho g - \nabla p + \mu \nabla^2 V \quad (2)$$

Momentum equation (2) consists of inertial, gravity, pressure and viscous forces in sequence. In order to take up fluctuations of turbulence, Reynolds Averaged Navier Stokes (RANS) equations should be used,

$$\frac{\partial \bar{u}_i}{\partial \bar{x}_i} = 0 \quad (3)$$

$$\rho \frac{\partial \bar{u}_i}{\partial t} + \rho \bar{u}_j \frac{\partial \bar{u}_i}{\partial x_j} = \frac{\partial}{\partial x_j} \left[\begin{array}{c} -\bar{p} \delta_{ij} \\ + \mu \left(\frac{\partial \bar{u}_i}{\partial x_j} + \frac{\partial \bar{u}_j}{\partial x_i} \right) \\ - \rho \left(\overline{u'_i u'_j} \right) \end{array} \right] \quad (4)$$

The last term in (4) is Reynolds tensor which should be defined in order to close momentum equation. RANS consists of more unknowns than number of equation system to be solved. Material derivative of (4) is,

$$\begin{aligned} \frac{D \overline{u_i u_j}}{Dt} = \frac{\partial}{\partial X_i} \left[\begin{array}{c} -\overline{u_i u_j u_i} \\ -\frac{p}{\rho} (\delta_{ji} u_i + \delta_{ji} u_j) \\ + \nu \frac{\partial \overline{u_i u_j}}{\partial X_i} \end{array} \right] \\ - \left(\overline{u_i u_i} \frac{\partial U_j}{\partial X_i} + \overline{u_j u_i} \frac{\partial U_i}{\partial X_i} \right) \\ - 2\nu \frac{\partial \bar{u}_i}{\partial X_i} \frac{\partial \bar{u}_j}{\partial X_i} + \frac{p}{\rho} \left(\frac{\partial u_i}{\partial X_j} + \frac{\partial u_j}{\partial X_i} \right) \end{aligned} \quad (5)$$

Right hand side of (5) consists of turbulent diffusion, molecular diffusion, production of Reynolds Stress and viscous dissipation [11]. In order to model Reynolds Stress terms there are lots of models developed, however Standard $k - \varepsilon$, RNG $k - \varepsilon$, Standard $k - w$, SST $k - w$ and Spalart Allmaras are taken into account in this study.

2.2 Turbulence Models

According to our investigation, RNG $k - \varepsilon$ was the most proper model found in test-case examinations. Turbulent kinetic energy equation is;

$$\frac{\partial(\rho k)}{\partial t} + \frac{\partial(k u_i)}{\partial x_i} = \frac{\partial}{\partial x_i} \left[\left(\alpha_k \mu_{eff} \right) \frac{\partial k}{\partial x_i} \right] + G_k + G_b - \rho \varepsilon - Y_M \quad (6)$$

Turbulent kinetic energy and rate of dissipation is shown with k and ε . The term G_k represents turbulent kinetic energy production due to the change of velocity in spatial, G_b is turbulent kinetic energy production due to the buoyancy forces, Y_M is the contribution of the fluctuating dilatation in compressible turbulence. The rate of dissipation;

$$\begin{aligned} \rho \frac{D\varepsilon}{Dt} = \frac{\partial}{\partial x_j} \left[\left(\mu + \frac{\mu_t}{\sigma_\varepsilon} \right) \frac{\partial \varepsilon}{\partial x_j} \right] \\ + C_{1\varepsilon} \frac{\varepsilon}{k} (G_k + C_{3\varepsilon} G_b) - C_{2\varepsilon} \rho \frac{\varepsilon^2}{k} \end{aligned} \quad (7)$$

In the turbulence model of RNG $k - \varepsilon$, rate of dissipation equation has advantage over Standard $k - \varepsilon$. Moreover it handles the rotating cases effectively. Prandtl numbers are based on analytical formulations, however Standard $k - \varepsilon$ model has constant numbers. Swirl dominated flows can be solved effectively due to the term R in rate of dissipation equation. RNG model is more responsive to rapid strain and streamline curvature than Standard $k - \varepsilon$ [12]. Flow around propeller is highly strained and this case can be solved in improved equation of

rate of dissipation.

2.3 Solver Type

The conservation equations and transport equations for turbulent scalars are solved in finite volume method. Therefore inside of the whole domain, mesh structure consisting of so many cells is built. Integral forms of transport equation for velocity, pressure and other scalars should be formed in each cell control volume. Pressure based solver is chosen in which velocity field is obtained by solving pressure correction equation. Integral form of transport equations (8) are transformed to algebraic form as in (9).

$$\int \frac{\partial \rho \phi}{\partial t} dV + \oint \rho \phi V \cdot dA = \oint \Gamma_{\phi} \nabla \phi \cdot dA + \int S_{\phi} dV \quad (8)$$

$$\begin{aligned} \frac{\partial \rho \phi}{\partial t} V + \sum_f^{N_{faces}} \oint \rho_f V_f \phi_f \cdot A_f \\ = \sum_f^{N_{faces}} \Gamma_{\phi} \nabla \phi_f \cdot A_f + S_{\phi} V \end{aligned} \quad (9)$$

Pressure segregated algorithm continues until convergence is satisfied. When the propeller rotation is not changing in time, steady flow is valid through process. Moving reference frame is used to represent rotation of propeller. Instead of stationary coordinate system, equations are written for moving reference frame. The velocity observed in rotating frame is,

$$V_r = V - \Omega \times r \quad (10)$$

Momentum equation in rotating frame can be written as,

$$\begin{aligned} S_m = \frac{\partial (\rho V)}{\partial t} + \nabla \cdot (\rho V_r V_r) + 2\Omega \times V_r \\ + \Omega \times \Omega \times r + \rho \frac{\partial \Omega}{\partial t} \times r \end{aligned} \quad (11)$$

On the other hand, sliding mesh should be used to handle inhomogeneous inflow while propeller is rotating especially to observe pressure fluctuations. However it sometimes require huge amount of calculations and high computer capacity. For Case-1 and Case-3, transient behavior was investigated through sliding mesh, but cavitation model would not be included in those cases due to the limitations of computation time.

2.3 Multiphase Flows

Cavitation is a multiphase flow consisting of discrete gaseous phase in a continuous fluid. A liquid may be subjected to a decreasing pressure which can below the saturated vapor pressure and resulting in sudden explosion of bubbles [12]. Approaches to multiphase modeling can be listed as; Euler-Euler Approach, VOF model, Mixture model and Eulerian Model. Mixture model is the appropriate method for two different phases in which

mixture momentum equation is solved and relative velocities are prescribed to describe the phases. Less computational effort is apparent in mixture model than Eulerian model due to the solution of smaller number of equations. This method solves the continuity, momentum and energy equation for mixture; volume fraction equation for secondary phases; algebraic expressions for relative velocities (slip velocity). On the other hand, slip velocities are neglected in cavitation model reducing to a homogeneous multiphase model. Continuity equation for the mixture is,

$$\frac{\partial \rho_m}{\partial t} + \nabla \cdot (\rho_m u_m) = 0 \quad (12)$$

where u_m and ρ_m is mass-averaged velocity and mixture density. Momentum equation can be shown as,

$$\begin{aligned} \frac{\partial \rho_m u_m}{\partial t} + \nabla \cdot (\rho_m u_m u_m) = -\nabla p + \nabla \cdot [\mu_m (\nabla u_m + \nabla u_m^T)] \\ + \rho_m g + F + \nabla \cdot \left(\sum_{k=1}^n \alpha_k \rho_k u_{dr,k} u_{dr,k} \right) \end{aligned} \quad (13)$$

n is the number of phases, F is a body force and μ_m is the viscosity of the mixture. $u_{dr,k}$ is the drift velocity for secondary phase k ,

$$u_{dr,k} = u_k - u_m \quad (14)$$

Cavitation models are based on Rayleigh-Plesset equation which describes the growth of a single vapor bubble in a liquid [12]. Vapor transport equation is,

$$\frac{\partial (\alpha \rho_v)}{\partial t} + \nabla \cdot (\alpha \rho_v u_v) = M_e - M_c \quad (15)$$

M_e, M_c states mass transfer between vapor and liquid phases and they are modeled based on Rayleigh-Plesset equation which describes the growth of a single vapor bubble in a liquid. In Zwart-Gerber-Belamri model, mass transfer rate per unit volume M is calculated using mass change rate of a single bubble and bubble radius,

$$M = n \times (4\pi R_B^2 \rho_v \frac{DR_B}{Dt}) \quad (16)$$

Then mass rate is conducted with Rayleigh-Plesset equation, nucleation site volume fraction α_{nuc} , condensation and evaporation coefficients and bubble radius. If $P \leq P_v$,

$$M_e = F_{vap} \frac{3\alpha_{nuc}(1-\alpha_v)\rho_v}{R_B} \sqrt{\frac{2}{3} \frac{P_v - P}{\rho_l}} \quad (17)$$

If $P \geq P_v$,

$$M_c = F_{cond} \frac{3\alpha_v \rho_v}{R_B} \sqrt{\frac{2}{3} \frac{P - P_v}{\rho_l}} \quad (18)$$

3 TEST-CASE STUDIES

Experiments were performed at Potsdam Model Basin (Germany) by Schiffbau-Versuchsanstalt Potsdam Team (SVA-PPTC) for three different cases. All the required geometry datasheet and solid cad models are presented in [15]. Coordinate axes are located in propeller as in Figure 1.

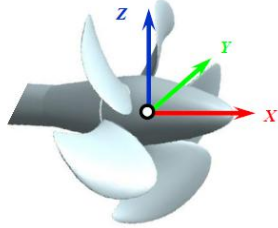


Figure 1: Coordinate axes representation.

3.1 Test Case - 1

In this case propeller is operating in a pull configuration (Figure 2) and propeller is inclined that flow becomes inhomogeneous [15]. Forces generated in three axes are requested in terms of non-dimensional values. Properties are listed in Table 1.

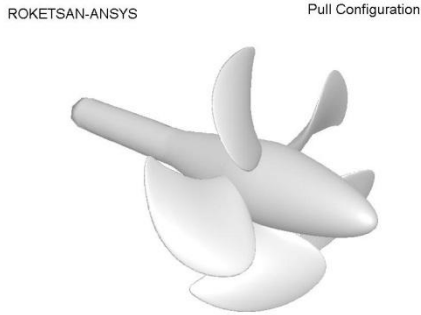


Figure 2: Pull configuration model.

TABLE 1: FLOW PROPERTIES

Property	Symbol	Dimension	Value
Water density	ρ	kg/m ³	998.62
Kinematic viscosity of water	ϑ	m ² /s	1.057E-06
Rate of revolutions	n	1/s	15
Inclination angle	φ	°	12

Dimensionless parameter of advance coefficient, thrust coefficient and torque coefficient are,

$$J = \frac{V_A}{nD} \quad K_t = \frac{T}{\rho n^2 D^4} \quad K_q = \frac{Q}{\rho n^2 D^5} \quad (19)$$

K_{Tx} , K_{Ty} and K_{Tz} are requested for advance coefficients $J=0.6, 0.8, 1.0, 1.2$ and 1.4 .

3.2 Test Case - 2

Inclined propeller test was applied in cavitation tunnel as illustrated in Figure 3. It is requested to calculate cavitation pattern for three operation points for a blade position of 0°. For different volume fractions cavity surface and thrust coefficient with and without cavitation condition should be provided.

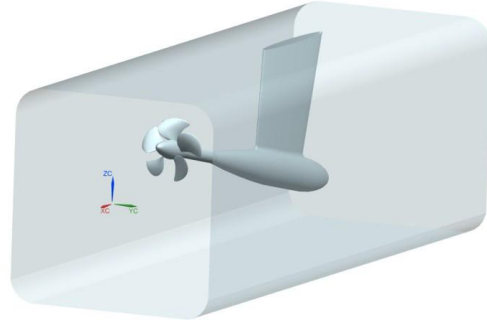


Figure 3: Inclined propeller test in cavitation tunnel

The inputs simulating the cavitation inflow are given in Table 2 for three operating points.

TABLE 2: THE FLOW INPUTS FOR THREE CONDITIONS

Property	Symbol	Dimension	Value
Advanced coefficient	J	–	1.019
Cavitation number	σ	–	2.024
Rate of revolutions	n	1/s	20
Water density	ρ	kg/m ³	997.78
Kinematic viscosity of water	ϑ	m ² /s	9.567E-07
Vapour pressure	p_v	Pa	2643
Oxygen saturation	α/α_s	%	46.05
Inclination angle	φ	°	12
Property	Symbol	Dimension	Value
Advanced coefficient	J	–	1.269
Cavitation number	σ	–	1.424
Rate of revolutions	n	1/s	20
Water density	ρ	kg/m ³	997.8
Kinematic viscosity of water	ϑ	m ² /s	9.591E-07
Vapour pressure	p_v	Pa	2626
Oxygen saturation	α/α_s	%	46.74
Inclination angle	φ	°	12
Property	Symbol	Dimension	Value
Advanced coefficient	J	–	1.408
Cavitation number	σ	–	2.000
Rate of revolutions	n	1/s	20
Water density	ρ	kg/m ³	997.41
Kinematic viscosity of water	ϑ	m ² /s	9.229E-07
Vapour pressure	p_v	Pa	2904
Oxygen saturation	α/α_s	%	42.54
Inclination angle	φ	°	12

Cavitation number is non-dimensionalized as,

$$\sigma = \frac{(p - p_v)}{0.5 \cdot \rho \cdot (n \cdot D)^2} \quad (20)$$

3.3 Test Case - 3

Inclined Propeller induced pressure pulses were measured at three different points located in caitation tunnel [15]. The positions of pressure sensors are sketched in Figure 4.

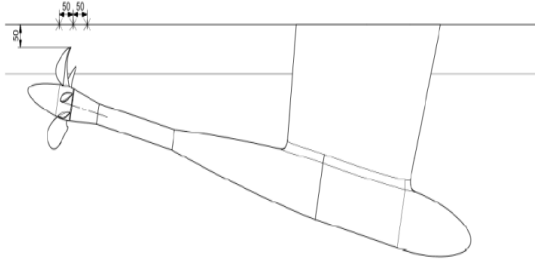


Figure 4: Locations of points for measuring pressure pulses

Enough small time step size should be selected and the pressure data has to be stored during 8 revolution of propeller for cavitation and non-cavitation. The operating condition is listed in Table 3.

TABLE 3: FLOW PARAMETERS TO SIMULATION

Property	Symbol	Dimension	Value
Advanced coefficient	J	—	1.019
Cavitation number	σ	—	2.024
Rate of revolutions	n	1/s	20
Water density	ρ	kg/m ³	997.38
Kinematic viscosity of water	ϑ	m ² /s	9.199E-07
Vapour pressure	p_v	Pa	2929
Oxygen saturation	α/α_s	%	55
Inclination angle	φ	°	12

4 NUMERICAL ANALYSIS

Solver type, discretization method, turbulence model and mesh structure had been already examined in different test-case studies as in [13]. According to this study, nearly same scheme and method is capable of being applied to the new case as described in this paper. On the other hand, unsteady conditions and cavitation behavior is a sophisticated area to study in a deeper way, therefore these effects can vary the result.

CAD models which are provided in website contain so many details, thus they have to be simplified in a systematic manner. Open water conditions are easy to implement the geometry and mesh. Cavitation tunnel walls alter the inflow due to the development of boundary layer on walls near blade tips and solution gets difficult to converge. Especially

computing the pressure pulses require huge amount of fine mesh near blade tips and tunnel walls on which pressure sensors are located. All those problems were investigated in this study.

4.1 CFD Simulation for Test Case - 1

The CAD model consists of blades, hub, cap and shaft as given in Figure 5. These shapes do not have any open surface, therefore it is easy to start mesh generation on surfaces without doing cumbersome modification.



Figure 5: The solid model for test case-1.

Fine mesh was implemented especially near tip, leading edge and trailing edge. Tetrahedral cell size gets bigger while moving away from propeller (Figure 6) .

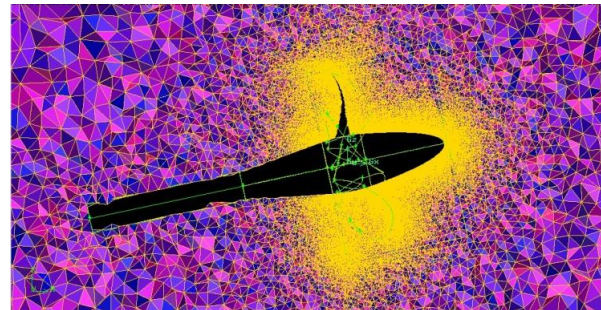


Figure 6: Mesh in domain for pull configuration.

Dyanometer walls are not interested, therefore coarse mesh is negligible in this area. Boundary layer was filled with fine mesh to handle shear strains. In order to avoid spoiling the solution accuracy, the grids are smooth and no large differences in volume or in stretching ratio of adjacent grid cells as stated in [10]. There are two different domains formed in whole case, one of them is rotating cylinder of propeller and the other one surrounds outer fixed flow. The total mesh size was approximately 5.8 million much of which was generated near blade profiles. Boundary conditions are described in Figure 7.

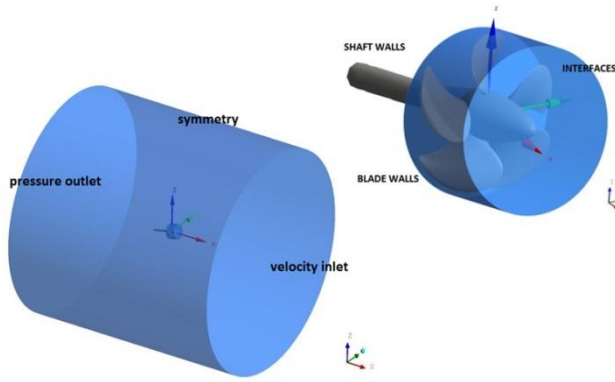


Figure 7: Boundary conditions on domain.

Due to the inhomogeneous inflow unsteady solution should be observed, thus sliding mesh and moving reference frame methods were compared. Moving reference frame allows simulating of rotation of propeller in the main flow. The interface surfaces should be defined matching each other as shown in Interpolation order in spatial discretization was investigated for first order and second order. Gungor and Ozdemir (2014) states that second order would have much accuracy but convergence is more difficult. Appropriate turbulence model should be examined especially for swirl dominated flows. The most apparent superiority of $RNG\ k - \varepsilon$ may be the modified rate of dissipation equation which consist swirl effects. Pressure based segregated algorithm was applied to solve the transport equations. Thrust coefficients for off-design and operation condition are given in Table 4.

TABLE 4: PREDICTED THRUST COEFFICIENTS IN THREE AXES

J	V [m/sn]	K_{tx}	K_{ty}	K_{tz}	K_q
0.6	2.25	0.6182	-0.0118	0.0467	-1.4219
0.8	3	0.5241	-0.0166	0.0640	-1.2547
1.0	3.75	0.4273	-0.0230	0.0848	-1.0801
1.2	4.5	0.3270	-0.0296	0.1078	-0.8887
1.4	5.25	0.2165	-0.0359	0.1318	-0.6677

Required time for convergence of sliding mesh (SM) method in transient solver was approximately 20 times higher than moving reference frame (MRF) method in steady solver. Therefore the point for advanced coefficient of 0.6 was simulated in unsteady solver. The difference between SM and MRF is approximately 10 percent. It can be concluded that mean values of those results are much meaningful.

4.2 CFD Simulation for Test Case - 2

Cross section of the whole mesh domain is given in Figure 8. Total mesh size is approximately 5.2 million.

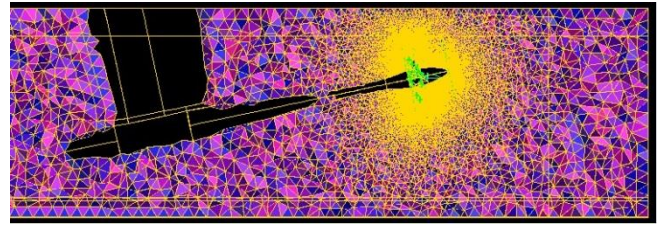


Figure 8: Whole mesh domain used in cavitation tunnel test

Highly strained flows containing swirl are tiresome to be converged and the turbulence model differs from case to case. However $RNG\ k - \varepsilon$ model was preferred for its superiorities over other turbulence models. The predicted thrust coefficients of non-cavitation and cavitation condition for three advance coefficients can be seen in Table 5.

TABLE 5: PREDICTED THRUST COEFFICIENTS

J	σ	V [m/sn]	K_{tx} noncav	K_{tx} cav
1.019	2.024	5.095	0.420	0.385
1.269	1.424	6.345	0.293	0.218
1.408	2.000	7.040	0.214	0.167

By considering the limitations of time and computer capacity, moving reference frame (MRF) is a pleasant technique to simulate behavior of propeller rotation compared to the pains of sliding mesh technique. Inlet flow sweeps the wake away from the blades, preventing extensive interference of circulation. Intense mesh generation is required around tip point and near hub region to illustrate eddies produced on curvatures successfully. The multiphase cavitation models are examined to find the most suitable one. Zwart-Gerber-Belamri cavitation model was appropriate for convergence criteria. Cavitation pattern of volume fraction of 40% and 60% on the propeller surface are given in order below. Illustrations for advanced coefficient of 1.019, 1.269 and 1.408 can be seen in Figure 9, Figure 10 and Figure 11. Green mark indicates %40 volume fraction while blue one is for %60.

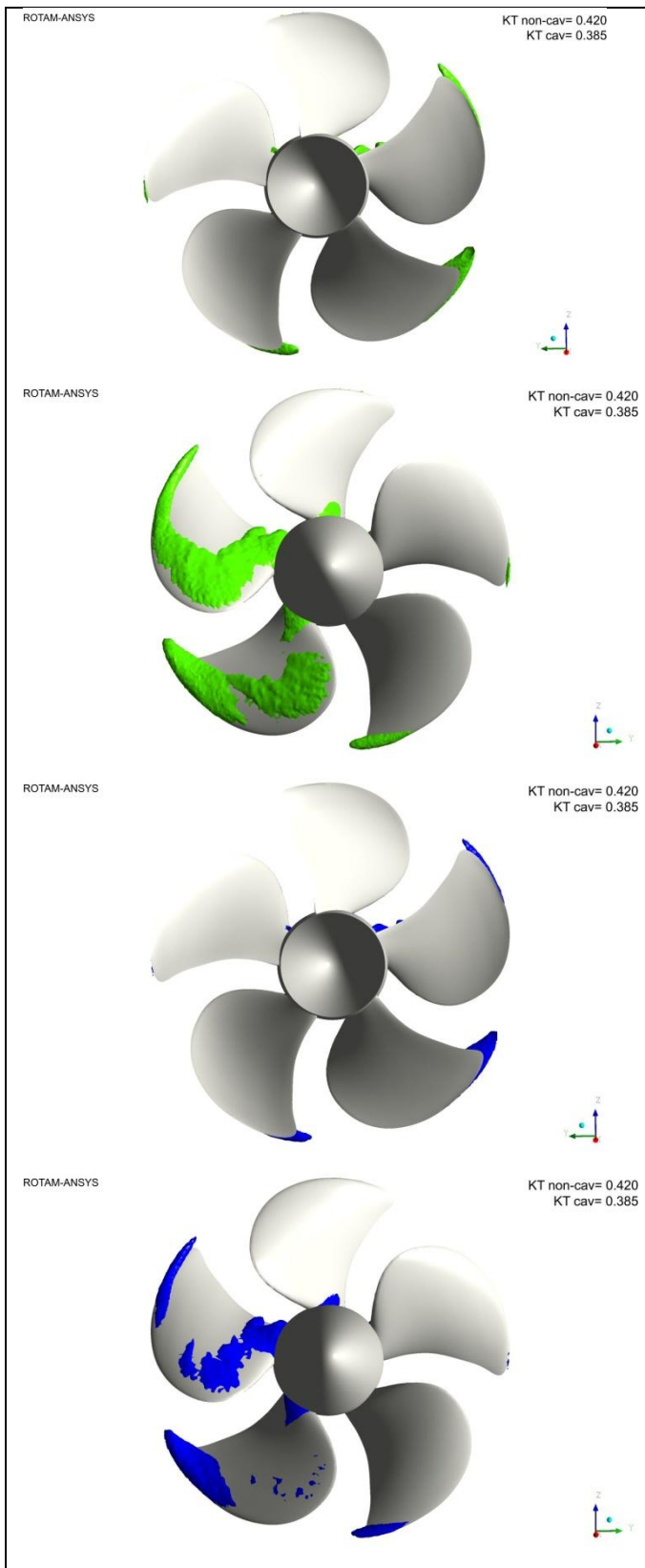


Figure 9: Predictions of cavitation patterns for advance coefficient of 1.019

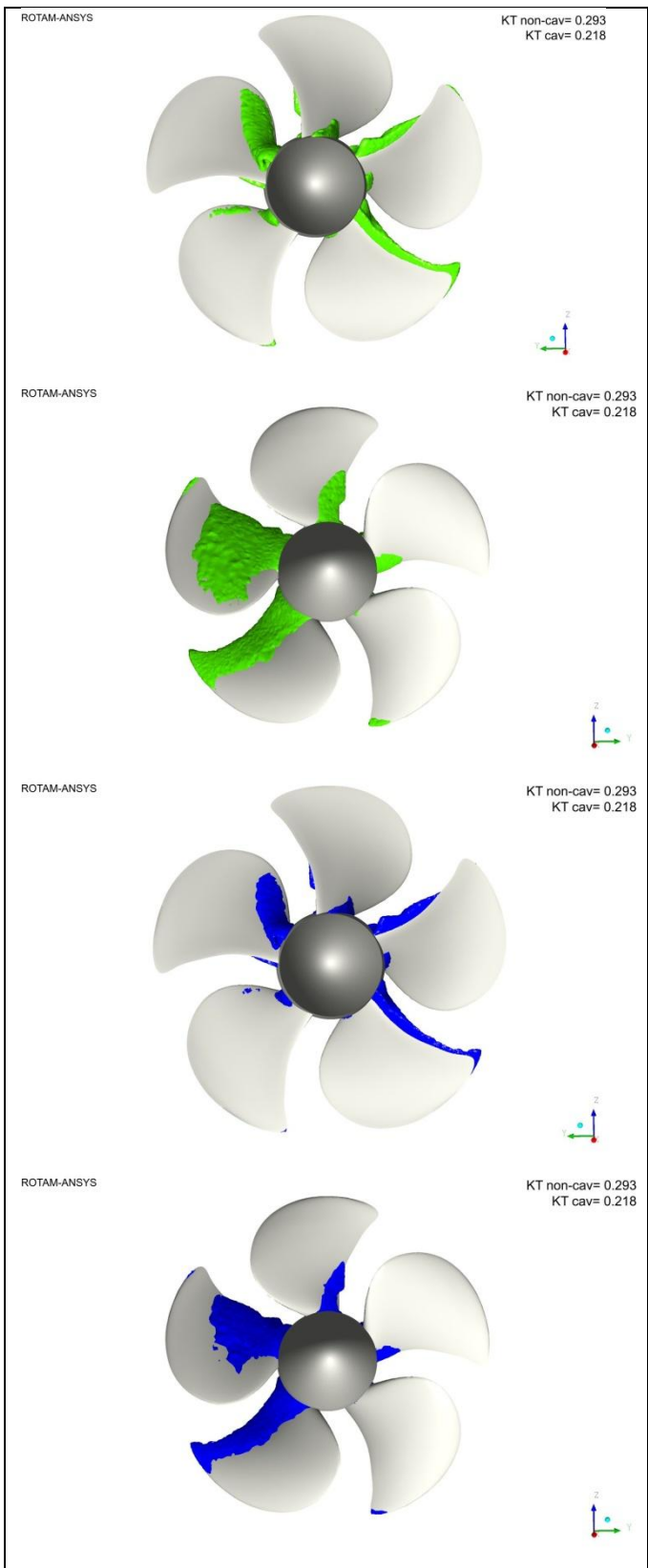


Figure 10: Predictions of cavitation patterns for advance coefficient of 1.269

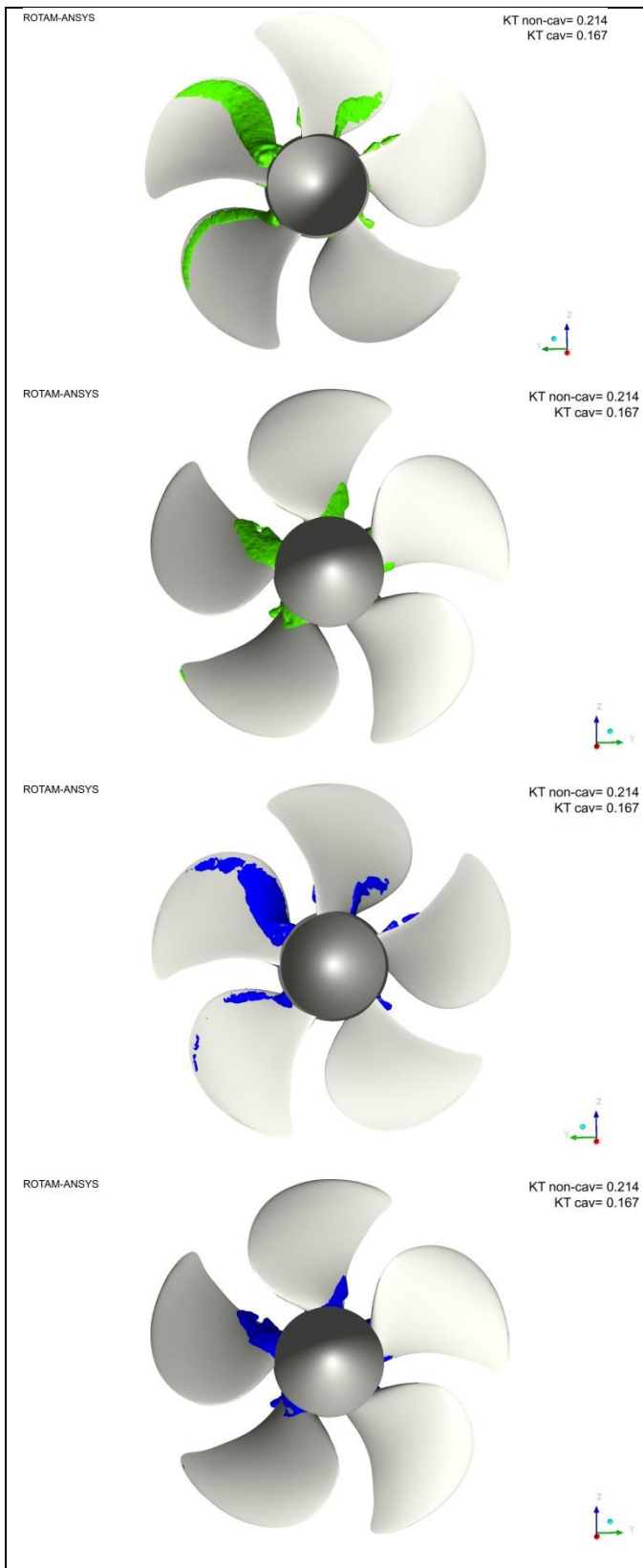


Figure 11: Predictions of cavitation patterns for advance coefficient of 1.408

The flow gains rotating velocity while passing through the blades and it heads towards to the centerline. This behavior indicates that the flow does not scatter outside. Turbulent kinetic energy (TKE) is produced due to the flow strains near the wall, especially near the blade tip. TKE is getting dense near blade root and it diffuses to back of blades by combining with boundary layer TKE until it disperses to the wake area. Flow velocity is the lowest near surfaces. Wake flow occurs at the back of hub in a wide range.

4.3 CFD Simulation for Test Case - 3

Unsteady solver was used to implement sliding mesh method which simulates propeller revolution. Time step size was calculated as following equation in which m equals 8,

$$t = \frac{1}{(n \cdot 2^m)} \quad (1)$$

Pressure pulses on three point p2, p5 and p10 were stored for advanced coefficient of 1.019. Figure 12 shows the whole revolution time history of pressure pulses.

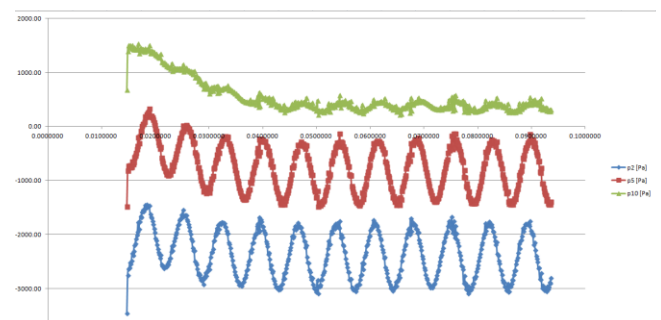


Figure 12: Revolution time history of pressure pulses.

4 CONCLUSION

As a consequence, test-case propeller was investigated via CFD method. Performance characteristics and cavitation patterns of test-case propeller were observed in finite-volume environment for off-design and operation conditions. It should be noted that computation based on *RNG k - ε* turbulence model, second order discretization, steady uncoupled solver for cavitation behavior, unsteady uncoupled solver for non-cavitation condition and unstructured tetrahedral mesh was used in this paper. On the other hand requested pressure pulses near the inclined propeller was performed using a specified time step size through time history. Approach in acoustic manner would be also a smart scope to research and to study this phenomenon in depth.

ACKNOWLEDGMENTS

Special thanks are directed towards the company ROKETSAN Missiles Inc. for its support and giving opportunity to attend SMP15 Conference and Workshop. I would like to thank Fluids Group and its Head (Prof. Bedii Ozdemir) for their support and technical supervision in previous so necessary studies.

REFERENCES

- [1] J. Kerwin, Hydrofoils and Propellers, USA: Massachusetts Institute of Technology, 2001.
- [2] J. Kerwin, "The Preliminary Design of Advanced Propulsors," in *Proc. of Propellers/Shafting 2003 Symposium, SNAME*, Virginia Beach, USA, 2003.
- [3] J. R. Boswell, "Design, cavitation performance, and open-water performance of a series of research skewed propellers," Department of the Navy Naval Ship Research Development Center, Washington, D.C., 1971.
- [4] S. Brizzolara, D. Villa and S. Gaggero, "A systematic comparison between RANS and Panel methods for propeller analysis," in *The 9th International Conference on Hydrodynamics*, Shanghai, China, 2010.
- [5] D. Liu and F. Hong, "The numerical predicted of SMP11 propeller performance with and without cavitation," in *The 2nd International Symposium on Marine Propulsors*, Hamburg, Germany, 2011.
- [6] C. Nathan, T. Michael and P. M. Carrica, "Overset Simulation of a Submarine and Propeller in Towed, Self-Propelled and Maneuvering Conditions," in *The 29th Symposium on Naval Hydrodynamics*, Gothenburg, Sweden, 2012.
- [7] H. Jang and K. Mahesh, "Large eddy simulation of crashback in ducted propellers with stator blades," in *The 29th Symposium on Naval Hydrodynamics*, Gothenburg, Sweden, 2012.
- [8] L. Xia, J. Lundberg and R. E. Bensow, "Performance prediction of a nozzle propeller," in *The 29th Symposium on Naval Hydrodynamics*, Gothenburg, Sweden, 2012.
- [9] S. B. Denny, "Cavitation and open-water performance tests of a series of propellers designed by lifting-surface method," Department of the Navy Naval Ship Research and Development Center, Washington, D.C., 1968.
- [10] J. Blazek, Computational Fluid Dynamics: Principles and Applications, Switzerland: Elsevier, 2001.
- [11] J. C. Ching and Y. J. Shenq, Fundamentals of Turbulence Modeling, Washington, DC: Taylor & Francis, 1998.
- [12] Ansys, "Ansys v13 Fluent User's Guide," USA, 2010.
- [13] E. Gungor, B. Ozdemir, Design and Analyses of a Propeller for Underwater Vehicles Using Computational Fluid Dynamics, 2014.
- [14] E. Gungor, B. Ozdemir, Investigation of Performance of Conventional Propellers and Design for Unique Propeller, 2015, to be published.
- [15] http://www.sva-potsdam.de/pptc_data_15.html

Prediction of pressure pulses and cavitation behavior of PPTC propeller in oblique flow with a 12° shaft inclination

Da-Qing Li

SSPA Sweden AB, Göteborg, SWEDEN

ABSTRACT

The paper describes SSPA's computational work in the 2nd International Workshop on Cavitating Propeller Performance during SMP'15. An incompressible multiphase mixture flow RANS solver with two sets of turbulence/cavitation models was employed to predict the cavitation behavior on the PPTC propeller (Case 2) and pressure pulses on the tunnel wall (Case 3). The first model-set is the standard SST k- ω turbulence model and Zwart's cavitation model, and the other set is a modified SST k- ω model based on Reboud's correction and Sauer's cavitation model. A wall-resolved mesh that ensures a $y^+=1$ of the first cell wall distance towards blade surface and consists of 12 million cells is used for the simulations.

It is observed that the method using Sauer's cavitation model and the modified SST k- ω model could to some extent capture the re-entrant jet effect at the tail of sheet cavity while the method using Zwart's model and the standard SST k- ω model did not predict any shedding. The former method also predicted slightly more extension of tip vortex cavitation. The pressure pulses predicted by the two methods do not differ very much except for Case 3.1.

Keywords

Cavitation, pressure pulses, cavitation model, turbulence model.

1 INTRODUCTION

A CP propeller, named PPTC, with extensive measurement data was kindly provided by model basin SVA in Potsdam for the 2nd International Workshop on Cavitation and Propeller Performance during SMP'15. The experiment datasets cover the open water characteristics in oblique flow with a 12° shaft inclination (Case 1), cavitation observations (Case 2) and pressure pulses measured on the tunnel wall in non-cavitating and cavitating conditions (Case 3). SSPA participated the validation Case2 and Case3. Case 1 was dropped due to lack of time.

2 PROPELLER MODEL

The PPTC propeller is a controllable pitch propeller. The dimensions are given in Table 1.

Propeller	unit	value
Diameter	[m]	0.25
Pitch ratio P/D at $0.7R$	[-]	1.635
Blade area ratio, A_E/A_0	[-]	0.77896
Chord length at $r/R = 0.7$	[m]	0.10417
Hub ratio, d_h/D	[-]	0.3
Skew angle	[°]	18.837
Number of blades	[-]	5

Table 1 Main dimension of PPTC propeller

3 NUMERICAL METHODS

3.1 Governing equations and numerical models

Commercial software ANSYS Fluent v15.0 is used in the present work. The multi-phase mixture model in ANSYS FLUENT assumes that the working medium is a single fluid with a homogeneous mixture of two phases (liquid and vapor).

Denoting the density of the mixture by ρ_m , the continuity equation for the mixture flow becomes:

$$\frac{\partial}{\partial t}(\rho_m) + \nabla \cdot (\rho_m \vec{v}_m) = 0 \quad (1)$$

The momentum equation for the mixture reads:

$$\begin{aligned} & \frac{\partial}{\partial t}(\rho_m \vec{v}_m) + \nabla \cdot (\rho_m \vec{v}_m \vec{v}_m) \\ & = -\nabla p + \nabla \cdot [\mu_m (\nabla \vec{v}_m + \nabla \vec{v}_m^T)] + \rho_m \vec{g} + \vec{F} \end{aligned} \quad (2)$$

The density relation of each phase in a mixture-flow cell is described by means of a scalar volume fraction as:

$$\rho_m = \alpha_v \rho_v + (1 - \alpha_v) \rho_l \quad (3)$$

where α_v is the volume fraction of vapor. To account for the mass transfer between phases a cavitation model is needed and a transport equation is thus solved for α_v as shown below. For turbulence closure, SST $k-\omega$ turbulence model with low-Reynolds number correction is adopted, which means that two more transport equations are solved.

The first cavitation model employed is Zwart's model (Zwart *et al.* 2004). It solves for the vapor volume fraction α_v with the following transport equation:

$$\frac{\partial}{\partial t}(\alpha_v \rho_v) + \nabla \cdot (\alpha_v \rho_v \vec{v}_m) = R_e - R_c \quad (4)$$

The source terms R_e and R_c were derived from the bubble dynamics equation of Rayleigh-Plesset and account for the mass transfer between the vapor and liquid phases in cavitation. They have the following form:

$$R_e = F_{vap} \frac{3\alpha_{nuc}(1-\alpha)\rho_v}{\mathfrak{R}_B} \sqrt{\frac{2(p_v - p)}{3\rho_l}} \quad (5)$$

when $p_v > p$, and

$$R_c = F_{cond} \frac{3\alpha\rho_v}{\mathfrak{R}_B} \sqrt{\frac{2(p - p_v)}{3\rho_l}} \quad (6)$$

when $p_v < p$. The model involves four parameters and default values are used. They are the bubble radius $R_B = 10^{-6}$ m, the nucleation site volume fraction $\alpha_{nuc} = 5 \times 10^{-4}$, evaporation and condensation coefficient $F_{vap} = 50$ and $F_{cond} = 0.001$.

The second cavitation model, Sauer's model, was developed by Schnerr and Sauer (2001). It also solves for the vapor volume fraction α_v with the transport equation (4), but has the following different formulation of source terms:

$$R_e = \frac{\rho_v \rho_l}{\rho_m} \alpha_v (1 - \alpha_v) \frac{3}{\mathfrak{R}_B} \sqrt{\frac{2(p_v - p)}{3\rho_l}} \quad (7)$$

when $p_v > p$, and

$$R_c = \frac{\rho_v \rho_l}{\rho_m} \alpha_v (1 - \alpha_v) \frac{3}{\mathfrak{R}_B} \sqrt{\frac{2(p - p_v)}{3\rho_l}} \quad (8)$$

when $p_v < p$. The bubble radius R_B can be determined by:

$$\mathfrak{R}_B = \left(\frac{\alpha_v}{1 - \alpha_v} \frac{3}{4\pi n_0} \right)^{1/3} \quad (9)$$

where n_0 is the bubble number density. A default value $n_0 = 10^{13}$ is used here. Furthermore, a modified SST $k-\omega$ model based on Reboud's correction is used in connection with Sauer's model. The Reboud's correction reduces the otherwise too high turbulent viscosity in the liquid-vapor mixture region thereby enhances the resolution of cavitation dynamics. See Li *et al.* (2009) for the application of Reboud's correction in cavitation prediction.

3.2 Numerical schemes

The numerical schemes are as follows:

- Multiphase mixture flow incompressible solver
- SST $k-\omega$ model for turbulence modelling
- Pressure and velocity solved in a coupled manner
- QUICK scheme for convection terms in all equations
- Propeller rotation handled by sliding mesh technique
- The 1st order implicit scheme for time-derivative
- Time-step = 1.9531×10^{-4} [s] based on the suggestion of Workshop organizer, i.e. each revolution is resolved by 2^8 (=256) time-steps.

4 GRIDS AND LOADING CONDITIONS

The computational domain is limited to the part of tunnel section whose geometry is provided by SVA. Figure 1 shows the computational domain and its boundaries. Note that the strut (or support) for the shaft is not included in the CFD model. Motivation for this simplification is because the strut is a fairly streamlined body and located farther downstream the propeller, its influence on the upstream propeller performance is thus assumed to be negligible. The domain is divided in two zones, one cylindrical zone closely surround the propeller and rotating with the blades, and one stationary zone filling the rest of domain.

Constant velocity, turbulence intensity and viscosity ratio are specified at the velocity inlet boundary, whereas a constant pressure is set at outlet boundary to realize the prescribed cavitation number for each cavitation case. The propeller blades, hub and shaft surface, and the tunnel wall are treated as no-slip walls.

The calculations for the cavitation cases are based on the given J-value and the propeller rate of revolution n . The computation starts with wetted flow simulation with the fixed n in a stationary MRF mode and then continued with the transient simulation using the sliding mesh technique.

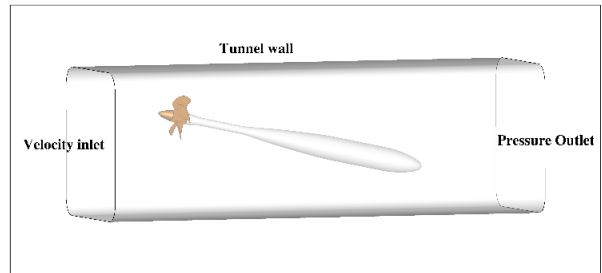


Figure 1 Computational domain

All grids are of hexahedral type. For the grid in the rotating zone, the grid nodes are refined in the wall normal direction to achieve a $y^+ = 1$ and also towards leading edge, trailing edge and tip of the blade. For the grid in the stationary domain, the nodes perpendicular to the tunnel wall are stretched to achieve a $y^+ = 30$. A grid cut-off at the central plane and the surface grid zooming to the propeller blades are

shown in Figure 2. The total number of grid cells is about 12 million. The propeller and the shaft/dynamometer are mounted at two different height for Case 2 and Case 3 (with a vertical installation difference ca 110mm), therefore, two different grids are generated, but the grid topology is the same.

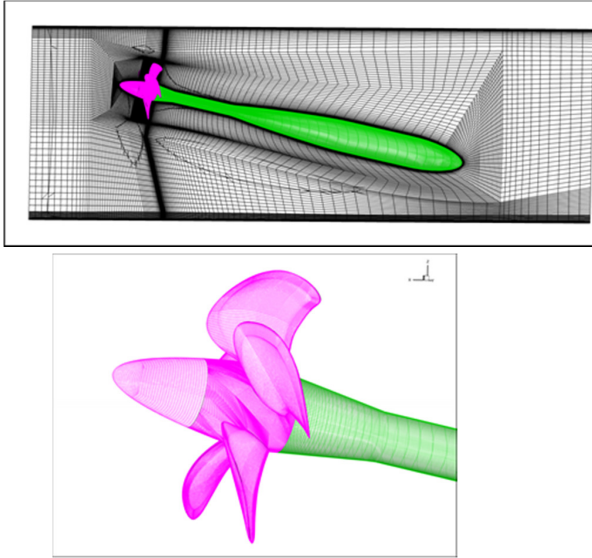


Figure 2 Grid cut-off at central plane (top) and surface grid on the propeller blades (bottom)

Table 2 The loading conditions

	n [1/s]	J [-]	K_T [-]	σ_n [-]
Case 1	15	0.2~1.4	Open water characteristics	-
Case 2.1/3.1	20	1.019	0.363/NA	2.024
Case 2.2/3.2	20	1.269	NA/NA	1.424
Case 2.3/3.3	20	1.408	NA/NA	2.000

The loading conditions for the test cases are summarized in Table 2. The sub-cases in Case 3 have the same loading as in Case 2. Further details of the case definition can be found in the workshop proceedings.

5 RESULTS AND DISCUSSIONS

5.1 Case 1 - Open water in oblique flow

Not computed.

5.2 Case 2 – Cavitation behavior

An example of pressure distribution (coefficient C_p normalized by $\frac{1}{2}\rho(nD)^2$) on the suction side blade in the non-cavitating and cavitation condition is depicted in Figure 3 for Case2.1. This off-design loading condition results in a rather large low pressure area on the suction side in the cavitating condition.

An example of typical turbulent vortex structures in the propeller wake is shown in Figure 4 for Case 2.2 with an iso-value of Q-criterion $Q=5000$ [s⁻²], colored by the turbulent viscosity ratio. As seen in the figure, the tip vortices in the near downstream region (up to a distance about 0.6D behind the propeller) are well captured, but they vanish quickly farther downstream. The character is typical of a RANS solution, which significantly under-resolves the turbulent structures in the wake. Lack of sufficient grid resolution in the downstream region (as can be seen from Figure 2) is another reason for the under resolved tip vortices.

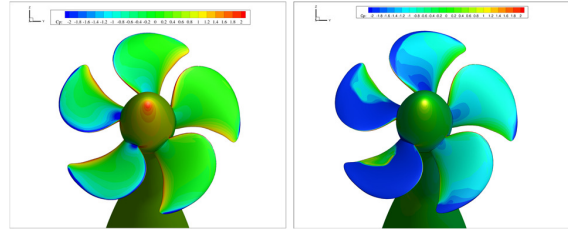


Figure 3 C_p on blade for Case 2.1, under no-cavitation (left) vs. cavitation (right) condition

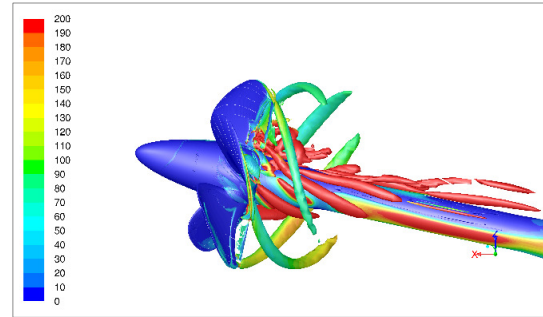


Figure 4 Turbulence structure in propeller wake, Case 2.2

The difference between the computed and the measured K_T is approximately -0.4% in the non-cavitating condition and 4.3% in the cavitation condition for Case 2.1.

5.2.1 Case 2.1

The cavitation surface is shown in Figure 5 with the iso-surface of vapor volume fraction $\alpha_v=0.6$ (in blue), compared with the observed cavitation pattern (sketches) at four blade positions from the experiment. The cavity surface plotted with the iso-surface of $\alpha_v=0.4$ shows little difference from that represented by $\alpha_v=0.6$, indicating that the cavity interface (between vapor and liquid) is rather sharp. Therefore, only the results with iso-surface of $\alpha_v=0.6$ are presented in the paper while all plots are submitted to the workshop organizer.

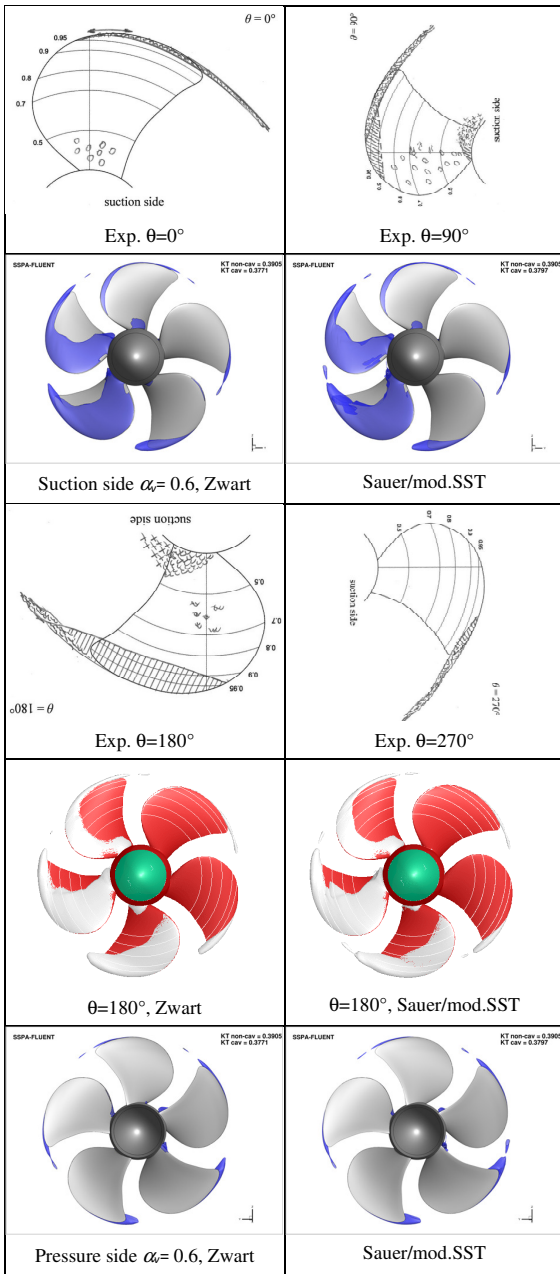


Figure 5 Cavitation pattern for Case 2.1

For Case 2.1 the predicted cavitation takes place only on the suction side. At 12 o'clock ($\theta=0^\circ$ blade angle) position a thin and narrow sheet cavity is developed along the leading edge. Towards the tip this cavity merges into the tip vortex cavity. However, the narrow sheet cavity was not present in the model test at $\theta=0^\circ$. At $\theta=72^\circ$ and 144° blade position, a much extended sheet cavity covering over 50% of blade area is observed. The cavitation at these blade angles can be compared with the sketch for $\theta=90^\circ$ in the model test, which

does not show the existence of sheet cavity on the blade area between $r/R=0.35$ and $r/R=0.87$. Instead, a group of cavity bubbles is observed in this area in the model test. It seems to imply that the used cavitation models may have failed to predict the bubble cavitation. In the present work only default values were adopted for all the parameters used in the cavitation models. Tuning the model parameter like bubble number density or bubble radius may improve the results.

Secondly, the tip vortex cavitation is present at all blade positions but it survives only a short distance downstream, the extension of TVC is much shorter than that observed in the experiment. Nonetheless Sauer's model with the modified SST k- ω model did capture slightly more TVC.

5.2.2 Case 2.2

The cavitation pattern for Case 2.2 is shown in Figure 6 with an iso-surface of $\alpha_s=0.6$. It is seen that cavitation is developed on both pressure and suction side. On the suction side a thin sheet cavity is developed over a large area on blade as the blade rotates through the starboard side. Tip vortex cavity is present but vanishes quickly downstream. There is also a significant amount of root cavitation at all blade positions. On the pressure side there is a thin and narrow sheet cavity occurring along the leading edge of blade in the range $180^\circ-20^\circ$. The most significant difference between the two models is at or near the cavity closure, where Sauer's model with Reboud's correction predicts the shearing effect of the re-entrant jet action whereas Zwart's model does not predict this. See the cross section plots in Figure 6.

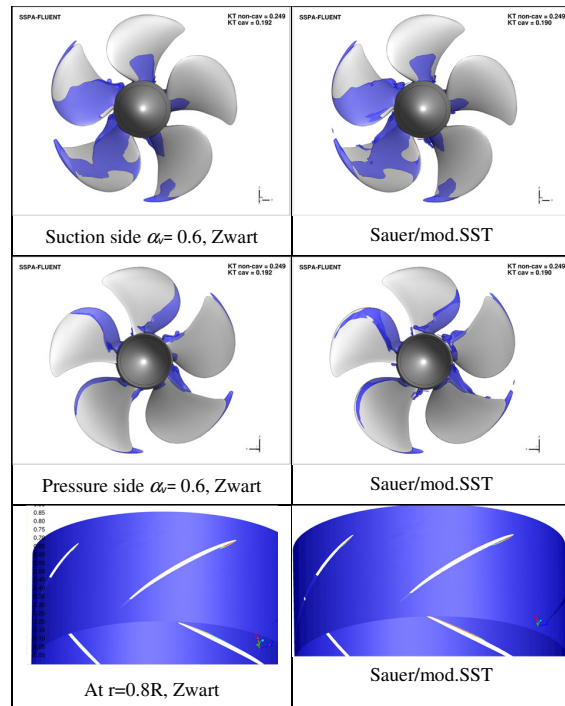


Figure 6 Cavitation pattern for Case 2.2

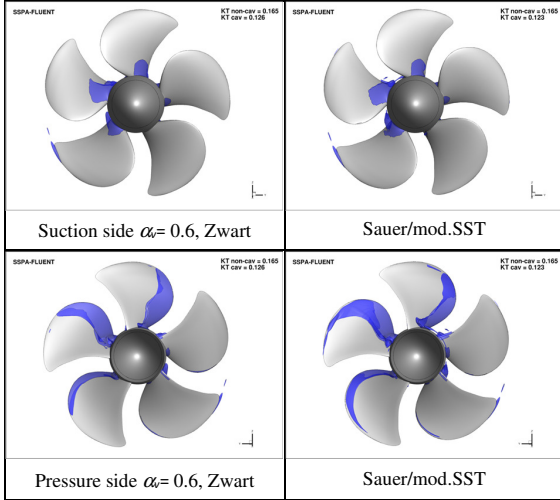


Figure 7 Cavitation pattern for Case 2.3

5.2.3 Case 2.3

The cavitation pattern for Case 2.3 is shown in Figure 7 with an iso-surface of $\alpha_v=0.6$. On the suction side there remains mainly root cavitation. On the pressure side a thin sheet cavity along the leading edge is noted in the range 170° - 50° . The difference between the two simulation results is near the cavity closure, where Sauer's model with the modified SST $k-\omega$ model predicts the shearing effect of the re-entrant jet action whereas Zwart's model does not predict this feature, as visualized on a cylindrical cut-off surface at radius $r=0.7R$ in Figure 8.

5.3 Case 3 – Pressure fluctuations

The pressure fluctuations at three positions on top of the tunnel wall were measured under non-cavitating and cavitating conditions. The pressure transducer locations in the model test are given in Figure 9, marked by p2, p5 and p10 in red. The pressure pulses (PP) are presented in form of K_p coefficient, defined as $K_p = \frac{2P_M}{\rho(nD)^2}$, where P_M is the single amplitude of the spectra of pressure signal.

5.3.1 Case 3.1

The predicted pressure pulses under non-cavitation and cavitation conditions are compared with each other in Figure 10. As seen in Figure 10, for the first blade rate (BR) harmonics the pressure pulse at transducer p2 in the non-cavitating condition is a bit higher than that in the cavitating condition. The K_p at transducer p5 is roughly at the same level, whereas the K_p at transducer p10 is much higher in the cavitating case than the non-cavitating case. For the higher order harmonics (2nd-5th BR), the K_p under cavitation

condition is clearly higher than that under non-cavitation condition. The high K_p level at higher order harmonics may be related to the tip vortex cavity (TVC) in Case2.1. There is also a rather large discrepancy in K_p at the 1st BR for the two cavitation models.

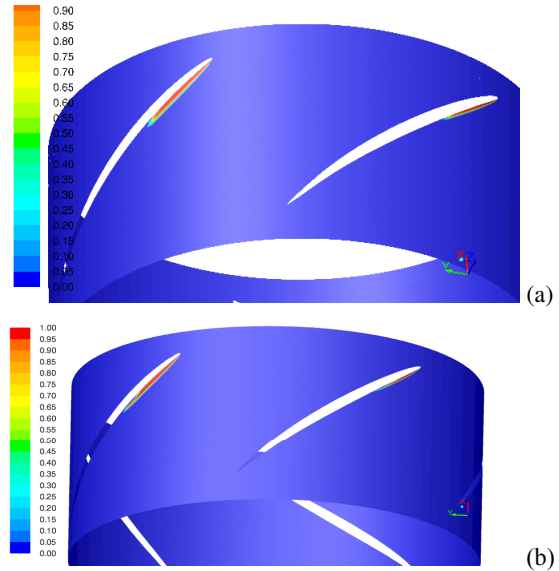


Figure 8 Pressure side cavity in Case 2.3 cross sectioned by a cylindrical surface of $r=0.7R$, predicted by Zwart model (a) versus Sauer/mod.SSTmodel (b). The reentrant jet effect at the tail of cavity is captured with Sauer/mod.SST model.

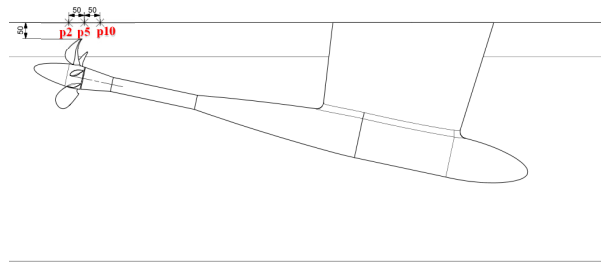


Figure 9 Pressure transducer locations in the experiment

5.3.2 Case 3.2

The K_p in non-cavitation condition is compared with that in cavitation condition in Figure 11. Similar to Case 3.1, the 1st BR harmonics K_p at transducer p2 and p5 is slightly higher in the non-cavitating case than the cavitation case. The 1st BR K_p at transducer p10 is considerably lower than those at p2 and p5, although the K_p in the cavitation condition is higher than that in non-cavitating condition as expected. So the 1st BR pressure fluctuations decrease in the streamwise

direction, from p2 to p10. For the higher order BR harmonics, the K_p in cavitating condition is slightly higher than in non-cavitating condition, but none of the K_p level at high order BR harmonics is of significance, probably due to a less severe TVC at this loading.

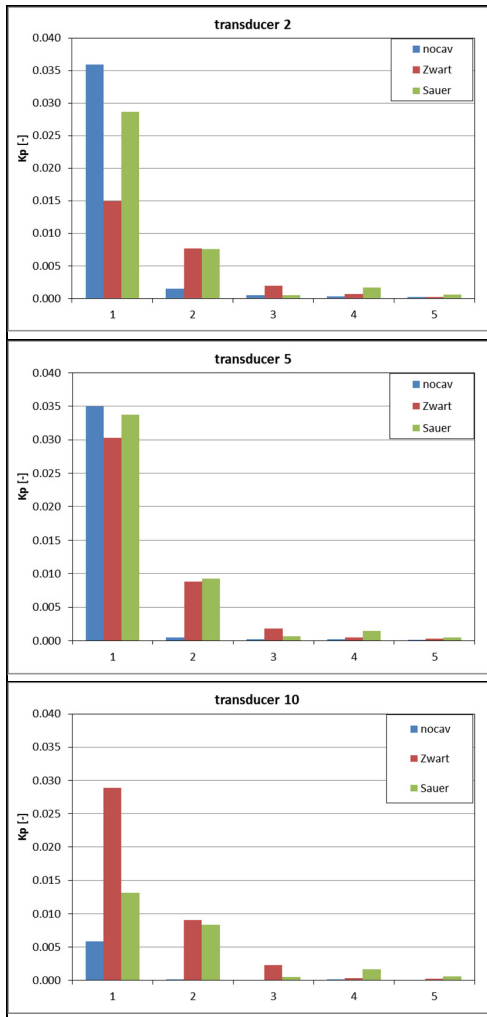


Figure 10 Pressure pulses in Case 3.1

5.3.3 Case 3.3

The K_p in non-cavitation and cavitation condition is compared in Figure 12. In non-cavitation condition the K_p is of significance mainly at the 1st BR harmonics and its magnitude decreases in the streamwise direction (i.e. from transducer p2 to p10). The cavitation pattern in Case 3.3 is quite similar to that in Case 2.3 (having the same loading). In the cavitating condition, the increase of K_p at the 1st BR harmonics seems to be in a reversed order, i.e. with a very low level at transducer p2, a notably high value at p5 and a further increase at p10. This behavior may be related to the fact that the dominant sheet cavitation occurs on the pressure

side of blade, which is about one blade thickness downstream of the suction side. Moreover, there is a less pronounced TVC in this case. The K_p at higher order harmonics (2nd-5th) remains to be on a low level, but cavitation does raise the K_p level to some extent as compared with the non-cavitation level. Compared with Zwart's model, Sauer's model predicts a slightly higher K_p level.

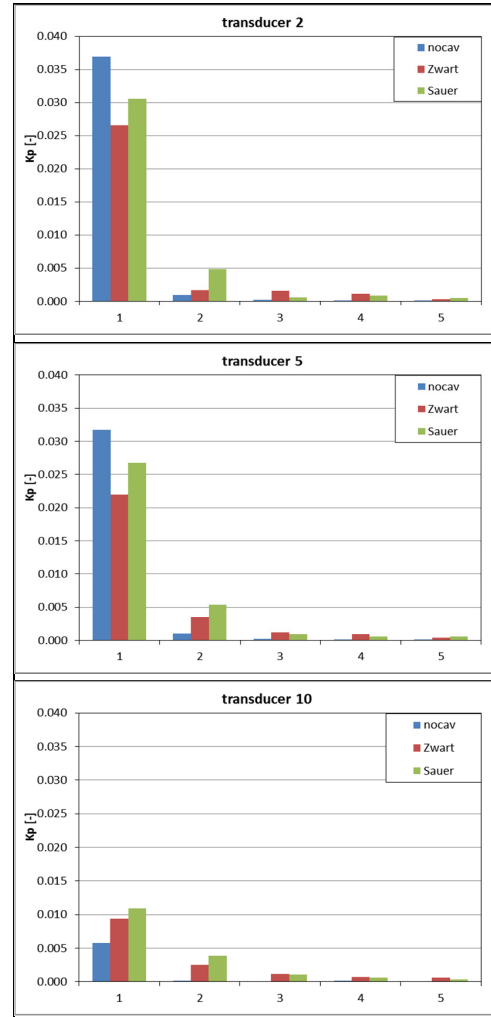


Figure 11 Pressure pulses in Case 3.2

6 CONCLUSIONS

A multiphase mixture flow RANS method with two sets of turbulence/cavitation models is applied to predict the cavitation dynamics and pressure pulses of the PPTC propeller under non-cavitation and cavitation conditions. Compared with the available model test result for Case 2.1, the cavitation models were able to predict the sheet cavitation, root cavitation, tip vortex cavitation on blade but failed to predict the bubble cavitation using the default model

parameters. Tuning of model parameters like bubble number density or bubble radius may improve the results but this is not explored.

The Sauer's model with the modified SST k- ω turbulence model captured to some extent the shedding dynamics due to re-entrant jet effect at the tail of sheet cavity. The pressure pulses predicted by the two models are about the same level except for Case 3.1.

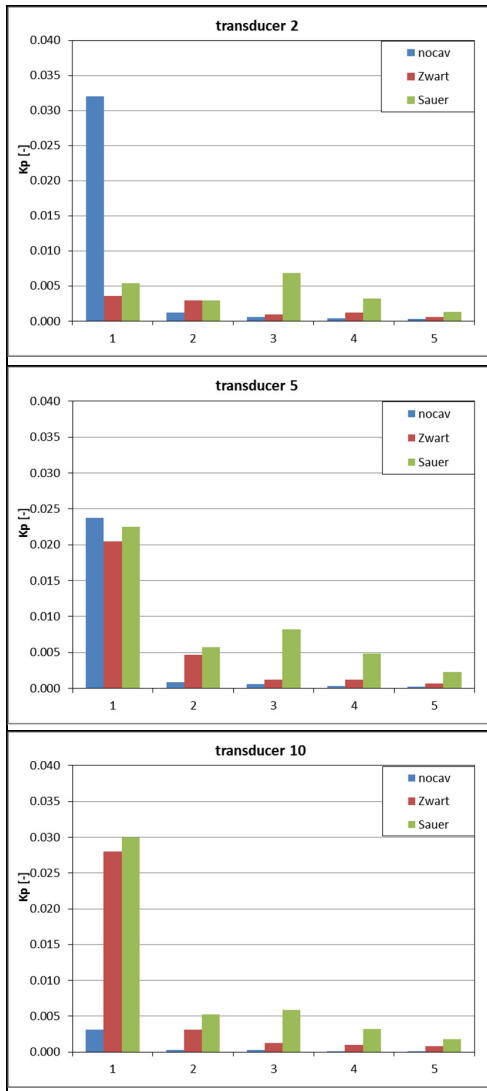


Figure 12 Pressure pulses in Case 3.3

7 REFERENCES

- Li, D.-Q., Grekula, M. and Lindell, P. (2009), 'A modified SST k- ω Turbulence Model to Predict the Steady and Unsteady Sheet Cavitation on 2D and 3D Hydrofoils', The 7th International Symposium on Cavitation (CAV2009), Michigan, USA.
- Reboud J.L., Coutier-Delgosha O. and Fortes-Patella R., (2003), "Evaluation of the Turbulence Model Influence on the Numerical Simulations of Unsteady Cavitation", Journal of Fluids Engineering, Vol. 125, Issue 1.
- Schnerr, G. H. and Sauer J., (2001), 'Physical and Numerical Modeling of Unsteady Cavitation Dynamics', In Fourth International Conference on Multiphase Flow, New Orleans, USA.
- Zwart, P. J. Gerber, A. G. and Belamri, T. (2004), "A Two-Phase Flow Model for Predicting Cavitation Dynamics". In Fifth International Conference on Multiphase Flow, Yokohama, Japan.

A Comparative Study on Computational Methods with regard to Propeller Simulation in Oblique Inflow

Martin Scharf¹, Keqi Wang², Sattar Al Jabair³, Moustafa Abdel-Maksoud⁴

^{1,2,3,4} Institute of Fluid Dynamics and Ship Theory, Technical University of Hamburg, Hamburg, GERMANY

ABSTRACT

A comparison between different numerical approaches to simulating the propeller flow is presented. Different test cases of the PPTC workshop will be considered. They feature an inclined propeller shaft and are designed to cover open water accuracy as well as cavitation prediction. The numerical methods employed are a BEM as well as two RANS solvers. All methods are able to predict propeller blade cavitation. Predicted forces acting on the propeller as well as cavitation will be compared.

Keywords

Propeller, oblique inflow, cavitation, BEM, RANS, PPTC

1 INTRODUCTION

In recent times propeller simulations in engineering are increasingly often performed with RANS solvers due to the continuously rising computational power. Nevertheless the simpler BEM methods still are widely used. Because of their good accuracy in combination with very low computation time they are employed as design tools. In this work both approaches will be applied to simulate a propeller operating in oblique inflow.

The different methods are expected give at least to a certain extent varying results depending on which physical mechanisms are captured by a particular method. The comparison of the results can give a good understanding of the effect those mechanisms and respectively the choice of the simulation method have in the present case. With a good idea of the strength of each method an efficient simulation approach can be selected individually for each prospective problem.

2 FORMULATION

2.1 Unsteady Panel Method

The potential flow solver *panMARE* used in this study is a low order panel method able to solve a wide range of flow problems. It allows for polygonal panels arranged both in unstructured and structured grids on lifting as well as nonlifting bodies. The code is steadily improved at TUHH.

The procedure follows closely the approach presented by Katz and Plotkin (2001). The total velocity \vec{V} of an incompressible medium is split into inflow velocity \vec{V}_0 and induced velocity \vec{V}^* . The flow field of the latter is assumed to be irrotational. Therefore a velocity potential Φ can be found that yields the unknown induced velocity through $\nabla\Phi = \vec{V}^*$ with $\nabla = (\partial/\partial x, \partial/\partial y, \partial/\partial z)$. Additionally the continuity equation simplifies to the Laplace equation $\nabla^2\Phi = 0$ and can be applied on the body surface to compute the potential. Because of its linear nature multiple solutions can be superimposed to a new valid solution. The value and its derivative in normal direction are regarded as doublet strength $\mu = -\Phi$ and source strength $\sigma = \nabla\Phi \cdot \vec{n}$ at the discrete panel collocation points.

To calculate the doublet strength of trailing wake sheets downstream of lifting bodies a Morino Kutta boundary condition is applied at each trailing edge segment of such a body. Those wake surfaces have zero thickness and are therefore material surfaces of the flow, i. e. they align with the local flow. This mechanism is implemented in the method by realignment of the wake sheet panels. In order to achieve faster convergence and numerically more stable simulations this realignment can also be restricted. For more accurate results at high propeller loadings it is for example beneficial to allow movement only in axial and tangential direction. In such a case only the components in permitted directions are considered.

2.2 Sheet Cavitation Model in Panel Method

The panel method *panMARE* includes a model to simulate sheet cavitation. It includes an approach based on Fine (1993) and Vaz (2005). At panels identified as afflicted by cavitation the dynamic boundary condition is applied to determine the doublet strength μ necessary to attain vapor pressure. Because it yields the corresponding velocity, to obtain the doublet strength the attained values are integrated across all cavitating panels upstream on the respective grid strip. The constant of integration in the form of the potential Φ_0 at the cavity starting point is determined using a third-order approach based on the potential at the three neighboring wetted panels upstream.

$$-\mu = \Phi_{cav} = \Phi_0 + \sum_{N_{cav,i}} \frac{\partial \Phi}{\partial s_1} \Delta s_1$$

The necessary numerical integration across all cavitating panels upstream $N_{cav,i}$ requires a panel grid of at least quasi-structured type containing quadrilateral panels.

To all remaining panels the source strength σ is applied according to the Neumann boundary condition using the normal vector \vec{n} and the velocity of the undisturbed inflow \vec{V} .

$$\sigma = \vec{n} \cdot \vec{V}$$

Finally a modified equation system is solved to set the remaining unknown singularities in accordance with the Laplace equation. This requires at least part of the panels to be solved using a Dirichlet boundary condition to ensure in addition to its derivative the correct level of potential and thus doublet strength.

Applying this procedure results in non-zero velocity components in the normal direction of the panel. They will be used to calculate the size of the cavity surface normal to the body surface, referred to as the cavity thickness in the following. Assuming the cavity surface C to be a solid boundary in the fluid with small thickness, the kinematic boundary condition can be applied on the body surface. This yields the cavity thickness on each panel.

$$\frac{D}{Dt} C(s_1, s_2, s_3) = \left(\frac{\partial}{\partial t} + \vec{V} \cdot \nabla \right) (s_3 - \eta(s_1, s_2, t)) = 0$$

The equation is transformed to a discretized form and solved in an equation system. The reference system used is the local panel coordinate system. The derivatives in directions in panel plane are approximated by a centralized second order approach. Unknowns determined are thicknesses at the edge centers upstream and downstream of panel centers. This allows for direct computation of cavity thicknesses at the boundaries.

Subsequently the cavity boundary is adjusted based on the obtained thicknesses. In case of positive thickness, the necessary extension downstream is estimated by a linear approximation based on the two known thicknesses upstream of the current boundary. Otherwise the boundary is moved upstream.

This procedure is repeated iteratively.

2.3 RANS Solvers

The equations which govern the behavior of an incompressible Newtonian fluid are the conservation equations of mass and momentum. By applying well-known assumptions they yield the Reynolds-averaged Navier-Stokes equations (RANS equations).

They are discretized with a cell-centered scheme and solved by a pressure-velocity coupling based on the PIMPLE algorithm. Employed solvers are both ANSYS CFX and OpenFOAM.

In OpenFOAM PISO and SIMPLE algorithms are combined while in ANSYS CFX the Rhie-Chow algorithm is employed. The approach of simulation for rotating motions is based on a multi domain definition of rotating and stationary parts, which were coupled with sliding interfaces.

2.4 Cavitation Models in RANS Simulations

In the finite volume approach the phase change between liquid and vapor phase is modeled. Both phases travel with the same velocity in a specific point. Hence the mass transport equation simplifies to an equation that describes mass transfer rate \dot{m}_l for liquid phase and \dot{m}_v for vapor phase. Different solutions that model mass transfer can be applied. In ANSYS CFX the Zwart model is implemented (Ansys (2015)). It considers vapor pressure p_v , vapour volume fraction α_v , volume fraction of nucleation sites r_{nuc} and the mean nucleation site radius R_{nuc} . Further a factor F takes into consideration that vaporization happens more quickly than condensation.

$$\dot{m}_l = -\dot{m}_v = F \frac{3r_{nuc}(1 - \alpha_v)\rho_v}{R_{nuc}} \sqrt{\frac{2|p_v - p|}{3\rho_l}} \text{sgn}(p_v - p)$$

$$F = \begin{cases} 0.01 & \text{for } p > p_v \\ 50 & \text{for } p < p_v \end{cases}$$

All parameters were set to their default values in the simulations carried out.

In OpenFOAM the Kunz model was used (Merkle (1998)).

3 COMPUTATIONAL SETUP

A detailed description of the simulated experiments can be found in the workshop documents for SMP '15. They will be referred to from here on.

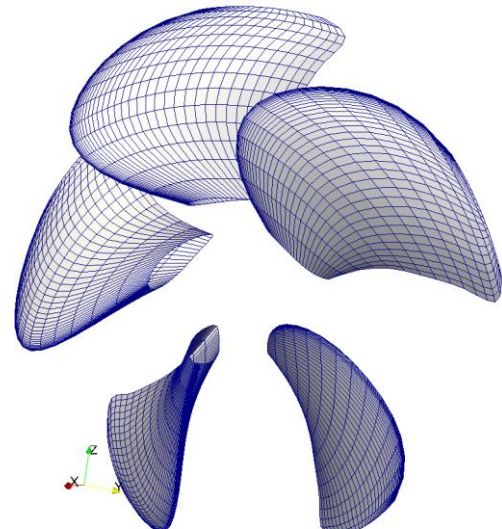


Figure 1: Propeller panel grid

3.1 Panel Method

3.1.1 Panel Grid

A grid of quadrilateral panels has been generated based on the propeller geometry as defined in the available *pff*-file. At the tip the data was modified slightly to achieve a nondimensional chord length equal to 1. All blades are included in the simulation because of the asymmetric flow field. They are modelled as lifting bodies with wake sheets extending a maximum amount of 1.5 revolutions downstream. The grid extends just up to $r/R = 0.99$ to avoid panels with high aspect ratios as well as non-planar geometry and the numerical problems arising. The hub is also not included. The development of *panMARE* is continuously ongoing and in this point not completed.

A grid study for the open water condition was performed to show consistency of the method and identify a reasonable grid resolution. As an indicator for this, the propeller thrust and torque were used. Calculations using a wide range of panel numbers for the blade grid were performed. The ratio between panels in radial and chordwise direction is kept constant, as well as the refinement functions. The quality of the results is evaluated based on the difference to the finest mesh. Results are shown in Figure 2 and Table 1. It is visible from the decreasing error that the results converge toward the results of the finest mesh. The lowest panel count reasonable before losing too much accuracy is 1080 per blade. A view of the corresponding panel grid is shown in Figure 1.

Table 1: Results of grid study for panel method

Panels	Δk_T [%]	$\Delta 10k_Q$ [%]
168	3,956	4,192
504	1,704	1,451
780	0,943	1,091
1080	0,152	0,260
1470	-0,426	-0,508
1794	0,122	0,112
2576	0,000	0,000

For Case 2 and Case 3 the tunnel walls are expected to have a considerable influence on the results and therefore they should be included in the simulation. The side walls are discretized with nonlifting panels, i.e. only the source strength is calculated. The top wall is included as a symmetry plane to reduce computational effort while the rounded corners are neglected. In order to evaluate pressure fluctuations in Case 3 panels are generated at the probe locations. An overview of the computational setup for case 3 is presented in Figure 3. In the lower half the actual geometry can be seen while the upper part shows the copy due to the

symmetry. For all simulations the propeller axis coincides with the global x-axis.

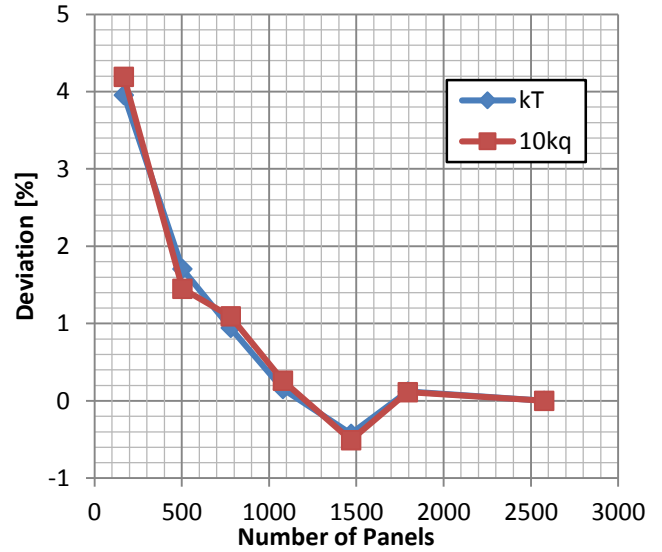


Figure 2: Results of grid convergence study for panel method

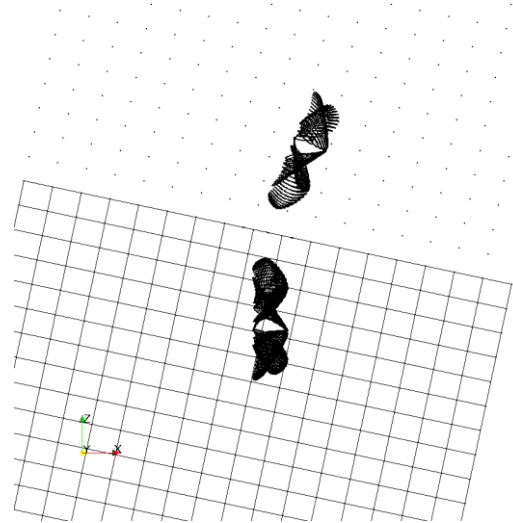


Figure 3: Panel method domain setup (case 3)

Hub and tip regions are excluded from the treatment of the cavitation model since locally high crossflow velocities are to be expected here. Thus, the flow does not follow chordwise grid strips as required in the dynamic boundary condition and therefore the cavitation model would yield unphysical results. Additionally, supercavitation and tip vortex cavitation occurs often in these regions, which is not implemented yet in the method.

3.1.2 Panel Method Setup

Friction forces are considered empirically with an approach to calculate the local friction coefficient for each panel based on the local Reynolds number. A transitional zone between laminar and turbulent approximations is included.

Hydrostatic pressure influence is considered with the gravity vector perpendicular to the top tunnel wall and downward.

In preliminary simulations it has been determined that the shape of the PPTC propeller requires a special treatment in the leading edge region. Because of the locally very high curvature discretized and actual geometry diverge. This causes large angles between neighboring panel normal vectors. Therefore the derivative of the potential to determine the local velocity is not calculated across the leading edge.

The strategy to determine the cavity inception location needs to be specified for the cavitation module. To achieve stability in the results a fixed position close to the leading edge was chosen, where low pressures are expected to occur.

3.2 Finite Volume Methods

3.2.1 Finite Volume Grids

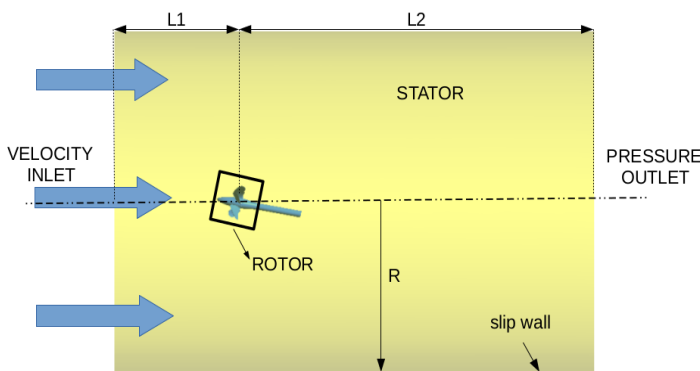


Figure 4: Domain setup in ANSYS CFX

A structured grid of hexaeder cells as shown in Figure 6 was generated using ICEM CFD and used in ANSYS CFX. For OpenFOAM an unstructured grid of hexaeders was created with HEXPRESS. An inlet condition was used to control the velocity according to the specific case, while the reference pressure was set at the outlet. All tunnel walls are modelled as no-slip walls. The domain was extended downstream in some cases with free-slip walls. Its dimensions are

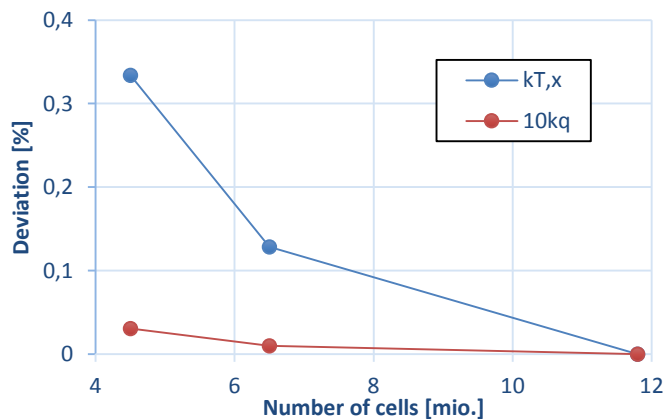


Figure 5: Results of grid convergence study for ANSYS CFX

summarized in Table 2. The boundary layer is discretized to ensure y^+ -Values lower than 30 on the blades.

Small changes were made in the geometry. The gap between hub and non-rotating parts was closed. To include the gap forces in the calculation a hub dummy was simulated at different operating points. The obtained forces were used to correct forces and torque from the propeller simulations.

As a first step a convergence study was carried out in ANSYS CFX for three different meshes. The results in Figure 5 show the difference in thrust and torque coefficients relative to results of the finest mesh. With increasing cell number the difference decreases in addition to already very low deviation for the coarsest mesh (4.5 million cells). This can be explained by the constant y^+ -Values in all meshes. Still the finest mesh was used in cases 2 and 3 to be able to capture as much of the cavitation as possible. The at the time low cluster utilization allowed us to use the same mesh for the open water simulations.

Table 2: Domain dimensions in FVM

Dimension	Case 1		Case 2 & 3	
	CFX	OpenFOAM	CFX	OpenFOAM
L_1	5D	3D	2.2D	
L_2	10D	8D	18.2D	
R	5D	4D	3.4D	

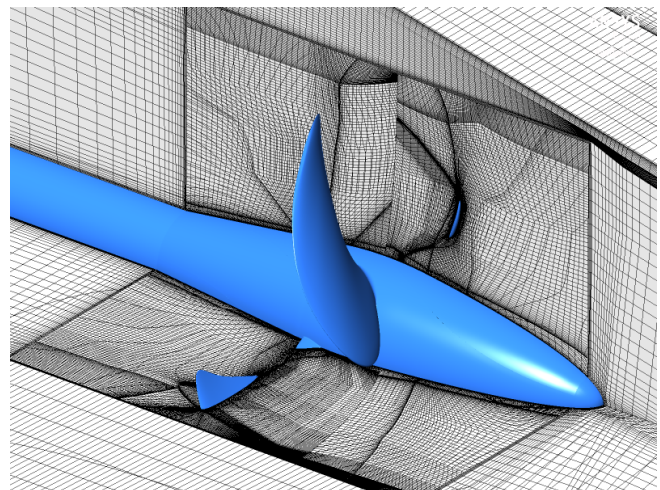


Figure 6: Propeller domain volume mesh (Case 3)

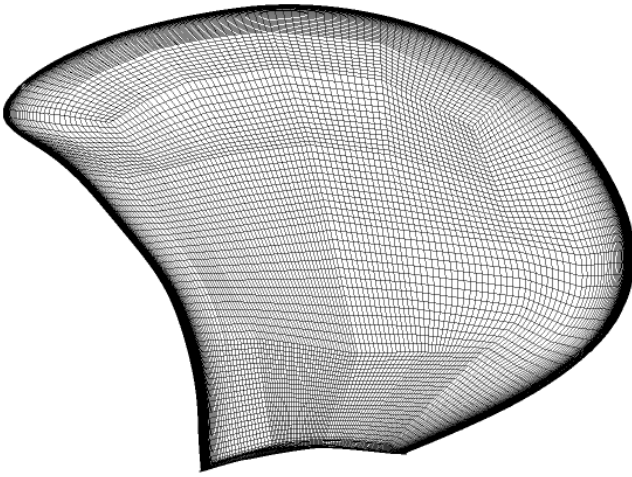


Figure 7: Blade surface block mesh (CFX)

3.2.2 Finite volume simulation setup

The SST $k - \omega$ turbulence model was used to model the boundary layer flow. Interfaces between rotating and stationary subdomains were employed to enable unsteady simulations. Buoyancy was not activated in any calculations.

In order to achieve faster convergence all unsteady calculations were initialized with the results of a suitable steady simulation.

4 RESULTS AND DISCUSSION

In this section results obtained with BEM and FVM methods are shown compared. Only parts of the workshop cases are shown for better clarity.

4.1 Open Water Test

The results of all simulations are summarized in the open water diagram (Figure 8). All forces were averaged across

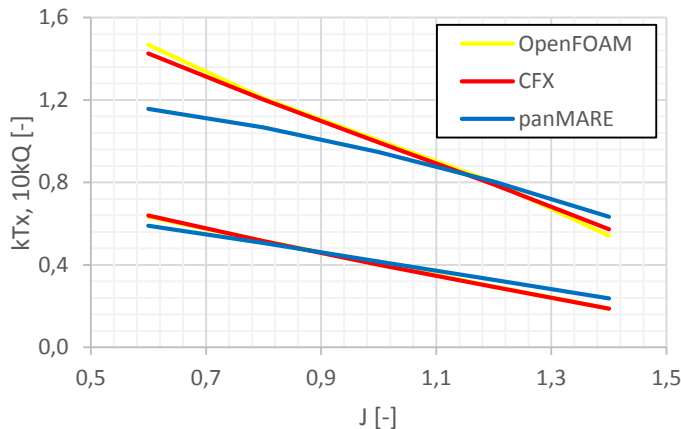


Figure 8: Open water diagram

multiple blade passages. Both RANS methods give results with only small deviations. At low advance coefficients the ANSYS CFX simulations predict higher thrust at lower torque, while at high advance coefficients OpenFOAM forecasts higher torque. This is likely caused by the different

meshing approaches and global as well as local refinements. To study the effects of solver and mesh individually, the simulations would have to be rerun with the respective other mesh.

Thrust and torque obtained by panel method simulations differ largely at most analyzed operating points. This indicates that significant components of those forces cannot be accounted for in a panel method using the described setup.

The limitation of the grid to 99% of the actual propeller radius causes lower thrust and torque. Another part of the difference might be attributed to the missing hub. It would increase the angle of attack locally and therefore thrust and torque acting in the hub region.

Regarding the side force components we refer you to the following workshop publications and narrow it down to a short summary: All methods predict side forces in the same direction while their magnitude differs. Surprisingly the forces show a significantly larger relative difference between ANSYS CFX results and OpenFOAM than in the predicted thrust shown above.

4.2 Cavitation Test

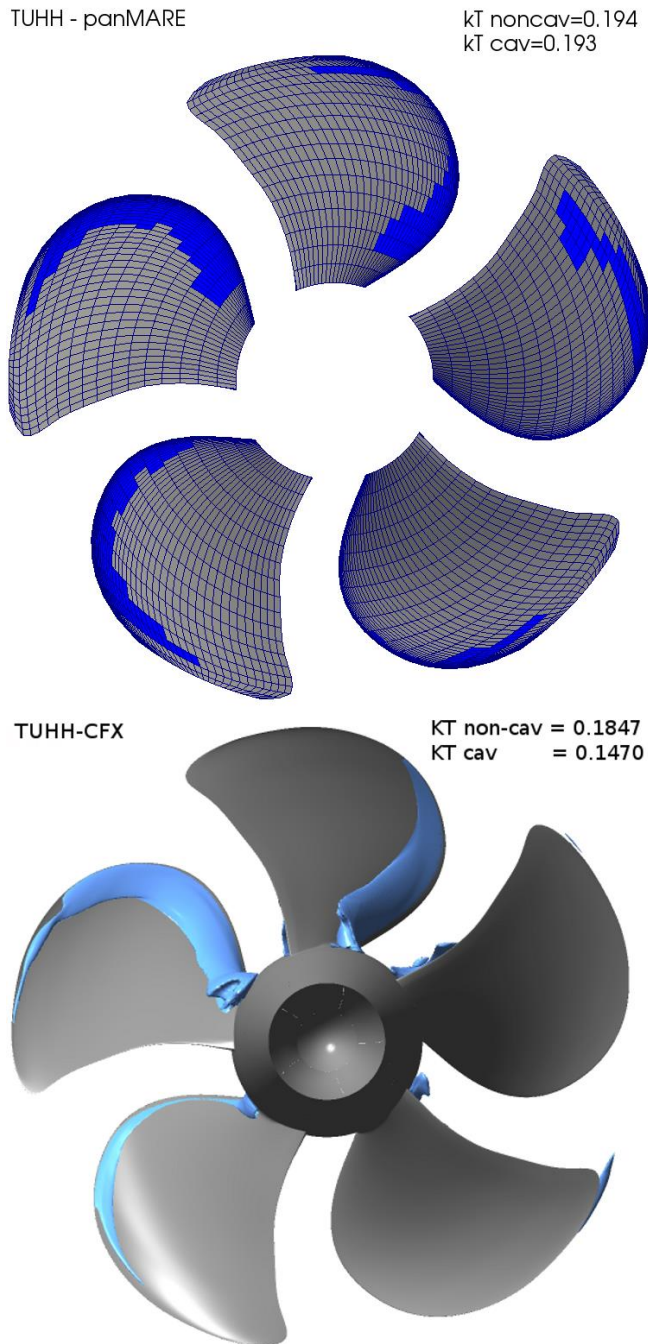
Case 2.3 was chosen exemplarily to compare the different computational methods. Unfortunately for OpenFOAM the highest angular rotation angle per timestep was around 0.25° due to stability reasons. Therefore the simulations could not be completed in time for this publication.

The cavity planform predicted by ANSYS CFX and *panMARE* show generally good agreement (see Figure 10). Differences can be observed in the tip and hub regions, where the RANS method exhibits both supercavitation and cavitating vortices. As described above those mechanisms cannot be simulated by the BEM method yet.

The thrust decrease predicted by RANS is in an expected range. However, a similar thrust loss is not present in the panel method results. The reason for that may be that the dynamic boundary condition is applied first. After the equation system is solved and the source strengths are determined it is no longer satisfied. Consequently the pressure in cavitating areas will be lower than vapor pressure. This problem will be addressed in future research. A higher thrust in the BEM results leads to a larger cavitating area on the blades because of the virtual change of operational point relative to the examined one in CFX.

Additionally, the leading edge vortex is not considered in the panel method. The RANS simulation shows a reduction of the cavity area on the blade near the 9 o'clock position compared to the BEM method results that is likely in part caused by the leading edge vortex. As a result the tip regions show less cavitation on all blades.

Evaluating the cavity inception locations the definition of a cavity inception location in *panMARE* leads to a good agreement with the RANS results. Yet in other cases this has caused the upstream cavity boundary positions to differ from the ones simulated by ANSYS CFX.



4.3 Pressure Pulses

Figure 10: Cavitation on blade pressure side (case 2.3)

In this section pressure pulses at one monitoring point are compared for test case 3.3. For the same reasons as presented in the previous chapter converged results with OpenFOAM

could not be achieved in time. The development of the monitored pressures is shown in Figure 9 for the timespan of roughly two blade passages. Unfortunately simulations with *panMARE* had to be run at a large time step to achieve good stability of resulting induced pressures. Therefore only simulation results with angular increment of 11.25° are presented.

Accounting for cavitation in both methods causes a higher amplitude relative to the fully wetted simulation results as expected in most cases. Furthermore amplitudes of higher harmonic frequencies than blade frequency are visible in results from both *panMARE* and ANSYS CFX. The BEM is able to capture the dominant mechanisms for pressure fluctuations as they were simulated with RANS. Because the induction of pressure is a potential effect this was expected and also proven in past research.

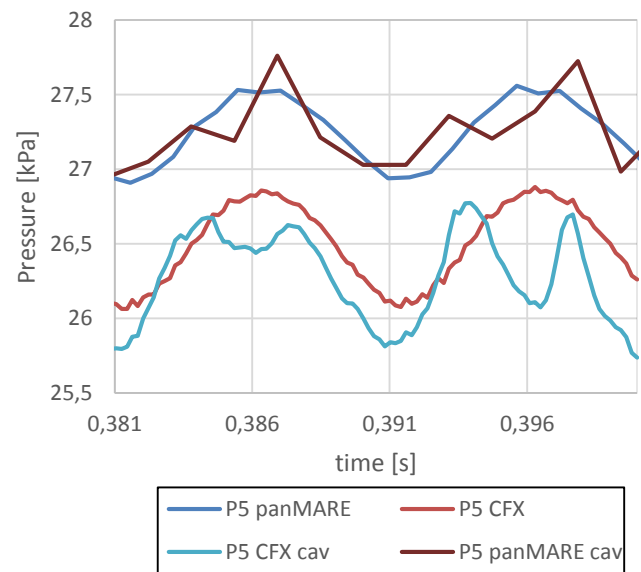


Figure 9: Pressure pulses comparison (case 3.3)

5 CONCLUSIONS AND FUTURE WORK

This work has shown a comparison of three numerical methods for the case of a propeller flow with inclined propeller axis. Open water experiments as well as experiments in a tunnels were simulated and the results presented. For open water conditions RANS methods delivered significantly different results at a high range of operation points than the BEM method. However, the cavity platform predicted by the BEM was mostly very close to the one obtained with RANS. Concerning the stability issues with *panMARE* it will be investigated which measures address this problem most efficiently. A second inner iteration could be a possible solution for example.

Acknowledgments

We would like to thank all of our colleagues that provided theoretical advice as well as CPU power. Without them this work could not have been completed in this scale.

REFERENCES

- ANSYS. ANSYS CFX 15.0 Documentation. Technical Report, ANSYS Inc., Canonsburg, USA, 2015.
- Vaz, G. (2005). Modelling of Sheet Cavitation on Hydrofoils and Marine Propellers using Boundary Element Methods. PhD Thesis, Universidade Técnica de Lisboa, Lisbon, Portugal.
- Fine, N. (1992). Nonlinear Analysis of Cavitating Propellers in Nonuniform Inflow. PhD thesis, Massachusetts Institute of Technology, Cambridge, USA.
- Katz, J. and Plotkin, A. (2001). Low Speed Aerodynamics. Cambridge University Press,
- Abdel-Maksoud, M. (2003). Numerical and Experimental Study of Cavitation Behaviour of a Propeller. Sprechtage Kavitration, Schiffbautechnische Gesellschaft. Hamburg, Germany.
- Lifante, Conxita, Frank and Thomas (2008). Untersuchung der Druckschwankungen höherer Ordnung am Hinterschiff unter Berücksichtigung der Kavitation am Propeller. Abschlussbericht, ANSYS Germany GmbH, Germany.
- Merkle C. L., Feng, J. and Buelow, P. E. O. (1998). Computational Modeling of the Dynamics of Sheet Cavitation. Third International Symposium on Cavitation, Grenoble, France.
- Dubbioso, G, Muscari, R and Di Mascio A. (2013). Analysis of the performances of a marine propeller operating in oblique flow. CNR-INSEAN, Roma, Italy.

Numerical Prediction of PPTC'2015 Propeller Performance in Oblique Flow

Matthias Tenzer¹

¹ Institute of Ship Technology, Ocean Engineering and Transport Systems, Department of Mechanical and Process Engineering
University of Duisburg-Essen, Duisburg, Germany

ABSTRACT

The paper presents results of open water characteristics in oblique flow (Case 1) for the PPTC'2015 propeller test case. Unsteady, incompressible, single-phase RANS computations with a $k-\omega$ -SST turbulence model using the commercial code ISIS-CFD within the Numeca FINE/Marine environment have been carried out. For a first validation of the method, the PPTC'2011 open water test case (Case 2.1) is calculated. On basis of the good agreement for the open water characteristics with the experimental data, a similar numerical setup in oblique flow is computed. This paper summarizes the settings and results of the open water characteristic for two different meshes.

Keywords

Propeller, RANS, open water test, oblique flow

1 INTRODUCTION

The investigation of ship's hull-propeller-rudder interaction is in focus of research since many years. Especially the interaction in flow states due to manoeuvring conditions in shallow water with ducted propellers and complex rudder geometries is of particular interest. A deeper understanding of this hydrodynamic problem is intended to improve the capabilities of ship handling simulators for inland waterway vessels.

The growing capacity of processor units in conjunction with capable numerical methods, such as Reynolds Averaged Navier-Stokes (RANS) solvers, can be regarded as a possible way of resolving this problem. For this purpose meaningful validation cases are needed to demonstrate the usability of the used numerical method.

2 NUMERICAL METHOD

Within the present study the commercial code ISIS-CFD is used. The code was developed by Ecole Centrale de Nantes (ECN) and Centre national de la recherche scientifique (CNRS) and is nowadays part of the Numeca FINE/Marine software package.

The code is capable of simulating turbulent flows by solving the incompressible unsteady Reynolds-averaged Navier Stokes equations (RANSE) and is based on the finite volume method (FVM) for the spatial discretization of the transport equations. It is a face-based method for three-dimensional unstructured meshes. Among a range of several turbulence models, the two-equation $k-\omega$ -SST model was used for all computations in this study. Although the code is able to solve multiphase-flows, all open water simulations in this paper were realized as single-phase calculations, considering a fluid region only. A comprehensive summary with mathematical description of the solver characteristics is given by Wackers et al. (2011).

3 NUMERICAL SETUP

The numerical grids used in the present study were generated with the mesh generation software HEXPRESS using the sliding interface technique. An inner cylindrical mesh contains the rotating propeller part, whereas a rectangular outer mesh contains the non rotating shaft and the far field.

Grid 1 refers to the PPTC'2011 geometry with spatial resolution of all gaps and is used for uniform and oblique flow calculations. Grid 2 is based on the simplified PPTC'2015 geometry without gaps. This grid is investigated in oblique flow conditions only. All calculations were carried out in model scale.

3.1 Grid 1

The first grid is modelled with the PPTC'2011 geometry with all gaps between the propeller blades and the root. The dimensions of the mesh are based on the size of the towing tank at SVA Potsdam (see Barkmann (2011)) with regard to breadth and depth. Instead of modelling the dynamometer, an extended shaft to the outlet is used.

Figure 1 shows the principle grid arrangement with dimensions and boundary conditions for the calculation of the PPTC'2011 case with straight inflow. The same configuration is used for modelling the PPTC'2015 case in oblique flow by adjusting the velocity components in x- and z-direction of the far field boundary conditions.

Additionally the boundary condition of the top is changed to a second outlet condition with zero pressure gradient. Figure 2 and 3 show the surface representation of the propeller and the gap resolution in detail.

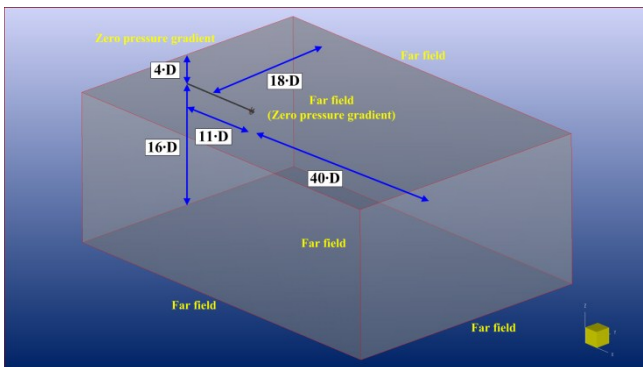


Figure 1: Dimensions and boundary conditions.

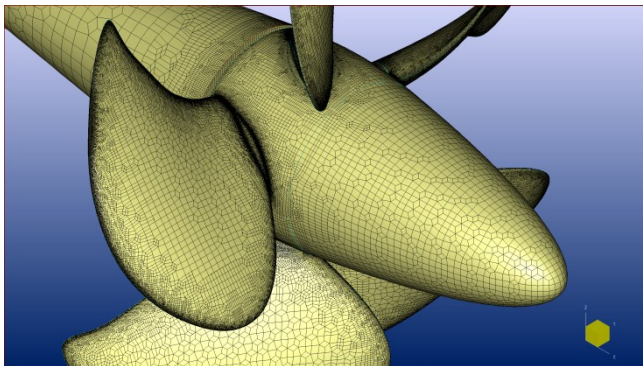


Figure 2: Surface representation of propeller.

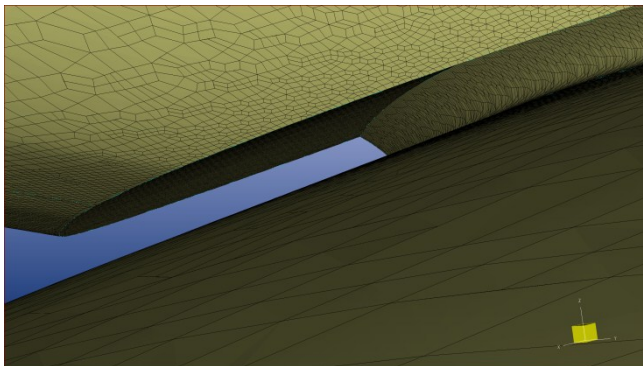


Figure 3: Mesh resolution of gaps.

The rotation of the propeller is included with the sliding interface technique. A cylindrical region around all rotating parts of the propeller represents the inner region.

The whole mesh consists of 8.3 million hexahedral cells with a prismatic layer, while 7.7 million cells belong to the inner region. This large amount of cells is the result of the fine propeller gap resolution for all five blades. For the PPTC'2011 straight flow calculations a mass density of $\rho=998.9$ [kg/m³] and a dynamic viscosity of $\eta=1.1\cdot 10^{-3}$

[Pa·s] is used. With propeller revolutions of 10 [1/s] a uniform time step of $\Delta t=1.0\cdot 10^{-3}$ [s] is used, which means a propeller rotation of 3.6 degree per time step. For the PPTC'2015 oblique flow calculations a mass density of $\rho=998.6$ [kg/m³] and a dynamic viscosity of $\eta=1.1\cdot 10^{-3}$ [Pa·s] is used. Although the propeller revolutions are increased to 15 [1/s], the same time step of $\Delta t=1.0\cdot 10^{-3}$ [s] is used, which means a propeller rotation of 5.4 degree per time step. Calculations are carried out with wall function and the boundary layer is applied for Y⁺-values of about 80.

3.2 Grid 2

The second computational domain has exactly the same dimensions, but contains the PPTC'2015 geometry without resolution of the gaps. Additionally the boundary condition of the top is put back to a far field condition. This grid is only used to simulate the PPTC'2015 case in oblique flow.

The whole mesh consists of 2.8 million cells, while 2.2 million cells belong to the inner region. In this case, with propeller revolutions of 15 [1/s], the time step is decreased to $\Delta t=5.0\cdot 10^{-4}$ [s], which means a propeller rotation of 2.7 degree per time step. Again the mesh is modelled with boundary layer using a wall function, applied for Y⁺-values of about 80.

4 COMPUTATIONAL RESULTS

4.1 Open water characteristics for the PPTC'2011 case

The open water characteristics were investigated on the basis of grid 1. Figure 4 shows the time series of the calculated propeller forces in x-direction. Within the first second the revolutions of the inner propeller region are increased with a sinusoidal ramp function.

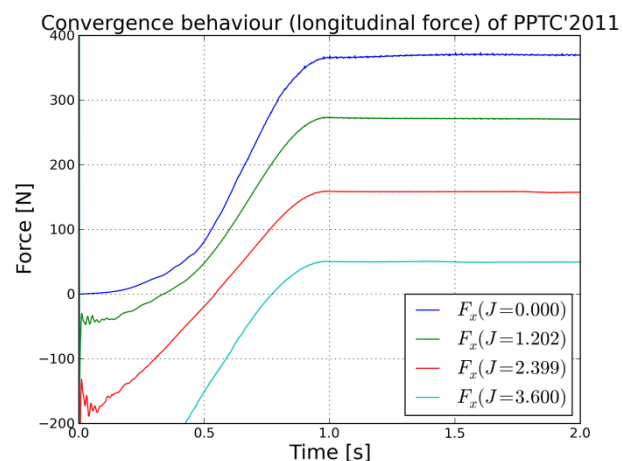


Figure 4: Convergence behaviour of propeller forces in longitudinal direction (PPTC'2011).

Shortly after a stationary condition is achieved, interesting forces and moments are averaged over a period of time. The

comparison of thrust and torque coefficients and the propeller efficiency is shown in Figure 5. All values show a good agreement between experiment and calculation.

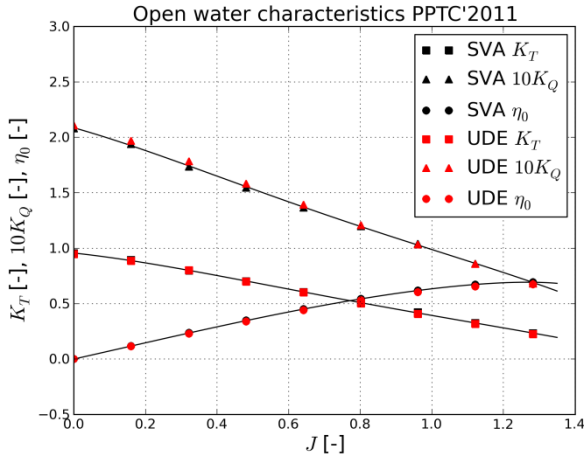


Figure 5: Open water characteristics (PPTC'2011).

Table 1: Deviations from the experiments (PPTC'2011).

J [-]	ΔK_T [%]	$\Delta 10 K_Q$ [%]
0.0000	-0.94	1.37
0.1599	-0.84	1.42
0.3218	0.11	2.72
0.4817	-0.28	2.38
0.6419	-0.45	1.92
0.8020	-1.53	0.83
0.9609	-3.19	-0.71
1.1211	-2.66	-0.13
1.2830	-3.35	-0.39

On the basis of the good agreement with the experimental data, the velocity inflow definitions for grid 1 are changed to simulate an inclination of 12°.

4.2 Open water characteristics for the PPTC'2015 case in oblique flow

Based on two available experimental data points, the calculations in oblique flow were validated for both calculated grids. For a better presentation in Figure 6, the calculations for K_{Tx} , K_Q and η_0 are represented as polynomials. Table 2 demonstrates at the same time a good agreement between the calculation and the experimental data. The abbreviations G1 and G2 stand for Grid 1 and Grid 2 respectively.

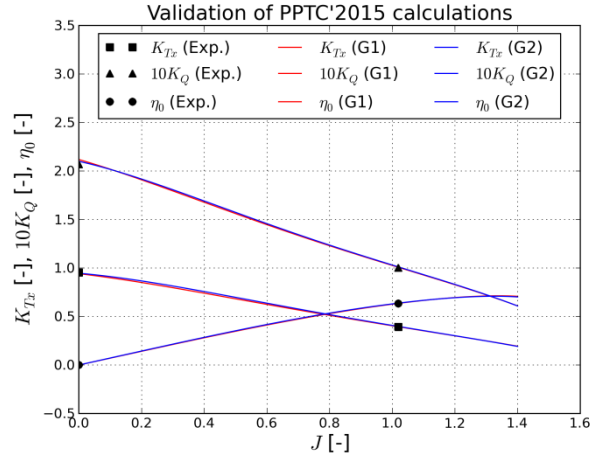


Figure 6: Validation of PPTC'2015 calculations in oblique flow with angle of attack of 12 degree.

Table 2: Deviations from the experiments (PPTC'2015) in oblique flow with angle of attack of 12 degree.

J [-]	ΔK_{Tx} (G1) [%]	$\Delta 10 K_Q$ (G1) [%]	ΔK_{Tx} (G2) [%]	$\Delta 10 K_Q$ (G2) [%]
0.0000	-1.40	2.19	-0.90	1.30
1.0190	n.a.	n.a.	1.51	1.00

Figure 7 shows all computed points of the PPTC'2015 test case with angle of attack of 12 degree for K_{Tx} , K_Q and η_0 and both grids. The results of grid 1 (with resolution of all gaps) are represented in red, the results of grid 2 (without gaps) are denoted in blue colour.

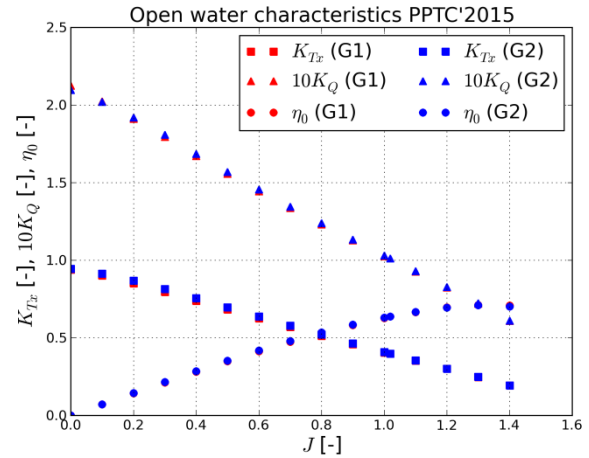


Figure 7: Open water characteristics of PPTC'2015 in oblique flow for both grids (K_{Tx} , K_Q and η_0).

Based on the oblique flow condition, force coefficients in y- and z-direction K_{Ty} and K_{Tz} are non-zero. Figure 8 shows the computed results for these coefficients for both grids.

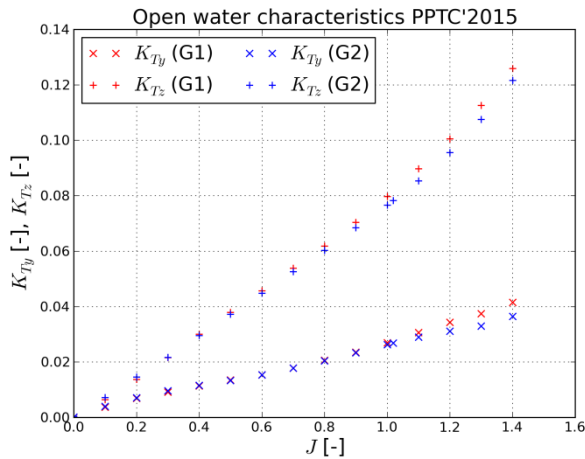


Figure 8: Open water characteristics of PPTC'2015 in oblique flow for both grids (K_{Ty} , K_{Tz}).

Table 3 summarizes the computed values of force and torque coefficients for grid 1 in oblique flow with an angle of attack of 12 degree.

Table 3: Computed values in oblique flow (Grid 1).

J [-]	K_{Tx} [-]	K_{Ty} [-]	K_{Tz} [-]	10 K_Q [-]
0.0	0.940	0.000	0.000	2.116
0.1	0.901	0.004	0.006	2.021
0.2	0.851	0.007	0.014	1.911
0.3	0.797	0.009	0.022	1.796
0.4	0.739	0.011	0.030	1.674
0.5	0.681	0.013	0.038	1.557

0.6	0.625	0.015	0.045	1.446
0.7	0.568	0.018	0.054	1.338
0.8	0.513	0.021	0.062	1.232
0.9	0.458	0.024	0.070	1.128
1.0	0.405	0.027	0.080	1.027
1.1	0.352	0.031	0.090	0.927
1.2	0.301	0.034	0.101	0.826
1.3	0.248	0.038	0.113	0.721
1.4	0.194	0.042	0.126	0.611

4 CLOSING REMARKS

The preliminary results point out, that the calculated values for both grids, do not differ considerably. This means the geometric resolution of all gaps is not of major importance. Nevertheless the submitted results for the workshop belong to grid 1 with spatial resolution of the gaps.

REFERENCES

- Wackers, J., Koren, B., Raven, H.C., van der Ploeg, A., Starke, A.R., Deng, G.B., Queutey, P., Visonneau, M., Hino, T. and Ohashi, K. (2011), "Free-Surface Viscous Flow Solution Methods for Ship Hydrodynamics", Archives of Computational Methods in Engineering, Vol. 18, 1-41.
- Barkmann, U. (2011), "Potsdam Propeller Test Case (PPTC) – Open Water Tests with the Model Propeller VP1304", Report 3752, Schiffbauversuchsanstalt Potsdam.

PPTC 2015 Test Case: simulating non-cavitating and cavitating propeller performances in oblique flow

Stefano Gaggero¹, Diego Villa² and Michele Viviani³

^{1,2,3} University of Genoa, Genoa, Italy

ABSTRACT

The analysis of the non-cavitating and cavitating unsteady performances of the PPTC propeller in oblique flow are presented. Calculations have been performed using the RANSE solver StarCCM+ that employs a homogeneous equation model, based on the immiscible mixture approach, for the solution of the water-vapor phase change. The *volume of fluid* approach is used to solve the multiphase flow while the mass transfer is modeled through the Schnerr-Sauer model. Finally, some calculations carried out with a Boundary Element Method are proposed in order to assess the reliability of this old-fashioned, but still widely adopted for design and optimization (thanks to its extremely higher computational efficiency), approach in a very demanding test case.

Keywords

Cavitation, PPTC Propeller, RANS, StarCCM+, BEM

1 INTRODUCTION

This paper presents the results of a computational study of the performance of the PPTC marine propeller in oblique flow conditions. Results are submitted to the workshop on cavitation and propeller performance PPTC'15 organized in the framework of the Fourth International Symposium on Marine Propulsors. Propeller hydrodynamics studies are performed by using both the commercial RANSE solver StarCCM+ (CD-Adapco, 2014) and a Boundary Element Method (Gaggero et al. 2010) specifically developed at the University of Genoa for the analysis of steady/unsteady, non-cavitating/cavitating propeller performances. RANSE calculations have been carried out using a homogeneous multiphase mixture approach solved with the *volume of fluid* approach. The Boundary Element Method is based on the solution of the inviscid, irrotational and incompressible potential flow equation for the perturbation potential (Morino and Kuo, 1974) with the partial non-linear model for the prediction of sheet laminar cavitation (Fine and Kinnas, 1993). Both the approaches have been extensively applied in the last years for the design (Bertetta et al., 2012, Gaggero et al., 2012a) and the analysis (Gaggero et al., 2010, Gaggero et al., 2012b, 2014a, 2014b) of marine propellers

performances in open water and in behind-wake conditions, under non-cavitating and cavitating conditions.

According to workshop specification, computations are applied to a five blade, right-handed, controllable pitch propeller, operating in oblique inflow conditions. Three cases, which measurements have been carried out at the SVA-Potsdam towing tank and cavitation tunnel, are proposed in the form of a “blind test”: prediction of oblique inflow (12° shaft inclination) non-cavitating open water performances (case 1), prediction of performances and cavity extension in oblique inflow (case 2) and prediction of unsteady non-cavitating and cavitating pressure pulses (case 3). The University of Genoa takes part to case 1 and case 2.

2 FORMULATION

2.1 RANS equations for Cavitating Flows

Even if most of the theoretical models for cavitation deal with the description of the dynamics of bubbles by solving for the vapor-liquid interface (the traditional Rayleigh-Plesset equation is probably the most known approach), in the framework of RANS solvers most of the cavitating engineering flows are solved using a mixture approach. The flow is treated, in fact, as a single variable density fluid, i.e. a homogeneous two-phase (vapor and liquid) mixture without explicit phase interfaces, whose dynamics are governed by tailored continuity and momentum equations for the mixture. Defining the vapor volume fraction α as the percentage of the volume domain (and, in discrete, of each computational cell) occupied by the vapor phase ($\gamma = 1 - \alpha$ is, of course, the liquid volume fraction):

$$\alpha = \frac{V_{vap}}{V_{liq} + V_{vap}} \quad (1)$$

the physical proprieties (in particular density, dynamic viscosity and velocity) of the mixture can be defined as a weighted mean between the physical proprieties of pure liquid and vapor phases:

$$\begin{aligned} \rho_{mix} &= \alpha\rho_{vap} + (1 - \alpha)\rho_{liq} \\ \mu_{mix} &= \alpha\mu_{vap} + (1 - \alpha)\mu_{liq} \\ \mathbf{u}_{mix} &= \alpha\mathbf{u}_{vap} + (1 - \alpha)\mathbf{u}_{liq} \end{aligned} \quad (2)$$

The resulting homogeneous mixture for compressible flows is governed, as usual, by continuity and momentum, expressed for the ideal mixture fluid as:

$$\begin{cases} \frac{\partial \rho_{mix}}{\partial t} + \nabla \cdot (\rho_{mix} \mathbf{u}_{mix}) = 0 \\ \frac{\partial (\rho_{mix} \mathbf{u}_{mix})}{\partial t} + \nabla \cdot (\rho_{mix} \mathbf{u}_{mix} \mathbf{u}_{mix}) = \nabla \cdot \boldsymbol{\sigma} + \mathbf{S} \end{cases} \quad (3)$$

in which $\boldsymbol{\sigma}$ is the stress tensor and \mathbf{S} represent the additional momentum sources (centrifugal forces, for instance). This system of equations can be closed introducing an additional equation that solves for the transport of the vapor volume fraction, through which the interaction between the vapor and the liquid phases is modeled. Combining, in fact, the expression of the mixed incompressible fluid density with the continuity equation, a conservative form of the incompressible transport equation for the fraction of vapor α can be written as:

$$\frac{\partial \alpha}{\partial t} + \nabla \cdot (\alpha \mathbf{u}_{mix}) = \frac{\dot{m}}{\rho_{vap}} \quad (4)$$

leading to the final form of the incompressible continuity and momentum equations for the mixture:

$$\begin{cases} \nabla \cdot \mathbf{u}_{mix} = \left(\frac{1}{\rho_{liq}} - \frac{1}{\rho_{vap}} \right) \dot{m} \\ \frac{\partial \mathbf{u}_{mix}}{\partial t} + \nabla \cdot (\mathbf{u}_{mix} \mathbf{u}_{mix}) = - \frac{1}{\rho_{mix}} \nabla p + \nabla \cdot \mathbf{T}_{Re} + \mathbf{S} \end{cases} \quad (5)$$

where \mathbf{T}_{Re} is the tensor of Reynolds stresses computed in accordance to the turbulent closure equations and $\dot{m} = \rho_v \rho_l / \rho_m \cdot d\alpha/dt$ is the interphase mass flow rate per unit volume. This set of equations is solved in StarCCM+ by using a *volume of fluid* approach (CD-Adapco, 2012).

The modeling of the interphase mass flow is the core of any cavitating flow approach within the RANS solvers. Merkle et al. (1998) proposed a chemical reaction analogy to model the phase transition that has been successfully applied by Kunz et al. (2000) to solve engineering flows cavitation. Many commercial codes (FLUENT and CFX, as in Ansys 2009) include this approach, together with the ‘‘full cavitation model’’ proposed by Singhal et al. (2002), based on two distinct continuity equations, one for the liquid and one for the vapor phase.

Unfortunately, the most important drawback of the Merkle/Kunz and the Singhal approaches is represented by the value of the constants of the models, whose values, in literature, are not unambiguous. Morgut and Nobile (2012) proposed, for instance, to calibrate (by optimization) these constants to obtain solutions consistent with the experiments but, in general, each new problem should require a specific analysis.

On the other hand, the alternative approach proposed by Schnerr and Sauer (2000, 2001), and adopted for instance in StarCCM+ (CD-Adapco, 2012), is based only on some

hypothesis about the nature of the vapor-liquid mixture. The vapor, in fact, is assumed to consist of N spherical bubbles ($n_0 = N/V_{liq}$ is the nuclei concentration per unit volume of pure liquid) of radius R , such that the vapor fraction can be expressed as:

$$\alpha = \frac{n_0 \frac{4}{3} \pi R^3}{1 + n_0 \frac{4}{3} \pi R^3} \quad (6)$$

On the light of equation (6) the time derivative of the vapor fraction is calculated as:

$$\frac{d\alpha}{dt} = \alpha(1 - \alpha) \frac{3}{R} \frac{dR}{dt} \quad (7)$$

where the bubble vapor-liquid interface velocity dR/dt is obtained through a simplified (but effective and largely adopted) Rayleigh relation:

$$\frac{dR}{dt} = \sqrt{\frac{2}{3} \frac{|p - p_{vap}|}{\rho_{liq}}} \text{sgn}(p_{vap} - p) \quad (8)$$

leading to a definition of the interphase mass flow rate \dot{m} , necessary to solve the set of equations (4) and (5), as:

$$\dot{m} = 3 \frac{\rho_{vap} \rho_{liq}}{\rho_m} \frac{\alpha(1 - \alpha)}{R} \sqrt{\frac{2}{3} \frac{|p - p_{vap}|}{\rho_{liq}}} \text{sgn}(p_{vap} - p) \quad (9)$$

that, with respect to the Merkle and the Kunz models, uses a symmetrical treatment of the grow and collapse of the vapor bubbles, even if from the second order Rayleigh equation the bubble collapse (when $p > p_{vap}$) is much more rapid. Depending on the sign of $|p - p_{vap}|$ the latest release of StarCCM+ (CD-Adapco, 2014) includes a modification of the mass transfer, that is multiplied by a custom factor in order to uneven the grow and the collapse of the vapor bubble. Present calculations, however, have been carried out with the unmodified formulation

2.1 Mesh and solver setup

The analysis of the PPTC propeller performances in non-cavitating and cavitating oblique inflow has been carried out by using a sliding interface approach, as presented in figure 1. Effectively StarCCM+ includes also chimera/overlapping mesh capabilities that, further than be extremely useful in the case of large mesh motions, may be applied also in the case of rotating geometries. However, by using polyhedral meshes, the interface conformity is granted for any choice of mesh arrangements and simulation time step, resulting in a more computational efficient (and, of course, usual) calculation setup. Calculations were performed, in both cases, adopting the same approach. An initial, coarse mesh, has been preferred, together with a relatively high time step, in order to initialize the flow field around the propeller. A fine regriding and a reduced time step were finally adopted to

carry out calculations until periodic convergence is reached. A total of 20 propeller revolutions was generally sufficient to achieve a converged solution.

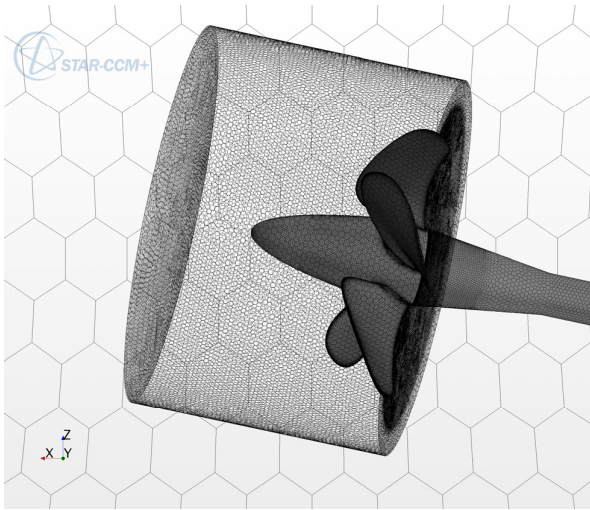


Figure 1: Inner and outer calculations domain.

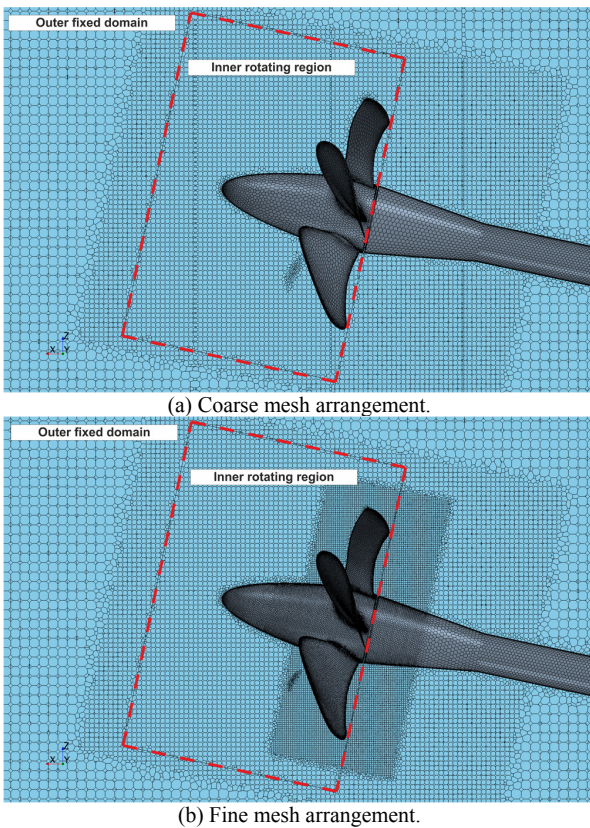
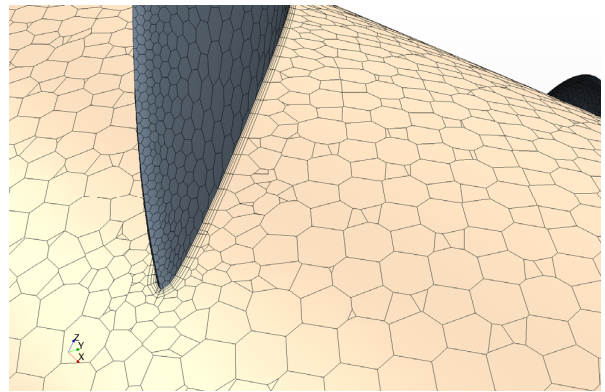
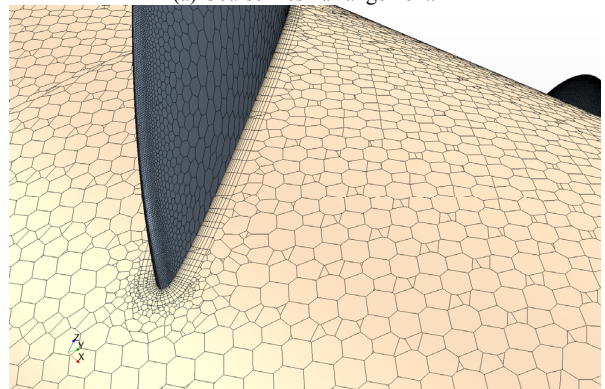


Figure 2: Mesh arrangement for non-cavitating calculations.



(a) Coarse mesh arrangement.



(b) Fine mesh arrangement.

Figure 3: Mesh arrangement for cavitating calculations. Details of the prism layers.

A summary of the main mesh parameters is reported in table 1 (non-cavitating calculations) and in table 2 (cavitating calculations). The fine mesh arrangement has been obtained by reducing the reference cell size on the blade surfaces and introducing some refinement regions to have a better description of the phenomena (including the risk of vortices from the hub) around the propeller (figure 2). Moreover, in the case of cavitating flow, a higher number of prism layers has been preferred to have cells as regular as possible in the most critic zones (figure 3).

Table 1: Main simulation parameters for non-cavitating calculations.

Mesh	cells	Prism layers/Total thick.	Sim. Δt
Coarse	1.7M	4 / 0.8 mm	6°
Fine	4.3M	4 / 0.8 mm	0.5°

This mesh setup, however, is far from the optimal choices, highlighted in Gaggero et al. (2014a), necessary for an accurate prediction of cavity inception point and

cavitating tip vortexes phenomena. The limitations of the computational resources, on the light of unsteady, moving mesh, calculations but also on the light of testing the reliability of affordable few-days engineering calculations, unfortunately force this choice of parameters.

Presented calculation, therefore, have been carried out with a mesh of about 4.3 and 5.0 Million of polyhedral cells respectively, with an equivalent time step of 0.5° . The realizable, two-layer $k - \varepsilon$ turbulence closure model has been selected on the light of previous works (Gaggero et al. 2014a) both for its overall reliability and proved accuracy (Kim and Rhee, 2004) in predicting frictional forces and for its lower smearing behavior of tip vortexes. The default parameters of the Schnerr-Sauer mass transfer model (numbers of nuclei and mean nuclei radius) were preferred (Gaggero et al, 2014a).

Table 2: Main simulation parameters for non-cavitating calculations.

Mesh	cells	Prism layers/Total thick.	Sim. Δt
Coarse	1.8M	4 / 0.8 mm	6°
Fine	5.0 M	8 / 1.5 mm	0.5°

3 RESULTS AND DISCUSSION

3.1 Test case 1

Results of case 1 (non-cavitating condition) are summarized in the graph of figure 4 while an example of the unsteady pressure distribution on the propeller blades is shown in figure 5.

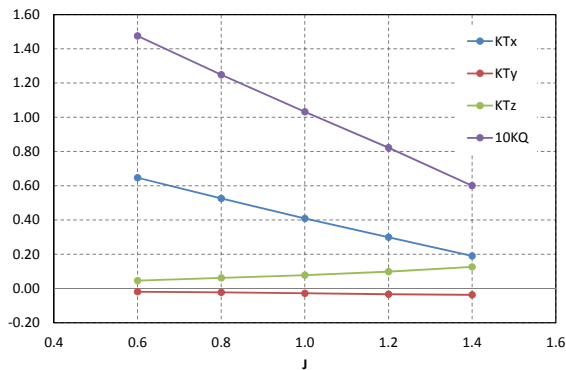


Figure 4: Propeller performances (K_{TX} , K_{TY} , K_{TZ} and $10K_Q$) as a function of the advance coefficient.

Calculations and results are presented only for the fine mesh arrangement. As a matter of fact the differences between the coarse and the fine mesh (having in mind, however, the limitations even of the fine mesh) are almost negligible. In terms of usual propeller forces (K_{TX} and $10K_Q$) the coarse mesh case differs from the fine arrangement of less than 2% (overestimated) up to an advance coefficient of 1.2, while in

off-design conditions ($J = 1.4$) differences are of about 3 and 4% (overestimated) respectively for the thrust and the torque coefficients.

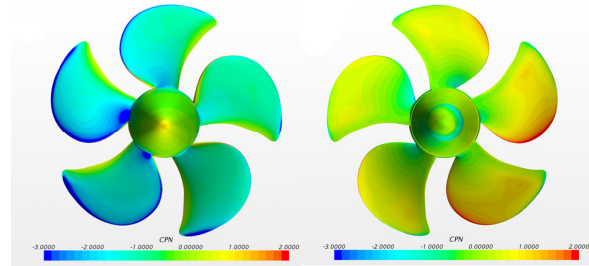


Figure 5: Pressure distribution (C_{PN}) on the suction and on the pressure side of the propeller, $J = 1.0$.

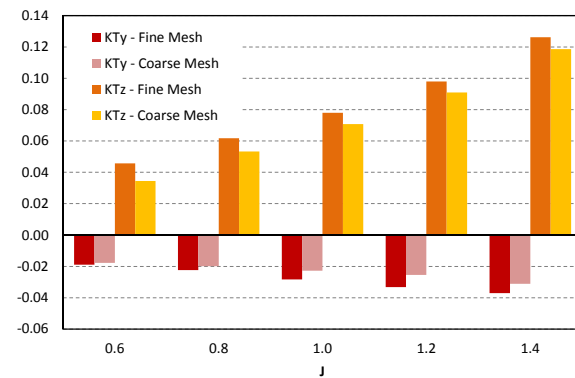


Figure 6: Comparison of vertical and transversal propeller forces computed with the Coarse and the Fine Mesh setup.

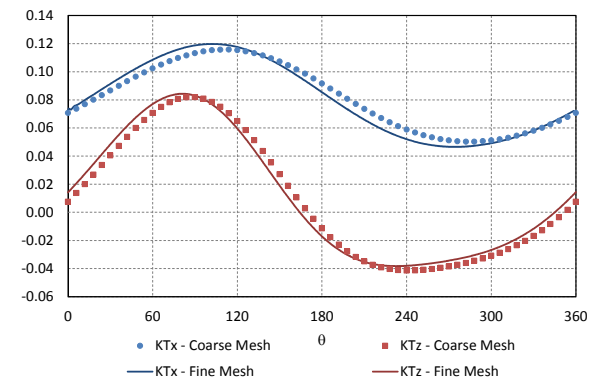


Figure 7: Single blade forces (K_{TX} and K_{TZ}). Coarse and Fine mesh comparison.

The influence of a more detailed mesh setup can be better appreciated, instead, looking at the forces on the transversal plane (K_{TY} and K_{TZ}). Computed vertical and transversal forces with the fine mesh are overestimated, in mean, by 10% and 15% respectively, as shown in figure 6.

Moreover the combined influence of a finer mesh arrangements and a reduced time step results in a slightly shift of the forces peaks, as evidenced in the analysis of the single blade forces along a single rotation shown in figure 7.

3.2 Test case 2

Results for the cavitating conditions (fine mesh setup) are reported in table 3. Figures from 8 to 10, moreover, compare the predicted cavity bubble for the two suggested values of volume fraction (60% in blue, 40% in green), both on the suction and on the pressure side of the blades. Predicted values are reasonably in agreement with the preliminary available cavitation tunnel measurements (case 2.1), even if some differences are worth to be highlighted. Predicted non-cavitating propeller performances are close (but slightly overestimated, +2.5%) to measurements, but the thrust breakdown due to cavitation is underpredicted: measured values show a thrust reduction of about 8% (from abt. 0.395 to 0.362 at $\sigma_N = 2.024$), while from computations only 4% of thrust reduction is evidenced. The nature of the cavitating phenomena, moreover, is rather different. At 0° position (figure 8) the numerical calculations shows a significant leading edge suction side (laminar) cavitation that is overestimated with respect to experiments, while the cavitating tip vortex is barely evidenced, due to a mesh arrangement not-adequate to prevent the numerical smearing of very local phenomena like those at tip. The tendency by StarCCM+ to overestimate the leading edge laminar cavitation is similar to that already evidenced, by many authors and by using different flow solvers, during the PPTC'11 SMP 2011 workshop on cavitating propellers in the case of propeller open water cavitation calculations (case 2.3.1) (Gaggero et al. 2011, Li, 2011, Sipila et al. 2011). At 90° and 180° the agreement with observations is slightly better except by the fact that the bubble cavitation shown, from root to $r/R = 0.8$, during the measurements is numerically mixed up with an uniform, even so very thin, sheet of vapor. The homogeneous mixture and the *volume of fluid* approach selected to simulate cavitating flows shows, for this particular phenomenon, all their limitations, suggesting that an Euler-Lagrange approach or calculations of the effective bubble dynamics (Hsiao and Chahine, 2008) should be preferred to simulate bubble cavitation. The bubble nature of the cavitating phenomena at $90-180^\circ$ (and this is much more clear for case 2.2 and 2.3) can be, however, deduced, on the light of the experimental and numerical experience of these kind of behavior, by the fact that the predicted isosurface of vapor fraction does not start its development at the blade leading edge. Its detachment line, on the contrary, is moved aft even if, due to a discretization arrangement constrained by computational resources, the leading edge is partially represented by a sharp edge (that should promote laminar sheet cavitation

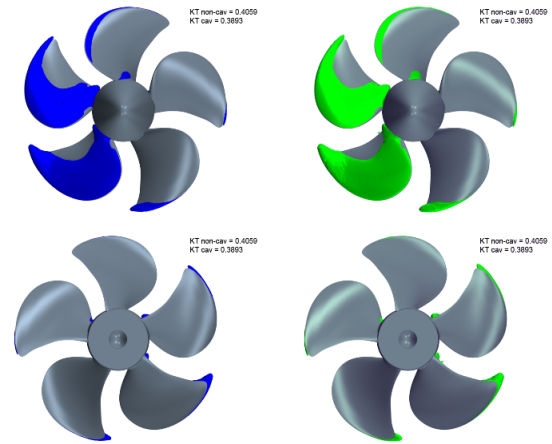


Figure 8: Isosurface of vapour fraction (60% in blue, left, 40% in green, right) for case 2.1.

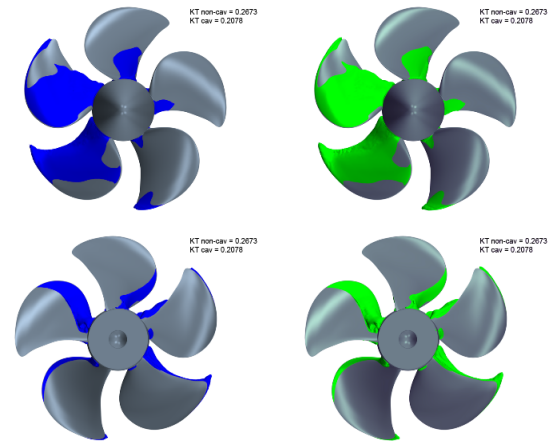


Figure 9: Isosurface of vapour fraction (60% in blue, left, 40% in green, right) for case 2.2.

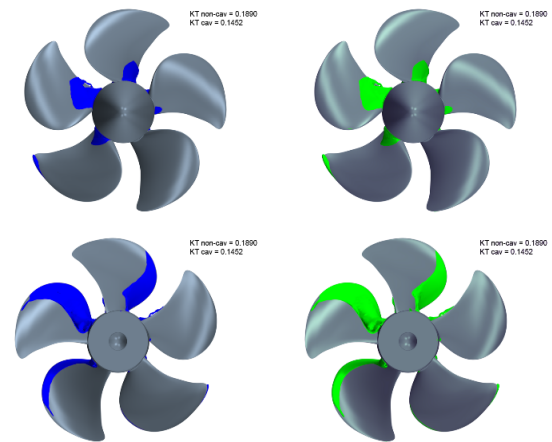


Figure 10: Isosurface of vapour fraction (60% in blue, left, 40% in green, right) for case 2.3.

rather than bubbles) instead than a perfectly rounded fillet. The comparison of the different vapor fraction isosurfaces highlights this behavior. At blade root the presence of a very thick suction side cavitation is fairly predicted while on the pressure side numerical calculations do not evidence the really small bubbles observed during cavitation tunnel tests.

Table 3: Predicted propeller performances in non-cavitating and cavitating conditions. RANS calculations.

	Case 2.1	Case 2.2	Case 2.3
J	1.019	1.269	1.408
σ_N	2.024	1.424	2.000
K_{TX} noncav.	0.406	0.267	0.189
K_{TX} cav.	0.389	0.208	0.145
10K_Q noncav.	1.015	0.749	0.589
10K_Q cav.	0.998	0.662	0.549

Obviously, the increase of the advance coefficient excites cavitation phenomena on the pressure side, as shown for case 2.2 (figure 9) and for case 2.3 (figure 10). The thrust breakdown computed in correspondence of these two conditions is higher (abt. 20%), the pressure side is characterized by a well-developed laminar cavitation at the blade leading edge while, similarly for case 2.1, the presence of bubble cavitation on the suction side and of thick bubbles at blade root can be deduced by the detachment point of the predicted isosurface of vapor regions.

3 BEM CALCULATIONS

In this last section case 1 and cases 2.1, 2.2 and 2.3 have been addressed by using the Boundary Element Method developed at the University of Genoa (Gaggero et al. 2010). Boundary Element Methods have been extensively applied for the analysis of the performances of marine propellers, both in steady and unsteady conditions including cavitation. Nowadays, with the increase of the computational resources, RANSE approaches are preferred for sheer analysis problems but in the design stage the computational efficiency of BEM approaches can be exploited to carry out systematic analyses and designs by optimization. Therefore the validation and a check on the accuracy of these approaches in very demanding cases like unsteady cavitating propellers in oblique inflow is still extremely important.

The Boundary Element Method developed at the University of Genoa is based on the Morino (Morino and Kuo, 1974) approach for the perturbation potential that solves the inviscid, incompressible and irrotational flow. Unsteady calculations are carried out with the *key blade approach* developed by Hsin (1990) while unsteady

cavitation is solved following the partial non-linear sheet cavity model proposed by Fine and Kinnas (1993). The propeller surface is discretized with hyperboloidal panels, an iterative Kutta condition scheme solves for the pressure jump at blade trailing edge while a simplified/semi-empirical wake alignment algorithm, instead than a fully unsteady alignment approach, has been preferred to avoid excessive computational time not worth in the design phase. Each blade has been discretized with a mesh of 1250 panels, while unsteady calculations were carried out with an equivalent time step of 4° .

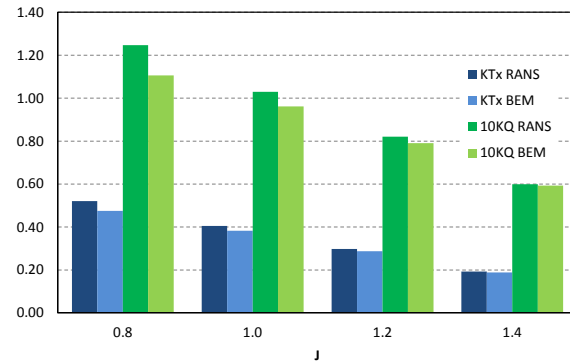


Figure 11: Comparison of RANSE and BEM predicted forces (K_{TX} and $10K_Q$) in non cavitating conditions.

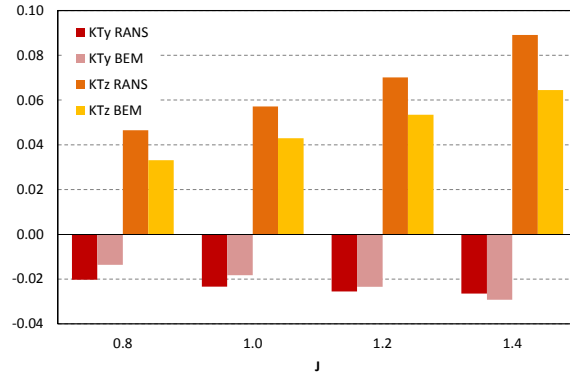


Figure 12: Comparison of RANSE and BEM predicted forces (K_{TY} , K_{TZ}) in non cavitating conditions.

Results of the unsteady non cavitating calculations, compared with RANSE, are shown in figure 11 and 12. For the sake of comparison, BEM and RANSE forces are only those of the blades, having the hub modeled for the potential calculations only an approximate cylindrical shape and being the potential approach not able to take into account the strong influence that viscosity plays in the case of blunt bodies, as the hub, in oblique inflow. The comparison, however, is quite satisfactory. Except very off-design conditions (the advance coefficient equal to 0.6 has

been consciously excluded by the analysis for these reasons), in correspondence of which viscous phenomena, unsteady leading edge separation forces (not accounted in these calculations), a more accurate representation of the trailing wake dynamics and, partially, the interaction with the hub flow and separated vortexes may strongly influence the performances of the propeller, predicted forces by the BEM are sufficiently in agreement with RANSE calculations. At lower advance coefficients BEM calculations are slightly underestimated (5%) for both thrust and torque coefficients, while close to design conditions (J abt. 1.2) the discrepancies are lower than 2.5%. Also for the forces on the transversal plane the Boundary Element Method shows a reasonably agreement with the more accurate RANSE calculations, at least in terms of trends.

Cavitating calculations results, for the three conditions under investigation, are summarized in table 4. With respect to RANSE and to the preliminary measurements the discrepancies are higher and this seems plausible on the light of the very complex cavity pattern evidenced both by observations and calculations. In particular, for case 2.1, in cavitating condition the propeller is not subjected to any thrust reduction; on the contrary thrust is increased due to an excessive pressure recovery at the cavitation bubble trailing edge. The solver, in its present configuration, is not able to take into account the influence of re-entrant jets, uses (and develops) a sheet laminar cavity model everywhere (precisely at the blade leading edge but also at midchord) the local pressure drops below the vapor tension (therefore observed bubble cavitation is modeled as a sheet laminar cavity bubble) and, inherently, cannot account for the very unsteady phenomena that, taking place in correspondence of the bubble closure region, could influence globally the propeller performances. For case 2.2 and 2.3 a rather better behavior of the BEM can be evidenced. In correspondence of the design advance coefficient the thrust reduction is of the order of 5% while for the higher advance coefficient the thrust reduction is of about 20%. The agreement between BEM and RANSE calculations is even better if cavity extensions are considered, as shown in figure 13, 14 and 15.

Table 4: Predicted propeller performances in non-cavitating and cavitating conditions. BEM calculations.

	Case 2.1	Case 2.2	Case 2.3
J	1.019	1.269	1.408
σ_N	2.024	1.424	2.000
K_{TX} noncav.	0.380	0.257	0.187
K_{TX} cav.	0.390	0.246	0.153
$10K_Q$ noncav.	0.960	0.731	0.586
$10K_Q$ cav.	1.010	0.743	0.541

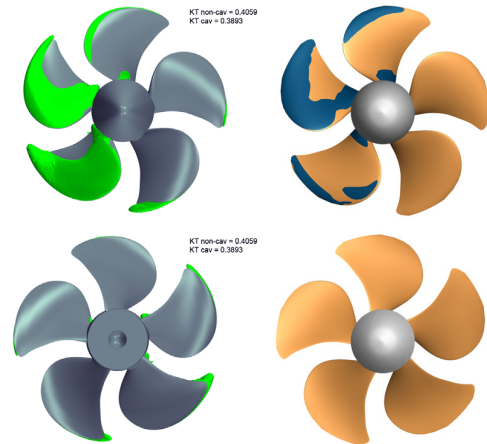


Figure 13: Comparison between RANS (60% vapour fraction, left) and BEM (right) for case 2.1.

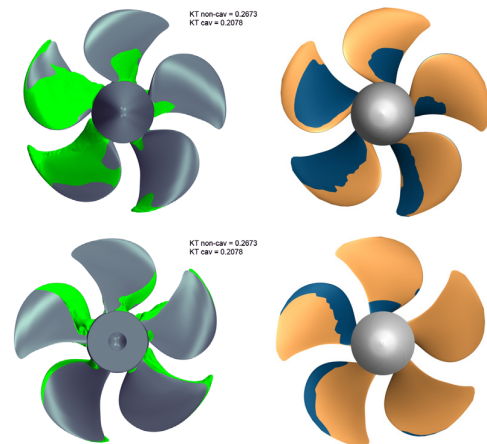


Figure 14: Comparison between RANS (60% vapour fraction, left) and BEM (right) for case 2.2.

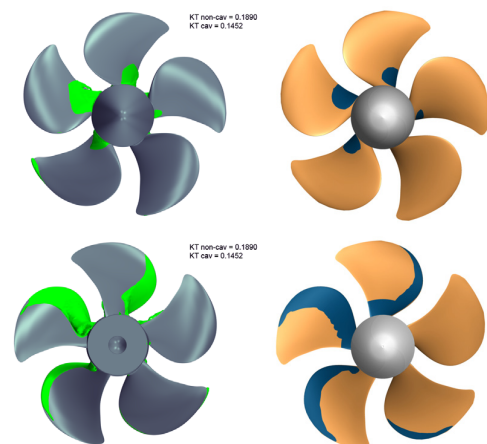


Figure 15: Comparison between RANS (60% vapour fraction, left) and BEM (right) for case 2.3.

Similarly to RANSE (and closely to the behavior already evidenced in the case of the open water calculations of the PPTC'11 SMP2011 test case) the leading edge laminar cavitation bubble is significantly overestimated at the blade leading edge in correspondence of the 0° blade position (case 2.1). At 90° and 180° the presence of bubble cavitation can be again deduced, as for RANSE, by the presence of the cavity bubble detaching far from the blade leading edge. At 180°, in particular, the predicted laminar cavity bubble close to the propeller tip is reasonably in agreement with the observations. In correspondence of case 2.2 and 2.3 BEM and RANSE predictions of cavity extension are even closer. BEM clearly evidences bubble cavitation from root to $r/R = 0.8$ and a slightly overestimated sheet laminar bubble on the blades pressure side. Also the thick cavity bubble at the blade root is similarly (extension and blade angular position) predicted.

4 CONCLUSIONS

The PPTC'15 test case (case 1 and 2) has been analysed by using a RANSE and a Boundary Element Method approach. Both unsteady propeller performances prediction and cavitation behaviour have been considered and a rather satisfactory agreement with the preliminary available measurements has been found. The mesh setup selected on the basis of the computational resources constraints and on the light of “weekly” affordable engineering calculations shows that overall propeller performances can be reasonably predicted with RANSE solvers. If, instead, the attention is focused on the prediction of local phenomena like tip vortex cavitation and bubble cavitation at midchord, much more detailed meshes, local refinements and advanced physical models like Euler-Lagrange bubble interactions are mandatory. On the other hand, once more Boundary Element Methods, if applied close to the design point, show an acceptable accuracy for their applications, as preliminary tools, for analysis and design issues.

REFERENCES

- ANSYS (2009). “Ansys Fluent 12.0 Theory Guide”. ANSYS.
- Bertetta, D., Brizzolara, S., Gaggero, S., Savio, S. and Viviani, M. (2012). “CPP propeller cavitation and noise optimization at different pitches with panel code and validation by cavitation tunnel measurements”. Ocean Engineering, Vol. 53, pp. 177-195.
- CD-Adapco, (2012). “StarCCM+ 7.04.006 Users Guide”.
- CD-Adapco, (2014). “StarCCM+ 9.04.009 Users Guide”.
- Fine, N. E., and Kinnas, S. A. (1993). “A Boundary-Element Method for the Analysis of the Flow around 3-D Cavitating Hydrofoils,” J. Ship Res., 37(3), 213-224.
- Gaggero, S., Villa, D. and Brizzolara, S. (2010). “RANS and Panel method for Unsteady Propeller Analysis”. Journal of Hydro-dynamics 22 (5): 564-569.
- Gaggero S., Villa, D. and Brizzolara S. (2011). “SMP Workshop on Cavitation and Propeller Performances: the Experience of the University of Genova on the Potsdam Propeller Test Case”. Proceedings of the Second International Symposium on Marine Propulsors. Workshop: Propeller Performance, SMP 2011, Hamburg, Germany.
- Gaggero S., Rizzo C.M., Tani G. and Viviani M. (2012a). “EFD and CFD design and analysis of a propeller in decelerating duct”. International Journal of Rotating Machinery, Volume 2012, Article ID 823831.
- Gaggero, S. Viviani, M., Villa, D., Bertetta, D., Vaccaro, C., Brizzolara, S. (2012b). “Numerical and experimental analysis of a CLT propeller cavitation behaviour”. Proceedings of the 8th International Symposium on Cavitation, Singapore, August.
- Gaggero, S., Tani, G., Viviani, M. and Conti, F. (2014a). “A study on the numerical prediction of propellers cavitating tip vortex”. Ocean Engineering, Vol. 92, pp. 137-161.
- Gaggero S., Villa D. and Viviani M. (2014b). “An investigation on the discrepancies between RANS and BEM approaches for the prediction of marine propeller unsteady performances in strongly non-homogeneous wakes”. Proceedings of the 33rd International Conference on Ocean, Offshore and Arctic Engineering, OMAE 2014, ASME, San Francisco, USA
- Hsiao, C.T., Chahine, G.L. (2008). Scaling of tip vortex cavitation inception for a marine open propeller. Proceedings of the 27th Symposium on Naval Hydrodynamics, Seoul, Korea, October.
- Hsin, C.Y. (1990). “Development and analysis of Panel Methods for Propellers in Unsteady Flows”. Ph.D. Dissertation, Massachusetts Institute of Technology.
- Kim, S.E., Rhee, S.H., (2004). “Towards high-fidelity prediction of tip-vortex around lifting surfaces – what does it take”. Proceedings of the 25th Symposium on Naval Hydrodynamics, St.John's, Newfoundland and Labrador, Canada, August.
- Kunz, R.F., Boger, D.A., Stinebring, D.R., Chyczewski, J.W., Gibeling, H.J., Venkateswaran, S., Govindan, T.R. (2000). “A preconditioned Navier–Stokes method for two-phase flows with application to cavitation prediction”. Comput. Fluids 29 (8), 849–875.
- Li, D.Q. (2011). “Prediction of non-cavitating and cavitating performance of a SVA Potsdam propeller”. Proceedings of the Second International Symposium on Marine Propulsors. Workshop: Propeller Performance, SMP 2011, Hamburg, Germany.

- Merkle, C.L., Feng, J., Buelow, P.E.O. (1998). "Computational modeling of the dynamics of sheet cavitation". Proceedings of the Third International Symposium on Cavitation. Grenoble, France.
- Morino, L. and Kuo, C.C. (1974). "Subsonic Potential Aerodynamic for complex configuration: a general theory". AIAA Journal, Vol. 12, pp. 191-197.
- Morgut, M., Nobile, E. (2012). "Numerical predictions of cavitating flow around model scale propellers by CFD and advanced model calibration". International Journal of Rotating Machinery, Volume 2012, Article ID 618180, 11 p., 2012. <http://dx.doi.org/10.1155/2012/618180>.
- Sauer, J., Schnerr, G. (2000). "Unsteady cavitating flows – a new cavitation model based on a modified front capturing method and bubble dynamics". Proceedings of the 2000 ASME Fluid Engineering Summer Conference. Boston, MA, June.
- Schnerr, G., Sauer, J. (2001). "Physical and numerical modeling of unsteady cavitation dynamics". Proceedings of the 4th International Conference on Multiphase Flow. New Orleans, USA.
- Singhal, A.K., Athavale, M.M., Li, H., Jiang, Y. (2002). "Mathematical basis and validation of the full cavitation model". J. Fluids Eng. 124 (3), 617–624.
- Sipila, T., Siikonen, T., Saisto, I. (2011). "FINFLO RANS-predictions for propeller performance". Proceedings of the Second International Symposium on Marine Propulsors. Workshop: Propeller Performance, SMP 2011. Hamburg, Germany.

FINFLO two-phase URANS predictions of propeller performance in oblique flow

V. Viitanen^{1,2} J. Martio¹ T. Sipilä¹

¹VTT Technical Research Centre of Finland, Tietotie 1 A, Espoo, PO Box 1000, FI-02044 VTT, Finland

²Corresponding author, email: ville.viitanen@vtt.fi

Abstract

The performance of the PPTC propeller in oblique flow conditions has been studied numerically. The investigations were performed according to the instructions given by the PPTC'15 Propeller Performance Workshop of SMP'15. The simulations have been conducted with the CFD solver FINFLO.

The tasks of the Workshop included predictions of the open water curves of the propeller, cavitation observations at three different operating points, and pressure pulses induced by the propeller at three different operating points. The performed analyses are blind tests, and only few global performance characteristics and cavitation sketches regarding these cases have been released to the participants prior to the Workshop.

The propeller open water performance in the inclined flow case was captured well. The differences between the computations on the different grid densities are within few percents. The cavitation predictions show qualitatively reasonable behaviour, when keeping in mind the limitations of the cavitation model.

Keywords

URANS, Propeller, Cavitation, Oblique flow

1. Introduction

The operation of a propeller in oblique flow differs greatly when compared to that in uniform axial inflow. In the inclined case, the inflow velocity to the propeller plane has a perpendicular component in addition to the axial one. When viewed in terms of the propeller relative velocities, this causes the resultant flow to the propeller blade to be inhomogeneous with respect to the propeller revolution. The velocity diagram in oblique flow configurations is shown in Fig. 1. If the angular position of $\theta = 0$ corresponds to the 12 o'clock position of a right-handed propeller, at $\theta = 90^\circ$ the perpendicular velocity component increases the angle of attack to the blade. Conversely, at $\theta = 270^\circ$ the perpendicular component decreases the angle of attack. This causes an asymmetric loading to the blade, resulting in thrust eccentricity and side force components. Additionally, the possible cavitation pattern will not be symmetric.

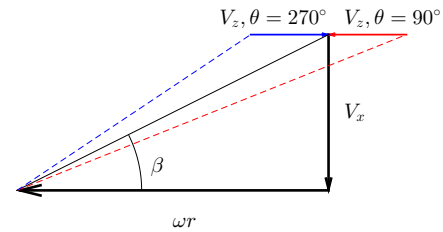


Figure 1: Velocity diagram for a propeller in oblique flow.

In this paper the FINFLO results of the SMP'15 workshop on cavitation and propeller performance in oblique flow are reported. The PPTC propeller is a five-bladed and right-handed, moderately skewed propeller with the diameter of $D = 0.25$ m in model scale. The propeller as well as the propeller coordinate system (PCS) are shown in Fig. 2.

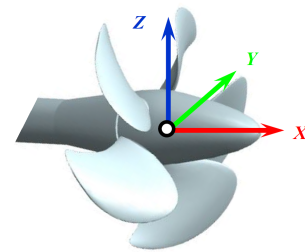


Figure 2: The PPTC propeller and the propeller coordinate system (PCS) used in the analyses.

The workshop consisted of three cases. The first case comprised of the predictions of the global performance open water curves for the torque, and the three force components. The second and third cases consisted of cavitation predictions in a cavitation tunnel, see Fig. 3. The tunnel geometry was provided by SVA Potsdam in IGES files. The second case consisted of observations of the propeller cavitation in three operation points in cavitation tunnel. Also, the global thrust coefficients for cavitating and wetted conditions at the three operation points were requested. In the third case, the time history of the pressure pulses at three measuring points on a plate above the propeller were requested. The pressure pulses were requested for wetted

and cavitating conditions. The plate was positioned 50 mm above the propeller in the cavitation tunnel. All of the simulations were done in uniform inflow conditions, but with the propeller axis inclined, making an angle of 12° , as can be seen in Fig. 3. This arrangement causes the flow to be inhomogeneous from the perspective of the propeller, since the tangential velocities act on one side with and on the other side against the direction of the propeller rotation. Consequently, all CFD analyses must be conducted in a time-accurate manner.

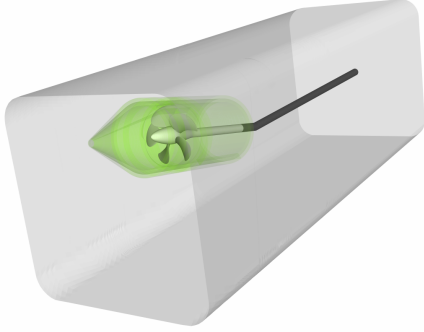


Figure 3: Computational domain for the calculations in the cavitation tunnel for Case 2. The propeller, hub and shaft are coloured with grey. The shaft is extended to the outlet by turning it 12° roughly four diameters downstream of the propeller. The darker grey denotes the non-rotating part. The green transparent parts denote the rotating blocks.

2. Numerical method

2.1. Finflo solver

The flow solution of in FINFLO is based on the control volume discretisation of the RANS equations (Siikonen et al., 1990). The equations are solved using a SIMPLE type pressure correction method. The iterative solution is based on approximately factorized time integration with local time stepping. In time-accurate simulations, a three-level fully implicit method is used. Approximately 100 inner iterations within each physical time step are used in the simulations. The inviscid fluxes are calculated using the Roe method, and the convective terms are evaluated using a third-order upwind biased scheme. The diffusive fluxes as well as the pressure gradients are evaluated using the second-order central difference scheme. FINFLO solves for the pressure, instead of the density, which is assumed to be a function of pressure and enthalpy. An algebraic multigrid method (AMG) with line Gauss-Seidel smoothing is employed to speed up the convergence.

For the two-phase simulations, a homogeneous mixture model is employed. The flow is assumed isothermal, which de-

ouples the energy equation from the system. Both phases share the same velocity, which simplifies the modelling, especially in the case of turbulence models. Furthermore, a single-pressure system is employed.

In the code, the continuity equation of the gas phase, and the momentum equations for the mixture are solved. The system of equations is in differential form

$$\frac{\partial \rho}{\partial t} + \frac{\partial \rho u_i}{\partial x_i} = 0 \quad (1)$$

$$\frac{\partial \rho u_i}{\partial t} + \frac{\partial \rho u_i u_j}{\partial x_j} = -\frac{\partial p}{\partial x_i} + \frac{\partial \tau_{ij}}{\partial x_j} \quad (2)$$

$$\frac{\partial \alpha \rho_g}{\partial t} + \frac{\partial \alpha \rho_g u_i}{\partial x_i} = -\Gamma \quad (3)$$

where ρ is the density of the mixture, u_i the velocity field of the mixture, p is the pressure, τ_{ij} the viscous stress tensor, α the gas volume fraction and ρ_g the density of the gas phase, and Γ is the mass transfer term. Note that in a two-phase system the liquid volume fraction follows from that of the gas phase as $\alpha_l = 1 - \alpha$.

The solution algorithm is based on finding a flux balance within each computational cell. This corresponds to a so-called explicit residual, which forms the driving force of the implicit stage. Before the implicit stage, the explicit residuals of the conservative variables are transformed to those of the primitive variables. The primitive variables are then updated at the end of each iteration cycle. The error in mass balance is eliminated from the residuals by the transformation of the explicit residuals.

The pressure-correction equation is derived from the continuity equation of the mixture. The mass residuals, weighed by the component densities, of both phases are summed together. The mass-transfer term is pseudo-linearized to enhance the diagonal dominance of the pressure-correction equation.

The turbulence model applied in the present calculations is the low Reynolds number SST $k - \omega$ of Menter (1994). Because of this, the heights of the first cells at the solid surfaces are adjusted such that $y^+ \approx 1$.

2.2. Cavitation model

The cavitation modelling in FINFLO is based on the mass transfer model of Merkle et al. (1998), *i.e.*

$$\Gamma = \frac{C_{dest} \rho_l \alpha_l \min(0, p - p_{sat})}{1/2 \rho_\infty V_\infty^2 (L_{ref}/V_{ref})} + \frac{C_{prod} \rho_g \alpha_g \max(0, p - p_{sat})}{1/2 \rho_\infty V_\infty^2 (L_{ref}/V_{ref})} \quad (4)$$

where $C_{dest} = 350$ and $C_{prod} = 350$ are the empirical parameters for the cavitation model; ρ_l is the density of the liquid phase and α_l is the volume fraction of the liquid phase; the ρ_∞ and V_∞ are the free stream density and velocity, respectively;

V_{ref} and L_{ref} are the reference velocity and length; p_{sat} is the saturation pressure. The saturation pressure is determined from the Antoine's equation

$$\log(p_{sat}) = A - \frac{B}{T_{sat} + C} \quad (5)$$

where the parameters are A , B and C are obtained empirically, and T_{sat} is the saturation temperature. (Lindstrom and Mallard, 2005; Miettinen et al., 2006)

2.3. Grids and boundary conditions

In the open-water analyses the propeller is operated in pull configuration, *i.e.*, the shaft is located behind the propeller. The blades, hub and shaft are modelled according to the IGES files that are given to the participants. The strut from which the propeller shaft emerges is not modelled for the present simulations, since its influence to the propeller is considered negligible as it is located roughly three-and-a-half diameters downstream of the propeller.

Table 1: Summary of the details of the grid used in the open water calculations for the three grid levels. The number of surface cells are given for one side of the blade.

	Fine grid	Medium grid	Coarse grid
Total number of cells	21 347 840	2 668 480	333 560
Surface cells in chordwise direction	144	72	36
Surface cells in spanwise direction	104	52	26

Three grid densities were used in the open water calculations. The details are summarized in Tab. 1. The grid has an O-O topology around the propeller blades. The finest grid levels consist of roughly 21 million cells in 90 blocks. The grid resolution around the leading edge is fine, and there are about 30 cells around the leading edge radius. Due to the O-O topology, the same resolution is applied around the blade tip and the trailing edge as well. The grid is refined normal to the viscous surfaces such that $y^+ \approx 1$ at the finest grid level. The grid details near the propeller are the same for all three cases. The grids on the suction side of the blades are shown in Fig. 4.

Due to the time-dependent nature of the problem, the whole propeller is modelled in the inclined flow calculations. The inlet is located five diameters upstream of the propeller, and the outlet is located ten diameters downstream of the propeller. The outer sides of the cylindrical domain are located four diameters from the propeller in the radial direction, and their effect is negligible in the calculations.

The blades, hub and shaft are modeled as no-slip rotational surfaces. A velocity boundary condition is applied at the inlet, and a pressure boundary condition is applied at the outlet. The outer side of the domain has a free-stream boundary condition. The whole computational domain is rotation with the given rate of rotation. The inflow velocity is set based on the advance numbers of the propeller.

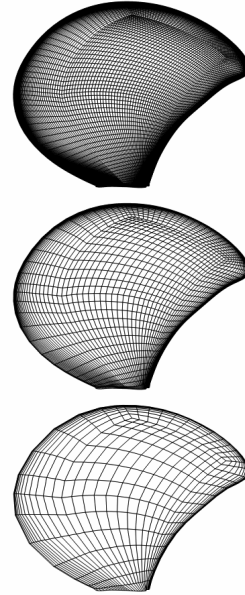


Figure 4: Grid resolution at the three grid levels on the suction side of the blade. From top to bottom: first grid level, second grid level, third grid level. The number of cells is the same on the pressure side of the blade.

The calculations are performed on three grid levels for the Case 1. At the coarser grid levels, every second point is taken into account compared to the finer level grid. A quasi-steady solution is used as an initial guess for the time-accurate calculations on each grid level.

The grid for the Case 2 is constructed based on the grid used for the first case. The geometry of the cavitation tunnel is provided in the IGES files. A sliding mesh technique is utilized to allow for the rotation of the propeller inside the tunnel, and a rotational no-slip boundary condition is used for the rotating solid surfaces. No-slip boundary condition is applied on the tunnel walls.

The computational domain used in the Case 2 is shown in Fig. 3. The grid close to the propeller is the same as that used in the first case, but with the cells similarly clustered in the propeller wake region as was done in the previous Workshop by Sipilä et al. (2011), *i.e.*, in vicinity of the cavitating tip vortex. The total number of cells on the first grid level is roughly 25 million in 103 grid blocks. However, calculations were performed only on the second grid level, which consists

of approximately 4 million cells.

The grid for the Case 3 based on the grid used for the second case. The grid is identical to the Case 2 grid with the exception that the propeller is lifted inside the tunnel such that the gap between the upper wall and the tip of the propeller is 50 mm. Calculations were performed only on the second grid level.

3. Results

3.1. Open water performance

The open water performance of the PPTC propeller is analysed with the advance number range of $J = 0.6, \dots, 1.4$ with the interval of $\Delta J = 0.2$. The advance number is defined as

$$J = \frac{V_A}{nD} \quad (6)$$

where V_A is the speed of advance of the propeller, $n = 15$ 1/s the rate of revolution and $D = 0.25$ m the diameter of the propeller. The thrust of the propeller is non-dimensionalized as

$$K_{T_i} = \frac{T_i}{\rho n^2 D^4} \quad (7)$$

where T_i denotes the thrust, or force, in the i -direction. Similarly, the torque about the X -axis is non-dimensionalized as

$$K_Q = \frac{Q}{\rho n^2 D^5} \quad (8)$$

where Q is the torque of the propeller. The open water efficiency of the propeller is defined as

$$\eta_0 = \frac{J}{2\pi} \frac{K_{T_x}}{K_Q} \quad (9)$$

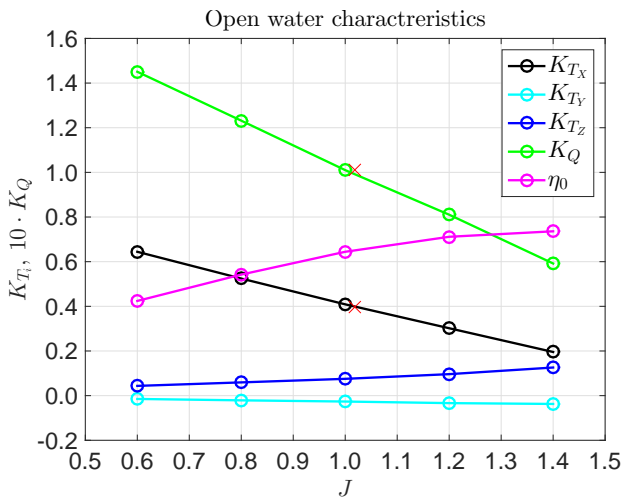


Figure 5: Open water characteristics of the PPTC propeller. The red crosses denote the results from the open water tests for the non-cavitating propeller that were provided prior to the workshop by SVA Potsdam.

The open water tests were performed using three different grid resolutions. The time step used in the simulations corresponds to half degrees of the propeller revolution.

The open water curves are plotted in Fig. 5. All curves show smooth behaviour over the entire investigated advance number range. The parameters K_{T_x} and K_Q , and consequently η_0 , resemble closely the form of the traditional open water curves with axially homogeneous inflow. The side force coefficients are significantly smaller in magnitude, the K_{T_z} being slightly larger than the K_{T_y} . The magnitudes of both seem to increase as the advance number is increased.

The model test results at $J = 1.019$ are shown in Fig. 5 with the red crosses. The computations show good comparison with the experimentally determined K_{T_x} , whilst showing slightly more discrepancy with the experimentally determined K_Q .

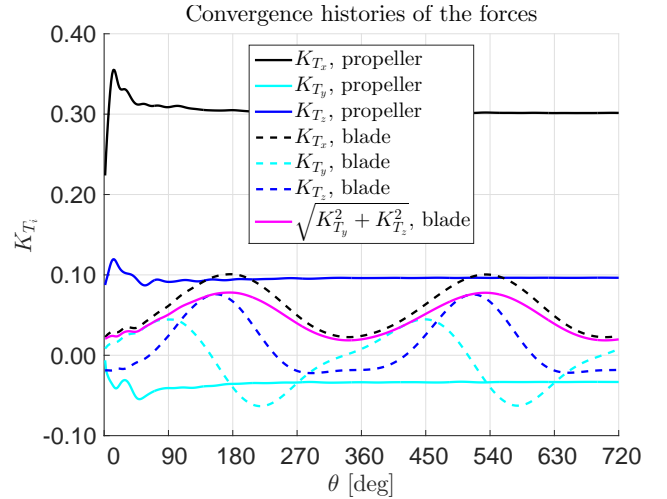


Figure 6: An example of the convergence histories of the thrust coefficients of the whole propeller and a single blade. The advance number is $J = 1.2$.

Table 2: Open water characteristics at $J = 1.2$ calculated on three grid levels

	K_{T_x}	K_{T_y}	K_{T_z}	$10 \cdot K_Q$
Coarse grid	0.295	-0.032	0.096	0.798
Medium grid	0.300	-0.033	0.096	0.807
Fine grid	0.302	-0.034	0.096	0.810

Examples of the convergence histories of the force coefficients are plotted in Fig. 6. The forces acting on the whole propeller seem to reach a steady level at around three-quarter revolutions. The coefficients for the single blade seem, however, to attain a periodic form slightly earlier, at around half a revolution. The simulations were extended to at least two propeller

revolutions to ensure the convergence. Computations made with the other advance numbers show similar behaviour. The K_{Tx} for a single blade exhibits distinct sinusoidal behaviour. The in-plane components do not show similar linear behaviour in this plot, but the resultant in-plane force for a single blade shows the sinusoidal shape, as shown in Fig. 6.

The grid dependency of the calculated open water characteristics at $J = 1.2$ is shown in Tab. 2. The grid density study was not performed using any systematic method, such as Richardson extrapolation. The relative error decreases with the increasing grid resolution. It is seen that the thrust coefficients at the medium and coarse grid levels differ about 1% and 3% when compared to the finest grid level, respectively. The horizontal force coefficient shows the largest differences on the coarse and medium grid levels, when compared to the finest grid level. The medium grid level result differs by 3% and the coarse grid level by 6%, when compared to the results on the finest grid. The calculated vertical force coefficient is the same on all grid levels. The torque coefficient differs by 0.4% and 1.5% on the medium and coarse grid levels, respectively, compared to the results on the finest grid level. This is due to the increased resolution for the boundary layer on the blade.

3.2. Cavitation observations

The cavitation tests have been conducted in the cavitation tunnel on the basis of thrust identity. The model tests have been conducted with a constant rate of revolutions of $n = 20$ 1/s and with three sets of different advance and cavitation numbers. The time step used in the simulations corresponds to half degrees of the propeller rotation.

The cavitation number based on n is defined as

$$\sigma_n = \frac{p - p_{sat}}{\frac{1}{2}\rho(nD)^2} \quad (10)$$

Three cases with different advance and cavitation numbers and simulated. The different cases are listed in Tab. 3. The advance number $J = 1.269$ is the propeller design point. The other tested performance points $J = 1.019$ and $J = 1.408$ are off-design points on both sides of the design point.

Table 3: Advance and cavitation numbers of the simulated cases.

Case	J	σ_n
Case 1	1.019	2.024
Case 2	1.269	1.424
Case 3	1.408	2.000

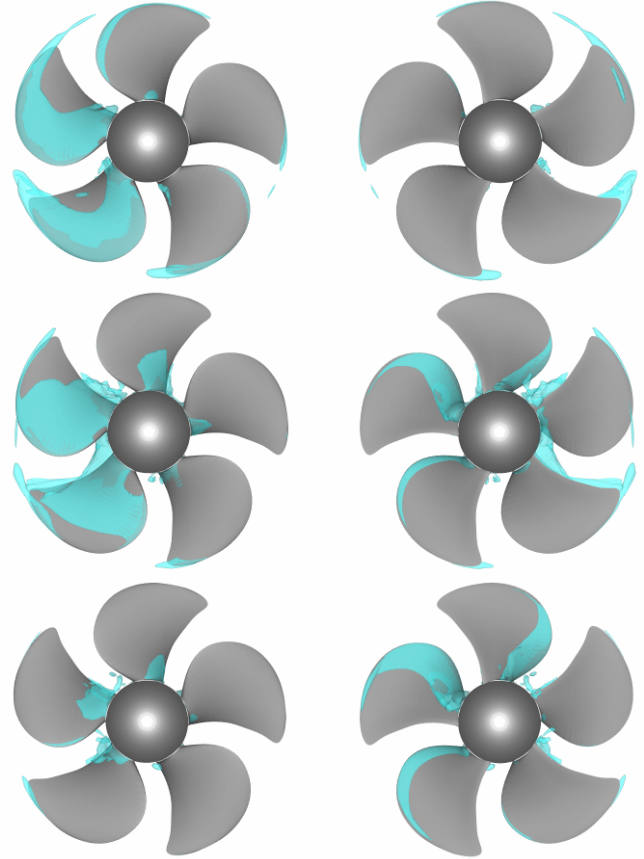


Figure 7: Iso-surfaces of $\alpha = 0.5$. The view toward the suction side of the propeller is on the left column, and the view toward the pressure side of is on the right column. From top to bottom: $J = 1.019$ and $\sigma_n = 2.024$; $J = 1.269$ and $\sigma_n = 1.424$; $J = 1.408$ and $\sigma_n = 2.000$.

Fig. 7 shows the cavitation patterns of the propeller in the three operating points. It is seen that in the regions where the angle of attack is increased, the suction side sheet cavitation dominates at the two highest loading conditions. At the operating point, the suction side sheet cavity passes the trailing edge of the propeller at around $\theta \approx 150^\circ$. The strongest tip cavitation incept as the propeller blades descend from the 12 o'clock position in all loading conditions. The severest tip cavitation occurs at the two highest loading conditions. In the regions where the angle of attack is increased, the cavitation extent on the suction side is the highest in all three operating conditions. Conversely, in regions where the angle of attack is decreased, the suction side cavitation mostly vanishes. The decreasing angle of attack seems, however, to cause pressure side cavitation at $J = 1.269$ and $J = 1.408$. The extent of the pressure side cavitation seems to increase with the increasing advance number. In the highest loading condition, there is no pressure side cavitation.

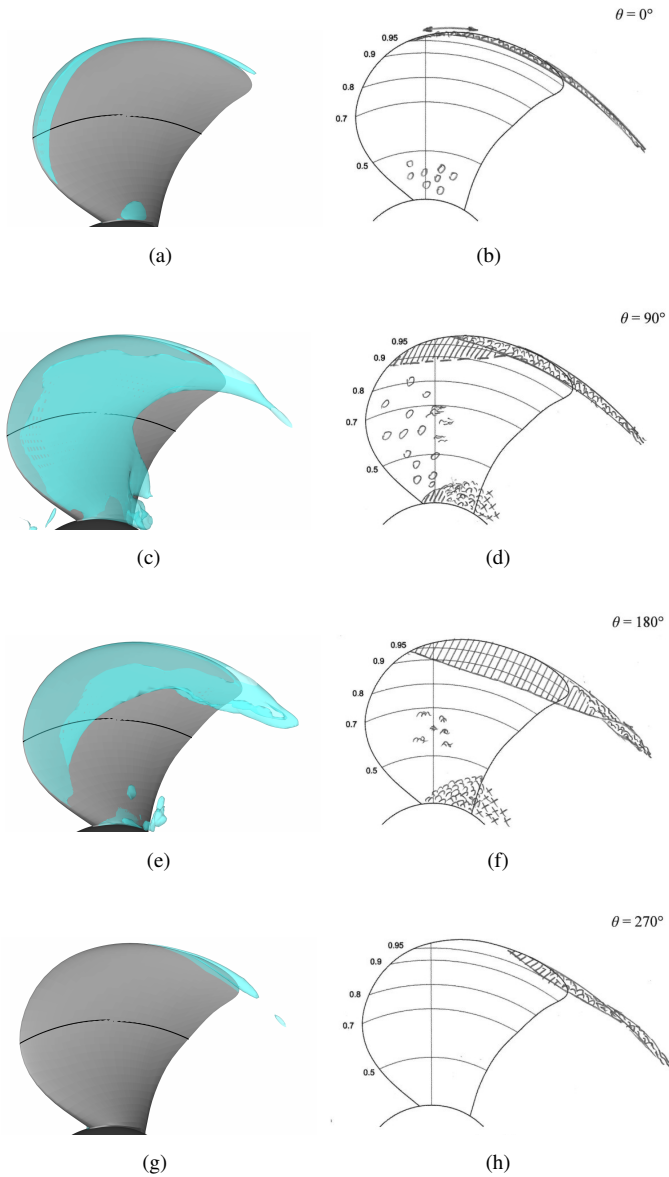


Figure 8: Cavitation patterns with $J = 1.019$ and $\sigma_n = 2.024$. The left column shows the simulated results. The right column shows the cavitation sketches from the model tests. The black circle in the simulated results denotes the radius $r/R = 0.7$. In the simulated results, the iso-surface of $\alpha = 0.5$ is shown.

Fig. 8 shows the comparison of the suction side cavitation patterns of the propeller at $J = 1.019$ and $\sigma_n = 2.024$ between the simulations and the model tests at different blade positions. A strong cavitating tip vortex is present both in the simulations and in the model tests. Root cavitation is also present both in the simulations and in the model tests. The extent of the sheet cavitation is significantly greater in the simulations than in the model tests. At this operating point it is observed, but not shown here, that the extent of the pressure side cavitation is

very small both in the simulations and in the model tests.

Examples of the convergence histories of the force coefficients of the whole propeller and a single blade are plotted in Fig. 9 at $J = 1.019$. The figure shows the third full revolution of the propeller in the cavitating and wetted conditions. In the wetted conditions, thrust coefficients of the propeller and the single blade converged to their final periodic values. It is seen that the thrust coefficients are more unstable in the cavitating conditions. The thrust coefficients also attain slightly lower values in the cavitating conditions than in the wetted conditions.

Table 4: Global performance characteristics at $J = 1.019$.

	Cavitating, $\sigma_n = 2.024$		Wetted	
	K_{T_x}	$10 \cdot K_Q$	K_{T_x}	$10 \cdot K_Q$
Test	0.362	0.959	0.393	1.005
Simulation	0.375	0.961	0.401	0.999
Difference	-3.6%	-0.2%	-2.0%	0.6%

Comparison of the global performance characteristics in cavitating and wetted conditions is done in Tab. 4. Both in the cavitating conditions and in the wetted conditions, the calculated torque coefficients agree very well with the tests. The thrust coefficients show slightly higher discrepancies. However, the differences are at most within four percent.

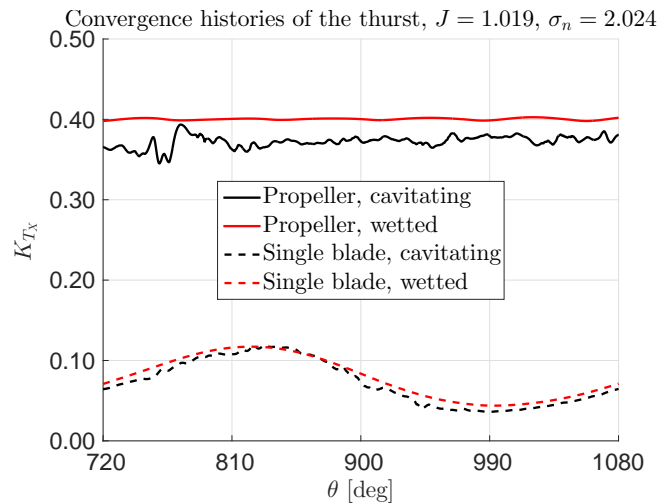


Figure 9: An example of the convergence histories of the thrust coefficients of the whole propeller and a single blade in cavitating and wetted conditions.

3.3. Pressure pulses

The time histories of the pressures are investigated at three points, located on the plate above the propeller in the cavitation tunnel. The three points are located on the center plane

of the propeller. One sensor is located directly above the propeller, and the other two are located 50 mm in front of it and behind it. Only the the wetted conditions were simulated for the workshop.

4. Discussions

The PPTC propeller was analysed by CFD solver FINFLO in inclined configuration in wetted and cavitating conditions. The whole propeller was modelled, and all calculations were performed in time-accurate manner. The mass transfer model in the two-phase simulations was the model of Merkle. All calculations were performed using the low Reynolds number SST $k - \omega$ turbulence model.

A wide model test program has been conducted for the PPTC propeller in oblique flow. The test program included also the cases simulated for the SMP'15 propeller performance workshop. However, only some global performance characteristics and few cavitation sketches from the test results were given to the workshop participants prior to the workshop.

The open water characteristics of the propeller in oblique flow in wetted conditions were analysed by FINFLO over a wide range of advance numbers. The open water characteristics were calculated with the shaft positioned behind the propeller. The simulated results agree well with the model tests at the published operating point. The grid density seems to be fine enough to reach grid independent global performance characteristics. The greatest deviation in the horizontal component might be anticipated since, from the perspective of the propeller, the flow field differs the most at the angular positions which lay solely on the horizontal axis because of the inclined axial inflow.

The cavitation behaviour of the propeller was studied at three different operating conditions: at the design point, and at lightly and highly loaded conditions. Due to the oblique flow, the cavitation pattern of the propeller is not symmetric. Additionally, the cavitation was unstable in the simulations even after several revolutions. It can be seen *e.g.* in Fig. 7 that small parts of either the sheet or root cavity continue to shed in the slipstream of the propeller in all loading conditions.

In the model tests, the inception of the sheet cavitation is delayed on the leading edge due to the laminar flow region, and only bubble cavitation was observed on the suction side. The Merkle model predicts cavitation when the local pressure drops below the vapour pressure. For this reason, the extent of the sheet cavitation is larger in the simulations than in the model tests.

A strong cavitating top vortex is present both in the simulations and in the model tests for the highest loading condition.

Root cavitation is also present both in the simulations and in the model tests. The cavitating tip vortex was mostly captured in the simulations due to the clustering of the grid points near the tip vortex. However, the clustering was done based on the axially straight inflow case; now the tip vortex or its location are not quasi-stead. In order to capture the tip vortices in oblique flow simulations, one would need an adaptive grid that follows the developing vortex based on some suitable criterion, *e.g.* vorticity.

In the future a grid sensitivity study on the behaviour of the cavitating propeller in oblique flow should be carried out. Here, this was not done due to the time limits.

Acknowledgements

The participation in the SMP'15 Propeller performance -workshop was made possible by Finnish Funding Agency for Innovation (TEKES) funded project PropNoise. The financial support is gratefully acknowledged.

References

- P. J. Lindstrom and W. G. Mallard. Eds., NIST Chemistry WebBook. NIST Standard Reference Database Number 69, National Institute of Standards and Technology, Gaithersburg MD. <http://webbook.nist.gov>, 2005.
- F. Menter. Two-equation eddy-viscosity turbulence models for engineering applications. *AIAA Journal*, 32(8):1598 – 1605, 1994.
- C.L. Merkle, J. Feng, and P.O.E. Buelow. Computational modeling of the dynamics of sheet cavitation. In *Proceedings of the third international symposium on cavitation*, pages 307 – 311, Grenoble, France, 1998.
- A. Miettinen, E. Salminen, and T. Siikonen. Kaksifaasivirtaus-simulointimenetelmien kehitystä ja sovelluksia. Technical report F-10. Finflo Oy, 2006. (in Finnish).
- T. Siikonen, J. Hoffren, and S. Laine. A multigrid LU factorisation scheme for the thin-layer Navier-Stokes equations. In *Proceedings of the 17th ICES Congress*, pages 2023 – 2034, Stockholm, Sweden, 1990.
- T. Sipilä, T. Siikonen, and I. Saisto. FINFLO RANS-predictions for propeller performance. In *Second International Symposium on Marine Propulsors (smp'11)*, Hamburg, Germany, 2011.

Prediction of Performance of Cavitating Propeller in Oblique Inflow

Ye Tian¹, Spyros A. Kinnas²

^{1,2} Ocean Engineering Group, Department of Civil, Architectural and Environmental Engineering
 The University of Texas at Austin, Austin, TX 78712, USA

ABSTRACT

The flows around a cavitating propeller subject to oblique inflow are simulated using potential flow methods only, or coupling with a Reynolds-Averaged Navier-Stokes (RANS) solver. Three experimental cases are considered: 1). a propeller in open water; 2). a propeller in a confined tunnel; 3). the propeller induced pressure fluctuation on the tunnel wall corresponding to case 2. The methods adopted in the numerical simulations of the three cases are described, and the corresponding results are reported as well.

INTRODUCTION

Unsteady cavitating propeller performance has drawn more and more attention in the ocean engineering community, in the meantime, brought challenges to potential flow methods, which are commonly used for quick evaluation of a design modification. In order to handle non-axisymmetric inflow, the numerical models using potential flow methods are often simplified. It is important to validate the numerical model so that the simplification can be justified. The experimental measurement in the Second International Workshop on Cavitating Propeller Performance provides valuable data for benchmarking our numerical tools.

The experiments are performed by SVA Potsdam GmbH., with emphasis on cavitating propeller performance subject to an oblique inflow. Three cases are investigated: 1). a propeller (Propeller VP 1304) in open water with inclined shaft; 2). the same propeller in a cavitating tunnel; 3) the propeller induced pressure fluctuation on the tunnel wall corresponding to case 2. Full details of the test cases are provided by 4th International Symposium on Marine Propulsors (SMP' 15).

In the following sections the numerical methods and the corresponding results for each case will be presented.

1 CASE 1

1.1 Experiment Setup

In the first case, the propeller is operating in a pull configuration, with the hub cap pointing upstream. The propeller axis is inclined by 12°. Fig. 1 shows the propeller in the experiment and the propeller coordinate system (PCS) according to which the propeller forces are requested.

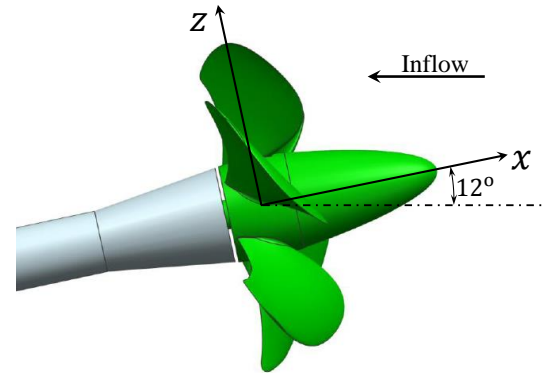


Figure 1: Propeller VP 1304 and the propeller coordinate system, with the y direction pointing inward.

The fully wetted performance of the propeller is measured in a towing tank for different advance ratios.

1.2 Numerical Approach

A boundary element method (BEM) code, PROPCAV is used to predict the open water characteristics of the propeller. In the method, the velocity field is decomposed into two components: the inflow and the perturbation velocity:

$$\mathbf{q} = \mathbf{U}_\infty + \mathbf{u} \quad (1)$$

where \mathbf{q} is the total velocity, \mathbf{U}_∞ is the inflow velocity and \mathbf{u} is the perturbation velocity. Assuming large Reynolds number, neglecting the effects of viscosity, the perturbation velocity is potential:

$$\mathbf{u} = \nabla\phi \quad (2)$$

where ϕ is the perturbation potential, which satisfies the Laplace equation:

$$\nabla^2\phi = 0 \quad (3)$$

Applying the Green's second identity, (3) can be written in the following boundary integral form:

$$2\pi\phi_p = \iint_{S_p} \left[\phi_p \frac{\partial G(p, q)}{\partial n} - \frac{\partial \phi_p}{\partial n} G(p, q) \right] dA + \iint_{S_w} \Delta\phi_w \frac{\partial G(p, q)}{\partial n} dA \quad (4)$$

where S_p represents the surface of propeller blades and S_w denotes the trailing edge wakes. $G(p, q)$ is the Green's function, which is defined as $1/R(p; q)$. R is the distance between the two points p and q . In PROPCAV, (4) is discretized using constant dipole and source panels. More details of the BEM can be found in (Hsin, 1989).

Since the propeller is subject to an oblique inflow, the most appropriate trailing edge wake model should be inclined and aligned with the flow field as well. Unfortunately the full wake alignment scheme proposed by Tian and Kinnas (2012) has not been extended into non-axisymmetric cases yet. A simplified wake model, namely PSF-2 type of alignment (Greeley and Kerwin, 1982) is adopted in our simulations.

1.3 Results

The propeller is simulated using 60×20 (chordwise \times spanwise) panels and 80×30 panels, as shown in Fig. 2.

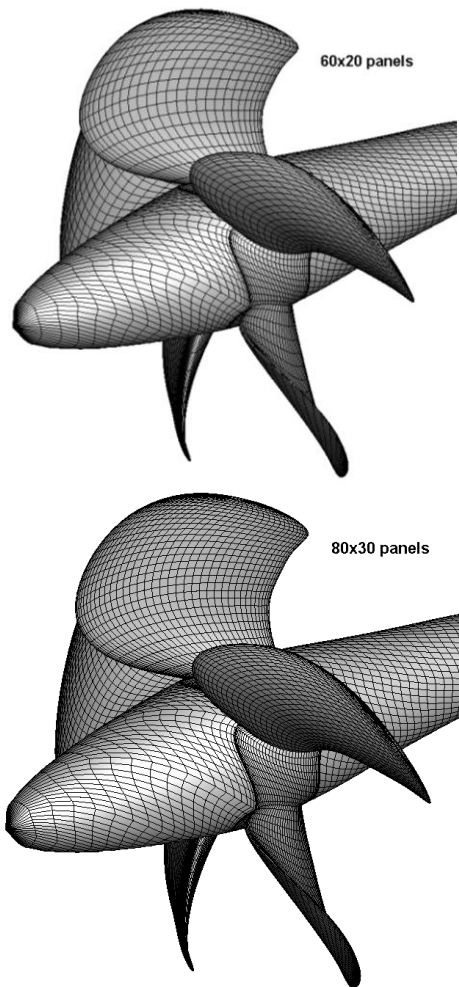


Figure 2: BEM panels for Propeller VP 1304. (Top: 60×20 panels; Bottom: 80×30 panels).

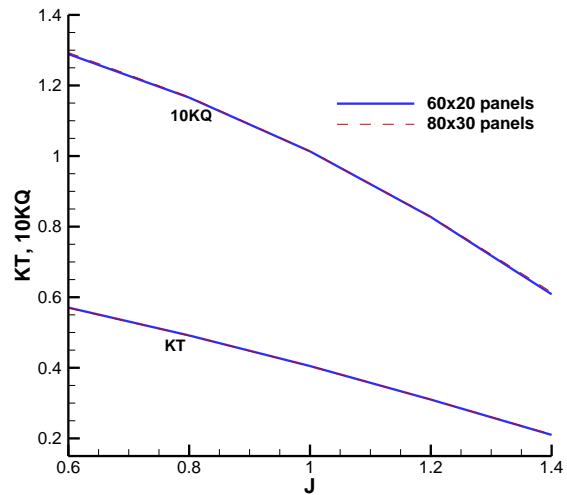


Figure 3: Predicted performance for Propeller VP 1304 in oblique inflow.

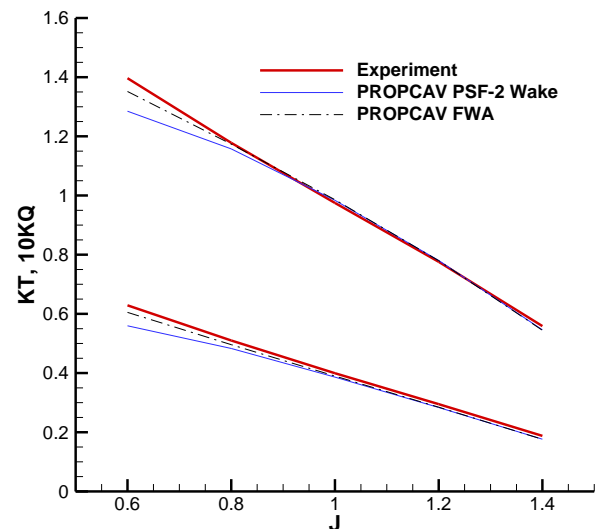


Figure 4: Predicted performance for Propeller VP 1304 in axisymmetric uniform inflow, where FWA stands for the full wake alignment scheme proposed by Tian and Kinnas (2012).

Fig. 3 shows the predicted KT and KQ from different spatial resolutions. Clearly the numerical solutions are convergent.

In order to validate the method, the propeller performance in axisymmetric uniform inflow is also analysed. In this case experimental measurement was performed in the first workshop on cavitating propeller performance (SMP'11). Fig. 4 plots the predicted KT and KQ from different wake models. Clearly the FWA scheme significantly improves the results at low J . However, as mentioned the FWA scheme has not been extended into non-axisymmetric cases yet, thus in this workshop only the results using PSF-2 type alignment are reported. Conceivably at low J the KT and KQ are under-predicted.

2 CASE 2

2.1 Experiment Setup

In this case, the unsteady cavitating performance of the propeller is investigated. The cavitation tests were conducted in the cavitation tunnel K 15 A of the SVA Potsdam. Fig. 5 shows a CAD model of the experimental facility.

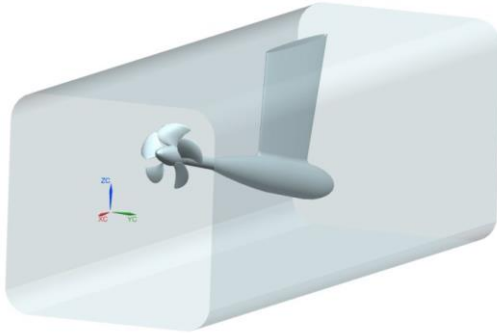


Figure 5: A CAD model of the experimental facility.

In this set of tests, the shaft of the propeller is still inclined by 12° . Propeller performance is measured on three operating conditions: 1). $J = 1.019$, $\sigma_n = 2.014$; 2). $J = 1.269$, $\sigma_n = 1.424$; 3). $J = 1.408$, $\sigma_n = 2.000$. For all the three cases, the rotational speed is kept the same ($n = 20$, where n stands for number of revolutions per second).

2.2 Numerical Approach

In this case, the BEM solver is still adopted to model the propeller. However, since the BEM solver does not have panels on the tunnel wall, an effective wake approach is used to incorporate the effects of the tunnel wall into the inflow. The effective wake approach was proposed by Kerwin et al. (1994) as an intuitive extension of the actuator disk concept to model ducted propellers. The approach was later improved by the Ocean Engineering Group (OEG) at the University of Texas at Austin, by coupling a Vortex-Lattice Method (VLM) solver, MPUF-3A, with a RANS solver. Recently the approach was used to simulate ducted propellers (Tian et al 2014) and thrusters/hull interaction (Tian and Kinnas 2015). The effective approach that couples a potential flow solver with a RANS solver was presented by Tian et al (2014) in detail.

The effective wake \mathbf{U}_{eff} is defined as the difference between the total velocity and the propeller induced velocity:

$$\mathbf{U}_{eff} = \mathbf{q} - \mathbf{u}_{prop} \quad (5)$$

where \mathbf{q} and \mathbf{u}_{prop} denote the total velocity and the propeller induced velocity respectively. Given an effective wake, the corresponding \mathbf{u}_{prop} and the pressure jump across the propeller blades can be evaluated. The pressure jump is then converted to body forces in the RANS solver, which provides a new total velocity field \mathbf{q} . The effective wake will be then updated using (5).

Once the effective wake gets converged, it carries the information of the boundary conditions which are not present in the BEM model. In the current method, the effective wake is determined for fully wetted flow, and used for both wetted and cavitating simulations.

The RANS grid is created using ANSYS ICEM CFD and ANSYS meshing. Fig. 6 shows a vertical slice of the grid cutting through the axis of the shaft. The grid has two zones connected via interface. Near the propeller and the shaft, dense structured cells are generated by revolving a 2D grid along the axis of the shaft, whereas away from the propeller and the shaft, unstructured Cartesian cells fill the rest of the computational domain. Totally 1.3 million cells constitute the grid. In order to simplify the grid generation process, the strut is not included. In the RANS simulation, standard $k - \epsilon$ turbulence model is adopted, along with QUICK scheme for spatial discretization.

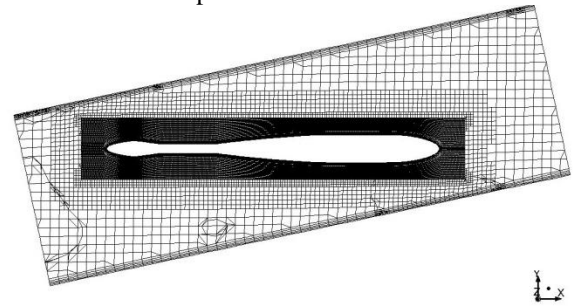


Figure 6: The RANS grid for the effective calculation in Case 2.

2.3 Results

Fig. 7 shows the total velocity field for case 2.1. Clearly the accelerated wake jet due to the presence of the propeller follows the direction of the tunnel wall. The total velocity fields for case 2.2 and 2.3 are similar to Fig. 7, thus will not be shown.

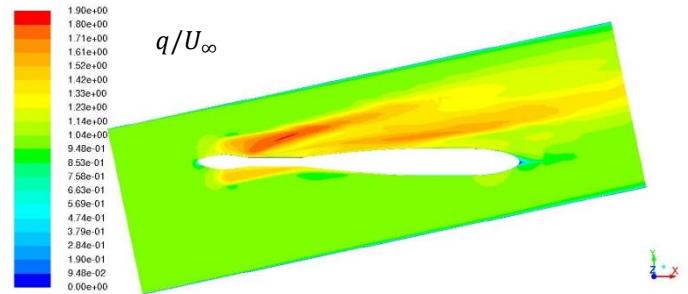


Figure 7: Total velocity field predicted by RANS/VLM coupling.

Fig. 8 shows the predicted effective wake in the propeller zone. In order to better visualize the effective wake, the inflow velocity on the mid-chord surface of the propeller is shown in Fig. 9. Clearly the velocity close to the upper tunnel wall is faster than the lower side, because the tunnel wall confines the flow passage. Fig. 10 and 11 plot the effective wake on the mid-chord surface for Case 2.2 and Case 2.3. It can be observed that as the propeller

loading reduces, the effective wake is more uniform, meaning less propeller and wall interaction.

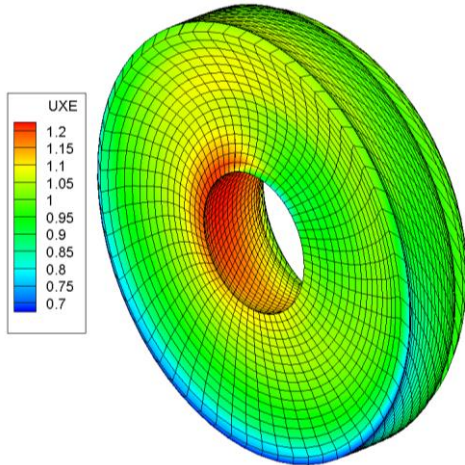


Figure 8: Predicted axial effective wake for Case 2.1, normalized by U_∞ .

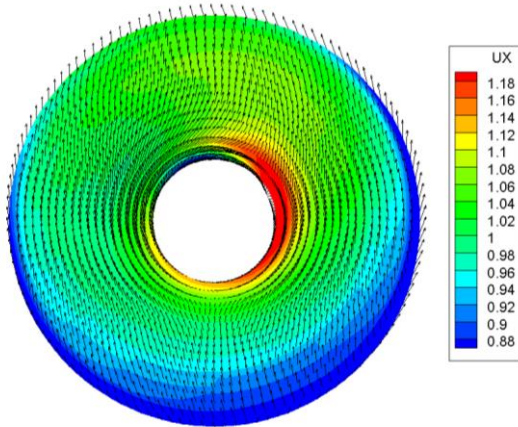


Figure 9: Predicted effective wake on the blade mid-chord surface for Case 2.1, normalized by U_∞ .

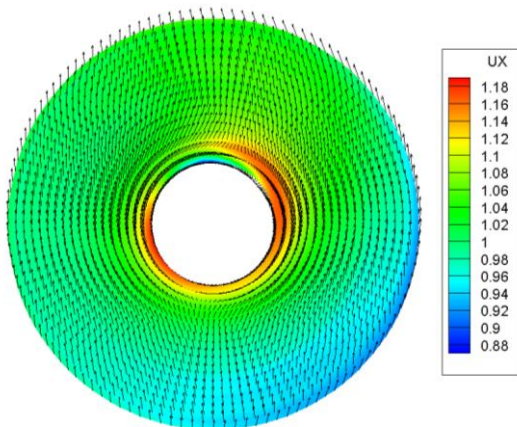


Figure 10: Predicted effective wake on the blade mid-chord surface for Case 2.2 normalized by U_∞ .

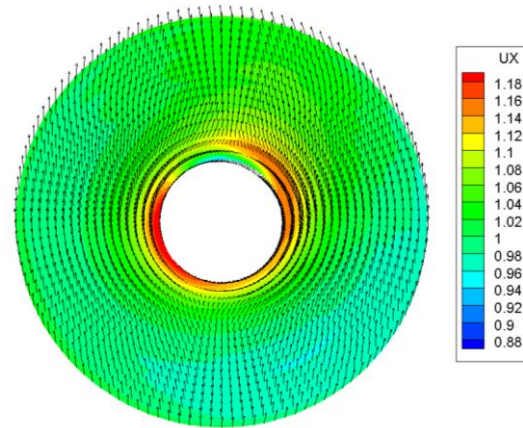


Figure 11: Predicted effective wake on the blade mid-chord surface for Case 2.3 normalized by U_∞ .

The predicted effective wakes are then used in PROPCAV to simulate the wetted and cavitating performance of the propeller on the operating conditions of Case 2.

For Case 2.1 and Case 2.2, PROPCAV can predict reasonable cavity patterns. Unfortunately the code crashes in Case 2.3. Thus the cavitating results for Case 2.3 are not shown in this paper.

Table 1 lists the wetted and cavitating KT and KQ for difference cases. For Case 2.1 a convergence study is performed and the results are also included in Table 1.

Table 1: Predicted KT/10KQ for Case 2, where (w) stands for wetted results and (c) stands for cavitating results.

	Case 2.1	Case 2.2	Case 2.3
60x20 (w)	0.395/0.992	0.262/0.714	0.186/0.539
60x20 (C)	0.367/0.964	0.167/0.534	--
80x30 (w)	0.398/0.100	--	--
80x30 (C)	0.368/0.969	--	--

Fig. 12 and 13 show the predicted cavity pattern for Case 2.1 and Case 2.2. For Case 2.1, only back side cavity is predicted. For Case 2.2, both back side and face side cavities are predicted. It is worth noting that for Case 2.2, a spurious thick cavity is shown near the hub. This unrealistic thick cavity definitely requires further investigation. In the meantime, since pressure under the cavity will be the vapour pressure of water no matter how thick the cavity is, the predicted KT and KQ should not be affected too much.

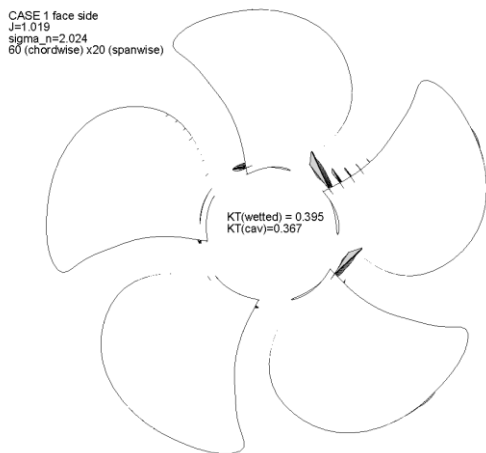
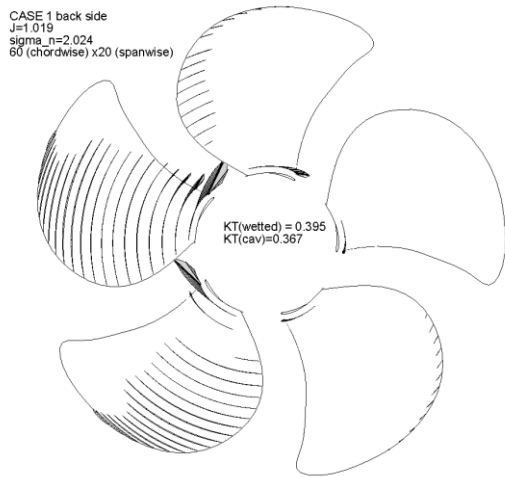


Figure 12: Predicted cavity pattern for Case 2.1 (Top: back side; bottom: face side).

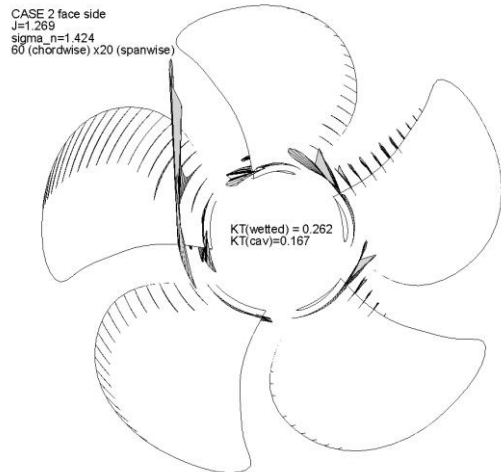
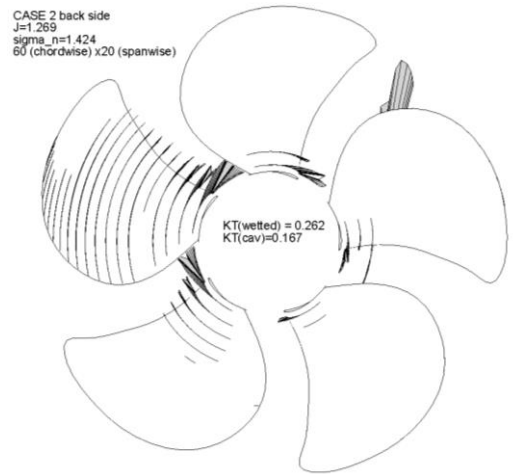


Figure 13: Predicted cavity pattern for Case 2.2 (Top: back side; bottom: face side).

3 CASE 3

3.1 Experiment Setup

In Case 3, the pressure fluctuation at three points on the top tunnel wall is measured for the three cases in Case 2. The arrangement of the three pressure sensors are shown in Fig. 14.

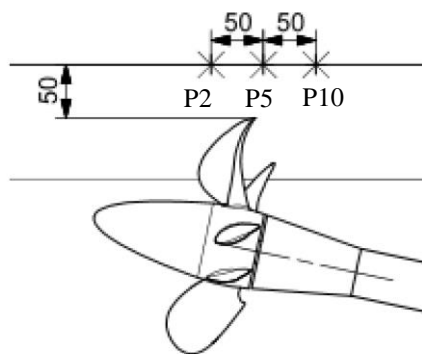


Figure 14: Arrangement of pressure sensors (unit: mm).

3.2 Numerical Approach

A BEM code, HULLFPP is developed at OEG at UT Austin, to predict the propeller induced pressure fluctuation on a hull. HULLFPP uses blade singularities from a pre-calculated propeller flow solution to find the propeller induced potential on the hull. The diffraction problem on the hull is then solved using BEM in frequency domain. The time derivative of the hull potential leads to the pressure fluctuation.

In order to approximate the top wall of the tunnel, a special hull is designed, as shown in Fig. 15. The side and bottom walls of the tunnel are neglected.

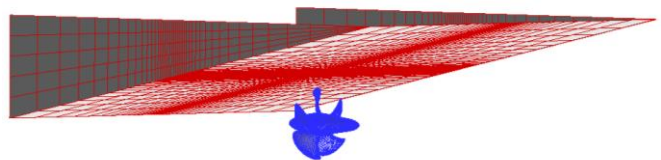


Figure 15: A wedge type hull resembles the top tunnel wall.

3.3 Results

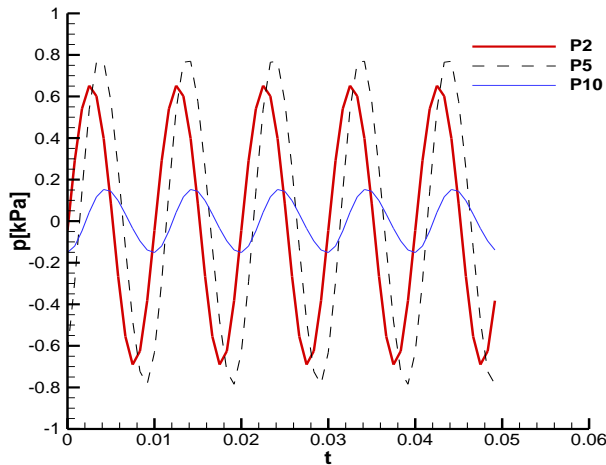


Figure 16: Pressure history at the three interrogating points for Case 3.1, fully wetted.

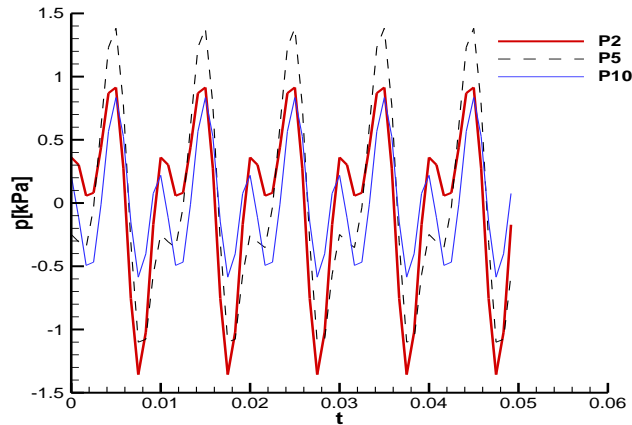


Figure 17: Pressure history at the three interrogating points for Case 3.1, cavitating.

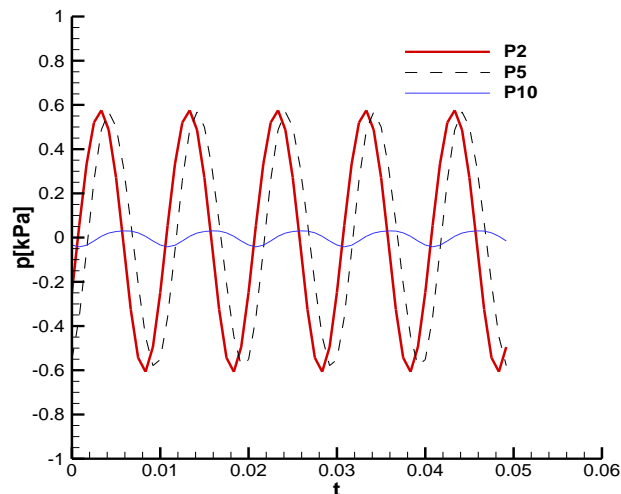


Figure 18: Pressure history at the three interrogating points for Case 3.2, wetted.

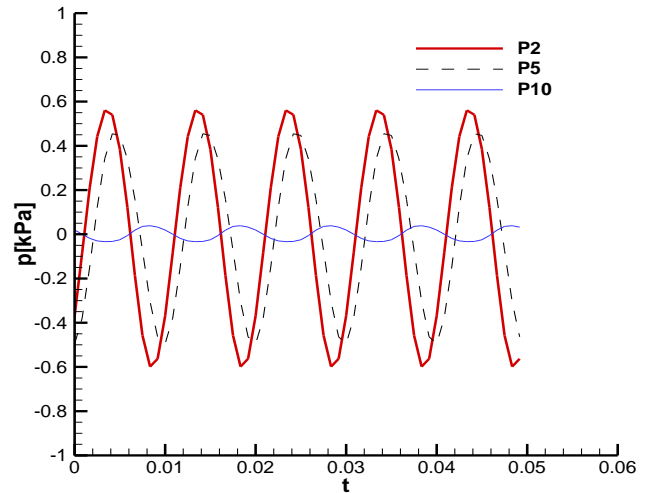


Figure 20: Pressure history at the three interrogating points for Case 3.3, wetted.

Fig. 16-20 show the predicted pressure fluctuation for different cases. The cavitating result for Case 3.2 is not shown because the very thick cavity shown in Fig. 13 induces nonsensical large pressure. Clearly the cavitating result is more affected by the high order harmonics than the fully wetted case.

CONCLUSIONS AND FUTURE WORK

The three test cases in the second international workshop on cavitating propeller performance were simulated. The numerical results were reported. The authors hope to take this chance to validate the methods that developed by the OEG at UT Austin.

While preparing the results presented in this paper, numerical difficulties on dealing with face cavitation were revealed. More investigation on the face cavity modeling will be carried out in the future.

ACKNOWLEDGMENTS

Support for this research was provided by the U.S. Office of Naval Research (Contract No. N00014-07-1-0616, Contract N00014-10-1-0931 and N00014-14-1-0303) and Phases V, VI and VII of the “Consortium on Cavitation Performance of High Speed Propulsors” with the following members: American Bureau of Shipping, Daewoo Shipbuilding and Marine Engineering Co. Ltd., Kawasaki Heavy Industry Ltd., Rolls-Royce Marine AB, Rolls-Royce Marine AS, Samsung Heavy Industries Co. Ltd., SSPA AB, Andritz Hydro GmbH, Wärtsilä Netherlands B.V., Wärtsilä Norway AS, Wärtsilä Lips Defense S.A.S., and Wärtsilä CME Zhenjiang Propeller Co. Ltd., Steerprop Ltd.

REFERENCES

- Kerwin, J. E., Keenan, D., Black, S. and Diggs, J. "A Coupled Viscous/potential Flow Design Method for Wake-adapted, Multi-stage, Ducted Propulsors using Generalized Geometry. Discussion. Authors' Closure". Trans. SNAME, 102, pp 23-56, 1994
- SMP'11: The Second International Symposium on Marine Propulsors: http://www.sva-potsdam.de/pptc_data.html#workshop
- SMP'15: The Fourth International Symposium on Marine Propulsors: http://www.cae.utexas.edu/smp15/smp_workshop_2015.html
- Greeley, D. S. and Kerwin, J. E. "Numerical methods for propeller design and analysis in steady flow". Transactions of Society of Naval Architects&Marine Engineers, 90:415-453., 1982.
- Hsin, C. "Development and Analysis of Panel Methods for Propellers in Unsteady Flow. PhD dissertation, M.I.T., Department of Ocean Engineering, 1989.
- Tian, Y. and Kinnas, S.A., "A Wake Model for the Prediction of Propeller Performance at Low Advance Ratios", International Journal of Rotating Machinery, Vol. 2012.
- Tian, Y., Jeon, C.-H., and Kinnas, S.A., "On the Accurate Calculation of Effective Wake/Application to Ducted Propellers", Journal of Ship Research, Vol. 58, No. 2, 2014.
- Tian, Y. and Kinnas, S.A., "Thruster and Hull Interaction", J. Offshore Mech. Arct. Eng. 137(4), 041801, Aug 01, 2015.



**4th International
Symposium on Marine Propulsors**
June 1-3 2015
Austin, Texas, USA

MARINTEK



Offshore Technology Research Center



THE UNIVERSITY OF TEXAS AT AUSTIN

**Civil, Architectural and
Environmental Engineering**